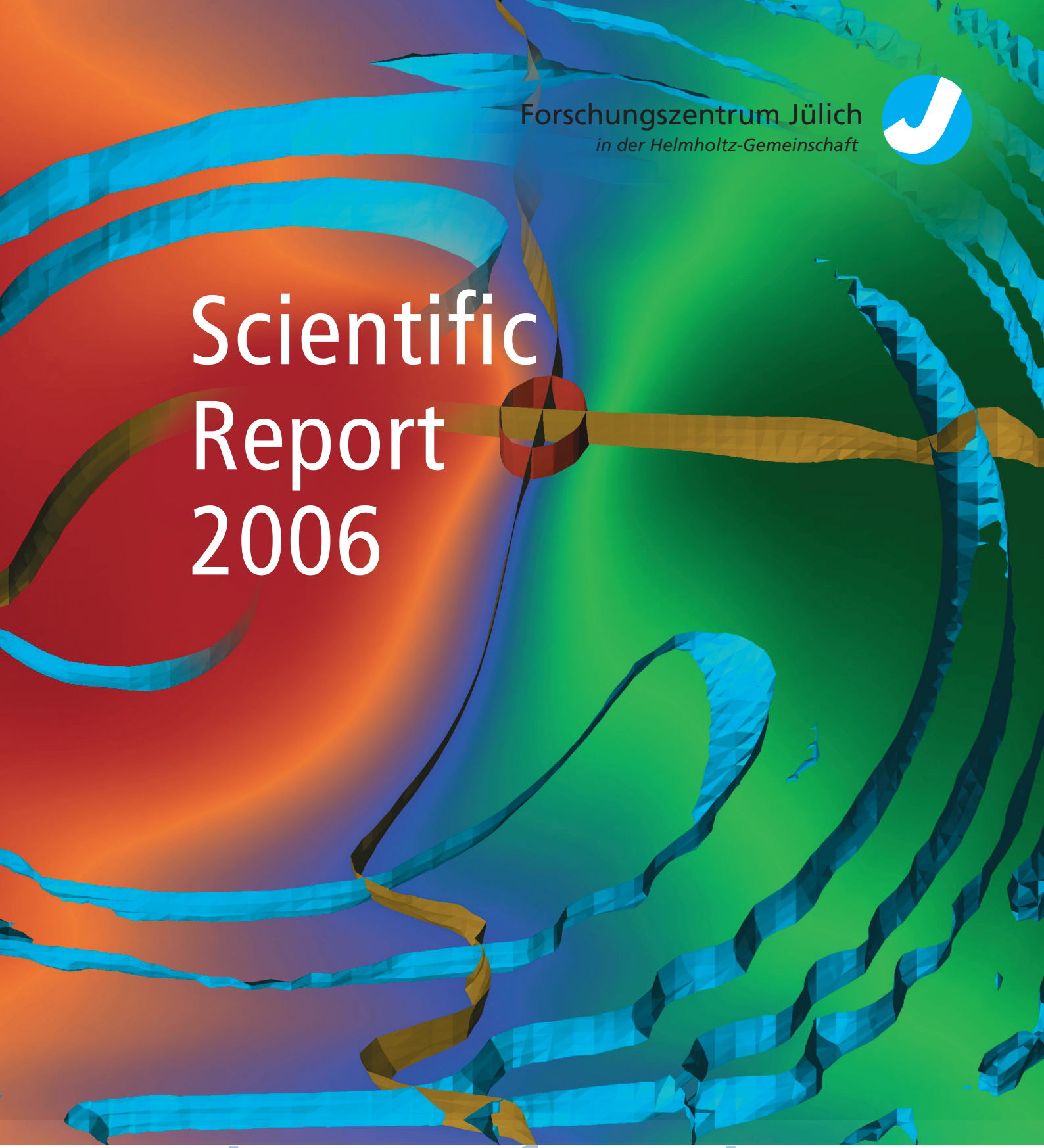

Forschungszentrum Jülich
in der Helmholtz-Gemeinschaft

Scientific Report 2006

Festkörperforschung

Institut für Festkörperforschung

Institute of Solid State Research

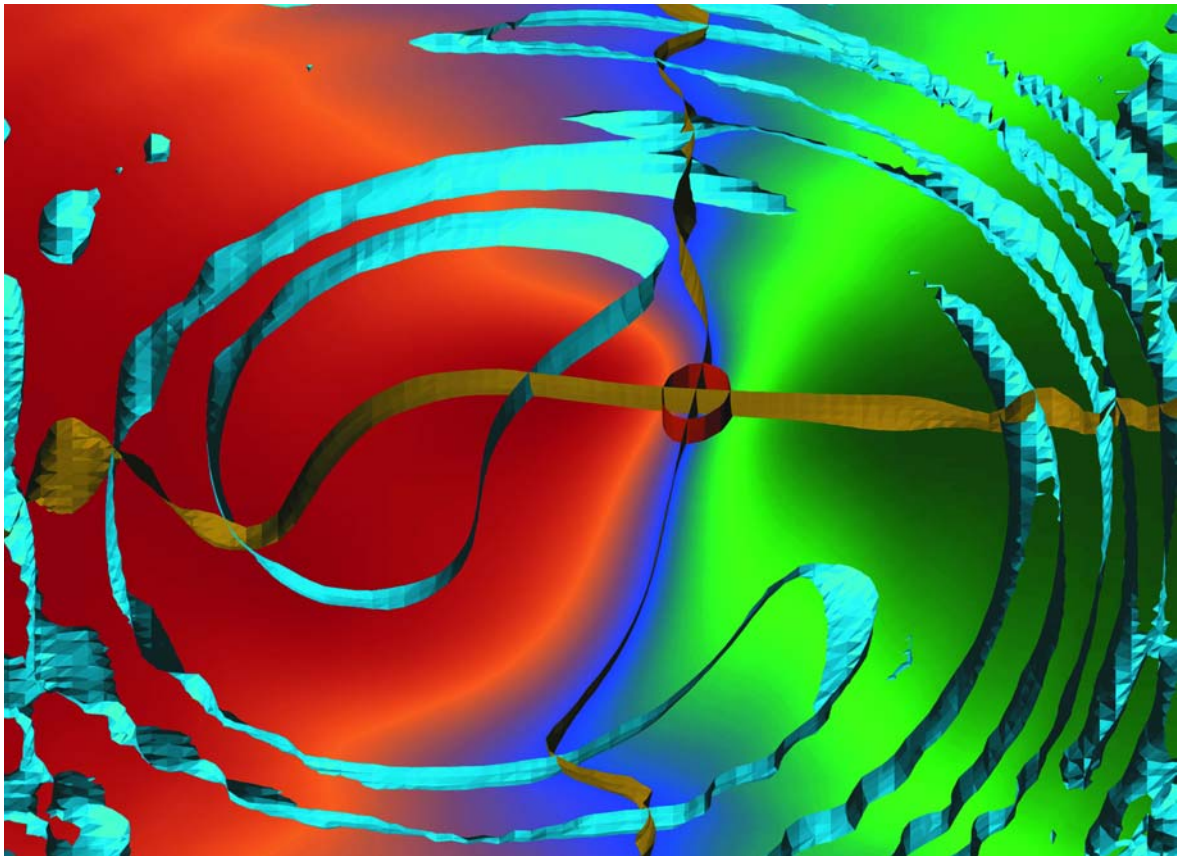

Exchange explosion: Sudden spin-wave emission after vortex-antivortex annihilation in a ferromagnetic platelet.
See page 60 for more information.

Contents

Directors of the Institute of Solid State Research (IFF) from left:

Prof. Dr. Jan K. G. Dhont (IFF-7: Soft Condensed Matter)
Prof. Dr. Knut Urban (IFF-8: Microstructure Research
Prof. Dr. Heiner Müller-Krumbhaar (IFF-3: Theory III)
Prof. Dr. Dieter Richter (IFF-5: Neutron Scattering)
Prof. Dr. Thomas Brückel (IFF-4: Scattering Methods)
Prof. Dr. Stefan Blügel (IFF-1: Theory I)
Prof. Dr. Rainer Waser (IFF-6: Electronic Materials)
Prof. Dr. Claus M. Schneider (IFF-9: Electronic Properties)
Prof. Dr. Gerhard Gompper (IFF-2: Theory II)

Editorial

2006 – This year marks an important step in the history and development of the "Institut für Festkörperforschung" (IFF). Looking back to a success story of more than 35 years, the IFF has implemented extensive and farreaching measures to prepare the Institute for the future challenges and to ensure its international competitiveness and leadership.

This annual report is intended to inform the international scientific community, including our scientific advisory board and the steering bodies of the Helmholtz Association of German Research Centres (HGF) about the scientific activities at the IFF during the past year. We have attempted to present a typical cross section through the research done at the IFF, including scientific highlights as well as results of long-term developments, for example, the construction of new instruments at large scale facilities. These contributions also reflect the participation of the IFF in the Helmholtz-Research Programmes "Condensed Matter Physics", "Information Technology with Nanoelectronic Systems", and "Large-Scale Facilities for Research with Photon, Neutron, and Ions".

Since 2003, the IFF is again in full operation with its nine institutes in the areas of hard and soft matter working on both experimental and theoretical aspects. Introducing the programme-oriented funding scheme in 2004, the IFF has taken the opportunity to further sharpen its scientific profile, at the same time including new topics of forefront research. One of these topics concerns magnetism in molecular structures and received a big push in 2006 by the establishing of a research group on synthetic chemistry headed by Prof. Dr. Paul Kögerler jointly with the RWTH Aachen. In the area of electronic phenomena and magnetism, the IFF was particularly successful in establishing young research groups, for example, on electronic correlations (Dr. Eva Pavarini) and micromagnetic simulations (Dr. Riccardo Hertel).

The neutron science, being a cornerstone of the IFF research on hard and soft matter since its very beginnings, witnessed the inauguration of the Jülich Center for Neutron Science (JCNS) opening up many new opportunities for state-of-the-art neutron-based research at world class external neutron sources: at the FRM II in Munich, at the Institute Laue-Langevin in Grenoble (France) and at the Spallation Neutron Source SNS in Oak Ridge (USA).

With this step made, Jülichs former home-base for research with neutrons, the reactor FRJ-2, could be permanently shut down on May 2nd. In its 44 years of operation, the FRJ-2 provided neutrons for excellent science, technical innovation and unique method development. The best instruments of FRJ-2 are currently being upgraded and transferred to the new research reactor FRM II, where they will be operated by a JCNS outstation.

The research on and with high-resolution electron microscopy, having a long tradition in the IFF, moved to a new quality. By founding the Ernst Ruska-Centre (ER-C) for Microscopy and Spectroscopy with Electrons, the IFF and the RWTH Aachen joined forces in advancing the frontiers of ultrahigh resolution electron microscopy and making this technique available within a user facility. Finally, after more than 30 years of successful operation, the IFF decided to put the Compact Cyclotron at rest, making room for new activities. It will find a new home and new users in Kharkov in the Ukraine. In the area of information technology, the IFF established the Nanoarchitecture Laboratory (jointly with the RWTH Aachen), addressing the alternative architectural concepts for future nanoelectronics devices.

The quality of the research at the IFF is accepted and honored by the scientific community. For his achievements in the advancement of high-resolution electron microscopy, Prof. Dr. Knut Urban received the Karl Heinz Beckurts Award 2006 and the von Hippel Award of the American Materials Research Society (MRS). With the discovery and his work on giant magnetoresistance (GMR) Prof. Dr. Peter Grünberg won the prize "European Inventor of the Year", an award bestowed by the European Patent Office and European Community. Being awarded the prestigious Helmholtz-Humboldt Research Prize, Prof. Dr. Charles S. Fadley from the Advanced Light Source at Berkeley (USA) has chosen the IFF as his base and partner for joint experiments on surface science and electron spectroscopy.

Our research is mainly driven by scientific curiosity, while still keeping an eye on potential applications. What scientists enjoy most is going where nobody has gone before and making new discoveries. I hope you will enjoy reading the report and learning about our activities in a similar spirit.

Prof. Dr. Claus M. Schneider
Managing Director of IFF 2007
Director of IFF-9 "Electronic Properties"
May 2007

Snapshots 2006

16 February:
Milestone in the history of the Jülich neutron research
The Jülich Centre for Neutron Science is founded. This centre – known as JCNS for short – focuses activities in Jülich and at external neutron sources, and establishes a branch laboratory at the new research reactor in Garching. Scientists from all over the world come to Jülich for the inauguration of the JCNS.

Thomas Rachel, Parliamentary State Secretary in the Federal Ministry of Education and Research (BMBF), describes the cooperation between Research Centre Jülich and Munich University of Technology as ground-breaking. "Science in Germany will profit from the close cooperation between university and non-university research." BMBF will provide the new centre with funds of about € 6 million annually, plus about € 18 million for investment in physical resources during the development phase.

260 participants from 19 countries come to the "JCNS Symposium and European User Meeting".

10 March:
50 years of innovation
This is the motto that Research Centre Jülich uses to attract participants to its very first Innovation Forum, which takes place as part of CeBIT 2006 in Hannover. The key issue: how will the knowledge society of tomorrow process information? Scientists from IFF present their current research along with their visions for the future in the field of nanoelectronics.

The participants of the Innovation Forum "Information". From left to right: Prof. Claus M. Schneider, Director at IFF Institute of Electronic Properties, Dr. Meyya Meyyappan, Director at NASA Ames Research Centre, Prof. Rainer Waser, Director of IFF Institute of Electronic Materials, Dr. Chris Van Hoof from IMEC, Prof. Andreas Offenhäuser, Director at the Jülich Institute of Thin Films and Interfaces (Bioelectronics), Niels Boeing, chairman of Innovation Forum Jülich, Prof. Markus Morgenstern from RWTH Aachen University, Prof. Kristof Szot from IFF.

Representatives from politics, science and industry debate the future prospects of nanoelectronics during the podium discussion. From left to right: Dr. Manfred Dietrich, BMBF, Prof. Rainer Waser, IFF, Niels Boeing, chairman, Dr. Chris Van Hoof, IMEC, Prof. Joachim Burghartz, IMS Chips, Dr. Christoph Kutter, Infineon Technologies.

2 May:
An era draws to a close
In the presence of numerous members of staff, guests and representatives of the regulatory authority, reactor operator Detlev Gottwald pushes the red button and permanently shuts down the FRJ-2 research reactor, also known as "DIDO". After almost 44 years or 15,875 days of operation, the neutron source that had long been the most powerful in Germany was thus extinguished. It had provided generations of physicists, chemists, biologists and geoscientists with a neutron beam, which they used to gain valuable knowledge on structures, physical characteristics, chemical compounds and living matter. Scientists at Jülich will soon be able to use Germany's most modern neutron source, the new Munich FRM II, for their research (see also "16 February").

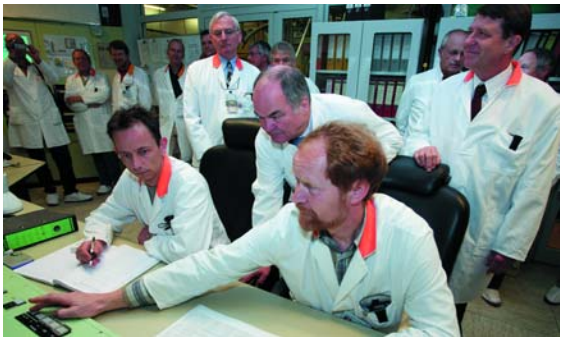

Detlev Gottwald shuts down the FRJ-2 research reactor; Prof. Joachim Treusch, Chairman of the Board of Directors at Research Centre Jülich until end September 2006, watches with interest.

After the decommissioning, the reactor team gathers in front of the monitoring area for a group photograph.

3 May:
"European Inventor of the Year"
The European Patent Office and the European Commission award this prize, which is bestowed for the first time, to Professor Peter A. Grünberg, IFF. A committee of representatives from industry, research and politics chose the winners from a selection of patent applications submitted between 1991 and 2000 that were successfully put into practice. Grünberg wins the prize in the "University and Research Institutions" category for his discovery of giant magnetoresistance (GMR) in 1988. The GMR effect led to the breakthrough in gigabyte hard discs and is used in more than 90 % of the hard discs produced today, as well as in MP3 players and ABS systems in cars. The GMR effect also opened the door into a completely new field of research: spin(elec)tronics. Exploiting spin, which along with charge is a vital property of electrons, could revolutionise the whole field of microelectronics.

Almost 400 visitors gathered at the Autoworld Museum in Brussels to see European Patent Office President Alain Pompidou and European Commission Vice President Günter Verheugen (from left) honour the European Inventors of the Year 2006 (right: Prof. Peter A. Grünberg).

Photo: European Patent Office

18 May:
Atoms in sight
The first national user centre for electron microscopy and spectroscopy is officially opened. With the opening of the Ernst Ruska-Centre, a globally unique access to the world of atoms is made possible. The Centre's main instruments, both of which are TITANs, are based on innovations in electron optics in which IFF played a decisive role: a cooperation between Darmstadt University of Technology, the EMBL research laboratory in Heidelberg and Research Centre Jülich led to the development of an instrument that generates microscopic images of almost inconceivable resolution. Today, the technology at the Ernst Ruska-Centre can be used by all interested researchers.

At the end of the event, which was attended by Ernst Ruska's widow and his sons, a bust of the researcher and engineer, who died in 1988, is unveiled. From left: Klaus Ruska, Burkhard Rauhut, Rector of RWTH Aachen University , Irmela Ruska, Jürgen Ruska, Prof. Joachim Treusch, Chairman of the Board of Directors at Research Centre Jülich until end September 2006, Prof. Knut Urban, Director at IFF Institute of Microstructural Research, Prof. Joachim Mayer, RWTH Aachen University.

In their welcome address, Professor Burkhard Rauhut, Rector of RWTH Aachen University, and Professor Joachim Treusch, Chairman of the Board of Directors of Research Centre Jülich until end September 2006, underline the trendsetting nature of the Ernst Ruska-Centre as an institution built on an equal partnership that will attract attention throughout Germany. Dr. Reinhard Grunwald, Secretary-General of the German Research Foundation, which financed one of the two TITAN instruments, refers to the Ernst Ruska-Centre as a shining example of cooperation between university and non-university research in Germany, from which both parties can profit.

14 July:
Compact cyclotron on the hook
An era in IFF comes to a close. A crane lifts the compact cyclotron CV 28 out of the basement of the cyclotron building and places it in a ready-and-waiting container. Its new destination is Kharkov in the Ukraine, where it will be rebuilt and put back into operation. The compact cyclotron was used between 1975 and the end of 2005 in the fields of materials science and basic research, as well as for the production of radioisotopes for nuclear medicine. The magnet in the cyclotron has a total weight of 25 tonnes.

Not something you see everyday! A compact cyclotron weighing several tonnes being lifted by a crane.

2 October:
Winner of Helmholtz-Humboldt Research Prize
Professor Charles S. Fadley from the University of California Davis and the Lawrence Berkeley Advanced Light Source starts work as a visiting scientist at IFF. He is conducting photoemission experiments on the characterization of magnetic systems. Such systems are used, for example, as magnetic data storage systems and as spintronics devices in information technology. During his visit to Germany, Fadley plans to perform investigations on instruments operated by the Jülich Competence Centre for Synchrotron Science at the synchrotron radiation sources BESSY in Berlin, DELTA in Dortmund and also DESY in Hamburg, using x-ray standing waves to study magnetic nanostructures among other things.

Fadley was one of ten scientists so far to be awarded the Helmholtz-Humboldt Research Prize in 2006 for his scientific achievements in the field of surface physics and electron spectroscopy.

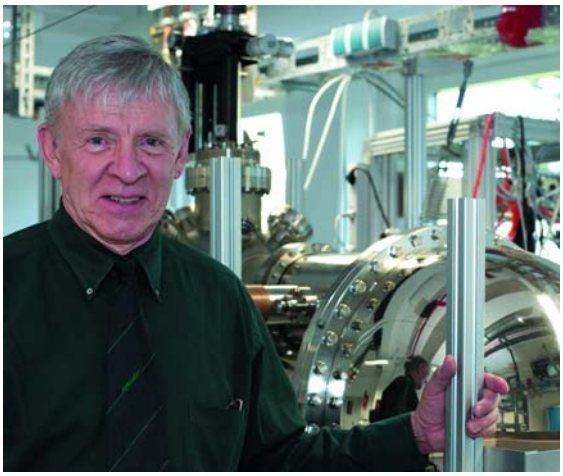

Prof. Charles S. Fadley

29 November:
Modern electron microscopy and quasi crystals
Prof. Knut Urban, Director at the IFF Institute of Microstructure Research, receives the Von Hippel Award of the American Materials Research Society. This is the highest honour awarded by the largest materials science society in the world. Urban is the first German to receive this award, which recognises his contribution to modern electron microscopy and the physics of defects in solids, namely in quasi crystals.

8 December:
Award for innovative scientists
Prof. Knut Urban, Dr. Maximilian Haider of CEOS GmbH, Heidelberg, and Prof. Harald Rose, formerly of the Technical University of Darmstadt, receive one of the two Karl Heinz Beckurts Awards 2006 for their decisive contribution to the sophistication of electron microscopes. The research team developed a new type of lens for electron microscopes. The lens behaves like an achromat in optical microscopes, which makes it possible to show materials and substances in atomic resolution.

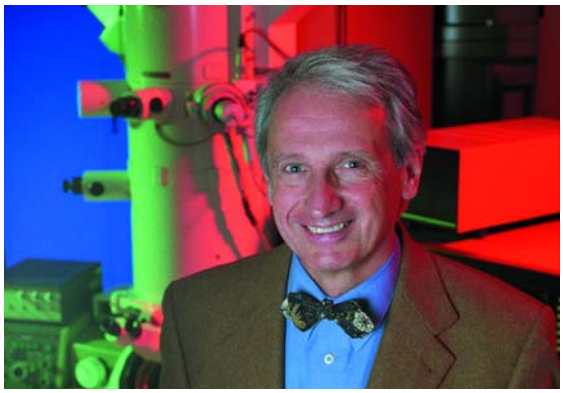

Prof. Knut Urban

Institute of Solid State Research (IFF)

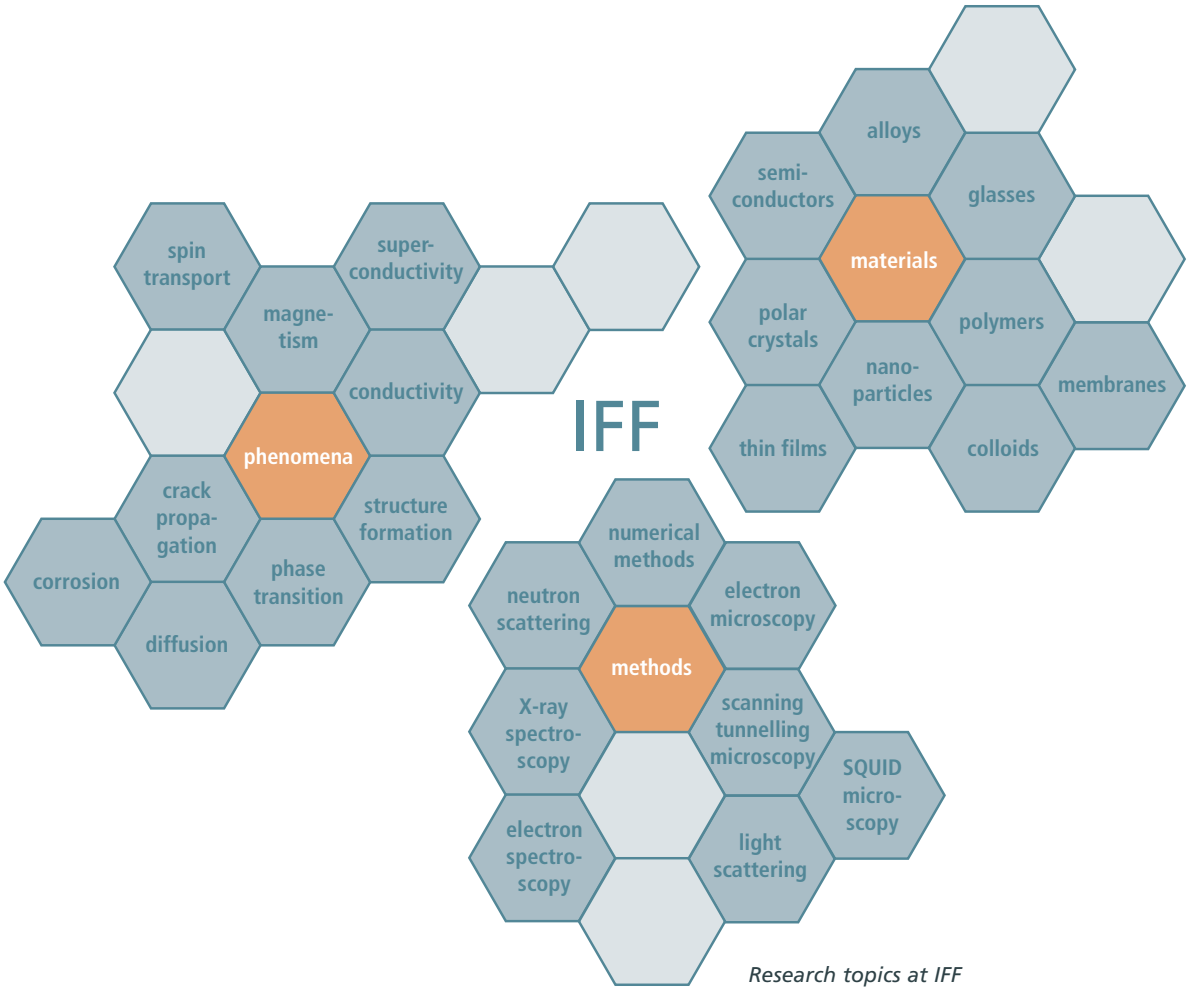

Research topics at IFF

Founded in 1969, the scientific reputation of the Institute of Solid State Research (Institut für Festkörperforschung – IFF) still owes much to the conception of its founders that new discoveries are made at the boundaries of disciplines. This is as true today as it was almost forty years ago. In this spirit, the IFF has pioneered new research fields such as spintronics and set trends towards multi- and cross-disciplinary activities in both fundamental research as well as technological innovations.

Today, the IFF is engaged in investigating a multitude of condensed matter phenomena with special emphasis on three prime objectives:

- studies of fundamental physical mechanisms and phenomena of condensed matter,
- the development and improvement of experimental and theoretical analysis methods, as well as
- the elucidation and utilization of new material properties in complex systems.

The corresponding research programmes follow the main theme to exploit the full scale of analytical and numerical methods to elucidate interrelations between structural, electronic, and magnetic properties of the solid state together with describing underlying physical mechanisms.

Research efforts are directed at obtaining a microscopic and atomistic understanding of phenomena based on fundamental interaction mechanisms. Research at the IFF rests firmly on quantum mechanics and statistical physics. On a microscopic scale, they describe the interaction of electrons and atomic building blocks and determine how these entities respond to external influences. Particular strengths encompass the theory of electronic structures, clusters and polymer physics, micromechanics of lattice imperfections, the dynamics of structure formation and phase transitions, materials and phenomena of magneto- and nanoelectronics, spintronics, spin dynamics, strongly correlated electron systems, as well as the instrumentation of electron, neutron, and synchrotron sources and their application to the study of condensed matter.

The experimental portfolio together with an acknowledged expertise enables the IFF to tackle complex problems in close cooperation with scientists and industry worldwide. Special state-of-the-art laboratories exist for thin film deposition and growth of bulk crystals as well as for the preparation of soft matter materials. In addition to standard methods for materials characterization, highly specialized techniques ranging from superconducting microscopy and spinpolarized microscopies to femtosecond laser spectroscopy are available at the IFF and are being constantly improved in performance.

Ernst Ruska-Centre
for
Microscopy and Spectroscopy
with
Electrons
ER-C

With the Ernst Ruska-Centre for Microscopy and Spectroscopy with Electrons (ER-C) the IFF operates a national user facility housing several of the world's most advanced electron microscopes and tools for nanocharacterization. In-house research programmes cover topical issues in condensed matter physics and – as a matter of course – future developments of subångström and sub-electronvolt microscopy.

JCCSS

Within the framework of the Jülich Competence Centre for Synchrotron Science (JCCSS) a broad variety of spectroscopy, microscopy, and scattering experiments at various synchrotron radiation facilities are designed and realized. The centre also provides expertise for the development of new beamlines and experimental concepts and, thus, acts as a valuable partner for synchrotron radiation laboratories throughout the world.

JCNS
Jülich Centre for Neutron Science

The Jülich Centre for Neutron Science (JCNS) operates advanced neutron scattering instruments at the worldwide most modern and highest flux neutron sources. As a complement to local research opportunities, instruments are designed and operated at external national and international neutron sources, such as the FRM II in Munich or the neutron spallation source in Oak Ridge, USA.

cni

The international networking of the IFF is a main pillar of its success; the institute initiated two EU Networks of Excellence (NoE) , “Soft Matter Composites” and “Complex Metallic Alloys”, and co-founded the Centre of Nanoelectronic Systems for Information Technology (CNI). CNI is a center of excellence for nanoelectronics at the Research Center Juelich and provides an excellent basis for future developments of nanoelectronics and information technology. To identify technology drivers the research areas cover quantum-electronics, magneto-electronics, ferro-electric and molecular nanostructures as well as Terahertz-electronics and bioelectronic signal processing.

The IFF is partner of more than one hundred universities and research institutions from all around the world.

Last but not least, the IFF has a long tradition in the teaching and training of students, not only through the approximately 30 IFF staff scientists steadily giving lectures at universities, but in particular through the annual IFF Spring Schools, Neutron Laboratory Courses, and the Nanoelectronic Days.

Actually representing a department, the IFF currently comprises six experimental and three theoretical divisions as well as joint service facilities, which, however, cannot be regarded separately. The divisions present themselves on the following pages.

Being an institute of the Research Centre Jülich – itself belonging to the Hermann von Helmholtz Association of German Research Centres (HGF) – the IFF provides key contributions to the strategic mission of the Helmholtz Association within three research programmes:

- Condensed Matter Physics (pages 26 – 117),
- Large-Scale Facilities for Research with Photons, Neutrons, and Ions (pages 118 – 167),
- Information Technology with Nanoelectronic Systems (pages 168 – 187).

As a matter of fact, much of the success of the IFF rests upon the inventiveness and initiative of its more than 300 staff members. The IFF supports independent research by encouraging the responsibility of individual scientists – a philosophy that contributes greatly to the stimulating atmosphere in the department. In order to sustain this level on the long run, special encouragement is given to young scientists.

The casual observer may be struck by the wide range of topics and extensive networking at the IFF, whose strength is to link complex issues together with its scientific and industrial partners. In the sixties, Germany seemed to be about to miss the boat in solid-state research. The success of the IFF demonstrates, how a leading global position may be achieved by a sound and clear-sighted research strategy, which is able to identify and address new developments and challenges at an early stage.

Department IFF

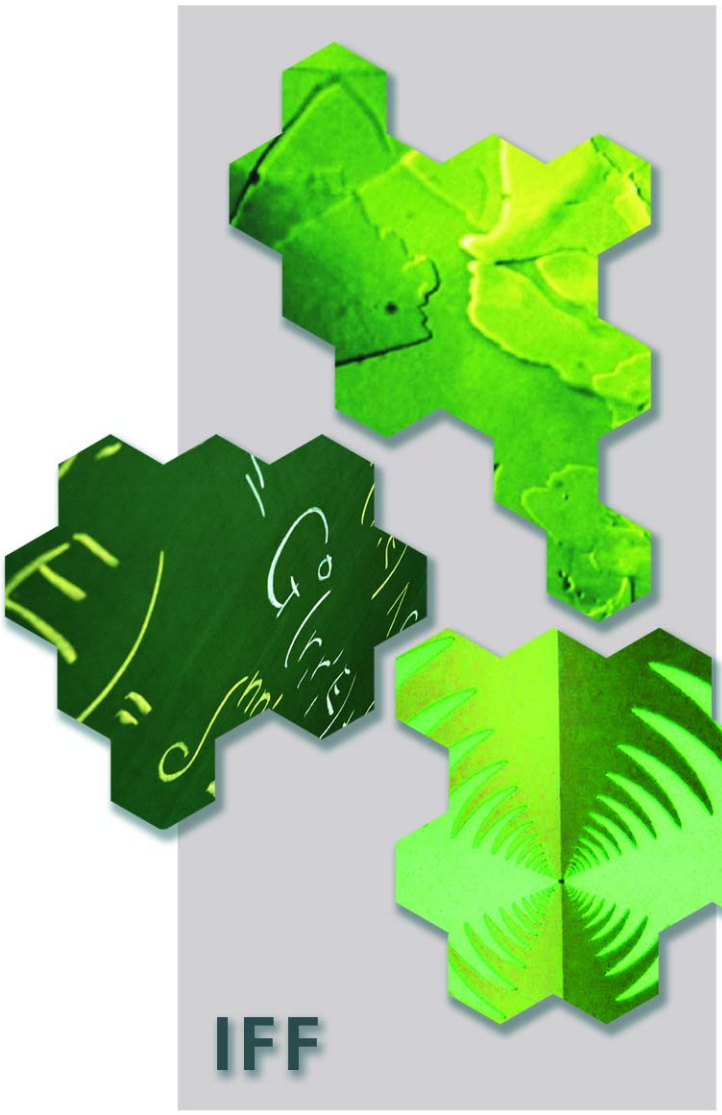

comprising the Institutes

IFF-1:	Theory I	Prof. Dr. Stefan Blügel
IFF-2:	Theory II	Prof. Dr. Gerhard Gompper
IFF-3:	Theory III	Prof. Dr. Heiner Müller-Krumbhaar
IFF-4:	Scattering Methods	Prof. Dr. Thomas Brückel
IFF-5:	Neutron Scattering	Prof. Dr. Dieter Richter
IFF-6:	Electronic Materials	Prof. Dr. Rainer Waser
IFF-7:	Soft Condensed Matter	Prof. Dr. Jan K. G. Dhont
IFF-8:	Microstructure Research	Prof. Dr. Knut Urban
IFF-9:	Electronic Properties	Prof. Dr. Claus M. Schneider

IFF-1: Theory I

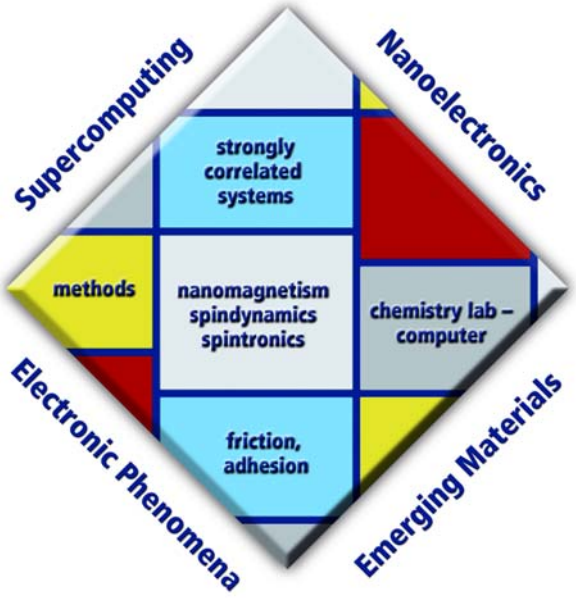

A major focus at "Quantum-Theory of Materials" (Theory I) is the analysis and computation of structural, electronic, magnetic, transport and chemical properties and processes in molecules and solids, in terms of both basic research and practical applications. The goal is to achieve a microscopic understanding of such complex phenomena.

Our research covers key areas of condensed matter theory, computational materials science, nanoelectronics and supercomputing. We explore the electronic and structural properties of systems from large organic (including biological) molecules, low-dimensional magnets, and magnetic multilayers, to complex solids. We consider transport properties across interfaces and molecules as relevant for spintronics and molecular electronics. We investigate the electronic excitations, and dynamical properties of atomic and molecular clusters, solids, and solid surfaces, as well as the quasiparticle behaviour of semiconductors, oxides and transition metals that results from electronic correlations. We analyze the physics of strongly correlated materials such as transition-metal oxides and molecular crystals paying particular attention to complex ordering phenomena. Other areas include nanoscale tribology, including friction, plastic deformation, adhesion, and brittle fracture, as well as nonlinear processes in the atmosphere and agrosphere.

A major asset of our institute is the competence in developing conceptual and computational methods based on density functional theory, molecular dynamics simulations, and Quantum Monte Carlo methods.

IFF-2: Theory II

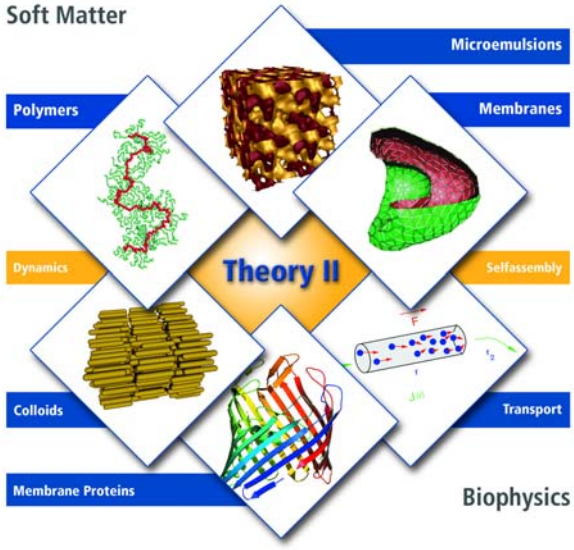

The main research topic of the Institute "Theoretical Soft Matter and Biophysics" (Theory II) is the theory of macromolecular systems. Soft matter physics and biophysics are interdisciplinary research areas encompassing statistical physics, materials science, chemistry, and biology. Our systems of interest include polymer solutions and melts, colloidal suspensions, membranes, vesicles and cells, but also composite systems ranging from colloids in polymer solutions to mixtures of surfactants and amphiphilic block copolymers.
A major focus is the hydrodynamic behaviour of complex fluids and biological systems, both in equilibrium and under flow conditions.

At IFF-2, a large variety of methods are applied. In fact, a combination of analytical and numerical methods is often required to successfully characterize the properties of these complex systems. In particular, simulation methods (Monte Carlo, molecular dynamics), mesoscale hydrodynamic simulation techniques, field theory, perturbation theory, and exact solutions are employed. Since the building blocks of soft matter systems often contain a large number of molecules, "simplified" mesoscale modelling is typically required, which is then linked to the molecular architecture.

A characteristic feature of soft-matter research is the fruitful interaction between theory and experiment. IFF-2 closely cooperates with the Institute for Neutron Scattering (Prof. Richter) and the Institute for Soft Condensed Matter (Prof. Dhont) to successfully tackle many of the essential aspects of the systems investigated.

IFF-3: Theory III

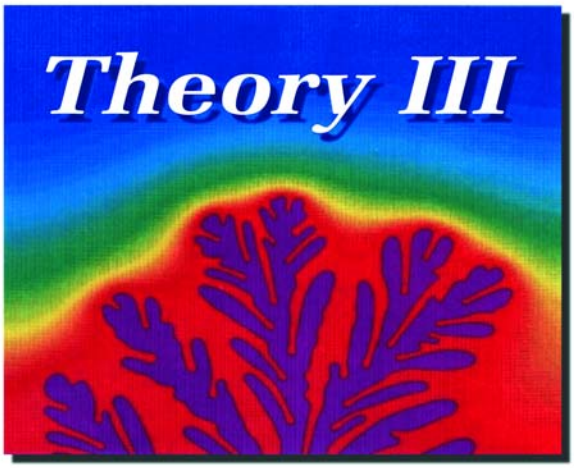

The research of the Institute "Theory of Structure Formation" (Theory III) is concerned with the mechanisms of the formation of structures and their consequences in condensed matter. The investigations start from electronic properties which define the shortest length and time scales, but they also encompass the macroscopic consequences. The analytical and numerical studies are in many ways closely connected to experimental research performed in other groups of the IFF, but also to activities in other institutes of the Research Centre Jülich. The institute contributes mainly to the research programmes "Condensed Matter Physics" and "Information Technology with Nanoelectronic Systems" of the Research Centre.

Central points of interest for the research in Theory III are in the field of electronic structure of solids, in particular effects of strong electronic correlations. A specific interest concerns materials relevant for Information technology. A second mainstream is formed by cooperative phenomena in condensed matter. Questions here aim at the dynamics of structure and pattern formation and the statistical mechanics of order and disorder processes. Specific activities concern the effect of long-range interactions like elastic effects in solids, friction and fracture phenomena, or hydrodynamic interactions in solid-liquid systems.

The research of Theory III employs all analytical and numerical techniques applicable to many-body problems of equilibrium and non-equilibrium phenomena in condensed matter. In addition, the development of new methodological concepts and numerical procedures is part of our research interest. The development of parallel programme codes adapted to massively parallel computers has received special attention in recent years.

IFF-4: Scattering Methods

At the Institute for Scattering Methods, we focus on the investigation of structural and magnetic order, fluctuations and excitations in complex or nanostructured magnetic systems and highly correlated electron systems. Our research is directed at obtaining a microscopic atomic understanding based on fundamental interaction mechanisms. The aim is to relate this microscopic information to macroscopic physical properties. To achieve this ambitious goal, we employ the most advanced synchrotron X-ray and neutron scattering methods and place great emphasis on the complementary use of these two probes. Some of our efforts are devoted to dedicated sample preparation and characterization from thin films and multilayers via nano-patterned structures to single crystals for a wide range of materials from metals to oxides.

A significant part of our activity is devoted to the development of novel scattering techniques and the construction and continuous improvement of instruments at large facilities in the framework of the Jülich Centre for Neutron Science JCNS and the Jülich Competence Centre for Synchrotron Science JCCSS.

IFF-5: Neutron Scattering

The Institute for Neutron Scattering is concerned with neutron research placing major emphasis on soft condensed matter, i.e. materials that react strongly to weak forces. Neutron scattering is a valuable tool for these systems because it reveals structure and dynamics of Soft Matter on the relevant length- and timescales.

A major part of the Soft Matter studies is done on polymers. Apart from their structure, we are interested in the dynamics of polymers in melts and solutions (e.g. gels, rubbery networks, aggregates). These polymers often have a complex architecture (copolymers, star-polymers etc.) to tailor them for industrial applications. Another field of interest are complex liquids such as microemulsions or colloid systems. Finally, biological materials (e.g. proteins) are studied concerning their structure and dynamics.

The institute has modern chemical laboratories for the synthesis, characterisation, and modification of Soft Matter. In order to complement neutron scattering experiments several ancillary techniques are used in the institute: rheology, light scattering, calorimetry, x-ray scattering, impedance spectroscopy, and computer simulation.

The Institute for Neutron Scattering is partner in the Jülich Centre for Neutron Science JCNS. In this position it operates several neutron scattering instruments at the research reactor FRM II in Munich, at the Institut Laue-Langevin in Grenoble, and at the Spallation Neutron Source in Oak Ridge, USA. These instruments are available to guest researchers on request. Another focus of research is the development of neutron instrumentation for research reactors and future spallation sources worldwide.

IFF-6: Electronic Materials

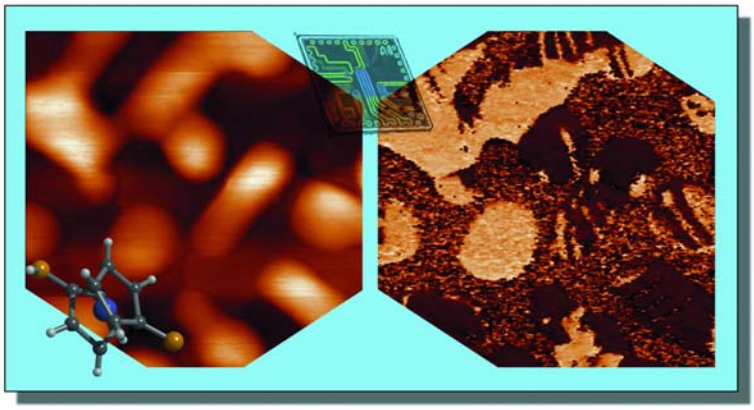

The Institute of Electronic Materials focuses on the physics and chemistry of electronic oxides and organic molecules, which are promising for potential memory, logic, and sensor functions. Our research aims at the fundamental understanding of nanoelectronic functions based on ferroelectricity, piezoelectricity, space charge effects, and electrochemical redox processes and at the elucidation of their potential for future device application.

In particular, true non-volatility and extended scaling represent the two major issues of Random Access Memories (RAM) dealt with in our institute. In the area of charge-based RAM, our research focuses on the scalability of ferroelectric RAM with respect to the vertical and lateral scaling limits. In addition, the impact of interfaces in epitaxial ferroelectric and superparaelectric thin films on the polar properties is investigated. In the area of resistance-based RAMs, we aim at the classification, the elucidation, and the subsequent exploitation of redox-based hysteretic switching phenomena. Other resistance switching phenomena such as the phase-change mechanism and potential tunneling-based effects are studied for comparison. Our research in technology aims at the deposition of ultrathin oxide films on 3D-structured surfaces by e. g. atomic layer deposition (ALD) and template growth techniques of nanostructures.

For execution these studies, our institute provides a broad spectrum of facilities reaching from dedicated material synthesis, atomically controlled film deposition methods, molecular self-assembly routes, and integration technologies, to the characterisation of processes, structures, and electronic properties with atomic resolution.

IFF-7: Soft Condensed Matter

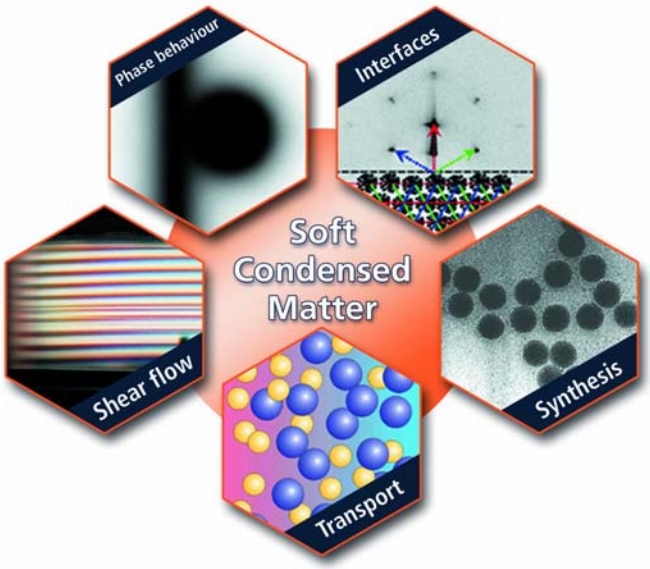

The Soft Condensed Matter group investigates the chemistry and physics of colloidal systems. Colloidal systems can be regarded as solutions of very large molecules which exhibit phase transitions and show non-equilibrium phenomena that are also found for simple molecular systems. Due to the slow dynamics of colloids and the tuneable interactions between the colloidal particles, however, there are many transitions and non-equilibrium phenomena that do not occur in simple molecular systems, like gellation and shear-band formation. The aim is to understand structure, dynamics and non-equilibrium phenomena on a microscopic basis with an open eye for possible technological applications.

The main topics that are studied include,

- the phase behaviour, pattern formation, phase separation kinetics and dynamics of suspensions of spherical and rod-like colloids under shear flow,
- mass transport induced by temperature gradients,
- dynamics and micro-structural properties of colloidal systems near walls and interfaces,
- the effects of pressure on interactions, the location of phase transition lines and gellation transitions and the dynamics of colloids and polymers,
- response of colloids to external electric fields,
- the equilibrium phase behaviour of mixtures of colloids and polymer-like systems,
- dynamics of various types of colloidal systems in equilibrium, and
- the synthesis of new colloidal model particles, with specific surface prop erties, interaction potentials and particle geometries.

IFF-8: Microstructure Research

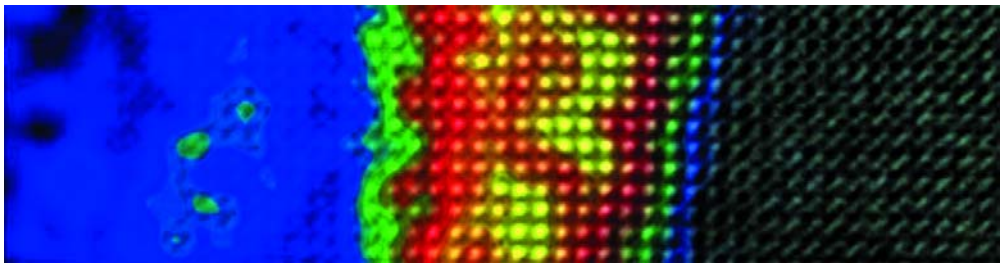

The Institute "Microstructure Research" focuses on the atomic and microstructural understanding of crystalline material properties with a special emphasis on electroceramics, metal alloys, nanostructured semiconductors and oxide superconductors. In some of these fields, the competence covers the whole range from basic research to the development and preparation of prefabricated technical devices. In other fields, access to novel material classes and intricate problems is provided by qualified collaborations. Current research programmes, performed either exclusively at the institute or in the framework of international cooperations, range from pure material preparation carried out hand in hand with all-embracing electron microscopic analyses to the design of electronic circuits and the development of advanced structural analysis techniques.

Over and above these general physics and technology-related projects, as a globally established organization, the institute continuously focuses and complements special competence in the field of advanced transmission electron microscopy techniques accompanied by the development of novel investigation methods. For these purposes, the institute operates and maintains the Ernst Ruska-Centre for Microscopy and Spectroscopy with Electrons (ER-C), which, as a supraregional user facility, benefits from the unique scientific expertise in the field of transmission electron microscopy, which is being continuously extended at the institute.

IFF-9: Electronic Properties

At the Institute "Electronic Properties" we explore the multifaceted interrelations between the electronic structure and the physical properties of matter. Our current research focus lies on magnetism, magnetic phenomena, and their exploitation in nanoscience and information technology. Systems of interest range from ultrathin films and thin film layer stacks through quantum wires and dots to clusters and molecules.

Magnetism displays a complicated interplay of competing interactions taking place on different length, energy, and time scales. We are particularly interested in the influence of the reduced dimensionality and the formation of quantum effects in nanoscale magnetic structures. The crosslinks between electronic structure and magnetism are addressed by a variety of spin-resolving spectroscopic techniques, such as spin-polarized photoemission and x-ray magnetooptics. These studies are carried out at dedicated beamlines at the synchrotron radiation facilities BESSY and DELTA.

The second line of research addresses the response of magnetic systems on short (magnetodynamics) and ultrashort timescales (spin dynamics). The magnetodynamics is experimentally accessed by pump-probe schemes and interpreted via micromagnetic simulations. Laser-based techniques provide high time-resolution, whereas time-resolved photoemission microscopy combines high lateral resolution with large magnetic sensitivity and element selectivity. In the realm of spin dynamics, we study energy and angular momentum transfer processes between the electron, spin, and lattice subsystems. Such experiments are performed by femtosecond pump-probe methods.

The third topic in the IFF-9 is Spintronics, i.e. the physics of spin-dependent transport processes. Resting on a long-standing experience with magnetoresistive phenomena, the current studies focus on the fundamental physics of spin transfer phenomena. This includes the development of new magnetic material systems and nanoscale devices. Particular emphasis lies on the exploration of smart magnetic switching alternatives involving spin-polarized electrical currents and photons.

The Ernst Ruska-Centre (ER-C) for Microscopy and Spectroscopy with Electrons houses several of the world's most advanced electron microscopes and tools for nanocharacterisation, which are available to interested users.

Condensed Matter Physics

Research in Condensed Matter is concerned with the complex interplay of the myriads of atoms in a solid or a liquid. Research in this field can thus be understood as the exploration of the „third infinity", being on equal footing with the exploration of the very small scales of elementary particle physics and the very large scales of astrophysics. The conceptual framework of quantum physics and statistical physics forms the basis for our understanding of Condensed Matter. The cooperation of the electrons and atoms within a many-body system is responsible for the different properties of the substances and determines why they are solid, fluid or gaseous, soft or hard, transparent or opaque, magnetic, metallic or even superconducting. Extreme length and time scales give rise to the characteristic complexity of Condensed Matter, ranging from subatomic sizes up to macroscopic measures, from electronic reaction times in the femtosecond range up to geological periods.

Our activities focus, in particular, on multi-scale phenomena in solid state and liquid phases and are organized in three topics:

- Electronic and Magnetic Phenomena,
- From Matter to Materials, and
- Soft Matter and Biophysics.

The studies in the first topic encompass electronic and magnetic quantum states and their properties. This includes problems in highly-correlated materials, superconductivity, magnetism in low dimensions and on short time scales. The second topic deals with phase transitions and transport processes, glass-like states, and complex metallic alloys, and finally structure formation and self-organization. In the third topic, structure formation and self-organization, mesoscopic dynamics and driven systems, as well as biology-inspired physics are addressed. The spectrum of the materials investigated covers a wide range from metals, semiconductors and ceramics, through macromolecular systems up to biological systems and cells. For this purpose, a broad portfolio of theoretical and experimental techniques is utilized, which are constantly improved and progressed. The experimental emphasis lies on neutron scattering, synchrotron-radiation methods and ultrahigh resolution electron microscopy, whereas the theoretical treatments range from quantum theory to statistical physics and involve both analytical and numerical procedures.

Massively Parallel Exact Diagonalization and Cluster Perturbation Theory: Understanding the Molecular Metal TTF-TCNQ

A. Dolfen and E. Koch

Division Quantum-Theory of Materials

In order to treat systems with strong correlations we have developed a parallel Lanczos code which runs efficiently on modern massively parallel supercomputers like JUBL, Jülich's new BlueGene/L system. To overcome the limitations of finite system-size we employ cluster perturbation theory (CPT), giving us access to the angular-resolved spectral function with high resolution. As a result we can resolve the spin-charge separation of the quasi one-dimensional molecular metal TTF-TCNQ.

The field of strongly correlated electrons features fascinating physics. This is due to the interplay between Coulomb repulsion and kinetic energy, yielding for instance effects of spin-charge separation in the one-dimensional metal TTF-TCNQ. The Ising model for strongly correlated systems is the Hubbard model

$$H = -\sum_{\sigma,\nu,i\neq j} t_{ij,\nu} c^{\dagger}_{i\nu\sigma} c_{j\nu\sigma} + U \sum_{i} n_{i\uparrow} n_{i\downarrow} \ , \qquad (1)$$

where the first term gives the kinetic energy, t_{ij} being the amplitude for an electron hopping from the Wannier orbital on site i to the Wannier orbital on site j. The second term represents the on-site Coulomb repulsion with Hubbard parameter U and $n_{i\uparrow} = c^{\dagger}_{i\uparrow} c_{i\uparrow}$. Unfortunately the corresponding Hilbert spaces are huge even for small systems and this makes the system hard to solve. Since there are four possible states for a single site(empty, filled with up or down electron, doubly occupied) the dimension of the Hilbert space for N sites is 4^N. Exploiting symmetries like spin and charge conservation improves the situation somewhat. We can, however, exploit the sparseness of the Hamiltonian. In the real space basis the Coulomb repulsion is diagonal. Moreover, since the systems we study are tightly bound, hopping occurs only between near neighbors and thus the hopping matrix t_{ij} and therewith the Hamiltonian is sparse.

For diagonalizing huge sparse matrices iterative methods are the methods of choice. Since we are interested in the ground-state eigenpair, i.e. the pair of ground-state vector and energy, we employ the Lanczos algorithm which needs three vectors of the size of the Hilbert space. Therefore its applicability is limited by the maximum amount of available main memory.

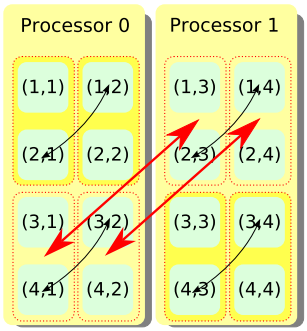

FIG. 1: Scheme of the transpose operation. The MPI communication (blue arrows) is realized by a `MPI_Alltoall` *call. The small black arrows indicate the local operations needed to complete the matrix transpose.*

On distributed memory systems the vector elements are distributed among all threads. Central to the Lanczos method is the multiplication of the Hamiltonian with the wave vectors. The kinetic energy term, though sparse, leads to non-local memory access patterns. A naive approach of implementing remote memory access is the use of MPI one-sided communication. It, however, gives extremely poor performance (see lower right panel of fig. 2). A simple yet important observation leads to an efficient implementation. The hopping part of the Hamiltonian conserves the electron-spin. Thus, writing the many-body vector as a matrix $v(i_\uparrow, i_\downarrow)$, where the indices label spin configurations we find that the hopping term only connects vector elements that differ in one index. Hence, when storing entire slices, i.e. $v(i_\uparrow, :)$, on one thread the kinetic term for the spin-down electrons is local to that thread. After transposing v the same is true for the hopping of the spin-up electrons. Therefore, the efficiency of the sparse matrix-vector multiplication depends on the performance of the matrix transpose operation which can be implemented with `MPI_Alltoall`. `MPI_Alltoall`, however, expects the data packages which will be sent to a given thread to be stored contiguously in memory. This does not apply to our case, since we would like to store the spin-down electron configurations sequentially in memory. Thus, the matrix is stored column wise. For `MPI_Alltoall` to work properly, we would have to bring the data elements in row-major order. This could be done by performing a local matrix transposition operation. The involved matrices are, however, in general rectangular,

leading to expensive local-copy and reordering operations. We can avoid this by calling `MPI_Alltoall` for each column separately. After calling `MPI_Alltoall` for each column (red arrows in figure 1) only a local strided transposition has to be performed (black arrows) to obtain the fully transposed matrix or Lanczos vector. The speedup (figure 2) shows that using collective communication is indeed very efficient, especially on BlueGene/L systems. Target for the development of the BlueGene system was high performance/price and performance/power consumption ratios. The main idea is to build the system out of a very large number of nodes, which taken for themselves have only a relatively modest clock rate and performance, leading to lower power consumption and low cost. Using relatively slow processors also implies a better balance between CPU speed and the usually considerably slower memory and network access. That this goal was achieved is evidenced by the main plot of figure 2, which shows the speedup for a calculation where in each iteration a state vector of 18 GB is "transposed" twice.

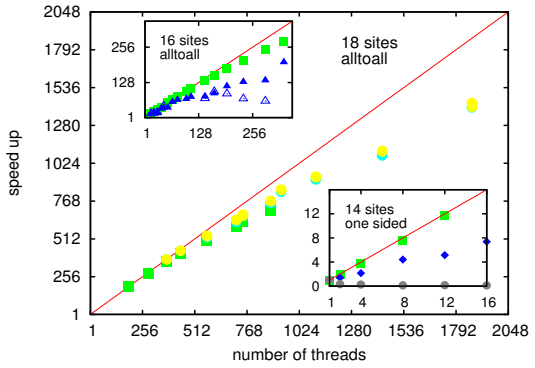

FIG. 2: Speedup of the Lanczos code on IBM Blue Gene/L JUBL (green (CO mode) and turquoise (VN mode) symbols) and IBM Regatta JUMP (blue (collective comm.) and grey (1-sided comm.) symbols) for different problem sizes.

In order to extrapolate to infinite systems we need to calculate the same system for different numbers of sites. Obviously we can only treat integer numbers of electrons in our calculations. Thus the number of sites must be chosen in such a way, that the filling constraints are met. For TCNQ for instance we have a filling of 0.6. Hence, we are restricted to 10 sites with 6 or 20 sites with 12 electrons. Moreover, in finite systems we have only a very limited k-resolution. When computing angular-resolved spectral functions in a system with periodic boundary conditions and L sites we have only $\lfloor L/2 \rfloor + 1$ independent angular-resolved spectral functions due to inversion symmetry.

A more advanced way of calculating infinite systems and to achieve an arbitrarily high k-space resolution is cluster perturbation theory (CPT). It works by diagonalizing a finite clusters exactly and then treating the hopping between identical clusters perturbatively, leading to an effectively infinite chain. For a single-site half-filled chain the spin-averaged Green's G^c function with respect to the chemical potential $\mu = -U/2$ and the Fourier transform of the inter-cluster hopping are given by $G^c = \left(\omega - \frac{U^2}{4\omega}\right)^{-1}$, $T(k) = -2t\cos(k)$ respectively. For the infinite system in CPT the Green's function is

$$G(k,\omega) = G^c(\omega)\left(1 - T(k)G^c(\omega)\right)^{-1} \quad (2)$$

$$= \left(\omega - \frac{U^2}{4\omega} + 2t\cos(k)\right)^{-1} . \quad (3)$$

which is just the Hubbard-I approximation for half-filling [4]. We use the CPT technique in combination with the Lanczos method to study the quasi one-dimensional molecular metal TTF-TCNQ. Isolated TTF and TCNQ molecules are stable, since they are closed-shell molecules. The HOMO of TTF is significantly higher in energy compared to the LUMO of TCNQ. Thus, when making a crystal out of these molecules charge is transferred from the TTF-HOMO to the TCNQ-LUMO. This charge transfer of about 0.6 electrons leads to partially filled bands and thus metallic behavior. The hopping of electrons occurs along the stack of like molecules, either TTF or TCNQ, giving rise to quasi one-dimensional bands. This low dimensionality in tandem with strong Coulomb repulsion compared to the kinetic energy leads to interesting many-body effects. Figure 3 shows the angular-resolved spectral function for TCNQ in a CPT calculation for a 20 sites t-U Hubbard model. At the Γ-point we observe signatures of spin-charge separation. The electron dispersion splits into a holon and a spinon branch.

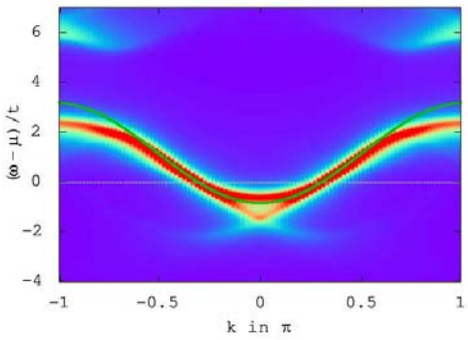

FIG. 3: Angular-resolved spectral function obtained by CPT for a 20 sites TCNQ-like t-U Hubbard model with 6 electrons of either spin ($U = 1.96$ eV, $t = 0.4$ eV). The white line shows the chemical potential, the green cosine the independent-particle band. Signatures of spin-charge separation are clearly observed in the vicinity of the Γ-point.

[1] A. Dolfen, diploma thesis Massively parallel exact diagonalization of strongly correlated systems (2006).

[2] L. Cano-Cortés, A. Dolfen, J. Merino, J. Behler, B. Delley, K. Reuter, E. Koch, submitted to Phys. Rev. Lett.

[3] A. Dolfen, E. Pavarini, E. Koch, InSiDe 4, p. 16, 2006

[4] J. Hubbard, Proc. R. Soc. A., **276**, pp. 238-257, 1963

Electron-Phonon Interaction and Antiferromagnetic Correlations

G. Sangiovanni[1], O. Gunnarssson[1], E. Koch[2], C. Castellani[3], and M. Capone[3]

[1]Max-Planck Institut für Festkörperforschung, Heisenbergstr. 1, D-70569 Stuttgart, Germany
[2]Institut für Festkörperforschung, Forschungszentrum Jülich, D-52425 Jülich, Germany
[3]Dipartimento di Fisica Università di Roma "La Sapienza" piazzale Aldo Moro 5, 1-00185 Roma, Italy

Phonons are suspected to play an important role in high-temperature superconductivity. To address this question we study the interplay of correlations and electron-phonon coupling in a model of cuprates at zero and finite doping using dynamical mean-field theory allowing for antiferromagentic correlations. We find that the AF correlations strongly enhance phonon effects on the electron Green's function with respect to the paramagnetic correlated system. Still, the net effect of the Coulomb interaction is a moderate suppression of the electron-phonon interaction. Doping leads to additional suppression, due to reduced antiferromagnetic correlations.

There are strong experimental indications that the electron-phonon interaction (EPI) plays a substantial role for properties of high-T_c cuprates [1, 2]. The Coulomb interaction in the copper-oxide plane is expected to strongly suppress charge fluctuations. This is often described in the Hubbard or t-J models, for which important phonons couple to such charge fluctuations [3]. One might therefore actually expect the Coulomb interaction to strongly suppress the EPI. This was indeed found with dynamical mean-field theory calculations in the paramagnetic phase (P-DMFT) [4].

The half-filled Hubbard model becomes an insulator for large U. In the P-DMFT the only mechanism for this is the quasiparticle weight Z going to zero. Such a reduction of Z tends to strongly suppress the EPI, which is an important reason for the small effects of the EPI in the P-DMFT. By allowing for antiferromagnetism (AF) in DMFT, it is possible to have an insulating state although Z remains finite. This suggests that it is important to allow for AF when describing the electron-phonon interaction.

We therefore use an AF-DMFT approach. In contrast to previous work, we find for the half-filled system that within the Holstein-Hubbard model the effects of the EPI on the electron Green's function are neither strongly suppressed nor enhanced by the Coulomb interaction. While previous work could only address the half-filled case, the present formalism makes it possible to treat doped metallic cuprates, which are of particular interest. We show that the EPI remains important for the electron Green's function as long as AF is important. Due to the weakening of AF correlations as the system is doped, we find that doping reduces the effects of the EPI on the electron Green's function and it weakens the tendency to polaron formation, in agreement with experiment [5].

We study the Holstein-Hubbard model

$$\begin{aligned} H &= -t\sum_{\langle ij\rangle\sigma}(c^\dagger_{i\sigma}c_{j\sigma}+\text{H.c.})+U\sum_i n_{i\uparrow}n_{i\downarrow} \quad (1)\\ &+ \omega_0\sum_i b^\dagger_i b_i + g\sum_i (n_i-1)(b_i+b^\dagger_i), \end{aligned}$$

where $c^\dagger_{i\sigma}$ creates an electron with spin σ on site i and $b^\dagger_i$ a phonon on site i, $t>0$ is a hopping integral, U the Coulomb interaction between two electrons on the same site, ω_0 is the phonon energy, g a coupling constant and n_i measures the number of electrons on site i. We assume an infinite-coordination Bethe lattice with the half band width D and the density of states $N(\varepsilon)=(2/\pi D^2)\sqrt{D^2-\varepsilon^2}$. We define a dimensionless coupling constant $\lambda = g^2/(\omega_0 D)$. For large U the Hubbard model is approximately equivalent to the t-J model. For a two-dimensional lattice, these models are related via $J/t = D/U$.

We solve the DMFT equations for $T=0$. The associated impurity problem is solved using the Lanczos method. The Hilbert space is limited by only allowing up to N_{ph} phonons, where $N_{ph}\sim 30$ depends on the parameters. The energies of and couplings to the bath levels are determined from a continued-fraction expansion for the large-U half-filled case and otherwise by a fit on the imaginary axis. We use up to 25 bath levels.

We here focus on the quasi-particle weight Z, since our criterion for polaron formation is Z being exponentially small and since Z_0, calculated for $\lambda=0$, is expected to be crucial for the electron-phonon interaction.

For noninteracting electrons the reduction of Z by the EPI is given by $(1/Z-1)/\lambda = 4/\pi$ for small λ and $\omega_0 \ll D$, as shown by the arrow in Fig. 1. To determine the effect of the EPI for interacting electrons ($U>0$), we calculate $(Z_0/Z-1)/\lambda$, shown in Fig. 1. This quantity measures how efficiently the EPI reduces the quasiparticle weight Z with respect to Z_0 obtained in the absence of EPI. In P-DMFT it is found that the EPI very quickly becomes inefficient when U is increased. In contrast, allowing for AF, we find that the EPI remains much stronger as U is increased, although it is still reduced compared to the noninter-

acting case. These results show that AF is crucial for the EPI of the half-filled system. For U/D values where the Hubbard and t-J models can be compared, the AF-DMFT and the SCBA agree well for $\omega_0 = 0.025D$. For larger phonon frequencies, however, we find that the EPI is appreciably more efficient in the SCBA than in the AF-DMFT.

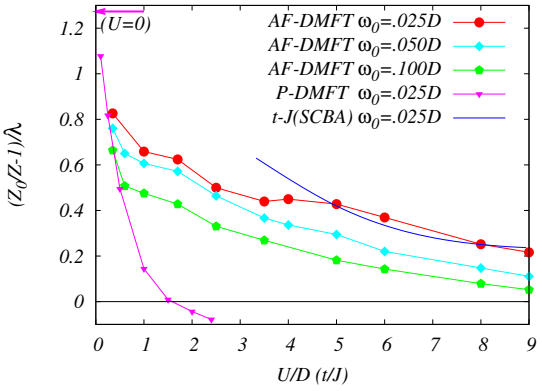

FIG. 1: $(Z_0/Z-1)/\lambda$ in the limit $\lambda \to 0$ for the Hubbard model according to the P-DMFT and AF-DMFT and for the t-J model according to the SCBA. This quantity indicates the effectiveness of the electron-phonon interaction (EPI) in the weak-coupling limit. The figure illustrates how the EPI is much more efficient in the AF-DMFT than the P-DMFT, and that AF-DMFT and SCBA agree rather well.

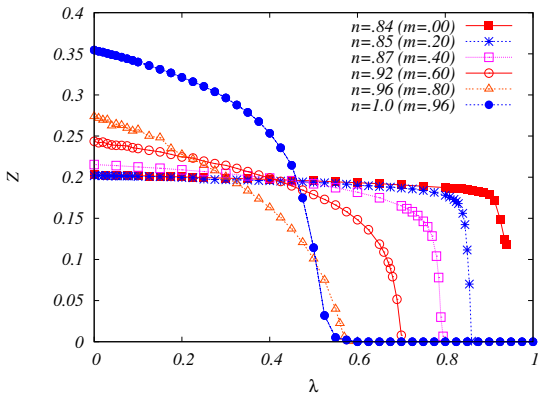

FIG. 2: Z as a function of λ for different fillings n and associated magnetic moments m for $U = 3.5D$ and $\omega_0 = 0.025D$. The figure illustrates how the critical λ_c is increased as the filling is reduced (doping is increased) due to a reduction of the the antiferromagnetic correlations.

In P-DMFT calculations it was found that the effective mass m^* depends only weakly on ω_0. In AF-DMFT we find a sizable isotope effect on m^* and for $\lambda \sim \lambda_c$ the effect is comparable to the experimental value [6]. So far we have discussed the half-filled system, since we can compare with other methods and test the reliability of the AF-DMFT. The doped cuprates, however, are more interesting and challenging, and we now focus on them. Fig. 2 shows Z as a function of λ for $U = 3.5D$ and for different dopings. As the filling is reduced (hole doping increased) the staggered magnetization m is reduced. The figure shows how this leads to an increase in λ_c. In a P-DMFT calculation, on the other hand, a reduction of the filling leads to a reduction of λ_c. The increase of λ_c in the AF-DMFT with increased doping is therefore indeed due to the reduction of m, since at constant $m = 0$, λ_c decreases with doping.

We find the AF-P transition for $U = 3.5D$ at $n = 0.84$, corresponding to a much larger doping (0.16) than found experimentally. This is only partly due to our neglect of second nearest neighbor hopping which would introduce magnetic frustration in the system. The main reason is that in the P state there are also AF correlations which lower the energy, but which are neglected in a DMFT calculation. The AF-DMFT calculation therefore favors the AF state. To obtain a balanced treatment it is necessary to use a cluster DMFT method. Such a calculation would introduce AF correlations also in the paramagnetic state, and like in the AF-DMFT calculation these correlations would weaken as the doping is increased. This should increase λ_c with doping in a qualitative similar way as in Fig. 2.

Experimentally, polaron formation is found to disappear as the system is moderately doped [5]. This may be partly due to screening of the EPI, leading to a reduction of λ. However, the suppression of polaron formation with doping for fixed λ, illustrated in Fig. 2, should also be an essential part of the explanation.

In conclusion, we have found that paramagnetic DMFT calculations for the Holstein-Hubbard model show that effects of the electron-phonon interaction (EPI) on the electrons (quasiparticle weight) are very strongly suppressed by the Coulomb interaction, we find that this suppression is only moderate when antiferromagnetic (AF) correlations are included. As the doping is increased, the AF is reduced and the EPI is more suppressed.These trends are consistent with experiment.

[1] A. Damascelli *et al.*, Rev. Mod. Phys. **75**, 473 (2003).

[2] L. Pintschovius, phys. stat. sol. (b) **242**, 30 (2005).

[3] O. Rösch and O. Gunnarsson, Phys. Rev. Lett. **92**, 146403 (2004).

[4] G. Sangiovanni *et al.*, Phys. Rev. Lett. **94**, 026401 (2005).

[5] K. M. Shen *et al.*, Phys. Rev. Lett. **93**, 267002 (2004).

[6] R. Khasanov *et al.*, Phys. Rev. Lett. **92**, 057602 (2004).

[7] G. Sangiovanni, O. Gunnarsson, E. Koch, C. Castellani, and M. Capone, Phys. Rev. Lett. **97**, 046404 (2006).

Subband Filling and Mott Transition in $Ca_{2-x}Sr_xRuO_4$

A. Liebsch[1] and H. Ishida[2]

[1]Institut für Festkörperforschung, Theorie I, Forschungszentrum Jülich, 52425 Jülich, Germany
[2]College of Humanities and Sciences, Nihon University, and CREST JST, Tokyo 156, Japan

A new concept is proposed for the paramagnetic metal insulator transition in the layer perovskite $Ca_{2-x}Sr_xRuO_4$. Whereas the pure Sr compound is metallic up to very large Coulomb energies due to strong orbital fluctuations, structural changes induced by doping with Ca give rise to a interorbital charge transfer which makes the material extremely sensitive to local correlations. Using dynamical mean field theory based on finite temperature multi-band exact diagonalization it is shown that the combination of crystal field splitting and onsite Coulomb interactions leads to complete filling of the d_{xy} band and to a Mott transition in the half-filled $d_{xz,yz}$ bands.

The layer perovskite $Ca_{2-x}Sr_xRuO_4$ has attracted wide interest during recent years because of the complex sequence of electronic and magnetic phases which arise when Sr is iso-electronically substituted by Ca. While the pure Sr compound exhibits unconventional superconductivity the structural distortions induced by the smaller Ca ions ultimately lead to an antiferromagnetic Mott insulator. The physical mechanism of how this multi-band material with four electrons per Ru ion evolves from the metal Sr_2RuO_4 towards the insulator Ca_2RuO_4 is presently not well understood.

According to band structure calculations the t_{2g} orbitals in Sr_2RuO_4 are approximately equally (2/3) occupied. Because of the planar geometry, these bands split into a wide, nearly two-dimensional d_{xy} band and two narrow, nearly one-dimensional $d_{xz,yz}$ bands (see Fig. 1). Clearly, the Mott transition in such an anisotropic system cannot be understood in terms of single-band models, or multi-band extensions assuming degenerate subbands.

We use finite temperature exact diagonalization (ED) DMFT [1] to study the nature of the Mott transition in $Ca_{2-x}Sr_xRuO_4$. LDA calculations show that the key effect caused by rotation, tilting and flattening of oxygen octahedra is the increasing d_{xy} orbital occupancy with increasing Ca concentration. To account for this charge transfer, we allow for a crystal field splitting Δ between d_{xy} and $d_{xz,yz}$ states.

The result of this work [2] is a new mechanism for the Mott transition in this multi-band system: For realistic values of the Coulomb energy U and crystal field Δ, we find a gradual filling of the d_{xy} subband with increasing U. Once the $d_{xz,yz} \rightarrow d_{xy}$ charge transfer is complete, i.e., $(n_{xy}, n_{xz}, n_{yz}) \rightarrow (1.0, 0.5, 0.5)$, a Mott transition takes place in the remaining half-filled $d_{xz,yz}$ bands. The critical U at which this transition occurs is lower for larger Δ. Thus, the present three-band system does not exhibit orbital selective Mott transitions.

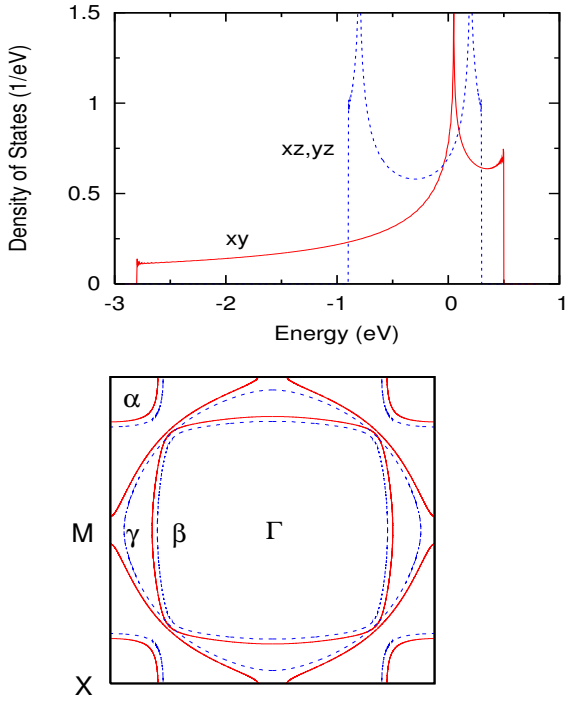

FIG. 1: Density of states of Sr_2RuO_4. Red: d_{xy}; blue: $d_{xz,yz}$. Below: Fermi surface for $\Delta = 0$ (blue) and $\Delta = 0.2$ eV (red).

Fig. 2 summarizes the variation of the t_{2g} orbital occupancies with onsite Coulomb energy U. In the case of Sr_2RuO_4 ($\Delta = 0$), a gradual charge transfer $d_{xz,yz} \rightarrow d_{xy}$ is found, in agreement with the trend found within QMC/DMFT for small U [3]. The system is seen to remain metallic up to very large U. This result is also consistent with previous calculations [4] which revealed no Mott transition up to $U = 4$ eV. Near $U_c \approx 10$ eV the interorbital charge transfer is complete with $n_{xy} = 1$. The remaining half-filled $d_{xz,yz}$ bands then undergo a Mott transition.

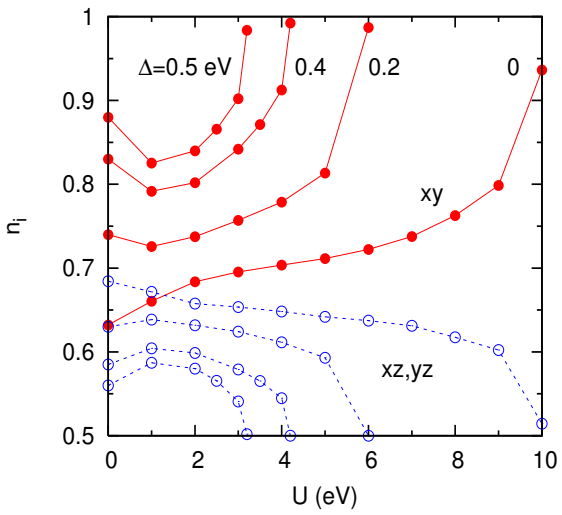

FIG. 2: Orbital occupancy n_i as a function of Coulomb energy for various crystal fields Δ. Red: n_{xy}, blue: $n_{xz,yz}$.

Note that the filling of the d_{xy} band for $\Delta = 0$ accelerates towards increasing U. The reason for this trend is that the larger d_{xy} occupancy reduces the intra-t_{2g} screening of U. Since at the same time the occupancy of the $d_{xz,yz}$ bands approaches one-half, the tendency for the latter bands to undergo a Mott transition becomes rapidly more favorable. In the absence of the d_{xy} band, the half-filled $d_{xz,yz}$ bands would exhibit a metal insulator transition at $U_c = 1.4$ eV. Thus the results for $\Delta = 0$ may be interpreted as $d_{xz,yz}$ Mott transition delayed by strong orbital fluctuations.

In view of this picture it is plausible that, at finite Ca concentrations, the greater initial occupancy of the d_{xy} band associated with $\Delta > 0$ gives rise to complete d_{xy} filling and a $d_{xz,yz}$ Mott transition at progressively lower values of U_c. This is confirmed by the results shown in Fig. 2. For Ca_2RuO_4 octahedral distortions lead to $\Delta \approx 0.4$ eV. The d_{xy} band filling and $d_{xz,yz}$ Mott transition is then shifted to $U_c \approx 4$ eV. Thus, the reduced orbital fluctuations greatly diminish the delay of the Mott transition in the half-filled $d_{xz,yz}$ bands.

In the range $0.5 \leq x \leq 2.0$ the octahedral distortions consist mainly of rotations about the z-axis, corresponding to $\Delta \leq 0.2$ eV. According to Fig. 2, the correlation induced d_{xy} filling and $d_{xz,yz}$ Mott transition then occur at $U_c \approx 6$ eV. In this doping region the system should therefore remain metallic. This result is consistent with angle resolved photoemission data and optical data which show that near $x = 0.5$ all t_{2g} states are itinerant.

A crystal field $\Delta = 0.1 \ldots 0.2$ eV is, however, large enough to push the d_{xy} van Hove singularity below E_F. This also agrees with the photoemission results which yield nearly the same Fermi surface for $Ca_{1.5}Sr_{0.5}RuO_4$ and Sr_2RuO_4, except that, because of the lowering of the van Hove singularity, the γ sheet has changed from electron-like to hole-like, as indicated in Fig. 1.

To prove that d_{xy} band filling and $d_{xz,yz}$ Mott transition coincide we have analyzed the t_{2g} quasi-particle spectra. For $\Delta = 0.4$ eV and $U = 3.0$ eV, the spectra for reveal that all subbands are metallic and exhibit appreciable spectral weight associated with lower Hubbard bands. In contrast, at $U = 4.5$ eV the d_{xy} band is filled and the half-filled $d_{xz,yz}$ bands exhibit a clear separation into upper and lower Hubbard bands. The transition between these two regions occurs at $U_c \approx 4.2$ eV.

To analyze the Mott transition in $Ca_{2-x}Sr_xRuO_4$ we have focused on the variation of the subband occupancies with Coulomb energy. In reality, U should be roughly constant as a function of x, with $U \approx 3.1$ eV and $J \approx 0.7$ eV according to constrained LDA calculations for $x = 2$. Thus, in Fig. 2 a vertical line near $U = 3$ eV should qualitatively cover the low temperature phase diagram. The result for $\Delta = 0$ with $n_{xy} = 0.70$, $n_{xz,yz} = 0.65$ corresponds to metallic Sr_2RuO_4. $\Delta = 0.2$ eV with $n_{xy} = 0.76$, $n_{xz,yz} = 0.62$ represents roughly the case $Ca_{1.5}Sr_{0.5}RuO_4$, which is also metallic. Finally, the results for $\Delta \geq 0.4$ eV indicate that the metal becomes unstable since n_{xy} increases rapidly towards complete filling, and $n_{xz,yz}$ towards half-filling: the favorable electronic configuration for a Mott transition.

In summary, the paramagnetic metal insulator transition in the layer perovskite $Ca_{2-x}Sr_xRuO_4$ has been investigated within multi-band finite temperature ED/DMFT. The results suggest a new concept following from the enhanced d_{xy} occupancy induced by Ca doping. Instead of sequential, orbital-selective Mott transitions, we find a common transition where the d_{xy} is completely filled and the remaining half-filled $d_{xz,yz}$ bands undergo a standard metal insulator transition. In the pure Sr compound, with nearly equally occupied t_{2g} bands, strong orbital fluctuations preclude this transition, despite the narrow width of the t_{2g} subbands. Thus, realistic Coulomb energies give rise only to a weak $d_{xz,yz} \rightarrow d_{xy}$ charge transfer. Substitution of Sr via smaller Ca ions leads to octahedral distortions and to an enhancement of this charge transfer. Accordingly, orbital fluctuations are reduced, and the material becomes highly sensitive to local correlations. In the Ca rich compound orbital fluctuations are sufficiently weak, so that the Mott transition occurs at realistic values of U. On the basis of this picture it would be very interesting to study the region $x \leq 0.5$ more closely in order to understand the orbital selective mass enhancement and the rich magnetic phases of this material.

[1] C.A. Perroni, H. Ishida, and A. Liebsch, Phys. Rev. B **75**, 045125 (2007); see also: A. Liebsch, Phys. Rev. Lett. **95**, 116402 (2005); A. Liebsch and T.A. Costi, Eur. Phys. J. B **51**, 523 (2006).

[2] A. Liebsch and H. Ishida, cond-mat/0612539; Phys. Rev. Lett. **98**, 216403 (2007).

[3] A. Liebsch and A. Lichtenstein, Phys. Rev. Lett. **84**, 1591 (2000).

[4] A. Liebsch, EuroPhys. Lett. **63**, 97 (2003).

Correlating Structural and Magnetic Properties in $La_{1-x}Sr_xMnO_3$ Manganites

H. F. Li[1], Y. Su[1], E. Gorelik[1], J. Persson[1], P. Meuffels[2], Th. Brückel[1]

[1] Institute for Scattering Methods
[2] Institute for Electronic Materials

A systematic study of structural and magnetic transitions using Rietveld refinement of neutron powder diffraction (NPD) data on polycrystalline and single-crystalline $La_{7/8}Sr_{1/8}Mn_{1-\gamma}O_{3+\delta}$ compounds has been performed. In addition, new insights on low-temperature charge/orbital ordering (CO/OO) phenomenon at this doping have been gained from resonant scattering experiments carried out in the hard and soft x-ray regimes.

$La_{1-x}Sr_xMnO_3$ is one archetypal correlated electron system. The compounds in this system are technologically interesting materials, exhibiting intriguing structural, magnetic and electronic properties. The ground states of magnetism and transport, and the colossal magnetoresistance (CMR) effect could be qualitatively but not quantitatively understood on the basis of strong Hund's coupling and double-exchange mechanism. The x = 0.125 compound is of particular interest, as double transitions from paramagnetic insulator to ferromagnetic metal and then to ferromagnetic insulator occur on lowing the temperature. The nature of the low-temperature ferromagnetic insulating (FMI) phase is still being strongly debated. Nevertheless, the importance of charge and orbital degrees of freedom as well as Jahn-Teller (JT) distortion has been recognized. Various low-temperature structures such as triclinic, monoclinic, orthorhombic and rhombohedral have been reported for nominal doping x = 0.125, strongly owing to the different preparation methods and various synthesis conditions. The structural and magnetic properties are substantially different in the literature, e.g. (i) the Curie temperature T_c, (ii) the structural evolutions versus temperature and Sr doping level and (iii) the phase diagram including monotonic variations of the phase boundaries [1]. Thus, the defect chemistry, e.g. cation nonstoichiometry, excess oxygen, etc, is a crucial issue for the understanding of manganites. In spite of intensive investigations, the exact and detailed CO/OO model is still a puzzle just because of the bewildering structures. In this report, in order to complete the structural study, solve issues in solid state reactions and clarify the difference between polycrystalline and single-crystalline samples, we have systematically studied the effects of Ar and O_2 annealings on the properties of $La_{0.875}Sr_{0.125}Mn_{1-\gamma}O_{3+\delta}$ manganites [2]. A complete NPD investigation of the structural transition, magnetic order and coherent JT distortion in powder material crushed from a single-crystalline $La_{1-x}Sr_xMnO_3$ ($x \approx 1/8$) perovskite from 5 to 300 K has also been performed. These studies were complemented by resonant x-ray scattering experiments in the hard (APS, USA) and soft (BESSY, Germany) x-ray ranges to study the CO/OO phenomenon.

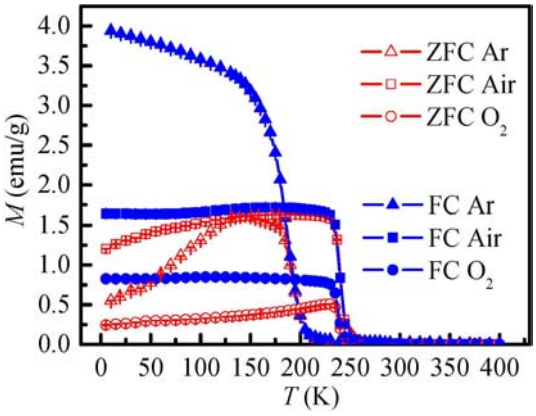

FIG. 1: ZFC and FC magnetization M versus temperature measured at H = 20 Oe.

Ar and O_2 annealings cause a decrease of the Curie temperature T_c from 240(1) K (Air) via 237(1) K (O_2) to 192(1) K (Ar) (Fig. 1). The Curie temperature is reduced by ~20% for the sample with orthorhombic structure (Ar) as compared to the samples with rhombohedral structure (Air and O_2). This is explained by a decrease of the total strength of magnetic interactions, due to the changed Mn-O-Mn bond angle, the decrease of the numbers of nearest magnetic neighbors. The possible reasons for the decrease of Mn site occupancy after Ar and O_2 annealings and the sources of apparent excess oxygen are discussed in [2]. Our results clearly demonstrate that extremely small changes in the stoichiometry can have huge effects on the structural and magnetic properties in these compounds based on the perovskite structure. Only ~2.2% relative decrease of oxygen content can lead to a structural transition from rhombohedral to orthorhombic and to a decrease of the transition temperature by ~20%. Such a huge response on small changes of parameters is characteristic of this complex system. All samples show different sequences

of phase transitions and transition temperatures [3].

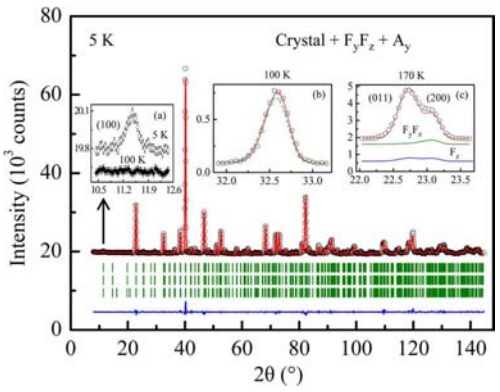

FIG. 2: Rietveld refinement plot of the NPD data from a powdered $La_{1-x}Sr_xMnO_3$ ($x \approx 1/8$) single crystal in $P12_1/c1$ symmetry at 5 K. The contributions to the calculated intensity (solid line) are from chemical, ferromagnetic (FM) (F_yF_z) and A-type antiferromagnetic (A-AFM) (A_y) structures. F_y, F_z and A_y denote the FM moments along the b and c axes and the A-AFM moment along the b axis, respectively. Insets (b) and (c) contrastingly show the quality of fits for refinements with different FM models F_yF_z and F_z.

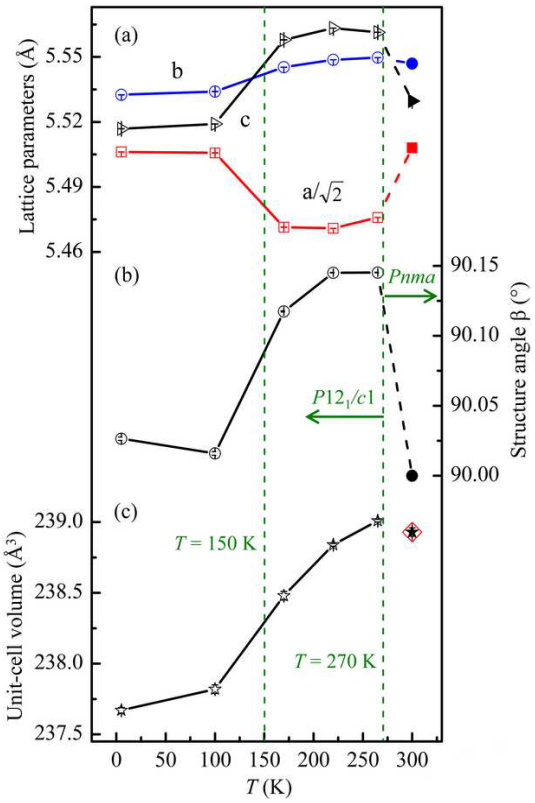

FIG. 3: Temperature variations of (a) the lattice parameters, (b) the crystal structure angle β and (c) the unit-cell volume of a $La_{1-x}Sr_xMnO_3$ ($x \approx 1/8$) singel crystal. The symbol ◊ in panel (c) represents the refined unit-cell volume using $P12_1/c1$ space group for observed 300 K NPD data.

The data from the powdered single crystal is of particular interest for establishing a basic view of the CO/OO pattern, where the information is usually obtained from single crystal x-ray investigation at a synchrotron. Fig. 2 gives an example of a Rietveld refinement at 5 K and Fig. 3 shows the temperature dependence of the refinement results from 5 to 300 K. The data at $T_{CO/OO} < T < T_{JT}$ for the first time were verified to have a monoclinic ($P12_1/c1$, M') structure. The data in the FMI region were also refined using the monoclinic ($P12_1/c1$, M") model. The panel (a) of Fig. 3 indicates a very strong JT distortion between 150 and 270 K. The FM structure was best fitted using a model with the total moment located in crystallographic b-c plane, i.e. F_yF_z. The AFM model was determined as Ay, indicated by the appearance of a characteristic A-AFM (100) peak shown in the inset (a) of Fig. 2. In addition, clear resonant enhancements of the CO/OO reflections are observed utilizing the resonant x-ray scattering technique.

To summarize, (i) the physical properties of manganites are strongly dependent on their structures formed under various synthesis conditions; (ii) we have established the right low-temperature structural data for single-crystalline $La_{0.875}Sr_{0.125}MnO_3$, providing the basis for establishing the right CO/OO pattern standing test of time; (iii) the spin model at 5 K for a single-crystalline $La_{0.875}Sr_{0.125}MnO_3$: short-range A-AFM domains are embedded in the long-range ordered FM domains. In addition, FM and A-AFM domains have an identical spin orientation, possibly attributing to the phase separation and (iv) our results reveal the importance of spin, charge, orbital and lattice interactions in manganites.

[1] D. E. Cox, T. Iglesias, E. Moshopoulou, K. Hirota, K. Takahashi, Y. Endoh, Phys. Rev. B **64**, 024431 (2001).

[2] H. F. Li, Y. Su, J. Persson, P. Meuffels, J. M. Walter, R. Skowronek, Th. Brückel, J. Phys.: Condens. Matter **19**, 016003(12pp) (2007).

[3] H. F. Li, Y. Su, J. Persson, P. Meuffels, J. M. Walter, R. Skowronek, Th. Brückel, J. Phys.: Condens. Matter **19**, 176226(12pp)(2007).

Dephasing by Kondo Impurities: Comparsion With Experiments

T. Micklitz[2], T. A. Costi[1], A. Altland[2], A. Rosch[2], C. Bäuerle[3], F. Mallet[3]

[1]Institut für Festkörperforschung, Forschungszentrum Jülich, 52425 Jülich, Germany
[2]Institute for Theoretical Physics, University of Cologne, 50937 Cologne, Germany
[3]NEEL Institut, Department of Nanoscience, 38042 Grenoble, France

We investigate the dephasing rate, $1/\tau_\varphi$, of weakly disordered electrons due to scattering from diluted dynamical impurities using the numerical renormalization group method, which is ideally suited to this type of problem. Our previous result for the weak-localization dephasing rate is generalized to *arbitrary* dynamical defects. For magnetic impurities, we compare the calculated dephasing rate to recent measurements on quasi-one-dimensional Ag wires doped with Fe Kondo impurities of different concentrations n_s and Kondo temperature $T_K \approx 4.3K$. We find that the experiments are well described by our results for the fully screened Kondo model, and we are able to exclude an explanation in terms of an overscreened or an underscreened Kondo model.

The destruction of phase coherence in a quantum system occurs due to interactions with its environment and can be studied, for example, in mesoscopic metals and semiconductors where the quantum-mechanical wave nature of the electrons leads to a variety of novel transport phenomena at low temperatures. The destruction of phase coherence is also important in the context of qubits whose quantum mechanical behaviour is influenced by the various sources of electromagnetic noise, as can arise, for example, during the read out process.

At low temperatures the dephasing rate, $1/\tau_\varphi$, depends on a number of inelastic scattering mechanisms. For metals, without dynamical impurities, the main source of dephasing at low temperatures is believed to be due to inelastic electron-electron scattering. This typically becomes important below about 1 K and was first calculated by Altshuler, Aronov and Khmelnitsky (AAK), who showed that it vanishes at low temperatures, T, with some power of T, depending on the dimensionality of the system [1].

In the last decade several groups performed magneto-resistance experiments [2, 3] to probe the influence of dephasing on weak localization in disordered metallic wires. An important new mechanism for dephasing in these systems is the presence of extremely low concentrations of dynamical impurities, such as atomic two-level systems [5] or magnetic impurities [3, 4]. The interaction of these dynamical impurities with the electronic environment, in the presence of disorder, makes this a challenging theoretical problem. Until recently, quantitative results for the dephasing rate due to dynamical impurities were only available for asymptotically low and high temperatures [6]. We have recently derived an exact expression for the dephasing rate due to magnetic impurities [7], valid over the whole temperature range of interest in experiments, and we have evaluated this exactly by using the numerical renormalization group (NRG) method [8]. In addition, we have generalized this expression to arbitrary dynamical scatterers, thereby allowing comparisons with a wide range of systems [9].

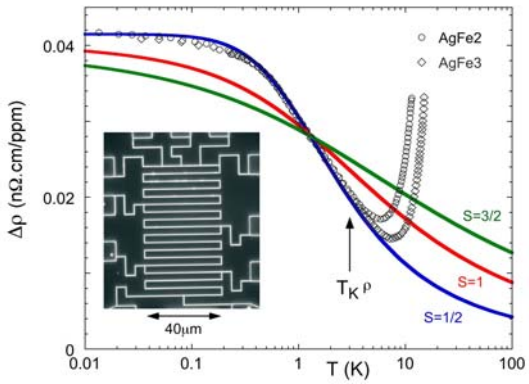

FIG. 1: Resistivity per magnetic impurity concentration as a function of temperature for sample AgFe2 ($n_s = 27\mathrm{ppm}$) and AgFe3 ($n_s = 67.5\mathrm{ppm}$). The electron-electron contribution has been subtracted. The increase above $T \approx 5K$ is due to phonons. The solid curves are the NRG results for the magnetic contribution for the fully screened $S = 1/2$ Kondo model (blue), and two underscreened models with $S = 1$ (red) and $S = 3/2$ (green). Figure taken from [10].

In parallel to these developments, experiments on controlled doping of clean Ag and Au wires with magnetic impurities [2, 3, 4] have become possible using nano-fabrication and ion-implantation techniques. These allow a quantitative comparison to the theoretical predictions of [7]. For such a comparison to be meaningful, a system is required with a Kondo scale T_K of a few K so that measurements can probe both the low temperature behaviour $T \ll T_K$ and the interesting crossover regime $T \approx T_K$ without, however,

having the peak in the dephasing rate at $T \approx T_K$ [7] completely masked by the large phonon contribution. A Kondo system which satisfies these requirements is Ag/Fe with a Kondo scale of $T_K \approx 4.3K$. Fe is expected to be characterized by both an orbital degree of freedom and a spin, $S = 2$, coupling to electrons in up to five angular momentum channels. The relevant theoretical model depends on the position of the Fe within the Ag crystal structure, crystal field effects and the strength of the spin-orbit coupling and is presently not known. We therefore consider, as a model for the magnetic impurities, a general multichannel Kondo model with n_c channels screening a spin S with a Kondo exchange given by

$$H_S = J \sum_{\alpha=1}^{n_c} \hat{\mathbf{S}} c^\dagger_{\alpha\sigma}(\mathbf{x}) \sigma_{\sigma\sigma'} c_{\alpha\sigma'}(\mathbf{x}). \qquad (1)$$

Figure 1 shows the magnetic impurity contribution to the measured resistivity as a function of temperature from recent experiments [10], together with a comparison of the calculated resistivity for underscreened Kondo models with $n_c = 1$ and $S = 1, S = 3/2$ and also for the $S = 1/2$ fully screened Kondo model. From this comparison it is clear that essentially all Kondo impurities behave like fully screened Kondo impurities.

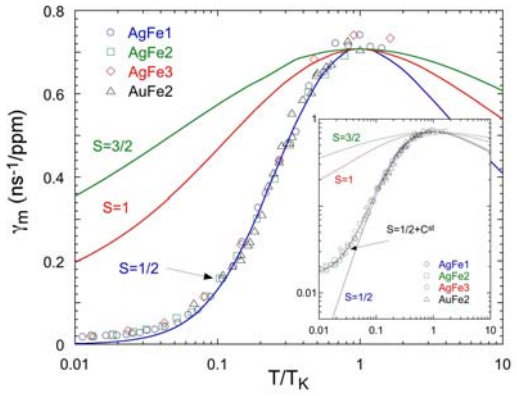

FIG. 2: Dephasing rate per magnetic impurity as a function of (T/T_K). The NRG results, for $S = 1/2$ (blue), $S = 1$ (red) and $S = 3/2$ (green) have been scaled in temperature such that the maxima coincide with the experimental data. The black solid line in the inset corresponds to S=1/2 where we add a constant background. Figure taken from [10], where full details of sample data can be found.

Fig. 2 shows the measured magnetic impurity contribution, γ_m, of the dephasing rate compared to the theoretical predictions for the fully screened Kondo model. Contributions from electron-electron and phonon scattering have been subtracted out as described in [10]. One sees that there is excellent agreement over the whole temperature range, with the experimental data for all samples collapsing onto the predicted universal scaling curve as a function of T/T_K. Notice, that the corresponding predictions for the underscreened Kondo models give a much broader maximum at $T \approx T_K$ and a slower decay of the dephasing rate at low temperatures than shown by the experiments. Therefore, we can rule out the possibility that all, or a large fraction, of magnetic impurities are underscreened. We can also exclude an overscreened Kondo model $n_c > 2S$ as the experiments with which we compare show a decrease of the dephasing rate with decreasing temperature whereas one expects a finite dephasing rate for an overscreened Kondo model [11].

In conclusion, we have carried out numerical renormalization group calculations for the resistivity and dephasing rate of electrons scattering from Kondo impurities using the theory developed in [7] and recently generalized to arbitrary dynamical scatterers in [9]. A quantitative comparison of these results to recent experiments on Fe impurities in Ag wires shows surprisingly good agreement to the theoretical prediction for the fully screened $S = 1/2$ Kondo model [10]. Similar agreement to this theory has been found in independent experiments [12]. We are able to rule out a purely underscreened or overscreened Kondo scenario to describe the above experiments. Calculations for higher spin fully screened Kondo models would be of interest in the future.

[1] B. L. Altshuler, A. G. Aronov and D. E. Khmelnitsky, J. Phys. C: Solid State Phys., **15**, 7367-7386 (1982).

[2] P. Mohanty and R. A. Webb, Phys. Rev. B **55**, R13452 (1997).

[3] F. Schopfer *et al.*, Phys. Rev. Lett. **90**, 056801 (2003); F. Pierre *et al.*, Phys. Rev. B **68**, 085413 (2003).

[4] C. Bäuerle, *et al.*, Phys. Rev. Lett **95**, 266805 (2005).

[5] A. Zawadowski, *et al.* Phys. Rev. Lett. **83**, 2632(1999); Y. Imry, H. Fukuyama and P. Schwab, Europhys. Lett. **47**, 608-6714 (1999).

[6] M. G. Vavilov and L. I. Glazman, Phys. Rev. B **67**, 115310 (2003).

[7] T. Micklitz, T. A. Costi, A. Altland and A. Rosch, Phys. Rev. Lett. **96**, 226601 (2006).

[8] T. A. Costi, A. C. Hewson and V. Zlatic, J. Phys.: Condens. Matter **6**, 2519 (1994).

[9] T. Micklitz, T. A. Costi, and A. Rosch, Phys. Rev. B**75**, 054406 (2007).

[10] F. Mallet, J. Ericsson, D. Mailly, S. Ünlübayir, D. Reuter, A. Melnikov, A. D. Wieck, T. Micklitz, A. Rosch, T. A. Costi, L. Saminadayar, and C. Bäuerle, Phys. Rev. Lett. **97**, 226804 (2006).

[11] A. Zawadowski, J. v. Delft, and D. C. Ralph, Phys. Rev. Lett. **83**, 2632 (1999).

[12] G. M. Alzoubi and N. O. Birge, Phys. Rev. Lett. **97**, 226803 (2006).

Thermal Collapse of Spin-Polarization in Half-Metallic Ferromagnets

M. Ležaić, Ph. Mavropoulos, J. Enkovaara, G. Bihlmayer, S. Blügel

Institut für Festkörperforschung, Forschungszentrum Jülich, D-52425 Jülich, Germany

The temperature dependence of the magnetization and spin-polarization at the Fermi level is investigated for half-metallic ferromagnets. We reveal a new mechanism, where the hybridization of states forming the half-metallic gap depends on thermal spin fluctuations and the polarization can drop abruptly at temperatures much lower than the Curie point. We verify this for NiMnSb by *ab initio* calculations. The thermal properties are studied by mapping *ab initio* results to an extended Heisenberg model which includes longitudinal fluctuations and is solved by a Monte Carlo method.

Half-metallic ferromagnets (HMFs)[1] are ferromagnetic metallic compounds showing, in the ideal case and at zero temperature, a spin polarization of $P = 100\%$ at the Fermi level E_F. This means that the spin-resolved density of states (DOS) shows a metallic character only for one spin direction; the other spin direction behaves like an insulator with E_F inside a band gap. This exotic behavior has inspired research in spintronics, since the extreme spin polarization suggests that HMFs are ideal for inducing and manipulating the transport of spin-polarized electrons. However, it is clear that the ideal half-metallic property ($P = 100\%$) cannot be present at elevated temperatures. Fluctuations of magnetic moments will mix the two spin channels, and at latest at the Curie point, T_C, the spin polarization will vanish together with the magnetization. Thus, for application purposes one seeks HMFs with T_C significantly higher than room temperature, reasonably assuming that the temperature dependence of the spin polarization, $P(T)$, approximately follows the magnetization, i.e., $P(T) \propto M(T)$.[2] Motivated by these considerations, we try to elucidate theoretically the problem of magnetization and spin polarization at $T > 0$.[3]

The decrease of P in the presence of non-collinear fluctuations arises due to three mechanisms: (1) Firstly, the local axis $\hat{e}_{\rm loc}$ of a region with short-range order is in general not parallel to the global magnetization axis $\hat{e}_{\rm glob}$. Thus, there is always a projection of locally spin-up states to the globally spin-down direction in the gap region. (2) Secondly, the spin axis of each atom varies with respect to that of its neighbors, so that spin-up wavefunctions of each atom are partly projected into the spin-down states of its neighbors within the gap. (3) Importantly, there is a hybridization effect (change in hybridization strength), leading to a closure of the gap by shifting the conduction and valence band edges. Fig. 1a shows schematically how the three mechanisms affect the minority-spin DOS.

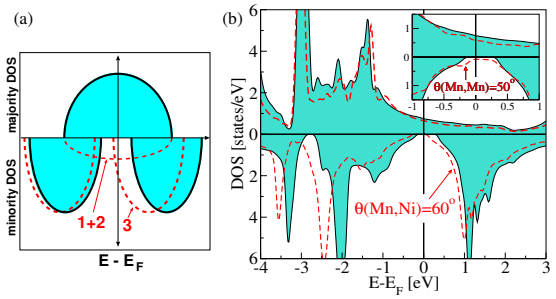

FIG. 1: (a): Modification of spin-down DOS around E_F reducing the spin polarization due to mechanisms (1)–(3) as discussed in text. (b): DOS of NiMnSb in the ground state (full curve) and in the state when the Ni moment has been constrained to an angle of 60° with respect to the Mn moment (dashed curve). Inset: Dashed curve: Mn moments of (001) neighboring layers form an angle of 50° with respect to each other, while the Ni moments are allowed to relax. DOS are projected to the global frame.

We turn now to the NiMnSb compound. We approach the finite-temperature properties within the adiabatic approximation for magnon spectra. We employ the full-potential linearized augmented plane-wave method (FLAPW) [5] within density-functional theory (DFT). In the ground state, the Mn local magnetic moment is large ($M_{\rm Mn} = 3.7\ \mu_B$), while the Ni moment is weak ($M_{\rm Ni} = 0.26\ \mu_B$) and originates mainly from the hybridization of the d orbitals of Mn with the ones of Ni (the same mechanism which opens the gap).[4] Consequently, the Ni moment does not really arise from strong intra-atomic exchange interactions (Hund's rule).

The treatment of the weak Ni moment requires an extension of the traditional Heisenberg model allowing fluctuations of the magnitude of $M_{\rm Ni}$. To this end, the energy needed for constraining the Ni moment is calculated within DFT and fitted by a fourth-order function. At each Ni site i the neighboring atoms, placed at sites j, act as an exchange field $\vec{B}_i = \sum_j J_{ij}\vec{M}_j$ polarizing the Ni atom. The energy expression for the

Ni atom at i includes the magnitude of the local moment M_i and the neighbor-induced polarizing field, and the total Hamiltonian reads

$$H = -\tfrac{1}{2}\sum_{i,j} J_{ij}\vec{M}_i\cdot\vec{M}_j + \sum_{i\in\{\mathrm{Ni}\}}(a\,M_i^2 + b\,M_i^4 - \vec{B}_i\cdot\vec{M}_i). \quad (1)$$

Note that, although the Ni moment is small and resulting from hybridization, a remnant of intra-atomic exchange still exists in Ni, enhancing the on-site susceptibility. This assists the local moment formation and is reflected in the values of a and b. Thus, the system can be regarded as an alloy of a strongly magnetic subsystem (Mn) with a paramagnetic subsystem with Stoner-enhanced susceptibility (Ni). The Monte Carlo calculation according to Eq. (1) yields the sublattice magnetizations $M_{\mathrm{Mn}}(T)$ and $M_{\mathrm{Ni}}(T)$, and the susceptibilities $\chi_{\mathrm{Mn}}(T)$ and $\chi_{\mathrm{Ni}}(T)$, shown in Fig. 2a. Evidently, the overall thermodynamics are governed by the mighty Mn moment. The phase transition is clearly seen by the peak in the susceptibility $\chi(T)$, which grossly coincides with the Mn sublattice susceptibility $\chi_{\mathrm{Mn}}(T)$, yielding $T_{\mathrm{C}} \approx 860$ K (experimental value is $T_{\mathrm{C}} = 730$ K). The surprising feature, however, is the behavior of $M_{\mathrm{Ni}}(T)$ and $\chi_{\mathrm{Ni}}(T)$. Already at 50 K, $M_{\mathrm{Ni}}(T)$ shows a rapid drop and $\chi_{\mathrm{Ni}}(T)$ a corresponding narrow peak. If we exclude the longitudinal fluctuations and work within the traditional Heisenberg model, an unpronounced behavior can be seen (broad maximum in $\chi_{\mathrm{Ni}}^{\mathrm{transv}}(T)$ at around $T = 300$ K). We conclude that the Ni sublattice magnetic order is lost to its great extent. We believe the peak of χ_{Ni} and the drop of M_{Ni} at low T to be connected to the so-far unexplained experimental findings of an anomaly in the temperature dependence of the magnetization and resistivity at approx. 80 K.[6]

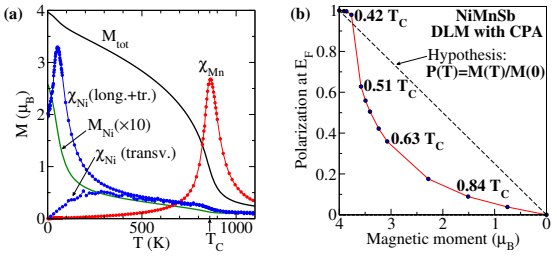

FIG. 2: (a): Monte Carlo results for the T-dependent magnetic properties. The Ni moment M_{Ni} (magnified by a factor 10) drops at 50 K, fluctuating transversely and longitudinally; a susceptibility peak (χ_{Ni}(long.+tr.)) is evident. If only transverse fluctuations are allowed, χ_{Ni}(transv.) has a less pronounced maximum. (b): Polarization at E_F as function of total spin moment for the DLM states NiMn$^{\uparrow}_{1-x}$Mn$^{\downarrow}_{x}$Sb calculated with the CPA.

Since the gap originates from the d-d hybridization between Ni and Mn spin-down states, and since the Ni d states are below E_F for both spin directions, a rotation of the Ni moment causes a hybridization of the Mn d spin-down states partly with the Ni spin-up states and partly with the Ni spin-down states. Consequently, the d-d hybridization remains, but the gap is reduced. The DOS is shown in Fig. 1b, for the case of the Mn moments remaining in a ferromagnetic configuration, while the Ni moments are at a 60° angle relative to Mn (M_{Ni} is reduced to 0.16 μ_B). The reduction of the gap follows from a reduction of the hybridization strength: as the Ni moment is reduced, its spin-down states move lower in energy and hybridize less with the Mn spin-down states. Thus, the spin-down "conduction band" ultimately reaches E_F and half-metallicity is lost. The inset of Fig. 1b shows the state when Mn moments of neighboring layers form an angle of 50° with respect to each other. A protrusion appears just 0.2 eV under E_F. This can cause a collapse of P if the protrusion reaches E_F.

For a quantitative estimate of $P(T)$, we describe the system at $T > 0$ in a mean-field manner via the disordered local moment (DLM) state. A Mn site can have a "down" orientation Mn$^{\downarrow}_{x}$ (opposite to the magnetization) with probability x, or an "up" orientation Mn$^{\uparrow}_{1-x}$. The ferromagnetic ground state ($T = 0$) corresponds to $x = 0$, while T_{C} corresponds to $x = 0.5$. The electronic structure of the DLM state for each x is found within the coherent potential approximation (CPA), utilizing the Korringa-Kohn-Rostoker full-potential Green function method[7] within DFT. This yields the average magnetic moment $M(x)$, and the polarization $P(x)$. We study the DLM states, NiMn$^{\uparrow}_{1-x}$Mn$^{\downarrow}_{x}$Sb, with varying concentration $0 < x < 0.5$. Within this approach, $P(T)$ cannot be directly found, if the explicit connection between x and T (or $M(T)$) is not known. However, one can check the hypothesis $P(T) \sim M(T)$.[2] As shown in Fig. 2b, such a relation does not hold. Instead, from a certain M on, P drops much faster than M. The reason can be traced back to the change in hybridization as x (or T) increases: each Ni atom has on average $4(1-x)$ Mn$^{\uparrow}$ neighbors and $4x$ Mn$^{\downarrow}$ neighbors. The occupied d states of the latter hybridize with the occupied spin-down states of Ni, push them higher in energy and diminish the gap; E_F reaches finally the valence band and P collapses. By approximating of $M(T)$ by the use of the Brillouin function $B_{5/2}$, we assigned the temperature values shown in Fig. 2b. We see that, up to $T = 0.42\ T_{\mathrm{C}}$ (this is about room temperature), $P(E_F)$ remains close to 100%, but then it collapses.

[1] R. A. de Groot *et al.*, Phys. Rev. Lett. **50**, 2024 (1983).

[2] R. Skomski and P. Dowben, Europhys. Lett. **58**, 544 (2002).

[3] M. Ležaić *et al.*, Phys. Rev. Lett. **97**, 026404 (2006).

[4] I. Galanakis *et al.*, Phys. Rev. B **66**, 134428 (2002).

[5] `http://www.flapw.de`

[6] C. Hordequin *et al.*, J. Magn. Magn. Mater. **162**, 75 (1996).

[7] `http://olymp.cup.uni-muenchen.de/ak/ebert/SPR-TB-KKR`

Inversion-Asymmetry Driven Magnetic Spirals at Surfaces Investigated by Electronic-Structure Calculations

M. Heide[1], G. Bihlmayer[1], S. Blügel[1], M. Bode[2], K. von Bergmann[2], P. Ferriani[2], S. Heinze[2], A. Kubetzka[2], O. Pietzsch[2], R. Wiesendanger[2]

[1] Institute "Quantum-Theory of Materials"
[2] Institute of Applied Physics and Microstructure Research Center, University of Hamburg, Germany

At surfaces, and in other geometries with broken inversion symmetry, magnetic structures are subject to an antisymmetric exchange interaction. This Dzyaloshinskii-Moriya interaction favors spiral magnetic structures of a specific handedness. We develop a computational scheme, that allows to estimate the strength of the Dzyaloshinskii-Moriya interaction from first-principles electronic-structure calculations. With the aid of this computational method, we investigate a monolayer of Mn atoms deposited on the W(110) surface and show, that the Dzyaloshinskii-Moriya interaction is indeed strong enough to induce a spiraling magnetic ground state in this system.

In a wide class of magnetic materials, the magnetic structure changes on a mesoscopic length scale and can be described by a continuous vector field $\mathbf{m}(\mathbf{r})$ with $|\mathbf{m}| = \text{const.}$. In the simplest case, $\mathbf{m}$ varies only along one spatial coordinate x and the energy of a magnetic configuration can be described by a simple Landau-Lifshitz functional of the form

$$E_0[\mathbf{m}] = \int \mathrm{d}x \left(A \left(\frac{\mathrm{d}\,\mathbf{m}(x)}{\mathrm{d}\,x}\right)^2 + \mathbf{m}(x)^{\dagger} \cdot \mathsf{K} \cdot \mathbf{m}(x) \right) . \quad (1)$$

Thereby, the spin stiffness A represents the exchange interactions that favor collinear spin alignment, and the symmetric anisotropy tensor K accounts for the preferred orientation of the magnetization with respect to the crystal lattice. The exchange term $A\,(\frac{\mathrm{d}\,\mathbf{m}}{\mathrm{d}\,x})^2$ is symmetric with respect to the rotational direction, i.e. the energy does not depend on the sign of $\frac{\mathrm{d}\,\mathbf{m}}{\mathrm{d}\,x}$. In some systems, however, an additional antisymmetric term of the form

$$E_{\mathrm{DM}}[\mathbf{m}] = \int \mathrm{d}x \left(\mathbf{D} \cdot \left(\mathbf{m}(x) \times \frac{\mathrm{d}\,\mathbf{m}(x)}{\mathrm{d}\,x} \right) \right) \quad (2)$$

has to be included. This term describes the Dzyaloshinskii-Moriya (DM) interaction [1, 2]. Expression (2) implies, that the energies for right- and left-handed spin rotations differ. This can be the case only if the underlying crystal structure does not posses inversion symmetry. Prominent examples for such structures are surfaces and interfaces [3]. Fig. 1 illustrates how a surface can break the symmetry between right- and left-handed spiral magnetic structures.

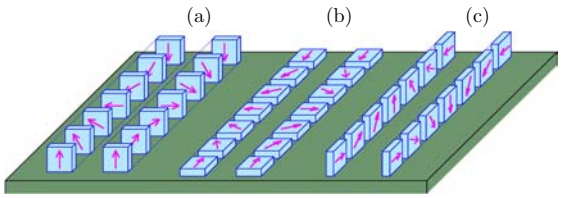

FIG. 1: Spin spirals with different rotation axes on a symmetric surface. For each rotation axis, a right- and a left-handed spiral is shown. For (a) and (b), the right- and left-handed spirals are mirror images of each other. In the case (c), however, the surface breaks the mirror symmetry. Therefore, the two spirals in (c) are not equivalent to each other and may differ in energy.

The DM term competes with the symmetric exchange and the anisotropy energy: The latter terms favor collinear spin alignment, whereas the DM term favors a spatially spiraling magnetic structure of a specific rotational direction. The resulting ground state was already discussed in 1965 for a simplified energy functional [4], but the actual values of the corresponding parameters (in particular the size of $\mathbf{D}$) are still unknown in most cases.

One can expect, that the DM term is of particular importance in atomically thin magnetic films that are deposited on non-magnetic surfaces: In such systems the local environment of all magnetic atoms is inversion asymmetric. On the other hand, such low-dimensional structures usually show a large magnetocrystalline anisotropy that favors collinear spin alignment. We want to find out, to what extent the DM interaction can modify the the magnetic ground state of such systems. For the exemplary system Mn/W(110), we estimate the model parameters (A, $\mathbf{D}$, K) from first-principles, i.e. by electronic-structure calculations in the framework of the density functional theory. We use the FLAPW method as implemented in the Fleur code.

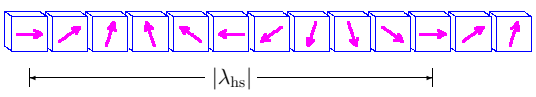

FIG. 2: Homogeneous spin spiral with period length $|\lambda_{\mathrm{hs}}|$. The angle between the magnetization directions of two adjacent lattice sites is constant.

We deduce the values of the spin stiffness A and the size and sign of the $\mathbf{D}$-vector from the electronic energies of homogeneous spin spirals. Such spirals are characterized by a fixed rotation axis and $(\frac{\mathrm{d}\,\mathbf{m}}{\mathrm{d}\,x})^2 = \mathrm{const.}$ (cf. Fig. 2). For these spirals Eqs. (1-2) simplify to

$$\frac{E_0 + E_{\mathrm{DM}}}{|\lambda_{\mathrm{hs}}|} = 4\,\pi\,A\,\lambda_{\mathrm{hs}}^{-2} + 2\,\pi\,D\,\lambda_{\mathrm{hs}}^{-1} + \mathrm{const.}\,, \quad (3)$$

where the integration is performed over one period length $|\lambda_{\mathrm{hs}}|$, the sign of λ_{hs} distinguishes between right- and left-handed spirals, and D depends on the size and orientation of $\mathbf{D}$. The treatment of spirals and other noncollinear magnetic structures is well established within the FLAPW method [5], but in our case the size of the system imposes a problem: Since the DM interaction is weak compared to the main interactions that contribute to the symmetric exchange, it induces only a small deviation from the collinear spin alignment. Thus, we have to consider spirals of very large period lengths. In order to deal with this large magnetic periods, we make use of the fact that spin-orbit coupling (SOC) (that relates the orientation of the magnetic moments to the orientation to the crystal lattice) is small compared to the main interactions that contribute to the symmetric exchange. In a first step we neglect SOC, then the individual lattice sites in a homogeneous spin spiral are all equivalent and we can calculate the spiral's electronic structure within a small unit cell by employing a generalized Bloch theorem [6]. Based on this intermediate results, we add the SOC operator in a perturbative scheme that allows us to estimate the energy corrections due to SOC [7].

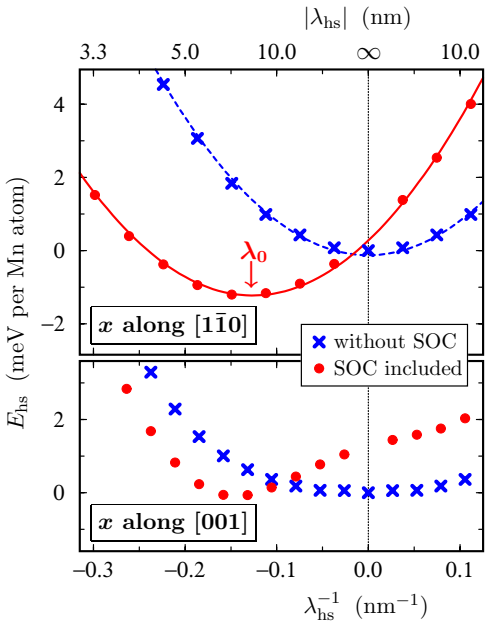

FIG. 3: Electronic energy of a homogeneous spin spiral depending on the period length $|\lambda_{\mathrm{hs}}|$. The sign of λ_{hs} depends on the rotational direction. The data points show the results obtained from the electronic-structure calculations and the lines indicate the fits with the terms of Eq. (3).

In the following, we report on the results of our computational scheme for a monolayer of Mn atoms deposited on the W(110)-surface. The magnetic structure of this system is well studied experimentally by spin-polarized STM. Locally it shows a $\mathrm{c}(2\times2)$-antiferromagnetic structure [8] (this does not conflict in with our ansatz, since the vector field $\mathbf{m}$ in Eqs. (1-2) represents only the spatial modulations on larger length scales). In Fig. 3, the calculated energies are shown for spin spirals propagating along the high-symmetry lines and the rotation axes aligned parallel to the corresponding $\mathbf{D}$-vectors. When SOC is neglected the curves represent the symmetric exchange, whereas the DM interaction and the anisotropy terms are a consequence of the SOC. From the figure, we can directly identify the homogeneous spiral of lowest energy (indicated with λ_0). In order to permit other magnetic structures, we obtain the parameters of Eq. (3) from fits to the calculated data and insert these values in the functionals (1-2). This way, we predict for the system Mn/W(110) a DM-driven left-handed spin spiral propagating along the $[1\bar{1}0]$-direction with a period $|\lambda| = 7.9\,\mathrm{nm}$. Since we are describing an antiferromagnet, the mesoscale magnetic structure shows a period of $\frac{1}{2}\,|\lambda|$. We find nice agreement with a recent experimental result that is presented in Fig. 4.

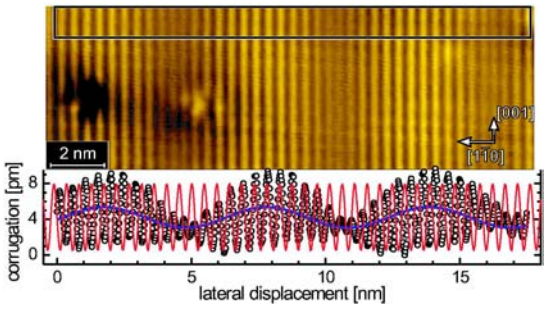

FIG. 4: Magnetic structure of Mn/W(110) imaged with spin-polarized STM. The stripes on the nanometer scale represent the local antiferromagnetic structure. On a larger length scale, however, the image shows a spiral structure that is driven by the DM interaction.

The studied system nicely illustrates the impact, that the DM interaction can have on magnetic structures of low symmetry. Our calculations show, that this interaction is indeed strong enough to compete with the spin stiffness and anisotropy. We expect this interaction to be relevant in a wider class of magnetic nanostructures.

We acknowledge support from DFG, grant BI823/1-1.

[1] I. E. Dzialoshinskii, JETP **5**, 1259 (1957)

[2] T. Moriya, Phys. Rev. **120**, 91 (1960)

[3] A. Fert, Materials Science Forum **59&60**, 439 (1990)

[4] I. E. Dzyaloshinskiĭ, JETP **20**, 665 (1965)

[5] P. Kurz et al., Phys. Rev. B **69**, 024415 (2004)

[6] L. M. Sandratskii, J. Phys. Cond. Mat. **3**, 8565 (1991)

[7] M. Heide, Ph.D. thesis, RWTH Aachen (2006)

[8] S. Heinze et al., Science **288**, 1805 (2000)

Approaching the Ground State of the Kagomé Antiferromagnet

W. Schweika[1], M. Valldor[2]

[1]Institute for Scattering Methods
[2]II. Physikalisches Institut Universität zu Köln

In low dimensions, antiferromagnetic order is suppressed at finite temperatures and geometrical frustration raises the complexity of ground states with finite entropy and non-collinear, chiral spin structures. $Y_{0.5}Ca_{0.5}BaCo_4O_7$ contains kagomé layers of Co ions, whose spins are strongly coupled, with a Curie-Weiss temperature of -2200 K. At low temperature, $T = 1.2$ K, our diffuse neutron scattering study with polarisation analysis reveals characteristic spin correlations close to a predicted two-dimensional coplanar ground state with staggered chirality. The absence of three dimensional long-range antiferromagnetic order indicates negligible coupling between the kagomé layers. The scattering intensities are consistent with high spin $S = 3/2$ states of Co^{2+} in the kagomé layers and low spin $S = 0$ states for Co^{3+} ions on interlayer sites. Our observations agree with previous Monte Carlo simulations indicating a ground state of effectively short range, staggered chiral spin order.

The topology of many crystal structures has an important influence on the collective behavior of interacting magnetic moments. In lattices with triangular networks the antiferromagnetic (AF) coupling between all spins can not be satisfied simultaneously owing to geometrical frustration that strongly reduces the ordering temperature and disturbs the settling of the system into a long range ordered state. A hallmark of frustration is the large degeneracy of complex, non-collinear ground states of finite entropy and the appearance of chiral correlation[1]. According to the Mermin-Wagner theorem [2], in low dimensions, the AF order that would reveal the ground state properties, is suppressed at finite temperatures. The famous two-dimensional kagomé lattice comprises both low dimensionality and geometrical frustration challenging the theoretical understanding of its unusual ground state properties. There are two competing ground states with either uniform or staggered chirality, see Fig. 1.

According to predictions for the classical Heisenberg AF the staggered chiral structure is favored [3, 4], because local zero energy modes, so-called *weathervane* defects which are common spin rotations on hexagons, cause a larger degeneracy. This entropical selection has been termed as the principle of order by disorder [5].

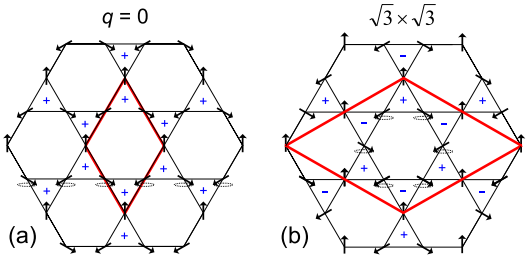

FIG. 1: Infinitely degenerate AF ground states on the kagomé lattice. (a) The q_0-structure with uniform chirality; (b) the staggered chiral structure, which has a larger unit cell by $\sqrt{3} \times \sqrt{3}$. The chirality is denoted by the sign inside the triangles. The dashed ellipses represent thermal fluctuations of zero energy: (a) common spin rotations in an infinite chain; (b) the weathervane defect, a common local spin rotation on a hexagon around the axis of the spins on the edges of the unit cell.

According to MC simulations, domain walls in the staggered chiral structure are moved by *weathervane* defects, which apparently destroys the long-range chiral order [4] and may give rise to residual entropy in analogy to ice [6] and spin-ice systems [7]. However, it is not clear whether the ground state is long-range ordered. We measured the diffuse neutron scattering of polycrystalline $Y_{0.5}Ca_{0.5}BaCo_4O_7$, see Fig.2, on the DNS instrument in Jülich, applying polarization analysis, which allows one to separate the magnetic scattering contribution.

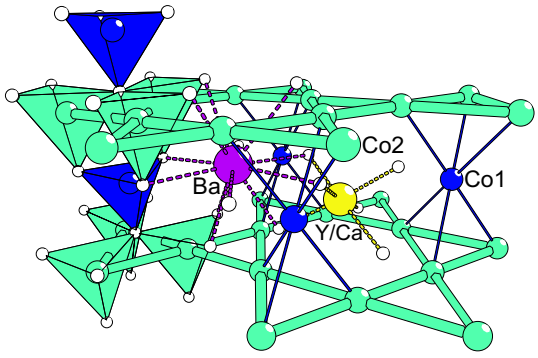

FIG. 2: The $Y_{0.5}Ca_{0.5}BaCo_4O_7$ crystal structure. Thicker bonds between the Co2 atoms highlight the kagomé layers.

At low temperatures, we observed a strong diffuse peak of asymmetric shape indicating low dimensional spin correlations, see Fig. 3. Remarkably, no long-range magnetic order appears even at 1.2 K. The magnitude of the magnetic scattering provides a quantitative estimate of the average magnetic moment of Co. Quantitative agreement is found if Co^{2+} ions (5/8 of all Co) are in high spin state $S = 3/2$ and Co^{3+} ions (3/8 of all Co, located on the interlayer Co1 position) are in low spin state $S = 0$, which rationalizes the absence of any significant interlayer coupling and, hence, the ultimate suppression of 3-D long-range order.

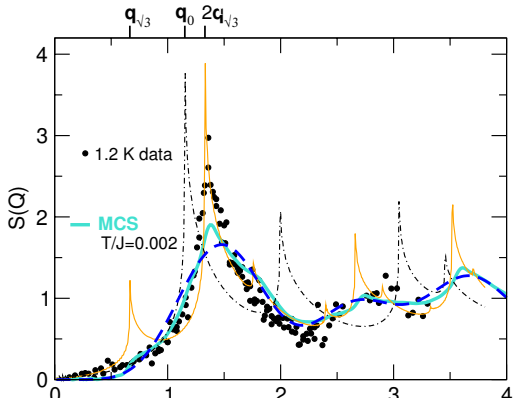

FIG. 3: Modeling of 1.2 K magnetic scattering data (normalized to the scattering of a random spin configuration). (i) power law decay of spin correlations in the q_0 and (ii) $\sqrt{3} \times \sqrt{3}$ structures respectively (dashed dotted black and solid orange lines); (iii) MC data (thick cyan line) for a classical Heisenberg AF at $T/J = 0.002$ [4]; (iv) $weathervane$ model (dashed blue line).

The wave-vector dependence of the diffuse scattering reveals characteristic spin correlations as expected for a $\sqrt{3} \times \sqrt{3}$ ground state, and agree favorably with the classical 2-D MC simulations. The ground state is approached much closer in our experiment than in the MC simulations, although temperature and Curie-Weiss constant of approximately $-2200\,\mathrm{K} \approx 4J$ [8], where J is the exchange energy, match closely the conditions of the simulation, $T/J = 0.002$. This can be understood by the lack of ergodicity in the simulations at low temperature. Both, the data and the MC-simulations do not show a peak at $Q = q_{\sqrt{3}}$ which reveals that the ground state must exhibit a specific type of disorder that can be related to $weathervane$ defects allowing domain wall motion. A modeling of spin correlation for a $weathervane$ hexagon shows the absence of the $q_{\sqrt{3}}$ peak.

Essentially these hexagon spin correlations survive at higher temperatures. However, these zero-energy modes show a fast correlated relaxation as seen in the quasi-elastic broadening at 150 K in Fig. 4. A relaxation rather than tunneling dynamics for the $wheathervane$ modes, even at low T, has been predicted based on a destructive quantum interference phenomenon (vanishing tunneling amplitudes) for $wheathervane$ modes in half integer spin systems [9].

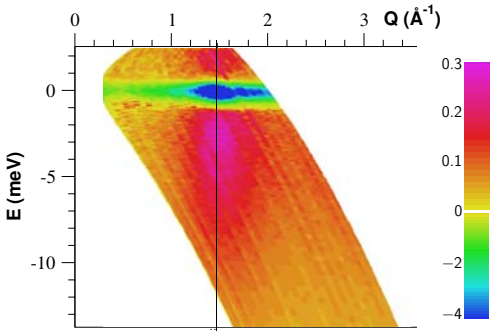

FIG. 4: Quasi-elastic broadening due to thermal spin fluctuations. The difference of S(Q,ω) measured at 150 K and 40 K in time-of-flight mode reveals a loss of elastic intensity (blue) and a relaxation response (red) with a Q-dependence consistent with $weathervane$ modes. The vertical line corresponds to the peak of model (iv) in Fig. 3.

In conclusion, the present neutron scattering study [10] with polarisation analysis on a new compound, realizing the $S = 3/2$ kagomé AF, agrees in surprising detail with the complexity of the ground state of the classical Heisenberg AF for only nearest neighbor interactions. The remarkable survival of only short-range 2D spin correlations at low temperature results from $S = 0$ low spin states of Co^{3+} ions at the interlayer sites, which decouple the kagomé layers. Despite the diverging range of spin correlations when approaching the ground state, the data indicate a short-range nature of chiral spin correlations, where the relevant feature is the $weathervane$ mode of spin hexagons.

[1] R. Moessner and A.T. Ramirez, Physics Today **59**, 24 (2006).

[2] N.D. Mermin and H. Wagner, Phys. Rev. Lett. **17**, 1133 (1966).

[3] D. A. Huse and A. D. Rutenberg, Phys. Rev. B **45**, 7536 (1992).

[4] J. N. Reimers and A. J. Berlinsky, Phys. Rev. B **48**, 9539 (1993).

[5] J. Villain *et al.*, J. Phys. (France) **41**, 1263 (1980).

[6] L. Pauling, *The nature of the chemical bond*, Cornell U. Press, Ithaca, NY (1945).

[7] M. J. Harris *et al.*, Phys. Rev. Lett. **79**, 2554 (1997).

[8] M. Valldor, Solid State Sci. **8**, 1272 (2006).

[9] J. von Delft and C. L. Henley, Phys. Rev. Lett. **69**, 3236 (1992).

[10] W. Schweika, M. Vallldor and P. Lemmens, Phys. Rev. Lett. accepted December 2006.

Magnetic Structure of Multiferroic $TbMnO_3$

J. Voigt, J. Persson, W. Schweika, Th. Brückel
Institute for Scattering Methods

Multiferroic compounds combine two usually uncoupled ordering phenomena in a single material. In the case of $TbMnO_3$, (anti)-ferromagnetic order is coupled to the formation of a ferroelectric polarization. It arises, when the magnetic structure changes its symmetry at $T_c = 28$ K. At this temperature it was assumed that the Tb^{3+} ions order for the first time, while at higher temperature only the Mn^{3+} ions are ordered magnetically. Using an element-specific probe for magnetism, namely resonant magnetic x-ray scattering (RMXS), we are aiming to clarify the magnetic structure of the Tb^{3+} ions.

"The revival of the magneto-electric effect" [1] was triggered strongly by the observation of multiferroic behavior in $TbMnO_3$ [2, 3]. Magneto-electric materials exhibit a strong coupling between magnetic properties, which are e.g. employed for data storage in hard disk drives, and electrical/optical properties. Hence such materials may be used for devices, which are based on a combination of optical and magnetic properties. Unfortunately, a strong magneto-electric effect is rather rare. The conventional mechanisms for ferroelectricity and magnetic order exclude each other. Hence scientist were very excited about the recent observation of a strong magneto-electric effect in $TbMnO_3$ and $TbMn_2O_5$. Moreover, the ferroelectric transition is directly connected to a change in the magnetic structure. In our study we intend to reveal the microscopic mechanism responsible for this unusual behavior.

Recently the magnetic structure has been investigated by neutron diffraction [4]. The authors could model their data by two different magnetic structures, which are schematically shown in Fig. 1. The scheme shows only the magnetic moment of the Mn^{3+} ions. According to this model, the magnetic structure, which coexists with the ferroelectric order, involves the ordering of the Tb^{3+} ions for $T < 28$ K, while only magnetic moments of Mn^{3+} ions are ordered in the 'high' temperature phase 28 K $< T <$ 41 K. To probe the magnetic order element specific, we employed resonant magnetic x-ray scattering at MuCAT beamline of the Advanced Photon source in Argonne, USA.

The resonant scattering process involves virtual transitions from core levels into exchange split valence levels. This process can only appear if the incoming x-ray energy fits the energy difference between both levels.

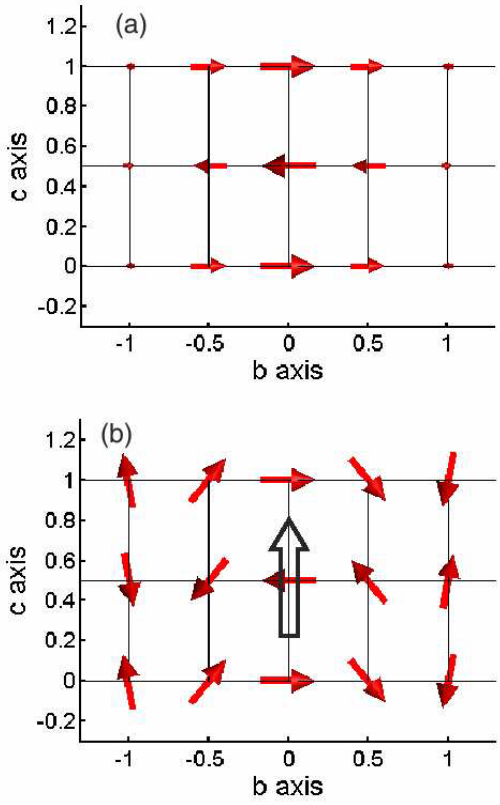

FIG. 1: Supposed scheme of the magnetic structure for the Mn ions as a result from neutron diffraction: (a) 28 K $< T <$ 4 1 K. The magnetic moments are modulated along the $\vec{b}$ direction of the crystallographic lattice. Each magnetic moment points along the $\vec{b}$ direction, too. (b) $T < 28$ K. The scheme shows a chiral magnetic structure with the magnetic moment rotating in the $\vec{b}\vec{c}$ plane. From [4]

Since this difference is specific for each element, the magnetic structure can be probed exclusively for one element. The element specific resonance enhancement is demonstrated in Fig. 2, where the energy dependence of the magnetic Bragg scattering is shown for all relevant absorption edges. Unusual features are observed, such as the pre- and post-edge peaks and a large resonance enhancement at the Mn K edge.

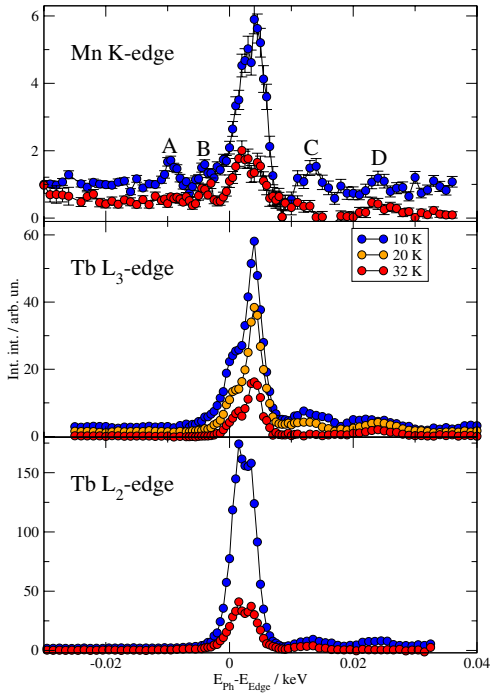

FIG. 2: Energy dependence of the peak intensity (0 q_m 0) for the different absorption edges at different temperatures. The data are corrected for absorption. The zero of the energy scale is given by the point of inflection from the fluorescence at the different absorption edges, respectively (not shown): $E_{Mn,K} = 6.549$ keV, $E_{Tb,L_{III}} = 7.515$ keV, $E_{Tb,L_{II}} = 8.253$ keV.

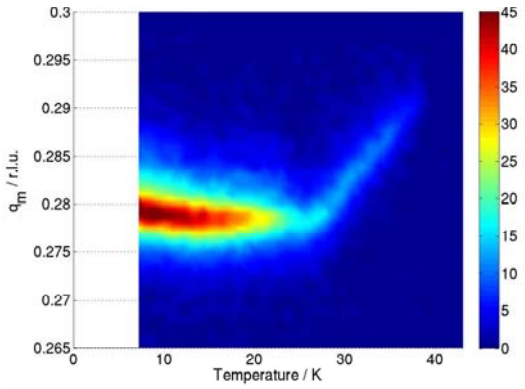

FIG. 3: RMXS at the Tb $\mathbf{L_{II}}$ edge $E = 8.255$ keV as a function of temperature and scattering vector q_m.

In Fig. 3, the intensity of the RMXS is shown as a color plot. The energy was tuned to the Tb $\mathbf{L_{III}}$ absorption edge. Only the spin polarization at the Tb ions contribute to the scattered intensity. The magnetic propagation vector shows a strong temperature dependence above 25 K, indicative of an incommensurate modulated structure. Below 25 K the propagation vector is nearly constant, but a true lock-in to a commensurate structure is not observed. From the width of this magnetic peak, we determine the magnetic correlation length, which remains at a constant value of 0.075(6)μm throughout the entrire temperature range. A comparable value is obtained for the magnetic order of the Mn ions. This shows, that significant magnetic disorder is present in this material as well for the Tb as for the Mn subsystems.

The most surprising observation of our study is the non-vanishing intensity at the Tb edges above 28 K. In Fig. 4 we present the integrated intensity of the RXMS signal. We have recorded the signal not only at the Tb $\mathbf{L_{II}}$ edge, but also at the $\mathbf{L_{III}}$ edge ($E = 7.515$ keV) and the Mn K absorption edge ($E = 6.549$ keV). In all three curves we observe a kink at about $T \approx 25$ K. We could fit all three curves with a model which assumes that the magnetic order of the Mn ions induces a spin polarization in the Tb $5d$ states. Above 25 K the shape of the curves can be described by the same spin quantum number $S = 2$, characteristic for Mn^{3+}. At lower temperatures, additional scattering, described by a angular momentum $J = 6$ is observed at the Tb absorption edges, characteristic for Tb^{3+} ions. We conclude, that below this temperature also the Tb $4f$ magnetic moments are ordered.

To summarize, we have observed element and band specific magnetic order in multiferroic $TbMnO_3$ [5]. In addition to the proposed magnetic structure derived from neutron scattering, RXMS reveales a spin polarization in the $5d$ states of Tb induced by the magnetic order of the Mn ions. These results show the strong interdependence of the electronic states of Mn and Tb ions, which might play a crucial role for the formation of ferroelectricity.

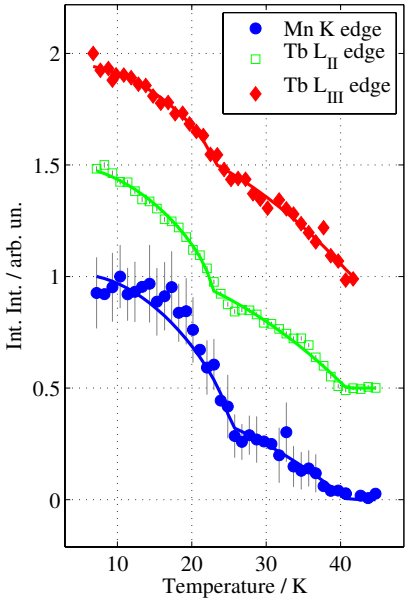

FIG. 4: Integrated intensity of the RMXS at the Mn K edge ($E = 6.549$ keV), the Tb $\mathbf{L_{III}}$ edge ($E = 7.515$ keV) and the Tb $\mathbf{L_{II}}$ edge ($E = 8.255$ keV). The solid lines show a fit to the data.

[1] M. Fiebig, Jour. Phys. D: Appl. Phys **38**, R123 (2005).

[2] T. Kimura *et al.*, Nature **426**, 55 (2003).

[3] T. Kimura *et al.*, Phys. Rev. B **71**, 224425 (2005).

[4] M. Kenyelmann *et al.*, Phys. Rev. Lett **95**, 087206 (2005).

[5] J. Voigt *et al.*, submitted.

Magnetism in Confined Geometry: Magnetic Critical Scattering of MnO Nanoparticles

M. Feygenson [†][1], W. Schweika[1], A. Ioffe[1], Th. Brückel[1], S.B. Vakhrushev[2]

[1] Institut für Festkörperforschung, Streumethoden
[2] A. F. Ioffe Physico-Technical Institute, 194021, St. Petersburg, Russia

We studied the magnetic order and phase transition of MnO nanoparticles embedded in a porous glass by polarized neutron scattering using the DNS-instrument at the research center in Jülich. The nanopores filled with MnO are wormlike structures with a typical diameter of 70Å. From the temperature dependence of the magnetic ($\frac{1}{2}$ $\frac{1}{2}$ $\frac{1}{2}$) Bragg intensity we obtained that for the MnO nanoparticles the phase transition is continuous with a Néel temperature $\mathbf{T_N = 122K}$. This is in contrast to bulk MnO, which exhibits a first order phase transition at $\mathbf{119K}$. Furthermore, we observed that a part of the MnO nanoparticle material remains disordered even at 2K, which indicates frustration at the interface MnO to glass. We interpret the higher $\mathbf{T_N}$ to be due to strain on MnO embedded in nanopores. The continuous character of the transition and the unusual temperature dependence with a reduced order parameter were described and modelled by surface induced disorder.

Confined geometries impose finite size effects and material dependent interactions with interfaces, which may alter the thermodynamic behavior. Wetting phenomena near interfaces maybe observed for instance in alloys and magnets near to order-disorder phase transitions.

We studied the MnO embedded in porous vicor glass matrix. The matrix has random wormlike pores with a narrow size distribution of pore diameters of 70 ± 3Å filled with MnO.

Golosovsky et al. [1] have found in non-polarized neutron powder diffraction a continuous phase transition of such MnO nanoparticles, whereas bulk MnO undergoes a discontinuous order-disorder phase transition. The critical exponents were obtained using the phenomenological approach from the magnetic ($\frac{1}{2}$ $\frac{1}{2}$ $\frac{1}{2}$) Bragg peak. However, due to the strong nuclear background from the glass matrix the critical behavior cannot be studied in enough detail to extract reliable critical exponents.

In our experiment we investigated the temperature dependence of the magnetic ($\frac{1}{2}$ $\frac{1}{2}$ $\frac{1}{2}$) Bragg peak using polarized neutrons with the wavelength of 5.24 Å within the temperature range from 2K up to 130K. An advantage of using polarized neutron scattering with the polarization analysis is that it allows to separate the diffuse magnetic scattering and the large background from the glass matrix. As the reference, the MnO powder was investigated between 11K and 140K with the same setup.

The order parameter as a function of temperate was obtained from the line-shape analysis of the magnetic peaks at different temperatures.

As seen from the Fig.1 the phase transition for MnO nanoparticle becomes continuous at $T_N = 122K$. The magnetic neutron scattering indicated that a part of MnO nanoparticles remains disordered even at very low temperatures, resulting in a flat background. From the peak-to-background ratio at $10K$ we estimated that 61% of atoms inside a MnO nanoparticle remain disordered. This disorder probably comes from interactions of the nanoparticles with glass walls.

The frustration due to broken bonds at the interface can lead to surface induced disorder and may explain why the order parameter of the MnO glass is lower compared to the bulk behavior and resembles a continuous phase transition.

In order to describe the phase transition we used the model of a critical wetting for semi-infinite systems [2] which can be applied to the surface-induced disordering [3]. The model describes a situation when a layer of disordered phase gradually introduces at the surface and penetrates into the bulk. Because of the surface inhomogeneity we use this model instead of the description involving single critical exponents.

The order parameter of a nanoparticle depends on an order parameter in every atomic layer:

$$\Psi = \sum_n N_n \psi_n \qquad (1)$$

where, N_n is the number of atoms in atomic layer n and ψ_n is the order parameter in this layer. Here, we neglect a size distribution of pores because it is extremely narrow.

The order parameter in n-th layer is expressed as [3]

$$\psi_n = \psi_{max} \left[1 + exp\left\{-2\xi_\perp^{-1}(n - \hat{n})\right\}\right]^{-1} \qquad (2)$$

where, n is the number of atomic layer, $\hat{n}$ is the interface position, ψ_{max} is the maximum order parameter of a system (typically equal to 1), $\xi_\perp$ is the interfacial roughness.

For dimensionality $d = 3$ it was found that the critical behavior at the wetting transition depends on the value of dimensionless parameter ω:

$$\omega = k_B T_{cb}/(4\pi\tilde{\Sigma}\xi_d^2) \qquad (3)$$

were, k_B is the Boltzmann constant, $T_{c,b}$ is the phase transition temperature of bulk, $\tilde{\Sigma}$ is the interfacial stiffness between ordered and disordered phase, ξ_d is the correlation length of order parameter fluctuations in the disordered bulk phase.

The interface between ordered and disordered phases behaves differently for the large interfacial stiffness ($0 < \omega \leq 1/2$) and for the small interfacial stiffness ($\omega > 1/2$). The preliminary simulations show that for our system the second condition is fulfilled, therefore [2]:

$$\begin{aligned} \xi_\perp &= \xi_d\sqrt{\omega}\,[ln(1/t)]^{1/2} \\ \hat{n} &= \sqrt{2\omega}ln(1/t) \end{aligned} \qquad (4)$$

where, $t = 1 - T/T_{c,b}$ is the reduced temperature.

In order to fit the measured temperature behavior of the order parameter Ψ the following routine was used.

The number of atoms inside each atomic layers was calculated assuming the cylindrical shape of the MnO nanoparticles with a radius of 35Å. Using this assumption and the lattice constant of MnO bulk (4.44Å) we calculated the number of atoms N_n in every atomic layer. These numbers were constrained to be constants during the fit as well as $\psi_{max} = 1$. We found that within such a nanoparticle there are 8 atomic layers.

The bulk correlation length was fixed to $\xi_d = 2$ lattice units, according to MnO powder neutron measurements of Shull et al [4].

As it was mentioned before 61% of atoms in nanoparticles are disordered due to the possible interaction with glass walls and cannot be described in the frame of the model. Therefore, we excluded three atomic layers from the surface by putting the number of atoms within these layers to zero: $N_{1-3} = 0$.

The bulk transition temperature was obtained from MnO powder measurements $T_{c,b} = 119K$.

Then, only ω parameter was fitted. The best fit is shown in Fig.1 as a solid line.

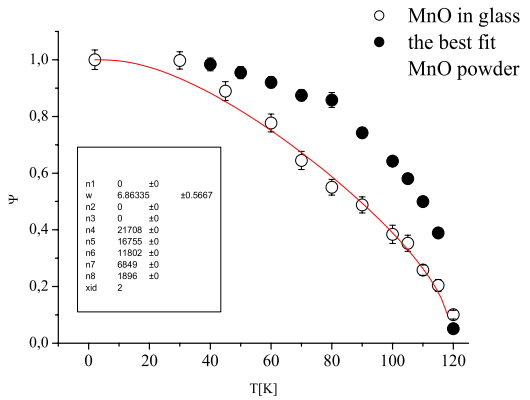

FIG. 1: The order parameter Ψ for MnO powder (filled circles) and MnO nanoparticles (open circles) as a function of temperature. The solid line represents the best fit for MnO nanoparticles (see text for details)

The overview of parameters used in the fit is given in inset of Fig.1.

We found $\omega = 6.8 \pm 0.57$ which indicates a relatively smooth interface between order and disordered phases as it was expected for $\omega > 1/2$. Using this value we reconstructed the profile of the order parameter ψ_n in every layer (see Fig.2).

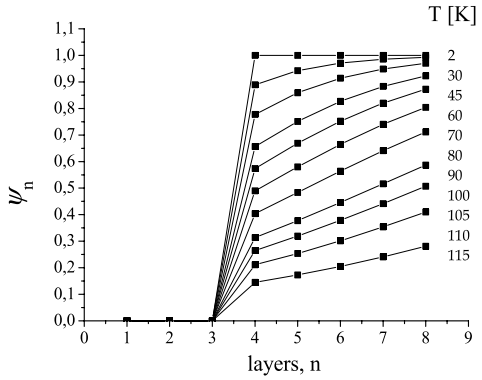

FIG. 2: The order parameter ψ_n in every atomic layer.

In conclusion, we have shown that surface induced disorder can explain the observed continues phase transition for MnO nanoparticles over the whole temperature range using a single free parameter related to the interface stiffness of the Mn spins in MnO.

[†] Present address: Institut für Festkörperforschung, Forschungszentrum Jülich GmbH, D-52425 Jülich

[1] Golosovsky et. al., Phys.Rev.Lett. 86 (2001)

[2] Lipowsky, Ferroelectrics 73(1987)

[3] Schweika et. al., Phys.Rev.B 53, 8937 (1996)

[4] C.G.Shull et.al., Phys.Rev. 83 (1951) 333

Magnetic Anisotropy Energies of Metal-Benzene Sandwiches

N. Atodiresei, Y. Mokrousov, G. Bihlmayer, S. Blügel

Institut für Festkörperforschung, Quanten-Theorie der Materialien

We report on ab initio calculations of the electronic and magnetic properties of metal-benzene sandwiches $\mathbf{M_n(C_6H_6)_m}$ $(\mathbf{M = V, Nb, Ta})$ and infinite wires based on the density functional theory (DFT). Due to increasing influence of the spin-orbit interaction on the magnetic properties, as going from V to Ta, a significant increase of the magnetic anisotropy energy (MAE) in the molecules is observed. In particular, an infinite Nb-benzene wire is predicted to change its ballistic conductance upon changing of magnetization direction (ballistic anisotropic magnetoresistance). The origin of the peculiar magnetic properties of the molecules is analyzed, and new possible technological applications are proposed.

The newest developments in ultra-high density magnetic recording aiming at non-volatility, low energy consumption and short access times for reading and writing rely on the miniaturization of the structures used in modern nanotechnology. Current technologies using nanostructured magnetic materials made of layered inorganic solids[1] will reach at some point the limit of nanopatterning, which motivates the search for completely new approaches. Molecular magnets moved to the frontier of research as ideal candidates for the smallest possible magnets. In designing molecular magnets several requirements should be fulfilled: beside a ferromagnetic coupling of local magnetic moments, a significant magnetic anisotropy energy (MAE) is requested. Crucial for practical applications, this quantity, arising predominantly from the spin-orbit coupling (SOC), gives an estimate for an energy barrier necessary to stabilize the magnetic order against quantum tunneling and thermal fluctuations. In this paper we focus on one-dimensional (1D) magnetic organometallic sandwiches @ S molecules, exhibiting large MAE and the recently proposed ballistic anisotropic magnetoresistance (BAMR) effect[2], which opens a vista for new device concepts in spintronics due to the change of the ballistic conductance upon changing the magnetization direction.

Several experimental and theoretical studies have been performed on magnetic sandwiches formed by V and benzene, $V_nBz_m(Bz = C_6H_6)$. Stern-Gerlach type magnetic deflection experiments[3] on V_nBz_{n+1} $(n = 1, 2, 3, 4)$ complexes suggest the increase of magnetic moment with the number of V-atoms in the molecule indicating that the magnetic moments of the V-atoms couple ferromagnetically. Synthesis, infrared spectroscopy and electric dipole measurements on MBz (half-sandwich) and $M(Bz)_2(M = Nb, Ta)$ compounds have also been reported[4].

Method. We performed calculations within the framework of the density functional theory (DFT) in the generalized gradient approximation (GGA-PBE). We employed a realization of the full-potential linearized augmented plane-wave method for one-dimensional-systems (1D-FLAPW). Single molecules were calculated using unit cells repeated exclusively along the symmetry axis (z-axis). The z-axis of the system points through the V atoms and the centers of gravity of the C_6H_6 molecules.

Geometry. Our calculations show that stable structures of these molecules are sandwiches with the metal atom above the center of gravity of C_6H_6 molecules, as was also confirmed by other theoretical and experimental investigations[3]. For all sandwiches the planarity of the outer C_6H_6 molecules is broken with the planes of C and H hexagons parallel but slightly shifted relative to each other along the z-axis.

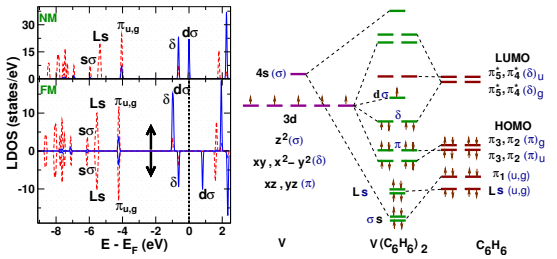

FIG. 1: Left: Local densities of states (LDOS) for the $V(C_6H_6)_2$: LDOS at the carbon site (dashed line) and LDOS at the vanadium site (full line); the upper part shows the nonmagnetic (NM) densities of states and the bottom part shows the spin-polarized ferromagnetic (FM) DOS with spin-up and spin-down channels indicated by arrows. Right: schematic orbital interaction scheme for $V(C_6H_6)_2$.

Electronic Properties. Insight into the mechanisms responsible for the bonding in the molecules $M_n(C_6H_6)_m$ can be gained on the basis of a schematic analysis of the orbitals of metal and benzene which are classified in terms of the pseudoan-

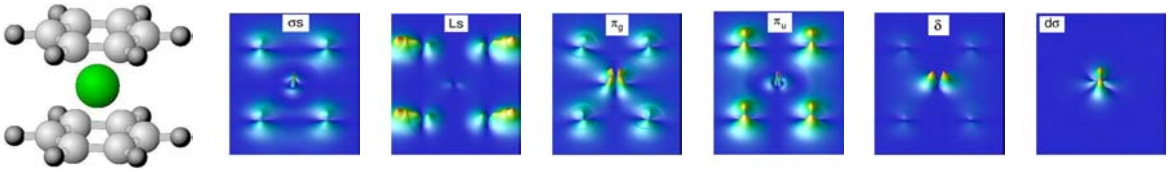

FIG. 2: Charge density plots in a plane cutting the vanadium and four carbon and hydrogen atoms for the electronic states of $V(C_6H_6)_2$. The plots are labeled by the names of the states as indicated in Fig. 1 (left).

gular momenta around the z-axis. The five $3d$-orbitals of the metal atom can be divided according to their symmetries into one $d\sigma\,(d_{z^2})$, two $d\pi\,(d_{xz}, d_{yz})$, two $d\delta\,(d_{x^2-y^2}, d_{xy})$ and a $4s$ orbital classified as $s\sigma$ orbital. The six π-orbitals of C_6H_6 form one $L\sigma\,(\pi_1)$, two degenerate $L\pi\,(\pi_2, \pi_3)$ (HOMO), two degenerate $L\delta\,(\pi_4^*, \pi_5^*)$(LUMO) and one $L\phi\,(\pi_6^*)$ orbital. When the benzene molecules and metal atoms are brought together, the HOMO and LUMO orbitals of C_6H_6 interact with the metal d orbitals (3d, 4d, 5d) of the same symmetry and hybridization occurs (see Fig. 1, 2).

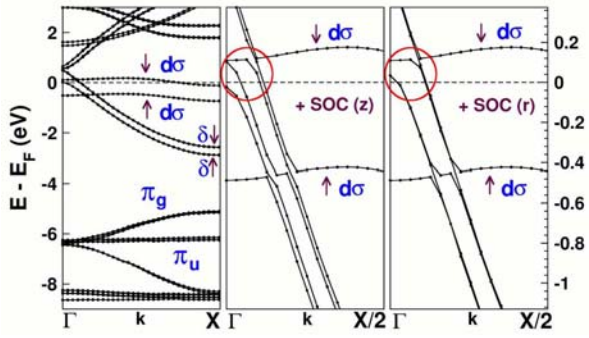

FIG. 3: (a) Calculated electronic band structure in the 1D Brillouin zone for an infinite wire, $(NbBz)_\infty$, with the spin-up and spin-down bands indicated by arrows, in (a) the absence of spin-orbit coupling, in (b) the presence of SOC with the spin-quantization axis along the z-axis, z, and in (c) the plane of the benzenes, r. The $(NbBz)_\infty$ wire shows a ballistic anisotropic magnetoresistance[2] with a change of the ballistic conductance upon the change of the magnetization direction.

Magnetic Properties. We found that all the $V_nBz_{n+1}(n = 1, 2, 3, 4)$ molecules and the infinite wire $V(C_6H_6)_\infty$ are magnetic with a large gain in total energy compared to the nonmagnetic solution (see Table 1 in Ref. [5]) is also the case for the compounds MBz and $(MBz)_\infty$, $(M = Nb, Ta)$, isoelectronic to V. For the V_nBz_m complexes the magnetic moments of the V-atoms are strongly localized for $n, m = 1, 2$, while for $n > 2$ a delocalization of the $d\sigma$ orbitals (dz^2-symmetry type) along the z-axis occurs with the corresponding redistribution of the spin density among V-atoms. For the molecule with $n = 1, 2, 4$ and in the infinite wire $(VBz)_\infty$, ferromagnetic (FM) ordering is preferred to the antiferromagnetic (AFM) one. For the double-sandwich ($n = 2$) the difference in energy between FM and AFM solutions is 3 meV, while for $n = 4$ it constitutes already 31 meV, reaching the value of 57 meV in the infinite wire. The molecule with $n = 3$ has an antiferromagnetic ground state with the total magnetic moment of $1\mu_B$, which is consistent with the experimental value at 56K[3]. By including the spin-orbit coupling in the total energy calculations we considered two possible symmetry-determined directions of the magnetization in the molecules and wires: along the z-axis (z), and radial, parallel to the plane of the benzenes (r). The magnetic anisotropy energy (MAE) is defined as a total energy difference between these two configurations. It is well-established, that systems on the nanoscale can reveal large values of MAE due to the unquenching of the orbital moments and strong tendency towards magnetism resulting from the lack of the nearest neighbors. We find, that for the V_nBz_m compounds the MAE is quite small (50 eV) for $n, m = 1, 2$ and increases by two orders of magnitude for $n > 2$ accompanied by a change in the magnetization direction for large n. These values of the anisotropy barrier, however, can still be easily overcome due to magnetic field or vibrations of the molecules. Furthermore, our calculations show, that substituting V atoms with the heavier Nb and Ta leads to a substantial increase in the values of MAE up to 7 meV for a TaBz half-sandwich, which would result in a stable superparamagnetic regime already at 100K . It is important to realize, however, that desired significant values of the magnetor esistance anisotropy are a consequence not only of the electronic structure at the Fermi energy, but also of a large spin-orbit splitting of the bands. We observe, that for a NbBz infinite wire a lucky combination of the two happens (Fig. 3). Significant spin-orbit splitting of the σ-bands at the Fermi energy leads to the fact that the number of states crossing the Fermi level is different for two different magnetization directions allowing to manipulate the conductance in the system with the means of an external magnetic field. This is the effect known as the ballistic anisotropic magnetoresistance (BAMR)[2], experimental realization of which opens a road for many possible spin-dependent transport applications.

[1] S. Maekawa, T. Shinjo, Spin dependent transport in magnetic Structures, London (2002).

[2] J. Velev et al., Phys. Rev. Lett. **94**, 127203 (2005).

[3] K. Miyajima et al., (a) J. Am. Chem. Soc., **126**, 13202 (2004); (b) Eur. Phys. Jour. D **34(1-3)**, 177 (2005).

[4] J.T. Lyon et al., Phys. Chem. A, **109**, 431 (2005).

[5] Y. Mokrousov, N. Atodiresei, G. Bihlmayer, S. Blügel, Int. J. Quant. Chem., **106**, 3208 (2006).

Interfacial Magnetization in Exchange-Coupled Fe/Cr/Fe Structures

A. A. Rzhevsky[1,2], D. Bürgler[1], B. B. Krichevtsov[2], C. M. Schneider[1]

[1]Institut für Festkörperforschung IFF-9, Forschungszentrum Jülich, 52425 Jülich, Germany,
[2]Ioffe Physical Technical Institut, Russian Academy of Sciences, 194021 St. Petersburg, Russia

Magnetic interlayer coupling is a crucial ingredient in building complex magnetic structures. Depending on the coupling strength, the magnetic properties of the participating layers, and the applied magnetic field, a wide variety of magnetic configurations may arise. We addressed this issue by means of magnetic optical second harmonic generation (MSHG) in the model system Fe/Cr/Fe. We clearly observe the field-induced transformations of the magnetic state at the interfaces in the trilayer in the SHG signal. The strong variations of the SHG signal with light polarization, experimental geometry (longitudinal or transversal), and in-plane orientation of the magnetic field H can be understood on the basis of a model accounting for nonmagnetic and magnetic contributions to SHG from the interfaces, as well as for changes of the interfacial magnetization orientation.

The interaction between the magnetizations $\mathbf{M_1}$ and $\mathbf{M_2}$ in magnetic films separated by a thin paramagnetic or diamagnetic metallic layer is characterized by the presence of bilinear ($E_{bl} = -J_1\hat{\mathbf{M}}_\mathbf{1}\hat{\mathbf{M}}_\mathbf{2}$, where $\hat{\mathbf{M}}_\mathbf{i}$ is a unit vector along the magnetization direction of layer i) or biquadratic ($E_{bq} = -J_2(\hat{\mathbf{M}}_\mathbf{1}\hat{\mathbf{M}}_\mathbf{2})^2$) interlayer exchange coupling [1]. Depending on the interlayer thickness bilinear coupling might lead to ferromagnetic ($\mathbf{M_1} \uparrow\uparrow \mathbf{M_2}, J_1 > 0$) or antiferromagnetic ($\mathbf{M_1} \uparrow\downarrow \mathbf{M_2}, J_1 < 0$) magnetzation orientations. The biquadratic exchange coupling stimulates an orthogonal orientation of the magnetizations ($\mathbf{M_1} \perp \mathbf{M_2}, J_2 < 0$). To date the magnetic properties of such coupled structures have been mainly addressed by such methods as ferromagnetic resonance, Brillouin light scattering, magnetoresistance, and magnetooptical Kerr effect [1]. All of these methods reflect the behavior of the volume-averaged magnetization $\mathbf{M_1}$ and $\mathbf{M_2}$ in the coupled layers. At the same time the interfacial magnetizations play important role in bilinear and biquadratic coupling formation. Therefore, investigations of the interfacial magnetization by specific interface-sensitive techniques are of particular interest.

For this purpose, we studied the interfacial magnetization in exchange coupled heterostructures Fe/Cr/Fe by magnetic-field-induced second harmonic generation (MSHG). The method is proved to be a highly sensitive tool to probe surface and interfacial magnetic properties of thin films and multilayers [2]. Epitaxial heterostructures Fe(50 Å)/Cr(10 Å)/Fe(100 Å)/Ag(1500 Å)/Fe(10 Å)/GaAs(100) grown by MBE served as model systems. To prevent the structure from the oxidation it was covered by a 20 Å Cr cap layer. The thickness (d=10 Å) of the Cr spacer layer corresponds to the first antiferromagnetic maximum of the $J_1(d)$ dependence [3]. Thus, in the absence of a magnetic field the system assumes a ferrimagnetic structure ($\mathbf{M_1} \uparrow\downarrow \mathbf{M_2}, \mathbf{M_1} > \mathbf{M_2}$). The structure displays biaxial in-plane magnetic anisotropy, with the easy and hard axes in the Fe layers pointing along [100] and [110]-type directions, correspondingly. The second harmonic generation was excited by short ($\sim$ 200 fs) light pulses from a Ti:Sapphire laser at $E_{ph} = 1.55$ eV. The measurements have been performed in reflection at the incidence angle of 5°. The magnetic field variations of SHG have been studied at room temperature in pp, ss, ps, and sp combinations of the light polarizations with magnetic field applied along the easy or hard axis in longitudinal (magnetic field is applied parallel to light incident plane) or transversal (magnetic field is applied perpendicular to light incident plane) geometries. The linear magneto-optical Kerr effect (MOKE) has also been measured in longitudinal geometry at light incidence angle of 35°.

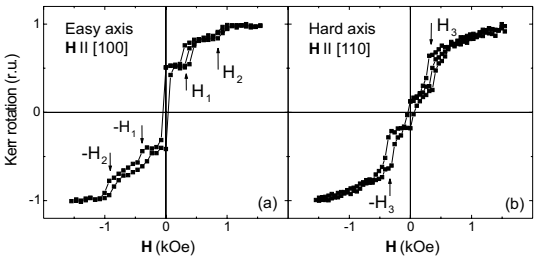

FIG. 1: Field variations of the normalized longitudinal magneto-optical Kerr effect measured in a Fe/Cr/Fe structure with the magnetic field along easy (a) and hard (b) axes.

In Fig. 1(a,b) and Fig. 2(a-d) field dependencies of the MOKE and MSHG are presented. The MOKE curves are odd functions in $\mathbf{M}$. The jump-like features appearing at certain values of the applied field ($\pm H_1, \pm H_2$ and $\pm H_3$) may be associated with magnetic switching events involving different mutual

orientations of the layer magnetizations shown in Fig. 3(a,b). For example, when $\mathbf{H}$ is applied along the easy axis (comp. Fig. 1(a) and Fig. 3(a)) at $H \approx 0$ the inversion of the magnetization directions in the layers takes place, while at H_1 and H_2 the transitions into the orthogonal ($\mathbf{M_1} \perp \mathbf{M_2}$) and saturated states ($\mathbf{M_1} \| \mathbf{M_2} \| \mathbf{H}$) take place.

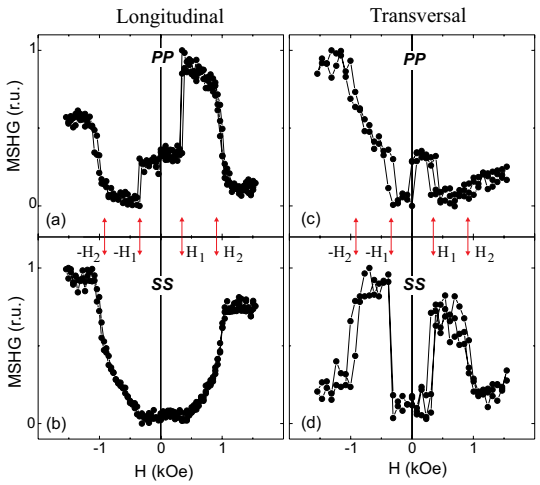

FIG. 2: Field variations of the normalized MSHG signal measured on a Fe/Cr/Fe structure at magnetic field along the easy axis in longitudinal (a,b) and transversal geometries (c,d) for different combinations of light polarizations, as indicated.

The field-induced variations of MSHG signal Fig. 2(a-d) principally differ from those in MOKE. In particular, in longitudinal pp (a) and ss (b), as well as in transversal ss (d) combinations of the polarizations the jump near $H = 0$ is absent. In the ss configurations the MSHG signals are even functions of the magnetic field, while in the pp configurations they have no defined parity. The difference in the field variations of MOKE and MSHG is due to the fact that MOKE probes mainly the bulk response, whereas MSHG originates from the interfacial magnetizations.

The linear on $\mathbf{M}$ contribution to SHG arises from an interference of light waves at frequency 2ω caused by magnetic field-dependent and independent components in the nonlinear optical susceptibility tensor χ [4]. To describe the MSHG response we employed the effective susceptibility model accounting for the surface and the Cr/Fe(1), Fe(1)/Cr and Cr/Fe(2) interfaces as possible sources of SHG. The validity of the model is based on the assumption that all interfaces have the same C_{4v} point symmetry, rendering the structure of χ the same for different interfaces. The model assumes the field-induced changes of the magnetic states at the interfaces to take place analogously to that in the bulk of the films (see Fig. 3) and the magnetic properties of the interfaces formed by the first and second iron layers to be identical. The intensity of the SHG signal accounting for a mutual orientation of interfacial magnetizations can be written:

$$I^{2\omega}_{\alpha\beta} = A|r^1_{\alpha\beta\gamma} m_{1\gamma} + r^2_{\alpha\beta\gamma} m_{2\gamma} + r_{\alpha\beta}|^2, \qquad (1)$$

where A is a parameter depending on the intensity of the fundamental light, $\mathbf{m_1}$ and $\mathbf{m_2}$ are interfacial magnetizations of the first and second iron layer, α and β are indices meaning s or p depending on the light polarization, and $\gamma = x, y, z$. The coefficients $r_{\alpha\beta}$, $r^1_{\alpha\beta\gamma}$ and $r^2_{\alpha\beta\gamma}$ are effective nonlinear susceptibilities.

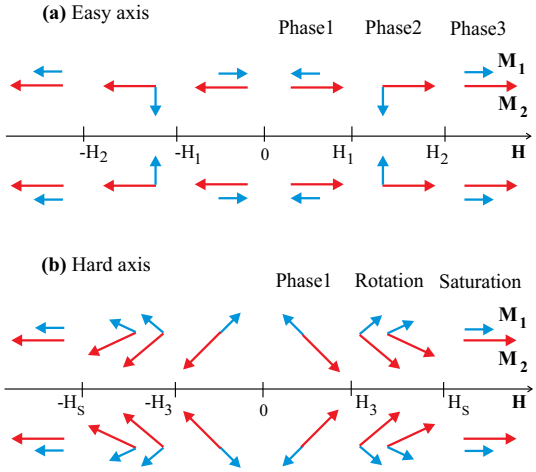

FIG. 3: Magnetic configurations arising during magnetization reversal with the field applied along easy (a) and hard (b) axis, respectively. The energetically equivalent states are shown above and below field axis.

Such an approach describes the salient features of the MSHG experiment. The comparison of the experimental and modelled field variations shows that using different combinations of input and output light polarizations and directions of the magnetic field (longitudinal or transversal) gives a possibility to independently investigate the magnetization components of $\mathbf{m_1}$ and $\mathbf{m_2}$ at the interfaces. We also find that the magnetization rotation processes appear much more pronounced in MSHG than in MOKE, and MSHG is able to clearly resolve magnetic switching events in the trilayer, which are not seen by linear Kerr effect [5].

[1] D. E. Bürgler, P. Grünberg, S. O. Demokritov, and M. T. Johnson, "Interlayer exchange coupling in layered magnetic structures", in Handbook of magnetic materials, Vol. **13**, edited by K. H. J. Buschow (Elsevier Science, 2001).

[2] A. Kirilyuk and Th. Rasing, J. Opt. Soc. Am. B **22**, 148 (2005).

[3] C. M. Schmidt, D. E. Bürgler, D. M. Schaller, F. Meisinger, and H.-J. Güntherodt, Phys. Rev. B **60**, 4158 (1999).

[4] K. H. Bennemann, J. Magn. Magn. Mat. **200**, 679 (1999).

[5] A. A. Rzhevsky, D. Bürgler, B. B. Krichevtsov, C. M. Schneider, Phys. Rev. B **75**, 144416 (2007).

Influence of MgO Overlayers on the Electronic States of bct Co(001)

F. Matthes[1], M. Müller[1], C. M. Schneider[1], L.-N. Tong[2], C.-L. Deng[1], and C.-G. Lee[3]

[1]Institut für Festkörperforschung IFF-9 "Elektronische Eigenschaften"
[2]Inst. Mat. Sci. Engin., Anhui University of Technology, Ma-An-Shan, 243002, Anhui, China
[3]School of Nano and Advanced Materials Engineering, Changwon National University, Changwon, Korea

Magnetic tunnel junctions involving single-crystalline MgO barriers and Co-based ferromagnetic electrodes exhibit very large spin-dependent tunneling effects at room temperature. This technologically very important effect is attributed to specific details in the band structure of Cobalt in the bcc structural modification. Little is known yet about the electronic states at the interface between Cobalt and MgO, which should crucially influence the spin-dependent transport properties. In order to shed light on the interfacial electronic properties in this system, we have performed spin-polarized photoemission experiments on bct-Co(001) films covered by MgO overlayers of various thicknesses. Beside a strong reduction of the spectral weight originating from the minority Δ_5 band in the photoemission spectra, we find that the electronic structure of the bct-Co films is not altered by stoichiometric MgO overlayers.

Spin-dependent transport mechanisms are at the heart of spinelectronic functionality, as they provide a control of the flow of the polarized charge carriers by means of the magnetic state of the electrodes. The most popular spin transport effects, which are already being exploited in commercially available devices are giant magnetoresistance (GMR) and tunneling magnetoresistance (TMR) [1]. Recently, an epitaxial single-crystalline model system – Fe/MgO/Fe – has attracted great attention due to its very high magnetoresistance effect [2, 3]. The origin of the high TMR ratio in MgO-based single-crystal magnetic tunneling systems is attributed to a coherent spin-polarized tunneling process, involving a particular matching of the Δ_1 symmetry electronic states in the ferromagnet and the tunneling barrier. In this context the electronic structure of the entire magnetic tunneling junction (MTJ) including the spin properties at the interfaces between the ferromagnetic electrode and the oxide barrier plays an important role. However, the nature of the electronic states in the electrode and at the interface, and their role on the spin-polarized tunneling process is not well understood yet. Therefore, we have started a program addressing the interfacial ground-state electronic properties of MgO-based TMR systems by means of spin-polarized, angle-resolved photoelectron spectroscopy. In the following, we focus on the Co/MgO(001) system. Theoretical calculations performed by Zhang and Butler [4] predicted TMR values for bcc-Co based MTJ's that significantly exceed those in the Fe/MgO/Fe system.

Besides theoretical predictions, there are to our knowledge, no experimental band structure data available in literature that can give experimental evidence for the electronic structure of bcc Co(100) and its possible changes introduced by a MgO overlayer.

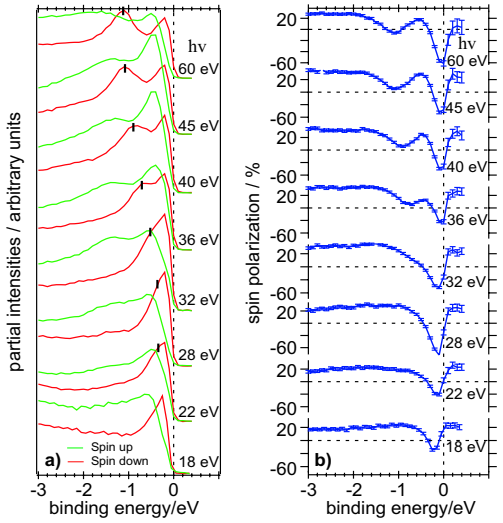

FIG. 1: Spin-resolved photoemission spectra for the 8 ML bct-Co film for different photon energies. (a) Partial intensities with majority (green) and minority spin character (red). (b) Corresponding intensity asymmetry spectra (blue).

The spin- and angle-resolved photoemission experiments were performed at the undulator beamline U-125-1 PGM at BESSY (Berlin). The measurements were carried out in magnetic remanence with the p-polarized light impinging under $45°$ to the surface normal. Analyzing only the photoelectrons along the surface normal, the non-relativistic dipole selection rules allowing direct transitions from initial bands with Δ_1 and Δ_5 spatial symmetry are exploited. In a first step, we determined the dispersion of the electronic states of the uncovered Co-film for a wide range of photon energies $h\nu$, covering the $\Gamma - \Delta - \mathrm{H}$ line in the Brillouin zone.

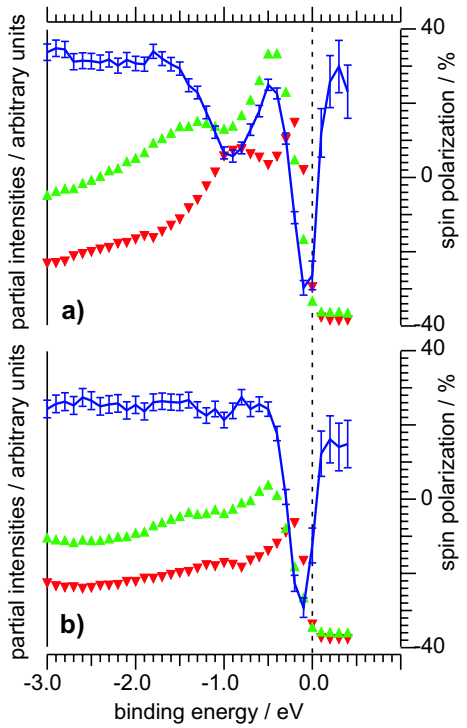

FIG. 2: Comparison of spin-polarized photoemission from a clean Co film (a) to that from a film with a MgO overlayer (b). Given are the spin polarization distribution (blue, right scale), and the majority (green) and minority spin (red) partial intensities (left scale).

From the measured total intensity the spin polarization (Fig.1b) and the spin-resolved intensity contributions (partial intensities) of spin-up (majority spin) and spin-down character (minority spin) can be determined. The dispersion of these spectral features is interpreted on the basis of a calculated electronic band structure for bct-Co, the structural parameters (a=0.287 nm, c=0.2793 nm) being taken from [5]. For the calculation we employed the Munich SPRKKR package [6]. On this basis in the minority channel of the photoemission spectra we can identify the dispersion of the $\Delta_5^\downarrow$ band (marked by vertical bars in Fig.1a). The band intersects the Fermi level for transitions at 22 eV excitation energy and approaches Γ at 60 eV, having a binding energy of -1.1 ± 0.2 eV. This band dispersion is accompanied by a pronounced minimum in the spin polarization spectra of the detected photoelectrons. The distinct appearance and dispersion of the $\Delta_5^\downarrow$ band indicates that the 8 ML Co film has indeed a three-dimensional electronic structure. Another pertinent feature is the majority spin peak around -0.8 eV below E_F arising from the $\Delta_1^\uparrow$ initial state band.

For the central issue of the study, the pronounced minority spin peak at -0.2 ± 0.2 eV binding energy is of further importance. Scanning the excitation energy does not lead to noticable peak dispersions within our energy resolution, but the spin polarization spectra display a minimum of -55 % spin polarization at 60 eV excitation energy. This minority spin feature at E_F, however, does not have a direct counterpart in the band structure of bcc-Co (lattice constant a=0.282 nm), because of a band gap in the $\Delta_1^\downarrow$ band. Theoretical calculations for tetragonal distorted bcc Co move this band closer to E_F, having its maximum located only 0.1 eV above Fermi energy with small contributions even below E_F. We also note that depending on the underlying structure and also to some extend on the growth conditions different values for the tetragonal distortion have been reported in literature. It is clear that altered lattice parameters lead to a shift of the individual band positions. The important finding in our studies is the occurrence of $\Delta_1^\downarrow$ band contributions at E_F. This may strongly influence the achievable TMR values, because the spin dependent tunneling conductivity can be increased in the case of antiparallel alignment of the Co electrodes, if the $\Delta_1^\downarrow$ band shifts below the Fermi level.

In the presence of an ultrathin MgO overlayer, the spin-resolved spectra change in a distinct manner, an example being given in Fig. 2 for $h\nu = 40$ eV. On the one hand, we note that the photoelectrons are still significantly polarized, i.e. the bonding at the Co/MgO interface does not significantly affect the magnetism in the interfacial Co layers. The same is found for the other photon energies as well. On the other hand, the spectral shapes change significantly. The spectral weight originating from direct transitions of initial $\Delta_5^\downarrow$ minority band is suppressed when compared to all other peaks in the photoemission spectra. This phenomenon is clearly reflected in the spin polarization spectra of the measured photoelectrons. Fig. 2 shows that the minimum located at -1.0 eV is smeared out upon coverage with MgO. We reported an analogue effect for transitions originating from $\Delta_5^\downarrow$ minority band in the case of bcc Fe/GaAs(001) upon coverage with MgO [7]. The origin of the selective suppression is still under discussion. It cannot be excluded yet, that the introduced changes are only relevant for processes occurring only during photoelectron emission. More information on this topic may be found in Ref. [8].

[1] I. Zutic, J. Fabian and S. D. Sarma, Rev. Mod. Phys. **76** (2004) 323.

[2] S. Yuasa, A. Fukushima, T. Nagahama, K. Ando, and Y. Suzuki, Jpn. J. Appl. Phys., Part 2 **43** (2004) L588.

[3] S. S. P. Parkin, C. Kaiser, A. Panchula, P. M. Rice, B. Hughes, M. Samant, and S.-H. Yang, Nat. Mater. **3** (2004) 862.

[4] X.-G. Zhang and JW. H. Butler, Phys. Rev. B **70** (2004) 172407.

[5] S.K. Kim, C. Petersen, F. Jona, and P.M. Marcus, Phys. Rev. B **54** (1996) 2184.

[6] H. Ebert, The Munich SPR-KKR package, version 2.1, http:// olymp. cup.uni-muenchen.de/ak/ebert/SPRKKR.

[7] F. Matthes, L.-N. Tong, and C. M. Schneider, J. Appl. Phys. **95** (2004) 7240.

[8] F. Matthes, M. Müller, C. M. Schneider, L.-N. Tong, C.-L. Deng, C.-G. Lee, Phys. Rev B. 73 (2006) 214401.

Magnetooptics in the XUV Regime

H.-Ch. Mertins[1], S. Valencia[2], P. M. Oppeneer[3], S. Cramm[4], C. M. Schneider[4]

[1]University of Applied Sciences Münster, D-48565 Steinfurt, Germany
[2]BESSY GmbH, D-12489 Berlin, Germany
[3]Department of Physics, Uppsala University, S-75121 Uppsala, Sweden
[4]Institut für Festkörperforschung IFF-9, Forschungszentrum Jülich, 52425 Jülich, Germany

The fast progress in the field of modern magnetism and the challenges brought about by spin-electronics ask for new characterization methods. Of particular importance are all-optical techniques, as they are compatible with high magnetic fields. We show that by accessing the shallow core levels of a ferromagnet in a resonant manner, large magnetooptical effects both in transmission and reflection can be observed in the extreme ultraviolet (XUV) spectral range. This XUV-magnetooptics forms the missing link between the magnetooptic effects in the visible and the soft and hard X-ray resonant magnetic scattering (XRMS) phenomena.

Magneto-optical (MO) spectroscopies using polarized high-energy photons [1] allow element selective studies due to the specific energies of the absorption edges, which are characteristic for every element. In addition, a resonant enhancement of the transition probabilities at the absorption edges occurs, which leads to MO responses exceeding those in the visible range by orders of magnitude. These features explain the recent popularity of x-ray MO spectroscopies. Currently exploited techniques are the well-known x-ray magnetic circular and linear dichroisms [2], resonant magnetic reflectometry, but also more mundane phenomena such as the x-ray Voigt [3] and Faraday effects [4]. These MO effects appear in various geometries and modes such as transmission, reflection or absorption. The size of the MO response relates both to the spin-orbit (SO) and exchange (EX) interactions of the electronic states involved in the optical transitions.

Up to now, most of the magneto-x-ray spectroscopic work focused on the $2p$ absorption edges of the $3d$ transition metals. Here the SO-coupling causes the $2p_{3/2}$ and $2p_{1/2}$ states to split by Δ_{SO}∼13-16 eV, which is larger than the EX-interaction of the 3d valence states (Δ_{EX}∼1-2 eV), and much larger than the EX-interaction of the $2p$ core levels (Δ_{EX}∼0.3-0.9 eV). At more weakly bound (shallow) core levels e.g., at the $3p$ states, however, the SO-splitting is reduced by about a factor of ten, while the EX-splitting of the 3p states increases, making these interaction energies comparable (∼1 eV). Thus, accessing the shallow core levels resonantly by extreme ultraviolet (XUV) light promises sizable MO effects paired with elemental selectivity.

In the following, we will demonstrate the kind of magneto-optical effects that can be observed in this spectral range. The experiments have been carried out on magnetic thin films of Co in the photon energy range of $h\nu$∼40-80 eV, using the BESSY reflectometer [5] and linearly polarized light delivered by the U-125/PGM undulator beamline at BESSY (Berlin).

The first experiment addresses the magneto-optical Faraday effect in a 50 nm thick Co film. As the Faraday effect requires a transmission geometry, the film was sputter-deposited on a 100 nm Si_3N_4 membrane and covered by a 3 nm Al cap layer. When the light passes through the film, the Faraday effect will cause a magnetization-dependent rotation of the polarization plane of the light φ_F, as well as a change in ellipticity ϵ_F. In a polar geometry this may be simply described by a complex index of refraction $n_\pm$ for two circularly polarized eigenmodes of the linearly polarized light

$$n_\pm = 1 - (\delta \pm \Delta\delta) + i(\beta \pm \Delta\beta) \qquad (1)$$

the subscript $+(-)$ referring to a parallel (antiparallel) alignment of photon helicity and magnetization direction of the sample. The real part ($\delta \pm \Delta\delta$) describes the dispersion, while the imaginary part ($\beta \pm \Delta\beta$) contains the absorption. The effect of the magnetization is contained in the respective MO constants $\Delta\delta$ and $\Delta\beta$, being nonzero for magnetized ferromagnets.

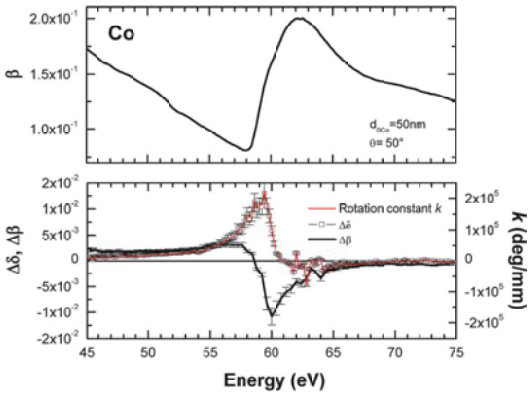

FIG. 1: Absorption and MO constants obtained for the Ni 3p edge. Top: absorption constant β. Bottom: MO constants $\Delta\delta$, $\Delta\beta$ and Faraday rotation constant k.

The results obtained from the Faraday effect measurements are displayed in Fig. 1. The top panel clearly shows the strong variation of the absorption β across the energy position of the Co $3p$ core level caused by the resonant excitation. The Faraday rotation and ellipticity can be determined by means of a multilayer polarization analyzer implemented into the reflectometer. In principle, from φ_F and ϵ_F one can directly calculate the magneto-optical constants. However, we have to consider the fact that thin films have their easy axis of magnetization in the film plane due to the shape anisotropy. Therefore, in a simple polar geometry the wave vector $\vec{k}$ of the incident light would be perpendicular to the magnetization and the effect will vanish. Instead, we have to incline the sample by an angle Θ_i to generate a magnetization component along $\vec{k}$. This leads to a slightly more elaborate analysis procedure, which yields $\Delta\delta$. The quantity $\Delta\beta$ is then obtained via Kramers-Kronig transformation.

For an incidence angle of $\Theta_i = 50°$ the MO constants $\Delta\delta$ and $\Delta\beta$ are displayed in the bottom panel of Fig. 1. We clearly see that both quantities exhibit peak values at the position of the absorption edge and more or less vanish further away from the edge. This proves that the MO response is directly related to the resonant excitation of the $3p$ level into the unoccupied density of states below the vacuum level. As expected, the peak position of $\Delta\delta$ differs slightly from that of $\Delta\beta$. The quantity $\Delta\delta$ is also directly related to the Faraday rotation constant k as $\Delta\delta = k\lambda/(2\pi)$. The peak value of k reaches 1.5×10^5 deg/mm, which is about one order of magnitude higher than the values known for the visible range. This result proves that even in the case that spin-orbit and exchange interaction are of comparable magnitude, strong magneto-optical effects show up. For further details, the reader is referred to Ref. [6].

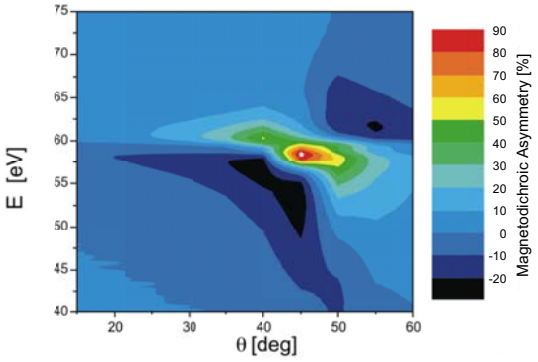

FIG. 2: Variations of T-MOKE signal (magnetodichroic asymmetry A_T) from a 50 nm thick Co film as a function of photon energy E and angle of incidence Θ. The color code gives the magnitude of A_T.

In the second experiment we employ a reflection geometry. For this purpose a similar Co thin film system was prepared on a SiO_2 template. Also in this experiment we have to fulfill a certain geometrical relationship to access the magnetooptical effects. We have therefore chosen the electric field vector of the incident light to be parallel to the scattering plane, whereas the magnetization vector of the sample is perpendicular to this plane. This is also known as transverse Kerr geometry, giving rise to the transverse magneto-optical Kerr effect (T-MOKE). A particular feature of the T-MOKE in the visible regime is that the magneto-optical response shows up directly as an intensity modulation in the reflected beam, due to the influence of the metal optics. Therefore, no polarization analyzer is needed to measure the T-MOKE signal.

Exactly the same behavior is found in the XUV regime. In Fig. 2 we display the entire angular and photon energy dependence of the T-MOKE signal, which in this experiment is defined as the normalized intensity difference between opposite magnetization directions M_+ and M_-

$$A_T = [I(M_+) - (M_-)]/[(M_+) + (M_-)]. \quad (2)$$

As we have already seen in the Faraday effect above, the data in Fig. 2 show that the magneto-optic response peaks as a function of the photon energy in a narrow interval related to the resonant excitation of the $3p$ level. Moreover, the T-MOKE signal exhibits also a very pronounced angular dependence, taking maximum values at around $\Theta_i = 45°$, corresponding to the Brewster angle of the system. We should note that close to the Brewster angle, the intensity of the reflected beam is reduced by 4 orders of magnitude as compared to the specular reflection. Nevertheless, in this region the T-MOKE signal may easily reach a magnetization-induced variation of close to 100%. It can therefore be conveniently employed, for example, to measure element-selective hysteresis loops in magnetic thin film systems. As the wavelength of the XUV radiation is at least one order of magnitude higher than the individual layer thickness in functional magnetic layer stacks, which is in the nm-range, the angular variations of the T-MOKE signal from such structures is much less complicated by multiple-diffraction effects.

[1] H. C. Mertins, S. Valencia, A. Gaupp, P. M. Oppeneer and C. M. Schneider, Appl. Phys. A **80**, 1011 (2005).

[2] J. Stöhr and H. Siegmann: Magnetism (Springer-Verlag, Berlin, 2006).

[3] H. C. Mertins, P. M. Oppeneer, J. Kuněs, A. Gaupp, D. Abramsohn and F. Schäfers, Phys. Rev. Lett. **87**, 047401 (2001).

[4] [9] H. C. Mertins, F. Schäfers, X. Le Cann, A. Gaupp and W. Gudat, Phys. Rev. B **61**, R874 (2000).

[5] F. Schäfers, Appl. Opt. **38**, 4074 (1999).

[6] S. Valencia, A. Gaupp, W. Gudat, H.-Ch. Mertins, P. M. Oppeneer,D. Abramsohn and C .M. Schneider, New J. Phys. **8**, 254 (2006).

Observing Ultrafast Magnetization Dynamics

S. R. Woodford, A. Bringer, and S. Blügel

Quanten-Theorie der Materialien, Institut für Festkörperforschung, Forschungszentrum Jülich

In order to understand ultrafast magnetization dynamics, experiments must yield not only a qualitative description, but also quantitative information. We theoretically investigate the measurement of magnetization dynamics using ultrashort light pulses. By solving the Maxwell's equations for a variety of experimental parameters, we determine experimental conditions under which quantitative analysis of the magnetization dynamics is possible. Furthermore, we highlight the difficulties that will be faced if these conditions are not met.

Increasing the speed at which data may be written or recovered is one of the challenges to the ever-increasing speed of computation. One of the most promising ultrafast methods is the "inverse Faraday effect", where circularly polarized light provides an effective magnetic field, that switches the magnetic state [1]. This effect, which uses ultrashort light pulses of around 50fs duration, is a nonresonant effect; the light is not absorbed, meaning that the system does not need any cooling-down time between writing cycles (which causes significant delays in other optical switching methods). However, as with many ultrafast magnetization experiments, it is difficult to estimate the strength of the effect, since a quantitative analysis of the experimental results is lacking.

The difficulty inherent in measuring ultrafast magnetization dynamics is essentially due to their ultrafast nature. That is, experiments must be able to resolve dynamics on scales shorter than 1ps; conventional magnetization measurements are unable to achieve this. At present, only optical measurements are able to resolve this timescale, since it is possible to generate laser pulses with a time-width of less than 50fs. Since the interaction of light with magnetization is indirect (that is, the magnetization affects the dielectric properties of the material, which in turn affect the light), the interpretation of optical measurements is quite imprecise. For this reason, optical experiments have never been seriously considered as a quantitative measure of magnetization. We have been working to correct this deficiency. Specifically, we have considered a quantitative analysis of the Faraday effect, in which linearly polarized light passes through the medium (which is transparent) and we measure the emergent polarization ellipse.

The difficulty of constructing a quantitative theory was hinted at above. The interaction between light and magnetization is indirect. As the magnetization vector changes (in the case of Ref.[1], $\mathbf{m}$ oscillates in time), the dielectric properties of the material change. For a complete theory, we need to accurately know all the changes that occur, and determine how these changes affect the passage of light through the medium. The changes to the dielectric tensor have proved to be difficult to ascertain accurately [2].

There is one case in which the Faraday effect is very simple to assess. That is the case of an isotropic paramagnet. In this case, an external magnetic field produces a magnetization in the sample, which affects the off-diagonal elements of the dielectric tensor. In this case, the incident linearly polarized light decomposes into equal quantities of right- and left-circularly polarized eigenmodes, which propagate with different speeds. When these emerge, their phase relation has changed due to the differing phase velocities, and they recombine to form linearly polarized light with a rotated polarization axis. The angle of rotation is linearly proportional to both the magnetic field and to the thickness of the sample, with a coefficient that is independent of the sample geometry or size. If this coefficient is known, we could measure an unknown magnetic field using this method (although it is certainly not the easiest method of doing so).

However, the orthoferrites (which are the materials considered in [1]) are neither isotropic nor paramagnetic. (Paramagnets would be of little use for magnetic storage!) They are orthorhombic crystals, which have a weak ferromagnetic order. The orthorhombic nature of the crystal means that the optical eigenmodes travelling along one of the crystal axes are linearly polarized, with the polarization axis along one of the crystal axes. These two modes propagate at different speeds, even in the absence of magnetization; this is known as optical birefringence. The weak ferromagnetism is caused by the presence of two inequivalent magnetic sublattices, which couple antiferromagnetically. Since the sublattices are not identical, the antiferromagnetism is not complete and there is a residual magnetic moment. The inequivalence of the magnetic sublattices has the additional feature that the light couples to both the magnetic moment and the antiferromagnetic moment, which is a further complication.

Parameters describing the effect of the ferromagnetic and antiferromagnetic moment on the dielectric tensor have been determined previously [2]. Generally, these are known to very low accuracy; however, the relationship between the magnetization and the dielectric tensor is known qualitatively.

Using the qualitative relationship, we have solved Maxwell's equations for linearly polarized light travelling along one of the crystal axes. In general, the emergent light is rotated and elliptically polarized, with both of these features exhibiting a complicated dependence on both the sample thickness and the initial angle between the polarization axis and the crystal axes. Optical birefringence makes the rotation periodic in the sample thickness. (The rotation may even vanish for certain sample thicknesses.) This means that errors are magnified, since a small change to the argument of a periodic function may change the value of the function by an order of magnitude (or even make it change sign). Therefore an accurate estimate for the magnetization requires almost perfect values for all the optical constants. In addition to this, we have found that if the angle between the incident light's polarization axis and the crystal axis is not taken into account, estimates may be wrong by several orders of magnitude. Certainly, our results have shown that under general experimental conditions, there is no chance of obtaining a reliable estimate for the magnetization dynamics.

However, we have found that under certain circumstances, a quantitative theory is possible [3]. This makes use of the fact that even in equilibrium, light will be rotated, due to the equilibrium ferromagnetic moment m_0 . Therefore we may determine a reference angle of rotation, β_0 , which may be measured extremely accurately. Assuming that β_0 is not extremely small, and also assuming that the incoming light is polarized along one of the crystal axes, we find the formula

$$\frac{\beta - \beta_0}{\beta_0} = -\zeta \frac{m - m_0}{m_0}. \qquad (1)$$

Here, β is the measured angle, $m = |\mathbf{m}|$ is the magnetization (we assume the direction coincides with that of the equilibrium magnetization), and ζ is a parameter that measures the effect of the antiferromagnetic moment relative to the ferromagnetic moment. For dysprosium orthoferrite (used in Ref.[1]), ζ is known to about 50% accuracy: $\zeta = 0.23 \pm 0.13$ [2]. However, this is the only significant source of error in eq.(1), and will certainly not change estimates of m by an order of magnitude. We should note also that (1) does not rely on $\frac{m-m_0}{m_0}$ being small. Eq.(1) has been derived assuming that the system is close to magnetic equilibrium, but since the magnetic order is dominated by the antiferromagnetic vector, values of m such as $m = 2m_0$ or $m = 0$ may be considered as "near equilibrium".

In short, we have shown that the Faraday effect may only be used to make a quantitative estimate of magnetization dynamics provided the equilibrium sample causes a measurable (and not too small) rotation, and provided the incident light has its polarization axis accurately aligned along a crystal axis. Under these conditions, Faraday rotation provides a reasonably accurate estimate of the magnetization dynamics. We hope that our work will stimulate further experiments to determine ζ more accurately, which will then allow the Faraday effect to become an accurate quantitative measure of magnetization on an ultrafast timescale.

[1] [A.V. Kimel, A. Kirilyuk, P. A. Usachev, R. V. Pisarev, A. M. Balbashov and Th. Rasing, Nature **435**, 655 (2005)

[2] A.V. Zenkov, B. B. Krichevtsov, A. S. Moskvin, K. M. Mukimov, R. V. Pisarev and M. M. Ruvinshtein, Sov. Phys. JETP **69**, 792 (1989)

[3] S. R. Woodford, A. Bringer and S. Blugel, J. Appl. Phys. **101**, 053912 (2007)

Dynamic Properties of Arrays of Ferromagnetic Rectangular Bars

Roman Adam[1], Riccardo Hertel[1], Yuri Khivintsev[2], Robert Camley[2], Zbigniew Celinski[2] and Claus M. Schneider[1]

[1] Institute of Solid State Research, Research Center Jülich, D-52425 Jülich, Germany
[2] Center for Magnetism and Magnetic Nanostructures, University of Colorado at Colorado Springs, Colorado 80918

A detailed understanding of the magnetization dynamics is a crucial requirement for the design of future high frequency devices based on magnetic materials. Possible high-frequency applications include magnetic recording, current-induced microwave generation and switching, domain wall- and spin-manipulation, and spin-wave logic. We present an analysis of the magnetization dynamics in patterned Permalloy (Py) and Cobalt (Co) films subjected to a continuous microwave pumping and, alternatively, to a picosecond magnetic pulse excitation. We employed these two experimental techniques to study the dynamics in our ferromagnetic systems in the regimes of driven oscillations and free relaxation.

Fabrication. Our structures are fabricated on top of GaAs/LT-GaAs substrates. First we pattern a set of coplanar waveguides (CPW) by lift-off of a 200 nm thick Au film prepared by thermal deposition. CPWs designed for the time-resolved measurements contain a metal-semiconductor-metal photoconducting switch for magnetic pulse generation. After the CPW completion we pattern the arrays of rectangular bars with 1:2 and 2:1 aspect ratios and dimensions ranging from 4 $\times$ 8 μm^2 to 75 $\times$ 150 μm^2 on top of the central CPW lines.

Experimental Results.
To measure the high-frequency behavior of the small ferromagnetic bars in the regime of driven oscillations we employ Network Analyzer Ferromagnetic Resonance (NA-FMR) measurements. The samples are first placed in static magnetic field aligned along the CPW lines. Then we apply a continuous microwave field with the driving frequency continuously increasing up to $\sim$ 20 GHz. The resulting peak in the frequency dependence of the FMR absorption corresponds to the natural precession frequency of the ferromagnetic system tested.

Fig.1a shows FMR measurements on 100 nm thick Py bars oriented with their long axis perpendicular and parallel to the static magnetic field. Changing the bar orientation from the perpendicular to the parallel results in an increase of the resonant frequency by up to $\sim$ 2 GHz, as well as a linewidth broadening by 0.3-1 GHz.

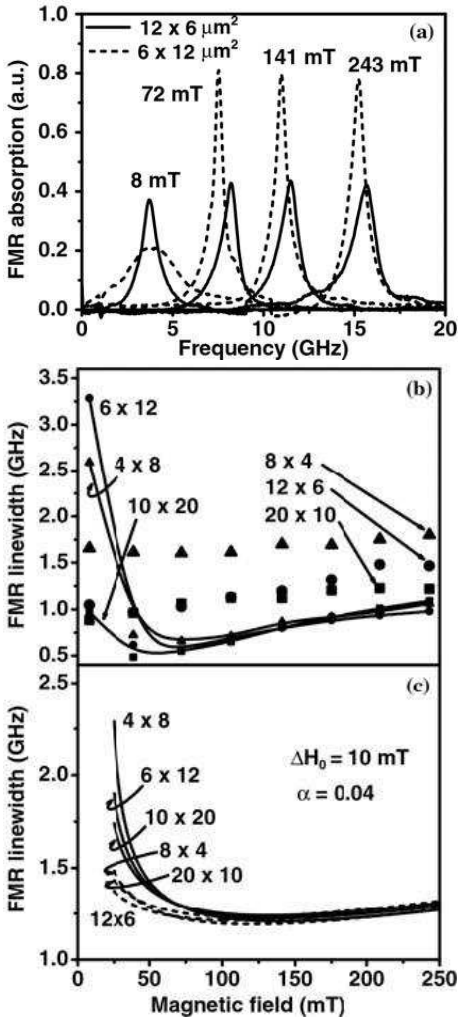

FIG. 1: FMR measurements on arrays of Py bars. Resonance frequency as a function of field (a); 12 $\times$ 6 μm^2 indicates a bar with long axis (12 μm) parallel to the static magnetic field. Field dependence of linewidth from experiment (b), and field dependence of linewidth from theory (c).

The observed frequency shift is in reasonable agreement with calculations of the ferromagnetic resonant frequency ω in an external static field H_0 obtained from Kittels formula[1] taking into account the difference of demagnetizing factors for the two alignments, and assuming a synchronized response of non-interacting ferromagnetic bars. The FMR linewidth

$\Delta\omega$ of the bars with the long axis perpendicular to the static field is narrow at high fields and broadens markedly in small fields (Fig.1b). The bars with their long axis parallel to the applied field have a much flatter response. The general behavior of the linewidth as a function of magnetic field corresponds reasonably to calculations[2], as shown in Fig.1c, except that the experimental linewidths for the bars with long axis parallel to the applied field are much larger than expected from the theory. It still must be clarified whether the effect is due to film growth, patterning or due to an effect not included in the calculations.

To understand the high-frequency behavior of the ferromagnetic bars in the regime of free oscillations we employ pulsed time-resolved magneto-optic Kerr effect (TR-MOKE) experiments. We place our ferromagnetic arrays in the static magnetic field and apply a train of $\sim$ 10 ps long magnetic field pulses perpendicular to the static field orientation. Pulses are generated by the LT-GaAs photoconductive switch excited by 120-fs short laser pulses. The synchronized linearly polarized probe beam is then reflected from the surface of ferromagnetic structures. The polarization state of the probe beam corresponds to the instantaneous average magnetization of the structures. We acquire the temporal evolution of the magnetization by varying the time delay between the excitation and the probe pulses.

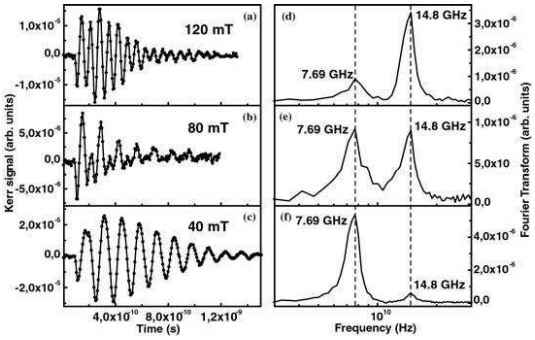

FIG. 2: Experimentally measured TR-MOKE signal corresponding to 40 mT, 80 mT, and 120 mT static magnetic fields (a)-(c), and Fourier transforms of the corresponding time resolved traces (d)-(f).

Oscillatory transient signals are displayed in Figs.2a-c and the corresponding Fourier transforms (FT) are shown in Figs.2d-f. The amplitude of oscillations during the first few oscillation cycles in Figs.2a and Figs.2c shows a gradual increase followed by a field-dependent exponential decay. The decreasing signal envelope is the measure of the system relaxation time. Contrary to the FMR measurements, the power spectrum maxima show not only one, but several pronounced oscillatory modes and strongly nonlinear amplitude dependence with increasing magnetic field. We ascribe the latter observations to the energy transfer between the oscillatory modes in varying static magnetic field.

To explain the TR-MOKE data we apply micromagnetic modeling to simulate the magnetization dynamics in a thin rectangular 400$\times$200$\times$1.5 nm^3 cobalt element subjected to the Gaussian-shaped $\sim$10 ps magnetic pulse.[3,4] The inset of Fig.3 shows the time evolution of the average out-of-plane magnetization component $< m_z(t) >$ of the bar following the pulse excitation. Similar to TR-MOKE measurements, the power spectrum of the calculated response displays several distinct maxima (Fig.3). We used windowed back-transformation of the simulated $< m_z(t) >$ response into real space to identify the modes corresponding to the power spectrum maxima. The simulations show that the main high- and low-frequency maxima arise due to the oscillatory modes at the center and at the borders of the bar, respectively. Snapshots corresponding to the oscillatory modes are shown at the top of the Fig.3.

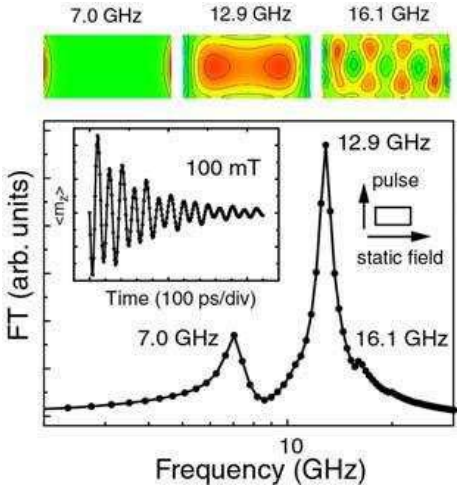

FIG. 3: Fourier transform of the calculated $< m_z(t) >$. Oscillatory modes corresponding to the power spectrum maxima are shown at the top of the figure.

In conclusion, we performed NA-FMR and TR-MOKE experiments to test the magnetization dynamics in Permalloy and Cobalt ferromagnetic arrays in the regimes of the driven and free oscillations. The frequency shift observed in FMR with changes in orientation of the bars is consistent with the shift due to the demagnetization factors, and the linewidth behavior can be qualitatively accounted for by employing the calculations including field dependence of the FMR resonant frequency. Time-resolved measurements reveal the presence of multiple oscillatory modes within the rectangular structures. We employed micromagnetic simulations to reproduce main features of the TR-MOKE signal and to identify the oscillatory modes in the pulse excitation regime.[5]

[1] Kittel, Ch. *Phys. Rev.*, **1948**, 73, 155.

[2] Kuanr, B.; Camley, R. E.; Celinski, Z. *Appl. Phys. Lett.* **2005**, 87, 012502.

[3] Brown, W. F. Jr. **1963**, *Micromagnetics, Wiley Interscience, New York, London.*

[4] Hertel, R.; Wulfhekel, W.; Kirschner, J. *Phys. Rev. Lett.* **2004**, 93, 257202.

[5] Adam, R.; Khivintsev, Y.; Hertel, R.; Schneider, C. M.; Hutchison, A.; Camley, R.; Celinski, Z. *J. Appl. Phys.* **2007**, 101, 09F516.

Magnetization Dynamics of Vortex-Antivortex Annihilation Processes

Riccardo Hertel, Sebastian Gliga, Claus M. Schneider

Institute of Solid State Research (IFF-9), Research Center Jülich, D-52425 Jülich, Germany

The study of dynamic magnetization processes in nanoscale magnets on the picosecond time scale is currently a very active field of research; important for both fundamental physics and for future applications of nanomagnets in spin-electronic devices. A typical topological object occuring in magnetization structures of thin-film nanomagnets is a vortex, where the magnetization circulates in the film plane around a core region with perpendicular magnetization. The static and dynamic properties of magnetic vortices have been studied intensively by several groups over the last years. The so-called antivortex is the counterpart of a magnetic vortex, which has a similar magnetic structure. A vortex and an antivortex can annihilate when they meet. By means of micromagnetic finite-element simulations we have investigated the dynamics of annihaltion processes of vortex-antivortex pairs in a Permalloy thin-film element of 100 nm size and 10 nm thickness. The results show that the relative orientation of the magnetization in the core of the vortex and the antivortex (being either parallel or antiparallel) has a drastic impact on the dynamics of the annihilation process. In the antiparallel case, the annihilation occurs via a sudden, burst-like emission of spin waves ("exchange explosion"). With this study we obtained a detailed description of a previously unexplored fundamental process in nanomagnetism. The annihilation of vortex-antivortex pairs as studied here has recently been proposed as a sub-process for a new mechanism to switch magnetic vortex cores.

Soft-magnetic thin-film elements tend to form magnetic flux-closure domain patterns, like the well known Landau domain structure [1]. Such flux-closure patterns contain an interesting region of only a few nm in size where the magnetization direction circulates by 360° around one point. These magnetic vortices have attracted much attention over the last years, since they have particular static [2, 3] and dynamic properties [4, 5]. It has been predicted theoretically and demonstrated experimentally [2, 3] that the core region of a magnetic vortex displays a magnetization direction perpendicular to the film plane, known as the vortex polarization. The antivortex is a structure similar to the vortex, in the sense that the magnetization direction in the film plane changes by 360° on a closed loop around one point, however with a different "winding number" (see below). The core of the antivortex is perpendicularly magnetized, as it is the case for a vortex. Fig. 1 schematically shows the structure of a vortex (a) and an antivortex (b). The winding number is defined as the normalized line integral on a closed loop S over the angle α that the magnetization $\vec{M}$ encloses with the x-axis: $W = \oint \alpha(\phi)/2\pi \, \mathrm{d}S$ (cf. Fig. 1c). Antivortices can occur in a certain type of magnetic domain walls, known as cross-tie walls [6].

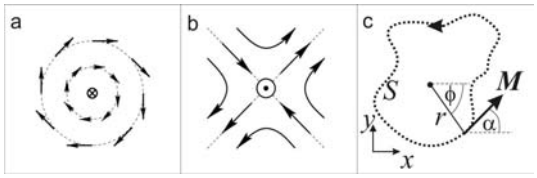

FIG. 1: Schematics of a magnetic vortex (a) and an antivortex (b). In the core of the (anti-)vortex, the magnetization is perpendicular to the plane. (c):Sketch on the definition of the winding number.

We have simulated the annihilation of an antivortex and a vortex in a cross-tie domain wall structure in a Permalloy thin-film element of 100 nm $\times$ 100 nm size and 10 nm thickness [7]. A Permalloy platelet of this size is too small to permanently sustain a cross-tie structure. If such a magnetic structure is imposed as an initial magnetic configuration, it decays into a simple vortex state. This domain structure conversion can only occur via a vortex-antivortex annihilation process. At zero field, the conversion into a vortex state occurs within $\sim$ 200 ps. The simulations were performed with the micromagnetic finite-element code based on the Landau-Lifshitz-Gilbert equation already used in previous studies [8]. We used a finite element mesh with about 200.000 tetrahedral elements of about 1.3 nm size. The results show [7] that the vortex-antivortex annihilation process is relatively simple if the vortex and the antivortex have the same polarization. Before the annihilation, the vortex cores approach each other on spiralling orbits and finally meet in the center, where the antivortex is. During this approach, the magnetization between the antivortex and the vortex rotates out of plane, thereby dissolving the complicated ini-

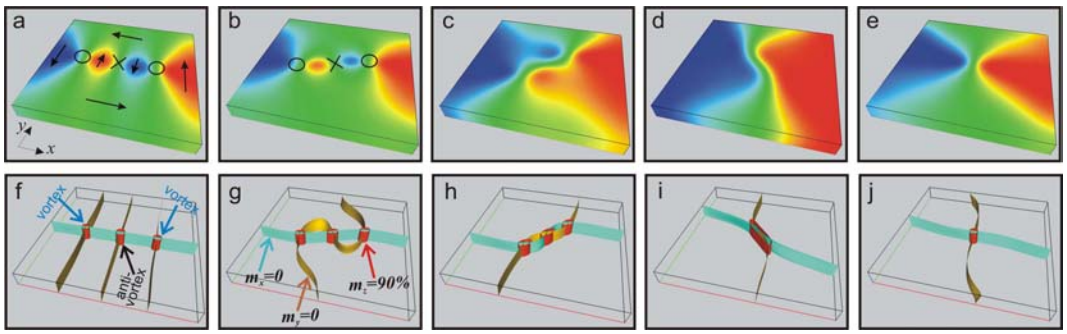

FIG. 2: Dynamics of a vortex-antivortex annihilation process with opposite polarization. In the panels a-e, a visualization with isosurfaces has been used, as described in the text. The configurations are shown at 5 ps (a,f), 110 ps (b,g), 135 ps (c,h), 138 ps (d,i) and 141 ps (e,j). In the bottom row, the panels f-j, show magnified top views on the region of interest. In addition, the isosurfaces $m_z = 0$ are displayed as green ribbons.

tial magnetic structure. In this case, the annihilation is a smooth, continuous rearrangement of the magnetization. The situation is very different if the antivortex has opposite polarization with respect to the neighboring vortices. To study this case, an unstable cross-tie structure is chosen as initial configuration, similar to the previous case, but now the polarization of the antivortex is negative, while the vortices have positive polarization. Using an isosurface representation of the magnetic structure [7], the dynamics of the annihilation process is shown in Fig. 2. The extended isosurfaces display the areas where $m_x = 0$ and $m_y = 0$, respectively. These isosurfaces allow for a precise localization of the cores: The (anti-)vortex cores are the only points in the sample where the z-component of the magnetization reaches 100%. Both the x and y-component are zero in the core center, hence the cores are at the intersections of the $m_x = 0$ and $m_y = 0$ isosurfaces. The cores are encircled by cylindrical isosurfaces displaying the regions where $m_z = 90\%$. The blue cylinder around the antivortex is the isosurface of $m_z = -90\%$. In this antiparallel case, the annihilation process begins with a relatively slow approach of the antivortex towards one of the vortices (here: on the left). This proceeds until the cores of the vortex and the antivortex meet in one point, leading to a dramatic and sudden annihilation, accomplished by a propagating micromagnetic singularity [9] (Bloch point, BP).

Isosurfaces and their intersections are not only helpful for locating vortex cores. They can also help identifying and locating BPs. In the panels f-j of Fig. 2, the $m_z = 0$ isosurface is displayed in addition to the $m_x = 0$ and $m_y = 0$ ribbons. A singularity occurs when these three isosurfaces intersect in one point: There –and only there– $|\boldsymbol{M}|$ is equal to zero inside the sample. In panel i of Fig. 2, the intersection of the cyan colored $m_x = 0$, the green $m_y = 0$, and the yellow $m_z = 0$ ribbon marks the point where a BP is formed. As the BP leaves the sample on the surface, the vortex-antivortex structure is dissolved and a large amount of exchange energy is released. The energy is converted into spin waves, recognizable as wave fronts emitted from the region where the BP was formed.

In conclusion, high-resolution micromagnetic simulations have been used to unveil the complicated magnetization dynamics of vortex-antivortex annihilation processes. When vortex and antivortex are polarized oppositely, the annihilation involves a sudden, burst-like emission of spin waves (exchange explosion). In that case, the annihilation is mediated by a propagating BP. The vortex-antivortex annihilation is considered to be an important sub-process of a complicated, recently observed vortex core reversal mechanism triggered by field pulses [5]. Our simulations provide detailed insight into crucial aspects of this process, and we have thus made the first step towards a theoretical understanding of a new micromagnetic mechanism [10], which opens the possibility of using magnetic vortex cores for data storage purposes [5, 11].

[1] L. Landau and E. M. Lifshitz, Phys. Z. Sowjet. **8**, 153 (1935).

[2] A. Wachowiak, J. Wiebe, M. Bode et al., Science **298**, 577 (2002).

[3] T. Shinjo, T. Okuno, R. Hassdorf, K. Shigeto, and T. Ono, Science **289**, 930 (2000).

[4] S. B. Choe, Y. Acremann, A. Scholl et al., Science **304**, 420 (2004).

[5] B. Van Waeyenberge, A. Puzic, H. Stoll, K. W. Chou, T. Tyliszczak, R. Hertel et al., Nature **444**, 461 (2006).

[6] E. E. Huber Jr., D. O. Smith, and J. B. Goodenough, J. Appl. Phys. **29** 294 (1958).

[7] R. Hertel and C. M. Schneider, Phys. Rev. Lett. **97**, 177202 (2006).

[8] R. Hertel, W. Wulfhekel, and J. Kirschner, Phys. Rev. Lett. **93** 257202 (2004).

[9] W. Döring, J. Appl. Phys. **39**, 1006 (1968).

[10] R. Hertel, S. Gliga, M. Fähnle, and C. M. Schneider, Phys. Rev. Lett. **98** 117201 (2007).

[11] M. Bode, Physik Journal **6**, 17 (2007).

The Guest Dynamics in Germanium Clathrates

R. P. Hermann, W. Schweika

Institute for Scattering Methods

Thermoelectric materials are useful for converting between electric and thermal energy whenever maintenance free or silent operation is crucial or when waste heat is available. A good thermoelectric material must exhibit low thermal conductivity and good electric conductivity. The insertion of guest atoms in cagey crystalline structures provides an efficient mechanism impeding thermal transport without hindering electric transport. We have studied the dynamics of the *R* = Sr, Ba, or Eu guests in $R_8Ga_{16}Ge_{30}$ clathrates by inelastic neutron scattering and nuclear inelastic scattering. Both methods confirm the local character of the guest vibrations and yield the energy and typical broadening caused by phonon collisions.

In a society that has both growing needs in energy and growing ecological concerns the development of better functional materials for energy transformation is a high priority. Thermoelectric energy conversion [1], although still suffering from a relatively low efficiency, provides an interesting route for realizing substantial reduction in energy consumption in some specific but important cases. In particular, the use of thermoelectric conversion could significantly contribute to the needs in electric power in the automotive industry by harnessing the engine waste heat[2]. Further, such materials are ideally suited for niche applications in which reliability or noise free operation is crucial, such as the radioisotope thermoelectric generators aboard deep space probes or the refrigeration systems aboard submarines.

An essential characteristic for an efficient thermoelectric material is its behavior as electron crystal and phonon glass[3]. A good electric conductivity is required in order to minimize resistive dissipation in the material and a bad thermal conductivity is required in order to maintain the thermal gradient between the hot and cold points. The requirement of a small lattice thermal conductivity can be fulfilled, for example, through nanostructuration or amorphisation, or, more generally, the addition of any efficient phonon scattering mechanism. Such scattering mechanism must however preserve the electric conductivity. One particular route for achieving this reduction is the insertion of loosely bound guests in crystalline structures that exhibit a cage like structure, such as skutterudites[4, 5] or clathrates[6, 7]. This insertion has been shown to preserve the electric conductivity while significantly reducing the thermal conductivity and allows for optimization of the doping of these semiconductors. The key for the achieved reduction in thermal conductivity resides in the dynamics of the guests in the cage, dubbed guest "rattling". This "rattling" model assumes Einstein oscillator like vibrational modes that are localized, $i.e.$ the motions of the guests are uncorrelated. A signature of such localized motion is the absence of dispersion in the associated phonon modes, which in turn implies a prominent peak in the phonon density of states, DOS.

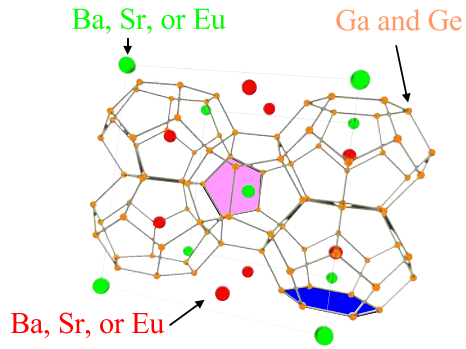

FIG. 1: In the type-I clathrate structure one quarter of the guests, $R(A)$, in green, is located in the smaller dodecahedral Ge-Ga cages, pink face, and three quarter, $R(B)$ in red, in the larger tetrakaidecahedral Ga-Ge cages, blue face. The substitution of Ge by Ga on the clathrate framework is required for charge compensation when the divalent Sr, Ba, or Eu cations are inserted.

We have determined the DOS for polycrystalline $Ba_8Ga_{16}Ge_{30}$ and $Sr_8Ga_{16}Ge_{30}$ clathrates by inelastic neutron scattering on the DNS cold neutron time of flight instrument located at the FRJ-II research reactor. The DOS has been obtained by integration over all scattering vectors, $\vec{Q}$. The europium specific DOS in $Eu_8Ga_{16}Ge_{30}$ clathrate powder has been measured at the European Synchrotron Radiation Facility on beamline ID22n by using nuclear inelastic scattering. In contrast to Mössbauer spectroscopy, in which the recoil free absorption cross section is measured, nuclear inelastic scattering measures the delayed fluorescence associated with phonon assisted nuclear absorption [8, 9, 10]. Our measurements of

the phonon DOS in $Ba_8Ga_{16}Ge_{30}$, $Sr_8Ga_{16}Ge_{30}$, and $Eu_8Ga_{16}Ge_{30}$ all indicate the presence of "rattling" guests[11].

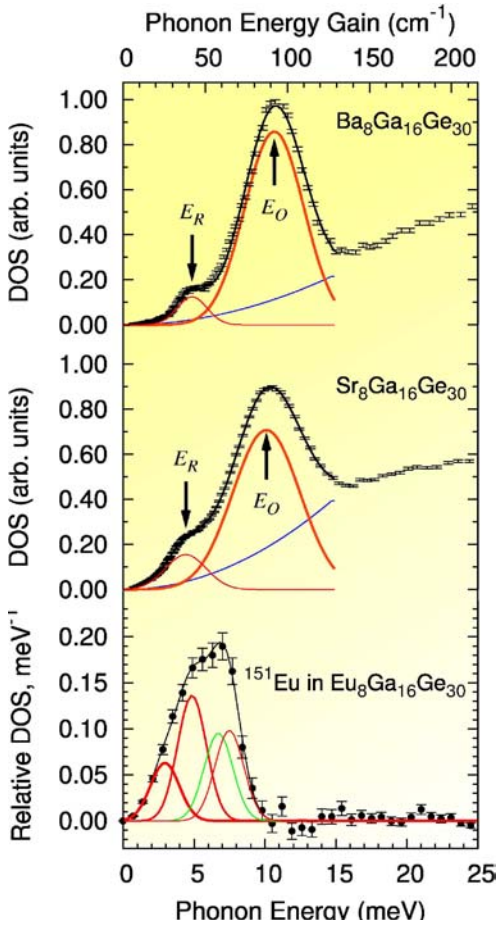

FIG. 2: The experimentally weighted DOS obtained by inelastic neutron scattering on $Ba_8Ga_{16}Ge_{30}$, top, and $Sr_8Ga_{16}Ge_{30}$, middle. The blue, thick orange, and red lines correspond to the acoustic phonons, the framework phonons, peaked at E_O, and the lowest localized mode contributions from $R(B)$ peaked at E_R, respectively. The europium partial DOS obtained by nuclear inelastic scattering on $Eu_8Ga_{16}Ge_{30}$, bottom. The three red lines and the green line correspond to three Eu(B) and one Eu(A) mode, respectively.

We have modeled the inelastic neutron scattering data with a phenomenological three term model, see Fig. 2, the three terms corresponding to a parabolic contribution for the acoustic phonons, a broad Gaussian contribution for the framework optical phonons, centered at E_O, and a contribution for the lowest lying "rattler" mode, centered at E_R. The lack of dispersion in the $|\vec{Q}|$-dependent scattering is consistent with the localized character, not shown. The energies E_R for the lowest Ba(B) and Sr(B) localized mode, 4.9(1) and 4.4(1) meV, respectively, are in good agreement with earlier determinations, summarized in Ref. [11]. It is quite surprising that the Einstein energy, E_R, is larger for Ba than for Sr, because the frequency of a harmonic oscillator is inversely proportional to its mass. Our observation indicates that there must be a stronger bonding of Ba to the clathrate framework.

The europium partial DOS in $Eu_8Ga_{16}Ge_{30}$ has been modeled by the sum of four Gaussian contributions, see Fig. 2. Because the tetrakaidecahedral cage in which Eu(B) is located is anisotropic, three vibrational modes are expected, whereas a single mode is expected for the more isotropic dodecahedral cage around Eu(A). We have obtained a description of the europium partial DOS that is consistent with earlier studies[11]. Remarkably and independently of any model, our observation indicates that the Eu guests in this clathrate do not participate significantly in any vibrational mode above 10 meV.

For all three studied clathrates, we have observed that the experimental width of the observed "rattler" peaks is larger than the instrumental resolution. This observation, combined with the lack of dispersion observed for the Sr and Ba filled clathrates, indicates broadening induced by the short phonon lifetime. Short phonon lifetimes arise from the frequent phonon collisions that lower the thermal conductivity. In particular, the linewidth, or the collision frequency, observed for the Sr(B) and Ba(B) local modes, 1.6 and 0.9 meV, respectively, are inversely proportional to the room temperature thermal conductivities of 10 and 17 mW/cm/K observed in $Sr_8Ga_{16}Ge_{30}$ and $Ba_8Ga_{16}Ge_{30}$, respectively.

[1] B. C. Sales, D. Mandrus, and R. K. Williams, Science **272**, 1325 (1996).

[2] J. Yang and T. Caillat, MRS Bulletin **31(3)**, 224 (2006).

[3] G. A. Slack, C. R. C. Handbook of Thermoelectrics (Chemical Rubber Company, Boca Raton, FL, 1995). p. 470.

[4] V. Keppens, D. Mandrus, B. C. Sales, B. C. Chakoumakos, P. Day, R. Coldea, M. B. Maple, D. A. Gajewski, E. J. Freemann, and S. Bennington, Nature **395**, 876 (1998).

[5] R. P. Hermann, R. Jin, W. Schweika, F. Grandjean, D. Mandrus, B. C. Sales, and G. J. Long, Phys. Rev. Lett. **90**, 135505 (2003).

[6] J. L. Cohn, G. S. Nolas, V. Fessatidis, T. A. Metcalf, and G. A. Slack, Phys. Rev. Lett. **82**, 779 (1999).

[7] B. C. Sales, B. C. Chakoumakos, R. Jin, J. R. Thompson, and D. Mandrus, Phys. Rev. B **63**, 245113 (2001).

[8] M. Seto, Y. Yoda, S. Kikuta, X. W. Zhang, and M. Ando, Phys. Rev. Lett. **74**, 3828 (1995).

[9] W. Sturhahn, T. S. Toellner, E. E. Alp, X. Zhang, M. Ando, Y. Yoda, S. Kikuta, M. Seto, C. W. Kimball, and B. Dabrowski, Phys. Rev. Lett. **74**, 3832 (1995).

[10] G. J. Long, R. P. Hermann, and F. Grandjean, ESRF Highlights pp. 22-23 (2006).

[11] R. P. Hermann, W. Schweika, O. Leupold, R. Rüffer, G. S. Nolas, F. Grandjean, and G. J. Long, Phys. Rev. B **72**, 174301 (2005).

Temperature Induced Differences in the Nanostructure of Hot-Wire Deposited Silicon-Germanium Alloys Analyzed by Anomalous Small-Angle X-ray Scattering

G. Goerigk

Institute for Scattering Methods

The nanostructure of hydrogenated amorphous silicon-germanium alloys, a-$Si_{1-x}Ge_x$:H (x=0.62 to 0.70), prepared by the hot-wire deposition technique was analyzed by anomalous small-angle x-ray scattering experiments. For all alloys the Ge-component was found to be inhomogeneously distributed. The results from the structural and quantitative analysis have been correlated to the materials photoconductivity. A clear improvement of the photoconductivity was achieved by optimizing the substrate temperature (between 130 and 360 °C) due to the reduction of hydrogen containing voids in coincidence with the formation of mass fractal structures of Ge with the fractal dimension p < 1.6 and a size of about 40 nm. The two processes cause the structural re-organization of Hydrogen from voids into Ge-fractals with enhanced Ge-H bonding improving the materials photoconductivity.

Hydrogenated amorphous silicon-germanium alloys are used in solar cell technology, where the germanium is added to produce lower band gap material to absorb the longer wavelength photons of the solar spectrum and to achieve higher efficiences for the conversion into electrical energy. However, Ge-alloying invarialy results in degraded opto-electronic properties compared with the base a-Si:H material. This behavior is closely related to the materials nanostructure, which can be analyzed by small-angle X-ray scattering (SAXS) on a mesoscopic length scale between 1 and 100 nm. Anomalous small-angle X-ray scattering (ASAXS) introduces the energy dependence into the SAXS-technique by making use of the X-ray continuum of the synchrotron radiation. When measuring the energy dependent small-angle X-ray scattering in the vicinity of the K-absorption edge of Ge (11.103 keV) at in minimum three energies a special separation algorithm allows the separation of the scattering due specifically to Ge-composition fluctuations from those associated with microvoids and/or hydrogen.

In recent years a group at NREL (National Renewable Energy Laboratory, U.S.A.) found evidence of improved photoresponse from a-SiGe:H alloys with narrow bandgaps deposited at different filament temperatures, filament diameters, and optimized substrate temperatures with hot-wire chemical-vapor deposition (HWCVD). Here we report on ASAXS results from a series of narrow bandgap films (1.21 eV < Gap (E_{Tauc}) < 1.32 eV) made at NREL by HWCVD at different substrate temperatures T_S. The deposition conditions are described elsewhere along with some opto-electronic properties of the first series of such alloys made by the HWCVD method [1]. The ASAXS measurements were carried out at the JUSIFA beamline at HASYLAB, DESY Hamburg.

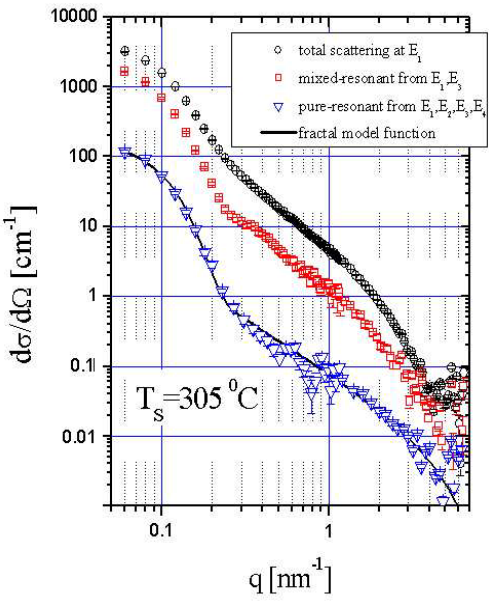

FIG. 1: Total scattering, mixed-resonant scattering and the form factor of the pure-resonant scattering contribution of a amorphous SiGe:H-alloy prepared by HWCVD-techniques at a substrate temperature of 305° C.

Figure 1 shows the scattering curves of an alloy prepared at the substrate temperature, T_S=305 °C. The circles represent the total scattering curves measured at 10053 eV (inhomogeneously distributed Ge and voids/hydrogen), while the squares show the separated scattering curves (mixed-resonant) obtained from SAXS measurements at the two energies 10053 and 11083 eV. The triangles represent the scattering due specifically only to the inhomogeneously distributed Ge-component in the alloy obtained from a separation algorithm explained in more detail in [2]. The solid line passing through the data points is a fitted model functions according to the fol-

lowing q-dependence:

$$S_{Ge}^{form}(q) = A \cdot \exp(\frac{-q^2 R_g^2}{3}) \quad (1)$$
$$+B \cdot \exp(\frac{-q^2 R_{sub}^2}{3}) \left\{ \frac{[\mathrm{erf}(qR_g/\sqrt{6})]^3}{q} \right\}^p$$

where q is the magnitude of the scattering vector [=$(4\pi/\lambda)\sin\Theta$], 2Θ is the scattering angle and λ the X-ray wavelength. Eq.(1) represents the Unified Exponential/Power-Law Approach of G. Beaucage [3] and can be used for the analysis of small-angle scattering curves from complex systems that contain multiple levels of related structural features such as mass fractals, where two structural levels are the overall radius of gyration R_g and a substructural length R_{sub}. The fractal nature of the system can be deduced from the power-law exponent p. If I(q) varies as q^{-p} in a q-range with $qR_g \gg 1$, then $p<3$ denotes a system that may be a mass fractal and $3<p<4$ corresponds to a surface fractal. The solid line in Figure 1 represents a mass fractal with p=1.56 and a gyration radius of 19.3 nm.

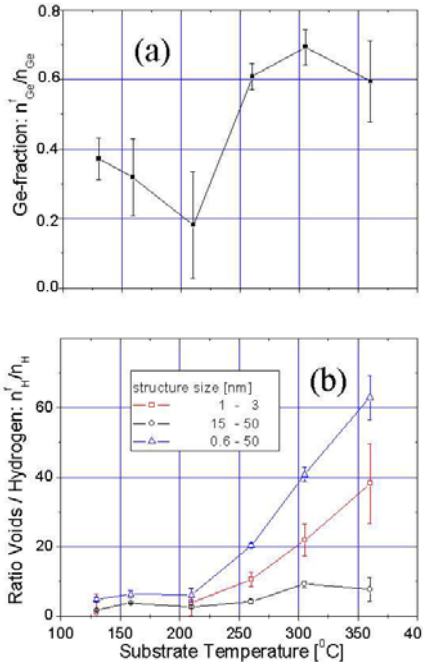

FIG. 2: The fraction of Ge atoms implemented in the fractals (a). The ratio of void scattering relative to the scattering expected from the hydrogen implemented in the amorphous matrix (b).

From the quantitative analysis of the Ge-related form factor the amount of Ge-atoms implemented in the mass fractals could be deduced. Figure 2a summarizes the results for six alloys deposited at different substrate temperatures. In this diagram two groups of samples can be distinguished, which correspond to the sharp decrease in Figure 2a at a substrate temperature below 260 °C. At T_S=260 °C and beyond, more than 60% of the Ge-atoms are located in the fractal structures, while at lower T_S the amount of Ge-atoms incorporated into the fractals is strongly reduced. Structural and quantitative information about the hydrogen clusters or voids can be gained from the analysis of the non-resonant scattering contribution. The triangles in Figure 2b represent the ratio of hydrogen atoms calculated from the non-resonant scattering contribution normalized to the hydrogen content of the alloys. Especially for the temperatures beyond 250 °C the ratio shows values which are far too high, i.e. 20, 40 and 60 times higher than expected from the hydrogen concentration. From this the conclusion can be drawn that the non-resonant scattering represents not only the scattering of hydrogen-filled inhomogeneities but also gives evidence for the existence of voids with a size of several nm, which dominate the non-resonant scattering contribution at higher substrate temperatures. These voids are strongly reduced when the substrate temperature is reduced and the optimum is reached, when the formation of the Ge mass fractals reaches a relative maximum in coincidence with a strongly reduced void fraction.

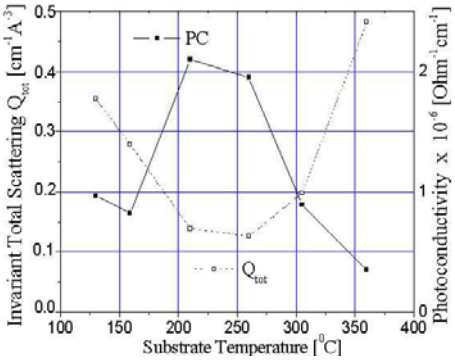

FIG. 3: Total integrated scattering and photoconductivity (right ordinate) of the six alloys plotted vs the substrate temperature.

This is confirmed by the correlation of the integrated total scattering Q_{tot} with the measured values of the photoconductivity shown in Figure 3. The photoconductivity reaches maximum values where the integrated total intensities Q_{tot} reaches minimum values at T_S= 210 and 260 °C. The minimum value at 260 °C is produced by the high amount of the mixed-resonant contribution at this temperature indicating a strong overlap of the spatial distribution functions of the Hydrogen and Germanium atoms. From this it can be concluded, that a larger amount of H atoms is probably bonded to Ge atoms removing trapping centers from the band gap and improving the photoconductivity drastically [2]. This is confirmed by IR-results, which show a maximum of Ge-H bonding fraction at 260 °C [4].

The work has been done in collaboration with D.L. Williamson, Department of Physics, Colorado School of Mines. The samples were supplied by National Renewable Energy Laboratory, USA.

[1] B.P. Nelson, et al., Mater. Res. Soc. Symp. Proc. 507, 447 (1998)

[2] G. Goerigk, and D.L. Williamson, J. Appl. Phys. 99, 084309 (2006)

[3] G. Beaucage, J. Appl. Cryst. 28, 717 (1995)

[4] Y. Xu, B.P. Nelson, D.L. Williamson, L.M. Gedvilas, and R.C. Reedy, Mater. Res. Soc. Symp. Proc. 762, A 10.2 (2003)

Multilayer Buffer for High Temperature Superconductor Devices on MgO

M. I. Faley, S. B. Mi, C. L. Jia, U. Poppe, and K. Urban

Institut für Festkörperforschung, Forschungszentrum Jülich GmbH, Jülich, Germany

Multilayer buffer layers containing $BaZrO_3$ thin films on the bottom and $SrTiO_3$ thin films on the top were successfully applied to improve the epitaxial growth of the $YBa_2Cu_3O_{7-x}$ (YBCO) films on the MgO substrates, which have the best correspondence of the thermal expansion coefficient with YBCO. The HRTEM and x-ray diffraction studies demonstrated pure c-axis orientation and absence of the in-plane misoriented grains in the YBCO films grown on the buffered MgO substrates. A high quality of superconducting parameters and no cracks were observed in such YBCO films even at thicknesses $\gg$ 1 μ m. Multilayer flux transformers having total thickness $\sim$ -2 μ m were prepared on the buffered MgO substrates and demonstrated an improved insulation between the superconducting layers and an increased dynamic range compared to flux transformers on $SrTiO_3$ substrates [1].

The epitaxial films of high-temperature superconductor (HTS) $YBa_2Cu_3O_{7-x}$ (YBCO) are typically prepared at substrate temperatures 700 - 900°C higher than their storage and operation temperatures. Due to the difference in the thermal expansion coefficients of the substrates and films an essential tensile strain in the YBCO films appears, which degrades their superconducting properties and can even crack the films when their thickness exceeds some critical value. Thick multilayer HTS thin film structures like multiturn flux transformers are, for example, required for the production of sensitive SQUID magnetometers [2]. A high critical current of the HTS films is also beneficial for high-Q microwave resonators and filters used for communication technique as well as for HTS tapes intended for generation and transport of electrical power.

MgO substrates have similar thermal expansion coefficients to that of YBCO. The main disadvantage of MgO substrates is the degradation of their hygroscopic surface in ambient air. These substrates also show a lattice mismatch of $\sim$9% with YBCO and a different crystal structure. These properties usually lead to a significant amount of in-plane 45° misoriented grains in YBCO films deposited on MgO substrates, which significantly suppresses the average critical current density of the HTS films. Deposition of buffer layer materials like $SrTiO_3$ (STO) or $BaZrO_3$ (BZO) have been suggested in order to improve the epitaxial growth of YBCO films on MgO substrates (see, e.g., [3]). The buffer layer can preserve the hygroscopic surface of the MgO substrates from degradation in air and/or during lithographic procedures. At least two buffer layers are required to deposit YBCO on MgO: the first one should provide the epitaxial growth of films with perovskite structure on the rock-salt structure of MgO, while the second buffer layer should match the lattice constants.

In the present work we describe a multilayer thin film buffer, which provided an epitaxial passivation of the surface of the single crystal MgO substrates and allowed a significant improvement of the epitaxial growth of the relatively thick crack-free YBCO films and multilayer structures.

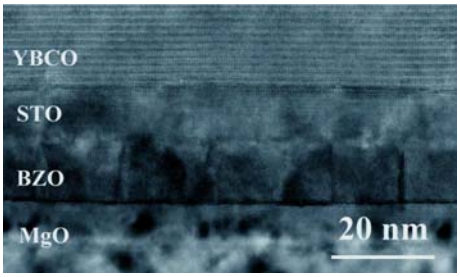

FIG. 1: Cross sectional HRTEM image of the BZO-STO-YBCO heterostructure deposited on the MgO (100) substrate.

High-oxygen-pressure sputtering was used to deposit the thin film buffer layers and YBCO films on STO, $LaAlO_3$ (LAO), $NdGaO_3$ (NGO) and MgO single crystal substrates. A single crystal STO wafer was used as a target. We have observed that the epitaxial STO buffer layer significantly improved the c-axis oriented epitaxial growth of YBCO and $PrBa_2Cu_3O_{7-x}$ (PBCO) films on the STO, LAO, and NGO substrates. The pristine MgO substrates were first investigated by atomic force microscope (AFM) to select the non-degraded substrates with a root-mean-square roughness of the surface $<$0.2nm for further processing. The epitaxial passivation of MgO substrates consisted of two buffer layers made of different compounds. The first deposited 30-nm-thick BZO layer served to change the crystal structure of the surface from the rock-salt to perovskite type. Above the BZO

layer a 30- to 300-nm-thick STO layer was deposited to achieve a better matching of the lattice constant of the buffer layer surface with YBCO.

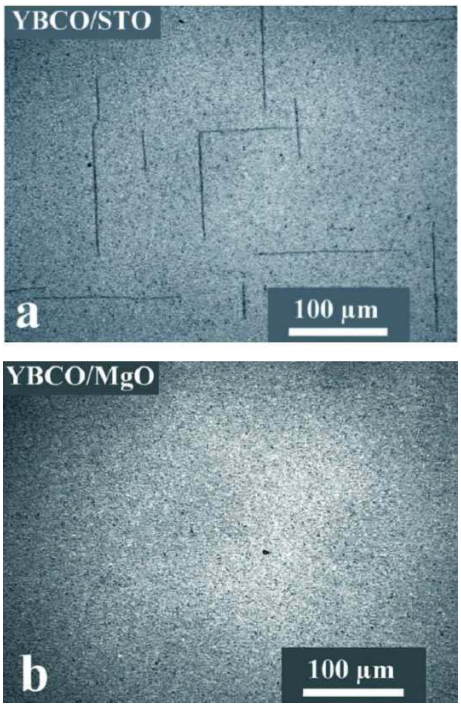

FIG. 2: Optical images (green filter) of crack structures in $\sim 2\mu$ m thick YBCO films deposited at similar conditions on (a) $SrTiO_3$(100) and (b) buffered MgO(100) substrates.

A cross sectional high-resolution transmission electron microscopy (HRTEM) image of the BZO-STO-YBCO heterostructure deposited on an MgO (100) substrate is shown in Fig.1. Column-like growth of the BZO layer observed by HRTEM was stopped at the BZO-STO interface. The STO layer also significantly smoothed the ∼1nm root-mean-square roughness of the surface, which had appeared on the BZO layer. An STO layer thickness of∼10nm was found to be sufficient for complete coverage of the substrate and epitaxial growth of the YBCO films.

Crystal structure and orientation of the deposited oxide films was investigated by 2Θ and ϕ scans with x-ray diffraction (XRD). The XRD patterns demonstrated a perfect c-axis and in-plane orientation of the YBCO film. The in-plane orientation of $\sim 1\mu$ m thick YBCO films deposited on buffered MgO (100) substrate was checked by YBCO (103) XRD ϕ scans and plan view HRTEM. No misoriented grains were observed for the YBCO films deposited on the buffered MgO substrates.

Cracks in the $\sim$ 2 μ m thick YBCO films were observed on all investigated substrates except MgO ones (see Fig.2). It was observed that the cracks for the LAO (100) and NGO (110) substrates started to appear in ~ 0.5-μ m-thick YBCO films whereas for the STO substrates they appeared in the YBCO film at a thickness of $\sim 1\mu$ m.

The YBCO films deposited on the buffered MgO substrates had typical critical current densities J_c ∼2 - 5 MA/cm^2 at 77.4K, and the superconducting transition temperature T_c exceeded 91K. The thickness dependences of the room temperature dc-resistance of the YBCO films deposited at similar conditions on LAO, STO, and buffered MgO substrates are shown in Fig.3. Only the YBCO films on buffered MgO substrates demonstrated resistance inversely proportional to the film thickness. The resistance of YBCO films on other substrates saturated or even increased when the thicknesses exceeded the critical values where cracks appeared in the films.

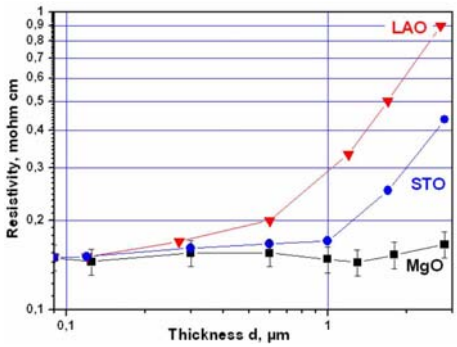

FIG. 3: Thickness dependence of the effective room temperature specific resistivity for YBCO films deposited at similar conditions on LAO (▼), STO (●), and buffered MgO (■) substrates.

We used buffered MgO substrates mainly for the preparation of multilayer flux transformers. For the first time it was possible to increase the thickness of all layers in such a heterostructure containing two YBCO layers and one PBCO non-superconducting layer for about twofold up to a total thickness of $\sim 2\mu$ m. This helped us to improve the insulation between the superconducting layers and increase the critical current of the flux transformer. Thus the reproducibility and dynamic range of the flux transformers was significantly improved.

In conclusion, an epitaxial multilayer thin film buffer served for passivation of the single crystal MgO substrates and improved the epitaxial growth of the YBCO films. The multilayer buffer preserved the surface of the MgO substrate from degradation during patterning of the multilayer HTS structures and devices.

[1] M. I. Faley, S. B. Mi, A. Petraru, C. L. Jia, U. Poppe, and K. Urban, Appl. Phys. Lett. **89**, 082507 (2006).

[2] M.I.Faley, U.Poppe, K.Urban, D.N.Paulson, T.Starr, and R.L.Fagaly, IEEE Transactions on Appl. Supercond., **11**, No.1, 1383 (2001). M.I.Faley, C.L.Jia, U.Poppe, L.Houben, and K.Urban, Superconductor Science and Technology, **19**, S195 (2006).

[3] R.Hühne, D.Selbmann, J.Eickemeyer, J.Hänisch, and B.Holzapfel, Superconductor Science and Technology, **19**, 169 (2006).

Multiphase Modeling of Fracture

R. Spatschek, E. A. Brener, C. Müller-Gugenberger, D. Pilipenko, H. Müller- Krumbhaar

Institut für Festkörperforschung, Forschungszentrum Jülich, 52425 Jülich, Germany

We present a continuum theory to describe fracture processes and the influence of elastic effects on surfaces and interfaces. A multiphase field method allows to investigate the dynamics of these nonequilibrium pattern formation processes. The theory predicts the fast steady state growth, the interaction and coarsening of cracks. Stress intensity factors for stationary or moving cracks even with extended tip can be extracted. We demonstrate the application of the theory to delamination processes in composite structures.

Understanding the phenomenon of fracture is very important for many applications and a challenging task for physics and materials science. The fundamental basis of fracture was discovered by Griffith [1]: according to his findings the growth of cracks is determined by a competition of a release of elastic energy if a crack extends and a simultaneous increase of the surface energy. During the past years, phase field modeling has emerged as a promising approach to model fracture by continuum methods. Recently, we developed a minimum theory of fracture [2, 3] which is only based on well-established thermodynamical concepts. This is also motivated by experimental results showing that many features of crack growth are rather generic [4]; among them is the saturation of the steady state velocity appreciably below the Rayleigh speed and a tip splitting for high applied tension.
In the spirit of our work [3] the propagation of cracks is understood as an interfacial pattern formation process. We therefore developed multiphase field methods to describe fracture and the influence of elastic effects on phase transformations with more than two phases. The volume fraction of each phase is described by a field variable ϕ_k, $k = 1, \ldots, N$, with N being the number of phases. In the sharp interface limit, inside the bulk phases one phase field variable is one, and the others are zero. The temporal evolution is given by

$$\frac{\partial \phi_k}{\partial t} = -\frac{2D}{3\xi}\left(\frac{\delta U}{\delta \phi_k} - \lambda\right), \qquad (1)$$

where we introduced a Lagrange multiplier to maintain the phase conservation, $\sum_{k=1}^{N} \phi_k = 1$. The phase field interface width is denoted by ξ, D is a kinetic coefficient. The expression for the Lagrange multiplier is given by $\lambda = 1/N \times \sum_{i=1}^{N} \delta U/\delta\phi_k$. The individual energy terms which contribute to the total free energy $U = U_{el} + U_s + U_{dw}$ are $U_{el} = \int \left(\mu(\Phi)\epsilon_{ij}^2 + \lambda(\Phi)(\epsilon_{ii})^2/2\right) dV$ for the elastic energy density (ϵ is the strain tensor), $U_s = 3\xi/4 \times \sum_{i,j=1}^{N} \gamma_{ij} \int (\phi_i \nabla\phi_j - \phi_j \nabla\phi_i)^2 dV$ as interfacial energy density, and the generalization of the standard double well potential $U_{dw} = 3/\xi \times \sum_{i,j=1;i\neq j}^{N} \gamma_{ij} \int \phi_i^2 \phi_j^2 dV$. Here, the interpolated elastic constants are $\mu(\Phi) = \sum_{i=1}^{N} h(\phi_i)\mu^{(i)}$ and $\lambda(\Phi) = \sum_{i=1}^{N} h(\phi_i)\lambda^{(i)}$, with $\mu^{(i)}$ and $\lambda^{(i)}$ being the elastic constants of the individual bulk phases. Also, we have mutual interfacial energies $\gamma_{ij} = \gamma_{ji}$ between phases i and j. Similarly, the elastic equation of motion is given by

$$\rho \ddot{u}_i = \frac{\partial \sigma_{ik}(\Phi)}{\partial x_k}, \qquad (2)$$

with the stress tensor $\sigma_{ik}(\Phi) = 2\mu(\Phi)\epsilon_{ik} + \lambda(\Phi)\epsilon_{ll}\delta_{ik}$ and the mass density ρ. This set of equations leads to a well-controlled sharp interface limit as described in [3].

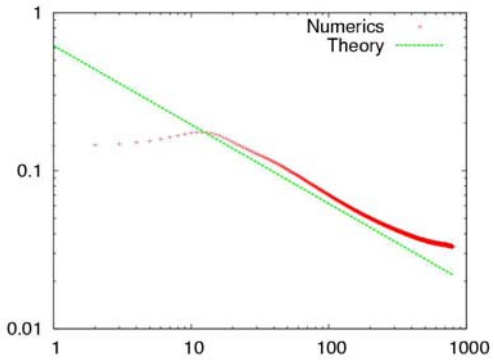

FIG. 1: Determination of a dynamical stress intensity factor. The value of the vertical stress component σ_{yy} as a function of the distance from the tip is shown in a logarithmic presentation. In an intermediate regime, the square-root behavior is clearly visible.

Close to crack tips, stresses become large, exhibiting characteristic square-root singularities which are related to stress intensity factors K, and the phase field code can also be used to extract them. For cracks

with finite tip radius r_0, the stress scaling $\sigma \sim Kr^{-1/2}$ at a distance r from the tip is only valid in an intermediate regime in finite systems: Close to the tip, higher order terms can appear,

$$\sigma_{ij} = \frac{K}{(2\pi r)^{1/2}} \left(f_{ij}^{(0)} + \sum_{n=1}^{\infty} \frac{A_n f_{ij,d}^{(n)} + B_n f_{ij,s}^{(n)}}{r^n} \right), \quad (3)$$

which are suppressed only for sharp tips. Here, the functions $f_{ij,d}^{(n)}(\theta_d, \upsilon)$ and $f_{ij,s}^{(n)}(\theta_s, \upsilon)$ are the universal angular distributions for the dilatational and shear contributions; A_n and B_n are the coefficients of expansion. From an intermediate region, the stress intensity factor can be extracted. This is done here for a fast moving crack with propagation velocity $\upsilon/v_R = 0.68$ (v_R is the Rayleigh speed) subjected to a mode I loading (see Fig. 1); a deviation of about 10% for the dynamical stress intensity factor from its theoretical expectation is due to the fact that the crack opening is rather large in comparison to the system size.
A competition between adjacent cracks takes places because the cracks mutually reduce the effective driving force due to the elastic relaxation behind the crack tip. Therefore, for low driving forces, the cracks will attract each other and finally fuse in order to minimize the surface energy. In a large sample, many microcracks can exist for higher driving forces, grow and merge, finally leading to complete rupture (see Fig. 2).

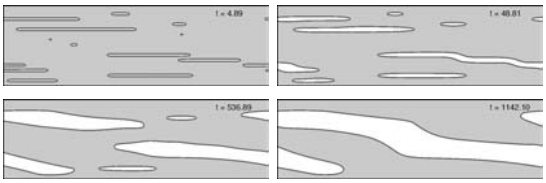

FIG. 2: Coarsening of an irregular arrangement of cracks in a uniaxially strained solid with periodic boundary conditions in lateral direction. Large cracks grow at the expense of smaller cracks. The parameters used here are $\Delta = 6$, $D/\xi v_R = 2.32$, and the system size is 1000×300 grid points. Time is given in units D/v_R^2.

The late stage of crack coarsening processes has been studied analytically in [5]. A conventional mean field behavior breaks down and multiple lengthscales become relevant in this process.
As another example, we assume that a small cavity has formed between two layers of material as an initial interfacial crack. The system is vertically loaded by a fixed displacement. For simplicity, we assume the two solid phases to be identical, but of course each phase can in principle have individual elastic properties. The "broken phase" has negligible elastic coefficients, which leads to stress free boundaries on the crack. In contrast to normal crack growth, the presence of the interlayer boundary leads to the formation of a triple junction. In full thermodynamical equilibrium, the material is completely broken and therefore all stresses have vanished. In contrast, for full lamination, the solid is homogeneously stretched and its elastic energy density is $U_{el} = \sigma_{ik}\epsilon_{ik}/2$. Complete rupture leads to an increase of the surface energy (per length of the system) by $\mathcal{U}_s = \gamma_1 + \gamma_2 - \gamma_{12}$, where γ_1 and γ_2 are the surface energies of the solid phases and γ_{12} is the cohesive interfacial energy of the laminate. With L being the height of the sample, the condition of energy equilibrium $U_{el}L = \mathcal{U}_s$ defines a generalized Griffith threshold for the laminate. Above the Griffith threshold, delamination occurs, and a typical evolution of such a process is shown in Fig. 3. Here, the propagation of the crack is rather fast in comparison to the sound speed. Dissipation at the crack tips leads to the emission of sound waves which can be detected at the boundaries of the sample.

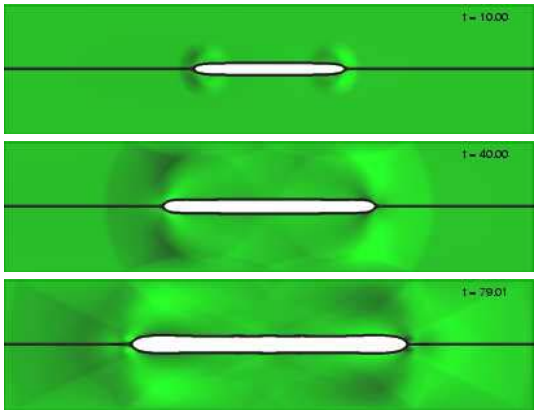

FIG. 3: Delamination of two elastic strips. Time is given in units D/v_R^2 with v_R being the Rayleigh speed of the bulk phases and D the kinetic coefficient for the delamination process. The delaminated phase is shown in white. The green color coding illustrates the wave propagation: bright regions correspond to positive horizontal velocities, $\dot{u}_x > 0$, dark regions to $\dot{u}_x < 0$.

[1] A. A. Griffith, Philos. Trans. R. Soc. A, **21**, 163 (1921).

[2] E. A. Brener and R. Spatschek, Phys. Rev. E **67**, 016112 (2003).

[3] R. Spatschek, M. Hartmann, E. Brener, H. Müller-Krumbhaar, and K. Kassner, Phys. Rev. Lett. **96**, 015502 (2006).

[4] J. Fineberg and M. Marder, Phys. Rep. **313**, 1 (1999).

[5] E. Brener, V. Marchenko, H. Müller-Krumbhaar, and R. Spatschek, Phys. Rev. Lett. **84**, 4914 (2000); E. Brener, H. Müller-Krumbhaar, and R. Spatschek, Phys. Rev. Lett. **86**, 1291 (2001).

Diffusion in a Binary Amorphous Metal: Pair-Correlation in $Cu_{33}Zr_{67}$

M. Kluge, H. R. Schober

Institute IFF-Theory III

Glasses and amorphous materials are found ubiquitously both in nature and high technology. Seen on length scales of several nm they are disordered, whereas they have nearly complete near neighbour order. This interplay between order and disorder is basic to many applications but also poses many challenging questions. Glasses are formed by all sorts of chemical compounds, e.g. polymers, covalent systems, ionic systems etc.. This chemical diversity opens numerous avenues to novel applications. Despite this great variety all glassy materials show common "glassy properties". Metallic glasses, besides their manifold usage, are considered the prototype of simple glasses for the study of such glassy properties. In the present work computer simulation was employed to study the atomic diffusion around the transition from an undercooled melt to a glassy solid. In particular the differences between the two components in a binary glass were investigated.

In recent years considerable insight into the diffusion mechanisms in amorphous metals and their undercooled melts has been gained. This was achieved by combining results from experiment, computer simulations and theory as shown in the recent review by Faupel $et\ al$ [1]. It is undisputed that in a hot melt, diffusion is by flow, whereas, in the glassy state, well below the transition temperature, it is by hopping processes. Theory predicts a freezing of flow at a critical temperature T_c, well above the glass transition temperature T_g [2]. The mechanism of the transition from flow to hopping is still an open question, closely connected with the atomistic nature of the hopping process itself.

A key to the atomistic nature of diffusion in metallic glasses and their undercooled melts was found in measurements of the isotope effect of diffusion. Because of the $1/\sqrt{m}$-dependence of the atomic velocities E is of order unity for diffusion via single vacancy jumps in densely packed lattices where essentially single atoms jump. In contrast both in glasses [3] and in undercooled metallic melts [4] nearly vanishing isotope effects were observed. This has a natural explanation if one assumes a collective diffusion mechanism, both above and below the glass transition. Computer simulations [5, 6] systems have shown that, driven mainly by densification, collectivity rapidly grows upon cooling and diffusion is highly collective already well above T_c. Chains of ten and more atoms move together [7, 8, 9]. This collective motion is closely correlated to quasi-localized vibrations [7, 10].

This picture of collective motion in the undercooled melt, as well as in the glass, is supported by pressure experiments which generally show small activation volumes [1]. In computer simulations four temperature regions could be distinguished in the activation volume [11]. At high temperatures when binary collisions dominate, the activation volumes are of the order of the atomic volume. They drop to a much lower plateau value in the undercooled melt. At T_c the activation volume shows a spike, related to the $1/(T-T_c)$ singularity predicted by mode coupling theory [2]. In the glass, the activation volume seems to attain values similar to the ones in the undercooled melt.

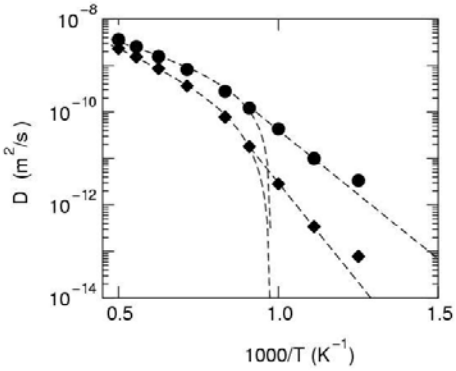

FIG. 1: Diffusion coefficients in $Zr_{67}Cu_{33}$ (Zr: diamonds, Cu: spheres) The dashed lines represent a fit with mode coupling theory, using the same temperature T_c for both components, in the undercooled melt and an Arrhenius fit in the glass [12].

In our previous paper [12] we have shown that diffusion in $Cu_{33}Zr_{67}$, both in the undercooled melt and in the glass near T_g, can be described in terms of atomic hopping with a smooth distribution of hopping lengths as would be expected from collective jumps. In this work [13] we study the time evolution of the pair correlation, Fig. 2, for temperatures ranging from

the hot melt to the glass. The investigation shows marked differences in the time evolution of the pair correlation of the two components Zr and Cu. This is exemplified in Fig. 3 which shows the filling of the self-hole in the pair correlation function $g_{\alpha\beta}(r,t)$.

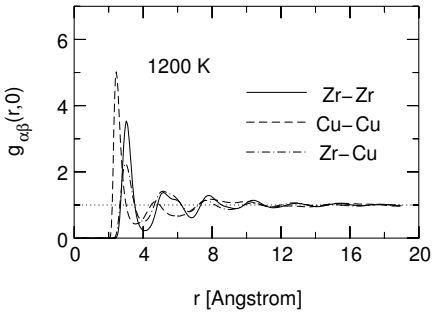

FIG. 2: Static pair correlation functions in $\mathrm{Zr_{67}Cu_{33}}$ *at* $T = 1200$ *K.*

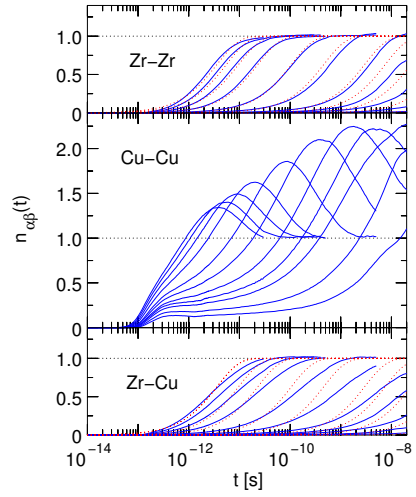

FIG. 3: Time dependence of the relative number of atoms in the self-hole of the pair correlation function.Temperatures from left to right: 2000, 1800, 1600, 1400, 1200, 1100, 1000, 960, 900, 800 and 700 K. The dotted line shows a simple estimate using the diffusion coefficient of Zr, see text.

We define a relative number of atoms in a shell

$$n_{\alpha\beta}(T_0,t) = \frac{1}{V_{12}} \int_{r_1}^{r_2} g_{\alpha\beta}(r,t) 4\pi r^2 dr \Big|_{T=T_0} \qquad (1)$$

where V_{12} is the integration volume. $n_{\alpha\beta}(T,t)$ measures the number of atoms of species β in the volume V_{12}, normalized to their random ($t = \infty$) value, under the condition that at time $t = 0$ a different atom (species α) was at $r = 0$. By definition, therefore, $n_{\alpha\beta}(T, t = \infty) = 1$. To calculate the relative occupation number of the self-hole we set $r_1 = 0$ and $r_2 = 1.9$ Å for all components. The figure shows two effects. First, whereas the filling of the self-hole in the Zr-Zr correlation follows a simple exponential law, as to be expected for random motion without a fixed jump length, the Cu-Cu correlation overshoots. The decay time for the faster component Cu is longer than for the slower Zr. Secondly. No qualitative change of the behaviour is seen at the glass transition temperature $T_g \approx 965$ K.

We conclude, the temporal evolution of the pair correlation functions in the binary CuZr system supports the general diffusion scenario in metallic glasses as outlined in the review [1]. Both above and below the glass transition temperature diffusion is by collective jumps of chains of atoms, where single atoms move only a fraction of the nearest neighbor distance and there is no typical jump length. Despite this general behavior there are characteristic differences on a microscopic level which reflect the different mobilities and the dynamic heterogeneity of the glass. The more mobile atoms, in particular the ones of the smaller minority component, move in a semi-rigid matrix. This causes a preference to occupy sites near previous atomic positions. Due to this effect the correlations of the faster moving component (Cu-Cu) decay slower than the ones of the more sluggish Zr. This effect has to be accounted for when comparing macroscopic measurements of tracer diffusion to microscopic probes.

[1] F. Faupel, W. Frank, M.-P. Macht, H. Mehrer, V. Naundorf, K. Rätzke, S. K. Sharma, H. R. Schober, H. Teichler, Rev. Mod. Phys. **75** (2003) 237.

[2] W. Götze, A. Sjölander, Rep. Prog. Phys **55**, (1992) 241.

[3] F. Faupel, P. W. Hüppe, and K. Rätzke, Phys. Rev. Lett. **65** (1990) 1219.

[4] H. Ehmler, A. Heesemann, K. Rätzke, F. Faupel, U. Geyer, Phys. Rev. Lett. **80** (1998) 4919.

[5] M. Kluge, H. R. Schober, Phys. Rev. **62** (2000) 597.

[6] H. R. Schober, Solid State Commun. **119** (2001) 73.

[7] H. R. Schober, C. Oligschleger, B. B. Laird, J. Non-Cryst. Sol. **156**, (1993) 965.

[8] H. R. Schober, C. Gaukel, C. Oligschleger, Defect and Diffusion Forum **143-147** (1997) 723.

[9] C. Donati, J. F. Douglas, W. Kob, S. J. Plimpton, P. H. Poole, S. C. Glotzer, Phys. Rev. Lett. **80** (1998) 2338.

[10] C. Oligschleger, H. R. Schober, Phys. Rev. B **59** (1999) 811.

[11] H. R. Schober, Phys. Rev. Lett. **88** (2002) 145901.

[12] M. Kluge, H. R. Schober, Phys. Rev. B **70** (2004) 224209.

[13] M. Kluge, H. R. Schober, J. Non-Cryst. Solids **352**, 5093 (2006).

Adsorption of Molecular Layers on Metal Surfaces: A Density Functional Study

N. Atodiresei[1], V. Caciuc[2], K. Schroeder[3]

[1] Institut für Festkörperforschung, Quanten-Theorie der Materialien
[2] Physikalisches Institut, Westfälische Wilhelms-Universität, Münster
[3] Institut für Festkörperforschung, Theorie der Strukturbildung

Anchoring organic molecule on metal surfaces is a prerequisite for many applications, e.g. as sensors, where specific reaction sites for atoms and molecules are created, as devices in molecular electronics where switchable molecules between electrodes are used, as templates for reactions like polymerization, or for biological activity e.g. chiral selectivity. We have studied by density functional calculations the adsorption geometry, the bond formation, and the electronic structure of molecules like formate, thiophene carboxylate or terephthalic acid, which use the carboxylate group to chemisorb on the Cu (110) surface. We find that for high coverage all molecules adsorb with the molecular axis perpendicular to the surface, and the oxygen atoms of the carboxylate group bind to Cu atoms of the first layer in a monodendate fashion.

Surface reactions involving organic molecules have attracted increasing attention recently. Apart from the traditional use in a vast number of economically important surface processes such as catalysis in chemical production, corrosion, the fabrication of computer chips or magnetic storage devices, the behavior of biomaterials and organic functionalization of the metallic surfaces has important applications. [1] In addition, electronic transport involving organic molecules adsorbed on metal surfaces is considered as a promising pathway to nanoelectronic devices.

The binding and ordering of molecules on surfaces is in general controlled by a delicate balance between competing molecule-substrate and intermolecular interactions. The adsorption on metal surfaces may change the geometrical and electronic properties of the molecule and the exact adsorption conformation may play an important role for the electron transfer from the metal to the molecule. A detailed insight into the binding geometries and ordering of the molecules on surfaces and the specificity of the interactions that occur between anchored molecules can be obtained by performing ab initio calculations. The first question concerns the adsorption geometry and the atomic positions. The next step is the understanding of the electronic structure and the hybridization of orbitals in the formation of the bonds.

We have investigated the bonding of molecules via the carboxylate (OCO) group on Cu(110) by density functional calculations. [2, 3] These include formate (HOCO) as the simplest molecules, and also molecules where the H atom is replaced by a 5-atom ring (like thiophene carboxylate with a S heteroatom) or a 6-atom ring and an additional formic acid group like terephthalic acid.

As an example we show the adsorption geometry of the 5-atom ring molecules thiophene carboxylate and its relatives, which contain O, Se, Te instead of a sulfur heteroatom in the ring (Fig. 1). The bridge position (each O atom binds to one Cu atom and the OCO group forms a bridge between two Cu surface atoms) is always the most stable adsorption site. As can aslo be seen in Fig. 1, the ring plane is rotated with respect to the carboxylate plane. This is contrary to the conformation of the isolated molecules in the gas phase, which all have planar geometry. The reason for the rotation is the steric hindrance of the rings when the molecules are adsorbed in high coverage on the Cu surface.

The binding of the carboxylate group is established by orbital hybridization between O and Cu, as shown in Fig. 2 for formate on Cu(110). The oxygen p-band is split due to the formation of hybrides. In the lower part of the Cu d-band (between -4 eV and -2.5 eV) bonding hybrids are formed and in the upper part (between -2 eV and -1 eV) antibonding hybrids are formed. Examples are shown in Fig. 2.

If one changes the heteroatom in the 5-rings, the binding energy of the molecules to the Cu surface varies between 2.8 eV (for Te) and 3.3 eV (for O) due to the variation of the electronegativity of the heteroatoms. [2]

We did not find any indication of a hydrogen bond between neighboring molecules. From the calculation of the packing energy (energy gained by putting the molecules in the same density and arrangement as in the adsorption geometry, but without the Cu surface) we conclude that the interaction between the molecules has contributions due to Coulombic forces from the heterogeneous charge distribution and due to the (repulsive) steric hindrance. We are currently investigating the extension of the molecular π-system in spite of the ring plane rotation. This is important for the use of such molecules as switchable leads be-

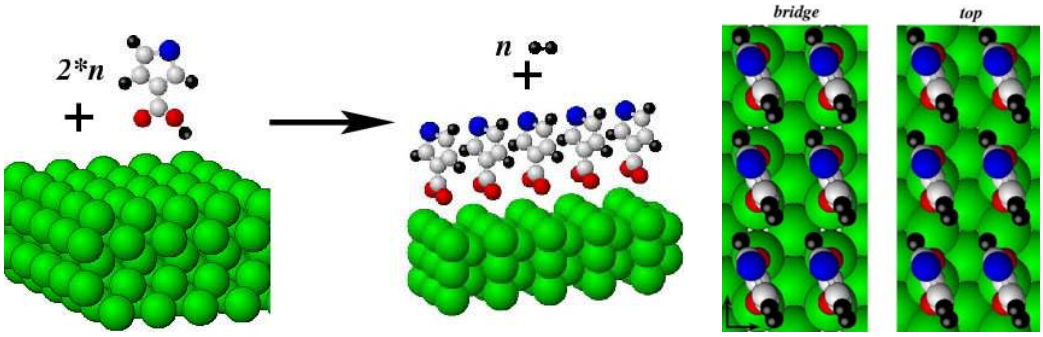

FIG. 1: When molecules which contain carboxylic acid (OCOH) are adsorbed on metal surfaces they release the H atom. The O atoms of the carboxylate group (OCO) attach to Cu surface atoms and the molecular axis is perpendicular to the surface. Contrary to the conformation in the vacuum (flat molecule) the 5-atom ring is rotated by ≈24° due to steric reasons.

tween metal electrodes.

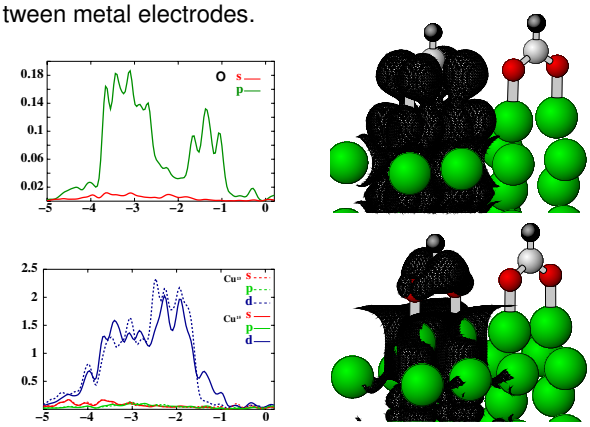

FIG. 2: Electronic structure of the bonds between O atoms of the carboxylate group and Cu surface atoms for formate. The left panels show the partial local density of states at the O and Cu atoms. The oxygen p-band is split due to the formation of bonding hybrids in the lower part of the Cu d-band (between -4 eV and -2.5 eV) and antibonding hybrids in the upper part (between -2 eV and -1 eV). Two orbitals are shown on the right: the upper panel shows an antibonding orbital, and the lower panel a bonding orbital.

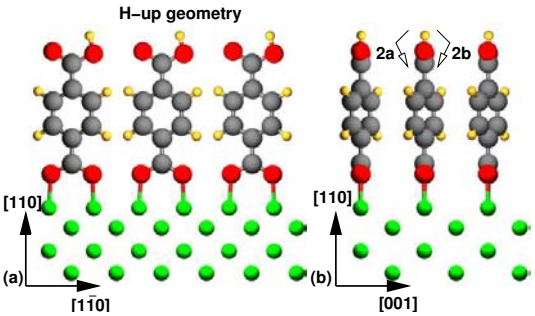

FIG. 3: Ball-and-stick model of the TPA adsorbed on Cu(110). At high coverage, the TPA molecule adsorbs with an upright orientation with the carboxylate groups (COO) aligned along $[1\bar{1}0]$ direction. In the adsorbtion configuration with lowest energy the H atom of the carboxylic group (COOH) is pointing towards the vacuum (H-up geometry). The lateral interactions between adjacent TPA molecules induces a rotation of the benzyne rings (C_6H_4) with respect to the carboxylate plane by an angle of 24.7° .

We also investigated the adsorption of molecules which contain a reactive acid group exposed to the vacuum. One example is terephthalic acid with a 6-atom benzene ring and two opposing formic acid groups (see Fig. 3). One of these is used for the attachment of the molecules to the metal surface, the other one (exposed to the vacuum) remains intact, and makes the adsorbed molecular layer a template for further reactions.[3]

The important question is the position of the acidic H atom at the vacuum side, which determines the possible reactions this template can undergo. We have calculated the adsorption geometry and energy for several conformations of the molecule changing the position of the acidic H atom. Several conformations (one with the H atom pointing straight towards the vacuum and one with the H atom pointing towards the neighboring molecule) have very similar energies. The calculated activation energy for transitions between these configurations is 0.85 eV, which means that the transition is quite probable slightly above room temperature. Thus, terephthalic acid adsorbed on Cu is a promising template for further reactions, e.g. to extend the backbone of the molecule. It is currently used in experiments to obtain switchable molecular leads.

[1] R. Raval, Current Opinion in Solid Science **7**, 67 (2003).

[2] N.Atodiresei, K.Schroeder, and S.Blügel, Phys. Rev. B **75**, 115407 (2007)

[3] N.Atodiresei, V.Caciuc, K.Schroeder, and S.Blügel, submitted to Phys. Rev. B (2007).

Liquid-to-Glass Transition in Bulk Glass Forming $Cu_{60}Ti_{20}Zr_{20}$

X. J. Han[1,2], Helmar Teichler[2]

[1]IFF Theory III, Forschungszentrum Jülich
[2]Inst. f. Materials Physics, University of Göttingen

The present work reports results from molecular dynamics studies about microscopic structure and dynamics of the ternary, bulk metallic glass forming $Cu_{60}Ti_{20}Zr_{20}$. An atomic interaction potential model was constructed and used for simulation. $Cu_{60}Ti_{20}Zr_{20}$ is found to be characterized by a structure with marked intermediate range order. The dynamics of the system fulfils in most respects the predictions of the mode coupling theory (MCT), up to an absence of the algebraic t^{-a}-decay in the early β-range. Comparison with the calculated memory kernel shows that this absence can be traced back to deviations of the kernel from its approximate form analysed in the MCT.

With favorable mechanical behavior and good resistance to corrosion, multi-component bulk metallic glasses (BMGs) have attracted extensive research interest [1, 2, 3] since the first synthesis of the La-Al-Ni BMG by copper mold casting in 1989.[1] However, despite the great achievements in preparation and characterization of these materials, the specific details of the liquid-to-glass transition of multi-component BMGs have not been fully understood yet and are still an open question. Here we present results of a molecular dynamics (MD) analysis of the BMG forming $Cu_{60}Ti_{20}Zr_{20}$ ternary alloy.

Molecular dynamics simulations are performed for a system containing 1372 atoms at constant temperature and zero external pressure. In order to generate the ternary liquid structure, we start with hypothetic face-centred-cubic configuration, which is equilibrated at 1700K for 5ns, leading to a homogeneous liquid state. Then the system is cooled down to given temperatures with a cooling rate of $3x10^{10}$K/s. The resulting configurations are relaxed by additional isothermal annealing runs, and then production runs are carried out and used for detailed data analysis at the selected temperature.

In order to describe the atomic interactions in the ternary Cu-Ti-Zr alloy, a microscopic model is applied similar to the one used for the binary Ni-Zr [4, 5] and the ternary Ni-Zr-Al alloy[6]. The pair potentials take the form of Stillinger-Weber potential. For estimating the pair-potential parameters, information from Hausleitner–Hafner hybrid-dized nearly free-electron tight-binding-bond model [7, 8] and experimental data are combined. We determined the total radial distribution function of $Cu_{60}Ti_{20}Zr_{20}$ alloy in the glassy state of 300K on basis of this model. The simulation result is presented in Fig. 1, which also includes the experimental data from an X-ray diffraction [9]. Our model reproduces well the experimentally determined total radial distribution of $Cu_{60}Ti_{20}Zr_{20}$ [9], which is a clear indication that the model meets well the steric conditions of the system. Regarding further details of the structure, our investigation shows that the overall structure seems to be built by groups of Ti and Zr atoms wrapped by sheets of Cu atoms, which provide the coupling between the Ti-Zr-groups. The system displays a complex intermediate range structure, which reflects a complicated interplay between the short ranged chemical bonding between the three components, steric conditions enforced by the size of the components, and optimization of the chemical potential when forming the space filling structure.

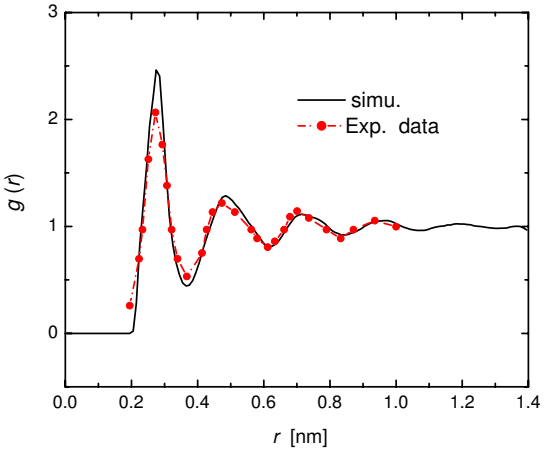

FIG. 1: Total radial distribution function of experimental [9] and simulated amorphous $Cu_{60}Ti_{20}Zr_{20}$ at 300 K.

From enthalpy and specific heat, the glass transition temperature is found to be around 750K, which is close to the experimental 710K. The critical temperature T_c is approximated as 850K from self-diffusion coefficient, dynamical susceptibility, α-relaxation time, and the memory kernel $F(t)$. The analysis of the intermediate scattering function, $\Phi(t)$,

in terms of the MCT and its modification [10, 11] shows that the present ternary $Cu_{60}Ti_{20}Zr_{20}$ behaves in this respect like the common binary glass forming melts, e.g. the NiZr alloys [4, 5] or the Lennard-Jones model [12]. We have in particular deduced that the present system fulfils well the predictions of the schematic MCT [10, 11] on the interrelationship between the β-parameter in the Kohlrausch-Williams-Watts time law for the α-decay around T_c and the critical exponent γ that governs the temperature dependence of the α-relaxation time τ_α or the shift of the α-relaxation frequency peak ω_α above T_c.
In contrast to this agreement with the results of the schematic MCT, the algebraic t^{-a} decay predicted by the MCT for the early β-regime was not found for the present system. Already in the early MD simulation by Lewis and Wahnström [13], absence of this decay was attributed to masking effects by single particle vibrations, not taken into account in the MCT.
The present analysis provides a direct confirmation of this argument from transforming the time dependence of the memory kernel $F(t)$ by use of $\Phi(t)$ into an $F(\Phi)$ relationship. For T around T_c, we find that only for Φ values below a critical Φ_b the kernel $F(\Phi)$ has the smooth, polynomial-like Φ-dependence assumed by the schematic MCT. Above that value, $F(\Phi)$ exhibits a rather different behaviour, as illustrated in Fig. 2.

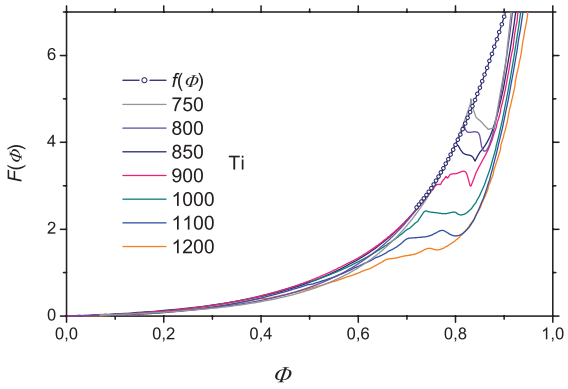

FIG. 2: $F(\Phi)$ at various temperatures and its Taylor expansion $f(\Phi)$ at 850 K for Ti in simulated $Cu_{60}Ti_{20}Zr_{20}$. (With increasing temparture the kink, resp. intermediate maximum in the $F(\Phi)$ curves shifts to lower F-values.)

From comparison with $\Phi(t)$, the Φ-range above Φ_b is just the range where the decay of the correlator $\Phi(t)$ with time is governed by the atomic vibrations. Since Φ_b is only slightly above the plateau value of the correlator, there is nearly no Φ-range left for developing the t^{-a}-decay. This is the reason why the system is absent of the t^{-a}-decay.
In conclusion, on basis of the developed potential model, the microstructure of $Cu_{60}Ti_{20}Zr_{20}$ is found to be characterized by a marked intermediate range order. The dynamics of liquid to glass transition of this system fulfils in most respects the predictions of schematic MCT. The absence of the t^{-a}-decay in the early β-range is ascribed to the deviation of memory kernel from its approximate form analysed in the MCT.

[1] A. Inoue, T. Zhang, and T. Masumoto, Mater. Trans., JIM **30**, 965 (1989).

[2] Inoue, A. Kato, T. Zhang, S. G. Kim, and T. Masumoto, Mater. Trans., JIM **32**, 609 (1991).

[3] A. Peker and W. L. Johnson, Appl. Phys. Lett. **63**, 2342 (1993).

[4] H. Teichler, Phys. Rev. E **53**, R4287 (1996).

[5] A. B. Mutiara and H. Teichler, Phys. Rev. E **64**, 046133 (2001).

[6] M. Guerdane and H. Teichler, Phys. Rev. B **65**, 014203 (2001).

[7] C. Hausleitner and J. Hafner, Phys. Rev. B **45**, 115 (1992).

[8] C. Hausleitner and J. Hafner, Phys. Rev. B **45**, 128 (1992).

[9] N. Mattern, J.Sakowski, A. Concustell, P. Jovari, M. D. Baro , and J. Eckert, in : Jahresbericht des HASYLAB am Deutschen Elektronen –Synchrotron DESY, Hamburg, Germany, 627-628 (2003).

[10] W. Götze and L. Sjögren, Rep. Prog. Phys. **55**, 241 (1992).

[11] W. Götze and L. Sjögren, Transp. Theory Stat. Phys. **24**, 801 (1995).

[12] W. Kob and H. C. Andersen, Phys. Rev. E **52**, 4134 (1995).

[13] L. J. Lewis and G. Wahnstrm, Phys. Rev. E **50**, 3865 (1994).

Elastic Domains in Antiferromagnets on Substrates

Efim A. Brener[1], V. I. Marchenko[2]

[1] Institut für Festkörperforschung, Forschungszentrum Jülich, D-52425 Jülich, Germany
[2] P. L. Kapitza Institute for Physical Problems, RAS 119334, Kosygina 2, Moscow, Russia

We consider periodic domain structures which appear due to the magnetoelastic interaction if the antiferromagnetic crystal is attached to an elastic substrate. The peculiar behavior of such structures in an external magnetic field is discussed. In particular, we find the magnetic field dependence of the equilibrium period and the concentrations of different domains.

Spontaneous breaking of any discrete rotational symmetry in monocrystals leads to the appearance of degenerate phases characterized by different orientations of the order parameter. The phase boundaries have a positive (free) energy, otherwise the system would be thermodynamically unstable. Thus, in equilibrium one should observe a single phase. This is, however, not the case for the phases with spontaneous magnetization (or electrical polarization). Periodic domain structures are formed in such materials in order to reduce the large, proportional to the volume, energy of the magnetic (or electric) field.

Using the electron spin resonance technique, Janossy $et\ al.$ [1, 2] demonstrated the existence of the equilibrium domain structure in antiferromagnetic $YBa_2Cu_3O_{6+x}$ and in $Y_{1-x}Ca_xBa_2Cu_3O_6$. The domain structure was easily modified by the external magnetic field, and restored after switching the field off. The resonance method does not provide information about characteristic sizes and the arrangement of the domains. Recently Vinnikov, $et\ al.$ [3] directly observed periodic domain structures in antiferromagnetic $TbNi_2B_2C$ by the "finest magnetic-particle decoration technique" [4]. Neither spontaneous magnetization, nor electrical polarization is seen in this material. Nevertheless, regular and reversible (by the change of the temperature and magnetic field) domain structures are realized with a periodicity of the order of a few microns in the samples of plate shape with a thickness 0.5 mm.

In this report we discuss a possible scenario for the appearance of such periodic domain structures and the behavior of the structures in an external magnetic field. If a monocrystal is attached to some elastic substrate, the domain structure should inevitably arise in any orientational phase transition in order to minimize the strain energy. Indeed, the stress free (but not strain free) monodomain state is realized if we discuss free surface boundary conditions. If the monodomain crystal is attached to some elastic substrate, stresses arise, and we loose a large, proportional to the crystal volume, energy. In this case, the appearance of the domain structure, with a period much smaller than the crystal size, will drastically diminish the energy of elastic deformations.

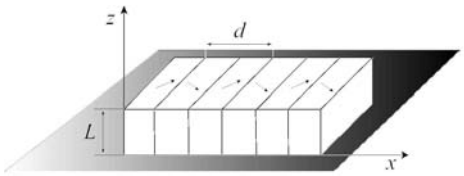

FIG. 1: Schematic presentation of the domain structure in the antiferromagnetic crystal attached to an elastic substrate.

All materials studied in the experiments of Ref. [1, 2, 3] are collinear easy plane antiferromagnets with tetragonal crystal symmetry. For definiteness' sake we discuss this case. For the description of the antiferromagnetic states we use the exchange approximation [5], treating the effects of the magnetic anisotropy, magnetoelastic effects and the external magnetic field as perturbations. By a proper choice of the orientation of the coordinate system (say, the x axis can be oriented along the [110] or [100] direction) we can write the anisotropy energy in the easy xy-plane as

$$F_{an} = -\beta l_x^2 l_y^2, \qquad (1)$$

with a positive constant β; here l_x, and l_y are the components of the antiferromagnetic unit vector $\mathbf{l}$. The four states $l_x^2 = l_y^2 = 1/2$, differ by the signs of the x, y-components ($\nearrow$, $\searrow$, $\swarrow$, $\nwarrow$), and correspond to the minimum of the energy, Eq. (1).
The elastic strain arises in the crystal due to the magnetoelastic interaction

$$F_{me} = \gamma_1 l_x l_y u_{xy} + \gamma_2 (l_x^2 - l_y^2)(u_{xx} - u_{yy}), \qquad (2)$$

where u_{ik} are the components of the strain tensor. For simplicity, we consider the magnetoelastic effects to be small compared to the anisotropy, Eq. (1). The second term in Eq. (2) is zero for the discussed states with $l_x^2 = l_y^2$. The elastic energy of tetragonal crystals can be written as a sum of 6 invariants:

$$F_{el} = \mu_1 u_{xy}^2 + \mu_2 (u_{xz}^2 + u_{yz}^2) + \mu_3 (u_{xx} - u_{yy})^2 + \mu_4 u_{zz}^2 + \mu_5 u_{zz}(u_{xx} + u_{yy}) + \mu_6 (u_{xx} + u_{yy})^2. \qquad (3)$$

Minimizing the sum of the energies, Eq. (2) and Eq. (3), we find that, in the monodomain state of the unstressed crystal, the only nonzero component of the strain tensor is

$$u^0_{xy} = \frac{\gamma_1}{2\mu_1} l_x l_y = \pm \frac{\gamma_1}{4\mu_1}. \qquad (4)$$

Consider the antiferromagnetic crystal, of plate shape, attached to a flat elastic substrate. Let the main axis of the crystal be normal to the plate. The domain structure that appears in this case is schematically presented in Fig. 1. The state of each domain far from the crystal-substrate boundary is one of the unstressed ground states. Additional energetic contributions arise from i) the energy of the domain walls, and ii) the elastic energy localized near the crystal-substrate boundary in a layer of thickness of the order of the domain structure periodicity d. Minimization of these two contributions with respect to d leads to the equilibrium period of the domain structure. This argumentation is close in spirit to arguments of Ref. [6] (see also [7, 8, 9]). The elastic interaction between domains and point defects was discussed in [10]. However, we stress that the additional elastic energy term appears only near the crystal-substrate boundary and does not appear near the free surface. This is a crucial difference between these elastic domains and the domains in ferromagnets. Finally we find for the equilibrium period of the domain structures [11]

$$d = d_0 = \left(\frac{(2\mu + \sqrt{\mu_1 \mu_2})\sigma_0 L}{\nu \mu \sqrt{\mu_1 \mu_2} (u^0_{xy})^2} \right)^{1/2}. \qquad (5)$$

The classical law $d \propto L^{1/2}$, in the limit $d \ll L$, is the crucial point for the experimental verification of the domain structure theory. In the case of antiferromagnetic domains there exists an additional valuable experimental possibility, namely to study the behavior of the structure in the external magnetic field.
The magnetic field changes the orientation of the antiferromagnetic vector. The corresponding term in the energy is

$$F_H = -\frac{\chi_\perp - \chi_\parallel}{2} [\mathbf{lH}]^2, \qquad (6)$$

where $\chi_\parallel$ ($\chi_\perp$) is the magnetic susceptibility parallel (perpendicular) to the vector $\mathbf{l}$. In collinear antiferromagnets $\chi_\parallel < \chi_\perp$.
If the magnetic field $\mathbf{H}$ is oriented along the y-direction, the minimization of the sum of the energies, Eq. (1) and Eq. (6), gives $l_x^2 - l_y^2 = h^2$ for $H < H_c$, and $l_y = 0$ for $H > H_c$; here $h = H/H_c$, $H_c^2 = 2\beta/(\chi_\perp - \chi_\parallel)$. Firstly, the magnetic field leads to the appearance of homogeneous deviatoric stresses $\sigma_{xx} = -\sigma_{yy} = \gamma_2(l_x^2 - l_y^2)$ due to the second term of the magnetoelastic energy, Eq. (2). These stresses are equal in the coexisting domains, and do not affect the periodicity. The second effect is the renormalization of the equilibrium strain tensor, Eq. (4), by the factor $(1 - h^4)^{1/2}$. The third effect is the renormalization of the energy of the domain walls. The explicit dependence of the period of the domain structures on the magnetic fields is given in [11].
The behavior of the domain structure will be much more complicated if one applies a field with some arbitrary orientation. Then the nearest-neighbor domains should have different widths. We have calculated the concentrations of different domains, c^+ and c^- ($c^+ + c^- = 1$), in the limit of small magnetic fields, $H_x, H_y << H_c$ and, as before, assuming magnetoelastic effects to be small compared to the anisotropy [11]:

$$c^\pm = \frac{1}{2}\left(1 \pm \frac{H_x H_y}{H_{me}^2}\right), H_{me}^2 = \frac{\gamma_1^2}{4\mu_1(\chi_\perp - \chi_\parallel)} << H_c^2. \qquad (7)$$

The domain period cannot be found analytically at arbitrary field orientations. In this case there are no symmetry arguments forcing the domain walls, near the sample-substrate boundary (at distances of the order of the period), to be flat and oriented along the z-axis. The domain walls should be inclined and curved in this case.

[1] A. Janossy *et al.*, Phys. Rev. B **59**, 1176 (1999).

[2] A. Janossy, T. Feher, and A. Erb, Phys. Rev. Lett. **91**, 177001 (2003).

[3] L.Ya. Vinnikov *et al.*, JETP Lett. **77**(9), 502 (2003).

[4] L.Ya. Vinnikov, I.V. Grigor'eva, and L.A. Gurevich, Springer Ser. Mater. Sci. **23**, 89 (1993).

[5] A.F. Andreev, and V.I. Marchenko, Sov. Phys. Uspekhi **23**, 21 (1980).

[6] A. G. Khachaturyan, *Theory of Structural Transformation in Solids* (Wiley, New York, 1983).

[7] B. Horovitz, G. R. Barsch, and J. A. Krumhansl, Phys. Rev B **43**, 1021 (1991).

[8] B. Horovitz, Phys. Rev B **69**, 140501(R) (2004).

[9] E. Gomonay, and V. M. Loktev, J. Physics : Condens. Matter **14**, 3959 (2002); Phys. Solid State **47**, 1755 (2005).

[10] V. M. Kalita, A. F. Lozenko, S. M. Ryabchenko and P. A. Trotsenko, JETP **99**, 1054 (2004)[Zh. Eksp. Teor. Phys. **126**, 1209 (2004)].

[11] E. A. Brener and V. I. Marchenko, Phys. Rev. Lett. **97**, 067204 (2006).

Improving the Charge-Density Normalization in KKR Green-Function Calculations

R. Zeller

Institute Theory III

In electronic structure calculations the KKR Green-function method is not often used for semiconducting and insulating systems, since the correct position of the Fermi energy cannot be obtained from the Green function. The difficulty arises because the necessary truncation of the angular momentum expansion of the Green function leads to an inexact charge-density normalization. It is shown that this problem can be solved by a technique which circumvents the truncation error by exploiting direct density-of-states determinations by Lloyd's formula. The technique is explained and illustrated by calculations for a half-metallic dilute magnetic semiconductor, where it leads to an exact integer value of the magnetic moment, and for a metal-semiconductor multilayer, where it leads to an appropriate band alignment.

The Korringa-Kohn-Rostoker (KKR) Green-function (GF) method is a well established method to calculate the electronic structure of complex materials with an economical computational effort. Instead of solving the Schrödinger equation for the wavefunctions by using basis sets and variational principles, the KKR-GF method solves the Dyson equation for the Green function by using the concept of reference systems. For instance, starting from free space, where the Green function is analytically known, the electronic structure of an adatom on a surface can be calculated in steps by using an ideal bulk crystal and a clean surface as intermediate reference systems with the advantage that in each step existing periodicities and localized perturbations of the electronic potential can be exploited.

Despite these advantages the KKR-GF method is not often applied to semiconducting or insulating materials. The difficulty is the inexact charge-density normalization, which arises from the necessary truncation of the angular momentum expansion in the multiple-scattering representation of the Green function. Whereas in metals missing or extra charge can be counterbalanced by a usually small and often negligible shift of the Fermi level E_F, this option is not available in semiconducting or insulating materials. In these materials the correct position of E_F is in the gap and the calculated charge density remains practically unaffected, if E_F is varied within the gap. The required shift for a correct normalization inevitably puts E_F either into the valence or conduction band with the unpleasant consequence that these materials are then treated as metallic systems.

The use of Lloyd's formula [1] to determine E_F has been suggested in the past, but it has remained unclear how to obtain a charge density, which is consistent with this Fermi level. Lloyd's formula directly expresses the number of states in terms of scattering matrices and thus avoids the truncation error of the angular momentum expansion of the Green function. The appropriate position of E_F can be obtained, but unfortunately not the correct charge-density normalization since the charge density cannot be calculated from Lloyd's formula, but only from the angular momentum expansion of the Green function.

Recently [2] the expectation was expressed that charge-density normalization errors in the KKR-GF method can be compensated by application of energy dependent renormalization factors along the complex-energy charge-density integration contours. It was speculated that the factors could be calculated by Lloyd's formula if divergences arising from the real part of the Green function can be treated in a suitable way.

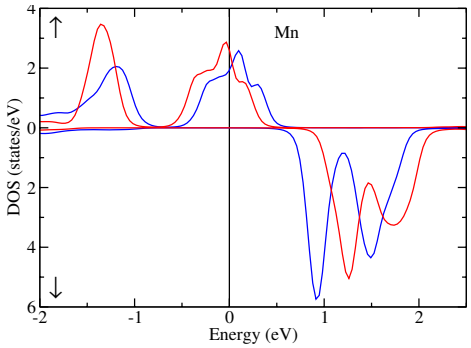

FIG. 1: Calculated density of states as function of energy relative to E_F for the Mn atom in a $MnGa_{15}N_{16}$ supercell. The red and blue curves are obtained by use of the improved charge-density normalization and by use of a simple (incorrect) Fermi level adjustment. Minority spin contributions are plotted downwards.

In the meantime a solution for the divergence problem was found [3]. The advantages of the resulting technique, which will be explained below, are now

illustrated for a dilute magnetic semiconductor Mn doped zinc-blende GaN and for a periodic multilayer Fe_8Si_{12}.
In Fig. 1 the density of states (DOS) of the Mn atom in a $MnGa_{15}N_{16}$ supercell is shown for energies in the vicinity of E_F. The DOS is typical for a half-metallic ferromagnet where a gap occurs around E_F for one spin direction, here for the minority spin, so that only majority spin states contribute to the conductance. For a correct normalization as obtained by the new technique, the minority band is below the gap are fully occupied, which leads to an integer number of minority states and an integer magnetic moment of 4.00 μ_B per unit cell. On the other hand by the standard procedure based on a simple adjustment of E_F, a non-integer value 3.18 μ_B is obtained. The large reduction of 0.82 μ_B, which is responsible for the reduced spin splitting seen in Fig. 1, arises because the few majority Mn states available at E_F must compensate all normalization errors of the many GaN states in the unit cell. The large reduction occurs not only in supercell calculations, but also in KKR-CPA calculations for disordered dilute magnetic semiconductors and can only be avoided by a correct charge-density normalization.

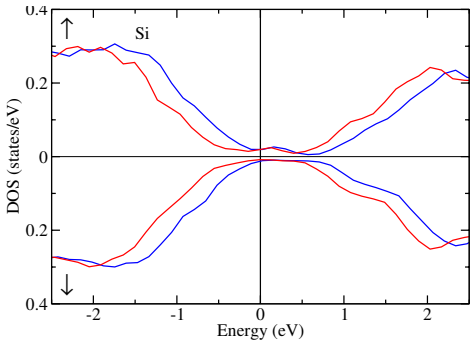

FIG. 2: Calculated density of states as function of energy relative to E_F for the Si atom in the middle of a Si layer in a Fe_8Si_{12} multilayer. The curves are assigned as in Fig. 1.

While dilute magnetic semiconductor with integer moments are interesting systems, the improved charge-density normalization is even more important for metal-semiconductor junctions. Here the simple procedure of adjusting E_F produces large errors for the energetic positions of states in the semiconducting region, whereas the energetic positions of states in the metallic and interface regions are described almost correctly. This leads to an unacceptable band-bending. For a Fe_8Si_{12} multilayer, here studied as an example, the adjustment puts E_F into the upper part of the valence band and consequently raises the semiconducting states compared to the metallic states as shown in Fig. 2, where an upward shift of about 0.3 eV is found for the DOS of a Si atom in the middle of the semiconducting region. The behaviour of the bands throughout the semiconducting region can be visualized by plotting the energy levels of Si core states (see Fig. 3), since core states respond to the average layer potential in a similar way as bands. The improved charge-density normalization leads to an almost constant value for Si 1s core energies except for Si atoms in the first and second layer at the interface, whereas the standard procedure with a simple adjustment of E_F clearly produces a band-bending with an upward shift of about 0.3 eV in the middle of semiconducting region in agreement with the DOS in Fig. 2.

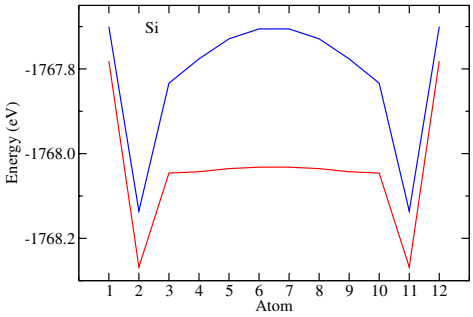

FIG. 3: Calculated 1s core level energies for the Si atoms in a Fe_8Si_{12} multilayer as function of the atomic layer index. The curves are assigned as in Fig. 1.

After the presentation of these illustrative examples, the last part of this report now describes the technique used to obtain the improved charge-density normalization. In principle, the technique is very similar to the procedure applied in all basis-set methods, where a finite subset from an infinite complete set of basis functions is chosen to expand the wavefunctions. For different subsets the wavefunctions contain changed partial contributions from the individual basis functions, but no change occurs for the always correct overall normalization of wavefunctions and charge density. In the KKR-GF method the values of the Green function along the complex-energy charge-density integration contour are the corresponding quantities, which should be normalized always correctly. The basic idea that the normalization can be provided by energy dependent factors determined by use of Lloyd's formula is not easily put into practice. The primary difficulty arises from divergent contributions of the real part of the Green function. By subtracting similarly divergent contributions of a suitably chosen reference system most divergent terms cancel. The very small remaining terms are then taken into account by an energy independent scaling factor. Another difficulty is the usually complicated correct determination of the phases of multivalued imaginary parts of complex logarithms, which appear in Lloyd's formula. Here a recently developed numerically accurate and reliable procedure [2] is rather useful and enabled to obtain the results shown above for the dilute magnetic semiconductor and the metal-semiconductor multilayer.

[1] P. Lloyd, Proc. Phys. Soc. London, **90**, 207 (1967).

[2] R. Zeller, J. Phys.: Condens. Matter, **17**, 5367 (2005).

[3] R. Zeller (to be published).

Phase Transformation Behaviour and Enhancement of Piezoelectricity in Nanoscale $NaNbO_3$

C. Pithan

Institut für Festkörperforschung, Elektronische Materialien

The noncentrosymmetric crystal modification of nanoscale $NaNbO_3$, which is usually known as an antiferroelectric and therefore non-polar compound has been characterized by temperature- and pressure-tuning Raman-spectroscopy. The transition towards the bulk-like, antiferroelectric phase has been observed in the temperature range from 280 to 360 °C. Successive pressure induced phase transitions were observed at 2, 6.5 and 10 GPa respectively. Above 7 GPa the Raman-scattering profiles correspond to those reported for bulk $NaNbO_3$. The temperature-induced spectral changes were found to be completely reversible in the region between -150 and 450 °C, whereas those obtained under pressurization were not completely reversible between ambient pressure and 15.9 GPa. Piezoresponse force microscopy revealed enhanced piezoelectric response for $NaNbO_3$ crystals with a particle-size between 200 and 400 nm.

The effort for substituting lead containing piezoelectric ceramics such as $Pb(Zr_{1-x}, Ti_x)O_3$ has been driven forward energetically in the recent years [1-2]. In this context compositions based on alkaline niobates such as $(K_{1-x}, Na_x)NbO_3$ have been of particular interest. $KNbO_3$, one of the end members in the potassium sodium niobate system reveals the same phase transition behaviour which is also typical for the ferroelectric model phase $BaTiO_3$. $NaNbO_3$ on the other hand shows a much more complex transition characteristic through the displacement of Nb ions and tilting of NbO_6 octahedra. At room temperature this material is antiferroelectric but certain oxides dissolved in $NaNbO_3$ promote a transition from the antiferroelectric towards a ferroelectric state as in the case of $(K_{1-x}, Na_x)NbO_3$. Recently a novel noncentrosymmetric modification of $NaNbO_3$ which can be assigned by the crystallographic space group $Pmc2_1$ for crystallites with reduced dimensions (200-400 nm) has been discovered [3]. The thermodynamic stability of this phase is, however, unknown up to now. For this reason the present study reports on the phase transition behaviour of $NaNbO_3$ with $Pmc2_1$ symmetry in dependence of temperature and pressure. These aspects are of technological interest since ceramic grains in the nanoscale range are expected to show enhanced piezoelectric activity. In order to monitor the structural transitions induced by both these thermodynamic intensive variables, temperature and pressure tuning Raman spectroscopy has been applied. Finally piezoresponse force microscopy (PFM) has been performed.

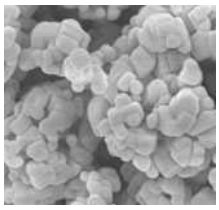

FIG. 1: SEM image obtained from nanoscale $NaNbO_3$ powders.

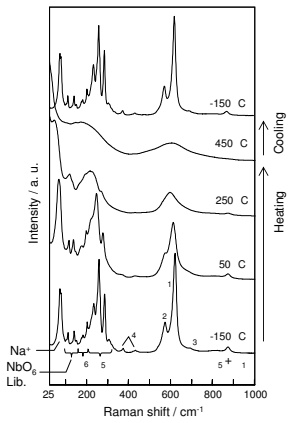

FIG. 2: Raman spectra recorded for nanoscale $NaNbO_3$ powders at various temperatures upon heating and after cooling.

Figure 1 shows a SEM image obtained for nanoscale $NaNbO_3$ powder obtained via microemulsion mediated hydrolysis of Na-isopropoxide [4] followed by an annealing treatment at 800 °C for 12 hours. The average particle diameter was evaluated using the line intercept method to 0.3 $\pm$ 0.1 μm. XRPD patterns modelled by Rietveld refinement yielded the following lattice parameter of the orthorhombic structure: a=0.776778(5), b=0.551759(2) and c=0.556829(2) nm. The space group is $Pmc2_1$.

Figure 2 shows the evolution of the Raman spectra recorded for nanoscale $NaNbO_3$ powder on sequential heating from -150 up to 450 and after cooling down again to -150 °C. The Raman active normal modes of the space group $Pmc2_1$ are represented by $16A_1 + 13A_2 + 12B_1 + 16B_2$. According to

the assignments for bulk $NaNbO_3$, the bands below 80 cm^{-1} are assigned to Na+ translational modes against the NbO_6-octahedra. The librational and internal modes of NbO_6-octahedra appear in the regions from 80 to 160 cm^{-1} and above 160 up to 900 cm^{-1}, respectively. The number of bands decreases and the individual bands broaden with increasing temperature. Temperature-induced spectral transitions are reversible on heating and cooling. Figure 3 shows the wavenumber shift of the NbO_6 librational mode at 118 cm^{-1}. Although most of the bands shift towards lower frequencies with increasing temperature, this mode shows a gradual shift towards higher frequencies.

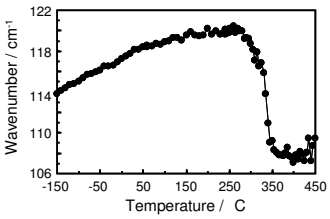

FIG. 3: Wavenumber shift of the NbO_6-librational mode on heating.

Drastic softening of this mode starts at 280 °C and continues up to 360 °C. Above 300 °C the Raman scattering profiles become simpler. This indicates, that the crystal structure transforms into a higher symmetry at high temperature. A comparison of these profiles with the ones obtained for bulk or coarse $NaNbO_3$ reveals that the high temperature modification of nanoscale $NaNbO_3$ corresponds to the normal stable one reported in the literature. Finally it could be concluded that the described phase transition behaviour is completely reversible on temperature change as long as temperature rising does not result in a coarsening of the particles. Figure 4 shows representative Raman spectra recorded at various increasing pressures up to 15.9 GPa at room temperature. The spectra obtained after the pressure has been released and a reference spectrum for coarse $NaNbO_3$ are also indicated. At pressures above 7 GPa the scattering profiles take the characteristics of the bulk coarse phase and the transition upon pressing and pressure release were found to be almost reversible. The noncentrosymmetric phase is stable up to pressures of at least 1 GPa.

Piezoelectric materials do not present an inversion centre in the unit cell of their crystal structure. Therefore, an enhancement of converse piezoelectricity is expected for the noncentrosymmetric phase of the present study in comparison with the centrosymmetric bulk phase. A direct indication was given by a PFM analysis. Figure 5a and 5b show the topography of nanoscale powder and a coarse reference powder respectively monitored using the constant force mode of the microscope. In the case of the nanoscale sample (Fig. 5a) several grains of approximately 200 to 300 nm in diameter can be recognized. For example in the top left corner of Fig. 5a very clearly an almost spherical particle of ca. 200 nm can be seen. On the other hand Fig. 5b shows a crystal which has dimensions exceeding the scanned area of this picture. The corresponding mappings of the in-plane piezoresponse signal in arbitrary units are shown in Figs. 5c and 5d. For the coarse reference sample (Fig. 5c) only a very small and noisy signal with maximum amplitude of 0.6 a.u. is recorded. Only very locally this low intensity response can be detected. No correlation between the response and the topography can be found. On the other hand much larger piezoelectric displacements are measured for the nanoscale crystals (Fig. 5c). Regions of maximum piezoactivity correspond to the locations of grains identified in the topography image and show a maximum signal up to 8 a.u., which is 10 times the value observed for the coarse reference.

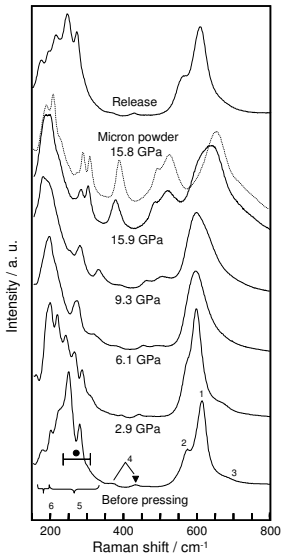

FIG. 4: Evolution of the Raman spectra upon pressing and after pressure release recorded for nanoscale $NaNbO_3$. The spectrum obtained for micron $NaNbO_3$ at 15.8 GPa (dotted curve) is stacked above the spectrum at 15.9 GPa.

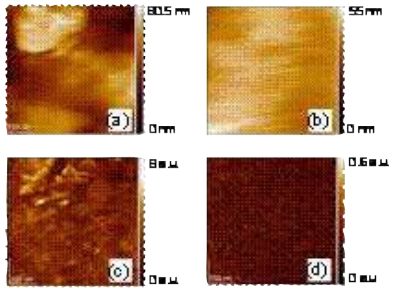

FIG. 5: Results of the AFM and in-plane PFM measurements (a,b) topological images (500 x 500 nm) and (c,d) mapping of piezoresponse for nanoscale (left) and coarse (right) $NaNbO_3$ respectively.

[1] E. Cross, Nature 432 (2004) 24.

[2] Y. Saito, H. Takao, T. Tani, T. Nonoyama, K. Takatori, T. Homma, T. Nagaya, M. Nakamura, Nature 432 (2004)

[3] Y. Shiratori, A. Magrez, J. Dornseiffer, F.-H. Haegel, C. Pithan, R. Waser, J. Phys. Chem. B 43 (2005) 20122.

[4] C. Pithan, Y. Shiratori, J. Dornseiffer, F.-H. Haegel, A. Magrez, R. Waser, J. Cryst. Growth 280 (2005) 191.

Influence of Plastic Deformation on the Distribution of Dislocations in Reduced $SrTiO_3$ Single Crystals

P. Meuffels[1], W. Speier[2]

[1]Institut für Festkörperforschung, Elektronische Materialien
[2]Wissenschaftlich Technische Planung

The electrical transport properties of $SrTiO_3$ – a model material for perovskite-type oxides – are traditionally considered as bulk phenomena and are explained on the basis of a point defect description. There are, however, some indications that the role of extended defects such as dislocation networks has also to be taken into account. $SrTiO_3$ single crystals were plastically deformed by bending experiments at room temperature in order to introduce dislocations into the lattice and to change their distribution within the crystals. After thermal reduction under high vacuum conditions, the local electrical conductivity on the surface of the deformed crystals was mapped by means of atomic force microscopy with a current probe at room temperature. Within the shear band regions which are characterized by an intense plastic deformation and thus a high dislocation density, numerous locations were found with an appreciably enhanced electrical conductivity compared to that in the un-deformed regions of the crystals. This observation indicates that networks of dislocations in reduced $SrTiO_3$ crystals are potential short-circuit pathways for the electrical transport.

Pervoskite-structured oxides ABO_3 show a wide span of electronic properties from insulating, ionically conducting, semiconducting to metallic and even superconducting behavior. The partial electrical conductivities of such materials, i.e. the ionic and/or electronic transport properties, can be changed, in many cases, by orders of magnitude by varying temperature, composition, concentration of aliovalent impurities (acceptor-type and donor-type) and high-temperature annealing conditions after material synthesis. This results in an enormous spectrum of possible applications for these materials as, e.g., sensors, electrodes, permeation membranes and heterogeneous catalysts.
The dependencies between the partial conductivities and the above mentioned parameters are traditionally considered as bulk phenomena and are explained on the basis of a point defect description [1, 2]. Within the framework of such models, it is assumed that the oxide systems behave as classical solid solutions with randomly distributed point defects. In real crystals, however, various forms of so-called extended defects such as dislocations, defect clusters, stacking faults, micro-do mains and shear planes exist. There is some evidence that extended defects and networks of extended defects can have an influence on the transport properties of pervoskite-type oxides [3, 4, 5] and that their influence cannot be viewed as to be of secondary nature.
In order to understand the role of extended defects with respect to macroscopic transport properties, their local transport properties have to be analyzed. At first, our investigation concentrated thus on the influence of dislocations and dislocation networks on the local electrical transport properties. Among all types of extended defects dislocations are of great importance because they are by nature present in every real material.
The study was performed on the perovskite-type oxide $SrTiO_3$ which serves as a model material for electroceramic oxides in general and for perovskites in particular. It is known that dislocations can act as easy diffusion paths for oxygen in $SrTiO_3$ [4] and there are indications that they can modify the electronic conductivity [5]. Recent work has shown that $SrTiO_3$ crystals can be plastically deformed even at low or moderate temperatures [6]. This offers an opportunity to artificially introduce dislocations into the lattice and/or to change their spatial distribution within the crystals.

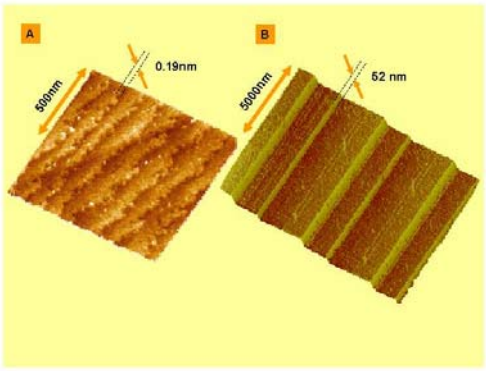

FIG. 1: Surface topography of an un-deformed (A) and plastically deformed (B) $SrTiO_3$ (100) crystal after thermal reducti on under high vacuum conditions as obtained by scanning force microscopy.

Verneuil-grown, nominally un-doped $SrTiO_3$ single crystals with (100)-orientation and dimensions of 10 x 5 x 1 mm^3 were used for our experiments. The crystals were plastically deformed by bending experiments at room temperature and then thermally reduced under high vacuum conditions at temperatures 700 – 900 °C. Fig. 1 shows the surface topographies of an un-deformed and plastically deformed $SrTiO_3$ (100) crystal after thermal reduction. The measurements were performed by means of scanning force microscopy at room temperature. It is clearly seen from fig. 1 (B) that the deformation is not homogeneous but concentrated in shear bands which appear as steps at the surface of the deformed crystal. Fig. 2 shows mappings of the local electrical conductivity on the surfaces of an un-deformed and a plastically deformed crystal after thermal reduction. The scanned surface region of the deformed crystal was selected in such a way that the exit of one shear band could be covered. The local conductivities were measured at room temperature by means of an atomic force microscopy with a current probe (LC-AFM).
The LC-AFM measurement on the un-deformed crystal shows a number of randomly distributed locations on the surface which possess an enhanced electrical conductivity compared to the surrounding matrix indicating filamentary electrical conduction. In the case of the plastically deformed crystal, a quite different picture is obtained. Numerous locations with an enhanced electrical conductivity are now found within the shear band region, whereas the un- or less-deformed parts of the crystal seem to be free from exit points i of electrically conducting filaments.

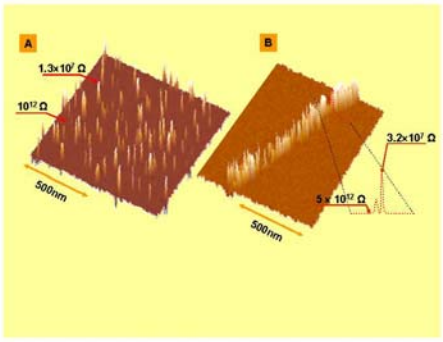

FIG. 2: Mapping of the local electrical conductivity on the surface of an un-deformed (A) and mechanically deformed (B) $SrTiO_3$(100) crystal after thermal reduction under high vacuum conditions. The data were obtained by means of scanning force microscopy with a current probe at room temperature. The measurement on the deformed sample covers the exit location of a shear band.

As intense plastic deformation of the crystal occurs on the shear bands, it is reasonable to assume that a large amount of dislocations are introduced into these regions and/or that existing dislocations pile up owing to dislocation motion as a consequence of mechanical stress. The enhanced local electrical conductivity within the shear bands seems thus to be correlated to the enhanced density of dislocations forming an extensive network. This finding indicates that dislocations in reduced $SrTiO_3$ are - compared to the surrounding matrix - potential short-circuit pathways for the electrical transport. Furthermore, the experiments show that dislocations in $SrTiO_3$ crystals can be easily arranged by simple application of mechanical stress.
There are two underlying mechanisms which might explain why dislocations are potential short-circuit pathways for the electrical transport. On the one hand, dislocations posses a disturbed crystallographic structure in comparison with the surrounding lattice. This by itself can give rise to a differing lattice dynamics and a deviating electronic structure within the core [7] and thus a deviating electrical conductivity within the dislocation core region. On the other hand, dislocations can act as sources and sinks for vacancies, i. e. one can view them as – so to speak - “one-dimensional inner surfaces” which might induce segregation effects in the nearest neighborhood [8]. Accompanying changes in the defect chemistry around the dislocation core could thus indirectly impinge on the electrical transport properties.

[1] A. A. Griffith, Philos. Trans. R. Soc. A, **21**, 163 (1921).

[2] J. Mizusaki: Solid State Ionics 52 (1192) 79.

[3] A. Nemudry , E. L. Goldberg, M. Aguirre, M. A. Alario-Franco: Solid State Sciences 4 (2002) 677.

[4] A. E. Paladino: J. Am. Ceram. Soc. 48 (1965) 476.

[5] K. Szot , W. Speier, R. Carius, U. Zastrow, W. Beyer: Phys. Rev. Lett. 88 (2002) 075508.

[6] S. Taeri, D. Brunner, W. Sigle, M. Rhle: Z. Metallkd. 95 (2004) 433.

[7] K. Szot, W. Speier, G. Bihlmayer , R. Waser: Nature Materials 5 (2006) 312.

[8] J. D. Eshelby, C. W. A. Newey, P. L. Pratt, A. B. Lidiard: Phil. Mag. 3 (1958) 75.

Synthesis of Uniform Silica Rods, Curved Silica Wires and Silica Bundles Using Filamentous Fd Virus as a Template

Johan Buitenhuis and Zhenkun Zhang

Forschungszentrum Jülich GmbH, IFF–Weiche Materie, D-52428 Jülich, Germany

We explored fd as a template to direct the formation of silica nanomaterials with different morphologies through simple sol-gel chemistry. Depending on the conditions silica nanowires can be formed, which seem to accurately transcript the bending conformation and the length of the fd viruses in solution. But also surprisingly straight silica rods may be formed, and under other conditions bow-tie-shaped bundles of rods are formed, which have a remarkably well defined shape and dimension.

One dimensional anisotropic inorganic nanostructures such as tubes, rods, wires, fibers, etc. are in the focus of research interests due to their potential applications, for example in optical, electronic and mechanical devices, sensors and catalysis[1, 2]. The synthesis of these anisotropic nanostructures is a big challenge, because most inorganic materials do not form the desired structure by themselves. In contrast to inorganic systems, biological and organic materials, especially supramolecular systems, usually have a well defined structure down to the nanoscale. Using (bio)organic materials as a template to build up anisotropic inorganic nanostructures has therefore emerged as a highly attractive method in recent years[3]. The results described in the present paper may serve as a basis for the further development of the synthesis of inorganic materials using biopolymers as a template. Similar routes of synthesis occur spontaneously in nature, for instance, in the formation of the silica cell wall of the Diatom, which is formed with an amazingly perfect pattern[4]. For the synthesis of nanomaterials, rod-like viruses, carbon nanotubes, lipid nanotubes, rod-like structures formed from organogelators, single DNA etc. offer many templates to direct the formation of anisotropic inorganic materials with special structures and properties.

In this paper, the filamentous fd virus is used as a template to regulate the formation of silica nanomaterials with well-defined morphologies. Fd viruses have a length of 880 nm and a diameter of 6.6 nm. Each virus consists of a single-stranded circular DNA molecule packed in a sheath of 2,700 identical coating proteins. Besides of its role in biochemistry where it is used for molecular cloning, fd has also been used as a rod-like model system to understand some fundamental problems of complex fluids, because it is monodisperse in size and has a nearly hard rod conformation (persistence length 2.2μm)[5]. M13, a virus which is almost identical to fd, differing only in one amino acid per coating protein, has been intensively explored by Belcher, Hammond and co-worker as a template in the synthesis of metallic and other magnetic and semiconducting nanowires[6, 7]. Their strategy is to modify the coat protein of M13 via genetic engineering specifically for each metal or oxide, so that the coat protein can selectively induce precipitation or assembly of that specific metal or oxide on the surface of the virus. However, as far as we know, there is no report concerning the application of fd or M13 as a template for silica precipitation.

In contrast to the complicated genetic engineering route used with the M13 virus, we show here that wild-type fd virus can also be used as a template in the synthesis of inorganic materials using simple sol-gel chemistry. Under different conditions, using acid-catalyzed hydrolyzation and condensation of tetraethoxysilane as silica precursor, three kinds of morphologies are observed: 1) silica nanorods with a diameter of 20 nm and a homogeneous silica layer, 2) nanowires with a curved shape and 3) bow-tie-shaped bundles with well-defined shape and hierarchy. As far as we know, we are the first to use fd as a template for material synthesis and have observed several interesting structures.

All coating procedures were carried out at low pH where fd is positively charged and the amount of silica precursor (tetraethoxy silane) was estimated so that a silica layer of 1 nm could be formed on all fd viruses. At an fd concentration of 6 mg/mL and a pH of 2.3 straight silica rods are obtained. Along the axis of the rods, the diameter is constant and the silica layer is homogeneous (see Fig.1, top image). The surface of these rods is smooth under the maximum resolution of the TEM we used and the shape of the ends of the rods is semi-spherical. Although fd is semi-flexible and somewhat curved in dispersion, most of the rods are straight and only a few slightly curved rods are seen. Long rods with a length comparable to the length of intact fd are observed along with short rods, which might form from the silica coating of the fragments of decomposed fd. Some of the rods show a clear core-shell structure with a low contrast part along the center of the whole rod (Fig.1, top image). The low contrast part might be fd.

Bow-tie-shaped bundles of silica rods are formed (Fig.1, bottom left) if the straight rod dispersion de-

scribed above is mixed with a methanol/ammonia mixture. This morphology is remarkable because as far as we know, no similar morphology has been reported for any other virus or organic template in the past. The formation of the bow-tie-shaped bundles itself seems to originate from an aggregation of (silica coated) fd viruses (and granular silica) after addition of the methanol/ammonia mixture, but the exact reason for the shape and size of the bundle remains unclear.

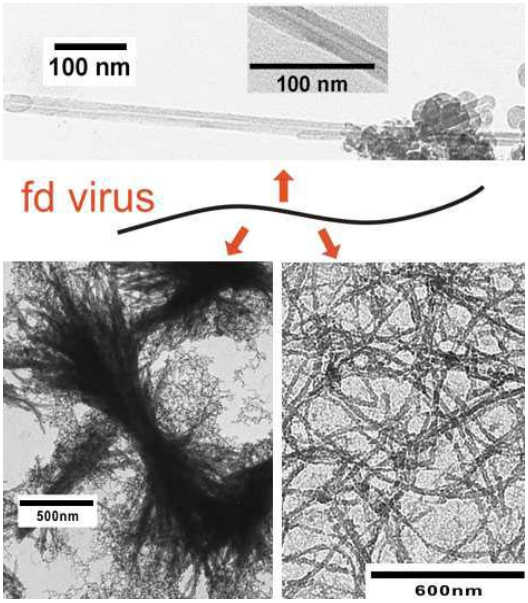

FIG. 1: Three different silica structures observed using the filamentous fd virus as a template.

At lower fd concentration and a slightly lower pH, long, curved wires are observed entangled with each other (Fig.1, bottom right). The surface of these wires is less smooth than that of the straight rods described before, and the diameter of these wires shows a less sharp distribution. The contour length of these wires is in the range of that of intact fd, while long wires with a length twice that of fd are also observed. The longer wires seem to consist of two viruses sticking together by partial parallel overlap. These results imply that most fd remains intact during wire formation, in contrast to the case of the straight rods described above, where many rods much shorter than fd are observed. The curved shape of these wires probably originates from the bending configurations of the semi-flexible fd virus in aqueous media. Therefore, these hybrid silica wires show an example of a quite precise transcription of the template, here, semi-flexible fd. Whether or not the silica coating solidifies the fd virus completely so that the flexibility is lost is not clear.

For the templating mechanism to work, the affinity of the surface of the fd virus towards silica deposition has to be high enough, so that heterogeneous nucleation of silica onto the surface of the fd virus can compete with the homogeneous nucleation of silica in the solution (so-called secondary nucleation). In the present study the formation of silica is not limited exclusively to the surface of the fd virus, but also a lot of granular silica (Fig.1, top and bottom left) due to secondary nucleation is observed. Furthermore, the amount of silica precursor was taken such that it can form a 1 nm layer of silica around all fd viruses. Because the actual layer thickness observed is much larger than 1 nm and in addition part of the silica is lost in the secondary nucleation, this means that many fd viruses are not coated at all. It is not clear why some of the fd viruses are coated with a smooth silica layer with a narrow distribution of the diameter, while some other fd viruses are not coated at all.

We demonstrated the capability of fd viruses to be used as a template for the formation of 1D silica nanomaterials. Three nanostructures with distinct morphologies have been observed under different sol-gel conditions using TEOS as silica precursor: silica rods, wires and bow-tie-shaped bundles. Silica wires seem to transcript the bending conformation and length of intact semi-flexible fd, but under somewhat different reaction conditions also remarkably straight silica rods are formed. The bow-tie-shaped bundles may form from an aggregation of (silica coated) fd viruses under the conditions adopted here, leading to bundles with a defined dimension and shape. Compared with many other organic templates, fd is almost perfect because of its narrow size distribution and the homogeneous properties of its surface. Work devoted to further understanding the results obtained in this paper and exploring the above problems is ongoing.

[1] Y. N. Xia, P. D. Yang, Y. G. Sun, Y. Y. Wu, B. Mayers, B. Gates, Y. D. Yin, F. Kim, and Y. Q. Yan, Advanced Materials **15**, 353 (2003).

[2] G. R. Patzke, F. Krumeich, and R. Nesper, Angewandte Chemie-International Edition **41**, 2446 (2002).

[3] K. J. C. van Bommel, A. Friggeri, and S. Shinkai, Angewandte Chemie-International Edition **42**, 980 (2003).

[4] M. Sumper and E. Brunner, Advanced Functional Materials **16**, 17 (2006).

[5] Z. Dogic and S. Fraden, in Soft Matter, Volume 2: Complex Colloidal Suspensions., edited by G. Gompper and M. Schick (WILEY-VCH Verlag GmbH & Co. KGaA, Weinheim, Germany, 2006), Soft Matter, pp. 1–86.

[6] C. B. Mao, D. J. Solis, B. D. Reiss, S. T. Kottmann, R. Y. Sweeney, A. Hayhurst, G. Georgiou, B. Iverson, and A. M. Belcher, Science **303**, 213 (2004).

[7] K. T. Nam, D. W. Kim, P. J. Yoo, C. Y. Chiang, N. Meethong, P. T. Hammond, Y. M. Chiang, and A. M. Belcher, Science **312**, 885 (2006).

Colloidal Particles Close to a Wall: Dynamics and Interaction Potentials

P. Holmqvist, D. Kleshchanok, P. R. Lang

Institut für Festkörperforschung, Weiche Materie

The influence of the hydrodynamic drag effect on the near wall dynamics of colloidal particles is studied by evanescent wave dynamic light scattering (EWDLS). Spherical particles as small as 27 nm in radius are shown to follow theoretical predictions for the creeping flow limit with stick boundary conditions. The presence of a second component in the colloid suspension causes an additional slowing down of the near wall dynamics, which can not be explained by the standard mean field approach.

If a particle suspended in a quiescent solvent approaches a hard wall, the so called viscous drag effect causes the particles mobility to decrease and to become ansiotropic. The theoretical description of this effect has a history of almost hundred years [1] and was cast into its widely accepted final form in the sixties of the last century by Brenner and coworkers [2]. These authors showed that the diffusion coefficient of the particle close to the wall is related to the bulk diffusion coefficient ,D_0, by the direction dependent hydrodynamic friction terms, $\lambda_{\parallel}$ and $\lambda_{\perp}$. The latter are complicated functions of the particle radius, R, and the particle–wall separation distance, z. Differently, from the theoretical achievements, experimental investigations of this effect are rather new. For macroscopic, i. e. non–Brownian particles, the theoretical predictions have been proven valid in sedimentation measurements of large spheres in highly viscous liquids [3]. With modern microscopic and optical trapping techniques it was shown that colloidal particles with a radius, R, larger than about 100 nm also behave as expected [4, 5].

We have recently improved the experimental and theoretical basis of evanescent wave dynamic light scattering (EWDLS) [6, 7], in a way that allows us to study the near wall dynamics of particles as small as ca. 25 nm in radius. In this method the evanescent wave, which is created upon total reflection of a laser beam is used as a the incident radiation for a dynamic light scattering experiment (see sketch in Figure 1).

With our novel instrumental design it is possible to vary the normal, $Q_{\perp}$, and the parallel, $Q_{\parallel}$, component, of the scattering vector (that is the difference between the wave vector of the scattered wave and the evanescent wave, $\mathbf{Q} = \mathbf{k}_S - \mathbf{k}_e$) independently.

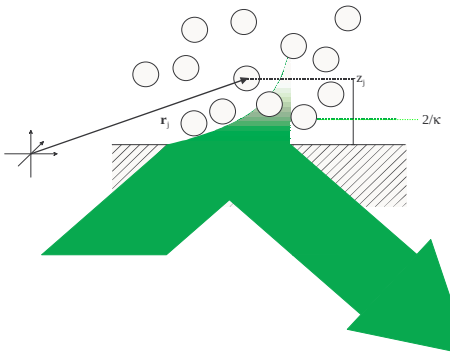

FIG. 1: Upon total reflection of a laser beam an evanescent wave is created, which has an exponentially decaying electric field strength with a penetration depth $\kappa/2$. The evanescent wave is used as the radiation source for a dynamic scattering experiment in EWDLS.

By this means it becomes possible to distinguish between the particle mobility parallel and normal to the interface. For a thorough data analysis, it was further necessary to derive a theoretical expression for the initial decay rate; Γ, of the time auto correlation function of the scattered field, $g_1(t)$, which takes into account hydrodynamic and static interaction between the colloidal particles and the wall. Combining the new set-up and the expression for Γ it is possible to determine normalized mean particle diffusivities parallel and normal to the wall

$$\frac{\langle D_{\parallel,\perp} \rangle}{D_0} = \frac{\int_{z>R} dz \exp\{-\beta\phi(z)\} \exp\{-(z-R)\kappa/2\} \lambda^{-1}_{\parallel,\perp}(z)}{\int_{z>R} dz \exp\{-\beta\phi(z)\} \exp\{-(z-R)\kappa/2\}} \quad (1)$$

Here $\beta\phi(z)$ is the static particle–wall interaction potential in units of the thermal energy. The integrations are performed inherently in the experiments, i. e. $\langle D_{\parallel,\perp} \rangle$ are the mean values of the diffusivities, which are averaged over the entire z–range that is illuminated by the evanescent wave.

In Figure 2 we show experimental data of $\langle D_{\parallel,\perp} \rangle / D_0$ vs. the scaled penetration depth $\xi = \kappa/(2R)$ from dilute solutions of two colloidal samples with different radii in a solution of 10mM additional electrolyte. Under these conditions the particles may be regarded as hard spheres. Accordingly the experimental data coincide well with the theoretical curves according to

eq. 1 with $\beta\phi(z) = 0$ for $z > R$ (see square symbols and full lines in Figure 2).

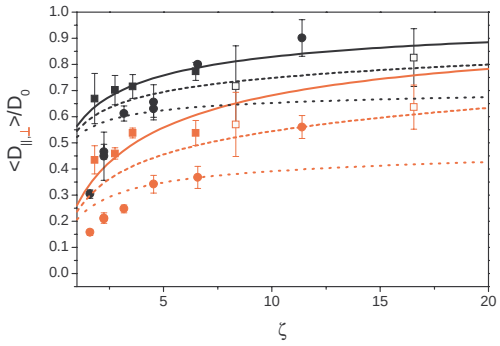

FIG. 2: Normalized mean diffusivities vs. scaled penetration depth. Different colors refer to the diffusivity parallel (black) and normal (red) to the wall. Symbols are experimental data from spherical particles with $R = 85$nm (full symbols) and $R = 27$nm (open symbols) in pure salt solution (squares) and in the presence of fd-virus (bullets). Full lines represent theoretical predictions for different contact values of the depletion potential according to eq.2: full line: $\alpha = 0$, dashed line $\alpha = 2k_BT$ and dotted line $\alpha = 5k_BT$

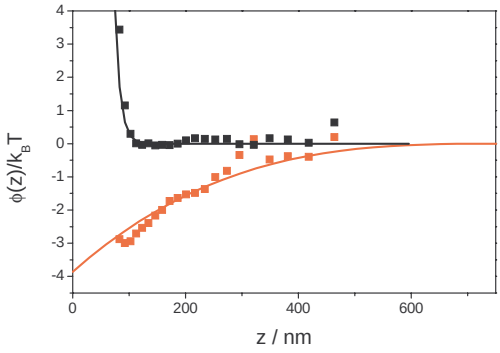

FIG. 3: Interaction potentials between a wall and a Polystyrene sphere with $R = 2.7\mu$m. Symbols are experimental data and full lines are parameter free calculations according to eqs. 2 and 3. Different colors represent the electrostatic (black) and the depletion (red) contribution to the total potential.

If an additional polymer or colloidal component is added to such a solution, this leads to an effective attractive potential between the wall an the particles, the so–called depletion interaction. In the present case we studied the influence of the depletion interaction induced by rod–shaped colloids (fd-viruses) on the near wall dynamics of colloidal spheres. The depletion interaction induced by a rod of length L has the form

$$\beta\phi_{depl}(z) = -\alpha\left(1 - \frac{z}{L}\right)^3 \qquad (2)$$

in the Derjaguin–approximation, i. e.if the radius of the spherical particle is much larger than the rod length. Here the contact value α is an increasing function of the rod number density, the rod length and the particle radius.

Using Total Internal Reflection Microscopy (TIRM) [8] we are able to measure directly the interaction potential between a single sphere and a wall [9]. In Figure 3 we show experimentally determined contributions to the total interaction potential between a charge stabilized sphere with radius $R = 2.7\mu$m and a like charged wall. The electrostatic contribution can be well described in the Debye–Hückel approximation

$$\beta\phi_{DH}(z) = B\exp\{-\kappa_{DH}z\} \qquad (3)$$

where the amplitude, B, is related to the charge density on the particle and the wall surface and κ_{DH}^{-1} is the Debye screening length, which can by tuned by the addition of electrolyte to the colloid solution. The experimental data for the depletion interaction fit well with the expression of eq. 2 where α was calculated without any adjustable parameter.

The influence of the depletion potential induced by fd-virus on the near wall dynamics of colloidal spheres with $R = 85$nm is displayed also in Figure 2. As compared to the fd–free case the mean diffusivities decrease significantly and the anisotropy of the mobility increases. A comparison of the experimental data with the theoretical predictions according to eq. 1 however shows that the theory grossly underestimates the additional slowing down especially at low penetration depths and for the case of the diffusivity normal to the interface.

This implies that it is not possible to describe the influence of the second co–solute on the near–wall dynamics of colloidal spheres by an effective mean field depletion potential. We conjecture that the rods have to be treated as a second component which couples hydrodynamically to the mobility of the spheres. We plan to do Brownian Dynamics computer simulations in the future to clarify this point.

[1] H. A. Lorentz, Abh. Theor. Phys. **1**, 23 (1907).

[2] H. Brenner, Chem. Eng. Sci. **16**, 242 (1961).

[3] Z. Adamcyzk, M. Adamcyzk and T. G. M. Van De Ven J. Colloid Interface Sci. **96**, 204 (1983).

[4] B. Lin, J. Yu, and S. A. Rice, Phys. Rev. E **62**, 3909 (2000).

[5] L. Joly, C. Ybert, and L. Bocquet, Phys. Rev. Lett. **96**, 046101 (2006).

[6] P. Holmqvist, J. K. G. Dhont, and P. R. Lang, Phys. Rev. E **74**, 021402 (2006). DOI: 10.1103/PhysRevE.74.021402

[7] P. Holmqvist, J. K. G. Dhont, and P. R. Lang, J. Chem. Phys. **126**, 044707 (2007).

[8] D. C. Prieve, Adv. Colloid Interface. Sci. **82**, 93 (1999).

[9] D. Kleshchanok, R. Tuinier, and P. R. Lang Langmuir **22**, 9121 (2006). DOI: 10.1021/la061657m

The Hydrodynamics in Dense Rod Suspensions as Studied by Video Microscopy and Multi-Particle Collision Dynamics Simulations

M. P. Lettinga[1], S. Messlinger[2], Z. Zhang[1], and G. Gompper[2]

[1]Institute Soft Condensed Matter
[2]Institute Theory of Soft-Matter and Biophysics

The effect of hydrodynamic interactions on the diffusion of rods in dense rod suspensions is studied. We do this experimentally by fluorescent microscopy on charged rod-like viruses with and without polymer coating and theoretically by computer simulations with and without solvent particles. Thus we have we have a handle on hydrodynamic interactions both in experiment as in simulations. We observe that the anisotropy in the diffusion of rods in the nematic phase is set by the effective excluded volume, while the absolute diffusion is set by hydrodynamic interaction.

The diffusion of colloidal particles in a complex network is a field of research that is of both physical and practical interest. The most common examples in biology are transport phenomena in the cell, which is practically a dense packed system with often a backbone structure of actin filaments. In order to systematically investigate the diffusion properties in complex systems often model systems are used like colloids in an actin network [1]. These model systems consist in most cases of an unordered host matrix probed by a spherical tracer particles, whereas in nature ordering plays an important role and the diffusing particles are anisotropic. One important example is the cell nucleus, where DNA is most efficiently packed and unpacked when the DNA molecules are aligned, i.e. when they form a nematic phase. To mimic this type of diffusion one should investigate the diffusion of rods in the isotropic (I) and nematic (N) phase.
This diffusion has been studied extensively throughout the past decade for both lyotropic and thermotropic liquid crystals. Experimentally the diffusion of boehmite rods and polymeric liquid crystals have been studied using fluorescence recovery after photo-bleaching, while for rod-like viruses diffusion was directly observed with fluorescence video microscopy [2]. In all cases it was shown that the phase transition from the isotropic to the nematic phase causes a splitting up of the diffusion matrix in a fast component parallel to the nematic director and a slow component perpendicular to it. Now the splitting up of the diffusion has been well established, the next step is to understand on which parameters the diffusion depends and how it takes place. Nowadays, computer simulations can help understanding the microscopic details of rod diffusion. In literature one can find several examples of computer simulations of rod-like colloids. However, there are no simulations which explicitly take one of the most important ingredients of rod suspensions into account, namely the solvent. For single rods in infinite dilution it is known that hydrodynamic interactions due to the solvent strongly affects rod diffusion. Analytical calculations show that the diffusion constant $D_{||}$ of diffusion in the direction parallel to the rod axis is about twice as large as that one for perpendicular diffusion $D_{\perp}$. In addition to this diffusion anisotropy, the total diffusion constant, defined by $D_{tot} = 1/3(D_{||} + 2D_{\perp})$, is larger than the diffusion constant

$$D_0 = \frac{k_B T}{\eta} \frac{1}{3\pi L} \qquad (1)$$

in an imaginary solvent without hydrodynamic interactions where η is the viscosity of the solvent. It was shown that

$$\frac{D_{tot}}{D_0} = \ln(\frac{L}{d^{hyd}}) \qquad (2)$$

holds for leading orders in the d^{hyd}/L. Here L is the rod length and d^{hyd} denotes the hydrodynamic rod diameter. For concentrated rod suspensions, an other rod diameter plays a role, namely the effective diameter d^{eff}. This diameter defines a minimum lateral distance between two rods due to direct repulsive rod-rod interaction, and is crucial e.g. for the static phase behaviour. To this day, there is no theory which gives an analytical expression of the diffusion matrix for such systems. In this report we therefore approach this question with experiments as well as simulations.

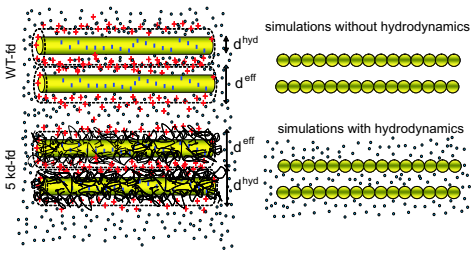

FIG. 1: The $in\ vitro$ and $in\ silica$ systems.

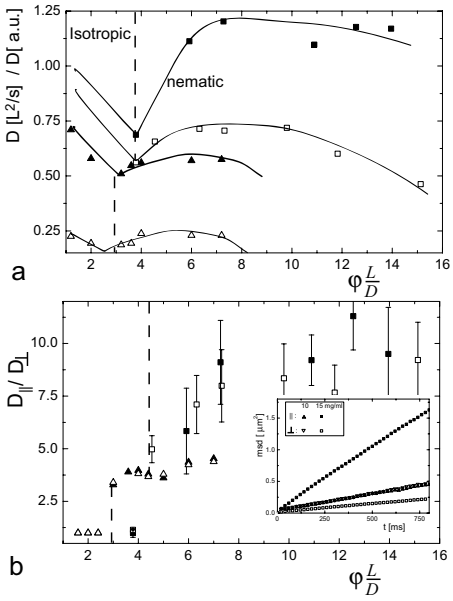

FIG. 2: (a) The scaled absolute diffusion as a function of the scaled concentration for wild type (■) and coated fd (□) and as found by simulations ($L/d = 20$) with (▲) and without (△) HD interactions. (b) The ratio of the diffusion parallel and perpendicular to the director. Symbols as in (a). The inset shows the mean square displacement parallel and perpendicular to the director in the nematic and isotropic phase. The dashed line in both plots indicates the phase transition concentration.

For the experiments we use fd viruses in combination with video microscopy [2]. The fd virus constitutes a very suitable model system because they are intrinsically monodisperse, very thin ($L = 880\ nm$, $D = 6.6\ nm$) and stiff (persistence length $P = 3.0\ nm$). Moreover, the effective diameter d^{eff} can be changed by decreasing the ionic strength, i.e. increasing the Debye screening length, or by coating the virus with poly-ethylene oxide (PEO). We use these features by doing measurements at an ionic strength of 20 mM and by using wild-type viruses and viruses coated with 5 kd PEO. Since the I-N phase transition of WT-fd and 5kf-fd at this ionic strength takes place at the same concentration, these rods have the effective diameter d^{eff}. They have, however, a different hydrodynamic radius d^{hyd} because for WT-fd solvent particles can go in penetrate between the rods when the effective diameters start to overlap, while this is not possible for 5kd-fd. Thus we have $d^{eff} = d^{hyd} = 14\ nm$ for 5kd-fd, and $d^{eff} = 14\ nm$ and $d^{hyd} = 6\ nm$ for WT-fd, see Fig. 1. For the video microscopy we used alexal488-labelled fd viruses in a host dispersion of unlabelled fd, at a ratio of 1:10000. We used a fluorescence microscope equipped with a EM-CCD camera operating at a frame rate of 50 frames per second. Tracking the individual rods we obtain the mean square displacement vs. time, the slope of which gives the diffusion rates of the rods. In the nematic phase the diffusion has a component parallel and a component perpendicular to the director. The orientation of the director is obtained from the anisotropy in the the diffusion and independently also from the average orientation of the rods. An example of the mean square displacement in the isotropic and nematic phase is given in the inset in Fig. 2b. In simulations [3], rod dynamics is solved using standard molecular dynamics (MD). For simulating the solvent, we use a novel particle based simulation method called "multiple particle collision (MPC) dynamics". This method provides both all hydrodynamic and thermodynamic properties which are essential for the rod dynamics. For a more detailed description see Ref. [4]. A modified version of the MPC algorithm, called "random MPC solvent", can be used in order to suppress hydrodynamic interactions. Thus it is possible to compare simulations with and without hydrodynamics, but with same thermodynamical properties. The aspect ratio of the simulated rods was 20.

The experiment and simulations yield two interesting parameters: the ratio $D_{||}/D_{\perp}$ of the two diffusion constants, which quatifies the anisotropy in the diffusion, and the absolute diffusion constant D_{tot}. We anticipate that both parameters depend differently on hydrodynamic interactions between the particles and the aspect ratio of the particles. These parameters are plotted as a function of concentration in Fig. 2. From the data of the absolute diffusion (Fig. 2a) we can draw two conclusions. First it shows for all studied systems that the total diffusion increases after the I-N phase transition, as was already found earlier. Second, and more interestingly, it shows that the absolute diffusion is strongly influenced by the hydrodynamic interactions: both the simulated and experimental data show that the diffusion constants are increased due to hydrodynamic effects by a factor of about two. Interestingly this factor is of the same order as in infinite dilution (see Equ. 2). Fig. 2b shows that anisotropy in the diffusion is not influenced by hydrodynamics. In other words the anisotropy is the same if the effective diameter d^{eff} is the same, independent of the hydrodynamic radius. It is therefore fully determined by the topological constraints.

To conclude, we observe both by experiments and simulations that the anisotropy in the diffusion of rods in the nematic phase is set by the effective excluded volume, while the absolute diffusion is set by hydrodynamic interaction.

[1] K. Kang et al., J. Chem. Phys **122**, 044905 (2005).

[2] M. P. Lettinga et al., Europhys. Lett. **71**, 692 (2005).

[3] S. Messlinger and G. Gompper, to be published

[4] R. G. Winkler et al., J. Chem. Phys **169**, 326 (2005).

Diffusion in Charge-Stabilized Colloidal Suspensions: Theory, Simulation and Experiment

G. Nägele, G. Meier, M. P. Lettinga, P. Holmqvist and M. G. McPhie

Institute Soft Matter

We report on a joint experimental-theoretical study of diffusion processes in dense suspensions of charge-stabilized colloidal spheres. Numerous transport properties have been calculated by means of a recently developed accelerated Stokesian dynamics simulation tool, and using methods of many-body theory adapted to soft matter. The simulation and theoretical methods describe quantitatively our static and dynamic scattering experiments on colloidal particles, globular proteins and DNA fragments. Salient results of this study comprise the absence of screening of hydrodynamic flow in salt-free suspensions, and a hydrodynamic explanation for the unexpected non-monotonic concentration dependence of self-diffusion in suspensions of moderately charged particles.

Charge-stabilized suspensions are composed of charged meso-scaled colloidal particles or macromolecules dispersed in a low-molecular polar solvent like water. The importance of these soft matter systems is based on the fact that they ubiquitously occur in chemical, environmental and food industry, and in many pharmaceutical, cosmetic and biological products. Examples include proteins and viruses, paint and clay particles, and well-characterized model systems consisting of spherical colloidal spheres. For the latter type of model systems, a considerable amount of work was done during the past years to explore and understand the dynamics of charged spheres on a microscopic basis.

The diffusion properties of charge-stabilized colloids are determined by a subtle interplay of electro-steric and hydrodynamic inter-particle forces. Charge-stabilized particles interact electrostatically by an exponentially screened Coulomb repulsion originating from the overlap of neutralizing electric double layers formed by surface-released counter-ions and residual or added salt ions. Hydrodynamic interactions (HI), on the other hand, are transmitted by complicated solvent flow pattern created by the moving particles. In unconfined suspensions of mobile particles, HI are very long-range and decay with the inter-particle distance r like $1/r$. The inherent many-body character of the long-range HI causes challenging problems in theoretical and computer simulation studies of particle diffusion. HI strongly affect the diffusion and rheological properties of suspensions, and they can give rise to unexpected dynamic effects.

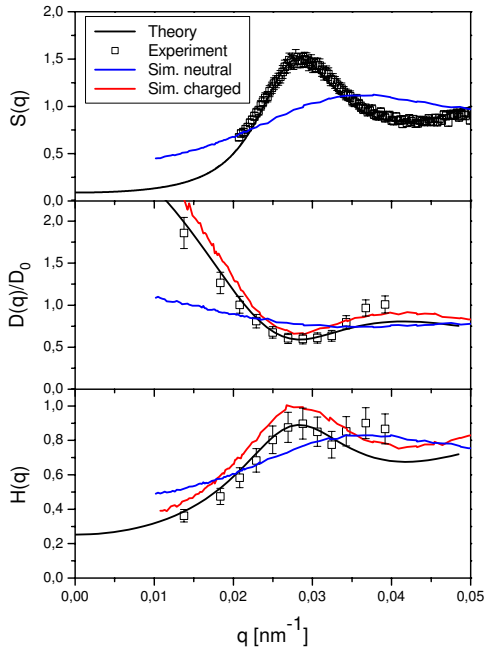

FIG. 1: Hydrodynamic function $H(q)$, diffusion function $D(q)$, and structure factor $S(q)$ of a low-salt suspension of polystyrene spheres. Shown are experimental results (open squares) in comparison to simulation results (red lines) and many-body theory (black lines). Blue lines: simulation data for neutral spheres at same concentration. For details see [2].

A salient measure of the influence of HI with regard to diffusion is given by the so-called hydrodynamic function $H(q)$. It can be determined by a combination of static and dynamic scattering experiments using visible laser light, X-rays or thermal neutrons. Without HI, $H(q)$ is equal to one. Any variation in its dependence on the scattering wave number q is a hallmark of HI. At large q, $H(q)$ becomes proportional to the short-time self-diffusion coefficient D_S. At small wave numbers it reduces to the mean sedimentation velocity of colloidal particles. In earlier work [1], it had been concluded that hydrodynamic

interactions between charged colloidal particles are screened in the important case of a low-salt suspension. This conclusion was based on the observation of experimentally extracted values of $H(q)$ that are smaller than for a suspension of neutral hard colloidal spheres at the same concentration. The interpretation of the strong hydrodynamic hindrance in terms of hydrodynamic screening caused a strong controversy since, according to theory, HI screening should not occur for liquid-state suspensions of mobile particles.

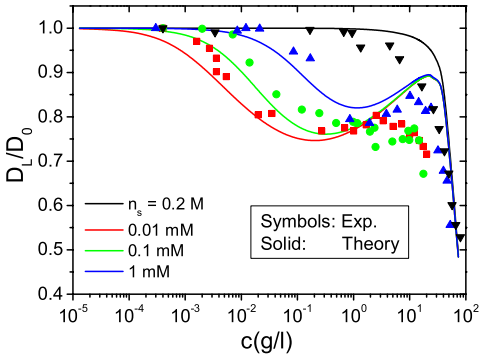

FIG. 2: Theoretical calculations with HI of the long-time self-diffusion coefficient, D_L, are compared to experimental fluorescence correlation spectroscopy data for weakly charged DNA fragments in water. The non-monotonic dependence of D_L on the DNA concentration is due to hydrodynamic interactions. For details see [6].

In two recent articles [2, 3], we have shown that, in fact, there is no hydrodynamic screening present in low-salinity systems. This important result has been obtained from combining dynamic synchrotron radiation measurements of $H(q)$ with static synchrotron measurements of the structure factor $S(q)$, performed on aqueous suspensions of fluorinated latex spheres, in comparison to dynamic computer simulations and predictions from a hydrodynamic many-body theory. The synchrotron experiments on the latex spheres have been done at the European Synchrotron Radiation Facility in Grenoble. The simulations were performed using a novel accelerated Stokesian Dynamics method. Our simulation results for $H(q)$ are the only ones available so far for charge-stabilized suspensions with significant many-body HI. All our experimental data on $H(q)$, and on the collective diffusion function $D(q) = D_0 H(q)/S(q)$, where D_0 is the diffusion coefficient of an isolated sphere, can be quantitatively described by the simulations, and by the many-body hydrodynamic theory. In particular, the behavior of $H(q)$ for de-ionized dense suspensions can be explained by many-body HI effects, without requiring to conjecture hydrodynamic screening. Experimental, theoretical and computer simulation results for $H(q)$, $D(q)$ and $S(q)$ of a low-salt system are shown in Fig. 1. The data are compared to simulation predictions for a suspension of neutral hard spheres of same radius and concentration. A similarly successful comparison between theory, simulation and experiment has been made for the diffusion properties of solutions of nano-sized globular apoferritin proteins [4].

The long-time self-diffusion coefficient, D_L, of colloidal particles is given by the long-time slope of the particle mean squared displacement. It is commonly expected that long-time diffusion slows down with increasing particle concentration because of enlarged particle interactions. Quite surprisingly, however, a non-monotonic concentration dependence has been observed for suspensions of moderately charged particles at low salinity like DNA fragments [5]. Using a hydrodynamic version of mode coupling theory, we can explain this unusual behavior of D_L by an interplay of short-range and long-range hydrodynamic force contributions (see Fig. 2).

In conclusion, by a concerted experimental-theoretical effort, we could explain and quantify the influence of hydrodynamic particle interactions on diffusion properties of charge-stabilized colloidal spheres and biological macromolecules. A consistent understanding of the micro-hydrodynamics of simple charge-stabilized model systems is important to gain improved insight into transport properties of more complex colloidal particles relevant to industry and biology.

[1] D.O. Riese, G.H. Wegdam, W.L. Vos, R. Sprik, D. Fenistein, J.H.H. Bongaerts and G. Grübel, Phys. Rev. Lett. **85**, 5460 (2000).

[2] A.J. Banchio, J. Gapinski, A. Patkowski, W. Häussler, A. Fluerasu, S. Sacanna, P. Holmqvist, G. Meier, M.P. Lettinga and G. Nägele, Phys. Rev. Lett. **96**, 138303 (2006).

[3] J. Gapinski, A. Patkowski, A.J. Banchio, P. Holmqvist, G. Meier, M.P. Lettinga and G. Nägele, J. Chem. Phys. **126**, 1 (2007).

[4] J. Gapinski, A. Wilk, A. Patkowski, W. Häußler, A.J. Banchio, R. Pecora and G. Nägele, J. Chem. Phys. **123**, 054708 (2005).

[5] A. Wilk, J. Gapinski, A. Patkowski and R. Pecora, J. Chem. Phys. **121**, 10794 (2004).

[6] M.G. McPhie and G. Nägele, to be submitted.

Thermal Diffusion Behavior of hard Sphere Suspensions: A new Approach to solve a 150 year old Problem

H. Ning, J. Buitenhuis and S. Wiegand

Soft Condensed Matter

The molecular origin of the thermal diffusion process or Ludwig-Soret effect is one of the unsolved problems. It relates to our poor understanding of non-equilibrium statistical mechanics pointing out our incapability of obtaining, in some cases, even qualitative predictions, which are of practical importance in separation processes (Thermal field flow fractionation of polymers and colloids, isotope separation), characterization of geochemical processes (Salton Sea geotherm, oil reservoir composition) and combustion. One of our strategies to tackle this problem is the investigation of a spherical colloidal model system with a short range repulsive interaction potential. We studied a colloidal dispersion in the intermediate concentration range (volume fraction $\phi < 10$ %) and found that the interactive part of the Soret coefficient agrees with an analytical theory. At higher concentration the Soret coefficient follows a power law. The temperature dependence of the Soret coefficient is mainly determined by single particle contributions and agrees to some extent with the temperature dependence of the surface coating material, octadecane, in toluene.

Colloidal particles are small enough to exhibit thermal motion commonly referred to as Brownion motion. Being just very large molecules in a solvent, colloidal particles show many physical phenomena that are also found in ordinary molecular systems. Consequently, colloids have been used frequently to study fundamental questions in physics. Therefore, it is expected that they are also a suitable model system to illuminate the microscopic mechanism underlying the Ludwig-Soret effect, which was discovered already 150 years ago [1]. This effect, also known as thermal diffusion, describes the diffusive mass transport induced by a temperature gradient in a multicomponent system. The scenario for a binary mixture of particles is sketched in figure 1.

A number of studies show that interactions play an important role for the thermal diffusion behavior, where long ranged repulsion between charged micelles and colloids has been considered [2, 3, 4].

Conceptually, thermal diffusive behavior of highly diluted and concentrated solutions can be differentiated. In dilute solutions, where colloid-colloid interactions can be neglected, the thermal diffusion coefficient of the colloids is determined by the nature of the interactions between single colloidal particles and solvent molecules (and possibly other solutes like ions that form a double layer around the colloids). Structural changes of the surrounding solvation layer due to temperature changes and/or changes of the solvent composition may induce a sign change of the thermal diffusive behavior of single colloidal particles. Usually, the mechanism leading to a sign change is system dependent. Although, for several aqueous mixtures with and without solutes such as polymers and colloids, we found the sign change concentration is almost system independent and strongly correlated with the breakdown of the hydrogen-bond network [5]. Also the temperature dependence of S_{T} for a large class of macromolecules and colloids in water shows a distinctive universal characteristic [6]. A pronounced concentration dependence of the Soret coefficient has been found in experiments [7, 2] and is predicted by theory [8].

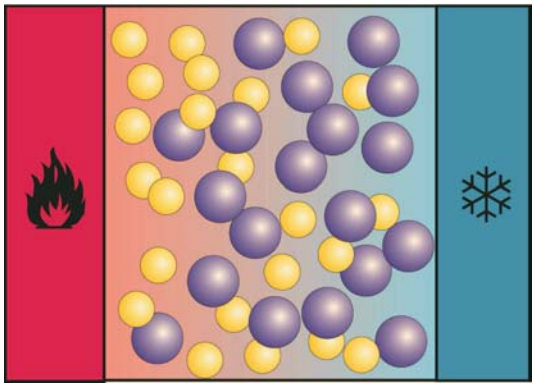

FIG. 1: Schematic illustration of the thermal diffusion process in a binary mixture in a temperature gradient. The small and big particles accumulate at the hot and cold side, respectively.

In recent years, modern optical techniques have been developed which allow the investigation of complex fluids with slow dynamics such as polymer solutions and blends, micellar solutions, colloidal dispersions and bio-molecules [4, 9, 6, 10, 11]. The main issues of interest were the derivation of scaling laws and to understand the sign change of the Soret coefficient for macromolecular and colloidal systems on the basis of existing theories for molecular fluids.

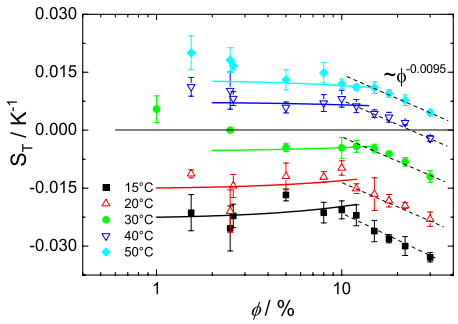

FIG. 2: Concentration dependence of the Soret coefficient at different temperatures. The solid line represents a fit of the data according to the theory by Dhont [8].

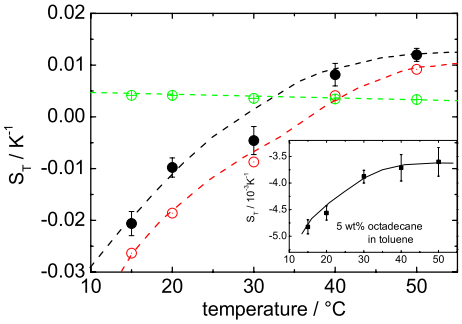

FIG. 3: The measured Soret coefficient (•) versus temperature for a colloidal suspension with a volume fraction of ϕ=10%. According to the theoretical approach by Dhont the single (⊙) and the collective part (⊕) of S_T can be separated. The dashed lines are guides to the eye. The inset shows S_T of octadecane in toluene versus temperature for a octadecane concentration of w=5 wt%.

In the past few years several theoretical concepts have been proposed to understand single particle and colloid-colloid interaction contributions to the thermophoretic motion of colloidal particles [12, 13, 14, 8]. While the majority of the theoretical approaches give expressions for the single particle contribution, the work by Dhont gives explicit expressions for the contribution of colloid-colloid interactions to the thermal diffusion coefficient D_T. These interaction contributions lead to a concentration dependence of the thermal diffusion coefficient. According to this theory, a sign change of the Soret coefficient as a function of temperature and concentration is possible for appropriate interaction parameters.

We studied spherical silica particles, sterically stabilized by octadecane, with a radius of $a = 27$ nm dispersed in toluene. The thermal diffusion behavior was studied in a concentration range between 1% and 30% by volume fraction and in a temperature range from 15-50 °C [15]. At low temperature the colloids move to the warm side, while at high temperatures the colloids move to the cold side. Typically, the movement of the solute particles to the cold side is an indication for poor solvent conditions, while under good solvent conditions the particles move to the warm side. In the intermediate concentration range the concentration dependence of the Soret coefficient can be described by theory for hard spheres [8]. At high concentrations S_T follows a power law as it also has been found for polymers approaching the glass-transition [11]. Although the exponent is two orders of magnitude smaller.

A separation of the Soret coefficient into a single particle contribution and an interactive part, shows, that the interactive part is almost temperature independent, while the single part shows a strong temperature dependence, which has the same tendency as the Soret coefficient of octadecane in toluene (cf. Fig. 3). But for the low molecular weight system no sign change occurs in the investigated temperature range. This might be an indication that also the silica core of the particles influences the thermal diffusion behavior. Also the fact that octadecane is bound to a surface might influence the thermal diffusion behavior. In general one can expect, that if the particle coating changes from " organophilic" to "organophobic" a sign change could be expected, but under which conditions this is the case needs to be clarified in further investigations.

[1] C. Ludwig, Sitz. ber. Akad. Wiss. Wien Math.-naturw. Kl 20, 539 (1856);C. Soret, Arch. Geneve 3, 48 (1879).

[2] R. Piazza, Phil. Mag. 83, 2067 (2003).

[3] K. Morozov, J. Magn. Magn. Mater. 201, 248 (1999).

[4] S. A. Putnam and D. G. Cahill, Langmuir 21, 5317 (2005).

[5] S. Wiegand, H. Ning, and R. Kita, J. Non-Equilib. Thermodyn., to be published.

[6] S. Iacopini, R. Rusconi, and R. Piazza, Eur. Phys. J. E 19, 59 (2006).

[7] H. Ning, R. Kita, H. Kriegs, J. Luettmer-Strathmann, and S. Wiegand, J. Phys. Chem. B. 110, 10746 (2006).

[8] J. K. G. Dhont, J. Chem. Phys. 120, 1632 (2004) and 1642 (2004).

[9] B. J. de Gans, R. Kita, B. Müller, and S. Wiegand, J. Chem. Phys. 118, 8073 (2003).

[10] S. Duhr and D. Braun, Phys. Rev. Lett. 96, 168301 (2005).

[11] J. Rauch and W. Köhler, Macromolecules 38, 3571 (2005).

[12] S. Fayolle, T. Bickel, S. Le Boiteux, and A. Würger, Phys. Rev. Lett. 95, 208301 (2005).

[13] E. Bringuier and A. Bourdon, Phys. Rev. E 67, 011404 (2003).

[14] A. Parola and R. Piazza, Eur. Phys. J. E. 15, 255 (2004).

[15] H. Ning, J. Buitenhuis, J. K. G. Dhont, and S. Wiegand, J. Chem. Phys. 125, 204911 (2006).

Dynamics of Vesicle Self-Assembly and Dissolution

Hiroshi Noguchi, Gerhard Gompper

Institute Theory II, IFF, Forschungszentrum Jülich, D-52425 Jülich, Germany

We have proposed a new particle-based membrane model, which is well suited to study the membrane dynamics with topological changes. The hydrodynamic interactions can be taken into account by the combination of this model with multi-particle collision dynamics. Using this model, we have clarified the features of the vesicle self-assembly and dissolution. In the assembly, disk-like clusters are first formed, aggregation of clusters into larger membrane patches, and finally vesicle formation. In the disassembly, vesicles dissolve via pore formation in the membrane. Hydrodynamic interactions are found to speed up the dynamics in both cases. Furthermore, hydrodynamics makes vesicle more spherical in the membrane-closure process.

INTRODUCTION

Bilayer membranes are biologically important as model systems for the plasma membrane and intracellular compartments in living cells. A closed membrane, vesicle exhibits rich dynamical behaviors far from equilibrium, where hydrodynamic interactions play a role as well as the thermal fluctuations. However, in comparison with equilibrium properties, the non-equilibrium phenomena are much less explored.

Lipids and other surfactant molecules spontaneously assembly and form vesicles in dilute solutions. The self-assembly dynamics was studied experimentally by time-resolved scatting techniques but the detailed shapes and dynamics are difficult to observe experimentally. The solubilization of vesicles is the inverse process of self-assembly. Detergents can dissolve lipid membranes into small micelles in various pathways dependent on the combination of detergent and lipid.

We have proposed a particle-based meshless membrane model [1], where the bilayer membrane is described as mathematical surface with curvature elasticity. We simulate the self-assembly from a random spatial distribution of monomers into membrane patches, the closure of flat membrane patches into vesicles, and the dissolution of vesicles after rupture [2]. Effects of hydrodynamic interactions are investigated by comparing Brownian dynamics (BD) with a particle-based mesoscale solvent simulations, multi-particle collision (MPC) dynamics [3].

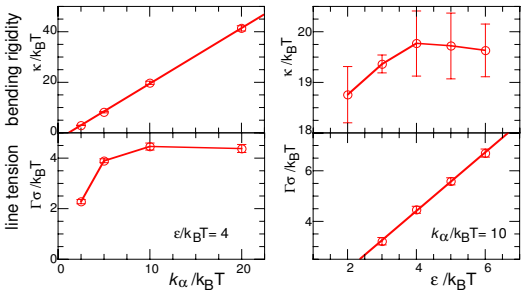

FIG. 1: k_α and ε dependences of the bending rigidity κ and line tension Γ.

MESHLESS MEMBRANE MODEL

A membrane consists of N particles, which interact via a potential

$$U = \varepsilon(U_{\rm rep} + U_{\rm att}) + k_\alpha \sum_i \alpha_{\rm pl}(\mathbf{r}_i), \qquad (1)$$

which consists of a repulsive soft-core potential $U_{\rm rep}$, an attractive potential $U_{\rm att}$, and a curvature potential. The curvature potential keeps particles to a quasi-2D plane. The aplanarity $\alpha_{\rm pl}$ is the degree of deviation from a plane and calculated from the weighted gyration tensor.

The free energy of a fluid membrane is given by

$$F = \int \left[\gamma + \frac{\kappa}{2}(C_1+C_2)^2 + \bar{\kappa} C_1 C_2\right] dA + \int \Gamma ds, \quad (2)$$

where C_1 and C_2 are the principal curvatures at each point of the membrane. In this model, the bending rigidity κ and line tension Γ can essentially be varied independently (see Fig. 1). κ increases linearly with k_α and is almost independent of ε. On the other hand, Γ increases linearly with ε and is almost independent of k_α. The saddle-splay modulus $\bar{\kappa}$ is roughly estimated as $\bar{\kappa} \simeq -\kappa$.

Self-assembly

Particles first self-assemble into disk-like clusters, and then the clusters aggregate into larger membrane patches. A vesicle is formed after the disk-like cluster becomes larger than the critical size. The critical size agrees with the energy calculation of the spherical-cap membrane [4], which shows that the vesicle is the equilibrium shape at $N > N_0 = \pi(\kappa/\Gamma)^2/a_0$ and there is an energy barrier between sphere and disk for $N < 4N_0$, where a_0 is the area per particle. The aggregation of disk-like clusters

shows growth law, the average cluster size $\langle n_c \rangle \propto t$. The assembly dynamics with hydrodynamic interactions (MPC) is faster than without hydrodynamic interactions (BD) but do not seem to change the dynamics qualitatively. This linear growth laws can be understood on the basis of Smoluchowski rate equations.

To investigate the closure dynamics into a vesicle in detail, we employ a flat square-shaped membrane with a fixed size as initial condition. All membranes close via bowl-like shape a little above the metastability limit $N > 4N_0$. However, for much larger vesicle with $N \gg 4N_0$, some of membranes are found to close via a S-shaped conformation and divide into two vesicles (see Fig. 2). We also studied the detailed dynamics via a bowl-shaped membrane. The membrane shape at large Γ/κ is the section of an oblate ellipse rather than sphere as shown in the left-bottom snapshot in Fig. 2. It is quantified by the calculation of the radius of gyration R_g and asphericity, which is the degree of deviation from a spherical shape. However, hydrodynamic interactions reduce this deviation and make the membrane more spherical.

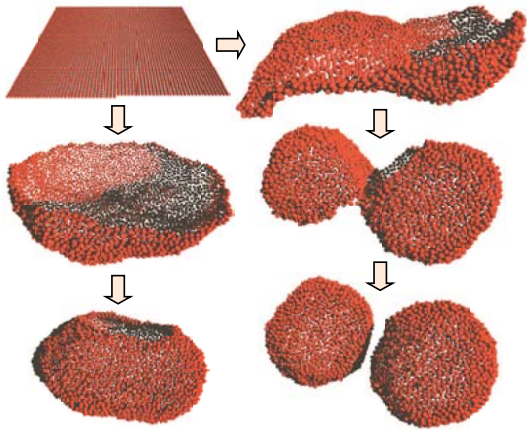

FIG. 2: Snapshots of closing membranes of BD at $N = 4000$, $k_\alpha/k_BT = 5$, and $\varepsilon/k_BT = 6$ ($N \gg N_0 = 30$).

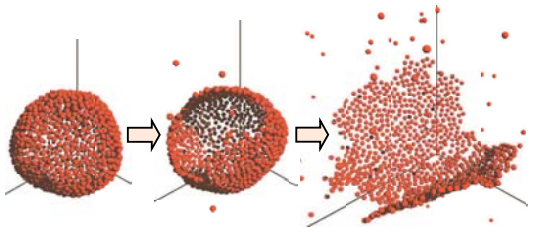

FIG. 3: Snapshots of the dissolution process of a vesicle in BD simulation with $N = 1000$, $k_\alpha/k_BT = 10$, $\varepsilon/k_BT = 1.3$.

The closing dynamics depends on the membrane viscosity η_{mb} as well as the solvent viscosity η_0. We postulate that the time scale can be written as $\tau = \eta_0(1 + \chi\eta^*_{mb}){R_{eq}}^2/\Gamma$, where $\eta^*_{mb} = \eta_{mb}/\eta_0 R_{eq}$. The $R_g(t)$ curves for different viscosities can be made to coincide in the early and late stage for $\chi \simeq 0.5$ and $\chi \simeq 1$, respectively. In the formation of the bowl-like shape, the membrane mainly moves perpendicularly so that η_0 has dominant effects. In the later stage of closure [$\theta_{po} < 0.3\pi$], membrane moves rather tangentially and the dynamics slow down with increasing membrane viscosity.

Dissolution

When the strength ε of the cohesive interaction between membrane particles is sufficiently reduced, the membrane disintegrates and a vesicle dissolves as shown in Fig. 3. The vesicle is still metastable and keeps its initial shape for a while. Then, a pore open and membrane particles dissolve from the edge of the pore. The rupture time shows the exponential dependence on ε, which suggests that the free-energy barrier of rupture and pore opening ΔF_{po} is proportional to ε. An exponential dependence of the free-energy barrier for pore opening has also been reported from micropipette-aspiration experiments.

The dissolution dynamics, after the membrane has opened up to a disk-like shape, can be understood from the decay equation of a circular cluster. Since particles dissolve mainly from the edge of the membrane, $dN/dt = -c\sqrt{N}$ where the dissolution rate is proportional to $R_{dis} \sim \sqrt{N}$, and not to N as in the standard "radioactive" decay processes. Thus, the membrane size is expected to decreases as $\sqrt{N(t)} = \sqrt{N_0} - ct/2$. The radius R_g of the cluster and $\sqrt{N}$ are both predicted to decrease linearly in time. These predictions agree very well with the simulation data.

Summary

We have studied the self-assembly and dissolution dynamics of membranes, both with and without hydrodynamic interactions. In our method, the hydrodynamic interactions can easily switched on or off. Static equilibrium properties can be investigated very efficiently by BD, since it needs much less computational time. Thus, our membrane model is very well suited to study other dynamical phenomena, such as the budding of vesicles or vesicle deformation under flow.

[1] H. Noguchi and G. Gompper, Phys. Rev. E **73**, 021903 (2006).

[2] H. Noguchi and G. Gompper, J. Chem. Phys. **125**, 164908 (2006).

[3] A. Malevanets and R. Kapral, J. Chem. Phys. **110**, 8605 (1999).

[4] P. Fromherz, Chem. Phys. Lett. **94**, 259 (1983).

Breakdown of Gallavotti-Cohen Symmetry for Stochastic Dynamics

R. J. Harris[1], A. Rákos[2], and G. M. Schütz[3]

[1] Fachrichtung Theoretische Physik, Universität des Saarlandes, 66041 Saarbrücken, Germany
[2] Present address: Department of Physics of Complex Systems, Weizmann Institute of Science – Rehovot 76100, Israel
[3] Institute Theory II

Recently discovered fluctuation theorems such as the Gallavotti-Cohen symmetry for entropy production generalize properties of fundamental thermodynamic relations to systems arbitrarily far from thermal equilibrium. In order to explore the range of validity of the Gallavotti-Cohen symmetry in a many-body system, we study current fluctuations in the one-dimensional partially asymmetric zero-range process with open boundaries. Significantly, exact computations and Monte-Carlo simulations show that the Gallavotti-Cohen symmetry has limited applicability and that such a breakdown can generally occur in systems with unbounded state space. We also observe a dependence of the asymptotic current distribution on the initial state even though the system is ergodic.

Substantial progress in the understanding of non-equilibrium systems has been achieved recently through so-called fluctuation theorems [1]. Specifically, the Gallavotti-Cohen fluctuation theorem (GCFT) can be loosely written as

$$\frac{p(-\sigma,t)}{p(\sigma,t)} \sim e^{-\sigma t} \qquad (1)$$

where $p(\sigma,t)$ is the probability to observe an average value σ for the entropy production in time interval t and $\sim$ denotes the limiting behaviour for large t. This theorem was first derived for deterministic systems [2] (motivated by computer simulations of sheared fluids [3]) and subsequently for stochastic dynamics [4, 5]. From [6] onwards there have been successful attempts at experimental verification, including for simple random processes such as the driven two-level system in [7]. Strictly the GCFT is a property of non-equilibrium steady states but, for systems with a unique stationary state it is usually also expected to hold for arbitrary initial states. We will refer to this more general property of the large deviation function as "GC symmetry". Specifically, we explore the GC symmetry in the context of a paradigmatic non-equilibrium model—the zero-range process [8]. We explicitly calculate the current distribution in this large-fluctuation regime and thus prove a breakdown of the symmetry relation (1). Significantly, we argue that our analytical approach predicts that this effect also occurs for more general models.

Let us begin by defining our model—the partially asymmetric zero-range process (PAZRP) on an open one-dimensional lattice of L sites [9]. Each site can contain any number of particles, the topmost of which hops randomly to a neighbouring site after an exponentially distributed waiting time. In the bulk particles move to the right (left) with rate pw_n (qw_n) where w_n depends only on the occupation number n of the departure site. Particles are injected onto site 1 (L) with rate α (δ) and removed with rate γw_n (βw_n). The quantity of interest is the time-integrated current $J_i(t)$ across a bond $i, i+1$, i.e., the net number of particles that have crossed this bond up to time t for a given initial configuration. In stochastic lattice gases such as the PAZRP the current is proportional to the entropy production [5].

For a fixed initial particle configuration the initial contribution to the asymptotic current distribution is always finite. However, for a normalized distribution over initial configurations (e.g., the steady-state) this contribution can also diverge (in the case where w_n is bounded) meaning that the asymptotic current distribution retains a dependence on the initial state. This has important consequences for measurement of the current fluctuations in simulation (or equivalent experiments). Suppose we start from a fixed initial particle configuration, e.g., the empty lattice, wait for some time T_1 and then measure the current in many realizations of the process over a time interval T_2. These are two noncommuting timescales—if we take $T_2 \to \infty$ faster than $T_1 \to \infty$ we will measure the asymptotic distribution of current fluctuations corresponding to the fixed initial condition which may differ from the asymptotic behaviour of steady-state current fluctuations obtained by taking $T_1 \to \infty$ before $T_2 \to \infty$.

In order to explore this theoretical possibility in a specific setting we first specialize to the case of the single-site PAZRP, i.e, one site with "input" (left) and "output" (right) bonds. For simplicity we consider $w_n = 1$, anticipating qualitatively the same effects for any bounded w_n. We assume an initial Boltzmann distribution for the particle number with fugacity $x = e^{-\beta\mu} < 1$. Notice that $x = 0$ corresponds to starting with the empty lattice (fixed initial state). For some explicitly known x^* the distribution is stationary [9]. Explicit computations yield an integral form for the generating function of the input current [10]. In order to extract the large-time behaviour we use a saddle-point method, taking careful account of the contributions from residues when the saddle-point contour is deformed through poles in the inte-

grand.
Via Legendre transformation we obtain the large deviation behaviour of $j_0 = J_0/t$. The resulting "phase diagram" is shown in Fig. 1 where

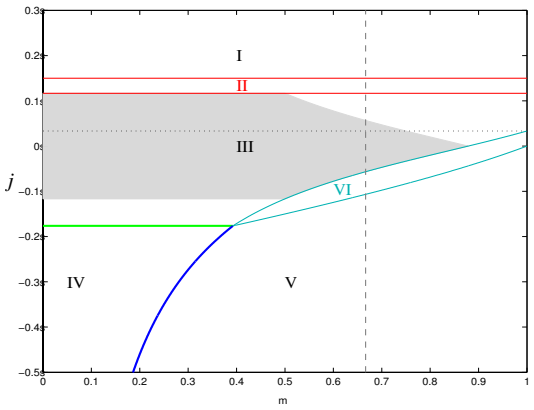

FIG. 1: Phase diagram for input current large deviations. Single-site PAZRP with $w_n = 1$, $\alpha = 0.1$, $\beta = 0.2$, $\gamma = 0.1$, $\delta = 0.1$. Dotted horizontal line shows mean steady-state current, dashed vertical line denotes steady-state initial condition. The symmetry (1) is obeyed in the shaded area inside III.

$\hat{e}_0(j)$ has the following forms in the different regions:

$$\hat{e}_0(j) = \begin{cases} f_j(\alpha,\gamma) & \text{I} \\ g_j\Big(\frac{(\alpha-\beta-\gamma+\delta)(\beta-\delta)}{\beta+\gamma-\delta}, \frac{\beta+\gamma-\delta}{\alpha}\Big) & \text{II} \\ f_j\Big(\frac{\alpha\beta}{\beta+\gamma}, \frac{\gamma\delta}{\beta+\gamma}\Big) & \text{III} \\ f_j(\alpha,\gamma) + f_j(\beta,\delta) & \text{IV} \\ f_j(\alpha,\gamma) + g_j(\beta(1-x)+\delta(1-x^{-1}), x) & \text{V} \\ g_j\Big(\frac{(1-x)\{\alpha\beta x - \delta[\beta(1-x)+\gamma]\}}{x[\beta(1-x)+\gamma]}, \frac{\gamma x}{\beta(1-x)+\gamma}\Big) & \text{VI} \end{cases} \tag{2}$$

with

$$f_j(a,b) = a + b - \sqrt{j^2+4ab} + j\ln\frac{j+\sqrt{j^2+4ab}}{2a} \tag{3}$$

$$g_j(a,b) = a + j\ln b. \tag{4}$$

Comparing with (1) one reads off that the GC-symmetry is satisfied only for small enough currents up to some critical initial fugacity.
We now turn to numerical results for a larger system with a different choice of bounded w_n, see Fig. 2.

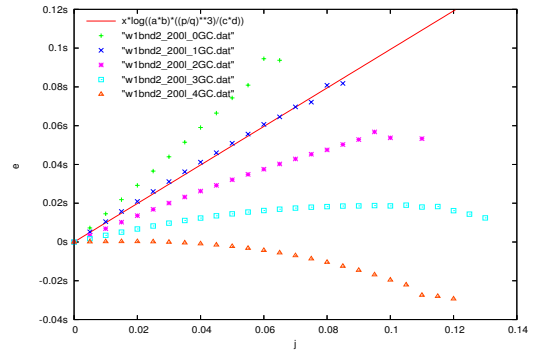

FIG. 2: Simulation results for $\log[p(j,t)/p(-j,t]$ in four-site PAZRP with $w_n = 1 - 0.5/n$, $\alpha = 0.1$, $\beta = 0.2$, $\gamma = 0.1$, $\delta = 0.1$, $p = 0.525$, $q = 0.475$ and $x = 0$. Points show data for five bonds at $t = 200$.

The GC symmetry states that, $\hat{e}(-j) - \hat{e}(j)$ should be a straight line. In the finite-time simulation regime one again sees indications of violation of GC symmetry with bond-dependent form. Physically, we argue that the inhomogeneity of the fluctuations across the two different bonds in the single-site PAZRP and the associated violation of the GC symmetry is a result of the temporary build-up of particles on the site [10]. In general, this possibility is expected to occur in any open-boundary zero-range process with $\lim_{n\to\infty} w_n$ finite (even when the boundary parameters are chosen so that there is a well-defined steady state, i.e., no permanent condensation).
Mathematically, the observed breakdown of the GC symmetry results from the divergence of the weighted probability sum of stochastic trajectories of the process and of the initial distribution to the current distribution. For models with bounded state space, these quantities are by necessity finite and the relation (1) holds for any initial state. However, the limit $N \to \infty$ does not necessarily commute with the $t \to \infty$ limit taken in (1) and (2). This non-commutation of limits leads in some cases to the violation of (1) even for steady-state initial conditions. This and the initial state dependence (due to non-commuting timescales) are the main issues highlighted by our work.

[1] D. J. Evans and D. J. Searles, Adv. Phys. **51**, 1529 (2002).

[2] G. Gallavotti and E. G. D. Cohen, Phys. Rev. Lett. **74**, 2694 (1995).

[3] D. J. Evans, E. G. D. Cohen, and G. P. Morriss, Phys. Rev. Lett. **71**, 2401 (1993).

[4] J. Kurchan, J. Phys. A: Math. Gen. **31**, 3719 (1998).

[5] J. L. Lebowitz and H. Spohn, J. Stat. Phys. **95**, 333 (1999).

[6] S. Ciliberto and C. Laroche, J. Phys. IV **8**, 215 (1998).

[7] S. Schuler, T. Speck, C. Tietz, J. Wrachtrup, and U. Seifert, Phys. Rev. Lett. **94**, 180602 (2005).

[8] F. Spitzer, Adv. Math. **5**, 246 (1970).

[9] E. Levine, D. Mukamel, and G. M. Schütz, J. Stat. Phys. **120**, 759 (2005).

[10] R.J. Harris, A. Rákos, and G.M. Schütz, Europhys. Lett. **75**, 227 (2006).

Mechanical Properties of Icosahedral Virus Capsids

G. A. Vliegenthart and G. Gompper

Theorie der Weichen Materie und Biophysik

Virus capsids are self-assembled protein shells in the size range of 10 to 100 nanometers. The shells of DNA-viruses have to sustain large internal pressures while encapsulating and protecting the viral DNA. We employ computer simulations to study the mechanical properties of crystalline shells with icosahedral symmetry that serve as a model for virus capsids. The shells are positioned on a substrate and deformed by a uni-axial force excerted by a small bead. We predict the elastic response for small deformations, and the buckling transitions at large deformations. Both are found to depend strongly on the number N of elementary building blocks (capsomers), and the Föppl-von Kármán number γ which characterizes the relative importance of shear and bending elasticity.

The deformation of thin elastic sheets is a fundamental problem with practical applications ranging from macroscopic materials (thin steel plates, rubber films, paper sheets) via mesoscopic materials (clay platelets, membrane of biological cells) to microscopic materials (virus particles, carbon nanotubes). We have focussed on the elastic and mechanical properties of a model for icosahedral virus capsids for which — inspired by recent experiments with an Atomic Force Microscope (AFM) — we have studied the response to an applied uni-directional force excerted by a small colloidal particle [1].

Historically, the study of thin elastic sheets dates back to the early work of Föppl and von-Kármán [2, 3]. In the Föppl-von Kármán formalism, a thin shell of a three-dimensional homogeneous elastic material with a three-dimensional Young modulus Y, Poisson ratio ν and thickness h can be described by a mathematical surface (of zero thickness) with a two-dimensional Young modulus K_0 and a bending rigidity κ [4]. The equations that describe the mechanical equilibrium are the von-Kármán equations. For most geometries and boundary conditions a general solution of these equations is not available; therefore, one is handed over to a numerical solution of the problem. Our strategy is to solve the elastic problem using classical molecular-dynamics computer simulations.

A viral capsid has a remarkably regular structure and is built up from a fixed number of copies of a single or a few kinds of capsid protein. Its geometry is that of an icosahedron or a helical cylinder, but more complex structures also exist. It was shown by Caspar and Klug [5] that the organization of proteins in spherical viruses is such that a few protein subunits form pentavalent and hexavalent morphological units that crystallize into an icosahedral shell. This shell can be characterized by two numbers p and q, which define the triangulation number (T-number) of the virus, with $T = p^2 + q^2 + pq$. The number of vertices N is then $N = 10\ T + 2$, the number of triangles is $N_T = 20\ T$, and the number of protein sub-units is $3\ N_T = 60\ T$. For most viruses the number of sub-units is small, so that consequently T and N_T are also small. The mechanical stability of these viruses is a direct consequence of the interactions between sub-units which are on the order of 100-400 kJ/mole per protein-protein bond. For DNA viruses, the magnitude of this binding energy has an obvious origin: the genetic material is tightly packed, resulting in a large internal pressure which drives the injection of genetic material during infection [6]. For other viruses the mechanical requirements are not so clearly understood yet. Recent experiments have shown that for some viruses the thickness of the protein shell and consequently the elastic properties of the shell change during virus maturation [7] and this might be relevant for virus entry in the cell.

All this suggests that the elastic properties of viral capsids play an important biophysical role. We therefore investigated the mechanical properties for a simple elastic model that, in contrast to recent finite-element calculations, correctly takes into account the geometric structure of the viral capsids. We performed a simulation study of virus indentation in a set-up very similar to the AFM experiments of Ref. [8]. This approach allows for a direct investigation of the effect of various parameters — like bending rigidity, Young modulus, capsid radius, 'tip' radius of the AFM, and capsid orientation — on the shape of force-deformation curves. We used a triangulated-surface model, where the number of vertices that is used to discretize the surface can be varied easily. This allows for a detailed analysis of finite-size effects; in the limit of a large number of nodes, the results should approach or become equivalent to the (unknown) solutions of continuum elasticity theory. The two dimensional Young modulus K_0, the bending rigidity κ and the average radius of the virus R_v are input parameters in the calculation. They can

be converted into a single dimensionless parameter $\gamma = K_0 R_v^2/\kappa$, the so-called Föppl-von Kármán number which measures the relative importance of the bending and stretching energy. Our results are important to properly interpret experimental force-deformation curves.

We measured force-deformation curves for a large number of parameters. In Fig. 1, we show force-deformation curves for several virus shells differing in triangulation number. For small γ, the data with increasing T-number quickly converge to an almost linear behavior up to large compressions. For large γ, this convergence is much slower [1]. For the smallest tringulation number of $T = 1$, a jump in the curve is visible, which correspond to buckling event, i.e. a sudden rearrangement leads to an instantaneous drop in the force on the sphere. Such buckling events are frequently observed also for large T in the case of large γ [1]. For small enough deformations all curves follow a universal scaling relation,

$$\frac{F R_v}{\kappa\sqrt{\gamma}} = C\left(1 - \frac{\Delta z}{2R_v}\right) \qquad (1)$$

where F is the force the capsid exerts on the sphere and Δz is the vertical deformation. The scaling factor $R_v/\kappa\sqrt{\gamma} = 1/\sqrt{K_0\kappa}$ is the same as was found for the scaling of the buckling force of spherical shells [4] and of stretching ridges in thin elastic sheets [9].

For large γ, the initial slope of the buckling curve can be described by the same scaling relation (i.e. with the same value of C) while for larger compressions a second linear regime is observed with a different (larger) effective spring constant. The details of these two regimes are discussed in Ref. [1].

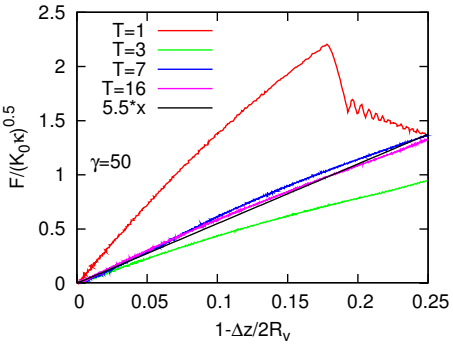

FIG. 1: Force deformation curves for the case that $\gamma = 50$ and the compressing sphere is small.

For both small and large γ, the initial deformation corresponds to a local deformation of the surface by the tip. For larger deformation the response becomes increasingly non-local. In Fig. 2 the generic deformation pathway, as found for all simulations with this geometry, is illustrated for a one particular system. From left to right configurations at different instants of time are shown. Figure 2 bottom shows the corresponding deformations. We find that upon compression the top face deforms first, followed by an inwards flip of one of the corners of the top face. This 'flip-in' corresponds to a buckling event. Further compression of the virus leads to a cascade of smaller and much more difficult to interpret buckling events.

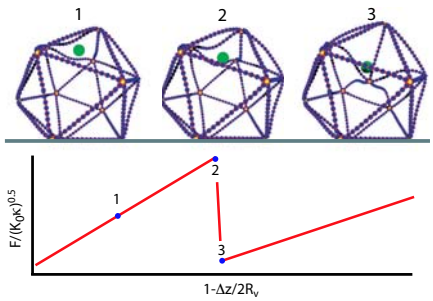

FIG. 2: Schematic illustration of the deformation pathway. Top: sequence of configurations corresponding to the deformations indicated by the numbers in the schematic deformation curve in the lower figure. '1' corresponds to a small deformation, '2' is the situation just before buckling, '3' the buckled state, and '4' indicates the final state (after more than one buckling event). For clarity only the vertices that are connecting the ridges are shown.

In recent experiments [8] force-deformation curves were measured for several different viruses. These data have been analyzed and interpreted so far using finite-element methods for spherical solid shells. Our results show how more precise information can be extracted from such experiments.

Finally, we want to mention that for very large Föppl-von Kármán numbers, a large number of small buckling events can be observed in the simulations, which resembles crumpling of a paper sheet. Indeed, the same model described above has been used to study the intriguing pattern of folds which appears on crumpled sheets [10].

[1] G. A. Vliegenthart and G. Gompper, Biophys. J. **91**, 834 (2006).

[2] A. Föppl, *Vorlesung über Technische Mathematik,* vol. 5 (B. G. Turner, Leipzig, Berlin 1907).

[3] Th. von Kármán, *Collected works* (Butterworths, London, 1956).

[4] L. D. Landau and E. M. lifshitz, *Theory of elasticity* (Butterworth-Heinemann, 1986).

[5] D. L. D. Caspar and A. Klug, Cold Spring Harbor Symp. on Quant. Biol. **27**, 1 (1962).

[6] D. E. Smith, S. J. Tans, S. B. Smith, S. Grimes, D. L. Anderson, and C. Bustamante, Nature **413**, 748 (2001).

[7] W. R. Wikoff, J. F. Conway, J. Tang, K. K. Lee, L. Gan, N. Cheng, R. L. Duda, R. W. Hendrix, A. C. Steven, and J. E. Johnson, J. of Struct. Biol. **153**, 300 (2006).

[8] I. L. Ivanovska, P. J. de Pablo, B. Ibarra, G. Sgalari, F. C. MacKintosh, J. L. Carrascosa, C. F. Schmidt, and G. J. L. Wuite, Proc. Natl. Acad. Sci. U.S.A. **101**, 7600 (2004).

[9] B. A. DiDonna and T. A. Witten, Phzs. Rev. Lett. **87**, 206105 (2001).

[10] G. A. Vliegenthart and G. Gompper, Nature Materials **5**, 216 (2006).

Tumbling Dynamics of DNA in Shear Flow

Roland G. Winkler

Institut für Festkörperforschung, Theorie der Weichen Materie und Biophysik

The dynamics of semiflexible polymers under the influence of shear flow is studied analytically. Power laws are derived for various conformational and dynamical quantities which are in agreement with experimental findings. In particular, the tumbling motion is analyzed and expressions are provided for the probability distributions of the orientation angles and the tumbling time. The calculations explain the similarities in the behavior of flexible and semiflexible polymers as well as free draining and non-draining systems.

The properties of individual DNA molecules can be studied by direct visualization via fluorescent staining in Fluorescence Microscopy experiments. In such studies, often DNA molecules are used for various reasons. On the one hand, DNA is the molecule of life and is thus of primary interest in biology and medicine. On the other hand, a DNA molecule is an ideal model system for a semiflexible polymer. Hence, single molecule experiments provide the opportunity to test theoretical models. Moreover, such experiments help to establish a direct link between microscopic quantities such as polymer conformations and macroscopic material properties like viscosity.

Experimental studies of individual DNA molecules in steady shear flow have provided a wealth of information on single polymer dynamics [1, 2, 3, 4]. In particular, these experiments reveal remarkably large conformational changes due to tumbling motion, i.e., a polymer stretches and recoils in the coarse of time [1, 2]. The dependence of the tumbling time on the shear rate (or Weissenberg number) was elucidated in Refs. [3, 4]. The authors of Ref. [4] were even able to measure orientational distribution functions of λ-DNA. A number of theoretical studies have been performed in order to achieve a microscopic understanding of the observed phenomena [3, 5], which provided various scaling relations for conformational und dynamical properties [4].

The dynamic behavior of a macromolecule in shear flow is governed by various parameters; aside from the shear rate, the finite chain extensibility is of major importance. To which extend hydrodynamic interactions, thermal fluctuations, and chain persistence play a role has been explored in Ref. [5].

The analytical results of Ref. [5] show that due to shear flow high order correlations in time and the whole history of time evolution of the system are important for structural as well as dynamical quantities. This is the origin of what is called intermittency phenomena in Ref. [4] – characterized by algebraic or exponential tails of distribution functions – although the underlying thermal process is Gaussian and Markovian and the equations of motion are linear. Thus, a polymer in shear flow is an example where a very complex system behavior is obtained despite the underlaying simple Gaussian process.

The dynamics of macromolecules in shear flow can be analyzed using a Gaussian semiflexible polymer model. The polymer of length L is described by a continuous, differentiable space curve $\boldsymbol{r}(s,t)$, where s is the contour coordinate along the chain ($-L/2 < s < L/2$). The equation of motion, including hydrodynamic interactions, is give by the Langevin equation [5]

$$\frac{\partial}{\partial t}\boldsymbol{r}(s,t) = \int_{-L/2}^{L/2} \mathbf{H}(s,s') \left[2\nu k_B T \frac{\partial^2}{\partial s'^2}\boldsymbol{r}(s',t) - \epsilon k_B T \frac{\partial^4}{\partial s'^4}\boldsymbol{r}(s',t) + \boldsymbol{\Gamma}(s',t) \right] ds' + \mathbf{K}\boldsymbol{r}(s,t), \quad (1)$$

with appropriate boundary conditions. The term with the second derivative in $\boldsymbol{r}$ captures the chain flexibility, i.e., it takes chain entropy into account. The term with the fourth derivative accounts for bending stiffness. Note, no excluded volume interactions are taken into account, which may affect the system behavior for small and intermediate Weissenberg numbers. The stochastic force $\boldsymbol{\Gamma}(s,t)$ is assumed to be stationary, Markovian, and Gaussian with zero mean. The shear rate tensor $\mathbf{K}$ possesses only one non-zero element: $K_{xy} = \dot{\gamma}$, where $\dot{\gamma}$ is the shear rate. k_B is the Boltzmann factor, T the temperature, $\epsilon = 3/(4p)$, where p is related to the chain persistence length (l_p) via $p = 1/(2l_p)$, and $\nu = 3p\mu/2$. The factor μ is determined from the constraint for the contour length $\int_{-L/2}^{L/2} \langle [\partial \boldsymbol{r}/\partial s]^2 \rangle \, ds = L$, where $\mu = 1$ at equilibrium. Hydrodynamic interactions are taken into account by the Rotne-Prager tensor and treated within the preaveraging approximation. For averaging, the equilibrium distribution function without shear is used. Equation (1) is then a linear equation with coefficients depending in a non-linear manner on the shear rate and can be solved by a normal mode analysis.

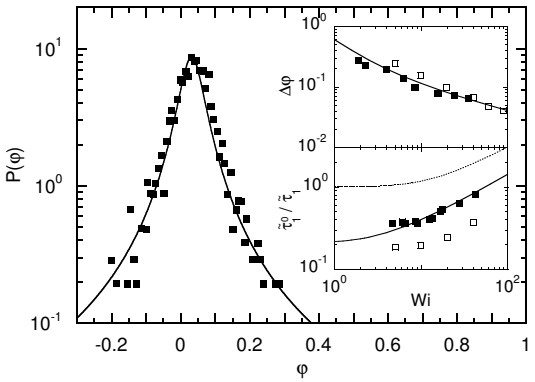

FIG. 1: Comparison of the theoretical probability density function of the angle φ (solid line) with experimental results on λ-DNA for the Weissenberg number $Wi = 25$ [4]. The top inset displays the width at half-height of $P(\varphi)$ and the bottom inset shows the tumbling time $t_T = \tilde{\tau}_1$ for the theoretical model (solid line), experiments (■), and simulations (□) [4]. The dotted line is $\mu(Wi)$. For the comparison, the theoretical Weissenberg numbers are set to four times the displayed experimental values.

Using the eigenfunction expansion, a general expression is obtained for the parameter μ containing the sum over all modes. In the limit $pL \gg 1$, and with the ratio of the relaxation times $\tilde{\tau}_n/\tilde{\tau}_1^0 = (1+\pi^2/(2pL)^2)/(\mu n^2)$ following for $\mu \gg 1$, where $\tilde{\tau}_1^0$ is the longest relaxation time $\tilde{\tau}_1$ at $\mu = 1$, this expression reduces to

$$\mu^3 - \mu^{5/2} - \frac{[1+(\pi/(2pL))^2]^2\pi^4}{540pL} Wi^2 = 0. \qquad (2)$$

Here, the Weissenberg number $Wi = \dot{\gamma}\tilde{\tau}_1^0$ is introduced. The solution of this equation deviates from the full expression by a few percent only for all Wi as long as $pL > 2$, i.e., the approximate expression applies even to rather stiff polymers. The reason is that in the derivation of Eq. 2 bending modes do not play a major role. Only the lowest modes contribute to the overall system behavior. For $Wi \gg 1$, Eq. (2) yields

$$\mu \approx Wi^{2/3} \sqrt[3]{\pi^4/(540pL)}. \qquad (3)$$

This relation is an important result, because the factor μ appears in the relaxation times and hence in all other quantities and determines the system behavior at large Weissenberg numbers. It is important to note that μ is only weakly dependent on the persistence length and does not depend on hydrodynamic interactions. Equation (2) suggests that for semiflexible polymers ($pL > 2$) a length and persistence length independent behavior is obtained if (measured) quantities are presented in terms of $Wi/\sqrt{pL}$. I like to point out that even for rodlike polymers the dependence $\mu \sim Wi^{2/3}$ ($Wi \gg 1$) is observed.

Using the derived expressions, various conformational properties of a semiflexible polymer can be calculated [5]. A particular interesting quantity, which has been measured in Ref. [4], is the probability distribution $P(\varphi)$ of the orientational angle (φ) of the main axis of the gyration tensor with the flow direction. Using the approximations indicated before Eq. (2), the latter reads

$$P = \frac{\sqrt{\pi^4 + 4\widetilde{Wi}^2(\pi^2-4)/\mu^2}}{2\pi\left[\pi^2 + 4\widetilde{Wi}^2\sin^2(\varphi)/\mu^2 - 4\widetilde{Wi}\sin(2\varphi)/\mu\right]},$$

with the abbreviation $\widetilde{Wi} = Wi[1+(\pi/(2pL))^2]$. This equation accounts for the full distribution function within a relative error of $4\ \%$ only for $pL \geq 5$ and $Wi > 1$.

Figure 1 displays the probability density function for λ-DNA. The only parameters appearing in the theoretical description are the product pL, the thickness of the DNA, and the Weissenberg number. Using the parameters of Ref. [4], namely $L = 21\ \mu$m and the radius of gyration $\boldsymbol{r}_g^2 = 0.53\ \mu\text{m}^2$, the DNA persistence length is $l_p \approx 70$ nm, i.e., $pL = L/(2l_p) = 150$. The DNA thickness is set to $d = 2$ nm. Applying the experimental Weissenberg number $Wi = 25$ leads to a pronounced mismatch between the measurements (symbols) and the theoretical distribution function. Only by using a four times larger Wi, i.e, $Wi = 100$ in the theoretical model, the very good agreement of Fig. 1 is obtained. I attribute this necessary adjustment to differences in the longest measured and theoretical relaxation times, respectively, used in the definition of Wi. The inset of Fig. 1 shows the width of $P(\varphi)$ at half height for various Weissenberg numbers. The theoretical curve reproduces the experimentally obtained dependence very well, when again four times larger theoretical Wi values are used.

The bottom inset of Fig. 1 compares the measured tumbling times and simulation results with the theoretical prediction $\tilde{\tau}_1^0/\tilde{\tau}_1 = \mu$. Taking four times large theoretical Weissenberg numbers and dividing $\tilde{\tau}_1^0/\tilde{\tau}_1$ by five instead of four, the latter adjustment might be related to differences in the definition of the tumbling time, the theoretical curve agrees qualitatively with the measured data. The comparison shows that the experimental values are in a crossover regime with respect to the Weissenberg number. The limiting behavior $t_T \sim \mu^{-1} \sim Wi^{-2/3}$, follows for larger Wi.

[1] D. E. Smith, H. P. Babcock, and S. Chu, Science **282**, 1724 (1999).

[2] P.LeDuc, C. Haber, G. Boa, and D. Wirtz, Nature **399**, 564 (1999).

[3] C. M. Schroeder, R. E. Teixaira, E. S. G. Shaqfeh, and S. Chu, Phys. Rev. Lett. **95**, 018301 (2005).

[4] S. Gerashchenko and V. Steinberg, Phys. Rev. Lett. **96**, 038304 (2006).

[5] R. G. Winkler, Phys. Rev. Lett. **97**, 128301 (2006).

Towards a Molecular Theory of Ion Conduction in Potassium Channels

J.-F. Gwan, S. Grudinin, M. Haan, and A. Baumgaertner

Institut der Theorie der weichen Materie und Biophysik

We have investigated the transport of potassium ions inside a nanochannel using molecular dynamics simulations. The atomic structure of the nanochannel was adopted from the structure of a biological ion channel. The channel contains an alternating sequence of ions and water molecules. The simulations reveal that the transport mechanism of such a single file can be described by hopping processes of ion-water pairs mediated by the flexible carbonyl groups lining the backbone of the nanochannel.

Although many biomolecular nanomachines have been identified [1], the relations between their structural and dynamical properties ("function") are still poorly understood. Recent breakthroughs in determination of crystal structures at the atomic resolution, however, have provided detailed insights into the molecular architecture of simple nanomachines. This is seen, e.g., in recent successful structural determination of the water-conducting aquaporin [2] and the bacterial potassium ion channel KcsA [3, 4].
Ion channels reside in cell membranes and are an important class of biomolecular machines. They work by selecting specific ions and by catalyzing the passive diffusion through its selectivity filter. Fig.1 shows the potassium ion channel KcsA [3, 4] in a ribbon representation.

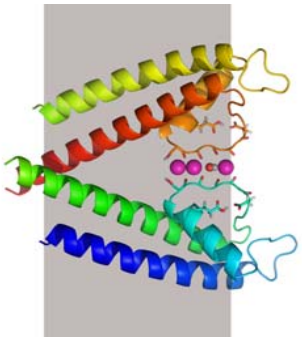

FIG. 1: Structure of the KcsA potassium channel. Only two monomers of the tetrameric protein are shown. The shaded area represents the membrane.

The cutaway view of the protein shows only two monomers of the tetrameric protein complex embedded in the cell membrane (shaded area). Each monomer consists of three helices depicted in different colors, one extracellular loop, and as the central part of the channel the selectivity filter containing three potassium ions (depicted by balls) and one water molecule between. The structural details of the filter are decisive for ion selectivity and transport. The selectivity filter facilitates the diffusion of potassium ions at rates approaching 10^8 ions per second under physiological electrochemical gradients [5]. The ability of potassium channels to conduct several K^+ ions simultaneously in a single file through the narrow pore at levels near the limit of diffusion is usually described in terms of concerted mechanisms [6, 7]. It has been suggested that to reach a high conduction rate in a long-pore channel, ions must move through the channel pore in a multi-ion fashion : the permeating ions line up in the narrow channel pore and move in a single file through the channel [6].. This is known as "the multi-ion permeation process", and is believed to be a common feature of the ion transportation process in all potassium channels [5]. The multi-ion theory has been acepted over decades, but the molecular mechanism of it remained elusive.

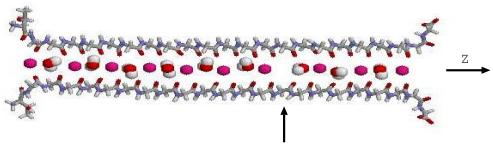

(a)

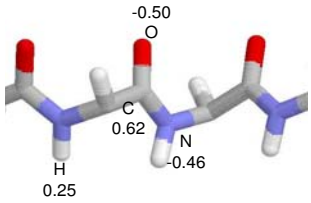

(b)

FIG. 2: (a) Geometry of the extended KcsA selectivity filter. (b) Conformation and charge distribution of the atoms on the peptide backbone (in electron units). C (grey), O (red), N (blue), and H (white)

Based on previous molecular dynamics simulation studies on the KcsA channel [8], we have em-

ployed [9] an extended KcsA channel ("nanochannel") in order to elucidate in more detail the molecular mechanism of ion transport through the channel. The nanochannel is constructed as a finite periodic continuation of the original KcsA selectivity filter of the potassium channel KcsA. The nanochannel, as shown in Fig.2(a), contains 21 binding sites At each binding site an ion or a water molecules is stably coordinated by eight carbonyl oxygens, four on each side. A carbonyl group, C-O, is a polar group where its oxygen end is negatively charged (Fig.2(b)). The width of such a binding site is about 3 Å. The periodicity of binding sites represents a one-dimensional lattice potential provided by the carbonyl groups of the backbone. In its conductive state the channel contains successive pairs of potassium ions (red balls) and water molecules [10]. In our simulations [9] the nanochannel contained one vacancy which is indicated by the arrow in Fig.2(a). This vacancy leads to an imbalance of the electrostatic interactions among the ions, which leads to movements of the ions.

The analysis of the simulations reveal a cooperative hopping of pairs or triples of ions and water molecules. This can be concluded from the time-dependent displacements, z(t), of all ions and water molecules as shown in Fig.3. According to their displacements it is observed that the movement of an ion located next to the vacancy occurs almost at the same time as the movement of its adjacent water molecule, both in the same direction. In addition, it was shown [8, 9] that the orientation of water molecules and carbonyl groups of the filter are cooperatively coordinated during the ion transport.

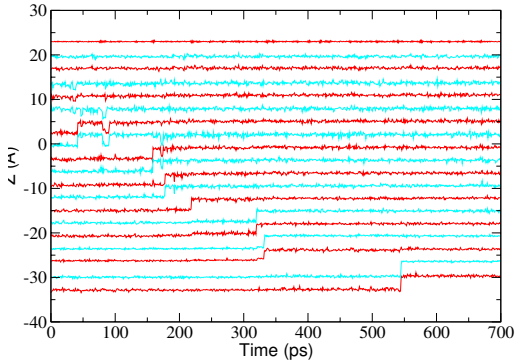

FIG. 3: Displacements of the ions (red) and the water molecules (blue) versus time t [ps].

Based on our molecular dynamics simulations we found three distinct features of the molecular mechanism.

(1) *The movements of neighboring ions and water molecules are strongly correlated.* They mostly moved in pairs or triples ("permons"). One important fact for the understanding of the efficiency of the correlated movements is that the periodicity of the pore potential, $\approx$ 3 Å, practically matches with the distance of the lowest Coulomb energy $U_{KW}(\Delta z)$ between one ion and one water molecule. The classical potential energy $U_{KW}(\Delta z)$ between a single ion and a single water molecule at distance Δz, consisting of Coulomb and van der Waals interactions, exhibits energy minima at characteristic distances of $\Delta z \approx 3$ Å("bound states"). The depth of the potential depends on the orientation of the water molecule with respect to the ion.

(2) *Permons are polarized.* The absolute minimum of $U_{KW}(\Delta z) \approx 30\ k_BT$ is at distance Δz = -2.65 Å and when the oxygen of the water dipol is oriented towards the ion ("polarized bound state"). If the ion hops to the vacancy, the ion's neighboring water molecule prefers to maintain its bound state and follows almost simultaneously the preceding ion towards the vacancy. This is the movement of a permon.

(3) *The movements of permons are rectified.* Another interesting observation from our MD simulations is that very rarely a water molecule has been observed to hop back to the vacancy and join the other ion to form a bound state. The absence of such an event is explained by the energy barrier imposed by the lattice potential on the water molecule. This implies that a water molecule acts as a "pawl" in a ratchet mechanism. This may have interesting consequences for our understanding of the transport mechanism in the natural KcsA ion channel [3, 4]. One implication is that the transport of ion-water pairs through an ion channel is much more efficient than the transport of ions only.

In summary, the high permeation rate at which ion and water molecules pass through the KcsA ion channel is based on the cooperative hopping of pairs of ions and water molecules mediated by the flexible charged carbonyl groups lining the backbone of the channel. These observations provide the basis of an atomistic concept of the molecular mechanism of the multi-ion transport mechanism [6, 5]. It may also provide the basis of a mathematical quasi-particle theory of collective ion conduction [11].

[1] A. Baumgaertner, Biomolecular machines, in Handbook of Theoretical and Computational Nanotechnology, edited by M. Rieth and W. Schommers, pages 000–000, American Scientific Publisher, 2005.

[2] K. Murata et al., Nature **407**, 599 (2000).

[3] D.A.Doyle et al., Science **280**, 69 (1998).

[4] Y. F. Zhou, J. H. Morais-Cabral, A. Kaufman, and R. MacKinnon, Nature **414**, 43 (2001).

[5] B. Hille, Ion channels of excitable membranes, Sinauer Associates Inc, Sunderland, Massachusetts, third edition, 2001.

[6] A. L. Hodgkin and R. D. Keynes, J. Physiol. **128**, 61 (1955).

[7] B. Hille and W. Schwarz, J. Gen. Physiol. **72**, 409 (1978).

[8] J. F. Gwan, The molecular mechanism of multi-ion conduction in K^+ channels, PhD thesis, Research Centre Jülich, Jülich, Germany, 2006.

[9] J. F. Gwan and A. Baumgaertner, J. Compt. Theor. Nanoscience **4**, 50 (2007).

[10] Y. Zhou and R. MacKinnon, J.Mol.Biol. **333**, 965 (2003).

[11] R. Elber, D. P. Chen, D. Rojewska, and R. Eisenberg, Biophys. J. **68**, 906 (1995).

The Influence of Surface Roughness on Superhydrophobicity

B. N. J. Persson and C. Yang

IFF, FZ-Jülich, 52425 Jülich, Germany

Superhydrophobic surfaces, with liquid contact angle θ greater than 150°, have important practical applications ranging from self-cleaning window glasses, paints, and fabrics to low friction surfaces. Many biological surfaces, such as the lotus leaf, have hierarchically structured surface roughness which is optimized for superhydrophobicity through natural selection. Here we present a molecular dynamics study of liquid droplets in contact with self-affine fractal surfaces. Our results indicate that the contact angle for nanodroplets depends strongly on the root-mean-square (rms) surface roughness amplitude but is nearly independent of the fractal dimension $\mathrm{D_f}$ of the surface.

The fascinating water repellents of many biological surfaces, in particular plant leaves, have recently attracted great interest for fundamental research as well as practical applications. The ability of these surfaces to make water beads off completely and thereby wash off contamination very effectively has been termed the Lotus effect, although it is observed not only on the leaves of Lotus plant, but also on many other plants such as strawberry, raspberry and so on. Water repellents are very important in many industrial and biological processes, such as prevention of the adhesion of snow, rain drops and fog to antennas, self-cleaning windows and traffic indicators, low-friction surfaces and cell mobility.

Most leaves that exhibit strong hydrophobicity have hierarchical surface roughness with micro- and nanostructures made of unwettable wax crystals. The roughness enhances the hydrophobic behavior, so that the water droplets on top tend to become nearly spherical. As a result the leaves have also a self-cleaning property: the rain drops roll away removing the contamination particles from the surface, thanks to the small adhesion energy and the small contact area between the contaminant and the rough leaf.

The hydrophobicity of solid surfaces is determined by both the chemical composition and the geometrical micro- or nanostructure of the surface. Understanding the wetting of corrugated and porous surfaces is a problem of long standing interest in areas ranging from textile science to catalytic reaction engineering. Renewed interest in this problem has been generated by the discoveries of surfaces with small scale corrugations that exhibit very large contact angles for water and other liquids—in some cases the contact angle is close to 180°. Such surfaces are referred to as superhydrophobic.

The contact angle θ between a flat solid surface and a liquid droplet depends on the relation between the interfacial free energies per unit area: solid/liquid γ_{sl}, solid/vapor γ_{sv} and liquid/vapor γ_{lv}. The Young's equation $\gamma_{\mathrm{sl}} + \gamma_{\mathrm{lv}}\cos\theta = \gamma_{\mathrm{sv}}$, results from the minimization of the total free energy of the system on a flat substrate surface. Complete wetting corresponds to $\theta = 0^\circ$, and typically happens on solids with high surface energy γ_{sv}. Liquids on low energy surfaces tend to form droplets with high contact angle θ.

It is well known that the roughness of a hydrophobic solid (with $\theta > 90^\circ$ on the flat substrate) enhances its hydrophobicity. If the contact angle of water on such flat solids is of the order of 100° to 120°, on a rough or microtextured surface it may be as high as 150° to 175°. Two distinct models have been proposed to explain this effect. The Wenzel model considers the increase of contact area due to the surface roughness: this leads to an increase of the effective free energy of the solid/liquid interface, making the surface more hydrophobic. The contact angle θ_0 on the rough surface is obtained from the contact angle θ on the microscopically flat surface of the same material through this equation

$$\cos\theta_0 = r\cos\theta \qquad \text{(Wenzel model)}, \qquad (1)$$

where $r = A/A_0$ is the ratio between the real substrate (area) and the nominal (or projected) area A_0. The Cassie model assumes that some air remains trapped between the drop and the cavities of the rough surface. In this case the interface free energy γ_{sl} must be replaced by a weighted average of three interface free energies γ_{sl}, γ_{lv} and γ_{sv}, with the weights depending on the fraction ϕ of the area where the contact between the liquid and the solid happens. The contact angle is given by

$$\cos\theta_0 = -1 + \phi(1+\cos\theta) \qquad \text{(Cassie model)}. \quad (2)$$

For a micro- or nano structured substrate, usually the droplet stays in the Cassie state, but the Cassie state can switch (irreversibly) to the Wenzel state when the droplet is pressed against the substrate. The Wenzel droplets are highly pinned, and the transition from

the Cassie to the Wenzel state results in the loss of the anti-adhesive properties generally associated with superhydrophobicity.

We have used Molecular Dynamics calculations to study the influence of surface roughness on superhydrophobicity. We have studied hydrocarbon liquid droplets on different self-affine fractal surfaces. The nano-droplet contained 2364 octane molecules C_8H_{18} at $T = 300$ K, which is between the melting and boiling points of octane. Because of the periodic boundary condition and the size of our system, the liquid droplet forms a cylinder with the central line along the y-axis, see Fig. 1.

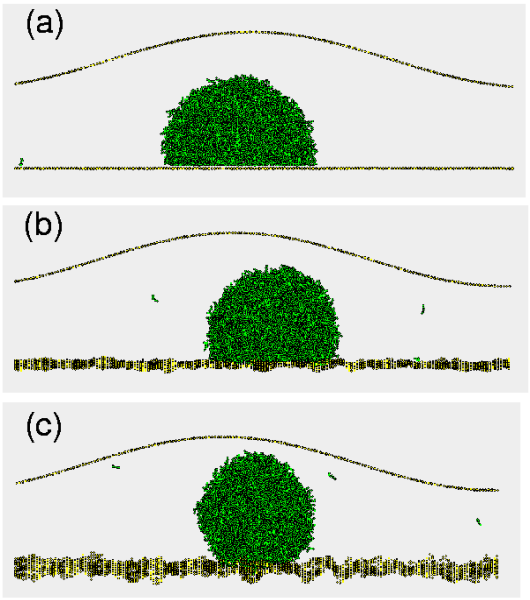

FIG. 1: Snapshots for different root mean square roughness. (a) the droplet is in contact with the flat substrate. (b) and (c) are for rough substrates with the root mean square amplitude $\sigma = 2.3$ Å and $\sigma = 4.8$ Å, respectively.

The apparent contact angle, θ_0, as a function of the root mean square roughness (rms), is shown in Fig. 2 with the fractal dimension $D_f = 2.2$. There is a strong increase in θ_0 with increasing rms-roughness amplitude. Fig. 3 shows how θ_0 depends on the Hurst exponent $H = 3 - D_f$. Note that θ_0 is almost independent of H.

Accordingly to the Wenzel equation, the apparent contact angle θ_0 depends only on the surface roughness via the ratio $r = A/A_0$. Calculations show that as H decreases from 1 to 0.4 (i.e., D_f increases from 2 to 2.6), A/A_0 increases by $\sim 50\%$. However, the MD-calculations show that the apparent contact angle θ_0 is almost independent of the fractal dimension, see Fig. 3. Thus the Wenzel equation cannot be used in the present situation. This is consistent with a visual inspection of the liquid-substrate interface which shows that on the rough substrates, the droplet is "riding" on the asperity tops of the substrate, i.e., the droplet is in the Cassie state. In order to quantitatively verify this, we have calculated the distances $h(x, y)$ between the bottom surface of the liquid drop and the rough substrate surface in the (apparent) contact area. From the distribution $P(h)$ of these distances we obtain the fraction ψ of the (projected) surface area where contact occurs. Note that due to the thermal fluctuations $\psi = \psi_0$ for flat surface is less than 1. Using the normalized $\phi = \psi/\psi_0$, the Cassie model predicts the variation of the contact angle with σ and H given in Fig. 2 and 3 (square points).

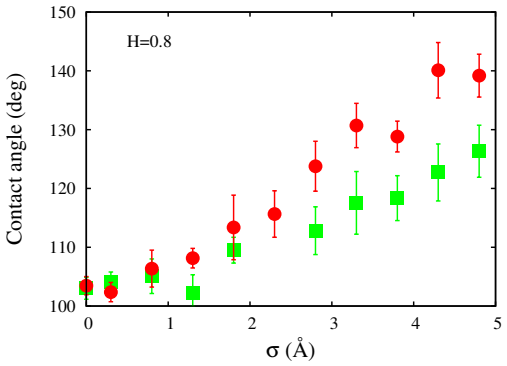

FIG. 2: The contact angle as a function of the root mean square roughness σ. The circle points are numerical results from the simulations, while the square points are obtained from the Cassie model (see Eq. 2). Each data point is an average over several snap-shot configurations. The fractal dimension is $D_f = 2.2$.

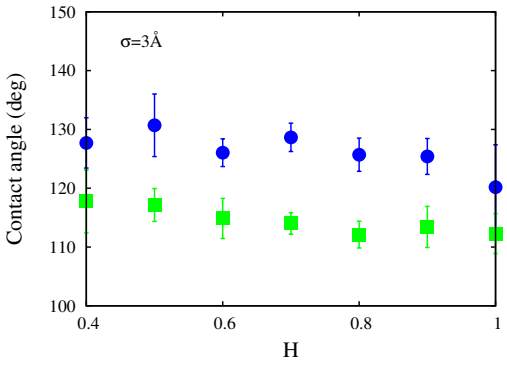

FIG. 3: The contact angle θ as a function of Hurst exponent H for the rms roughness $\sigma = 3$ Å. The circles and squares have the same meaning as that in Fig. 2 The fractal dimension is $D_f = 3 - H$.

Fig. 2 shows that the apparent contact angle θ_0 increases strongly with increasing rms-roughness amplitude, at fixed fractal dimension $D_f = 2.2$, while it is nearly independent of the fractal dimension D_f (see Fig. 3). Since increasing the fractal dimension at constant rms roughness amplitude mainly increases the short-wavelength roughness, we conclude that the nanoscale wave length roughness doesn't matter so much in determining the contact angle for hydrophobic surfaces, while the long wavelength roughness plays an important role. We attribute this fact to the strong thermal fluctuations in the height (or width) h of the liquid-solid interface which occur at the nanoscale even for the flat substrate surface.

[1] C. Yang, U. Tartaglino, B.N.J. Persson, Phys. Rev. Lett. **97**, 116103, (2006)

Effect of Surface Roughness on Superlubricity

B. N. J. Persson, U. Tartaglino, V. N. Samoilov

IFF, FZ-Jülich, 52425 Jülich, Germany

We study the sliding of elastic solids in adhesive contact with flat and rough interfaces. We consider the dependence of the sliding friction on the elastic modulus of the solids. For elastically hard solids with planar surfaces with incommensurate surface structures we observe extremely low friction (superlubricity), which very abruptly increases as the elastic modulus decreases. We show that even a relatively small surface roughness may completely kill the superlubricity state.

Friction between solid surfaces is a common phenomenon in nature and of extreme importance in biology and technology[1]. At the most fundamental level friction is (almost) always due to elastic instabilities at the sliding interface. At low sliding velocity an elastic instability first involves (slow) elastic loading, followed by a rapid rearrangement, where the speed of the rearrangement is much faster than, and unrelated to, the loading (or sliding) velocity. During the fast rearrangement the elastic energy gained during the loading phase is converted into irregular heat motion. The exact way of how the energy is "dissipated" has usually a negligible influence on the sliding friction force, assuming that the dissipation occurs so fast that no memory of it remains during the next elastic loading event. There are many possible origins of elastic instabilities, e.g., it may involve individual molecules or, more likely, groups of molecules or "patches" at the interface which we have denoted by stress domains. The most fundamental problem in sliding friction is to understand the physical origin and nature of the elastic instabilities.

Elastic instabilities occur only if the lateral corrugation of the interaction potential between the solid walls is high enough, or the elastic modulus of the solids small enough. Roughly speaking, elastic instabilities can only occur if a characteristic elastic energy is smaller than a characteristic binding (or rather barrier height) energy. In general, one must consider the whole interface. In this case, depending on the elasticity and lateral barriers and the size of the contact area, elastic instabilities may or may not occur. Assume first that an elastically very stiff solid slides on a rigid corrugated substrate. In this case the atoms at the bottom surface cannot adjust to the corrugated substrate potential, and (for an incommensurate system) as some atoms move downhill other atoms move uphill in such a way that the total energy is constant. Thus, no elastic instabilities will occur during sliding, resulting in a very low sliding friction; this state has been termed *superlubricity*. However, when the block is elastically soft the atoms can rearrange themselves so that at any moment in time almost all the atoms occupy positions close to the minima of the substrate potential. During sliding rapid jumps will occur from time to time where a particle changes potential well. In this case the friction is high and (at zero temperature) remains finite as the sliding velocity $v \to 0$. It is important to note that even if the solids are too stiff for elastic instabilities to occur on short length scale, the ratio between the effective elasticity and the amplitude of the lateral corrugation of the binding potential may decrease when the system is studied at a longer length scale, which may make elastic instabilities possible on a longer length scale.

It is well known that elastically hard solids tend to exhibit smaller sliding friction than (elastically) soft materials. One extreme example is diamond which under normal circumstances exhibits very low kinetic friction coefficient, of the order of 0.01, when diamond is sliding on diamond. This can be explained by the nearly absence of elastic instabilities because of the elastic hardness of the material.

Recently, superlubricity has been observed during sliding of graphite on graphite. When the graphite surfaces are in registry stick-slip motion and large friction are observed. When the flake is rotated out of registry, the forces felt by the different atoms start to cancel each other out, causing the friction force to nearly vanish, and the contact to become superlubric.

Graphite and many other layered materials are excellent dry lubricants. The most likely reason for this is that the solid walls of the sliding objects get coated by graphite flakes or layers with different orientation so a large fraction of the graphite-graphite contacts will be in the superlubric state. This will lead to a strong reduction in the average friction. However, the coated solid walls are unlikely to be perfectly flat and it is important to address how surface roughness may influence the superlubric state. Here we will show that even a relatively small surface roughness may kill the superlubric state.

We have used a recently developed multiscale

molecular dynamics model, where the block extends in the vertical z-direction a similar distance as along the x-direction[2]. The results presented below have been obtained using this code for an elastic flat block sliding on a rigid substrate[3].

The lateral size of the block is equal to that of the substrate, but for the latter we use different a lattice constant $b \approx a/\phi$, where $\phi = (1+\sqrt{5})/2$ is the golden mean, in order to hinder the formation of commensurate structures at the interface. We have used self-affine fractal surfaces (see Ref. [4]), with the fractal dimension $D_{\rm f} = 2.2$. The atoms at the interface between the block and the substrate interact with the Lennard-Jones potential.

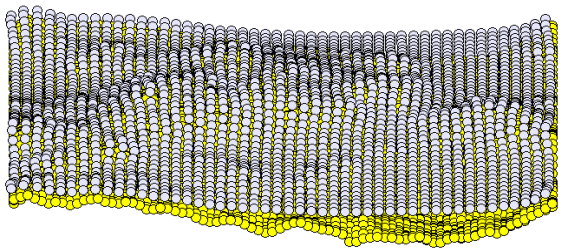

FIG. 1: The contact between an elastic block with a flat surface and a rough $rigid$ substrate. Only the interfacial layers of atoms are shown. The elastic modulus of the block is $E = 100$ GPa. The substrate is self-affine fractal with the root-mean-square roughness 3 Å, fractal dimension $D_{\rm f} = 2.2$. The applied pressure $p = 10$ GPa.

As an illustration, in Fig. 1 we show the contact between a flat elastic block (top) and a randomly rough $rigid$ substrate (bottom). Only the interfacial block and substrate atoms are shown. The substrate is self-affine fractal. Note the elastic deformation of the block, and that non-contact regions occur in the "deep" valleys of the substrate.

In all results presented below the upper surface of the block moves with the velocity $v = 0.1$ m/s, and the (nominal) squeezing pressure p is one tenth of the elastic modulus E of the block, i.e., $p = 0.1E$. The system is kept a low temperature by a viscous friction (a Langevin thermostat at $T = 0$ K) applied only to the topmost layer of block atoms, which are far away from the interface.

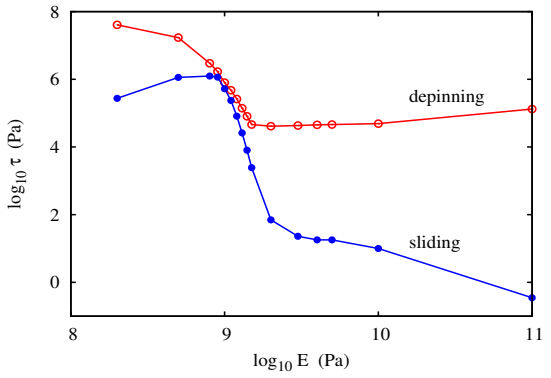

FIG. 2: The shear stress at depinning (static friction) and during sliding (kinetic friction) as a function of the elastic modulus E of the block, for the flat substrate. In the calculation we have used the squeezing pressure $p = 0.1E$ and the sliding velocity $v = 0.1$ m/s.

Let us first assume that both the block and the substrate have atomically smooth surfaces. Fig. 2 shows the shear stress as a function of the elastic modulus E of the block. Note the relatively abrupt decrease in the friction when the elastic modulus changes from $E_1 \approx 0.7$ GPa to $E_2 \approx 2$ GPa. For $E > E_2$ practically no instabilities occur and the friction is extremely small, while for $E < E_1$ relatively strong elastic instabilities occur at the sliding interface, and the friction is high. For $E = 0.2$ GPa the static friction $\mu_{\rm s} > 2$. This calculation illustrates that the transition from high friction to *superlubricity* can be very abrupt; in the present case an increase in the elastic modulus by only a factor of 3 (from 0.7 to 2.1 GPa) decreases the kinetic friction by a factor of $\sim 10^5$.

Let us now consider the influence of surface roughness on the sliding dynamics. In Fig. 3 we show average shear stress for an elastic block sliding on a rough substrate, as a function of the elastic modulus E of the block. The curves from top to bottom correspond to the substrate root-mean-square roughness amplitudes 3, 1, 0.3, 0.1 Å and 0 (flat substrate). For the substrate with the largest roughness, no superlubricity state can be observed for any elastic modulus up to $E = 10^{12}$ Pa.

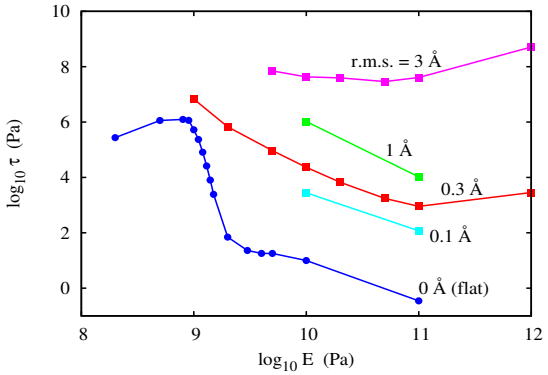

FIG. 3: The shear stress for an elastic block sliding on rough substrates, as a function of the elastic modulus E of the block. The curves from top to bottom correspond to the root-mean-square roughness amplitudes of the fractal substrate 3, 1, 0.3, 0.1 Å and 0 (flat substrate).

[1] B.N.J. Persson, *Sliding Friction: Physical Principles and Applications*, 2nd ed., Springer, Heidelberg, 2000.

[2] C. Yang, U. Tartaglino and B.N.J. Persson, Eur. Phys. J. E**19**, 47 (2006)

[3] U. Tartaglino, V.N. Samoilov and B.N.J. Persson, J. Phys.: Condens. Matter **18**, 4143 (2006).

[4] B.N.J. Persson, O. Albohr, U. Tartaglino, A.I. Volokitin and E. Tosatti, J. Phys. Condens. Matter **17**, R1 (2005).

New Cleaning Agents on the Basis of Microemulsions for Offset Printing

C. Frank[1], J. Allgaier[1], S. Pudzich[2], J. Adams[2]

[1] FZJ, Institute of Solid State Research – Neutron Scattering, Juelich, Germany
[2] Bernd Schwegmann GmbH&Co.KG, Grafschaft-Gelsdorf, Germany

For the cleaning of printing machines mostly cleaners are used which contain mainly organic solvents. This causes severe difficulties in terms of safety at work and protection of the environment. Therefore we developed a new generation of cleaners on the basis of microemulsions. Besides advantages with respect to safety and environmental aspects the new cleaners are superior to the solvent cleaners in their cleaning power.

Offset printing is nowadays the dominating printing process. Cleaning of printing machines is carried out usually using solvents on the basis of hydrocarbons (see Figure 1). Due to their low boiling points these conventional cleaners evaporate largely during use and therefore cause substantial difficulties with respect to safety at work and protection of the environment. Efforts to replace the low boiling cleaners by cleaners with high flame points were only partly successful. These cleaners on the basis of high boiling hydrocarbons or natural ester oils usually exhibit poor cleaning results. In addition, the solvent cleaners generally show a poor performance regarding the removal of polar dirts like paper dust or pigments. Therefore, the development of better cleaners is an important task. In a project co-funded by the Deutsche Bundesstiftung Umwelt (DBU) new microemulsion cleaners for offset printing machines were examined. Because of the combination of polar and non-polar properties, microemulsions should be useful for the removal of both polar dirts and non-polar dirts, printing inks for example. As they contain water, microemulsions should furthermore lead to a reduction of solvents and exhibit elevated flame points. Microemulsions for technical applications need to be stable over a wide temperature window. For this reason they contain large amounts of surfactants, usually in the order of 20-30%. This is economically disadvantageous and, in addition, creates new safety problems as surfactants are hazardous to skin and eyes. Therefore a procedure for increasing the efficiency of surfactants in microemulsions was used in this work to minimize the surfactant contents [1, 2]. As little was known about the use of microemulsions for the new application, in a preceding step several surfactants and surfactant mixtures were tested with respect to usability in the microemulsion cleaners. If the formulations fulfilled the stability criteria, application tests were carried out first in the laboratory and using the most promising formulations, additionally in printing plants.

FIG. 1: Cleaning of a printing machine.

In the first step several surfactant systems were tested with respect to their stabilizing properties. Because of the huge diversity of technical surfactants and the time consuming work associated with recording the corresponding phase diagrams, screening experiments were carried out with alcohol ethoxylates, sugar surfactants and anionic-nonionic mixtures. Alcohol ethoxylates are widely used for microemulsions in fundamental research. In our work such surfactants on the basis of C-8 to C-10 alcohols were useful for stabilizing microemulsions. However, they were responsible for bad smell in the final formulations and therefore could not be used. Alcohol ethoxylates on the basis of higher alcohols did not cause smell problems but led to high viscosities due to the formation of lamella phases, which in turn reduced the cleaning properties. Mixtures of ionic and non-ionic surfactants frequently yield very temperature insensitive microemulsions. For this reason alcohol ethoxylates in combination with different anionic surfactants were tested. Again under the requirements of the microemulsion composition, most of these systems led to relatively viscous formulations, being of little use for cleaning purposes. The situation was different for sugar surfactants, where two different types were tested, alkyl polyglycosides and sorbitan esters, the latter surfactant class being almost unknown in microemulsion research. Together with non-polar cosurfactants, sugar surfactants are known to form temperature insensitive microemulsions in analogy to the ionic/non-ionic mixtures. Several alcohols and lowly

ethoxylated alcohols were tested as co-surfactants. Such combinations finally allowed formulating relatively low viscosity cleaners. Besides these properties, sugar surfactants feature other important advantages. Their hazardous potential is minimal and they are produced mainly from renewable resources. In the next step the method for increasing the surfactant efficiency was applied. Originally polyalkane-PEO block copolymers were used as additives for this purpose. As these polymers were not available commercially and it turned out that their biodegradability is extremely bad, new additives had to be used. We succeeded finding a replacement using very hydrophilic alcohol ethoxylates. These materials also can be regarded as PEO equipped at one chain end with a short hydrophobic unit. It turned out that C-12 to C-18 anchors were sufficient to fully locate the additive molecules at the surfactant interface [3]. In other words this means that the new additives were fully equivalent to the formerly used block copolymers with respect to efficiency increase. Additionally their biodegradability was found to be excellent. Combining the sugar surfactants with the new additives gave ideal formulations with respect to safety and environmental requirements. In addition the surfactant content could be reduced to 5 - 10% and the stability window was kept at least between 10°C and 40°C. Figure 2 shows on the left hand side a cleaner based on a conventional microemulsion with high surfactant content and without efficiency increasing additive. The other cleaner was formulated on the basis of the efficiency increasing technology and contains few surfactants. Because of the low surfactant content the microemulsion is turbid.

FIG. 2: Microemulsion cleaners with high surfactant content (left) and low surfactant content (right).

Cleaners showing good stability properties were tested with respect to their cleaning properties. It soon turned out that viscosity is of crucial importance. Conventional solvent cleaners usually exhibit low viscosities around 1 mPas. In microemulsions usually viscosities between 10 and 100mPas were found. Additionally, it seemed that under shear many microemulsions tended to gel. This is of importance because strong shear forces are applied during the cleaning processes. The viscosity tests showed that especially cleaners on the basis of sugar surfactants had low enough viscosities and showed acceptable cleaning results. Besides viscosity additives are of importance to optimize the cleaning performance. Glycol ethers and salts were used for this purpose. As these additives also influence microemulsion stability, the cleaning tests were strongly interconnected with the corresponding stability tests. In the laboratory scale simple wipe tests were carried out first to estimate the cleaning power. Only formulations which passed all preceding tests were chosen for practical tests in printing plants. These tests were necessary because the complex situations during the cleaning processes cannot be fully simulated in laboratory experiments.

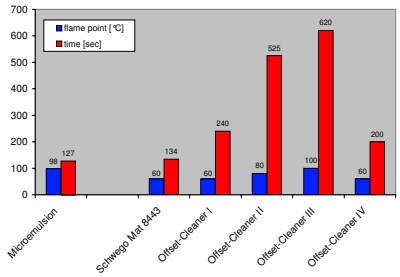

FIG. 3: Cleaning properties for printing inks (red columns) and flame points (blue columns) for different cleaners.

Figure 3 visualizes the cleaning powers and flame points of the newly developed microemulsion cleaner together with the results for commercial solvent based cleaners. The cleaning power is expressed in terms of the time needed in a standard test to solubilise a given amount of printing ink. The lower the time is, the better the cleaning power is. The results clearly demonstrate that for the solvent cleaners the cleaning power decreases with increasing flame point. The microemulsion cleaner, however, shows the best cleaning power although its flame point is almost the highest. It is also more versatile in its application than the standard cleaners as it clearly shows better cleaning results for hydrophilic dirts. In addition, the solvent content of the microemulsion cleaner is reduced by more than a factor of two. The Schwegmann company plans to commercialize this new cleaner in 2007.

[1] B. Jakobs et al., Langmuir **15**, 6707 (1999).

[2] European Patent No. 1 109 883.

[3] German Patent Application No. 10 2005 049 765.9-43.

Dynamics of Alcohol Dehydrogenase Observed by Neutron Spin Echo Spectroscopy

R. Biehl[1], B. Hoffmann[2], M. Monkenbusch[1], P. Falus[3], R. Merkel[2], D. Richter[1]

[1]Institut für Festkörperforschung, FZJ
[2]Institut für Bio- und Nanosysteme, FZJ
[3]Institut Laue-Langevin, Grenoble, France

The dynamic behaviour of proteins is a keystone to the understanding of their function as nanomachines or their mode of operation during the conversion to vitally important substances or while metabolising toxic by-products of other production processes. To understand these processes we need information on length scales comparable to the size of the protein and its domains, which determine their functionality. Here we focus on the alcohol dehydrogenase (AD) in solution to examine the domain mobility and the influence of a bound cofactor on the dynamics of the AD tetramer of horse liver.

Protein domain motions are critical for proteins to coordinate precise biological functions. Alcohol dehydrogenases belongs to a group of dehydrogenase enzymes that occur in many organisms and facilitate the conversion between alcohol and aldehyde and/or ketone. In humans and many other animals, they serve to break down alcohols, which could otherwise be toxic. In yeast and many bacteria they catalyse the opposite reaction as a part of fermentation. In figure 1 the tetramer of horse liver is shown with its 4 monomers in a flat structure. A key factor is the needed cofactor Nicotinamide Adenine Dinucleotide (NAD^+), which is bound into the gap between the two main domains of the AD monomer (see figure 1).

Between the main domains, depicted yellow and blue for a single monomer in figure 1, the NAD^+ Molecule is bound in conjunction with a narrowing of the gap recently observed by MD simulation.[1] Additional the Ethanol is bound into the gap. After metabolising the ethanol the protein has to release both molecules (NADH and acetaldehyde) and should reopen. We try to observe a difference between bound and unbound state of the protein.

Neutron Spin Echo Spectroscopy (NSE) measures the intermediate scattering function $S(q,\tau)/S(q,0)$ and is a versatile tool to observe the dynamics of small molecules on length scales of several nm and on timescales below a nanosecond to above 100 nanoseconds. The data were collected at wavelength between 6A (max fourier time 10 ns) and 15A (max fourier time 170 ns) in a Q range of $0.022A^{-1} < Q < 0.220A^{-1}$ at a temperature of 5°C. Within this Q range the $S(Q,t)/S(Q,0)$ spectra obtained by NSE mainly measure coherent scattering. The spectra can be approximated by the first cumulant representation with the leading term

$$\lim_{\tau\to 0}\frac{\delta}{\delta\tau}\ln\frac{S(Q,\tau)}{S(Q,0)} = -\Gamma(Q) = -Q^2 D_{eff}(Q) \quad (1)$$

resulting in the effective Diffusion constant D_{eff} for small fourier times τ.

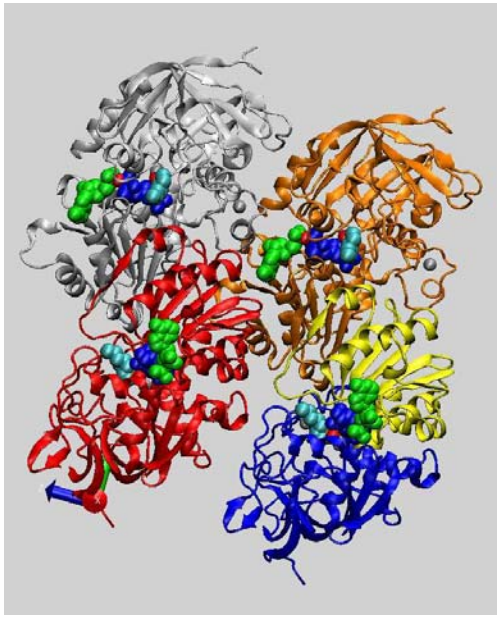

FIG. 1: The 4 monomers of horse liver AD (gray, orange, red and blue+ yellow) show a flat structure (gray-red parallel tor orange blue-yellow). The molecules between the monomer domains (blue and yellow) are NAD^+. The secondary structure is represented by ribbons for β- sheets and twisted α- helices.

For NSE experiments AD was dissolved in 99.9% D_2O buffer solution at neutral pH with a concentration of 10 and 50 mg/ml. To the sample with NAD^+ a concentration corresponding to 4 NAD Molecules per AD active centre was added. The buffer without NAD contained about 2 deuterated ethanol molecules per AD active centre to guaranty after some hours the metabolism of all possible NAD contamination from the stock powder.
Figure 2 shows the resulting effective diffusion coefficients for the 1% sample. For a first evaluation diffusion coefficients were fitted in different intervals to

discriminate between a short time (first half of fourier times) a long time (second half) and the overall behaviour.
We observe a similarity between the curves compared to the full interval. At small q we can discriminate a smaller value fo r the short times while the long times together with the complete interval has higher values. Also a small discrepancy at $q = 0.1A^{-1}$ is detected but is not significant. We measured the diffusion coefficient with dynamic light scattering (DLS) for c omparison. The resulting value of $2.3A^2/ns$ corresponds to the short time fit result at low q as single particle diffusion.
To model the overall shape with an increasing diffusion at increasing q rotational and translational diffusion has to be taken into account. The translational and rotational diffusion coefficients of $D_T = 2.38A^2/ns$ respective $D_R = 7.8 * 10^5 s^{-1}$ were calculated by the program HYDROPRO [2] which includes the full protein structure from the Protein Data Bank [3] and the hydrodynamic interactions with the surrounding fluid. The full scattering function was taken into account including the partially exchange of protons in the protein structure due to solvation in D_2O. For the effective diffusion of a rigid particle with scalar coefficients we yield

$$q^2 D_{eff}(q) = \sum_l S_l(q)[q^2 D_\tau + l(l+1)D_R] \qquad (2)$$

$$\text{with } S_l(q) = \sum_{|m|\leq l} \sum_i^{Atoms} |b_i j_l(qr_i) Y_{l,m}(\Omega_i)|^2$$

where b_i is the neutron scattering lengths of the i atom in the protein and r_i, Ω_i are the length and orientation of the i-th position vector. J_l and Y_{lm} are the spherical Bessel Functions and the Spherical Harmonics of order l and m.

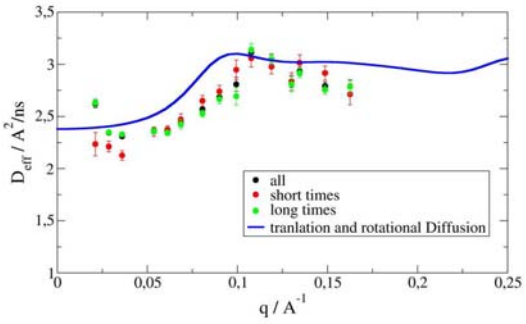

FIG. 2: The measured effective diffusion constant for the 1% sample with NAD compared to a model of scalar translational and rotational diffusion including the effect of the internal structure of the protein according to the partial deuteration of exchangeable protons.

The calculated value for lowest q is in good agreement with the DLS value and with the short time behaviour at low q representing the diffusion of a single particle. With increasing q when the observation length scale shrinks to the dimension of the protein (longest axis about 100A) the rotational diffusion rises its contribution and leads to an increase of the effective diffusion. The following modulation is due to the changing internal structure in the protein with changing observation length scale.
The increase of the long time diffusion at large length scales (small q) might be due to an upcoming interaction with other proteins but is not yet understood. The shift of the increase to higher q values compared with the calculated might be due to the small changes of the structure in solution compared to the crystal structure used for the calculations. Overall the dynamics is overestimated by the calculation. Figure 3 shows the result of the 5% sample with and without NAD as bound cofactor. The overall shape is the same as for 1% but at a smaller level. For the short time behaviour with cofactor we observe again a value near to the DLS value which is not observed without the bound cofactor. The long time behaviour shows the same values at low q as for the 1% sample. At about $0.1A^{-1}$ and at smaller q we observe again a difference between long and short time values but here with significance.

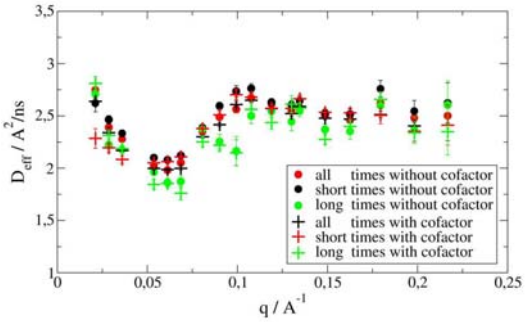

FIG. 3: Comparison of the effective diffusion for the 5% sample with and without cofactor.

The Neutron Spin Echo Measurements show a detailed image of the dynamics of alcohol dehydrogenase. While we observe no significant influence of the bound cofactor onto the dynamics of the protein we observe at $0.1A^{-1}$ a difference between long and short time behaviour possibly due to internal dynamics of the protein neglected in the rotational-translational diffusion model of a rigid protein. The simple model of a rigid object with translational and rotational diffusion gives a qualitative description but is not contenting. Additional independent measurement of the rotational diffusion coefficient is necessary and will be combined with a model taking the internal mobility of the protein domains into account to describe the observed features which cannot be described by the rigid body model.

[1] Hayward S., Kitao A. Biophysical Journal 911823-1831 (2006).

[2] Garcia de la Torre J. et al Biophys. J. 78, 719 (2000)

[3] http://www.pdb.org/

MAO Is a Polymer!

J. Stellbrink[1], A. Z. Niu[1], J. Allgaier[1], D. Richter[1], B. W. Koenig[2], R. Hartmann[2], L. J. Fetters[3], G. W. Coates[4]

[1]Institut für Neutronenstreuung
[2]Institut für biologische Informationsverarbeitung
[3]School of Chemical and Biomolecular Engineering, Cornell University, Ithaca, NY 14583-5201, USA
[4]Dep. of Chemistry and Chemical Biology, Cornell University, Ithaca, NY 14583-5201, USA

Modern polymerization techniques for the synthesis of olefin-based polymer materials often involve organo-metallic compounds as catalysts, which have to be activated by a co-catalyst. Since its discovery as a crucial co-catalyst in metallocene and post-metallocene olefin polymerizations methylaluminoxane (MAO) has retained commercial and academic status. We have used small angle neutron scattering (SANS) as the primary analysis tool for dilute MAO solutions in toluene. The main structure assayed is a linear polymer chain, $[\text{-Al(CH}_3\text{)O-}]_n$, with an average degree of polymerisation n≈300, a radius of gyration R_g ≈46Å showing a negative second virial coefficient. The latter fortifies the known state of play that toluene is a poor MAO solvent. Due to this low solubility we observe interchain branching with increasing concentration, which probably occurs via tetra-functional coordination of aluminium atoms.

Olefin-based polymeric materials, i.e. macromolecules made by polymerizing monomers containing a C-C double bond, are widely used as consumer products. For example more than 60 million tons of polyethylene (PE) are produced worldwide every year. Modern polymerization techniques often involve organo-metallic compounds as catalysts, which have to be activated by a co-catalyst. Methylaluminoxane ([Al/CH_3/O]–MAO) has held, since its discovery as a catalyst activator in 1980 [1], a near unique position as the activating co-catalyst for olefin based polymerizations. This generic dual catalyst combination has led to the commercialization of olefin homo- and co-polymerizations presumably carried by a single active center–the "single site" systems. The monolithic identity of the propagating site has led to unprecedented compositional, molecular weight distributions and tacticity control in olefin systems. In certain cases the propagation mechanism yields living system that provide control over chain molecular weights and polydispersity indices. Nevertheless, the absolute structural identities of the MAO aggregates and its catalyst complexed counterparts still remain ill defined [2]. We investigated MAO solutions in d-toluene using small angle neutron scattering (SANS) combined with static and dynamic light scattering (SLS/DLS) and ^{1}H-NMR [3]. The main structure of MAO is found to be a linear polymer chain, $[\text{-Al(CH}_3\text{)O-}]_n$, with an average degree of polymerisation n≈300 and a radius of gyration R_g ≈46Å. Another feature of MAO is its recognized non-solubility in alkane solvents and the poor solubility in toluene, which is confirmed in our experiments by the negative second virial coefficient A_2=5.9x10^{-4} cm^3 mol/g^2 obtained from model independent Zimm analysis. Probably this latent tendency towards phase separation induces the concentration dependent formation of chain-branching observed for concentrated solutions. All these results combine to support the notion that PMAO-IP is a polymer chain with a molecular weight (or chain length) well above those exhibited for the structures that have been based upon various theoretical exercises [2].

Experimental Polymethylaluminoxane-IP (PMAO-IP) was obtained from Akzo-Nobel as a transparent, colorless and precipitant free toluene solution. Sample preparation was carried out on a vacuum line and/or in an glove box under argon atmosphere to prevent contamination with air or moisture. Hence, the possibility of accidental sample adulteration was virtually eliminated.

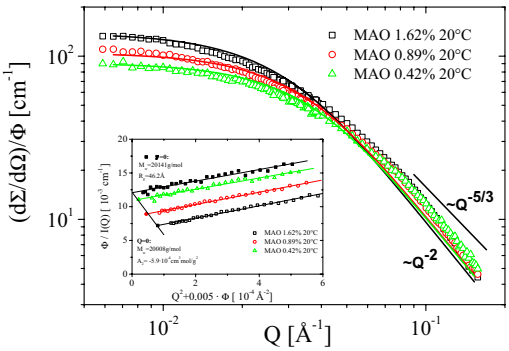

FIG. 1: Measured SANS intensity in absolute units vs. scattering vector Q for dilute PMAO-IP solutions in d_8-toluene. Solid lines: fit to the Debye funktions [4], see text. Inset: Zimm representation.

The SANS measurements were performed at the KWS1 instrument at the Forschungszentrum covering a Q-range of $2\text{x}10^{-3} \leq Q \leq 0.23\text{Å}^{-1}$, which corresponds to a spatial resolution $5\text{Å} \leq 1/Q \leq 500\text{Å}$. To achieve maximum contrast and minimum incoherent background, we investigated the PMAO-IP struc-

ture in d_8-toluene. In Fig. 1 SANS intensities given as the macroscopic cross section ($d\Sigma/d\Omega$) are shown as a function of the scattering vector Q= $4\pi\lambda \sin(\Theta/2)$, with λ the neutron wavelength and Θ the scattering angle. All data are normalized to volume fraction ϕ. Using this representation the volume fraction dependence should be eliminated, as found for high Q-vectors. Here, all data fall on top of each other as expected, because in this Q-range SANS is observing the local structure on the length scale of several tenths of Angstroms. This also proves without ambiguity that almost all of the PMAO-IP material is present in the chain-like structure. Towards low Q-vectors the curves split into a volume fraction dependent Zimm- or Guinier plateau, indicating the onset of particle-particle interactions. The simplest approach to describe interactions in dilute solution is a standard virial expansion, i.e.: $\phi/(d\Sigma/d\Omega)=1/V_w+2\cdot A_2\cdot\phi$, which, when combined with the Guinier law $P(Q)\sim\exp(-Q^2R_g^2/3)$ for describing the Q-dependence of the particle form factor P(Q), results in the well-known Zimm-plot [4]. A Zimm analysis is performed essentially without any assumption about the detailed molecular structure of the scattering particle (model-independent analysis) and reflects only its overall or global properties i.e. the molecular volume, M_w, the radius of gyration, R_g, and, if applicable, the second virial coefficient A_2. The Zimm plot of our data ($Q > 10^{-2}\mathring{A}^{-1}$) is shown in the inset of Fig. 1. The dual extrapolations to zero concentration (ϕ=0, filled squares) and angle (Q=0, filled symbols) lead to the following characteristics associated with the PMAO-IP structure: M_w = 20.1 kg/mol; n= 313; A_2 = -5.9x10^{-4} cm^3 mol/g^2; R_g = 46.2$\mathring{A}$; $< R^2 >_0/M$ = 0.637 $\mathring{A}^2$ mol/g while C_∞ = 4.3. Combined with results from elemental analysis we derive the following structure for PMAO-IP:$[$ -Al($C_{1.45}H_{3.89}$) O-$]_n$.

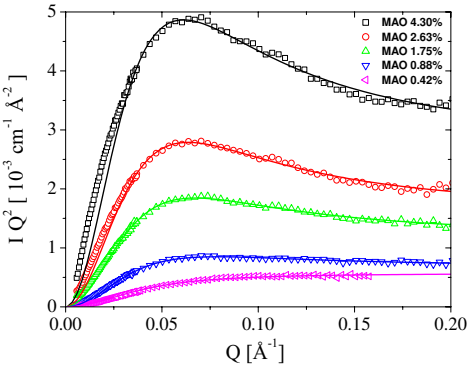

FIG. 2: Kratky representation of the SANS intensity measured for dilute to concentrated solutions of PMAO-IP solutions in d_8-toluene. Solid lines; Fit to the form factor of polydisperse star polymers [4], see text.

Fig. 2 shows a Kratky-representation of our data, i.e. plotting $(d\Sigma/d\Omega)\cdot Q^2$ vs. Q, which reveals the existence of branched polymer structures by a peak, whose height crucially depends on the degree of branching f. The form factor of a linear Gaussian chain (Debye function) [4], on the other hand, increases monotonically to an asymptotic plateau due to the power law I(Q) Q-2. Such a plateau is found in our experimental data only for the lowest volume fraction ϕ=0.42%, but the plateau height deviates from those of the Debye function. With increasing volume fraction a slight peak evolves, which becomes most clearly obvious for the highest volume fractions ϕ=2.63% and 4.30%. Analysing our SANS data in terms of form factors for branched polymer structures [2] we were not able to describe the data over the full experimental Q-range. Either we could describe the intermediate Q-range around $Q\approx 10^{-2}\mathring{A}^{-1}$, i.e. the Guinier- or Zimm regime, or the peak region $Q\geq 5x10^{-2}\mathring{A}^{-1}$ in the Kratky-representation. Whereas the former results corroborates the model-independent Zimm analysis for dilute solutions $\Phi \leq 2\%$, the latter gives a volume fraction dependent mean functionality f, which ranges from $f \approx 10$ at $\phi \leq 4.3\%$ to $f \approx 6$ at ϕ =0.88%. Due to this observed concentration dependence we expect that the branching occurs via tetra-functional interchain coordination. Possible branch sites are given in Fig. 3.

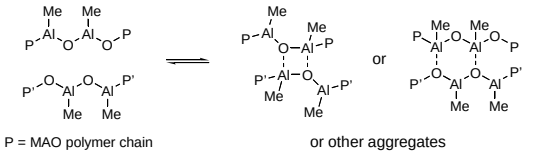

FIG. 3: Possible interchain branch sites via tetrafunctional coordination.

Conclusions: The unanticipated high polymer structure of the PMAO-IP as deduced from SANS and SLS/DLS is vastly different from the small, compact architectures favored theoretically for many years [2]. The scattering experiments have clearly shown that a high polymer-like self-assembled structure is formed by the aggregation of the $[$ Al/(R)/O $]$ units where, in our case, R denotes either the methyl or n-the n-octyl groups. As the PMAO-IP concentration increases branched structures commence to form.

[1] H. Sinn, W. Kaminsky, H.J. Vollmer, Angew. Chem., 19, 390, (1980).

[2] E. Zurek, T. Ziegler, Prog. Polym. Sci., 29, 107, (2004).

[3] J. Stellbrink, A.Z. Niu, J. Allgaier, D. Richter, B.W. Koenig, L. Hartmann, L.J. Fetters, G.W. Coates, accepted for publication in Macromolecules (2007).

[4] J. Higgins, H. Benoit, Polymers and Neutron Scattering, Oxford University Press, Oxford, (1994).

Polymer Chain Dynamics in a Random Environment

K. Niedzwiedz[1], A. Wischnewski[1], M. Monkenbusch[1], D. Richter[1], A.-C. Genix[2], A. Arbe[2], J. Colmenero[2,3], M. Strauch[4], E. Straube[4]

[1] FZJ, Institute of Solid State Research – Neutron Scattering, Jülich, Germany
[2] Donostia International Physics Center, Paseo Manuel de Lardizabal 4, 20018 San Sebastian, Spain
[3] Centro de Física de Materiales CSIC-UPV/EHU, Apartado 1072, 20080 San Sebastian, Spain
[4] Martin-Luther-Universität Halle-Wittenberg, Fachbereich Physik, D-06099 Halle, Germany

The question of what determines the behaviour of two polymers which are perfectly miscible on the one hand, but very different in their dynamical properties on the other hand, is at present matter of controversial discussion. We present a neutron scattering study on the miscible polymer blend poly(ethylene oxide)/ poly(methyl methacrylate) (PEO/PMMA) which due to the very different time scales of motion is a perfect candidate to address this topic. Only exploring different time and length scales allowed to identify the mechanisms of dynamic heterogeneity on a molecular scale.

The dynamics of a polymer chain in the melt is well described by the Rouse model [1]. Here, the relaxation of thermally activated fluctuations is balanced by entropic and viscous forces (friction). The relevant parameter in this model is the friction of the observed chain in a heat bath representing the adjacent chains. One important consequence of the fact, that the segments of a chain are linked to each other (chain-connectivity), is that segments exhibit a mean squared displacement proportional to the square root of time different to the displacement for a Fickian diffusion which is increasing linearly in time.

At present the investigation of dynamic miscibility in a blend of two different polymers is an active area of research. One of the important questions is how the segmental friction arises if a segment is surrounded by a chemically heterogeneous environment. The system PEO / PMMA is in particular interesting because of the significantly different glass transition temperatures ($T_g^{PEO} \approx 200$ K, $T_g^{PMMA} \approx 400$ K). In such a situation, for temperatures around and below T_g^{PMMA}, PEO moves in the random environment created by the frozen PMMA component [2].

Starry-eyed, one could assume that in a perfectly miscible polymer blend the friction of a given segment is determined by the average friction of the blend components.

We have investigated the PEO dynamics in PMMA by quasielastic neutron scattering. This has been realized by preparing a mixture of protonated PEO chains in deuterated PMMA. Samples with different concentrations (25%, 35% and 50% of PEO) have been measured at different temperatures between 350 K and 400 K. By neutron backscattering spectroscopy we have followed the mean square displacement (msd) of the PEO segments, the experiments were performed at the instrument BSS at the FZJ in Jülich.

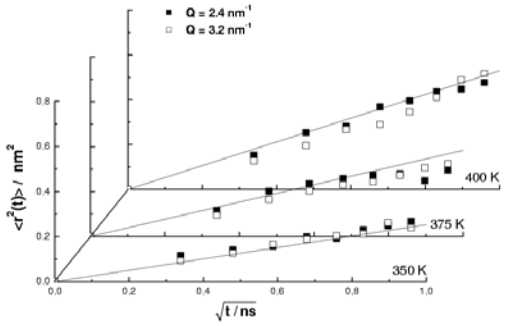

FIG. 1: Mean square displacements obtained from backscattering spectra from the 35% PEO/PMMA sample at different Q and temperatures.

Fig. 1 shows the result for a sample with 35% protonated PEO in 65% deuterated PMMA at two different momentum transfers Q. The data follow nicely straight lines when plotted against the square root of time in good agreement with the Rouse prediction. Depending on temperature, the maximum displacement of a PEO segment observed during about 1 ns amounts to less than 1 nm. The related values for the friction can be obtained from the slope of these lines. They show a temperature dependence very similar to the one found in pure PEO, however the friction is about one order of magnitude larger than in the pure system.

So far we may state that the dynamics of PEO in a matrix of PMMA at temperatures where PMMA is nearly frozen is in good agreement with Rouse dynamics characterized by an average friciton. From this one could conclude that the effect of blending is not more than imposing a different friction to a given segment, and therefore that the above mentioned naive assumption is true.

Fig. 2 displays neutron-spin-echo (NSE) measurements of the single chain dynamic structure factor of PEO chains in the PMMA matrix measured at the IN15 (ILL, Grenoble) up to about 80 ns. In order to achieve this result a deuterated PMMA matrix was used, where a mixture of deuterated and protonated PEO was immersed. The dotted lines in Fig. 2 are

a result of a Rouse description based on the average Rouse friction obtained from the backscattering data in fig. 1. Obviously this description fails grossly predicting a by far too fast decay. Apparently the motion is strongly slowed down towards longer times or larger length scales. We may roughly quantify this slowing down in fitting an effective smaller Rouse rate. This reveals retardations by factors 4 to 20 (depending on PEO-content and temperature) compared to the 1 ns scale and gives clear evidence for an additional effect of blending which has not been seen in the BSS data.

Finally, fig.3 shows Fourier transformed time-of-flight (TOF) data on the same blend measured at the FOCUS instrument (PSI, Villigen) at T=400 K. For the blend also the backscattering data are included. At high Q, quasielastic neutron scattering observes local processes. Compared to the spectrum from pure PEO, the blend data are strongly broadened demonstrating a broad distribution of local relaxation processes in the PMMA environment. From the decay we realize that a shift of the characteristic time from 1 ps in pure PEO to about 6 ps for PEO/PMMA is found –in excellent agreement with NMR data [3] and also with the ratio of the corresponding Rouse rates as determined by the backscattering experiment. However, the question remains where the extremely broad distribution comes from.

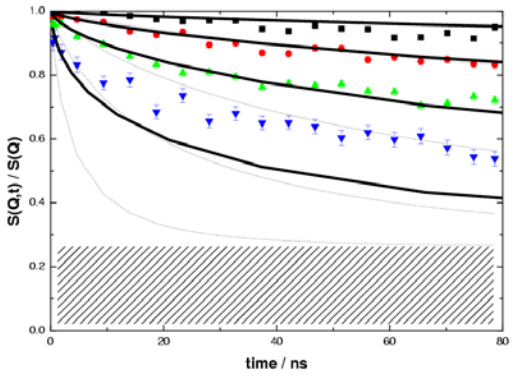

FIG. 2: Single chain dynamic structure factor of the 35% PEO/PMMA system at T=400 K. Q-values are 1 nm^{-1}, 1.5 nm^{-1}, 2 nm^{-1} and 3 nm^{-1} from top to bottom. The dashed base represents the elastic contribution to the scattering. The dotted lines illustrate the Rouse theory with Rouse relaxation rate obtained from the backscattering data. The solid lines show the results of the model with randomly distributed friction.

In the following we demonstrate that the contradictory experimental findings can be explained assuming that the mobile PEO chain experiences a heterogeneous environment imposed by the rather stiff PMMA matrix. This picture can be rationalized by a chain where the beads undergo a random friction with a distribution of friction coefficients.

The dynamic structure factor for such a chain has been calculated by starting with the Langevin equation for a polymer chain and introducing a set of bead mobilities following a log-normal distribution centered around the average mobility obtained from the backscattering data, the only adjustable parameter being its width. The solid lines in Fig. 2 show the best result which could be achieved for the 35 % PEO/PMMA sample. The three lowest Q values are in very good agreement with the experimental data, however, the highest Q data are reproduced at very short times only. The origin of this significant deviation at the highest Q and longer times is still unclear, though it might have to be related to additional confinement effects imposed by the matrix. The values of the width obtained by applying the same procedure to the other compositions and temperatures show the expected behaviour: the width of the distribution function increases with increasing PMMA concentration (in the limit of zero PMMA concentration it should go to zero) and within one blend it increases with decreasing temperature.

Having in mind that at high Q we observe directly the distribution of relaxation times, we now can try to describe the TOF spectra of the blend displayed in Fig. 3. Starting from the pure PEO spectrum we shift the relaxation rate by a factor obtained from the backscattering data for the blend. In a second step we convolve the thus shifted PEO spectra with the log-normal distribution function using the result from the NSE data. With this we obtain the solid line in Fig. 3 in perfect agreement with the observed spectrum. Having in mind that all parameters have been obtained from other measurements, the width from the NSE-data and the shift of the relaxation rate from the BSS data, this agreement which combines data over 5 orders of magnitude in time is remarkable.

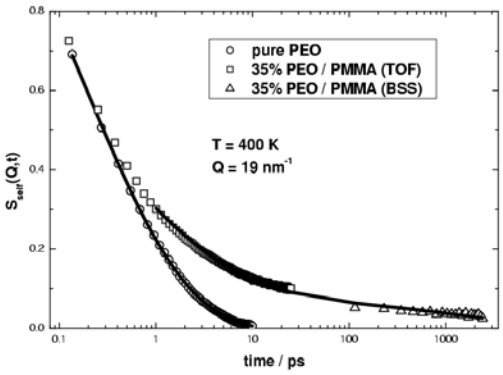

FIG. 3: Fourier transformed TOF data of pure PEO and 35% PEO/PMMA at T = 400 K. For the blend system also backscattering data are included. The solid line through the PEO data describes a fit with a stretched exponential (β = 0.5). Line through the blend data: see text.

[1] P. E. Rouse, J. Chem. Phys. **21**, 1272 (1953)

[2] A.-C. Genix, A. Arbe,F. Alvarez, J. Colmenero, L. Willner and D. Richter, Phys. Rev. E **72**, 031808 (2005)

[3] T. R. Lutz, Y. He, M. D. Ediger, H. Cao, G. Lin and A. A. Jones, Macromolecules **36**, 1724 (2003)

Anomalous Diffusion in Short Chain Polymer Melts

M. Zamponi[1], A. Wischnewski[1], M. Monkenbusch[1], L. Willner[1], D. Richter[1], M. Guenza[2], B. Farago[3]

[1] FZJ, Institute of Solid State Research – Neutron Scattering, Jülich, Germany
[2] University of Oregon, Oregon, USA
[3] Institut Laue-Langevin, Grenoble, France

The viscoelastic behavior of polymer melts is strongly influenced by the polymer chain length. The longer the chains the more important are the topological constraints due to entanglements of the chains. The dynamics of short polymer chains in the melt with a length about or below the entanglement length have been explored by neutron spin echo spectroscopy. Two different kinds of blends have been investigated: short chains with a length in the order of the entanglement length in a matrix of the same molecular weight and in a long chain matrix. Independent of the surrounding matrix chains the short chains are expected to perform free Rouse motion. While the monodisperse blends show at least qualitatively Rouse dynamics, the dynamics of the short chains in the long matrix is strongly retarded. In both cases deviation of the expected free diffusional center of mass motion is observed. In the monodisperse blend this deviation might be explained by interchain interactions whereas in the other case the short chains are subject to topological constraints even if they are shorter than the entanglement distance.

The dynamics of linear polymer chains in the melt depends strongly on the chain length: For short, unentangled chains the dynamics is determined by a balance of viscous and entropic forces which can be described by the Rouse model [1]. Here the chains interact solely by local friction with a heat bath, representing the neighboring chains. For long chains topological chain-chain interactions in terms of entanglements become important and are dominating the dynamical behavior. In the reptation model these topological constraints are described by a virtual tube which follows the primitive path of the observed test chain [2]. However, this definition means that a test chain with a length in the order of one entanglement distance can not be captured in a tube. Short chains below the entanglement weight are therefore expected to perform free Rouse motion independent of the chain length of the matrix chains.
Both models have been corroborated in their respectively regime on a molecular scale by neutron spin echo (NSE) spectroscopy [3, 4]. However, various simulation results (e.g. [5]) anticipate a deviation from the expected free Rouse diffusion even in the regime where Rouse dynamics should apply. The simulations show a subdiffusive regime of the center of mass mean squared displacement at early times. NSE allows to explore this regime experimentally. For a sample containing few protonated chains in a deuterated but otherwise identical environment NSE directly measures the single chain dynamic structure factor $S(Q,t)$. For short chains at small scattering wavevectors Q the center of mass diffusion dominates, internal relaxation modes are negligible. From the measured dynamic structure factor the center of mass mean squared displacement $< r^2(t) >$ can then be easily extracted.

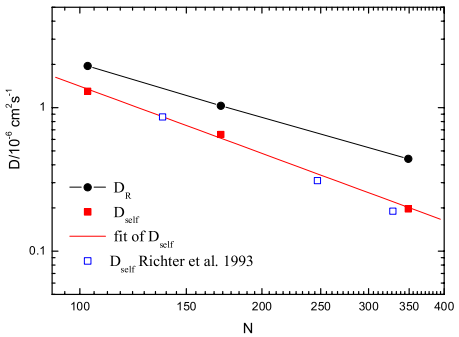

FIG. 1: Fitted diffusion constants in dependence of the chain length in comparison to the expected Rouse values and an earlier measurement [7] as indicated in the plot.

Short polyethylene chains with a length of about the entanglement molecular weight have been investigated by neutron spin echo spectroscopy in the melt (temperature T =509K). Although the measured dynamic structure factor displays at least qualitatively free Rouse motion, quantitative deviations occur. For small Q value and long times diffusion dominates, so that from a fit with the intermediate scattering function for simple diffusion $\exp(-Q^2Dt)$ the self diffusion constant of the short chains can be extracted. The fitted diffusion constants (fig.1) are significantly smaller than the expected Rouse diffusion constants $D_R = kT/N\xi$, with N the number of chain segments and $\xi(N)$ the segmental friction, where the molecular weight dependence of ξ for short chains [6] has been included here. The results agree nicely with an earlier measurement at short times by Richter et al. [7], where the diffusion constant has been estimated

from a mode analysis.

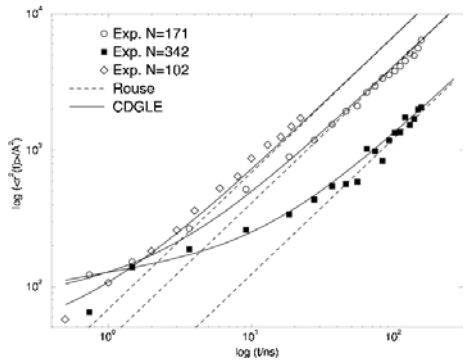

FIG. 2: Center of mass mean squared displacement for various short chain homopolymer melts in comparison to the mode coupling theory calculations by Guenza (solid lines).

For the smallest Q-value the center of mass mean squared displacement has been extracted from the measured dynamic structure factor $S(Q,t) = \exp(Q^2 < r^2(t) > /6)$. For normal diffusion a linear time dependence $< r^2(t) > \sim t$ is expected. This is found only for long times (see fig. 2), whereas at short times a subdiffusive regime with a power law $< r^2(t) > \sim t^{0.5} - t^{0.8}$ is found. This deviation is stronger than anticipated from the simulations but might be explained by intermolecular interactions as discussed by Guenza [8]. Following a mode coupling approach a modified Rouse model is derived, where the number of chains undergoing cooperative motions is the only fitting parameter. With this ansatz the smooth transition from subdiffusive motion to normal diffusion is nicely recovered (solid lines in fig.2). The transition roughly occurs at the Rouse time of the chain, the longest mode relaxation time. This experimental finding is in agreement with the model.

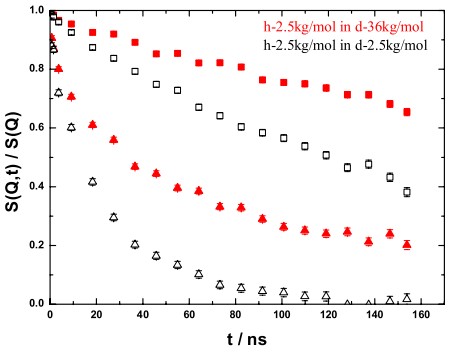

FIG. 3: Dynamic structure factor for 2 different Q-values of a short chain ($M_w \simeq M_e$) in a matrix of the same length (open symbols) and in a long chain matrix (closed symbols).

More surprising deviations for the same short chains in a long chain matrix have been observed. For chains around the entanglement molecular weight Rouse behavior is expected, independent on the matrix properties. But a strong retardation of the dynamics of the short chain in the long chain matrix in comparison to the same short chain in a short matrix is found (see fig. 3).The different dynamic structure factors for the same short chain can not be scaled onto each other, which would be the case if the deviation would stem only from a different segmental friction due to the different matrix chain lengths.
Again a clear subdiffusive regime of the center of mass mean squared displacement is found. Although the observed discrepancies are similar to the homopolymer melt they are qualitatively different. Now a clear subdiffusive regime with a $t^{1/2}$ dependence is found for all the different short chains in the same long chain matrix (see fig.4). The transition to normal diffusion takes place only at longer times far beyond the Rouse times of the short chains. The time at which this transition occurs increases with increasing chain length, but the data can be shifted onto one master curve by simply rescaling the time. For all the different chain lengths the transition to normal diffusion takes places at the same mean squared displacement. This indicates that the observed deviations are independent of the length of the test chain and therefore reflect a property of the matrix chains which may be related to the tube diameter. This would imply that the short chains are topologically constrained, although their length is below or about the entanglement distance.

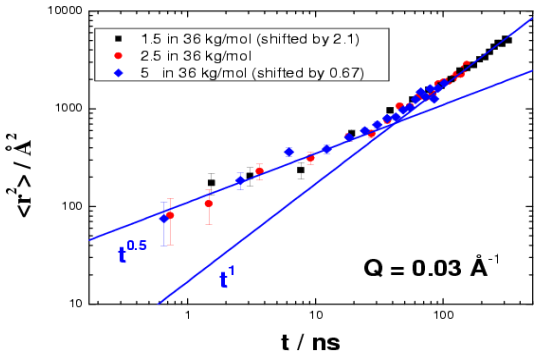

FIG. 4: Center of mass mean squared displacement of different short labelled chains in a long chain matrix (as indicated in the plot). Lines are guides for the eye.

[1] P. E. Rouse, J. Chem. Phys. **21**, 1272 (1953).

[2] P. G. DeGennes, J. de Phys. **42**, 735 (1981).

[3] D. Richter et al., Physica B **174**, (1991).

[4] P. Schleger et al., Phys. Rev. Lett. **81**, 128 (1998).

[5] G. D. Smith et al., Chem. Phys. **261**, 61 (2000).

[6] D. S. Pearson et al., Macromolecules **20**, 1133 (1987).

[7] D. Richter et al., Phys. Rev. Lett. **71**, 4158 (1993).

[8] M. Guenza, Macromolecules **35**, 2714 (2002).

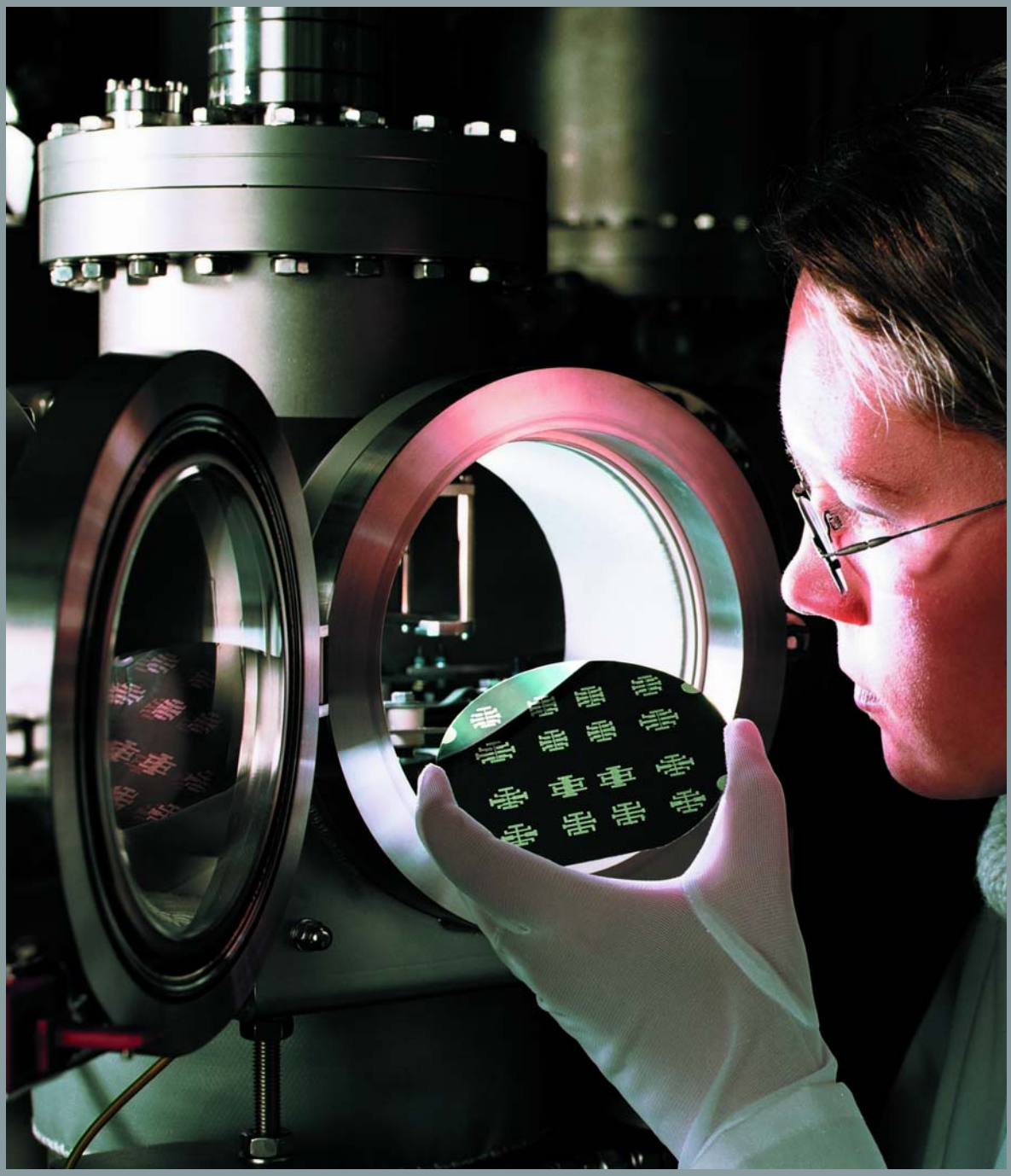

Physicists at the IFF are developing new materials for spintronics.

Information Technology with Nanoelectronic Systems

This research programme focuses on medium-term and long-term tasks in nanoelectronics, on emerging far-reaching concepts, and on issues of physics and technology well ahead of the mainstream development. On the eve of the transition from microelectronics to nanoelectronics, the traditional routes of down-scaling along the roadmap will no longer guarantee a long-term success. Exploratory research in the field of information technology is entering a new era and is unfolding into new degrees of freedom. This applies to all three major fields, information processing, information storage, and information transmission. The major routes of exploratory research in nanoelectronic systems to be followed are:

- scalability of device concepts,
- exploration of new material classes and phenomena,
- new concepts beyond conventional CMOS technology, and
- alternative architectures.

Our research towards these general goals utilizes three approaches, irrespective of the specific programme topics. One approach is dedicated to new electronic materials such as ferromagnetic and ferroelectric layer structures, group III nitrides, and electronically active organic molecules. These material classes are studied because of their potential for introducing improved or completely new functions onto Si chips and new emerging substrates. Another approach is devoted to process technologies for minimum feature sizes well below 100 nm. Apart from using conventional top-down approaches, which are limited to lithographically defined resolutions, we are investigating cost-effective bottom-up approaches, which aim at the generation and assembly of functions from self-organized inorganic nanostructures as well as tailored organic molecules at surfaces. Yet another approach explores novel electronic functions as the basis for new device concepts. These may aim at, for instance, bioelectronic applications, ultra-dense and non-volatile resistive memories, spin-controlled devices, Terahertz imaging systems, and self-organized semiconductor nanostructures.

Magnetic Properties of Polycrystalline $Co_2Cr_{1-x}Fe_xAl$ Alloys

M. Buchmaier[1], C. M. Schneider[1], J. Werner[2], D. Elefant[2], A. Teresiak[2], G. Behr[2], J. Schumann[2], E. Arushanov[3]

[1] Institut für Festkörperforschung IFF-9 "Elektronische Eigenschaften"
[2] Leibniz Institut für Festkörper- u. Werkstoffforschung IFW Dresden
[3] Institute of Applied Physics, Academy of Sciences of Moldova

Half-metallic ferromagnets have recently attracted considerable attention, because their conduction electrons are considered to be 100 % spin-polarized, making them a promising material class for spintronic applications [1], especially as electrodes in magnetic tunnel junctions. Co-based Heusler alloys are of particular interest, because they have comparatively high Curie temperatures, especially the full-Heusler compounds Co_2XY, which have been predicted to have a half-metallic band structure. We have investigated the magnetic properties of bulk $Co_2Cr_{1-x}Fe_xAl$ (CCFA) samples in the composition regime $(x = 0.3 - 0.5)$ [2]. Both, the bulk and surface properties have been investigated by appropriate experimental techniques. Additionally the dynamic spin wave properties, which are significant for the switching of fast magnetoelectronic devices have been investigated by Brillouin light scattering (BLS).

The Heusler phase $Co_2Cr_{1-x}Fe_xAl$ (CCFA) has first been proposed by Felser et al. [3] on the basis of LSDA calculations. The material is believed to exhibit a van-Hove singularity at the Fermi level giving rise to particular magnetic and electronic properties. However, these are strongly affected by composition, and chemical and structural disorder.

Bulk CCFA alloy samples were prepared by RF melting the elemental composites of 99.99 or better purity, 3 times in a Hukin-type copper crucible under Ar atmosphere. The samples were subsequently annealed in evacuated and sealed silica ampoules at 1100°C for 80 hours and afterwards quickly quenched in ice water. The composition of the polished samples, which was investigated by optical metallography and electron probe microanalysis, was found to vary mainly with respect to the Al and Cr content. The variation was found to be improved significantly by the annealing and quenching step, resulting in a homogeneity better than 5 %.

The crystal lattice parameter and structure has been investigated by X-ray diffraction on ball-milled powder samples and was found to change only very slightly with the Fe-content. The diffraction patterns of our alloy samples clearly indicate that the samples crystallized in the B2 structure, since the odd (111) superlattice lines indicative of the $L2_1$ phase were missing. From the influence of the Fe content x on the intensity ratio between the even superlattice reflexes (200) and (220), $I_{[200]}/I_{[220]}$, which is a measure for the degree of site ordering between the Co and Al [4], we conclude that an increasing incorporation of Fe in the lattice promotes a reduction of the site ordering of Co and Al.

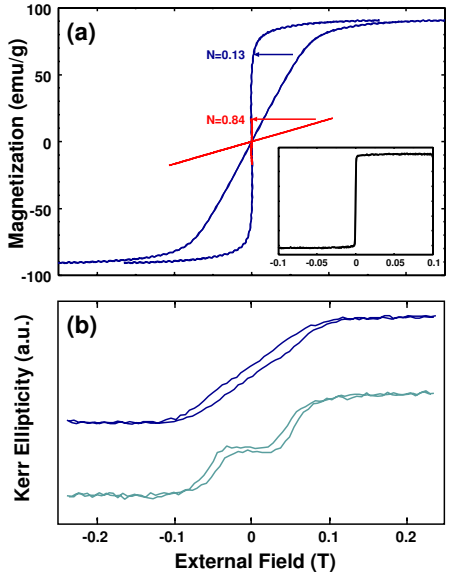

FIG. 1: $Co_2Cr_{0.5}Fe_{0.5}Al$. (a): Magnetization loops for an ellipsoid sample measured with AGM, and computed unsheared loops. The applied field is parallel to the long sample axis (red) and perpendicular to the surface (blue). (b): MOKE loops, taken in the center of the sample (dark blue) and near the edge (light blue).

The bulk saturation magnetization was measured at 300 K employing an alternating gradient magnetometer (AGM). The experimentally determined values, which are plotted in Fig. 2 (a), show a systematic increase of the total magnetic moment with increasing iron content. The magnetic moments should be compared with theoretical values calculated on the basis of the sum rule $M_t = Z_t - 24$ (M_t: total spin magnetic moment per unit cell; Z_t: total number of valence electrons), which should give reasonably accurate results for a half-metallic Co_2XY Heusler. Our results as well as the data in Ref. [4] exhibit, however, a relatively large deviation from the sum rule. This

cannot be explained by the B2 atomic site disorder, which is expected to have only little influence on the magnetic moment. Instead, the lack of magnetic moment can be explained by a significant A2-type disorder interchanging Co with Cr and Fe, which is expected to lead to a local antiferromagnetic coupling, and as a consequence to a magnetic frustration and a significant decrease in the magnetic moment with increasing degree of disorder [5].

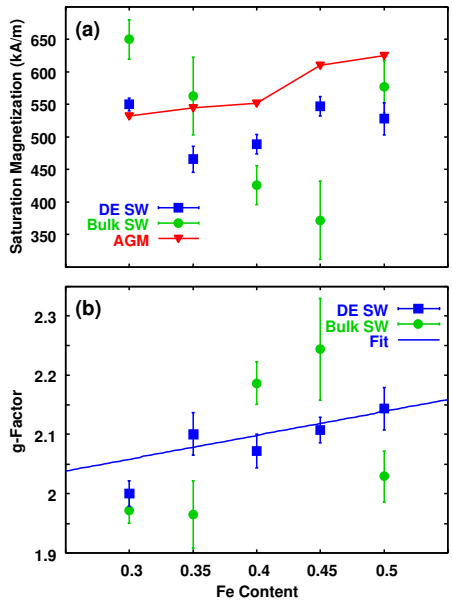

FIG. 2: (a): Saturation magnetization determined from AGM and BLS (bulk and DE modes). (b): gyromagnetic factor determined from BLS.

The hysteresis loops for the bulk material taken at different orientations of the externally applied magnetic field exhibit a large anisotropy. In order to clarify the origin of this anisotropy, we have prepared a geometrically regular CCFA sample with well-defined geometry and rounded corners. The blue and red graphs in Fig. 1 (a) show the experimental data with the magnetic field applied parallel to the longest and the shortest axes of the sample, respectively. Taking into account the appropriate demagnetizing factor N, the effect of the form anisotropy can be numerically removed from the hysteresis data to obtain the so-called unsheared loops, which are indicated by arrows in Fig. 1 (a). The inset of Fig. 1 (a) shows a hysteresis loop of a polycrystalline thin film sample prepared of the same material, with external field applied in the film plane. As the loop of the thin film sample, which should not be influenced by the form anisotropy, is in satisfactory accordance with the unsheared loops of the bulk crystal, we can conclude that geometry- and shape-dependent demagnetizing fields of the sample dominate the magnetization reversal process.

In order to clarify possible deviations from the bulk remagnetization behavior at the surface, we measured the magneto-optic Kerr effect in the longitudinal configuration. We have taken line scans with a lateral resolution of about 0.1 mm for each sample. Figure 1 (b) shows representative MOKE loops for a composition $x = 0.5$, where the dark blue graph corresponds to the sample center and the light graph has been acquired close to the sample edge. The order of magnitude of the saturation fields has been found to be in agreement with the bulk AGM loops. However, we have found a considerable variation of the loop shape and saturation field as a function of the position on the sample. From the clear position dependence of the loop shape, i.e. the plateau-like feature at low field of the loops recorded at the sample edge, which is missing in the sample center, the important influence of the stray fields on the hysteresis shape are highlighted. Another finding, which immediately catches the eye are the larger coercive fields appearing in the MOKE loops as compared to the AGM loops. These larger coercive fields at the sample surface as compared to the bulk are probably due to oxidation of the unprotected surface or defects, which might be introduced by the polishing process.

BLS spectra with variable external field (0-7 T) have been recorded while keeping the laser at a constant spot near the sample center. The spectra show a bulk-mode related band with a broad high-frequency tail, and an intense Damon-Eshbach (DE) surface mode peak, which are typical for bulk ferromagnetic samples with strong exchange (high Curie temperature). The effective dynamical saturation magnetization and the gyromagnetic g-factor extracted by fitting the field dependency of the DE and bulk frequencies are plotted in Fig. 2. The saturation magnetization values scatter strongly and in a general trend appear to be lower as compared to the AGM data (red graph), which possibly can be explained by (i) a significant magneto-crystalline anisotropy in conjunction with the polycrystalline nature of the samples and (ii) the dominant form anisotropy together with an insufficient control of the sample shape. As those extrinsic contributions do not affect the slope of the ν vs. B curves of the DE mode, which determines the g-factor, it is nevertheless possible to extract a g-factor with good accuracy. It shows a clear tendency to increase with increasing Fe content.

Our studies show the complex interplay between structural, chemical, and magnetic properties in the Co-based Heusler alloys in the B2 phase. The understanding of this interplay is very important to arrive at a reliable and reproducible preparation of single phase materials, which is the basis for a possible transfer to applications.

[1] G. A. Prinz, Science **282**, 1660 (1998).

[2] M. Buchmeier, C. M. Schneider et al., J. Magn. Magn. Mater. **313**, 157 (2007).

[3] C. Felser et al., J. Phys.: Condens. Matter **15**, 7019 (2003).

[4] S.Okamura, R. Goto et al., J. Appl. Phys. 96, **6561** (2004).

[5] Y. Miura, K. Nagao and M. Shirai, Phys. Rev. B **69**, 144413 (2004).

Half Metallic Antiferromagnetic Diluted Magnetic Semiconductors

L. Berqvist, P. H. Dederichs

Theory of Structure Formation, IFF

Based on electronic structure calculations and statistical methods we investigate a new class of materials for spintronic applications: halfmetallic antiferromagnetic diluted magnetic semiconductors (HMAF-DMS). As shown recently by Akai and Ogura these DMS systems contain equal amounts of low-valent and high-valent transition metal impurities, such that their local moments exactly compensate each other. Electronic structure calculations demonstrate, that the exchange coupling parameters in these systems are dominated by a strong antiferromagnetic interaction between the two impurities. The Neel temperatures are calculated by Monte Carlo simulations and in mean field approximation. It is shown that the latter method strongly overestimates the critical temperatures and that the more realistic values obtained by Monte Carlo are rather low.

In recent years, there has been a great interest in various materials aimed for applications in spintronics [1, 2]. The possibility of combining the electronic charge and spin degrees of freedom opens up for materials with new functionality. This include magnetic multilayers which are used in GMR readheads in harddisks, diluted magnetic semiconductors (DMS) and half-metallic ferromagnets like Heusler alloys. Especially DMS systems have attracted lots of attention[3, 4], both theoretically and experimentally, ever since the discovery of large-T_c ferromagnetism in Mn-doped GaAs by Ohno in 1998 [2]. In the last few years, more sophisticated control over defects in the samples and annealing have increased the critical temperature, T_c, from around 110 K to around 175 K for Mn-doped GaAs. Still, the T_c is well below room temperature which prohibits a practical use of this material for devices.

Recently, Akai and Ogura[5] proposed some new form of DMS systems, i.e. halfmetallic antiferromagnetic diluted magnetic semiconductors. They are very different from the standard ferromagnetic or disordered-local-moment (DLM) phases of DMS. Necessarily, they contain equal concentrations of two kinds of impurities, e.g. Cr and Fe in $Zn_{1-2x}Cr_xFe_xSe$ such that the moments of these impurities, i.e. of Cr and Fe, are equal and exactly compensate each other by antiparallel alignment. To obtain halfmetallicity, it is essential that both impurities are chemically different. Moreover, halfmetals have a 100 % spin polarization at the Fermi level being essential for spintronics.

Here we present extensive density functional calculations on halfmetallic antiferromagnetic DMS systems[6]. We present ground state calculations for the antiferromagnetic systems $Zn_{1-2x}Cr_xFe_xSe$ and $Zn_{1-2x}V_xCo_xSe$. Then we calculate the exchange coupling constants between the different impurity pairs and calculate the Neel temperatures of the antiferromagnetic systems and the Curie temperatures of the ferrimagnetic ones by Monte Carlo simulations. Due to the short range of the exchange couplings the critical temperatures of these systems are strongly reduced as compared to the mean field estimates, analogous to recent findings [7, 8, 9] in 'elemental' DMS systems.

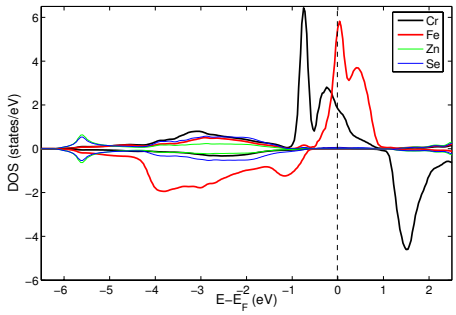

FIG. 1: Total DOS of $Zn_{0.9}Cr_{0.05}Fe_{0.05}Se$ using the KKR-ASA method in LDA approximation. Positive (negative) values corresponds to majority (minority) states.

In Fig. 1 the calculated density of states using the KKR-CPA method of $Zn_{0.9}Cr_{0.05}Fe_{0.05}Se$ is displayed. A halfmetallic ground state is found with zero total magnetic moment. Around the Fermi level a common impurity band in the spin-up channel originating from the Cr and Fe d-states is clearly present and is well understood from hybridization. The hybridization of these states lowers the band energy and also determines the magnetic coupling of the system.

In Fig. 2 the calculated magnetic exchange interactions using the LSDA approximation in $Zn_{0.9}Cr_{0.05}Fe_{0.05}Se$ and $Zn_{0.9}V_{0.05}Co_{0.05}Se$ are displayed as a function

of distance. Due to the halfmetallicity, disorder and the formation of a joint impurity band in the wide band gap, the exchange interactions are strongly damped with respect to the distance[7, 8]. Furthermore, the exchange interactions are essentially non-zero only for distances shorter than 1.5 lattice constants. The exchange interactions between a Cr atom to another Cr atom are ferromagnetic while the exchange interactions between a Fe atom to another Fe atom are weakly antiferromagnetic. The exchange interactions between a Cr atom to a Fe atom are strongly antiferromagnetic and basically determines the overall magnetic structure of the system. As discussed by Ogura and Akai, the strong antiferromagnetic Cr-Fe coupling arise from the double exchange mechanism in the joint impurity band. Since the d-states of Cr in this band are mostly filled and the Fe-DOS is shifted to higher energies, also superexchange plays an important role. In fact it is more or less impossible to distinguish both mechanism in this case.

The situation in $Zn_{0.9}V_{0.05}Co_{0.05}Se$ is slightly different (Fig. 2b). Here the exchange interactions between atom components of the same type (V-V and Co-Co) are ferromagnetic with a dominating nearest neighbour interaction.

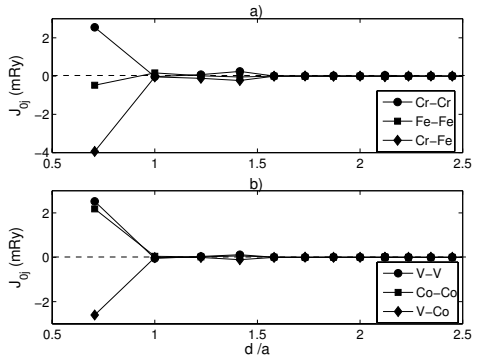

FIG. 2: Exchange interactions of a) $Zn_{0.9}Cr_{0.05}Fe_{0.05}Se$ and b) $Zn_{0.9}V_{0.05}Co_{0.05}Se$ using the KKR-ASA-CPA method and the LSDA approximation plotted as a function of distance d (in units of the lattice constant a).

The critical temperatures are evaluated using the above calculated exchange parameters and then applying statistical methods. The methods used are the mean field approximation (MFA) and the Monte Carlo simulations (MC). It should be noticed that MFA is using a virtual crystal approximation to treat the disorder while the MC simulations treats the disorder exactly without any approximations using large supercells. Since the calculated exchange interactions are rather short ranged it is expected that the MFA will strongly overestimate the critical temperatures, which is indeed the case as shown in Fig. 3.

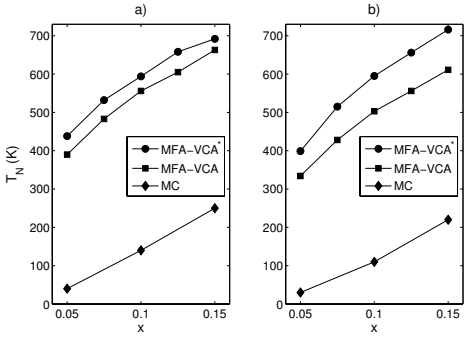

FIG. 3: Calculated critical temperatures of a) $Zn_{1-2x}Cr_xFe_xSe$ and b) $Zn_{1-2x}V_xCo_xSe$ in K using exchange parameters from LSDA. MFA-VCA denotes the mean field approximation where T_N is estimated from the total energy difference between the antiferromagnetic and DLM configuration, MFA-VCA denotes the mean field approximation results estimated from the exchange interactions and MC the result from MC simulations.*

Ultimately, spintronics systems should have a critical temperature well above room temperature in order to work satisfactory in applications. The mean field approximation give results that are above room temperatures for all concentrations considered. However, the numerically exact MC method gives much lower values for the critical temperatures, around 140 K for realistic concentration of magnetic ions, similar to the results for the elemental DMS [7, 8, 9].
Details of the calculations are found elsewhere[6].

[1] G.Prinz, Science **282**, 1660 (1998).

[2] H. Ohno, Science **281**, 951 (1998)

[3] T. Dietl, Semicond. Sci. Tech. **17**, 377 (2002).

[4] K. W. Edmonds, P. Boguslawski, K. Y. Wang, R. P. Campion, S. N. Novikov, N. R. S. Farley, B. L. Gallagher, C. T. Foxon, M. Sawicki, T. Dietl, M. Buongiorno Nardelli and J. Bernholc, Phys. Rev. Lett. **92**, 037201 (2004).

[5] H. Akai and M. Ogura, Phys. Rev. Lett. **97**, 026401 (2006).

[6] L. Bergqvist and P. H. Dederichs, J. Phys: Condens. Matter **19**, 216220 (2007).

[7] L. Bergqvist, O. Eriksson, J. Kudrnovský, V. Drchal, P. A. Korzhavyi and I. Turek, Phys. Rev. Lett. **93**, 137202 (2004).

[8] L. Bergqvist, O. Eriksson, J. Kudrnovský, V. Drchal, A. Bergman, L. Nordström and I. Turek, Phys. Rev. B **72**, 195210 (2005).

[9] K. Sato, W. Schweika, P. H. Dederichs and H. Katayama-Yoshida, Phys. Rev. B **70**, 201202(R) (2004).

Exchange Interactions in Dilute Magnetic Semiconductors: Local Environment Effects

P. H. Dederichs[1], K. Sato[2], H. Katayama-Yoshida[2]

[1]Institut für Festkörperforschung, Forschungszentrum Jülich, D-52425 Jülich, Germany
[2]ISIR, Osaka University, Ibaraki, Osaka 567-0047, Japan

Dilute magnetic semiconductors like $Ga_{1-x}Mn_xAs$ are considered as ideal materials for spintronics. They are half-metallic ferromagnets and exhibit a 100 % spin polarisation at E_F. Ferromagnetism is caused by the exchange interactions J_{ij} between neighboring Mn impurities. The disorder in these systems is usually described by the powerful coherent potential approximation (CPA), which averages over the substitutional disorder, and the exchange interactions J_{ij} are calculated by Liechtenstein's formula in connection with the CPA averaging. Here we investigate the validity of this approach, by embedding a whole cluster of impurities around the atoms i and j into the CPA medium, and by explicitly calculating the resulting exchange interactions as a function of the disordered environment. We find large fluctuations of the J_{ij} values and upon ensemble averaging significant deviations from the standard Liechtenstein-CPA formula, in particular for small distances $i - j$ and small concentrations.

Dilute magnetic semiconductors (DMS) like $Ga_{1-x}Mn_xAs$ are intensively studied for applications in spintronics. Due to their halfmetallicity they exhibit a 100 % spinpolarisation at E_F, being ideal for spin dependent devices. Due to their ferromagnetism and their structural similarity with semiconductors they are usually used as substitute for metallic ferromagnets in otherwise all semiconductor spintronics structures. For a theoretical analysis, the random disorder of the Mn-impurities in these systems is a serious complication. Therefore in most successful calculations the coherent potential approximation (CPA) is employed, providing a mean field description of the electronic structure.

Recent first-principles calculations based on density functional theory in connection with the CPA have proven to describe the electronic structure and magnetism of dilute magnetic semiconductors (DMS) with good accuracy. In particular, combining standard statistical methods with first principles methods, the measured Curie temperatures of DMS are reasonably reproduced for well studied systems such as (Ga, Mn)As and (Zn, Cr)Te [1, 2, 3]. The most successful approach is a hybrid method of Monte Carlo simulations (MCS) and first-principles calculations of effective exchange interactions by using Liechtenstein's prescription [4]. In this method, the configuration dependence of the exchange coupling constants J_{ij} between two impurities at sites i and j due to the presence of other impurities is averaged out by using the CPA Green's functions. The calculated exchange interactions are then concentration dependent, but otherwise depend only on the distance between the two sites i and j. In the MCS, first we generate a random distribution of impurities in a supercell, and perform MCS assuming the configuration-independent-CPA exchange interactions for each generated configuration, and then take the configuration average of the simulation results. Thus, rigorously speaking, this hybrid method is inconsistent with the CPA averaging procedure.

In this paper we go beyond the CPA and discuss local environment effects on the exchange interactions J_{ij} in DMS arising from the presence of other impurities on neighboring sites. To take the effects of local impurity configurations into account, we embed into the CPA medium a large cluster which includes in addition to sites i and j several other sites with random impurity occupancies. Within the cluster, multiple scattering at the different magnetic impurities is fully included and the calculated exchange parameters J_{ij} reflect the given local impurity configurations. In the present calculations, we calculate the electronic structure of DMS by using the Korringa-Kohn-Rostoker coherent potential approximation (KKR-CPA) method based on the local density approximation. We use the KKR-CPA package MACHIKANEYAMA2002 developed by Akai. The scattering path operators are calculated for the given embedded clusters and then the total energy change due to the rotation of magnetic moments at sites i and j are calculated by Liechtenstein's formula for the J_{ij} coupling constants [4].

The calculated results are shown for (Ga,Mn)As with 5 % Mn in Fig. 1a and for (Ga,Cr)N with 5 % Cr in Fig. 1b and with 10 % Cr in Fig. 1c.

For the realization of random impurity configurations, we prepare an $8 \times 8 \times 8$ supercell and choose magnetic sites randomly in the supercell. Then, for each impurity pair in the supercell, the coupling constant J_{ij} is calculated by taking the local impurity distribution into account. We consider two kinds of clusters, one is the smallest cluster which consists of only 2 impurities at site i and j (2-impurity embedding)

and the other considers the positions of impurities on the first nearest neighbor shells around both site i and site j. For the configuration average, we generate 10 different random supercell configurations. For simplicity in the calculations, we assume zinc blende crystal structure for (Ga, Cr)N.

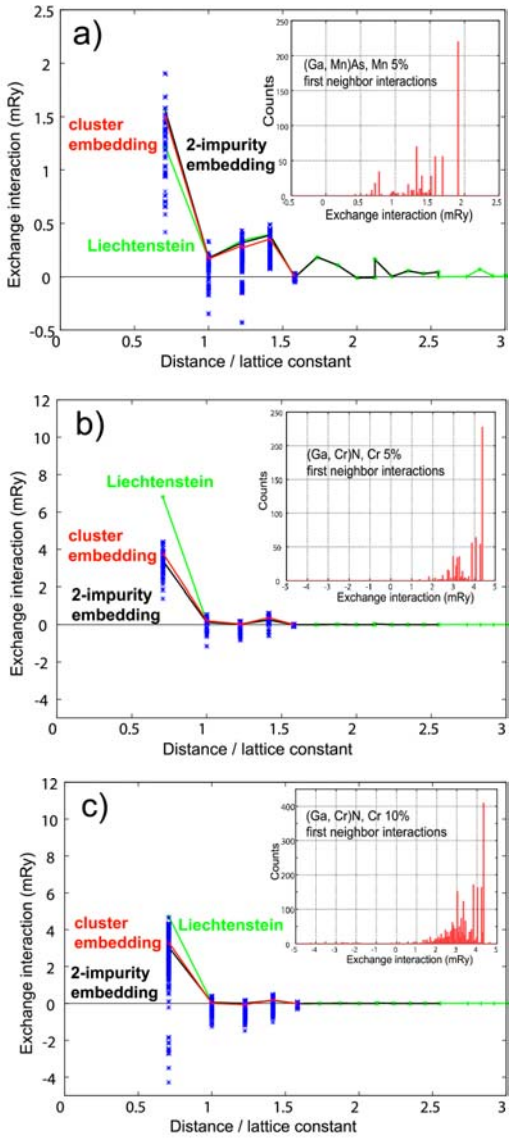

FIG. 1: Fluctuations of exchange interactions between magnetic impurities in DMS due to environmenta effects: a) (Ga,Mn)As for 5 % Mn, b) (Ga,Cr)N for 5 % Cr and c) (Ga,Cr)N for 10 % Cr. See text for details.

In Fig. 1 the data indicated by the crosses represent the results for the different impurity configurations, exhibiting large fluctuations resulting from a strong dependence on the positions of the other impurities. The fluctuations are so large that even negative values are obtained, in particular for the 2nd and 3rd neighbors. However the large spread is somewhat misleading, since the low and negative values have rather small weights, as it is indicated in the inset figure by the frequency histogram for the nearest neighbour interaction. The configuration average, as given by the red curve ("cluster embedding"), agrees very well with the two-impurities-embedded-in-CPA results (black curve), but disagrees with the standard Liechtenstein CPA formula (green curve). On the other hand all three curves agree very well for larger distances.

The obvious failure of the Liechtenstein CPA formula for small concentrations arises from the fact, that in this formula the multiple scattering between the impurities i and j are not fully included, i.e. the repeated back and forth scattering events are not taken into account in this formula, but are fully included in the embedded two-site or embedded cluster approach. For smaller concentrations this discrepancy becomes even larger, since for the nearest neighbour coupling Liechtenstein's formula yields a diverging contribution in the very dilute limit (at least for double exchange systems). On the other hand for larger distances all three curves agree well, since then repeated multiple scattering effects are less important. The same is valid for large concentrations. The good agreement of the configurational averaged results with the relatively simple two-impurity solutions is very gratifying, showing that vertex corrections to the CPA are of minor importance for the exchange interactions, provided the two-center problem is properly treated.

It is interesting that in Fig. 1 the configuration with the highest weight for the nearest neighbour pair exhibits also the largest exchange coupling. In this configuration the impurities i and j have no other impurities in their nearest neighbour shells. This means that (i) these values roughly represent the exchange couplings in the very dilute limit of vanishing concentrations and (ii) that due to the presence of third or fourth impurities the coupling is always reduced.

In conclusion we have discussed local environment effects on the exchange interactions in DMS. By embedding a whole disordered cluster around two impurities i and j in the CPA medium we find that (1) the exchange coupling J_{ij} exhibit large fluctuations depending on the positions of other impurities, that (2) the ensemble average over these configurations agrees well with the result obtained for the impurity pair (i, j) embedded in the CPA and that (3) the Liechtenstein CPA formula fails in the dilute limit.

[1] L. Bergqvist, O. Eriksson, J. Kudrnovsky, V. Drchal, P. Korzhavyi and I. Turek, Phys. Rev. Lett. **93**, 137202 (2004).

[2] K. Sato, W. Schweika, P. H. Dederichs and H. Katayama- Yoshida, Phys. Rev. B **93**, 201202R (2004).

[3] T. Fukushima, K. Sato, H. Katayama-Yoshida and P. H. Dederichs, Jpn. J. Appl. Phys. **43**, L1416 (2004).

[4] A. I. Liechtenstein, M. I. Katsnelson, V. P. Antropov and V. A. Gubanov, J. Magn. Magn. Mater. **67**, 65 (1987).

Spin-Polarized Tunneling Between an Antiferromagnet and a Ferromagnet

J. Enkovaara, D. Wortmann, S. Blügel

Institut für Festkörperforschung, Forschungszentrum Jülich, 52425 Jülich, Germany

By combining first-principles calculations with transport theory we investigate the origin of the magnetoresistance of a magnetic tunnel junction consisting of a ferromagnetic and an antiferromagnetic lead. The (001) oriented Fe/vacuum/Cr planar junction serves as model junction. Even though the conduction electrons of antiferromagnetic Cr are spin-degenerate, it is possible to observe magnetoresistance due to two mechanisms: Firstly, the surface magnetism of Cr creates a spin-dependent potential barrier, and secondly, exchange-split surface states and resonances result in a tunneling conductance which depends on the relative orientation of the Fe and Cr magnetizations.

The effect of spin-polarized tunneling of electrons through vacuum or an insulating barrier recently attracted inceased attention due to experimental progess in two fields: (i) the spin-polarized tunneling microscopy(SP-STM) [2] which developed into an important engine driving the field of nanomagnetism and (ii) the fabrication of planar tunneljunctions showing huge tunnelmagnetoresistance effects of well over 400% even at room temperatures[1].
The difference in the conductance due to a change in the relativ orientation of the magnetisation directions of tip and sample or of the two magnetic leads in the case of a planar tunnelbarrier, is frequently related to the spin-polarization of the conducting electrons. The simplest model proposing such a relation is due to Julliere and derives the magnetoresistance (MR), i.e. the relative differences of the resistances in the parallel R_P and antiparallel R_{AP} alignments of the magnetisation, from the density of states at the Fermi level $n^{L/R}_{\uparrow/\downarrow}$ for the two spin directions $\uparrow$ / $\downarrow$ and the two leads L/R

$$MR = \frac{R_{AP} - R_P}{R_P} = \frac{n^L_\uparrow n^R_\uparrow + n^L_\downarrow n^R_\downarrow}{n^L_\uparrow n^R_\downarrow + n^L_\downarrow n^R_\uparrow} - 1.$$

While this simple model can provide some insight into the basic mechanism of spin-polarized tunneling with ferromagnetic leads, it cannot easily be applied to tunneling between an ferromagnet and an antiferromagnet. The density of states of the antiferromagnet is spin-degenerate $n_\uparrow = n_\downarrow$ and consequently, Julliere's model (Eq.) predicts no magnetoresistance in such setups. In contrast to this finding, one of the most sucessfull realizations of SP-STM uses an antiferromagnetic Cr film tip. Similary to these SP-STM experiments showing a magnetic contrast with an antiferromagnetic tip, a large MR value has also be found in planar tunneljunctions where one electrode was an antiferromagnet. We will show that there are two mechanisms which give rise to a non-zero magnetoresistance in these cases: i) The surface magnetism of Cr leads to a spin-dependent potential barrier and ii) the presence of exchange-split surface states and resonances. Our findings are based on calculations carried out within the density functional theory (DFT) using the full-potential linearized augmented plane wave (FLAPW) method as implemented in the FLEUR-code (www.flapw.de). The boundary conditions corresponding to the semi-infinite Fe and Cr are treated with the embedded Green function method which has been recently implemented within the FLAPW-method. [3]

We investigate the case where the incident electrons travel normal to the surface, $i.e.$ we discuss electrons from the center ($\vec{k}_\parallel = 0$ or $\overline{\Gamma}$-point) of the two-dimensional Brillouin zone. In Fig. 1 we show the bulk band structures of Fe and Cr which project into the $\overline{\Gamma}$-point. In addition, the energy positions of the surface states are indicated. The Cr(001) surface is magnetic with an enhanced surface magnetic moment leading to exchange splitted surface states. The symmetry of the electronic states plays a key role in tunneling. Firstly, only those electronic states having the same symmetry on both sides of the barrier can couple. Secondly, the symmetry affects also the decay of the electronic wave function into the vacuum. This means that within the two-dimensional symmetry group of the Fe(001) and Cr(001) surfaces, states having Δ_1 symmetry decay slowest into the vacuum. The Δ_1 bands start at the $\overline{\Gamma}$ point at binding energies around -1 eV (1.5) eV for Fe majority (minority) states, and 1.1 eV for Cr, and they are dispersing upwards in energy. Additionally, the surface states marked in Fig. 1 are of Δ_1 symmetry. In the energy range acessible in tunneling experiments ($\sim \pm 1$ eV) the only bulk-like Δ_1-electrons originate from the Fe majority band. The minority Δ_1 surface states of both Fe and Cr may give additional contributions in this particular energy range.

The spin-resolved transmission probabilities $T^{\mathrm{P(AP)}}_{\uparrow(\downarrow)}$ for majority $(\uparrow)$ and minority $(\downarrow)$ states at the $\overline{\Gamma}$-point as function of the energy are shown in Fig. 2 for both magnetic configurations, where the magnetic mo-

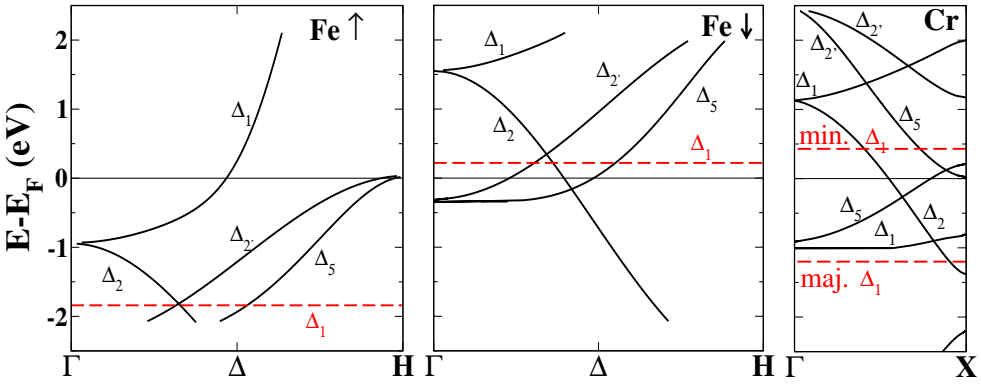

FIG. 1: Bulk band structures projecting onto $\overline{\Gamma}$-point. The positions of the surface states are indicated by the horizontal dashed lines. The left panel shows the Fe majority bands, the central one the Fe minority states and the right panel the Cr bands.

ments of the outermost Fe and Cr layers are aligned either parallel (P) or anti-parallel (AP). The terms majority (spin-up) and minority (spin-down) are defined with respect to the magnetic moment of the Fe surface. Hence, in the parallel configuration the Cr spin-up electrons are those with a larger density of states at the outermost Cr(001) surface layer while in the anti-parallel configuration the spin-down electrons are those with the larger the density of states in that layer.

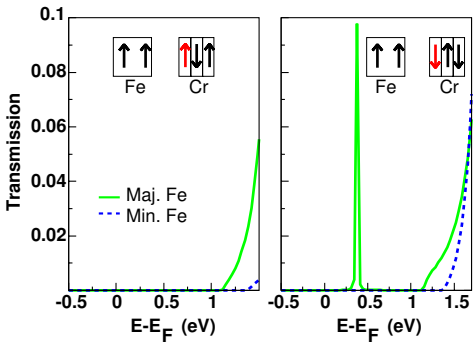

FIG. 2: Spin-resolved transmission probabilities at $\overline{\Gamma}$ as a function of the electron energy for parallel(P) (left panel) and and anti-parallel (AP) (right panel) alignment of tip and sample magnetization. The main solid (dashed) curve shows the the majority (minority) spin channel.

Cr exhibits a wide energy region without any Δ_1 state and therefore the bulk states with normal incidence will have a small transmission probability for both the parallel and anti-parallel magnetic alignments. Only at around 1.1 eV above the Fermi level, where the Δ_1 band of the Fe majority states overlaps with the Cr Δ_1 states a significant transmission probability can be found with a strongly increasing transmission at higher energies. For the Fe-minority states the overlap begins higher in energy and the transmission probability starts to increase at around 1.5 eV. One can see that for both spin-directions the energy at which a significant transmission sets in does not depend on the magnetic configuration. This point is determined only by the bulk band structure which is spin-degenerate for Cr. However, the surface magnetism of Cr results in a spin-dependent potential barrier and therefore the actual magnitude of transmission depends on the relative magnetic alignment of Cr tip and Fe sample.

For the anti-parallel alignment of tip and sample a narrow peak can be seen in the spin-up channel of the transmission probability arising from the Cr surface states. The Cr surface state near the Fermi level overlaps with the spin-up Δ_1 band of Fe which starts at -1 eV and thus can give a finite contribution to the conductance if the surface moments are properly aligned. When the magnetic alignment is parallel, the Cr surface state is of spin-down character and cannot tunnel into the bulk Δ_1 band of the Fe spin-up states due to spin-conservation during the tunneling process. However, in the antiparallel alignment the Cr surface state has the same spin as the overlapping Fe band, producing sharp feature in the tunneling conductance. Hence some conclusions can be drawn. As long as there is a Cr surface state near the Fermi level, a large change in the tunneling conductance, which is a Fermi-level property, at $\vec{k}_{\parallel} = 0$ with respect to the magnetic alignment can be expected, as this surface state contributes to the conductance only in the anti-parallel magnetic alignment.

[1] S. S. P. Parkin, et al. Nature Mat., 3:862, 2004.
S. Yuasa, et al. Nature Mater., 3:868, 2004.
S. Yuasa,et al. Applied Physics Letters, 89(4):042505, 2006.

[2] M. Bode. Rep. Progr. Phys., 66:523, 2003.

[3] D. Wortmann, H. Ishida, and S. Blügel. Phys. Rev. B, 65:165103, 2002.
D. Wortmann, H. Ishida, and S. Blügel. Phys. Rev. B, 66:075113, 2002.

Large TMR Effect at High Voltage Drop for $Co_2Cr_{0.6}Fe_{0.4}Al$/MgO/CoFe Tunnelling Junctions

A. D. Rata, H. Braak, D. E. Bürgler, and C. M. Schneider

CNI-Center of Nanoelectronic Systems for Information Technology (IFF-9)

Polycrystalline $Co_2Cr_{0.6}Fe_{0.4}Al$ Heusler films combined with MgO barriers and CoFe counter electrodes are structured to magnetic tunnel junctions and yield almost 50% magnetoresistance at room temperature. The magnetoresistance shows a strong bias dependence with the maximum occurring at a voltage drop well above 1 Volt. This special feature is accompanied by only a moderate temperature dependence of the tunnel magnetoresistance. A large magnetoresistance effect at high voltage drop in combination with a weak temperature is of high relevance for spintronic applications.

Co-based Heusler alloys are predicted to belong to the material class of the half-metals [1]. They are characterized by a band gap at the Fermi energy for one spin direction and metallic properties for the other. Therefore, the charge carriers should be 100% spin-polarized. Due to this feature large tunnelling or giant magnetoresistance values are expected in layered structures incorporating Heusler alloys as one or both ferromagnetic electrodes. Among the Co-based full-Heusler compounds, $Co_2Cr_{0.6}Fe_{0.4}Al$ (CCFA) is a promising candidate for obtaining large tunnelling or giant magnetoresistance effects. CCFA has a large magnetic moment and a high Curie temperature (T_c). Several groups have successfully prepared thin films of CCFA on various substrates, showing improved structural order and magnetic characteristics [2-5]. Remarkable progress was obtained also by incorporating these compounds into magnetic tunnel junctions (MTJs). Fully epitaxial junctions with CCFA films and MgO tunnelling barriers showed 90% TMR ratio at room temperature (RT) and 240% at 4.2 K [2]. We report on large TMR values obtained at RT in MTJs combining a polycrystalline CCFA thin film with an MgO tunnel barrier and a CoFe counter electrode. The magnetoresistance shows (i) rather moderate temperature dependence and (ii) a strong bias dependence with the largest TMR value occurring at a high voltage drop clearly exceeding 1 V [6].

MTJs were grown directly onto Si wafers covered with native, amorphous SiO_2 by magnetron sputtering at RT. We used a stoichiometric CCFA target and the sputtering rates, measured with a quartz balance, were calibrated using x-ray reflectivity. After deposition, the Heusler films can be annealed in-situ up to 873 K. The structure of the films was identified $ex\text{-}situ$ by x-ray diffraction (XRD), and for the magnetic characterization we employed SQUID magnetometry. MTJs are prepared without breaking the vacuum with the following layer sequence: SiO_2/CCFA(25 nm)/MgO(3 nm)/CoFe(5 nm)/IrMn(15 nm). The MgO barrier was deposited by rf-stimulated discharge from a stoichiometric target. The completed structure is annealed in vacuum for 1 hour at 573 K. Junctions with area from 3×3 up to 15×15 μm^2 with crossed electrodes were patterned for magnetotransport measurements in the current-perpendicular-plane geometry by standard optical lithography. The transport measurements were performed with a DC setup in the 4-point geometry using a constant current source. As for the SQUID measurements, the magnetic field is always applied in the film plane.

Ideally, the full-Heusler compounds display the cubic, so-called $L2_1$ structure consisting of four interpenetrating fcc unit-cells. Structural disorder occurs easily in this type of crystallographic structure. XRD indicates the polycrystalline structure of our CCFA films deposited directly onto amorphous SiO_2 at RT. The films show a uniform distribution of grains with an average diameter of 40 nm and an rms roughness of 0.5 nm [5]. The films take the B2 structure (CsCl type), where Co occupies the proper sublattice, while disorder occurs between the other elemental constituents. Post-annealing has little influence on the crystallographic structure. More details about growth and structure characterization of CCFA films can be found in Ref. [5]. The Curie temperature of the CCFA films can be increased up to 630 K after annealing in vacuum at 773 K for 1 hour. The films display a soft ferromagnetic behaviour with coercive fields of about 6 mT. We estimated the total magnetic moments from the saturation magnetization at 5 K. We find, that annealing in vacuum increases not only T_c, but also the value of the total magnetic moment and obtained 2.56 μ_B per formula unit ($f.u.$). This value is lower than the predicted theoretical value of 3.8 $\mu_B/f.u.$ This difference indicates the presence of site disorder. Yet, the value of the total magnetic moment is comparable with results obtained from films grown at elevated temperatures [7].

Although an IrMn antiferromagnet is located next to the CoFe electrode, the two ferromagnetic layers do

not switch separately as observed in SQUID measurements performed on the extended multilayer before lithographically defining the MTJs. We mention at this point that no further treatment like annealing above the Néel temperature of IrMn and field cooling could be applied to this structure. Thus, the CoFe electrode is not exchange-biased. The bell-shaped magnetoresistance curves without separate switching fields are consistent with the SQUID measurements and indicate the presence of magnetic coupling between CCFA and CoFe. Antiferromagnetic, Néel-type and biquadratic coupling due to interface roughness are the most likely coupling mechanisms. This suggests a noncollinear orientation of the layer magnetizations in the field free state and, thus, the observed TMR values seems to be a lower limit.

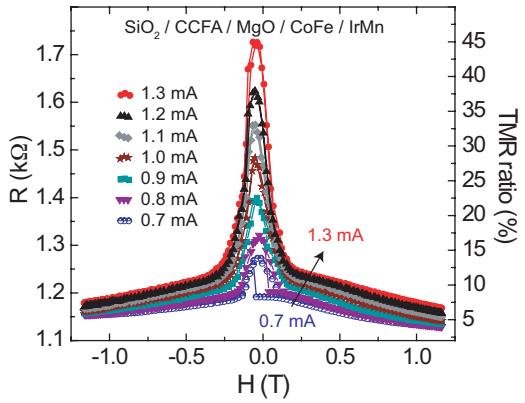

FIG. 1: Magnetoresistance curves measured by varying I_{bias} between 0.7 (bottommost curve) and 1.3 mA (topmost curve) in steps of 0.1 mA.

In Fig. 1 we plot several magnetoresistance curves measured at RT with different bias currents I_{bias}. For this experiment we used a constant current source and vary I_{bias} in steps of 0.1 mA. The TMR ratio is defined as TMR=$(R_{AP} - R_P)/R_P$, where R_{AP} and R_P are the resistances for the antiparallel and parallel magnetization configurations, respectively. We obtained a maximum TMR value of 46% for I_{bias}=1.3 mA. For smaller I_{bias} the TMR ratio is much lower (about 1% for $I_{bias} \leq 0.6$ mA) and also for larger I_{bias} the TMR ratio decreases, e.g. 18% for I_{bias}=1.4 mA and $<$ 7% for I_{bias}=1.5 mA. A variation of the bias current corresponds to a variation of the voltage drop across the junction. Multiplying the I_{bias} values in Fig. 1 by the corresponding resistance values in the saturated state, we obtain voltage drops in the range between 0.81 and 1.53 V. Therefore, the maximum TMR ratio occurs in these junctions at rather high voltages of more than 1 V. For all data presented here, the CCFA electrode is at positive voltage with respect to the CoFe counter electrode. The minimal resistance-area product is about 100 k$\Omega\mu$m^2. The measured junction resistances exceed 1 kΩ in all samples and, thus, are much larger than the lead resistances ($\approx$ 10-20 Ω), indicating that there is no geometrical enhancement in the TMR ratios. The TMR values we obtained at RT are much larger compared to the results reported by Inomata *et al.* [4] in similar structures also comprising a polycrystalline CCFA electrode. In Fig. 2 we present the temperature dependence of the TMR effect. Weak temperature dependence is observed with the TMR ratio increasing only by a factor of about 2 from 30% at RT to 56% at 20 K. The measurements are performed with a constant I_{bias} of 1 mA.

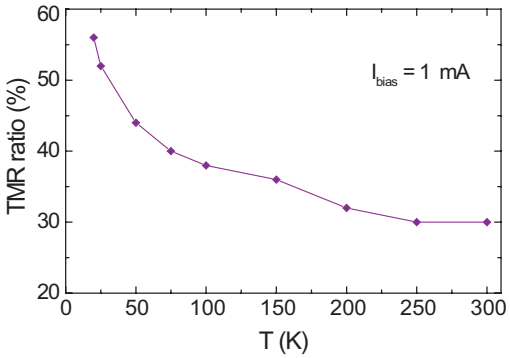

FIG. 2: Temperature dependence of the TMR ratio. The measurements are done with I_{bias}=1 mA.

In summary, CCFA films combined with MgO barriers yield almost 50% TMR at RT. Most surprising, the high TMR ratios occur only for high voltage drops across the junctions of up to 1.5 V. The question whether this special magnetoresisitive behaviour is related to spin filtering [8] at the MgO/CoFe interface of the 'negative' electrode or to density-of-states effects in the 'positive' CCFA electrode must be addressed in future experiments. These results are encouraging for further investigations of TMR structures consisting of highly oriented full-Heusler alloy films combined with possibly epitaxial MgO tunnelling barriers. From the application point of view, both the weak temperature dependence as well as the high voltage drop, which yields an output signal of 0.7 V at I_{bias}=1.3 mA, are of high relevance.

[1] R. A. de Groot, F. M. Mueller, P. G. van Engen, and K. H. J. Buschow, Phys. Rev. Lett. **50**, 2024 (1983)

[2] T. Marukame, T. Ishikawa, K. Matsuda, T. Uemura, and M. Yamamoto, Appl. Phys. Lett. **88**, 262503 (2006)

[3] D. D. Djayaprawira, K. Tsunekawa, M. Nagai, H. Maehara, S. Yamagata, N. Watanabe, S. Yuasa, Y. Suzuki, and K. Ando, Appl. Phys. Lett. **86**, 092502 (2005)

[4] K. Inomata, S. Okamura, R. Goto, and N. Tezuka, Jpn. J. Appl. Phys. **42**, L419, (2003)

[5] A. D. Rata, H. Braak, D. E. Bürgler, S. Cramm, and C. M. Schneider, Euro. Phys. J. B **52**, 445 (2006)

[6] A. D. Rata, H. Braak, D. E. Bürgler, and C. M. Schneider, J. Appl. Phys., **101**, 09J503 (2007)

[7] R. Kelekar and B. M. Clemens, J. Appl. Phys. **96**, 540 (2004)

[8] W. H. Butler, X. G. Zhang, T. C. Schulthess, and J. M. Mc Laren, Phys. Rev. B **63**, 054416 (2001)

Current-in-Plane Giant Magnetoresistance: The Effect of Interface Roughness and Spin-Depolarization Due to the Proximity of a Buffer Layer

M. Breidbach, D. E. Bürgler, and P. Grünberg

CNI – Center of Nanoelectronic Systems for Information Technology (IFF-9)

We report on proximity effects of a Au buffer layer on the current-in-plane giant magnetoresistance effect (CIP-GMR) in high-quality, epitaxial Fe/Cr/Fe(001) trilayers. The lower Fe layer is grown as a wedge and allows simultaneous preparation of 24 GMR stripes with different lower Fe thickness, $\mathbf{d_{Fe}}$. The layer-by-layer growth gives rise to (i) well controlled roughness changes from stripe to stripe as confirmed by reflection high-energy electron diffraction and (ii) to a varying influence of the underlying Au buffer. The oscillatory roughness variation yields an oscillatory GMR behaviour as a function of $\mathbf{d_{Fe}}$ and confirms our previous result that slightly increased interface roughness causes a higher GMR ratio. The proximity of the Au buffer to the GMR trilayer results in a decrease of the GMR ratio with decreasing $\mathbf{d_{Fe}}$. The latter effect is explained by spin-depolarization at the Fe/Au interface and in the bulk of the Au buffer. These results reveal limits for further decreasing the magnetic layer thickness in CIP-GMR structures.

Giant magnetoresistance in layered magnetic structures with the current flowing in the sample plane (CIP-GMR) is interpreted as due to spin-dependent electron scattering at the interfaces or in the bulk of the ferromagnetic films [1]. Hence, lattice defects, interface roughness, intermixing at interfaces, *etc.* should have an important effect on the GMR ratio. We present a comparison of the GMR in Fe/Cr/Fe samples, which differ only with respect to interface roughness and thickness of the lower Fe layer ($\mathbf{d_{Fe}}$), but are otherwise as much alike as possible [2]. We exploit the fact that in layer-by-layer growth, obtained by MBE, the growth front produces alternately smooth and rough surfaces as revealed by intensity oscillations in reflection high-energy electron diffraction (RHEED). We show the relation between interface roughness and GMR in a whole range of $\mathbf{d_{Fe}}$. Furthermore, a decrease of GMR with decreasing thickness of the Fe layer adjacent to the Au buffer is observed and attributed to the attenuation of GMR due to spin-depolarization induced by the proximity of the Au buffer.

A sketch of our sample structure is shown in Fig. 1. Details on the growth have been described in [3]. The Au buffer layer is necessary to obtain sufficiently good sample quality to enable the observation of RHEED oscillations for all layers. The lower Fe film is prepared in the form of a wedge. The sample is laterally structured by optical lithography and ion-beam etching into 24 stripes, each 8 mm long and only 50 μm wide, as indicated in Fig. 1. They run parallel to a magnetic hard axis of Fe(001), while the external field is applied along an easy axis. Therefore, contributions due to anisotropic magnetoresistance drop out of the difference $\Delta R_{max} = R_{B=0} - R_{sat}$ because the magnetizations are aligned along an easy axis and thus under an angle of 45° to the current direction at zero field as well as in saturation.

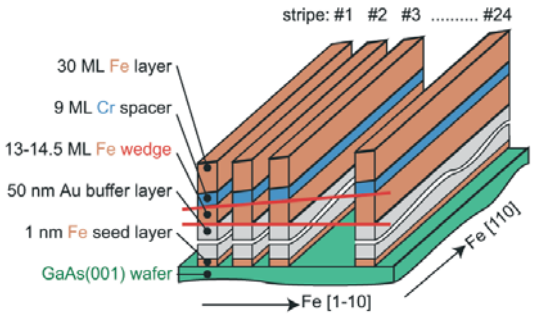

FIG. 1: Layer sequence and schematic layout of the 24 conducting stripes for GMR measurements. The lower Fe film has an increasing thickness d_{Fe} from left to right (red lines indicate the wedge shape).

The lateral variation of the surface roughness is characterized by monitoring the RHEED intensity while the sample is moved under the electron beam. The RHEED intensity oscillates along the Fe wedge before and after depositing the Cr spacer. In both cases, the oscillations reflect the thickness variation by 1.5 ML [red curve in Fig. 2b] and confirm that the roughness of both Fe/Cr and Cr/Fe interfaces varies along the wedge in phase [2]. In Fig. 2a, we display the dependence of the GMR ratio $\Delta R_{max}/R_{sat}$ on d_{Fe}. There is a continuous increase of the GMR ratio with d_{Fe}. This is opposite to the effect of shunting, which decreases the GMR ratio for increasing d_{Fe}. The observed decrease of GMR for decreasing d_{Fe} can be explained by the proximity of the Au buffer layer, which gives rise to spin-depolarization of the current. The mechanism leading to GMR is still thought to be mainly spin-dependent scattering at the Fe/Cr interfaces. But apart from the number

of such scattering events there has to be sufficiently high spin polarization for the GMR effect to occur. If a spin depolarizer such as non-magnetic Au is present within the mean free path for spin-flip scattering (λ), then this will have a destructive effect on the GMR effect. This basic idea is sketched in Fig. 3, where a cross-section of a wedge sample is shown. In CIP geometry, only electrons drifting in the sample plane within a distance of 1-2 times λ from the Cr spacer layer contribute to GMR, because they have a finite probability to move due to the Fermi velocity distribution from one Fe layer across the Cr spacer to the other Fe layer. This region centred at the Cr spacer is indicated in Fig. 3 by the two red lines. For ferromagnetic materials λ is typically only a few nm and thus exceeds the thickness of the lower Fe layer (left part) with two consequences: (i) The Fe/Au interface is within the reach of the electrons that contribute to GMR, and (ii) these electrons cover a part of their drift pathway inside the Au buffer. Spin-flip scattering events at the Fe/Au interface and in the bulk of Au depolarize the current, and the spin polarization P at the Fe/Cr interfaces is less than the Fe bulk value P_{bulk}. Of course, the spin-flip length in Au is larger than λ, but the travel distance along the interface (8 mm in our case) exceeds the spin-flip length by orders of magnitudes. With increasing d_{Fe}, these effects become less important and P is expected to behave like $P(d_{Fe}) \sim P_{bulk}\,[1-\exp(-d_{Fe}/\lambda)]$ as shown by the green curve in Fig. 3. For small d_{Fe} the GMR ratio is expected to exhibit a similar dependence as P with saturation before it again decreases due to shunting. The dashed lines in Fig. 3 indicate the Fe thickness range of our wedges, which is limited by the need for layer-by-layer growth. The exponential curve is rather linear in this part explaining the linear increase of the GMR ratio with d_{Fe} in Fig. 2a.

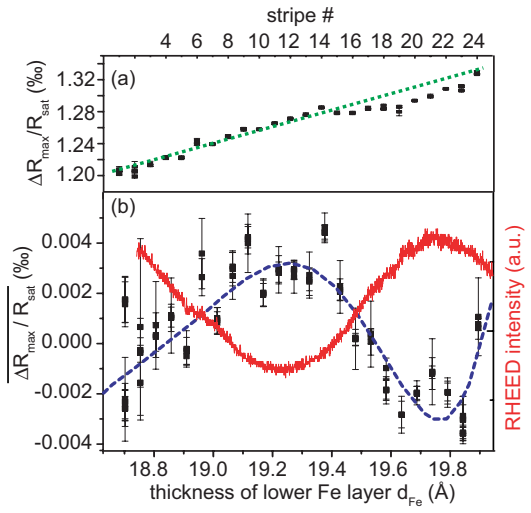

FIG. 2: (a) $\Delta R_{max}/R_{sat}$ as a function of d_{Fe}. The green line is a linear fit. (b) The $\Delta R_{max}/R_{sat}$ data of (a) after subtracting the linear background. The blue line is a guide to the eyes. The RHEED intensity curve taken along the surface of the Fe wedge is superimposed in red.

Figure 2b shows again the data of Fig. 2a but now after subtraction of the linear background. The blue line is a guide to the eye and indicates an oscillation. We superimpose in red the RHEED intensity curve taken along the Fe wedge of the same sample and find a clear correlation between interface roughness and GMR: The rougher the Fe/Cr and Cr/Fe interfaces (minimum RHEED intensity), the larger the GMR ratio. This very sensitive dependence confirms our previous findings [3] and can be understood by assuming that interface roughness increases the number of spin-dependent scattering sites, which are the origin of CIP-GMR.

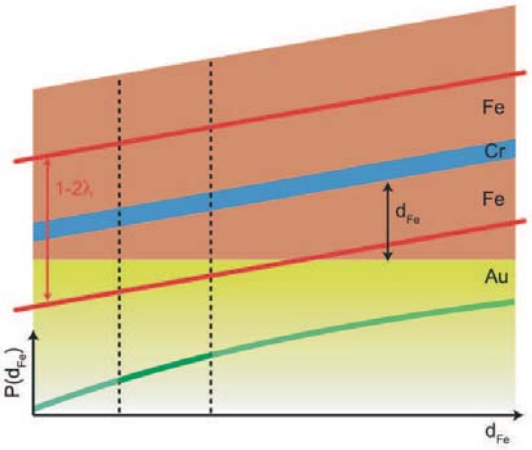

FIG. 3: Schematic drawing of the model for spin-depolarization due to the proximity of the Au buffer. The red lines mark the region around the Cr spacer within which electrons contributing to CIP-GMR are drifting.

In summary, it has been shown that in epitaxial Fe/Cr/Fe structures interface scattering at the Fe/Cr interfaces is the main source of CIP-GMR. The GMR ratio can be enhanced by moderately increasing the interface roughness. For optimizing CIP-GMR, in addition to the normal shunting effect in the bulk of the Fe layers and the underlying buffer, spin-depolarization effects due to the buffer and its interface towards the GMR trilayer have to be taken into account. This spin-depolarization poses a lower limit for the thickness of the ferromagnetic layers in CIP-GMR structures.

[1] A. Fert, P. Grünberg, A. Barthélémy, F. Petroff, W. Zinn, J. Magn. Magn. Mater. **140-144**, 1 (1995)

[2] M. Breidbach, D.E. Bürgler, P.A. Grünberg, J. Magn. Magn. Mater. **307**, L1 (2006)

[3] D. Olligs, D.E. Bürgler, Y.G. Wang, E. Kentzinger, U. Rücker, R. Schreiber, Th. Brückel, P. Grünberg, Europhys. Lett. **59**, 458 (2002)

Anisotropic FMR Linewidth of Triple-Domain Fe Layers on GaN(0001)

M. Buchmeier[1], D. E. Bürgler[1], P. A. Grünberg[1], C. M. Schneider[1], R. Meijers[2], R. Calarco[2], C. Raeder[3], and M. Farle[3]

CNI-Center of Nanoelectronic Systems for Information Technology ([1]IFF-9, [2]IBN)
[3]Fachbereich Physik, Universität Duisburg-Essen, Duisburg, Germany

We present a ferromagnetic resonance (FMR) study of 5 to 70 nm-thick Fe films on GaN(000), which grow in three differently oriented crystallographic Fe(110) domains. The samples show a strong (8 mT) 6-fold in-plane magnetic anisotropy with bulk-like thickness dependence and the easy axes oriented parallel to the Fe[001] directions. Thus, interface effects and averaged first order cubic or uniaxial anisotropies arising from the three domain orientations can be excluded. We qualitatively explain the 6-fold anisotropy by spin relaxation inside the grains. The FMR linewidth νs. frequency curves are linear and indicate a good homogeneity of the magnetic properties. However, the effective damping parameter α shows pronounced anisotropy and thickness dependence. The additional damping is explained by two-magnon scattering at defects, which are due to the triple domain structure. These results are of importance for envisaged spin injection devices based on Fe/GaN interfaces.

Spin damping in thin ferromagnetic films has recently gained attraction because of its importance for the switching of fast spintronic devices. In classical theory spinwave relaxation can be described via a scalar material parameter α in the Landau-Lifshitz-Gilbert equation. While experimental data on high-quality epitaxial, thin films have been successfully explained by the classical intrinsic Gilbert-type damping [1], there has been increasing evidence for the importance of non-classical damping mechanisms over the last years. The present ferromagnetic resonance (FMR) study [2] deals with Fe films grown in a triple-domain structure on top of hexagonal GaN. The structure of the films with thicknesses ranging between 5 and 70 nm has previously been investigated in detail [3].

We deposited 5 to 70 nm-thick Fe films on top of Al_2O_3/GaN(0001) templates [4] by electron-beam evaporation in ultra-high vacuum at room temperature. After deposition the samples were annealed *in-situ* for one hour at 500°C in order to improve the quality. The crystal structure was determined by *in-situ* low-energy electron diffraction (LEED) and *ex-situ* x-ray diffraction (XRD). It was found that bcc Fe grows with the (011) plane parallel to the interface. The in-plane crystal orientation was analyzed by comparing LEED pictures and XRD pole figures with simulations of different growth modes. A perfect match with the simulation was found for a triple-domain growth in the so-called Nishiyama-Wassermann orientation [5] with Fe[001]||GaN[11-20] [3]. The magnetization dynamics has been investigated by angle-dependent FMR with an in-plane static field. Measurements at resonance frequencies between 4.5 and 15.5 GHz have been performed using a home-build cylindrical resonator with variable length and a Hewlett Packard network analyzer, while a commercial Bruker EPR spectrometer was used for the 24 GHz frequency measurements.

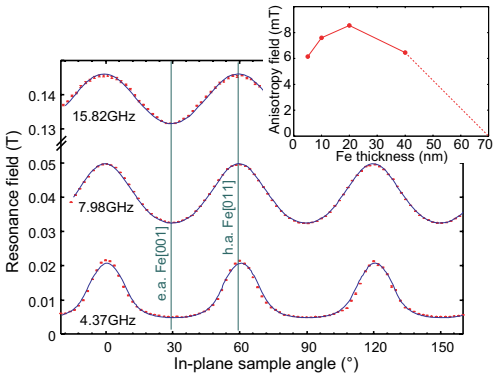

FIG. 1: Resonance field as a function of the azimuthal sample angle for the 20 nm-thick Fe film. Red symbols with error bars are experimental data, blue solid lines are least square fits. Inset: Thickness dependence of the 6-fold anisotropy field $2K_6/M_S^{eff}$ for 7.98 GHz driving frequency.

The resonance fields as a function of the sample angle for the 20 nm film are shown in Fig. 1. The curves clearly show a 6-fold in-plane anisotropy. The minima of the resonance field at 30°, 90°, and 150° correspond to the easy axes, while the maxima at 0°, 60°, and 120° indicate the directions of the hard axes. The easy axis has been determined from x-ray Laue pictures to lie parallel to GaN[11-20] and thus along the Fe[001] directions. The curves have been fitted taking into account an energy density $E_{K6} = K_6/9 \ \sin^2[3(\Theta_M - \Theta_{e.a.})]$ for the 6-fold in-plane anisotropy in order to extract the anisotropy strength K_6. The inset in Fig. 1 shows the thickness dependence of the anisotropy field $2K_6/M_S^{eff}$ ex-

tracted from the 7.98 GHz measurements. This data excludes an interfacial origin, which should result in an approximate 1/thickness behaviour. The fact that the strength of the 6-fold anisotropy is reduced at high frequency and corresponding high fields suggests spin relaxation inside the grains into the local easy axes of the magneto-crystalline anisotropy as the origin of the 6-fold anisotropy. In analogy to Slonczewskis explanation of the extrinsic biquadratic interlayer coupling by the fluctuation model [6], such a relaxation will lower the free energy of the system. This energy gain due to spin relaxation depends on the orientation of the external field and leads to an easy axis in the direction of largest energy gain. The effect has been addressed in detail by Heinrich $et\ al.$ [7], who conclude that any system that exhibits a lateral variation of the anisotropic free energy characterized by a particular angular power will also exhibit an effective anisotropic free energy corresponding to a higher angular power. In our case, the 4-fold anisotropy of Fe results in a 6-fold in-plane anisotropy as observed. Assuming the spin relaxation mechanism as the origin of the anisotropy, the spins get more and more aligned with increasing external field ($i.e.$ increasing frequency) resulting in the observed decreasing anisotropy, which will vanish when the field is eventually high enough to completely saturate the sample.

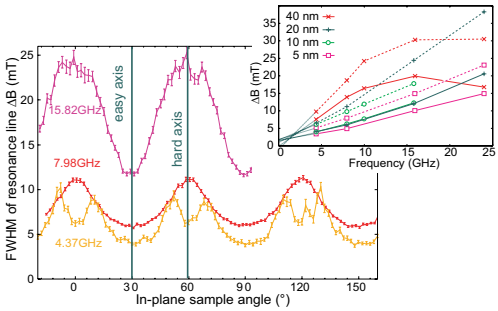

FIG. 2: Angular dependence of the linewidth (FWHM) ΔB for the 20 nm-thick Fe film. Inset: ΔB as a function of frequency for the 5, 10, 20, and 40 nm-thick Fe films. Solid and dashed lines correspond to easy and hard axes, respectively.

In Fig. 2 we plot the width of the resonance peak as a function of the sample angle for the 20 nm-thick Fe film and driving frequencies of 4.37, 7.98, and 15.82 GHz. All other samples show a qualitatively similar behaviour. At 7.98 and 15.82 GHz the width is maximal for the field parallel to hard axes of the 6-fold anisotropy. For the field parallel to the easy axes the linewidths have minima and are reduced to about half the value of the hard axes. As expected an increase of the linewidth with frequency can be observed. The pronounced 6-fold anisotropy is in disagreement with the intrinsic isotropic Gilbert damping and must be due to additional extrinsic damping mechanisms. In the inset of Fig. 2 the FWHM of the resonance peak for the field parallel to an easy (solid lines) and a hard (dashed lines) axis of the 6-fold anisotropy is plotted as a function of the driving frequency for all samples. The linear increase for Fe thicknesses of 5, 10, and 20 nm may be due to Gilbert damping. The effective damping parameter $\alpha_{eff} = \gamma\Delta B/2\nu$ can be extracted from the slope of the curves and ranges between 0.005 for the easy axis of the 5 nm-thick film and 0.035 for the hard axis of the thickest film at low frequency. A typical value for Fe(001) grown on GaAs(001) is α=0.004. The extrapolation of the curves to zero frequency yields very low offsets of about 1 mT, which means that there is no local resonance broadening and thus the samples are magnetically very homogeneous on a large scale. The two-magnon damping should saturate at high frequencies leading to a flattening of the curves in Fig. 2, which we indeed observe for the 40 nm-thick film. For the thinner films the highest employed frequency of 24 GHz is probably not high enough to saturate the broadening. The easy axis linewidth for the 40 nm film even decreases between 15 and 24 GHz. This decrease is compatible with realistic calculations of two-magnon scattering [8]. The observed linewidth variations must be attributed mainly to two-magnon scattering processes because (i) there is no significant local resonance broadening, (ii) the observed effective damping is much larger than the typical literature value for the Gilbert damping in Fe, (iii) the experimental α_{eff} increases strongly with film thickness, (iv) the damping is strongly anisotropic, and (v) a saturation of the linewidth is observed for the 40 nm-thick Fe film.

In summary, the peculiar triple-domain film structure of Fe/GaN(001) gives rise to interesting magnetic properties: (i) A 6-fold in-plane anisotropy with a strength of about 8 mT and bulk-like thickness dependence and (ii) a large FMR linewidth with 6-fold in-plane anisotropy. These specific magnetic properties must be taken into account when Fe/GaN-like interfaces are to be employed in spin injection devices.

[1] B. Heinrich, K.B. Urquhart, A.S. Arrott, J.F. Cochran, K. Myrtle, S.T. Purcell, Phys. Rev. Lett. **59**, 1756 (1987).

[2] M. Buchmeier, D.E. Bürgler, P.A. Grünberg, C.M. Schneider, R. Meijers, R. Calarco, C. Raeder, M. Farle, phys. stat. sol. (a) **203**, 1567 (2006).

[3] R. Meijers, R. Calarco, N. Kaluza, H. Hardtdegen, A. v. d. Ahe, H.L. Bay, H. Lüth, M. Buchmeier, D.E. Bürgler, J. Crystal Growth **283**, 500 (2005).

[4] H. Hardtdegen, N. Kaluza, R. Steins, P. Javorka, K. Wirtz, A. Alam, T. Schmitt, R. Beccard, phys. stat. sol. (a) **202**, 744 (2005).

[5] E. Bauer and J.H. van der Merwe, Phys. Rev. B **33**, 3657 (1986).

[6] J.C. Slonczewski, Phys. Rev. Lett. **67**, 3172 (1991).

[7] B. Heinrich, T. Monchesky, R. Urban, J. Magn. Magn. Mater. **236**, 339 (2001).

[8] R.D. McMichael and P. Krivosik, IEEE Trans. Magn. **40**, 2 (2004).

Fe/Si/Fe(001) Trilayers With Strong Antiferromagnetic Interlayer Exchange Coupling Prepared by Ion-Beam Sputter Epitaxy

T. Damm, M. Buchmeier, A. Steeb, D. E. Bürgler, P. Grünberg, and C. M. Schneider

CNI-Center of Nanoelectronc Systems for Information Technology (IFF-9)

We grow monocrystalline Fe/Si/Fe(001) trilayers by ion-beam sputter epitaxy on GaAs(001) and MgO(001) substrates and observe antiferromagnetic interlayer exchange coupling with coupling strengths of up to 2 mJ/m^2 at a Si thickness of 15 Å. Although the coupling is weaker than for similar Fe/Si/Fe structures grown by molecular-beam epitaxy, the observed coupling is still stronger than across most metal spacers. The results confirm that Si spacers represent a very special, although not yet fully understood case of interlayer exchange coupling. From a practical point of view this work demonstrates the transfer of the preparation of Fe/Si/Fe trilayer with strong coupling from molecular-beam epitaxy on high-quality Ag(001) buffer layers to the more application-friendly ion-beam sputter epitaxy on standard substrates.

Antiferromagnetic interlayer exchange coupling was discovered in monocrystalline Fe/Cr/Fe structures, which were carefully prepared by molecular-beam epitaxy (MBE) under ultra-high vacuum (UHV) conditions [1]. Subsequently, oscillatory interlayer exchange coupling was found for many non-magnetic metallic spacer layers and for alternative preparation methods, in particular sputtering techniques [2]. This opened the door to applications such as synthetic antiferromagnets in sensors and antiferromagnetically coupled storage media in hard-discs. The interlayer exchange coupling across non-metallic spacers is usually negligible except for epitaxial Si spacers in Fe/Si/Fe structures, which mediate very strong antiferromagnetic coupling exceeding the coupling strength of most metal spacers [3]. Previously, we have measured bilinear coupling constants J_1 in excess of 5 mJ/cm^2 for Fe/Si/Fe(001) trilayers grown by MBE [3]. Here, we report the preparation of similar structures by ion-beam sputter epitaxy, which show almost equally strong coupling [4].

Our ion-beam sputtering system is UHV compatible and features surface analysis tools, *e.g.* low-energy electron diffraction (LEED). It is equipped with a 2" RF ion gun, which is aligned towards the target (sputter gun) and a 4" electron cyclotron resonance (ECR) gun, which is aligned towards the substrate (assist gun) for pre-sputtering. The average target-to-substrate distance is 13 cm and therefore of the same order of magnitude as the mean free path for the typical sputtering gas pressure of 10^{-3} to 10^{-4} mbar. We use an Fe and a Si target with a purity of 99.95% and 99.999%, respectively. In order to prevent a charging of the Si target due to the bombardment with positive Ar ions, a beam-switch electronics is used. It allows pulsing the ion-beam with frequencies between 1 and 20 kHz with varying duty cycles. During the periods of no ion acceleration the sputter guns grid voltages can be inverted, so that electrons are extracted from the plasma. This broad electron beam hits the target and neutralizes any positive surface charge.

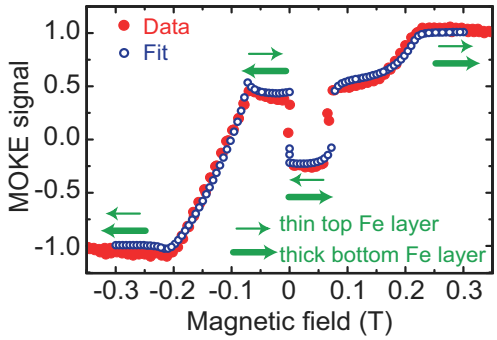

FIG. 1: MOKE loop of a 100 Å Fe/14 Å Si/50 Å Fe trilayer on GaAs. Red dots represent data and blue circles the best fit. The coupling parameters are: $J_1 = -0.81\mathrm{mJ/m^2}$, $J_2 = -0.15\mathrm{mJ/m^2}$. Green arrows indicate the magnetization directions of the thin, top and thick, bottom Fe layer, respectively, obtained from the fitting.

Furthermore, this beam-switch electronics can also be used to influence the deposition rate without changing any other sputtering parameter. The film thicknesses are monitored by a quartz crystal microbalance. GaAs(001) and MgO(001) substrates of 10×10 mm^2 size are mounted without any preceding treatment and are rotated during deposition at 5-8 rpm. The employed sputtering parameters have been obtained by optimizing the growth of Fe layers on GaAs(001) substrates [4]: deposition at 40°C, 15 s pre-sputtering to clean the air-exposed and thus oxidized substrates, deposition angle Φ=50°, beam energy U_{beam}=0.75 kV, and 1.8×10^{-3} mbar Ar pressure. Series of $substrate$/100 Å Fe/x Å Si/50 Å Fe trilayers with varying Si thickness x are deposited, where $substrate$ stands for GaAs(001) and MgO(001). LEED patterns of each layer confirm the

monocrystalline and epitaxial growth of the whole trilayer stack. *Ex-situ* performed magneto-optical Kerr effect (MOKE) measurements clearly show the presence of antiferromagnetic interlayer coupling for the trilayers on both substrate types.

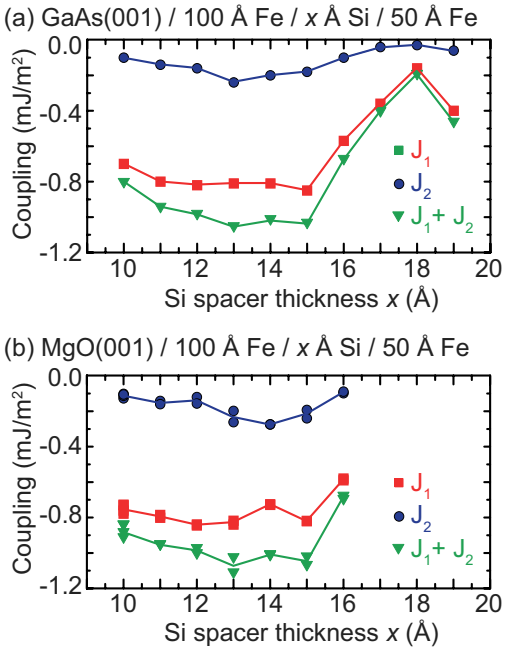

FIG. 2: Spacer thickness dependence of the coupling parameters J_1, J_2, and total coupling strength $J = J_1 + J_2$ derived by fitting MOKE loops of Fe/Si/Fe trilayers grown on (a) GaAs(001) and (b) MgO(001) substrates.

An example for a GaAs(001) substrate and a Si spacer thickness x=14 Å is shown in Fig. 1. The peculiar shape of the loop with the jump in small fields can be understood by taking into account that the thinner top Fe layer contributes stronger to the MOKE signal than the thicker bottom Fe layer. The reasons are the limited penetration depth of the laser light and reflections at the Fe/Si interfaces. Additionally, the signal contains strong 2$^{\mathrm{nd}}$ order MOKE contributions due to a large angle of incidence (only about 15° from the sample normal), which give rise to further asymmetries with respect to zero field. Taking all these effects into account, we are able to well reproduce the MOKE loops (see arrows and circles in Fig. 1) and fit the bilinear and biquadratic coupling constants J_1 and J_2 defined by the phenomenological expression for the areal free energy density of the coupling

$$E = -J_1 \cos(\Delta\Theta) - J_2 \cos^2(\Delta\Theta),$$

where $\Delta\Theta$ is the angle between the magnetizations of the two Fe layers. We take into account the in-plane 4-fold magnetocrystalline anisotropy, the Zeeman energy, and the possibly twisted magnetization state within each ferromagnetic layer [5]. The variation of the coupling strengths as a function of the Si spacer thickness x is displayed in Fig. 2 for trilayers grown on GaAs(001) as well as on MgO(001). In both cases, there is no sharp maximum for the total coupling strength $J = J_1 + J_2$, but an almost constant value of $|J|$ of the order of 1 mJ/m^2. This value is comparable to those typically found for fully metallic systems [2], but is clearly smaller than the 6 mJ/m^2 observed for MBE-grown Fe/Si/Fe(001) trilayers [3]. We relate the reduced coupling strength compared to MBE samples to intermixing at the Fe/Si interface due to the higher energy of the incident particles during the sputtering process. A metallic spacer could be the reason for the increase in (bilinear) coupling strength at a Si thickness of 19 Å in Fig. 2a, which possibly indicates oscillatory behaviour of the coupling. The hypothesis that enhanced intermixing reduces the coupling strength is confirmed in a further experiment, in which we increase the Si deposition rate by a factor of two from 0.3 to 0.6 Å/s in order to reduce diffusion and intermixing. Ion-beam sputtering allows us to keep all other sputtering parameters constant. As expected, the antiferromagnetic coupling strength increases. The maximum of the total coupling strength doubles to $|J| \approx 2$ mJ/m^2 at a Si thickness of 15 Å and exceeds the coupling strengths previously reported for sputtered Fe/Si/Fe trilayers [6-8].

In summary, monocrystalline Fe/Si/Fe(001) trilayers are grown by ion-beam sputtering on GaAs(001) and MgO(001) substrates and show strong antiferromagnetic interlayer exchange coupling. Under optimized conditions we measure a total coupling strength of 2 mJ/m^2, which is stronger than for most metal spacers. This work extends the observation of strong antiferromagnetic interlayer exchange coupling in monocrystalline Fe/Si/Fe(001) trilayers to standard substrates and to the ion-beam sputtering technique. Both aspects are of relevance for the application of antiferromagnetically coupled Fe/Si/Fe trilayers in devices.

[1] P. Grünberg, R. Schreiber, Y. Pang, M. B. Brodsky, H. Sowers, Phys. Rev. Lett. **57**, 2442 (1986)

[2] D. E. Bürgler, P. Grünberg, S. O. Demokritov, M. T. Johnson, in Handbook of Magnetic Materials, edited by K. H. J. Buschow (Elsevier, Amsterdam, 2001), Vol. 13, pp. 1 – 85

[3] R. R. Gareev, D. E. Bürgler, M. Buchmeier, R. Schreiber, P. Grünberg, J. Magn. Magn. Mater. **240**, 237 (2002)

[4] T. Damm, M. Buchmeier, A. Schindler, D. E. Bürgler, P. Grünberg, C. M. Schneider, J. Appl. Phys. **99**, 093905 (2006)

[5] M. Buchmeier, B. K. Kuanr, R. R. Gareev, D.E. Bürgler, P. Grünberg, Phys. Rev. B **67**, 184404 (2003)

[6] A. Chaiken, R. P. Michel, C. T. Wang, J. Appl. Phys. **79**, 4772 (1996)

[7] K. Inomata, K. Yusu, Y. Saito, Phys. Rev. Lett. **74**, 1863 (1995)

[8] Y. Endo, O. Kitakami, Y. Shimada, J. Appl. Phys. **85**, 5741 (1999)

Towards Flux Qubits: Josephson Tunnel Junctions With Ferromagnetic Interlayer

M. Weides[1], H. Kohlstedt[1], R. Waser[1], M. Kemmler[2], D. Koelle[2], R. Kleiner[2], E. Goldobin[2]

[1]Center of Nanoelectronic Systems for Information Technology (CNI), Institute for Electronic Materials, Research Centre Jülich, D-52425 Jülich, Germany

[2]Physikalisches Institut – Experimentalphysik II, Universität Tübingen, Auf der Morgenstelle 14, D-72076 Tübingen, Germany

We fabricated high quality Nb/Al_2O_3/$Ni_{0.6}Cu_{0.4}$/Nb superconductor-insulator-ferromagnet-superconductor Josephson tunnel junctions. Using a ferromagnetic layer with a step-like thickness, we obtain a 0–π junction, with equal lengths and absolute critical currents of 0 and π parts. The ground state of our $330\ \mu\mathrm{m}$ $(1.3\lambda_J)$ long junction corresponds to a spontaneous vortex of supercurrent pinned at the 0–π step and carrying $\sim 6.7\%$ of the magnetic flux quantum Φ_0. The dependence of the critical current on the applied magnetic field shows a clear minimum in the vicinity of zero field [M. Weides *et al.*, Phys. Rev. Lett. 97, 247001 (2006)].

In superconducting/ferromagnet (S/F) systems the superconductivity may be non-uniform [1]. The Cooper pair wave function extends from the superconductor to the ferromagnet with a damped oscillatory behavior. This results in novel and interesting physics, such as a non-monotonic critical current dependence on temperature or the realization of π coupling in Josephson junctions (JJs) with a ferromagnetic interlayer.

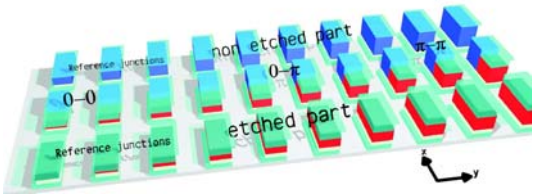

FIG. 1: Schematic layout of stepped JJs along with reference junctions. F-layers with thicknesses d_1 are denoted in red, and step Δd_F and d_2 in blue. The F-layer thickness increases from left to right. The actual F-layer thickness is much smaller than depicted.

In his classical paper [2], B. Josephson predicted that the supercurrent through a Josephson junction is given by $I_s = I_c \sin(\mu)$. Here, μ is the Josephson phase, and $I_c > 0$ is the critical current. When one passes no current ($I_s = 0$), the Josephson phase $\mu = 0$ corresponds to the minimum of energy (ground state). The solution corresponds to the energy maximum and is unstable. Later, it was suggested that using a ferromagnetic barrier one can realize JJs where $I_s = I_c \sin(\mu + \pi) = -I_c \sin(\mu)$ [3]. Such JJs obviously have $\mu = \pi$ in the ground state and, therefore, are called π JJs. The unstable solution $\mu = 0$ corresponds to the energy maximum. These SFS/SIFS-type junctions (I: tunnel barrier) are characterized by an intrinsic phase-shift of π in the current-phase relation or, in other words, a negative critical current.
We studied $\mathrm{Nb/Al_2O_3/Ni_{0.6}Cu_{0.4}/Nb}$ (i.e. SIFS-type) Josephson tunnel junctions with an ultrathin $\mathrm{Al_2O_3}$ tunnel barrier. The junction fabrication was optimized regarding the junction insulation and homogeneity of current transport [4].

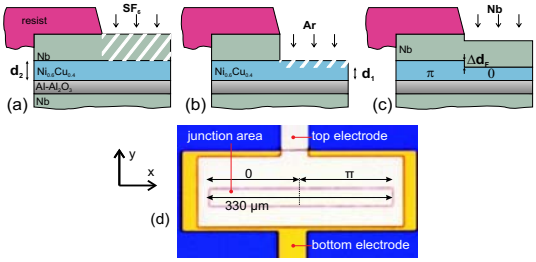

FIG. 2: The complete SIFS stack was protected in part by photoresist. (a) reactive etching of Nb with $\mathrm{SF_6}$ down to NiCu layer, (b) ion-etching of NiCu to set 0 coupling and (c) in situ deposition of cap Nb layer. (d) Picture of a $330 \times 30\ \mu\mathrm{m}^2$ stepped JJ (top view). The 0–π boundary/step in the F-layer (if any) is indicated by a dashed line.

The F-layer was deposited with a gradient of thickness in y-direction on the S/I stack, see Fig. 1. After the deposition of $40\ \mathrm{nm}$ Nb as cap layer and lift-off we obtained the complete SIFS stack with F-layer thickness $d_F(y)$, but without steps in d_F yet. To produce the desired step-like variation in d_F, the parts of the JJ that were supposed to have a larger thickness d_2 were protected by photoresist. The Nb cap layer was removed by reactive dry etching using $\mathrm{SF_6}$. A few tenth of nanometer ($\Delta d_F = d_2 - d_1$) of NiCu were Ar ion etched at a very low power and rate to avoid any damaging of the NiCu film under the surface and to keep a good control over the step height. When the F-layer thickness was reduced down to the thickness d_1 the etching was stopped and $40\ \mathrm{nm}$ of Nb were deposited in situ, Fig. 2 (a)-(c). Various structures on the chip were placed within a narrow ribbon along the x-direction and replicated along y-direction. One ribbon contained references JJs with the F-layer thicknesses d_1 (uniformly etched) and d_2 (non-etched) and a JJ with step in the F-layer thickness from d_1 to d_2. The length L_0 and L_π are within

lithographic accuracy of $\approx 1\ \mu\mathrm{m}$. A set of structures for different $d_F(y)$ with an increase in d_F for each row of about $0.05\ \mathrm{nm}$ was obtained. The increase of the F-layer thickness along y-axis was determined from reference films [5].

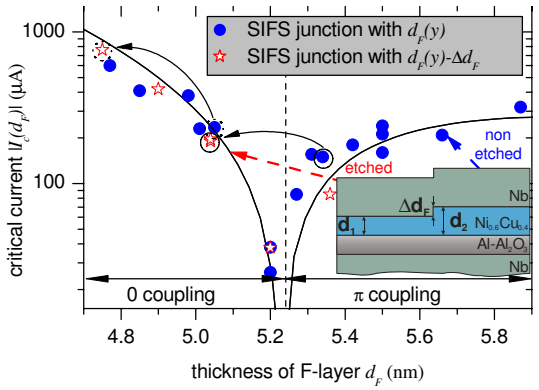

FIG. 3: Critical current $|I_c|$ of the uniformly etched (star) and non-etched (dot) SIFS junctions versus the F-layer thickness before etching d_F. The fit of the experimental data for non-etched samples is shown by the continuous line.

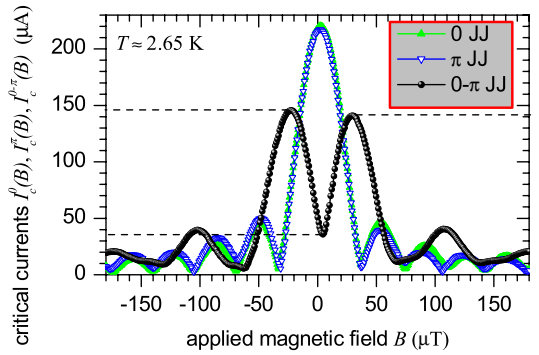

FIG. 4: Junction geometries $330 \times 30\ \mu\mathrm{m}^2$. $I_c(H)$ of 0–π JJ with H applied parallel to short (y) axis and step in the F-layer, along with the non-etched and etched reference SIFS junctions. At $T \approx 2.65$ K the 0–π JJ becomes symmetric.

Depending on the thickness of the ferromagnetic $Ni_{0.6}Cu_{0.4}$ layer, Fig. 3, and on the ambient temperature, the junctions were in the 0 or π coupled ground state [6, 7]. Using a ferromagnetic layer with a step-like thickness (inset of Fig. 3), a 0–π junction with equal lengths and absolute critical currents of 0 and π parts was obtained (Fig. 2 (d)). The ground state of this $330\ \mu\mathrm{m}$ ($= 1.3 \cdot \mathrm{Josephson\ penetration\ depth}\ \lambda_J$) long junction corresponded to a spontaneous supercurrent carrying a vortex of 6.7% of the magnetic flux quantum Φ_0 [8]. This fractional flux was pinned at the 0–π phase discontinuity and was generated by self-screening Josephson currents in absence of a driving bias current and an external field. The dependence of the critical current on the applied magnetic field $I_c(H)$ showed a clear minimum in the vicinity of zero field, see Fig. 4.

In summary, we have fabricated high quality $Nb/Al_2O_3/Ni_{0.6}Cu_{0.4}/Nb$ superconductor-insulator-ferromagnet-superconductor Josephson tunnel junctions. Using a ferromagnetic layer with a step-like thickness, we obtained the so-called 0–π Josephson junction. At $T \approx 2.65$ K the critical currents of 0 and π parts become equal and the junction carries spontaneous fractional flux in the ground state.The Al_2O_3 tunnel barrier allowed a rather low damping of plasma oscillations, which is desirable for many experiments especially in the quantum domain.

As an outlook the ferromagnetic 0-π Josephson junctions allow to study the physics of fractional vortices with a good temperature control of the symmetry between 0 and π parts. We note that symmetry is only needed for JJ lengths $\lesssim \lambda_J$. For longer JJs the semifluxon appears even in rather asymmetric JJs, and T can be varied in a wide range affecting the semifluxon properties only weakly.

The possibility to fabricate 0, π and 0–π Josephson junctions within the same process and having the same I_c and $V_c = R_n I_c$ opens perspectives for applications of the SIFS technology. It may be used to construct classical and quantum devices such as oscillators, RSFQ-logics with active π-junctions, memory cells, π flux qubits or semifluxon based qubits.[9]

[1] E. A. Demler et al., Phys. Rev. B **55**, 15174 (1997).

[2] B. D. Josephson, Phys. Lett. **1**, 251 (1962).

[3] L. Bulaevskii et al., JETP Lett. **25**, 7 (1977).

[4] M. Weides et al., Physica C **437-438**, 349 (2006).

[5] M. Weides et al., J. Appl. Phys. **101**, 063902 (2007).

[6] M. Weides et al., Appl. Phys. Lett. **89**, 122511 (2006).

[7] M. Weides, Ph.D. thesis, Universität zu Köln (2006).

[8] M. Weides et al., Phys. Rev. Lett. **97**, 247001 (2006).

[9] E. Goldobin et al., Phys. Rev. B. **72**, 054527 (2005).

Phase Change Memory: *The* Future of Computer Memory?

R. O. Jones[1], J. Akola[2]

[1]Institute 1: Quantum Theory of Matter
[2]Nanoscience Center, FI-40014 University of Jyväskylä, Finnland

Every user of a personal computer or laptop knows the frustration caused by the delay between switching on the computer and starting to use it. Customary random access memory (RAM) is "volatile", and its content is lost when the power is switched off. Disk storage limitations and the mechanical failure of disk drives that rotate at high speeds are also known to many. Phase change materials (PCM), which switch between *amorphous* and *ordered* structures when an electric current or a laser pulse is applied, are widely viewed as the most promising candidates for the memory of the future, although details of the structures involved are available in few cases. We have used the new IBM BlueGene/L computer to perform extensive simulations on the amorphous and ordered states of an alloy of germanium, antimony, and tellurium (GST) that is already used in DVD-RW optical disks. These simulations provide insight that can be obtained by no other means.

Memory devices that are independent of a power supply have obvious advantages, and some are familiar to us all. The ubiquitous USB-sticks can already be bought with 16 GB capacity, and SD memory cards can be used in digital cameras to store thousands of high resolution pictures. These devices are examples of flash memory, which is based on arrays of Si-SiO_2 junctions. The limitations of flash memory - in particular, the lower reliability that has accompanied scaling to smaller dimensions - have stimulated the search for other "non-volatile" memory devices.

The rapid and reversible transition between ordered and amorphous forms is the basis of phase change (PC) memory materials such as rewritable optical disks. In thin films of many such materials, amorphization can be driven by localized and short ($\sim$ 1 ns) laser heating to a temperature above the melting point T_m, and longer laser heating ($\sim$ 50 ns) to below T_m but above the glass temperature T_g leads to a metastable "crystalline" form. The phase change can be monitored by the accompanying large changes in resistivity or optical reflectivity. A memory cell where the phase change is driven by a current pulse is shown in Fig. 1. PC materials are widely viewed as prime candidates for the memory materials of the future, which ideally will be fast ($\sim$ 10 ns switching time), dense (bit diameter $\ll$ 50 nm), stable (several years per lost bit), long-lived ($> 10^{12}$ cycles per lost bit), and - naturally - with low manufacturing cost and power consumption. Such bit diameters would result in storage densities far in excess of those found in current commercial devices, such as those based on giant magnetic resonance (GMR).

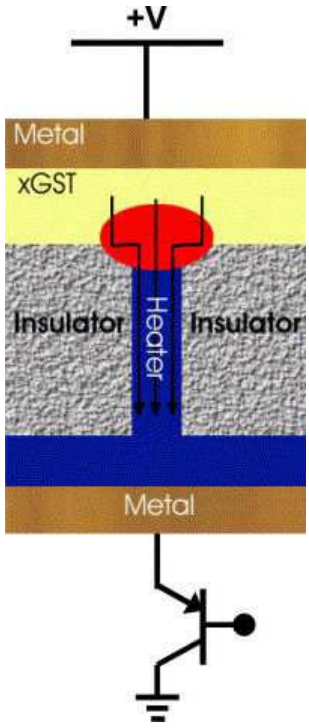

FIG. 1: Cross section of one type of PC memory cell [1]. The localized phase change in the GST film [red area] is driven here by a current pulse.

To satisfy these criteria, PC optical memory materials require: (a) an absorption edge in the visible or near infrared that changes with the transition, (b) a melting point T_m that is high enough to prevent spontaneous crystallization, but accessible to laser heating, (c) a rapid and stable transition. Work has then focused on semiconductors and semimetals with T_m between 500 and 1000°C, large atomic mobilities, and structures that are similar in the amorphous and crystalline phases. For more than a decade [2],

the pseudobinary compounds GeTe-Sb_2Te_3 have attracted much attention, and one of them ($Ge_2Sb_2Te_5$, GST) is already the basis of digital versatile disc-random access memories (DVD-RAM).

Central to the understanding of the properties of GST is a knowledge of the structures of the different phases, but these are difficult to obtain in a ternary alloy with a significant number ($\sim$ 20%) of vacancies. Yamada [2] proposed that the metastable phase has a rock-salt structure with Te atoms on all sites of one type, with the other site occupied randomly by Ge and Sb atoms and vacancies. However, as noted recently, "the local structural order of glasses in the ternary system $Ge_xSb_yTe_{1-x-y}$ is not well established" [3]. It is striking that systems whose structures are "not well established" should already be the basis for mass commercial products. We can expect that an improved understanding of the structures and the transitions between them will lead in turn to a much deeper understanding of material properties and ways that they can be improved.

The study of phase change mechanisms in ternary alloy systems is very difficult for both theory and experiment, and the analysis of the latter often requires wide-ranging assumptions about the atomic arrangements. The metastable nature of amorphous GST (bulk samples crystallize) has also restricted experimental studies of this material. A number of calculations have been performed on GST materials in recent years, and they have provided important clues to the phase change mechanism. Nevertheless, they have focused on a restricted ranges of structures using unit cells (typically ~ 60 atoms) that may be too small to describe the details of the mechanism. The simulation times (typically a few picoseconds) are probably too short to describe vibrational and other thermodynamic properties reliably.

The installation and availability of the new supercomputer in Jülich has enabled us to extend the range of density functional calculations on GST and related systems substantially. We have performed calculations on $Ge_2Sb_2Te_5$ in a unit cell containing 460 atoms, and we have carried out simulated annealing from a high temperature in order to avoid bias towards particular structural types. We have also simulated rock-salt (ordered) structures of $Ge_2Sb_2Te_5$, the corresponding liquid and amorphous structures (at 900 K and 300 K, respectively), as well as two well-studied forms of the Ge-Te alloy system: $Ge_{0.50}Te_{50}$ and $Ge_{0.15}Te_{0.85}$, the second of which has the lowest melting point (650 K) of Ge-Te alloys.

The calculations have resulted in a huge amount of data that we are still analyzing. Since we know the positions of each atom throughout the simulations, we can determine the pair correlation functions for all atom types. The structure factors derived from these agree remarkably well with the results of scattering experiments (x-rays, neutrons) where available. The vibration frequencies can be determined from well-equilibrated structures and from analysis of correlation functions obtained from long simulation trajectories. We would welcome more experimental information of the vibrational properties. The structures of the amorphous and ordered phases show similarities, as we expect from such a rapid phase change. A recent paper [4] pointed out that the ring statistics in amorphous GST were dominated by four- and sixfold rings, as found in the crystal phase, and similar patterns are evident in our work. A crucial component of these materials (and essential for an understanding of their properties) are the vacancies. The calculations provide us with insight into their distributions as well.

More details are not yet available, but this situation will change soon. We shall have plenty to say in the Annual Report next year, so you should return to this space then.

[1] A. L. Lacaita, Solid-State Electronics **50**, 24 (2006).

[2] N. Yamada, Mat. Res. Soc. Bull. **21**, 48 (1996).

[3] J. K. Olson, H. Li, and P. C. Taylor, J. Ovonic Res. **1**, 1 (2005).

[4] S. Kohara et al., Appl. Phys. Lett. **89**, 201910 (2006)

Co-Existence of Bipolar and Unipolar Resistive Switching in a Ot/TiO_2 Thin Film Stack

Doo Seok Jeong, Herbert Schroeder

CNI-Center of Nanoelectronic Systems for Information Technology (IFF-IEM), Forschungszentrum Jülich, 52425 Jülich, Germany

Bipolar and unipolar resistive switching (BRS and URS) behavior of Pt/TiO_2 (27 nm thick)/Pt thin film stacks were investigated. One of both, BRS or URS, could be observed depending on the current compliance during the electroforming process. With a lower current compliance ($<$ 0.1 mA) during electroforming asymmetric current-voltage (I-V) curves showing the BRS were observed in the voltage range -1.6 V to +1.1 V, while with a higher current compliance (1 to 10 mA) the URS behavior was observed. Furthermore, the permanent transition from BRS to URS was investigated by applying the voltage with a higher current compliance ($\sim$ 3 mA).

Resistive switching behavior of transition metal oxide (TMO) materials is a very attractive subject of scientific and technical research. TMOs, including TiO_2 and NiO, show bistable resistive switching behavior, i.e. reversible switching between a high resistance state (HRS) and a low resistance state (LRS) achieved by the applied voltage [1, 2]. This resistive switching is classified into unipolar resistive switching (URS) because the switching behavior hardly depends on the polarity of the applied voltage, so that both, the SET switching (HRS $\rightarrow$ LRS) and the RESET switching (LRS $\rightarrow$ HRS), occur regardless of the polarity of the applied voltage. The URS of TMOs gives potential for the application in resistive switching random access memory (ReRAM) devices due to the high off/on ratio and the inherent low geometric scaling problem compared to capacitance-based RAMs. However, a quite high current flow, a few tens of mA, is necessary for the RESET switching of the URS. It is therefore very important for the application to search for solutions with reduced RESET current.

Bipolar resistive switching (BRS), showing a dependence of the resistive switching on the polarity of the applied voltage, has been reported in perovskite-type oxides including $SrZrO_3$, $Pb(Zr_x,Ti_{1-x})O_3$, and $Pr_{0.7}Ca_{0.3}MnO_3$ (See Refs. in [3]). An interesting aspect of the BRS is the low RESET switching current of several hundreds of μ A or even less.

A 27 nm thick blanket TiO_2 thin film was deposited on a platinized Si-wafer at room temperature by reactive sputtering of Ti in an Ar/O2 environment. As top electrodes (TE) circle-shaped Pt spots with a radius of 100 μm were formed on the blanket TiO_2 film by dc sputtering using a lift-off process. The resistance of the as-produced Pt/TiO_2/Pt stack is in the GΩ range at 1 V showing good insulating properties [4]. Therefore, to induce URS or BRS, electroforming was carried out by applying a positive voltage of about 5 V on the TE with setting a proper current compliance to prevent permanent dielectric breakdown of the as-produced stack. The current compliance during the electroforming decides on the resistive switching mode: a high current compliance ($>$1 mA) leads to URS, while a low one ($<$0.1 mA) leads to BRS. However, in the current compliance range of 0.1-1 mA it is hard to define a dominant resistive switching mode because both URS and BRS may be activated [3].

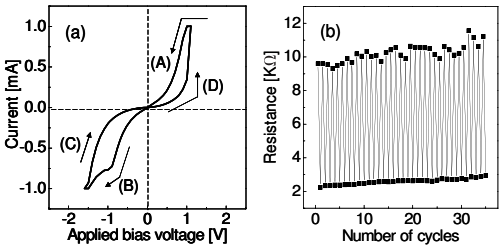

FIG. 1: (a) I-V curve of a Pt/TiO_2/Pt stack with a current compliance of 1 mA showing asymmetric switching in the BRS mode. (b) The resistances in the HRS and LRS at a read-out voltage of 0.3 V dependent on the number of cycles [3].

The I - V curve of TiO_2 undergoing BRS is shown in Fig. 1(a), measured with a current compliance of 1 mA and electroformed before by applying a positive voltage on the TE. Switching between HRS and LRS can be observed within the current range (- 1 mA to +1 mA). By decreasing the applied voltage from a starting voltage of +1.1 V, the current decreases along the path denoted by (A) in the LRS suggesting that the SET switching takes place by applying the starting voltage. Passing the origin point, negative current increases along the path (B). Around -1 V the RESET switching to the HRS starts with a gradual increase of resistance in the I-V curve until the current compliance (1 mA) is reached at about 1.6 V. Increasing the applied voltage to positive values (paths C and D) the SET switching takes place again around 1 V in the path (D). Both HRS and LRS are stable at a read-out voltage of 0.3 V, for which the resistance ratio of HRS to LRS is about 5 as can be seen in Fig.

1(b). Fig. 1(a) shows that the I-V curve in the LRS is almost symmetric as long as the applied voltage is less than the RESET switching voltage.

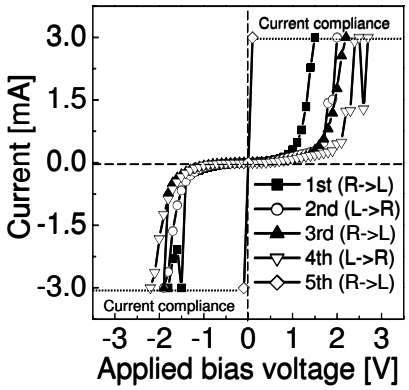

FIG. 2: Transition from BRS to URS mode by applying voltage sweeps with a current compliance of 3 mA. R → L and L → R indicate the voltage sweeps from +3 V to -3 V and from -3 V to +3 V, respectively [3].

Increasing current compliance during BRS gives rise to a transition from the BRS to the URS mode as demonstrated in Fig. 2. Several continuous voltage sweeps from +3 V to -3 V (R → L) and back to +3 V (L → R) were applied with a current compliance of 3 mA. Finally, the transition resulted in a linear I-V behavior (5th cycle in Fig. 2) corresponding to the LRS of the URS mode. After this transition stable URS behavior is observed in the I-V curves, an example is shown in Fig. 3(a). The ratio of HRS to LRS is larger than 1000 [see Fig. 3(b)].

Comparison of Fig. 1(b) and Fig. 3(b) shows that the resistance values of both resistance states of the BRS mode are in between those of the URS mode, i.e. the HRS and the LRS of the URS mode show higher and lower resistance values than the HRS and the LRS of the BRS mode, respectively. The RESET current of the URS is in the range of 30 - 50 mA, much higher than that of the BRS ($\leq$ 1 mA). In the shown example, Fig. 3(a), the current compliance for the SET switching was set to 1 mA, a value lower than the compliance current for the transition from BRS to the URS mode (3 mA) in Fig. 2. Therefore, the URS mode is stable as the HRS is very easily switched to the LRS even with a very low current compliance without a reverse transition to be the BRS mode. Another difference of the URS mode of TiO_2 is that the RESET switching is accompanied by a steep negative differential resistance phenomenon [see Fig. 3(a)]. Comparing Figs. 1(b) and 3(b) it can also be noted that the resistance values in the LRS with respect to the number of cycles are scattered much less than those of the HRS, especially in the URS mode.

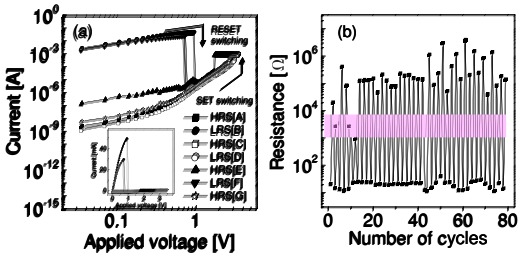

FIG. 3: (a) I-V curves in the URS mode in a logarithmic scale; the inset shows same curves in a linear scale. (b) The resistances of HRS and LRS at a read-out voltage of 0.3 V vs. the number of cycles [3]. The pink band indicates the resistance variation in the BRS mode.

In conclusion, it was shown for the first time that BRS and URS modes can be induced in a Pt/TiO_2/Pt thin film stack depending on the current compliance value during the necessary electroforming. The BRS mode can be transformed into the URS mode by increasing current compliance during continuous switching cycles, but the reverse transition has not been observed. For the technological application the BRS mode is favored due to its low SET switching current although its resistance ratio of HRS to LRS is much lower than in the URS mode. For a mechanistic modeling more experimental parameters such as temperature, TE area, TiO_2 thickness will be investigated together with microstructural observations.

[1] F. Argall, Solid-State Electronics **11**, 535 (1968).

[2] B. J. Choi, D. S. Jeong, S. K. Kim, C. Rohde, S. Choi, J. H. Oh, H. J. Kim, C. S. Hwang, R. Waser, B. Reichenberg, and S. Tiedke, J. Appl. Phys. **98**, 033715 (2005).

[3] D. S. Jeong, H. Schroeder, and R. Waser, Appl. Phys. Lett., accepted for publication.

[4] D. S. Jeong, H. Schroeder, and R. Waser, Appl. Phys. Lett. **89**, 082909 (2006).

Self-Assembly of Diblock-Copolymer Micelles for Template Based Preparation of $PbTiO_3$ Nanograins

S. Karthäuser[1], S. Rathgeber[2], S. Kronholz[1], H. Kohlstedt[1], S. Clemens[3], T. Schneller[3], R. Waser[1, 3]

[1]CNI-Center of Nanoelectronic Systems for Information Technology (IFF)
[2]Max-Planck Institute for Polymer Research, Mainz
[3]Institut für Werkstoffe der Elektrotechnik II, RWTH-Aachen

A bottom-up fabrication route for $PbTiO_3$ nanograins grown on predefined TiO_2 nanostructures used as seeds is presented. The structuring of the TiO_2 seeds was performed using a self-organized template built up by a gold loaded micellar monofilm. With this fabrication process TiO_2 seeds and $PbTiO_3$ grains with a diameter of 12 nm and 30 nm, respectively, were prepared without any e-beam lithographic step. The dimensions of the structure imposed by the micelle template are transferred over all process steps to the final $PbTiO_3$ grains. Furthermore it is shown that the inter-micelle distance and the degree of order in the dried monofilm is mainly determined by the preparation condition such as the pulling velocity in the dipping process and the strength of the surface-micelle interaction and not necessarily by the architectural properties (block length and ratio) of the diblock copolymers building the micelles. The inter-micelle spacing in the dried film is much smaller than the micelle dimension in solution and approaches the dimensions of a fully collapsed micelle in case the dipping process is performed slow enough.

In recent years especially ferroelectric or resistively switching perovskites have attracted considerable attention due to their potential for applications in non-volatile random access memories. Classical fabrication processes of defined nanostructures with certain periodicity are serial working, time consuming and thus expensive. Up to now some approaches exist which use hybrid top/down techniques based on templates or e-beam lithography to pattern nanograin structures which in a second step act as seeds for the deposition of ferroelectric or resistively switching perovskites by an additive technique [1, 2]. We realized a novel bottom-up fabrication route for $PbTiO_3$-grains with natural grown facets based on predefined TiO_2 nanostructures created by using a self-organized template. For details see Reference [3]. The process is schematically shown in Figure 1.

The first steps of the preparation process involve the formation of micelles from A-B diblock copolymers, poly(vinylpiridine)-b-poly(styrene) (PVP-b-PS), and the loading of the micellar core with Au salt. The micellar monolayer film is created on platinized silicon substrates with a titanium top-layer by a dip coating process. The micelles arrange regularly in a hexagonal pattern. In the subsequent process step the organic compounds are removed by reactive ion beam etching (RIBE) with O_2-plasma. The plasma treatment leads to a reduction of the Au salt and finally to one Au nanocluster per micelle by thermal annealing. The resulting Au nanoparticles are suitable as template for the structuring of the TiO_2-thin film with reactive ion etching (RIE) using CF_4-plasma. Subsequently the residual Au nanoparticles are removed by a RIBE Ar-plasma treatment step. In this way, TiO_2 seeds are produced for the controlled growth of $PbTiO_3$ nanograins by a chemical solution deposition technique. This additive growth technique results in crystals with natural growth facets.

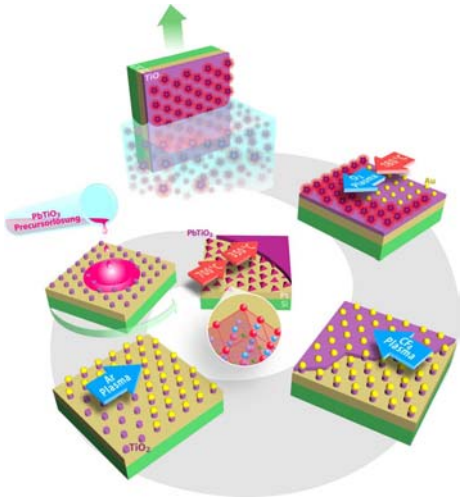

FIG. 1: Process flow of the template based preparation of $PbTiO_3$ nano-grains: (a) self- assembled gold loaded PVP-b-PS micelles, (b) gold nano-particles after reduction and temperature treatment, (c) gold covered TiO_2 seeds after RIE, (d) elimination of the Au template by RIE and (e) $PbTiO_3$ grains grown on TiO_2 seeds.

The developed process route enables the fabrication of TiO_2 seeds with a diameter of 12 nm, which can be used as nucleation sites for the growth of $PbTiO_3$ nanograins having a diameter of only 30 nm and an average spacing of 55 nm. In contrast to other top-down assisted approaches [1, 2] leading to $PbTiO_3$ nanograins with diameters $>$ 50 nm, no time consuming and thus expensive e-beam lithography step is involved. Figure 2 shows the scanning electron photographs and inter-particle distances obtained from

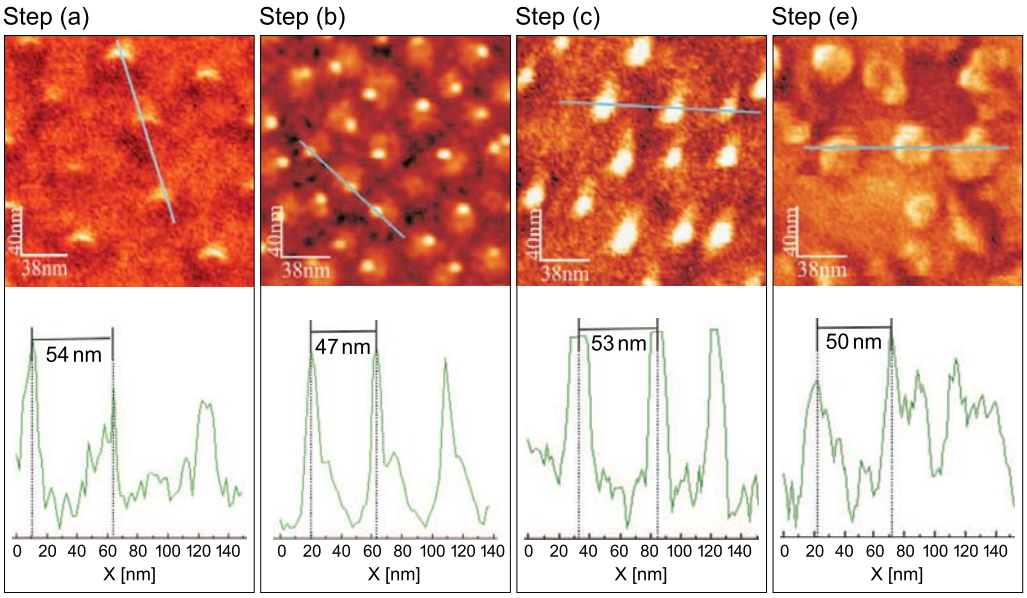

FIG. 2: SEM photographs and results of line scans yielding the inter-particle distances taken at process steps (a), (b), (c) and (e) [see Fig.(1)] during the preparation of $PbTiO_3$ nanograins on a TiO_2 surface.

line scans taken for samples at different steps of the preparation process. Obviously, the structure dimensions can be transferred from the micellar template over all process steps to the final $PbTiO_3$ nanograins. The great interest of using diblock-copolymer micelles as templates was partly based on the idea that the spacing can be easily varied by increasing the length of the block building the shell. By a combined approach of scattering experiments on the solution properties of the Au loaded micelles and surface characterizations of the dried monolayer films we were able to work out which impact the diblock-copolymer architecture and the monolayer film preparation conditions have on the characteristics of the template. We did light scattering and also small-angle neutron scattering to obtain information about the full form factor which allows us to determine the overall shape of the micelles in solution and the distribution of the gold load in the micelles.

In Figure 3 the density and mass distribution of a polymer micelle in solution and the gold distribution in the core for various gold loads are shown. We compared the micelle dimensions and average inter-micelle spacing in solutions with those obtained from dried monolayer films. The inter-micelle spacing in the dried film is much smaller than the micelle dimension in solution and approaches the dimension of a fully collapsed micelle in case the dipping process is performed slowly enough. The micelles collapse, but they still have a certain mobility to rearrange on the surface during the drying process resulting in a higher degree of order of the pattern. It turned out that inter-micelle distances and the degree of order of the dried monofilm is mainly determined by the preparation condition such as the pulling velocity in the dipping process and the strength of the surface-micelle interaction and not necessarily by the architectural properties of the diblock copolymers building the micelles.

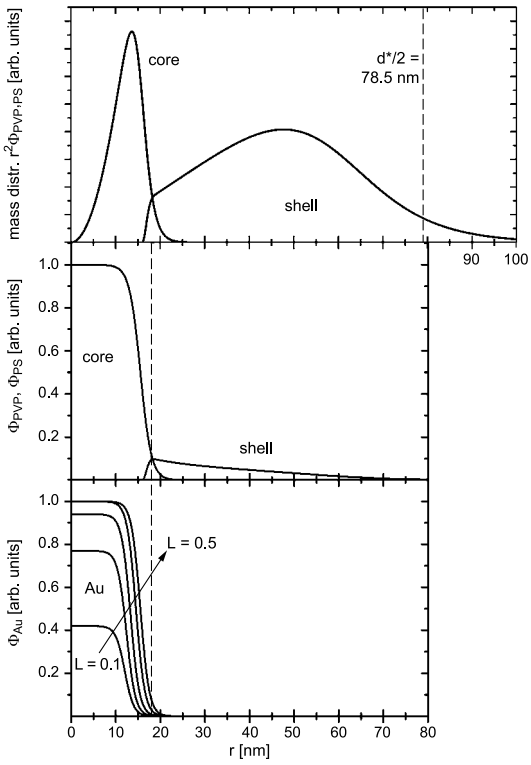

FIG. 3: Mass distribution (upper part) and density profile of a polymer micelle in solution (middle part) and gold distribution in the core (lower part).

[1] S. Bühlmann, P. Muralt, S. Von Allmen, Appl. Phys. Lett. **84**, 2614 (2004).

[2] S. Clemens, T. Schneller, A. van der Hart, F. Peter, R. Waser, Adv. Mater. **17**, 1357 (2005).

[3] S. Kronholz, S. Rathgeber, S. Karthäuser, H. Kohlstedt, S. Clemens, T. Schneller, Adv. Funct. Mater. **16**, 2346 (2006).

Combining Ferroelectricity, Magnetism, and Superconductivity in Tunnel Junctions

H. Kohlstedt[1], N. A. Pertsev[1, 2], A. Petraru[1], U. Poppe[1], R. Waser[1], E. Y. Tsymbal[3]

[1] Institut für Festkörperforschung, and CNI, Forschungszentrum Jülich GmbH, 52425 Jülich, Germany
[2] A. F. Ioffe Physico-Technical Institute, Russian Academy of Sciences, 194021, St. Petersburg, Russia
[3] Department of Physics and Astronomy, Nebraska Center for Materials and Nanosciense, University of Nebraska, Lincoln, NE 68588 USA

Complex oxides display a rich variety of physical phenomena including magnetism, superconductivity, and ferroelectricity. From many points of view it is an interesting approach to combine these (partly antagonistic) cooperative phenomena in tunnel junctions. On the one hand, new device functionalities are expected in such complex junctions. On the other hand, tunneling electrons are extremely sensitive to the barrier and interface excitations and, therefore, represent an ideal spectroscopic tool to extract material properties on the nanometer and even atomic scale. By combing ferroelectric or multiferroic tunnel barriers with ferromagnetic and/or superconducting electrodes, a whole "zoo" of novel tunnel junctions can be proposed.

Historically, the electron tunneling effect played a significant role for the development of quantum mechanics, because it provided proof for the particle-wave dualism [1]. Electron tunneling is described by wave functions and the Schrödinger equation. A typical tunnel junction consists of two metal layers separated by a thin insulator (tunnel barrier). Although classically forbidden, an electron can traverse a potential barrier exceeding the electrons energy, but only for ultrathin (nanometer-thick) barriers a significant tunneling probability is expected. Famous examples are metallic tunnel junctions based on the fundamental work of I. Giaever and M. Jullière [2, 3]. Recently, researchers, armed with a variety of methods, have grown entire magnetic perovskite oxide tunnel junctions made, e.g., of $(La_{0.67}Sr_{0.33})CoO_3$ or $(La_{0.67}Ca_{0.33})CoO_3$ electrodes and $SrTiO_3$ tunnel barriers grown on (100) single crystal $SrTiO_3$ substrates [4]. All mentioned tunnel junctions have two features in common. First, their specific properties are associated with a cooperative phenomenon (superconductivity or magnetism), which occurs in the electrodes. Second, the barrier material in both types of junctions belongs to the group of non-polar dielectrics, although the material is very different (amorphous Al_2O_3 vs. single-crystalline $SrTiO_3$). Here we consider another, very interesting type of tunnel junction, where a ferroelectric is used as the barrier material. The concept, here termed a *ferroelectric tunnel junction* (FTJ), is illustrated in Figure 1 [5]. This device can be used to study the interplay of ferroelectricity and electron tunneling. It may be noted that the discovery of ferroelectricity goes back to 1920 [6], i.e., approximately to the time period when the principles of quantum mechanical electron tunneling [1] have been formulated. Ferroelectricity is defined as a polar state of a material which can be reversed by an external electric field. The remanent polarization is typically in the range of tenths of $\mu C/cm^2$. The central question is: *How a ferroelectric tunnel barrier modifies the electron tunneling transport in comparison to a non-polar dielectric?* Since ferroelectrics possess several specific physical properties, the current-voltage characteristics of FTJs are expected to be different from those of conventional metal-insulator-metal junctions. In particular, the electric-field-induced polarization reversal in a ferroelectric barrier may have a pronounced effect on the conductance of a FTJ and may lead to resistive switching at the coercive field of the ferroelectric material. Indeed, the polarization switching alters the sign of polarization charges existing at a given barrier/electrode interface, changes positions of ions in ferroelectric unit cells, and modifies lattice strains inside the barrier. The polarization reversal, therefore, is expected to change the tunneling transmission coefficient and so may lead to a resistive switching at the coercive voltage [7, 8].

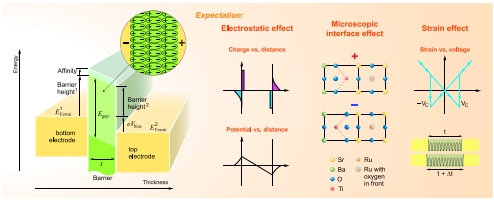

FIG. 1: Schematic of a ferroelectric tunnel junction and possible effects of polarization switching on the electron transport.

In order to realize a FTJ, a crucial condition has to be fulfilled, i.e., ferroelectricity must exist in films which are only a few unit cells thick. The pioneering work of Thomas Tybell [9] in the group of Jean-Marc Triscone in Geneva demonstrated the presence of a stable polarization in the 4-nm-thick epitaxial film of a perovskite ferroelectric $Pb(Zri_{0.2}Ti_{0.8})O_3$. Experimental evidence has been obtained by the Argonne group for the ferroelectric properties of epitaxial $PbTiO_3$ films with a thickness down to 1.2 nm on the basis of structural investigations by synchrotron radiation

[10]. The modern theoretical studies, performed either using the mean-field theory [11] or employing the first-principles approach [12], also support the existence of ferroelectricity in ultrathin films. Moreover, ferroelectricity has been observed experimentally in monolayers of polyvinylidene fluoride (PVDF) [13], which is a ferroelectric polymer and so represents completely different material class. Thus, the experimental and theoretical results indicate that FTJs may be realized in practice. In the above discussion, the electrodes in a FTJ were assumed to be in the normally conducting and paramagnetic state. Evidently, by replacing the paramagnetic electrodes in the FTJ by ferromagnets or superconductors, new types of tunnel junctions may be created (see Figure 2) [14, 15]. In these novel junctions, where the cooperative phenomena simultaneously exist in both the electrodes and the barrier, we can expect new physical effects. In particular, the electrostatic effect resulting from incomplete screening of the polarization charges at the barrier surfaces by the free charges in the electrodes [7, 8] may be very different in junctions with magnetic and/or superconducting electrodes. This "screening" effect may be pronounced in case of correlated oxide material electrodes because of their relatively low carrier density in comparison with metallic electrodes and sensitivity to external parameters. The influence of incomplete screening on the tunnel current can be considered as an electric field effect caused by the charge distribution at the ferroelectric/electrode interfaces. Moreover, an ionic screening effect existing within the first subsurface unit cells in the electrode was proposed recently [16]. Since the band structure is related to the mutual positions of atoms, a novel magnetoelectric interface effect has been predicted in case of magnetic electrodes [15].

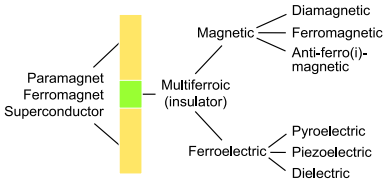

FIG. 2: The "zoo" of novel tunnel junctions

By looking even further into the future, we can predict the following scenarios. Many different material combinations in the electrode-insulator-electrode junctions are possible. Multiferroic [17] tunnel barriers, which exhibit simultaneous magnetic and ferroelectric properties, are challenging. Screening effects, strain and electric-field dependences of their properties could lead to interesting new phenomena. Multiferroic tunnel barriers in combination with superconducting electrodes are another exciting topic [17]. Probably the Josephson current as well as quasiparticle current will be influenced by the polar and magnetic nature of the barrier. Moreover, the multilayer junctions would offer even a higher degree of freedom. So far, there is no firm experimental evidence of even a single functioning FTJ or multiferroic junction. Many obstacles have to be overcome to realize and to prove the existence of these novel types of junctions. In addition, much better understanding of the polarization switching in nanometer-thick ferroelectric films is essential. On the other hand, tremendous achievements in the field of complex oxide epitaxy, the research on ultrathin ferroelectric polymers as well as the advent of advanced analytical methods (e.g., piezoresponse force microscopy) during the last years give hope that the realization of FTJs and multiferroic junctions might soon be possible. An important point is that parasitic effects, such as local conduction and inelastic electron transport via localized states, have to be eliminated. Conversely, if FTJs or multiferroic junctions really exist, we can use the tunneling electrons as an ultra-sensitive analytical tool to study ferroelectricity and magnetism on an Angstrom and nanometer scale. In other words, the powerful tool of electron tunneling spectroscopy [18] can be directly transferred to several kinds of novel tunnel junctions with new and fascinating properties.

[1] J. Frenkel, Phys. Rev. **36**, 1604 (1930).

[2] I. Giaver, Phys. Rev. Lett. **5**, 147 (1960).

[3] M. Jullire, Phys. Lett. A **54**, 225 (1960).

[4] Y. Lu, et al., Phys. Rev. B **54**, 8357 (1996).

[5] E.V. Tsymbal and H. Kohlstedt, Science **313**, 181 (2006) and reference therein.

[6] J. Valasek, Phys. Rev. **17**, 475 (1921).

[7] H. Kohlstedt et al., Phys. Rev. B **72**, 125341 (2005).

[8] M. Ye. Zhuravlev et al., Phys. Pev. Lett. **94**, 246802 (2005).

[9] T. Tybell, C.-H. Ahn, and J. M. Triscone, Appl. Phys. Lett. **75**, 856 (1999).

[10] D. D. Fong, et al, Phys. Rev B **72**, 020406 (2005).

[11] A. G. Zembilgotov, N. A. Pertsev, H. Kohlstedt, and R. Waser, J. Appl. Phys. **91**, 2247 (2002).

[12] J. Junquera and Ph. Ghosez, Nature **422**, 506 (2003).

[13] A.V. Bune, et al., Nature **391**, 874 (1998).

[14] M. Indlekofer and H. Kohlstedt, Europhys. Lett. **72**, 282 (2005).

[15] C.G. Duan et al., Phys.Rev. Lett. **97**, 047201 (2006).

[16] G. Gerra et al., Phys. Rev. Lett. **96**, 107603 (2006).

[17] M. Gajek et. al., cond-mat/060644 and references therein.

[18] E. L. Wolf, Principles of Tunneling Spectroscopy (Plenum, New York, 1985).

Thickness Dependence of Instrinsic Dielectric Response and Apparent Interfacial Capacitance in Ferroelectric Thin Films

N. A. Pertsev[1], R. Dittmann[1], R. Plonka[2], R. Waser[1,2]

[1] CNI-Center of Nanoelectronic Systems for Information Technology (IFF), Institut für Festkörperforschung, Forschungszentrum Jülich, 52425 Jülich, Germany
[2] Institut für Werkstoffe der Elektrotechnik II, RWTH Aachen

We studied theoretically the influence of the progressive strain relaxation and the depolarizing-field effect on the thickness dependence of the out-of-plane dielectric response of epitaxial ferroelectric thin films sandwiched between extended metal electrodes and compared it with the experimental data obtained for single-crystalline $SrRuO_3$/$Ba_{0.7}Sr_{0.3}TiO_3$/$SrRuO_3$ and Pt/$Ba_{0.7}Sr_{0.3}TiO_3$/$SrRuO_3$ thin-film capacitors. The calculations show that the inverse of the measured capacitance varies with the film thickness almost linearly in the most part of the thickness range at the majority of temperatures. Extrapolation of this linear dependence to zero thickness usually gives considerable nonzero intercept even in the absence of nonferroelectric interfacial layers. Remarkably, such apparent "interfacial capacitance" may be strongly temperature dependent and becomes negative in a certain temperature range.

Pronounced thickness dependence of the physical properties of ferroelectric thin films is a severe obstacle for the application of these materials in electronic devices which meet the demands of the current trend for miniaturization. Experimentally, the inverse of the measured capacitance c_t varies linearly with the film thickness. This observation led to a widely accepted interpretation of experimental data in terms of a "series capacitor model" (see expression in Fig. 1). This model implies that the permittivity ϵ_b of the film interior and the interfacial capacitances c_{i1} and c_{i2} are thickness-independent quantities. This assumption, however, seems to be generally incorrect for real ferroelectric capacitors, because the experimentally determined c_i values can be strongly temperature dependent and may even become negative (see Fig. 1). This renders the interpretation of c_i as an interface capacitance density questionable.

We used a nonlinear thermodynamic theory to study in detail the influence of strain relaxation and depolarizing field on the thickness dependence of the small-signal dielectric response of ferroelectric capacitors compressively strained by a dissimilar cubic substrate and sandwiched between continuous metal electrodes.

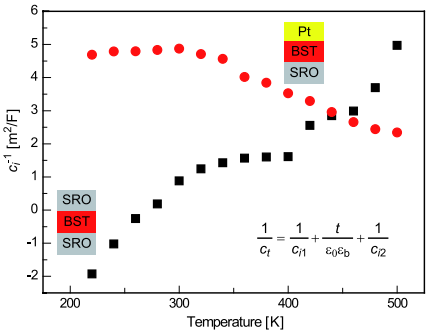

FIG. 1: **Equation** *according to the "series capacitor model":* ϵ_b *= permittivity of the film interior,* t *= film thickness, and* c_{i1} *and* c_{i2} *= interface capacitance of two interfaces.* **Graphs:** *Temperature dependence of the intercept* $c_t^{-1}(t \to 0)$ *extracted from the experimental data for Pt/*$Ba_{0.7}Sr_{0.3}TiO_3$*/*$SrRuO_3$ *and* $SrRuO_3$*/*$Ba_{0.7}Sr_{0.3}TiO_3$*/*$SrRuO_3$ *capacitors [1].*

The strain effect on film permittivity is closely related to the strain-induced shift of the paraelectric to ferroelectric phase transition. Within the stability range of the **paraelectric phase**, the relative out-of-plane permittivity ϵ_{33} of an epitaxial film depends on the misfit strain S_m as

$$\epsilon_{33} = \frac{K_s}{S_m S_m^*} \quad , \qquad (1)$$

where $K_s^{-1} > 0$ is the strain sensitivity of the film reciprocal permittivity, and $S_m^* < S_m$ is the temperature dependent critical misfit strain [2]. The progressive strain relaxation caused by generation of misfit dislocations in films with thicknesses t exceeding the critical value t_c results in the following thickness dependence of S_m:

$$S_m(t,T) \cong S_m^\infty(T) + \eta S_m^0(T_g)\frac{t_c}{t} \quad , \qquad (2)$$

where $S_m^\infty(T)$ represents the strain in a very thick epitaxial film ($t >> t_c$) and $\eta < 1$ allows for the fact that usually the equilibrium dislocation density is not reached due to kinetic limitations. According to Eqs. (1) and (2), at $t > t_c$ the reciprocal capacitance varies with the film thickness as

$$\frac{1}{c_t} = \frac{1}{\epsilon_0 \epsilon_{33}^\infty} + \frac{\eta S_m^0(T_g) t_c}{\epsilon_0 K_s} \quad . \qquad (3)$$

It can be seen that the extrapolation of c_t^{-1} to zero thickness gives a finite intercept caused by the

strain relaxation. Remarkably, when the in-plane film strains at T_g are compressive ($S_m^0 < 0$), the intercept $c_t^{-1}(t \to 0)$ is *negative*. For epitaxial films in the ferroelectric state, we discuss the range of relatively large negative misfit strains, where the tetragonal c phase with the out-of-plane spontaneous polarization ($P_1 = P_2 = 0, P_3 \neq 0$) becomes energetically most favorable. Near the second-order phase transition, where the P^4 approximation is valid, the dependence of the film permittivity ϵ_{33} on the misfit strain takes the form [1]

$$\epsilon_{33} = \frac{K_{sc}}{S_m^* S_m} \quad . \tag{4}$$

where $S_m < S_m^*$ and $K_{sc} = K_s/2$. The thickness dependence of reciprocal capacitance in the ferroelectric case becomes

$$\frac{1}{c_t} = \frac{1}{\epsilon_0 \epsilon_{33}^{\infty}} - \frac{\eta S_m^0(T_g) t_c}{\epsilon_0 K_{sc}} \quad . \tag{5}$$

It can be seen that the thickness-independent term in Eq. (5) differs from that in Eq. (3) by the opposite sign and by a two times larger magnitude. Since the c phase can form only at negative misfit strains [3], the strain $S_m^0(T_g)$ involved in Eq. (5) usually must be negative. Therefore, in the ferroelectric regime the intercept $c_t^{-1}(t \to 0)$ normally is expected to be positive. In summary, the strain effect leads to a change of sign of the intercept at the transition temperature.

We proceed now to the analysis of the influence of the **depolarizing field** on the dielectric response of a ferroelectric capacitor. This field appears when the polarization charges existing at the film surfaces are not perfectly compensated for by other charges. Since the electronic screening length in metals is finite, the depolarizing field may be significant even in short-circuited capacitors [4]. We model the ferroelectric/electrode interfaces by thin low-permittivity dielectric layers with a fixed thickness $d << t$ and permittivity ϵ_d. If variations of ferroelectric polarization near film surfaces are negligible, the above parameters can be evaluated as $d = \sqrt{\epsilon}_m l_{\mathrm{TF}}$ and $\epsilon_d = \epsilon_m$, where l_{TF} and ϵ_m are the Thomas-Fermi screening length and the lattice dielectric constant of the electrode material, respectively.

Assuming the film to be in a single-domain state, we can calculate the total capacitance density $c_t = \partial D_3(V)/\partial V$ as

$$c_t = \frac{c_i t}{(\epsilon_0 + c_i t)} \left[\frac{\epsilon_0}{t} + \frac{c_i}{1 + (\epsilon_0 + c_i t)\chi_{33}} \right] \quad , \tag{6}$$

[5] where $\chi_{33} = \partial E_3/\partial P_3$ represents the inverse susceptibility of the ferroelectric film in the capacitor, and $c_i = (1/2)\epsilon_0 \epsilon_d/d$ is the total capacitance density of two interfacial layers. The depolarizing field affects χ_{33} via suppression of the film out-of-plane polarization P_3. Whereas $c_t^{-1}(t)$ is linear in the P^4 approximation, this dependence becomes nonlinear in the P^6 and higher-order approximations. The numerical calculations, however, show that the nonlinearity is usually negligible when $c_t^{-1}(t)$ is plotted over a limited thickness range only. Hence the thickness dependence of the reciprocal capacitance may be approximated by the relation

$$c_t^{-1} \cong \frac{t}{\epsilon_0 \epsilon_{\mathrm{eff}}} - \frac{\kappa}{c_i} \tag{7}$$

involving two fitting parameters, ϵ_{eff} and κ. Remarkably, the extrapolation to zero thickness gives a negative intercept equal to $-\kappa/c_i$, which may significantly vary with the temperature.

For ferroelectric capacitors with film thicknesses outside the nanoscale range ($t > t_c$) and imperfectly screening electrodes, the influence of both the strain relaxation and the depolarizing field has to be taken into account. We performed numerical calculations of $c_t^{-1}(t)$ in the P_8 approximation for $BaTiO_3$ capacitors with two different interface capacitances c_i. Nonlinearity of the dependence $c_t^{-1}(t)$ was proved to be negligible at the majority of temperatures, and the intercept $c_t^{-1}(t \to 0)$ was plotted as a function of temperature (see Fig. 2). For both values of the interface capacitance, the intercept changes sign on crossing the phase transition region. In case of electrodes with good screening properties (c_i = 1 F/m^2), the strain effect dominates so that the intercept is positive at low temperatures and negative at high temperatures. For electrodes with poor screening ability (c_i = 0.2 F/m^2), the depolarizing-field effect overrides the influence of strain relaxation.

Thus, the observed two different types of the temperature dependence of the intercept, which are shown in Fig. 1, can be qualitatively explained by our calculations.

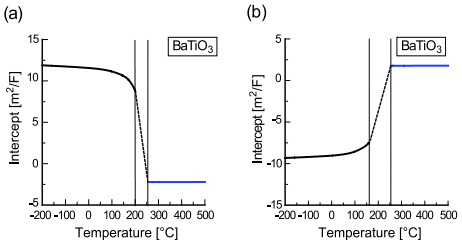

FIG. 2: Temperature dependence of $c_t^{-1}(t \to 0)$ calculated for $BaTiO_3$ thin-film capacitors sandwiched between electrodes with different screening ability: (a) c_i = 1 F/m^2, (b) c_i = 0.2 F/m^2. We assumed $S_m = -15 \times 10^{-3}, t_c = 10$ nm, η = 0.7, and $\partial S_m/\partial T = 4 \times 10^{-6} K^{-1}$ [5].

[1] R. Plonka, R. Dittmann, N. A. Pertsev, E. Vasco, and R. Waser, Appl. Phys. Lett. **86**, 202908 (2005)

[2] N. A. Pertsev, V. G. Koukhar, R. Waser, and S. Hoffmann, Appl. Phys. Lett. **77**, 2596 (2000).

[3] N. A. Pertsev, A. G. Zembilgotov, and A. K. Tagantsev, Phys. Rev. Lett. **80**, 1988 (1998); V. G. Koukhar, N. A. Pertsev, and R. Waser, Phys. Rev. B **64**, 214103 (2001)

[4] R. R. Mehta, B. D. Silverman, and J. T. Jacobs, J. Appl. Phys. **44**, 3379 (1973)

[5] N. A. Pertsev, R. Dittmann, R. Plonka, and R. Waser, submitted to J. Appl.

Nanoscale Ferroelectric Capacitors Studied by Atomic Force Microscopy

A. Petraru[1], H. Kohlstedt[1,3], V. Nagarajan[2], R. Ramesh[3], G. Schlom[4], U. Poppe[1] and R. Waser[1]

[1]Institut für Festkörperforschung and CNI, Forschungszentrum Jülich GmbH, Jülich, Germany
[2]School of Materials Science and Engineering University of New South Wales Sydney NSW 2052
[3]Dept. of Materials Science and Engineering and Dept. of Physics, University of California, Berkeley, USA
[4]Dept. of Materials Science and Engineering Pennsylvania State University, University Park, USA

We present a sensitive method to simultaneously acquire the C(V) characteristics and piezoresponse of sub-micron size ferroelectric capacitors using a Atomic Force Microscope(AFM). Model Pt/($La_{0.5}Sr_{0.5}$) CoO_3/$PbZr_{0.4}Ti_{0.6}O_3$/($La_{0.5}Sr_{0.5}$) CoO_3/La:$SrTiO_3$/Si nanocapacitors were fabricated by focused ion beam milling from $100\mu m^2$ down to $0.04\mu m^2$. With this AFM based capacitance measurement technique we show clear "double-humped" $C(V)$ for all sizes with no significant change in peak value of the ϵ_r down to capacitors with the smallest area of $0.04\mu m^2$. The smallest capacitance measured is only of the order a few femtofarads, demonstrating the high sensitivity of the technique. Simultaneously piezoelectric response is recorded for each measurement, thus the technique facilitates simultaneous piezoresponse and dielectric characterization of ferroelectric memory devices.

To make ferroelectric RAMs (FeRAMs) superior to current non-volatile memories such as Flash, it is critical to scale the ferroelectric cell size down to the nanoscale dimensions. Thus, the ability to successfully characterize ferroelectric properties of the small area capacitors, in the range of tens to hundred nanometers is of paramount importance. In the past few years, there has been tremendous progress in the use of atomic force microscopy (AFM) based techniques to investigate ferroelectric behavior. This includes direct hysteresis loop measurements, polarization switching experiments and piezoresponse domain imaging studies. The use of lock-in based current detection technique has been presented by Oh et al. [1] Impedance detection methods have also been investigated. Shao et al. and later on OHayre et al. [2] have reported an advanced impedance based AFM technique to detect small amounts of currents. Lee et al. have shown a lock-in based very sensitive local capacitance technique [3] where capacitance values as low as attofarads could be detected. Very few of the above have been applied to the dielectric measurements of nanoscale ferroelectric/dielectric capacitors. Measurements of the dielectric response in nanoscale ferroelectric capacitors are important because they can give us immense information such as scaling of the coercive voltage, tunability of the ferroelectric layer, presence of passive layers etc. Although well established scanned probe techniques such as Scanning Capacitance Microscopy [4] have been used to investigate the dielectric response of ferroelectrics at the nanoscale, extracting accurate quantitative information of the capacitance is still a challenge. At the same time it is often desirable to measure more than one functional property. In ferroelectrics particularly, it is known that the piezoelectric constants are strongly linked to the dielectric and the polarization behavior. Thus an approach that could measure both the piezoelectric and dielectric behavior simultaneously would be of immense potent. In this paper, we demonstrate an approach that allows the simultaneous quantitative measurement of the $C(V)$ curve and piezoresponse hysteresis loops for sub-micron sized ferroelectric capacitors with an area down to $0.04\mu m^2$.

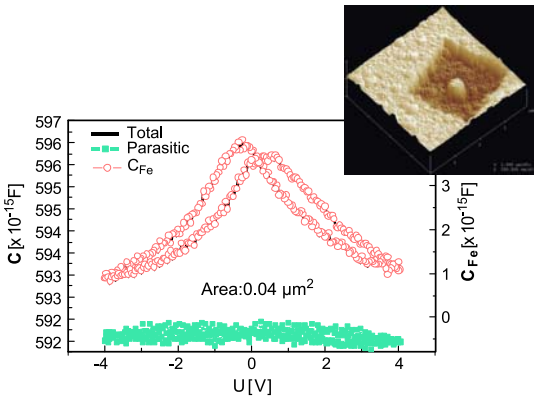

FIG. 1: $C(V)$ for a capacitor with an area of $0.04\mu m^2$: total capacitance, parasitic capacitance and ferroelectric capacitance. Inset: an AFM image of an FIB capacitor.

The measurement setup consists of an atomic force microscope (AFM) equipped with a conductive Pt-Ir coated cantilever, a waveform generator and two lock-in amplifiers. For piezoresponse measurements, a second lock-in amplifier receives the signal from the optical detector of the AFM. Thus, the out-of-plane deflection of the laser beam modulated by the excitation signal via the converse piezoelectric effect is recorded, and it is proportional to the corresponding piezoelectric coefficient (d_{33} in the case of c-axis oriented Pb(Zr,Ti)O_3 epitaxial films). In short epitaxial $PbZr_{0.4}Ti_{0.6O3}$ films were prepared by sol-gel deposition with top and bottom sputtered $La_{0.5}Sr_{0.5}0_3$ oxide

electrodes on La-doped $SrTiO_3$ (epitaxial conductive template layer) buffered Si substrate. The nominal thickness of the ferroelectric layer was 120 nm. Capacitors with varying sizes from $100\mu m^2$ to $0.04\mu m^2$ were fabricated via focused Ga ion beam milling (FIB) followed by annealing in an oxygen furnace at 500 °C to eliminate ion beam damage. In Figure 1 we plot the raw capacitance data obtained for the smallest capacitor having an area of $0.04\mu m^2$, measured via AFM topography scans and reconfirmed by SEM images. The loop (line) shows clearly a double-humped curve, thus indicating the ferroelectric nature of the nanoisland. Our approach is to measure very precisely the total capacitance in order to subtract the parasitic (stray) capacitance and obtain the real capacitance of the device [5].

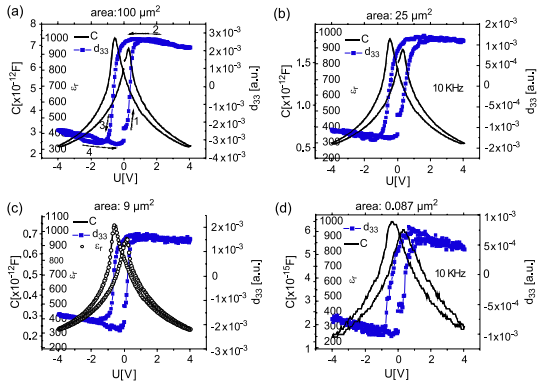

FIG. 2: Simultaneous measurements of the capacitance and piezoresponse of FIB PZT thin film capacitors having different areas.

In order to determine the actual value of dielectric constant of the nanocapacitors it is therefore important to determine very accurately the parasitic capacitance and to subtract it from the total capacitance. The traditional method to lift the tip and measure again is not very accurate, because the measured parasitic is strongly dependent on the distance to which the tip is lifted. Ideally the truest measurement of the parasitic capacitance is to use the same tip after it has lost the conductive coating from the very top. In this case the ferroelectric capacitor is disconnected from the circuit and precise parasitic capacitance is determined. Since this is not a practical solution (but good for checking the setup), our approach was to move the tip laterally, outside the milled electrode area (since the surrounding area is insulating) and then to measure the parasitic capacitance. This measurement of the parasitic capacitance is shown as the squares in the Figure 1. We find that it is strongly linear and deducting this from our raw data yields the true capacitance of the device. This is shown as the open circles and its magnitude is a few femtofarads.

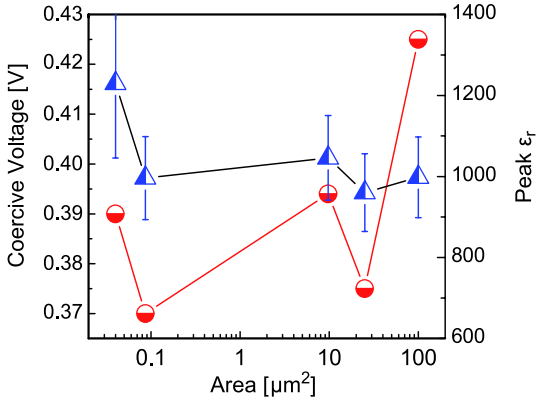

FIG. 3: Peak dielectric constant and the coercive voltage as a function of capacitor area.

Figure 2 shows the $C(V)$ together with the piezoresponse hysteresis loop for several device areas: $100\mu m^2$, $25\mu m^2$, $9\mu m^2$ and $0.09\mu m^2$. The value of the ϵ_r was derived assuming parallel-plate capacitors. Moreover the peak positions do not change with device size, suggesting an absence of scaling of the coercive voltage (and hence coercive field) with lateral dimensions, in contrast to the strong scaling shown by the coercive voltage when the thickness of the ferroelectric is varied. We do not find a significant variation in the tunability of the dielectric constant but we observe a broadening of the peak of the dielectric constant with decreasing size. In Figure 3 we plot the peak dielectric constant as a function of the capacitor area. The error bars represent a combination of the errors in the measurement of the area and statistical variation in the data. Within these error bars we find no significant scaling of the dielectric constant. The peak value is approximately 1000, in agreement with previous reports for the same kind of ferroelectric material. Normally smaller pads show an increase in their piezoelectric constant compared to larger clamped capacitors. Based on these results the dielectric constant was expected to also increase, therefore we find the above trend surprising. More detail investigations into the dielectric behavior of the ferroelectric layer as a function of size are therefore necessary.

[1] Oh, J. and R.J. Nemanicha, J. Appl. Phys. 92 (6) 2002.

[2] OHayre, M. Lee, and F.B. Prinz, JOURNAL OF APPLIED PHYSICS, 2004. 95(12): p. 8382.

[3] Lee, D.T., J.P. Pelz, and B. Bhushan, REVIEW OF SCIENTIFIC INSTRUMENTS, 2002. 73(10): p. 3525.

[4] Williams, C.C., W.P. Hough, and S.A. Rishton, Applied Physics Letters, 1989. 55(2): p. 203-205.

[5] A. Petraru, V. Nagarajan, H. Kohlstedt, R. Ramesh, D. Schlom, and R. Waser, Appl. Phys. A 84, 67 (2006).

Electrostriction Versus Polarization Reversal in Ferroelectric Nanoislands

S. Röhrig, A. Rüdiger

CNI-Center of Nanoelectronic Systems for Information Technology (ISG)

All ferroelectrics that are used in a wide range of non-volatile memory applications are necessarily piezoelectrics. Piezoresponse Force Microscopy (PFM) is thus using this structural property to indirectly determine the relative orientation of the ferroelectric polarization. The electromechanical response of ferroelectric nanoislands on a conductive substrate is stimulated and monitored by a conductive AFM tip in contact mode. For large electric fields, higher order terms of the mechanical response become significant, with the omnipresent electrostriction being quadratic in the externally applied field as the most prominent effect. As the experimental sensitivity requires the use of a Lock-In technique for the detection of the electro-mechanical response, the external voltage is modulated at ω_0 and consequently, electrostriction occurs at $2\omega_0$. We observed a deviation from this quadratic behaviour as the applied voltage exceeds coercivity. In this regime the polarization reversal creates another second harmonic mechanical response that periodically disrupts the electrical contact between tip and sample. These experiments suggest a novel sensing scheme for ferroelectric domain reversal and thus a new concept for ferroelectric data storage.

Ferroelectric domains are areas of different electrical polarization. They can be as narrow as a few unit cells and promise extremely high data storage capacities [1]. As the surface charge density decreases with area, the direct detection of charges was soon discarded and replaced by the detection of the piezoelectric response by amplitude and phase. Domains of antiparallel polarization are 180 degree out of phase in their piezoelectric response with respect to an external AC stimulus due to the relative orientations of the third rank piezoelectric tensor. Piezoresponse Force Microscopy (PFM) uses a metal coated contact-AFM cantilever to apply this external AC field to the sample and to monitor the deformation of the sample by the deflection of the AFM laser beam on a quadrupole photodiode [2]. With such a configuration both vertical and lateral components of the polarization are accessible. For vertical domain pattern writing and detection, a less demanding configuration that e.g. electrically determines the vertical motion of the cantilever is sufficient. Our recent findings suggest yet another way to detect the vertical polarization reversal purely electrically.

As indicated in Fig. 1, a sinusoidal excitation stimulates a sinusoidal strain response readily detectable by PFM. At 2 ω_0 electrostriction occurs with a qeuadratic dependence on the electrical field. As the external stimulus exceeds the coercive field of a ferroelectric the polarization switches upon scanning. What happens to the system as the polarization reverses depends on the initial state. If the structure is expanding under the external stimulus (external field parallel to the polarization), nothing will happen as the field exceeds coercivity. If however, the structure is contracting (external field antiparallel to the polarization), the electromechanical coupling will change its direction and the structure will out of a sudden expand at the speed of the transverse optical phonon (for thin films this happens faster than a nanosecond). The cantilever is pushed upwards. From now on the external field and the polarization will be antiparallel with every half-period creating an electromechanical response at 2 ω_0, similar to electrostriction with the main difference of still being linear in the electrical field. The overall signal at $2\omega_0$ should thus be a sum of quadratic electrostriction and this polarization reversal signal.

Our measurements were carried out at the perimeter of c-axis oriented structures of $\mathrm{Pb(Zr_{0.52}Ti_{0.48})O_3}$ on $\mathrm{SrTiO_3}$:iNb (100). At these slopes the lateral strain response is composed of various tensor elements, predominantly d31 which has the opposite sign of d_{33} (along the unit cell axis), see Fig. 2. In contrast to the aforementioned purely vertical detection with only a vertical cantilever deflection, while the cantilever is now pushed upwards by d_{33}, the inward lateral motion due to d_{31} deprives the cantilever of its contact to the sample as the mechanical resonance frequency even for lateral torsion is too low to instantaneously follow the motion of the sample surface. This disrupted mechanical contact disables the stimulation of electrostriction leaving a linear signal as illustrated in Fig. 3.

In practice this disruption should also be detectable by a current disruption across the sample. We are now elaborating an experiment with an electrical field above coercivity across these slopes. For an electrical field parallel to the polarization the current should be steady while an antiparallel field should at least

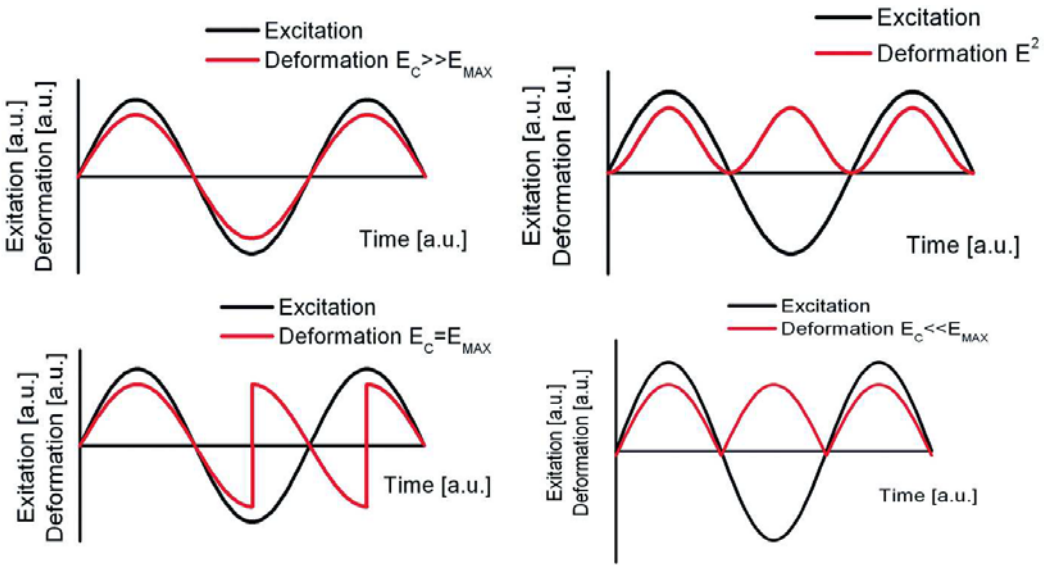

FIG. 1: Top left: sinusoidal electrical excitation and deformation are in phase with frequency ω_0. top right, electrical excitation and electrostriction with $2\omega_0$ and quadratic in the electric field, bottom left: deformation for an electrical stimulus E_{Max} that only just exceeds the coercive field E_C and bottom right: deformation for extremely high electric fields far above the coercive field

briefly discontinue this current flow. The time constant for this disruption is primarily determined by the spring constant of the cantilever for lateral torsion and ranges around a few 100 kHz enabling a new and fast detection scheme for ferroelectric polarization in nanoislands. This work is funded within the Volkswagen Project: “Nano-Sized Ferroelectric Hybrids”

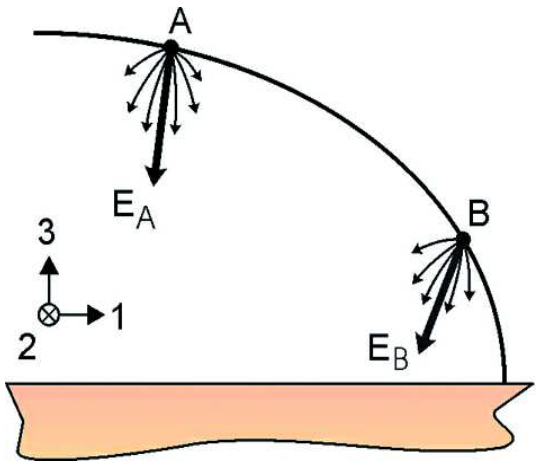

FIG. 2: Schematic field distribution at the perimeter of a ferroelectric nanostructure. The relative contributions of the piezoelectric tensor differ considerably between positions A and B according to ref. [3]

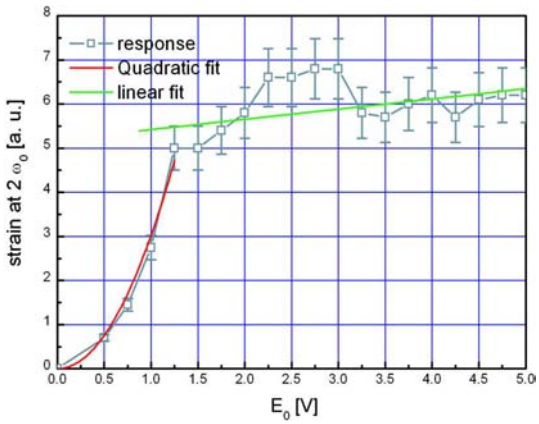

FIG. 3: Lateral strain response at $2\omega_0$ determined by piezoresponse force microscopy. The quadratic regime below 1.2 volts corresponds to electrostriction with a stable mechanical contact between tip and sample surface. As the coercive field is exceeded, the point contacted is disrupted at $2\omega_0$. This also causes the considerable errorbars due to a mechanically unstable situation with changing mechanical contact points over time. However the increasing linear trend anticipated from our model is clearly visible. The coercive voltage of 1.2 V is in good agreement with measurements thin films of equal thickness with macroscopic electrodes.

[1] Y. Cho et al., Appl.Phys.Lett., **87**, 232907 (2005)

[2] A. Rüdiger, R. Waser, Advances in Science and Technology, 45, 2392-2399 (2006)

[3] F. Peter et al. Appl. Phys. Lett., 87, 082901 (2005)

Resistive Switching in $Ge_{0.3}Se_{0.7}$ by Means of Copper Ion Migration

C. Schindler[1], X. Guo[1], R. Waser[1, 2]

[1]CNI-Center of Nanoelectronic Systems for Information Technology (IFF)
[2]Institut für Werkstoffe der Elektrotechnik II

Bipolar resistive switching in Pt/$Ge_{0.3}Se_{0.7}$/Cu cells was examined. By changing the bias voltage polarity on the electrodes, the cells were switched between high and low resistance states. The resistive switching was realized by means of Cu ion migration through the chalcogenide film. Switching voltages down to +/-100mV and a resistance ratio up to 200 have been achieved. Pulse measurements show that the two resistance states can be tuned by the applied voltage as well as by the pulse length. Due to their low switching voltages, non-destructive read out operation, and high scalability, these cells are very promising for memory applications.

Electrochemical memory cells become interesting as an alternative to established memory technologies, such as Static Random Access Memory (SRAM) or Dynamic Random Access Memory (DRAM), because they offer a high scalability, non-volatility, non-destructive read-out, cheap fabrication, and an easy integration into the standard CMOS line. The cells are based on chalcogenide materials, mainly CuS, Ag_2S [1], Ag-Ge-S, and Ag-Ge-Se [2]. These compounds are solid electrolytes, allowing easy diffusion of metal ions, such as Ag^+ or Cu^{2+}. Two stable states can be obtained by the formation or dissolution of metallic paths between an oxidizable (e.g. Cu) and an inert electrode (e.g. Pt). Only a few hundred mV are necessary to change the resistive state; therefore, the power consumption is low.

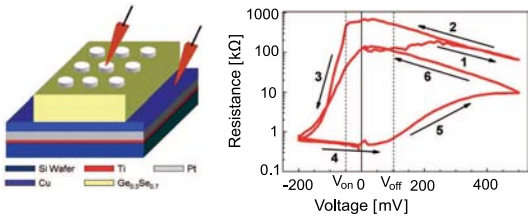

(a) (b)

FIG. 1: (a) Cell structure, and (b) characteristic R-V curves. For electrical characterization the bottom electrode was grounded. The initial high resistance is higher than the resistance in the following OFF-state.

Pt/$Ge_{0.3}Se_{0.7}$/Cu cells with $Ge_{0.3}Se_{0.7}$ thicknesses varying from 165nm to 50nm were fabricated. The actual cell structure is shown in Fig. 1(a). First, the bottom electrode was deposited on a Si substrate. Ti was used as adhesion promoter for a 100nm thick Pt layer. A 20nm Cu layer was deposited on Pt and this metal stack served as the oxidizable electrode later on. Optical lithography was used to structure the solid electrolyte and circular Pt top electrodes. All layers were deposited by rf magnetron sputtering.

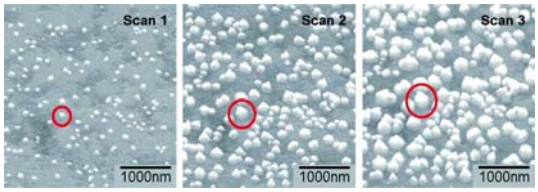

FIG. 2: Scanning electron microscopy (SEM) images of an area of 100nm $Ge_{0.3}Se_{0.7}$ film on 100nm Ag layer. The longer the area was exposed to the electron beam, the stronger was the Ag diffusion to the surface.

Current – voltage (I-V) measurements were done with a Digistant 4462 Burster as voltage source and a Keithley 617 electrometer as a current meter. A characteristic resistance- voltage (R-V) curve for a 165nm thick $Ge_{0.3}Se_{0.7}$ is given in Fig. 1(b). The Cu bottom electrode was grounded for all measurements. After fabrication, the cell was in the OFF-state with a high resistance of about 1MΩ. The ON-state with a resistance of about 500Ω was achieved by application of a negative voltage to the Pt top electrode. The following OFF-states show resistances around 100kΩ, which are lower than the initial film resistance, due to remaining Cu in the solid electrolyte after the first cycle.

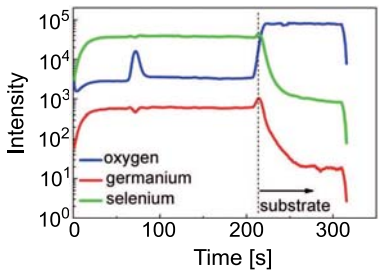

FIG. 3: ToF SIMS profile showing the oxide diffusion barrier in the solid electrolyte (by A. Besmehn).

For $Ge_{0.3}Se_{0.7}$ films with thicknesses between 50nm and 80nm, short circuits were observed in a lot of

cases. SEM pictures show that metals, such as Cu or Ag, easily diffuse through $Ge_{0.3}Se_{0.7}$ (Fig. 2) [3]. To prevent such a diffusion before voltage application, the $Ge_{0.3}Se_{0.7}$ films were deposited in two runs. After the first run, an oxide layer was allowed to form on the surface. Time of Flight Secondary Ion Mass Spectroscopy (ToF SIMS) (Fig. 3) shows the localized oxygen content inside the film, and XPS analysis proved it to be GeO. The GeO layer serves as diffusion barrier, but it can be overcome by the metal ions if a voltage is applied.

Resistive switching in the cells has been achieved by applying only a few hundred mV. If I-V measurements were done in sweep-mode, the resistance states were tuneable by variation of the maximum and minimum voltage applied to the Pt top electrode, while the Cu/Pt bottom electrode was grounded. Figure 4 (a) shows that the higher the positive voltage for erasing is, the higher is the resistance in the OFF-state. And the higher the negative voltage for writing is, the lower is the ON-resistance (Fig. 4(b)). The several resistance states per memory cell are advantageous, as this effect allows a higher storage density per cell.

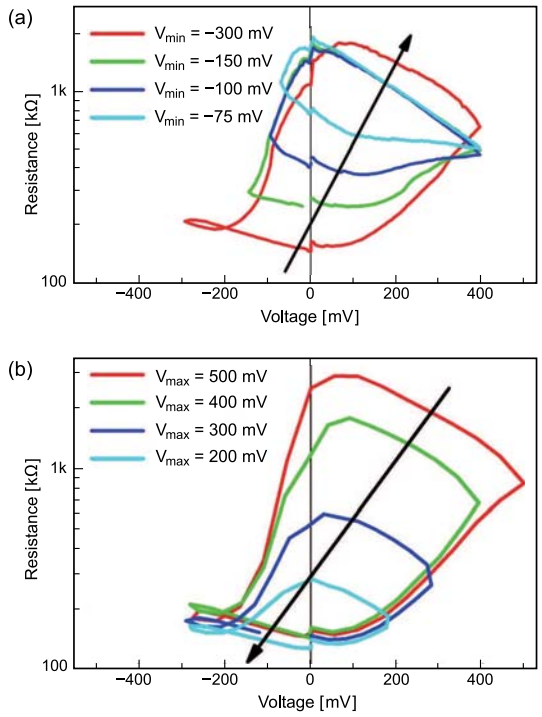

FIG. 4: (a) Tuning the ON-resistance by variation of the negative voltage applied to the top electrode. (b) Tuning the OFF-resistance by variation of the positive voltage applied to the top electrode. The voltage was increased stepwise at a rate of 10mV/s and the Cu bottom electrode was grounded.

From measurements in sweep-mode, it cannot be decided whether this effect is only due to the maximum and minimum sweep voltage or also due to the time of voltage application, as the rate of voltage increase was kept constant at 10mV/s. However, pulse measurements show that both parameters, voltage and time, have an impact on the two resistance states. Fig. 5 shows the dependence of the ON- and OFF-current and the resulting current ratio on (a) the voltage and (b) the time for switching to the OFF-state. Both parameters, a higher voltage and a longer time of voltage application, lead to a better dissolution of the conductive path, and thereby a lower OFF-current (Ioff). Just as Voff and toff mainly influence Ioff, the voltage and time for switching to the ON-state mainly influence the current in the ON-state.

In summary, switching voltages of a few hundred mV, an OFF/ON resistance ratio of about 200, and a non-destructive read-out with a voltage $<$20mV have been achieved for Pt/$Ge_{0.3}Se_{0.7}$/Cu cells in this work. The pulse measurements show that the switching voltage as well as the time of voltage application determine the strength of the conducive path between the two electrodes. Therefore, the resistance states become tuneable, allowing for the storage of more than two states per cell. This enables a higher memory density for future integration. The Pt/$Ge_{0.3}Se_{0.7}$/Cu cells are very promising for the future memory application.

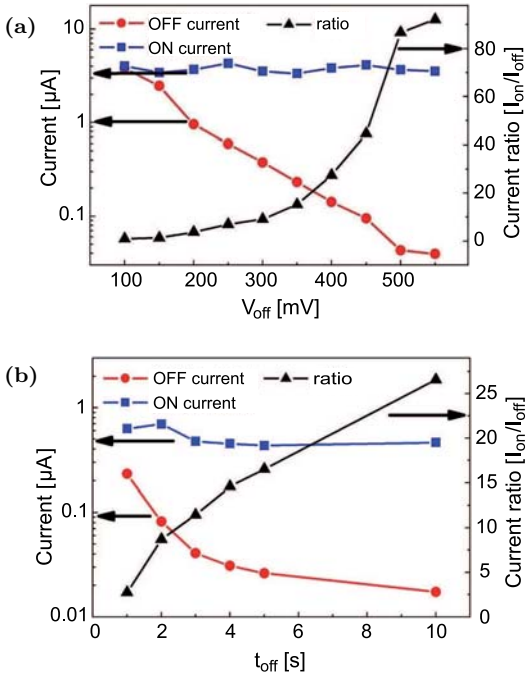

FIG. 5: Influence of (a) the switching voltage and (b) the time of voltage application on the current in ON- and OFF-state and on the current ratio. The experimental parameters are V_{on}=-400mV, t_{on}=1s, t_{off}=5s, V_{off}=400mV, V_{read}=10mV, and t_{read}=5s, respectively

[1] K. Terabe, T. Hasegawa, T. Nakayama, M. Aono, NATURE 433, 47-50 (2005)

[2] M.N. Kozicki, M. Park, M. Mitkova, IEEE Transactions on Nanotechnology 4, 331-338 (2005)

[3] C.P. McHardy, A.G. Fitzgerlad, P.A. Moirt, M. Flynn, J. Phys. C: Solid State Phys. 20, 4055-4075 (1987)

Nanoscale Resistive Switching in $SrTiO_3$ Thin Films

K. Szot[1,2], R. Dittmann[1], W. Speier[1], R. Waser[1,3]

[1]CNI-Center of Nanoelectronic Systems for Information Technology (IFF)
[2]Institut of Physics, University of Silesia, 40-007 Katowice, Poland
[3]Institut für Werkstoffe der Elektrotechnik II, RWTH Aachen

The local conductivity of $SrTiO_3$ thin films epitaxially grown on $SrRuO_3$-buffered $SrTiO_3$ single crystals has been investigated in detail with an atomic force microscope equipped with a conducting tip (LC-AFM). These experiments demonstrate that the conductivity of $SrTiO_3$ thin films originates from nanoscale well-conducting filaments connecting the surface to the $SrRuO_3$ bottom electrode. The electrical conduction of the filaments is shown to be reversibly modulated over several orders of magnitude by application of an appropriate electrical field. We analyze the resistive switching by ad-dressing individual filaments with the AFM tip as well as by scanning areas up to the μm scale. Temperature dependent measurements reveal that resistive switching on a macroscopic scale can be traced down to the insulator-to-metal transition of the independently switchable filaments.

The possibility to switch perovskite materials, e.g. $SrTiO_3$ (STO) between two different conducting states by application of an electrical field has attracted considerable interest [1] not only from a fundamental point of view, but also due to its technological potential for non-volatile resistive random access memories (RRAM). Our previous investigations have revealed the prototypic model system of STO single crystals as self-assembled system of closely packed bistable nanowires originating from a network of dislocations [2]. In this work, we extended this investigation to analyze the electrical conduction of ultra thin films of STO, here down to 10 nm, and to characterize the switching capability of such films from the nanometer to micrometer scale.

STO thin films with a thickness of 10nm have been grown epitaxially on $SrRuO_3$ buffered (100) STO substrates. Further detail s of the fabrication and the properties of the STO thin films have been published else-where [3]. A JEOL JSPM-4210A AFM set up equipped with Pt/Ir coated silicon tip operating in contact mode has been used to obtain simultaneously the topographica l and DC conductivity maps of the STO/SRO samples. All presented LC-AFM data are performed under vacuum conditions. Fig. 1a shows the conductivity map of a STO thin film. It depicts well-conducting spots with a density of $\sim$ 5 x 10^{11}/cm^2 imbedded in an insulating matrix. The spots visible in Fig. 1a have dimensions in the order of 10nm, but high resolution scans (Fig. 1b) reveal these patterns as bundles of spots with a diameter of 2-4nm. These nanosized spots are exits of conducting filaments which connect the surface to the conducting bottom electrode. According to their density, the filaments may be identified with dislocations [4].

We selected single spots on the surface and measured the current-voltage (I-V) curves by applying a DC voltage to the tip. Fig. 1c shows two different kinds of I-V curves measured on single-addressed spots in a voltage-driven mode with different current load. Both types of curves show a hysteresis but a completely different switching dynamic. The lower (blue) curve, recorded with a maximum current of 600nA switches between two branches with a similar non-linear I-V branch, resulting in a maximum ratio between the resitivities in high-conducting (on)- and low-conducting (off)-state (R_{on}/R_{off}) of 6. In contrast to it, the upper (red) curve in Fig. 1c recorded with a current compliance of 1μA, depicts switching between a linear on-state branch and a non-linear off-state branch. For this type of switching, a R_{on}/R_{off} of several orders of magnitude is obtained. The observed I-V curves can be well explained by regarding the conducting filaments as channels for easy diffusion for oxygen vacancies and location of a current-driven redox-process which induces a local metal-to-insulator transition [5].

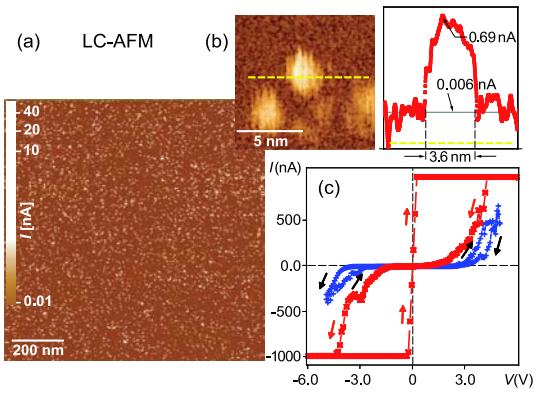

FIG. 1: A: Conductivity map (1μm x 1μm) of a 10nm thick STO thin film recorded by LC- AFM under vacuum conditions; B: Na noscale conductivity map (10nm x 10nm) and linescan performed along the dotted line; C: I-V- characteristics of 2 conducting spots with different current load;.

Within this model, the different switching curves shown in Fig. 1c can be attributed to different levels of reduction within the filaments. Only in the case where the amount of charge connected with the applied voltage is sufficient to completely reduce the filament, the on-state may be metallic (red curve). If the flowing charge is insufficient, parts of the filament remain semiconducting after reduction and cause a non-linear on-state branch in the I-V curve (blue curve).

In order to analyze the distribution of switching events on μm-scale areas and to simulate a macroscopic electrode, we recorded LC-AFM scans after polarizing the surface with a voltage bias of different amplitude and sign. Fig. 2a shows a LC-AFM scan which has been switched to the on- and off-state, respectively, on different scan areas. The density of filaments in these scans is so high, that the single filaments can not be resolved and the areas seem to be switched completely.

With respect to a deeper understanding of the current transport mechanisms in the different resistive states, information about the temperature dependence of I-V curves of individual filaments would provide a big step forward. Since the thermal drift of the tip prevents experimental access to this data for a single filament, we instead performed this measurement on large ensembles of filaments by statistically analysing current histograms of LC-AFM scans at different temperatures. The area below the histograms can be identified with the total current across a virtual top electrode with the dimension of the given scan area. Details of this analysis was explained in more detail in reference [3]. Since the filaments are statistically distributed in the sample, the thermal drift of the scan area has insignificant influence on the histograms.

The red curve in Fig. 2b shows the temperature dependence of the off-state current determined from the corresponding set of histograms. The noise level depicted in Fig. 2b was determined from a histogram recorded with a read-out voltage below the threshold for the observation of conducting spots and can be identified with the experimental noise of the LC-AFM I-V converter. It can be clearly seen, that the off-state current exceeds the noise level for all temperatures above 400K. The noise-subtracted off-state conductivity (blue curve in Fig. 2) which was determined from histograms at the corresponding temperature fits nicely to the Arrhenius law with an activation energy of 1.3eV.

The grey curve in Fig. 2b has been determined from current histograms of STO surfaces, polarized with a sufficient negative voltage to completely reduce the filaments. This procedure sets the filaments in the scan area to a linear on-state branch similar to the red I-V curve in Fig. 1c. Since the current determined from the corresponding histograms increases with decreasing temperature, the on-state is metallic and its conductivity exceeds the off-state conductivity by 4 orders of magnitude. These results prove that in case of a sufficient current transfer, the filaments are switched between a metallic on-state and a semiconducting off-state.

This scenario is an experimental upper limit for R_{on}/R_{off} with respect to a real macroscopic electrode, since scanning with LC-AFM gives a point-to-point galvanic contact on an atomic scale of the free surface and resembles a virtual, almost ideal macroscopic electrode. In real electrodes one has to take into account an imperfect contact with the sample surface or a preparation-induced damage of the interface. Even though many groups report about switching between two semiconducting branches with R_{on}/R_{off} in the order of 10 [1], a transition between metallic on-state and semiconducting off-state and a R_{on}/R_{off} of several orders of magnitude has already been realized with Pt-top electrodes [6].

In summary, evidence is given that the conduction of thin epitaxial films of STO is filamentary in nature. Depending on the charge transferred to the filaments, different types of hysteretic behaviour are observed. Maximum yield is reached by driving the filaments into the insulator-to-metal transition.

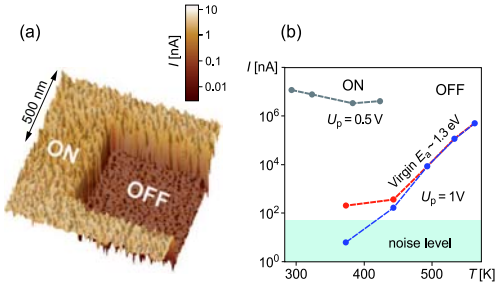

FIG. 2: A: LC-AFM scan of a 10nm STO thin film; The whole area is scanned with -6V and subsequently the inner area is scanned with +6V; B: Temperature dependence of the on-state (grey) and off-state current, determined from LC-AFM current histograms, with (blue) and without (red) noise subtraction (read-out voltage 0.5-1V; write voltage: 5-8V; erase voltage: 6V)

[1] A. Beck, J. G. Bednorz, Ch. Gerber, C. Rossel and D. Widmer, Appl. Phys. Lett. **77**, 139 (2000)K. Szot, R.

[2] K. Szot, W. Speier, G. Bihlmayer and R. Waser, Nature Materials **5**, 312 (2006)

[3] K. Szot, Dittmann, W. Speier, and R. Waser, Phys. stat. sol. (RRL) **1**, 2 (2007)

[4] S.H. Oh and C. G. Park, J. Appl. Phys. **9**5, 4691 (2004)

[5] K. Szot, W. Speier, W. Eberhardt, Appl. Phys. Lett. **6**0, 1190 (1992)

[6] K. Jung, H. Seo, N. Kim, Y. Kim, H. Im, J.-W. Park, M. K. Yang and J.-K. Lee, J. Korean Phys. Soc. **49**, 1071 (2006)

Liquid Injection Atomic Layer Deposition of $Pb(Zr,Ti)O_3$ Thin Films on Threedimensional Silicon Structures

T. Watanabe[1], S. Hoffmann-Eifert[1], R. Waser[1], C. S. Hwang[2], F. Dorn[3], A. Schwedt[3] and T. Weirich[3]

[1] Institute of Solid State Research and CNI-Center of Nanoelectronic Systems for Information Technology, Research Center Juelich, Germany
[2] School of Materials Science and Engineering, Seoul National University, Korea
[3] Central Facility for Electron Microscopy, RWTH Aachen Univerity, Germany

A liquid injection atomic layer deposition (ALD) process has been developed for conformal deposition of lead zirconate titanate thin films on three dimensional structured silicon substrates. Future applications of these structures address the field of non-volatile ferroelectric memory devices. PZT films were prepared by mixing the binary ALD processes of PbO_x, TiO_x, and ZrO_x. It was found that the type of precursors as well as the stacking sequence of the binary oxide layers is crucial for the control of film stoichiometry and for a saturation of the film growth behaviour characteristic for ALD processes. Using an optimized ALD process the molar ratios of Pb/(Ti+Zr) as well as Zr/(Ti+Zr) in the films show a saturation behaviour against an increasing precursor injection volume. $Pb(Zr_xTi_{1-x})O_3$ films deposited on 3D structured silicon exhibited a uniform film thickness and a homogeneous cation composition over the complex structure.

As the integration density of ferroelectric random access memories (FeRAMs) increases to >256 Mbit/chip, a conformal deposition of ferroelectric thin films over a 3-dimensional (3D) storage hole with a diameter <200 nm is required. However, ferroelectric thin films deposited by metalorganic chemical vapour deposition show a large distribution in the cation composition on complex structures [1], while the polarization switching property of ferroelectrics is the cation composition sensitive. This is an emerging issue for multi-component oxide films used on 3D structures in contrast to binary oxide, e.g., Ta_2O_5 for dynamic random access memory.

Atomic layer deposition (ALD) is characterized by the sequential gas supply process and the self-regulated growth rate per sequence. An ALD process typically consists of sequential precursor and reactant supply, and inert gas purges in between. The precursor molecule undergoes a chemisorption reaction with free bonds of the topmost surface molecules. Subsequently, in a purge turn, excessive precursors and reactants that did not contribute to the chemisorption are removed from the film's surface and pumped out of the reactor. As a result, these films show a constant growth rate defined by the chemisorption on the growing film surface even on wafers with a large dimension and complex nano-structures on the surface. In this work, we deposit quaternary $Pb(Zr_xTi_{1-x})O_3$ [PZT] films in a combination of binary ALD processes, aiming at a uniform coverage of 3D nano-structures both in the film thickness and the cation composition.

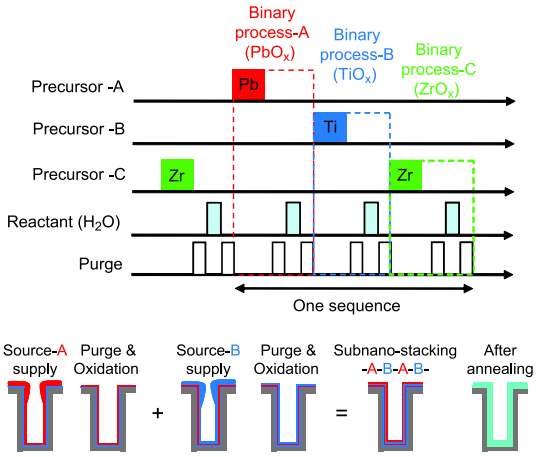

FIG. 1: Gas supply sequence for ALD of a quaternary oxide film (top) and schematic picture of the film growth process for a ternary film (bottom).

For this study, we configure a liquid-injection ALD tool, where precursor solutions are injected into a vaporizer kept at 200°C and thermally evaporated. Therefore, the precursors are not kept at high temperature to obtain high vapour pressure so that the lifetimes of the precursors are extended. This system expands the choice of precursors. The PZT films were grown by a liquid injection ALD tool with a horizontal cold wall reactor. One promising combination of precursors is $Pb(DPM)_2$, $Ti(O\mathit{i}\text{-}Pr)_4$, and $Zr(DPM)_4$ [DPM: $C_{11}H_{19}O_2$, dipivaloylmethanato; i-Pr: $CH(CH_3)_2$, iospropyl] dissolved in ethylcyclohexane (ECH) with a concentration of 0.1 M and water vapour. Before starting the multi-component ALD process, the thermal decomposition temperature was assessed for the all precursors via binary ALD processes [2, 3]. Since the ALD process is based on the chemisorption reaction, the molecular structures of the metalorganic precursors must be maintained as it reacts with the growing film's surface. For the ALD-PZT process, the deposition temperature was set at 240°C. This temperature is below the thermal

decomposition temperatures of all precursors mentioned above. Figure 1 shows the gas supply sequence used for the quaternary PZT-ALD process. The unit sequence was initially set as [(Pb-H_2O) - (Ti-H_2O) - (Zr-H_2O)]. Following this sequential gas supply, the saturation of film growth rate with increasing amount of injected precursor volume was examined changing the amount of injection of each precursor separately. Further experimental details are described in [3].

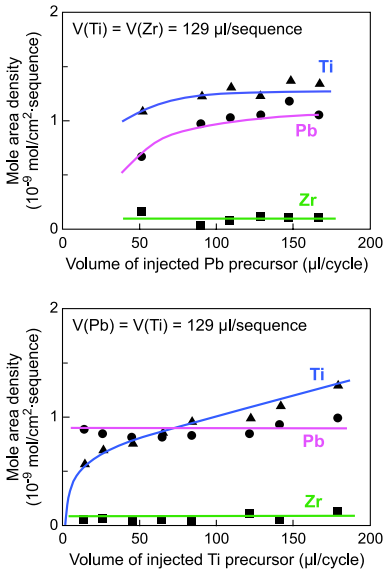

FIG. 2: Mole area density of each constituting element in the PZT film as a function of the input of the Pb solution (upper) and Ti solution (lower).

Figure 2 shows the deposition rate of each cation as a function of the volume of injected precursors. Two drawbacks can be identified which can be overcome by some modifications of the process: (1) the growth rate of Ti is not saturated against further increase of injected Ti precursor, and (2) A/B site composition and the Zr concentration in the PZT films have to be increased. All the other requirements for a saturated ALD type growth behavior were fulfilled. PZT films with Pb/(Zr+Ti)=1.1 were grown by a modified gas supply sequence presented as [2×(Pb-H_2O) - (Ti-H_2O) - (Zr-H_2O)].

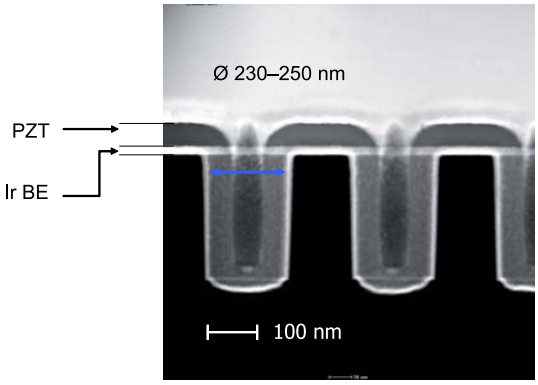

FIG. 3: Cross sectional TEM of a Pb(Zr,Ti)O_3 film deposited on a 3D silicon oxide structure pre-covered with an Ir bottom electrode layer.

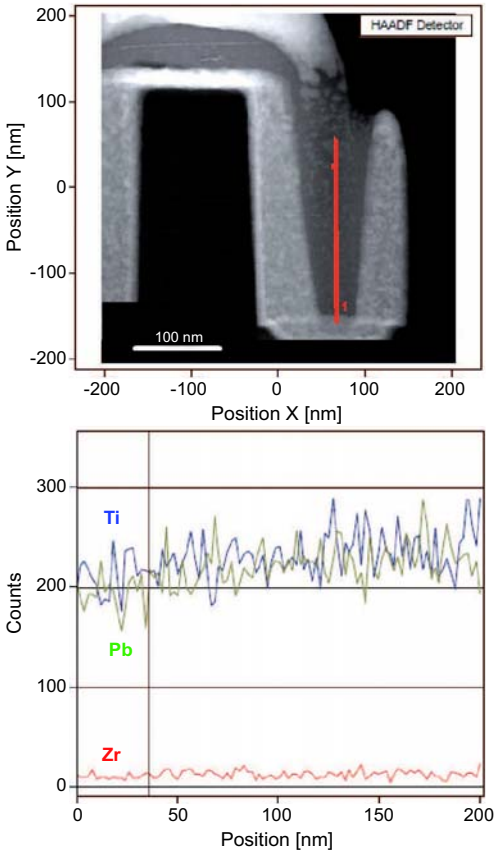

FIG. 4: STEM-EDS analysis of the cation composition uniformity in a 3D Pb(Zr,Ti)O_3 film. The lower figure demonstrate the result on the side wall as a representative of the three local EDS line scans shown in the upper figure.

Figures 3 and 4 show a cross sectional TEM picture and an STEM analysis of a PZT film deposited on a 3D structure pre-covered with Ir bottom electrode layer. The as-deposited PZT film was amorphous in accordance with XRD analysis. Although the process was not an ideally self-regulated one, the film thickness appears to be homogeneous (Fig.3) and the cation composition over the structure is nearly constant (Fig.4).

We conclude that the present set of precursors is promising for development of a future ALD-PZT process.

[1] A. Nagai, J. Minamidate, G. Asano, C.J. Choi, C-R. Cho, Y. Park, and H. Funakubo, Electrochem. Solid-State Lett. **9**, C15 (2006).

[2] T. Watanabe, S. Hoffmann-Eifert, S. Mi, C. Jia, R. Waser, and C.S. Hwang, J. Appl. Phys. **101**, 014114 (2007).

[3] T. Watanabe, S. Hoffmann-Eifert, R. Waser, and C.S. Hwang, 15th Inter. Symp. Appl. Ferro. Proc. (in press).

Resistive Switching of Rose Bengal Devices – a Molecular Effect?

S. Karthäuser[1], B. Lüssem[1], M. Weides[1], M. Alba[2], A. Besmehn[3], R. Oligschlaeger[4], R. Waser[1, 4]

[1] CNI-Center of Nanoelectronic Systems for Information Technology (IFF)
[2] Infineon Technologies
[3] Central Division of Analytical Chemistry
[4] Institut für Werkstoffe der Elektrotechnik II, RWTH-Aachen

The resistive switching behaviour of devices consisting of aluminium top electrode, molecular layer (Rose Bengal) and bottom electrode (zinc oxide, indium tin oxide) is examined. By measuring the current vs. voltage dependence of these devices frequency dependent and by systematically varying the composition of the device, we show that the switching is an extrinsic effect that is not primarily dependent on the molecular layer. It is shown that the molecular layer is short circuited by filaments of either zinc oxide or aluminium and that the switching effect is due to a thin layer of aluminium oxide at the zinc oxide/aluminium interface.

Switching effects in layers of organic molecules have already been known for more than thirty years [1]. Since then a wide variety of molecules have been proposed as basic materials for molecular memories. Recently, layers of Rose Bengal have been shown to switch resistively with high R_{OFF}/R_{ON} values, but the switching mechanism is still under discussion. Possible explanations are a change in electrical conjugation of the Rose Bengal molecule [2], a twist of the upper benzene ring [3], and the formation and breaking of metallic filaments. Similarly, some changes in the electrodes or the interface between the electrode and the molecular film can cause the resistive switching.

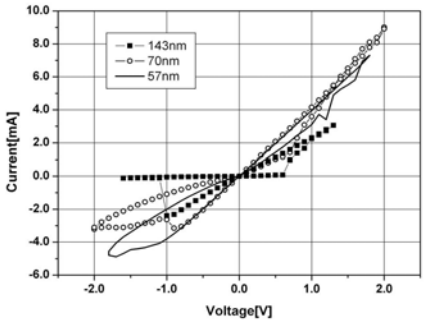

FIG. 1: IV characteristic of a layer of Rose Bengal (143nm, 70nm, 56nm) on ZnO with aluminium top electrodes.

To obtain layers of Rose Bengal, an ethanolic solution of Rose Bengal is spun onto zinc oxide or onto indium tin oxide (ITO) bottom electrodes at different revolutions per minute (rpm) resulting in varying film thicknesses (55nm - 143nm). For details of IV measurements and TOF-SIMS investigations see [4]. Figure 1 shows the IV characteristics of Rose Bengal layers with different thicknesses (143nm, 70nm, and 56nm). ON switching occurs at positive voltages, between 0.6V and 1V, and OFF switching at negative voltage (-1V). The ON state shows a linear IV characteristic, whereas the OFF state deviates from linearity at high voltages. For the (ZnO/143 nm RB/Al) device a R_{OFF}/R_{ON} ratio of 50 results. It can be seen from Figure 1, that R_{ON} has almost the same value for all thicknesses of the Rose Bengal layer, while R_{OFF} increases with increasing layer thickness resulting in a higher R_{OFF}/R_{ON} ratio.

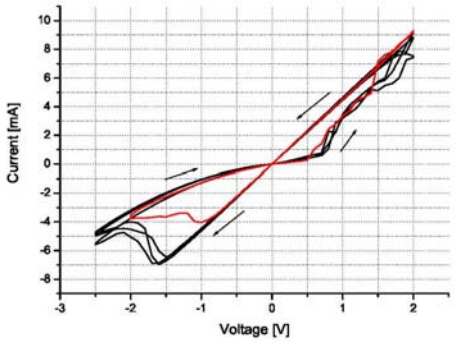

FIG. 2: Switching of a device consisting of ZnO, 5 nm Al_2O_3 and 80 nm Al. For comparison, a I/V characteristic of a ZnO/70nm Rose Bengal/Aluminium is shown in red. The characteristic of the switching is almost identical.

A systematic variation of the Rose Bengal device has been carried out by: substituting the ZnO bottom electrode by ITO, by changing the top electrode material and by changing the top electrode sizes (details see [4]). Generally, the switching of devices with ZnO and ITO bottom electrodes and with aluminium and titanium top electrodes show the same distinct features: the ON state is linear, whereas the OFF state deviates from linearity at higher voltages. The ON state resistance does not show a dependence on the pad size suggesting that the organic layer is short circuited in the ON state, most probably by conducting filaments between the electrodes.

To further verify that the switching effect we observe is strongly related to the switching of an oxide layer, the Rose Bengal layer is replaced by a 5 nm thick Al_2O_3 layer (Figure 2). Switching occurs in a very similar fashion: The ON state is linear, whereas the OFF state deviates from linearity and the ON switching occurs at lower voltages than the OFF switching pointing to the same switching mechanism. Furthermore even the same thickness dependence can be seen. A thicker aluminium oxide layer causes a higher resistance in the OFF state resulting in a higher R_{OFF}/R_{ON} ratio.

In addition SIMS depth profiles of the layered system Al/143nmRB/ZnO have been performed to investigate the interface between Al/RB and RB/ZnO, respectively and to gain information on the composition of the RB layer. This sample and reference systems were studied time dependent (details see [4]). In the fresh sample the O content within the Al is relatively high with respect to the Al which can be attributed to the specific properties of the Rose Bengal layer. One month after deposition (Fig. 3) the oxygen content within the RB layer decreases. The small hump at the Al/RB interface indicates the oxygen movement from the RB layer into the aluminium. This is a clear evidence for the oxidizing properties of Rose Bengal and indicates the formation of Al_2O_3 at the Al/RB interface.

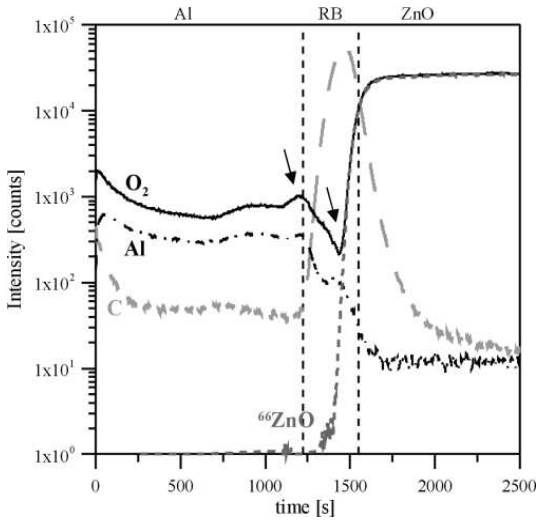

FIG. 3: Depth profile of a (Zn/143 nm RB/Al) device taken by TOF-SIMS one month after deposition.

The results presented here can be explained by the following model (Figure 4). In the ON state the molecular layer is short circuited due to paths of either aluminium or ZnO. This implies that the resistance of the device in the ON state is determined by the metallic path and thus independent of the molecular layer or thickness variations of the molecular layer. But, at least in the OFF state, a complete short circuit is avoided since at the contact of these paths with the opposite electrode, the aluminium is oxidized. This oxidation is analogous to the oxidation of an aluminium electrode which is directly deposited onto ZnO or ITO. But in case of a Rose Bengal layer located between the ZnO and Al electrodes, the oxidation of the Al electrode is enhanced due to the oxidation properties of Rose Bengal. However, although Rose Bengal does not directly originate the switching effect, it still has an indirect contribution. The R_{OFF}/R_{ON} ratio has been found to increase with increasing Rose Bengal layer thickness.

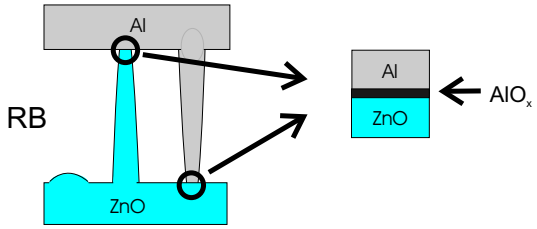

FIG. 4: Proposed model to explain the switching effect. The molecular layer is short circuited by either ZnO or Al filaments. At the Al/ZnO interface a thin layer of aluminum oxide is formed. Thereby, the switching is an effect of a thin aluminum oxide layer (compare figure 3) and thus not molecular.

We have shown that Rose Bengal thin films sandwiched between a ZnO or ITO bottom electrode and aluminium or titanium top electrode show resistive switching. By leaving out the molecular layer and depositing aluminium directly onto ZnO, we are able to exclude the molecular layer to generate the switching. It is proposed that filaments of either aluminium (titanium) or ZnO (ITO) grow through and short circuit the molecular layer. At the interface of ZnO and aluminium (titanium), a thin layer of aluminium oxide (titanium oxide) is formed. Due to the strong similarity of the switching of the Rose Bengal devices to the switching of an Al_2O_3 layer and due to the enhanced Al_2O_3 signal at the RB/Al interface obtained with TOF-SIMS, it is suggested that the switching is completely extrinsic, i.e. generated by the thin aluminium oxide layer at the interface.

[1] A. R. Elsharkawi, K. C. Kao, J. Phys. Chem. Sol. **38**, 95 (1977).

[2] A. Bandyopadhyay, A. J. Pal, J. Phys. Chem. B **107**, 2531 (2003).

[3] A. Bandyopadhyay, A. J. Pal, Appl. Phys. Lett. **84**, 999 (2004).

[4] S. Karthäuser, B. Lüssem, M. Weides, M. Alba, A. Besmehn, R. Oligschlaeger, and R. Waser, J. Appl. Phys. **100**, 094504 (2006).

Nanoimprint Lithography for Crossbar Arrays

M. Meier[1], C. Nauenheim[1], M. Prömpers[2], D. Mayer[2], C. Kügeler[1], R. Waser[1]

[1]CNI-Center of Nanoelectronic Systems for Information Technology (IFF)
[2]CNI-Center of Nanoelectronic Systems for Information Technology (IBN)

Nanoimprint lithography (NIL) is a powerful lithography method in the field of nanotechnology. Due to its high throughput, sub 10 nm resolution and low cost NIL is able to combine the advantages of conventional photo lithography and e-beam lithography in one tool [1]. In principle NIL works with a mold, which is pressed on a resist coated wafer to transfer the molds pattern into the resist layer. Now, we present first results of imprinted structures with a resolution of around 50 nm. Therefore thermal NIL as well as UV NIL is used. The molds are fabricated with e-beam lithography and reactive ion beam etching (RIBE).

Concerning the limits of conventional lithography methods for the realisation of nanostructures, it is necessary to focus on an alternative tool. With nanoimprint lithography (NIL) it is possible to overcome the resolution limit of optical lithography in a high throughput process. Our aim is to realise nanocrossbar arrays for logic and memory devices with NIL [2]. Therefore it is aspired to imprint a couple of parallel wires scaled with a few nanometers as well as rectangular contact pads in the range of microns within one step only (Fig. 2).

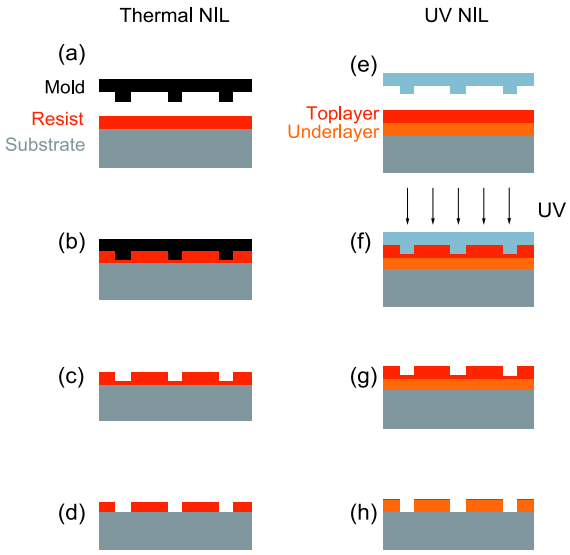

FIG. 1: Process flow of thermal NIL and UV NIL

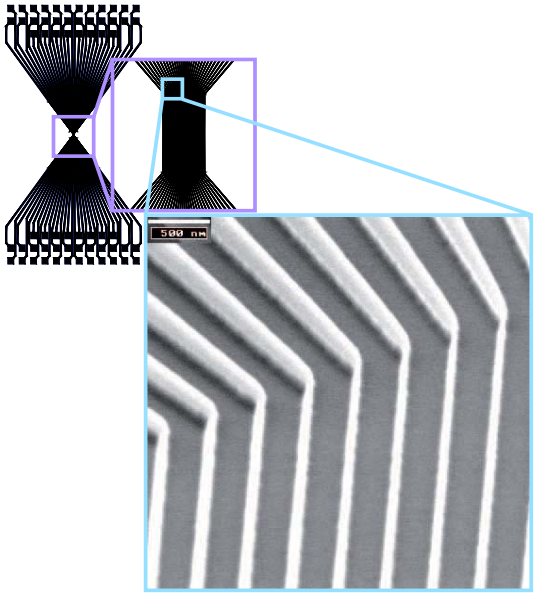

FIG. 2: SEM image of a thermal NIL mold fabricated with e-beam direct writing and reactive ion beam etching (line width $<$ 100 nm). The structure which was chosen for the image is schematically shown on the top. It pictures the bottom layer of a crossbar array structure (bottom electrode). Parallel lines in the dimension of nanometers define the centre of the array. Contact pads are needed for the electrical characterisation. The connection between the nanowires and the contact pads is realised by the so called fan out.

Dealing with NIL, it needs to be distinguished between thermal NIL and UV NIL. These two principles and their differences are shown in Figure 1. In both cases imprint resist is spun on a substrate (Fig. 1a and Fig. 1e). In a thermal imprint process, the resist is heated above its glass transition temperature (T_g) and at the same time the mold is pressed into the resist layer (Fig. 1b). Thus the resist gets deformed. Before removing the mold from the substrate the sample is cooled down below T_g, so that a replica of the mold stays in the hardened resist layer (Fig. 1c). In a final step the residual layer on the bottom of the imprinted trenches needs to be removed, typically within a dry etching process (Fig. 1d). For a UV imprint process a bi layer structure of resist is required. The top layer is photoactive whereas the under layer is more stable against etch processes and therefore suitable as etch mask. While pressing

the transparent mold into the resist on the substrate the top layer resist is crosslinked by applying UV light (Fig. 1f). After the release of the mold from the cured resist, the pattern is left in the top layer (Fig. 1g), so that the under layer can get structured in a final dry etching process (Fig. 1h). The most important advantage of UV NIL in comparison to thermal NIL is that there is no thermal impact during the process. Hence it is possible to handle temperature sensitive materials like organic molecules for example.
In the experiments a Nanonex 2000 imprint system is used for thermal NIL as well as UV NIL. The molds for thermal NIL are fabricated from silicon substrates with a silicon dioxide layer on the top which is structured by e-beam lithography and reactive ion beam etching (RIBE). Structures with a feature size of less than 100 nm and a height of around 110 nm are achieved (Fig. 2). Some results of thermal imprint are shown in Figure 3. Very homogeneous nano lines and at the same time large rectangular structures (e.g. contact pads) are nicely transferred into the resist within one step. During the imprint process the temperature and the pressure are set to 150°C and 200 psi respectively.

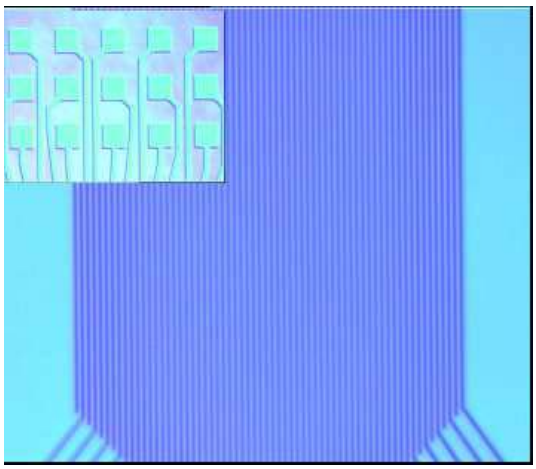

FIG. 3: Optical microscope image of a structure, which was realised in a thermal NIL process (line width 500 nm). On the top are shown rectangular structures (100 μm$\times$ 100 μm contact pads), which are also printed very homogenously.

The molds for UV NIL are fabricated on transparent quartz glass substrates. Due to charging effects during e-beam direct writing it is necessary to evaporate a thin titanium layer on the quartz wafer. After e-beam lithography the metal layer is patterned by RIBE and acts as a hard mask in the following dry etch process to transfer the nanopattern into the substrate material. By this approach an UV imprint mold with structures in the range of 500 nm down to 50 nm and a depth of 100 nm to 200 nm can be realised.
It is beneficial to evaporate an anti adhesion layer (typically perfluorosilane) on the surface of the mold, to ensure a successful release of the mold from the substrate after the imprint process. Figure 4 shows a SEM image of UV imprinted lines with a resolution below 100 nm. The sidewalls of the structures are very steep, smooth and the aspect ration looks convincingly. Furthermore structures with a resolution down to 50 nm are achieved with UV NIL as it can be observed in Figure 5. At 20 °C a pressure of 550 psi is typically applied to press the mold into the photo curable resist.

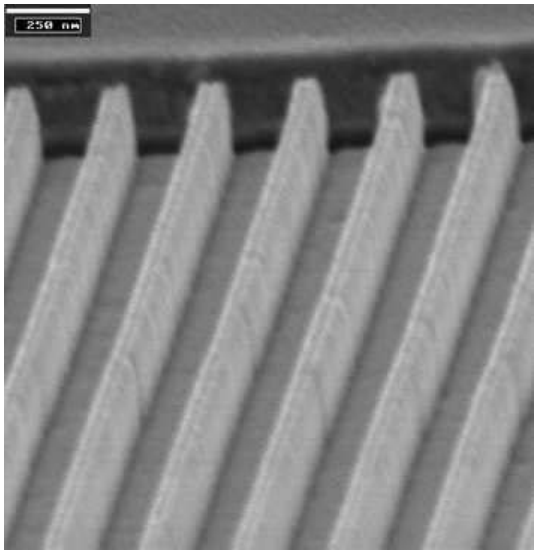

FIG. 4: SEM image of UV imprinted structures. The resolution is below 100 nm with steep sidewalls and a high aspect ratio.

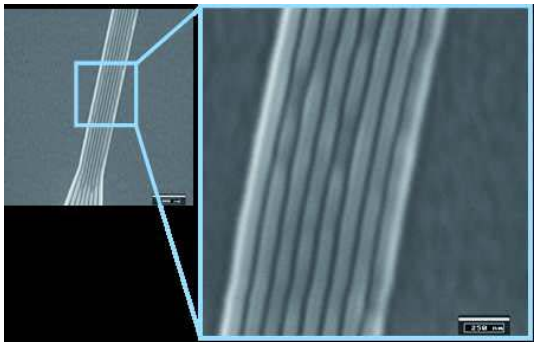

FIG. 5: SEM image of UV imprinted structures. The line width is around 50 nm.

In conclusion we present the fabrication of molds for thermal and UV nanoimprint lithography by e-beam direct writing and reactive ion beam etching. Using those molds we realised structures down to 50 nm whereas at the same time large feature sizes in micrometer range are also imprinted.

[1] S. Y. Chou, P. R. Krauss, P. J. Renstrom, J. Vac. Sci Technol. B **14(6)**, Nov/Dec (1996)

[2] G. Y. Jung, S. Ganapathiappan, D. A. A. Ohlberg, D. L. Olynick, Y. Chen, W. M. Tong, R. S. Williams, Nano Letters Vol. **4**, No. 7 1225 - 1229, (2004)

A Novel Reference Scheme for Reading Passive Resistive Crossbar Memories

J. Mustafa[1], R. Waser[2]

[1] Institut für Werkstoffe der Elektrotechnik II, RWTH Aachen
[2] CNI-Center of Nanoelectronic Systems for Information Technology (IFF)

A great effort today is concentrated on the development of resistive hysteretic materials and their related memory architecture. Resistive memories have a promising future to replace all current memory technologies to present an all-in-one memory solution. Passive resistive memories are of a special importance since they can be scaled into the nanometer range without losing their functionality. This work is concerned with a novel scheme for generating reference voltages for the read operation. The scheme can be used with any passive crossbar based memory, regardless of the materials used for the implementation of the memory elements.

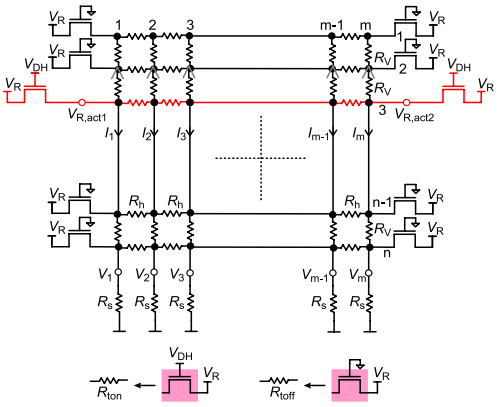

FIG. 1: Real crossbar array with row access transistors and sense resistors.

A crossbar resistive memory consists of vertical and horizontal conductive lines with a hysteretic resistive material separating them at the cross points. In a real crossbar, the resistances of the interconnects, the sensing elements, and the voltage source/s required for the read operation are considered as shown in Fig. 1.

To realize the read operation, voltage is applied to the rows using NMOS row access transistors which have an equivalent on-resistance R_{ton} when switched on and an equivalent off-resistance R_{toff} when switched off. R_{ton} and R_{toff} are considered to have values in the order $10^3\Omega$ and $10^7\Omega$ respectively [1]. Due to the voltage drops at the interconnects, the sensing elements and since the non-accessed cells are not isolated, parasitic currents will flow through the memory cells in the non-accessed rows. In addition, the resistance of the row access transistors will reduce the actual read voltage V_{Ract} applied to the row because they construct a voltage divider with the equivalent resistance of the rows.

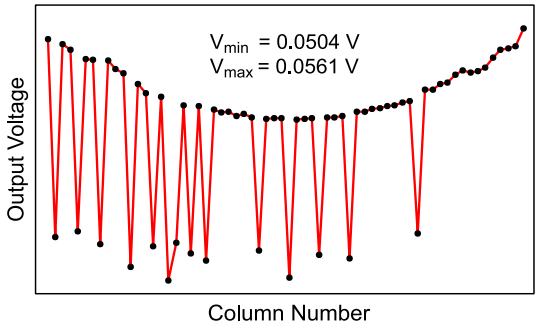

FIG. 2: Simulation result of a row from a 64x16 crossbar array considering the parasitic elements and a 0.8 probability of the "1"s.

The non-accessed rows are left open which means that the row access transistors are turned off and have an equivalent resistance of R_{toff}. To reduce the voltage degradation, voltage is applied from both sides of the array. The output voltages resulting from reading a row of a 64x16 bit array are shown in Fig. 2. The simulation parameters are $V_{\mathrm{R}} = 1$V, $R_{\mathrm{on}} = 10k\Omega$, $R_{\mathrm{off}} = 40k\Omega$, $R_{\mathrm{h}} = 10\Omega$, $R_{\mathrm{v}} = 10\Omega$, $R_{\mathrm{ton}} = 5k\Omega$, $R_{\mathrm{toff}} = 10M\Omega$, and $R_{\mathrm{s}} = 10k\Omega$. R_{on} and R_{off} are the resistances of the memory cell element in the "on" and "off" states respectively. R_{h} and R_{v} are the resistances of the horizontal and vertical interconnects between two adjacent cells respectively. The last parameter R_{s} is the value of the sense resistor. The pattern stored in the array is a random pattern with 0.8 probability of the "1"s.

It is obvious from the previous simulation that the output voltage levels are degraded when the parasitic resistances of the different memory elements are considered. Thus, it is not possible to use a constant reference voltage to differentiate between a "1" and a "0" especially if we considered that the voltage levels will change by changing the stored pattern. Since the degradation is severer for larger arrays, it will be a limiting factor for the maximum obtainable array size. Thus, an alternative method for generating a reliable reference voltage is required.

The cells in one row are locally strongly correlated re-

gardless of the values of the sense resistors, parasitic resistances of the different elements, or the stored pattern. This locality can be utilized to generate a reference voltage by dedicating some cells from each row to act as reference cells[2].

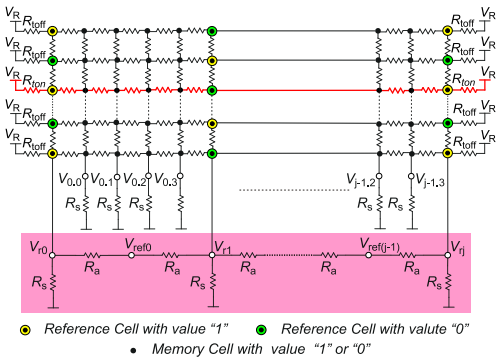

FIG. 3: The crossbar array after inserting reference cells and reference generating capacitors or resistors.

In this new reference scheme every two horizontally adjacent reference cells generate a local reference voltage for the cells between them as can be seen in Fig. 3. The number of the reference cells is determined depending on the grade of degradation of the output voltages. Higher voltage degradation will require more reference cells.

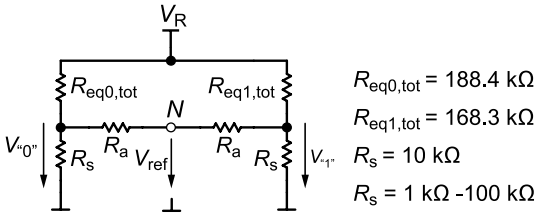

FIG. 4: Simplified equivalent circuit for generating the reference voltage by using resistors and real simulation results.

The values stored in the reference cells in a row are "1" and "0" (low and high ohmic) alternately. The first and last cells in a row are always reference cells. The horizontal position of the reference cells is identical in all rows, which constructs columns of reference cells (reference columns). Vertically adjacent reference cells have also values of "0" and a "1" alternately. Reference cells are physically the same as normal memory cells; however they are preprogrammed with constant values to generate reference voltages. An ideal reference voltage would be the average value of the "1" and "0" voltage levels. To generate the local reference voltages, every two adjacent reference columns are connected together using two identical resistors (R_a) as can be seen in Fig.3. The equivalent circuit of any two adjacent reference cells in any row is shown in Fig. 4.

The values of the used resistors Ra are not critical. To illustrate this, the total equivalent resistance connected to the two sense resistors is calculated from the voltage drops on them. After that, the effect of sweeping the value R_a on the voltages $V_{\text{"1"}}$, $V_{\text{"0"}}$, and V_{ref} is investigated. Which "1" or "0" is chosen from a row does not impose any restrictions on this concept. Thus we will consider the voltages of the "1" with the highest voltage and the "0" with the lowest voltage in Fig. 2. These voltages are 56.1mV and 50,4mV respectively which correspond to the equivalent resistances of 168,3 kΩ and 188,4 kΩ connected to the sense resistors as shown in Fig. 4. The simulation results obtained by sweeping the value of R_a from 1kΩ to 100kΩ are shown in Fig.5. As can be seen, $V_{\text{"1"}}$ and $V_{\text{"0"}}$ are degraded especially for small values of R_a but the reference voltage stays practically constant.

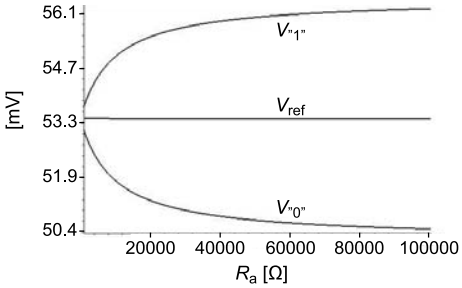

FIG. 5: Simulation results of sweeping the value of Ra from 1kΩ to 100kΩ.

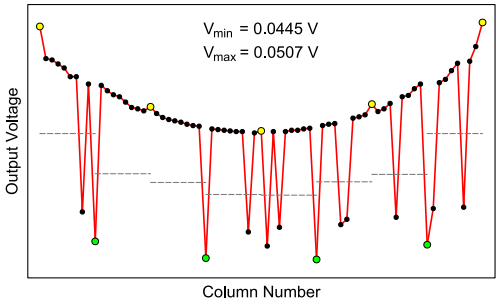

FIG. 6: The crossbar array after inserting reference cells and reference generating resistors.

Fig.6 shows the output voltages resulting from reading a row from 64x16 bit logical memory, which is physically 73x16 crossbar array after inserting the reference cells. In this simulation every ninth cell is a reference cell. The parameters used are the same as in the simulation in Fig.2. The large circles indicate the positions of the reference cells and the horizontal lines represent the local reference values generated from the reference cells. It can be clearly seen, that the reference values are adjusted according to the degradation of the output voltages. This yields a reliable read operation due to the higher voltage margin between the voltage levels of the "1"s and "0"s and their corresponding reference voltage.

[1] International Technology Roadmap for Semiconductors, 2005 Edition.

[2] J. Mustafa, R. Waser, A Novel Reference Scheme for Reading Passive Resistive Crossbar Memories, IEEE Transactions on Nanotechnology, Vol. 5, Issue 6, pp. 687-691, November 2006.

Integration of Resistively Switching TiO_2 Cells into Micro Crosspoint Cells

C. Nauenheim[1], C. Kügeler[1], A. Rüdiger[1], R. Waser[1,2]

[1] CNI-Center of Nanoelectronic Systems for Information Technology (IFF)
[2] Institut für Werkstoffe der Elektrotechnik II, RWTH Aachen

Non-volatile resistive switching binary cells of TiO_2 for memory applications are arranged in micro crosspoint and crossbar array form. This represents a first preliminary model for fabrication processes of nano crossbar arrays as proof of concept. These photolithography-fabricated devices are furthermore electrically measured by static I-V measurements. The results offer first insights into the general properties of passive two terminal devices arranged in crossbar arrays, as well as it contributes to the examination of the suitability of TiO_2. The determined resistance values and switching voltages point out the demands for arrays sizes and peripheral control logic.

The improvement of performance in information technology is a continual demand leading to a permanent enhancement of Moore's Law. To establish future ultra fast logic systems and high memory densities, the constant reduction of technology nodes far into the sub 32nm region will become a necessity. This is associated with an increasing number of technological and physical limits which, in turn require defect and failure tolerant systems based on reconfigurable devices. The 'Fat Tree' structure in combination with a 'Logic Array Based Architecture' implemented in the Teramac Concept by HP is a first paradigmatic change in this direction [1].

Our attempt is the development of a rewritable non-volatile memory cells in combination with a resistively switching material. These switches have also the potential for future investigations of diode resistor logic which is not addressed yet here. Aside from solid state electrolytes, organic charge transfer materials or molecular monolayers, binary oxides like TiO_2 are switching materials which seem to be suitable for this purpose [2]. Above all, this is justified by their thermal stability and simple compatibility with other materials, which is important for the combination with CMOS in a hybrid structure. The latter offers also an integration into a two terminal device that is automatically created at every junction of a crossbar array. These arrays with their perpendicular arranged set of simple parallel electrode lines, shown in Fig.1, present an appealing application for new fabrication methods like Nano Imprint Lithography, for example [3]. Additionally, theoretical approaches for the use of switching arrays in logic posses a prospect of logic and memory applications exclusively fabricated of these devices [4,5].

Resistive switches for memory applications show at least two resistive states, in which every state represents a binary value. Writing or erasing the information or the bit is performed by changing the state of a junction while exceeding a certain threshold voltage. Reading the information can be accomplished by applying a smaller voltage and measuring the resulting current without influencing the preassigned condition of the device. To reliably distinguish these states it is important achieve a stable ratio between R_{ON}/R_{OFF} with at least one to two orders of magnitude. Because the device is voltage controlled, its smallest resistance should also be considerably larger than the interconnect resistances to achieve a sufficient voltage drop and to reduce the influence for nearby cells in a high resistive state.

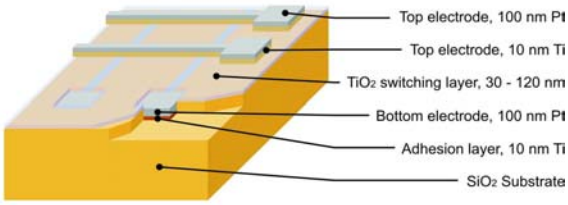

FIG. 1: SEM picture of an eight by eight bit micro crossbar. The width of the strip line amount to 1 μm which results in a cell size of 1 μm^2. The pitch of two adjacent lines is 1.5 μm.

For our first studies we composed a micro crossbar array. The 100nm thick Pt bottom-electrode is either buried in a SiO_2 substrate to reduce surface roughness or structured on top of the SiO_2 surface. As shown in Fig.2, we apply 30nm up to 90nm thick TiO_2 layers via reactive sputter deposition. This layer covers the whole sample surface and requires no further alignment. To gain a certain asymmetry at the interface between electrode and switching material, what we assume as necessity for a stable switching behavior, we deposited a 10nm thick Ti top-electrode under a second 100nm thick Pt electrode. The sample fabrication concludes with the uncovering of the contact pads of the bottom-electrode by a dry etching step. The generated samples contain single crosspoint structures for electrical characterization without any crosstalk as well as whole arrays with up to 8 by 8 bit and different cell sizes down to 1μm^2.

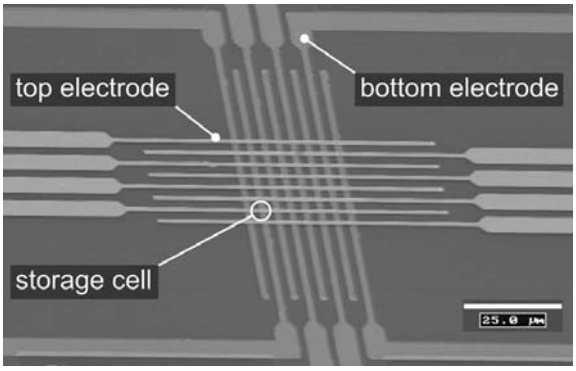

FIG. 2: Schematical assembly of a crossbar structure

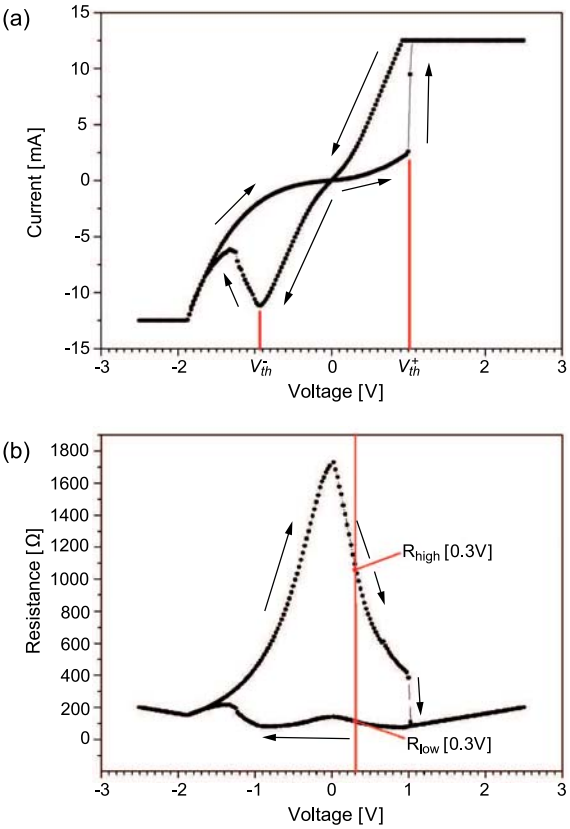

FIG. 3: (a) Static I-V trait of a binary cell with an area size of 5 × 7.5 μm^2 and a TiO_2 layer thickness of about 90 nm. Plotted are the measured currents against the predefined voltage values (current compliance set to 12.5mA). (b) R-V curve of the described I-V curve. The occurring resistance ratios represent up to more than one order of magnitude near the zero point. The red bar indicates the 0.3 V response that is used for read performance illustrations.

The single cells cycle through a closed switching I-V loop (Fig.3a) with two different resistive states (Fig.3b). Both indicate non-ohmic behaviors and are highly voltage dependent. The resistive state is changed by passing the appropriate threshold voltage. But by disconnecting the device from any voltage supply, the system remains in its resistive state and is considered as non volatile. However, long-term studies about the loss of information are still under investigation. The low resistive state is in the range up to several hundred ohm and switches stepless into the high resistive state. The latter exhibit a wide resistance range from several hundred ohm up to beyond thousand ohm for small voltages. Crossing the threshold voltage with a positive polarization at the Ti electrode results in an abrupt change of the resistance state. The current response varies analogical up to several milli amperes in the low resistive state, but it has to be limited by a current compliance to prevent an unintentional overstress. Our long-time investigations were also performed by static I-V measurements. Fig.4 displays every hundredth value of this measurement series. Whereas we present an exemplary read value determined at 0.3V showing an adequate R_{on}/R_{off} ratio. The last pair was taken at the 4800^{th} cycle after the break down of the cell.

The presented work is, as introductory mentioned, a first attempt with the objective of nano integration processes for crossbar arrays. For the time being, some material parameters will be optimized. The occurring threshold values for switching are sufficient. Although the maximum current values seem to be large, scaling down the crossbar system to the nanometer range by the usage of technologies like e-beam direct writing or nanoimprint lithography promises to reduce these values by orders of magnitude. This is appropriate for external CMOS amplifiers as well as other related circuit elements.

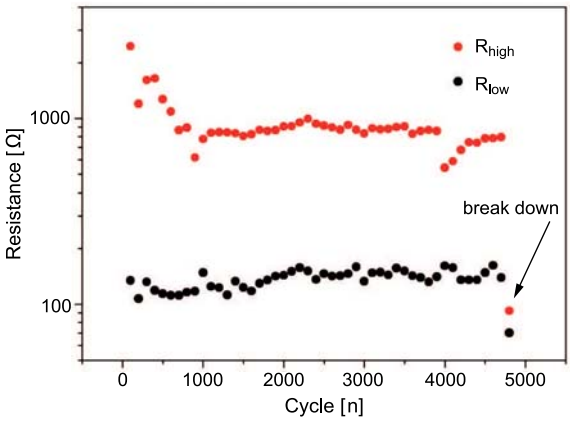

FIG. 4: Evaluation of a long-term static measurement. The cell is statically cycled with a voltage driven bipolar triangular signal. The presented values are extracted at 0.3 V. The first value is the initial state which contains no bistable switching but an open loop causing two different currents depending on the raising or falling of the voltage signal. The last points indicate the break down of the switching behaviour which is nearly static state.

[1] J.R. Heath, P.J. Kuekes, G.S. Snider, R.S. Williams, Science, **280**, pp.1716-21 (1998)

[2] M.D. Austin, H. Ge, W. Wu, M. Li, Z. Yu, D. Wasserman, S.A. Lyon, and S.Y. Chou, APL, **84**, 5299-301 (2004).

[3] H. Pagnia, N. Sotnik, Phys. Stat. Sol. (a), **108**, 11-65 (1988)

[4] G.S. Snider, P.J. Kuekes, T. Hogg, and R.S. Williams, Appl. Physics A, **80**, pp.1183-95 (2005)

[5] M.M. Ziegler, M.R. Stan, IEEE Trans. Nanotechnology, **2** (4), pp.217-30 (2003)

Bistable Resistive Switching of Atomic Layer Deposited (ALD) TiO_2 Thin Films

L. Yang, T. Watanabe, C. Kügeler, A. Rüdiger, R. Waser

CNI-Center of Nanoelectronic Systems for Information Technology (IFF)

Bistable resistive switching was found in atomic layer deposited TiO_2 thin films (60 nm) sandwiched between a Cu top electrode and a Pt bottom electrode. Bistable switching between a high ohmic and a low ohmic state is observed at low voltages (<2V) for more than 2000 continuous switching cycles.

Bistable resistive switching is intensively researched in many materials for its possible application to fabricate high density non-volatile memory devices. Binary transition metal oxide thin films such as TiO_2, NiO, Al_2O_3 exhibit such electric field induced resistive switching behaviour between a high resistance state (off) and a low resistance state (on) [1-3]. For future applications such memory devices should operate at low voltage and low current.

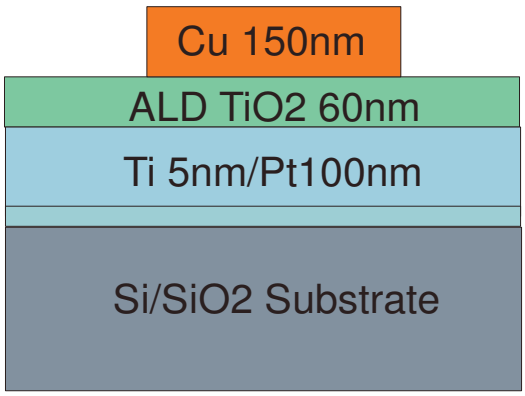

FIG. 1: Schematic of the lateral sample structure and the film compositions.

Fig. 1 describes the sandwich structure of the samples. A 5 nm Ti adhesion layer and a 100 nm Pt layer are evaporated on an oxidized Si wafer. Then 60 nm TiO_2 are deposited by atomic layer deposition at 240°C followed by 150 nm Cu top electrodes fabricated by evaporation and lift-off technique.
Electrical measurements are performed with an Agilent semiconductor parameter analyzer B1500A in combination with a Süss probestation at room temperature. There are two kinds of switching found in those samples - low current switching from several μA to about 120 μA and high current switching about 30 mA. Fig. 2 shows a typical low current I/V measurement. During the measurement the Pt is connected to ground. The arrows and the number describes the voltage sweep direction. The voltage applied to the Cu top electrode sweeps first from 0 V forwards to 1.3 V. At about 0.5 V the current jumps instantaneously from high resistive state to low resistive state. The maximum resistance reaches 10^8 Ohm, whereby the low resistance state is stable at about 6000 Ohm. In order to avoid a breakdown of the samples a compliance current (CC) is used to limit the maximum current flowing through the thin film. Therefore the rising resistance between 0.4 V and 1.3 V and the constant current are an artifact of this compliance current of the measurements equipment. The state of resistance can be toggled by applying a reverse voltage.

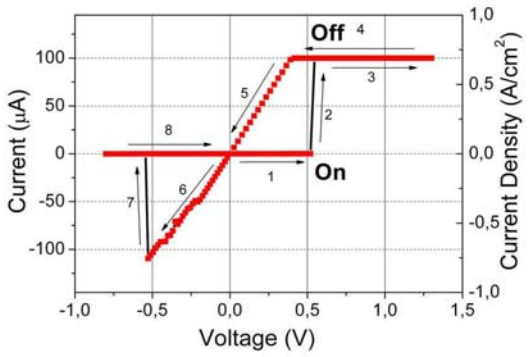

FIG. 2: Typical I/V curve measured on ALD TiO_2 thin films at room temperature.

Fig. 3 illustrates clearly a stable "on" resistance during stage 5 and 6 until the voltage reaches about -0.5 V, whereby the low resistance state jumps to the high resistance state more than 2 orders of magnitude.

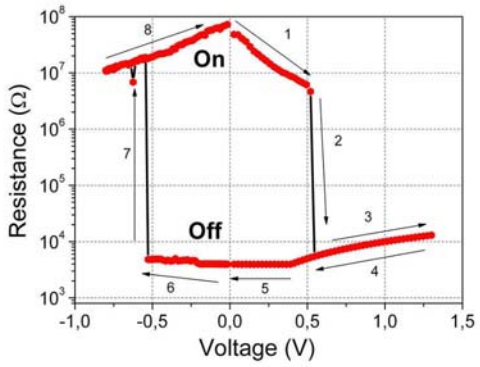

FIG. 3: Typical R/V curve measured on ALD TiO_2 thin films at room temperature.

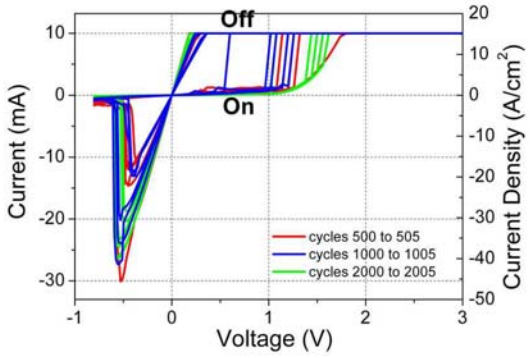

FIG. 4: Three groups of I/V curves from the 2000 consecutive switching measured on the ALD TiO_2 films at room temperature.

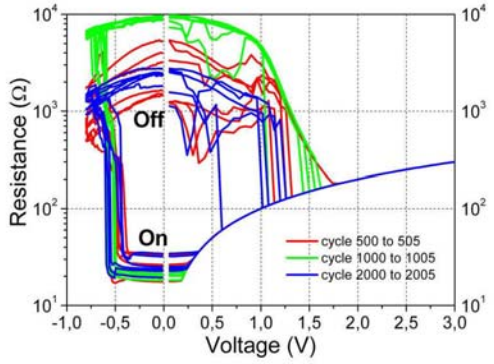

FIG. 5: Three groups of R/V curves from the 2000 consecutive switching measured on the ALD TiO_2 films at room temperature.

Fig. 4 and 5 show the typical I/V and R/V characteristics of the high current switching. More than 2000 consecutive switching cycles could be performed. Their resistance of the "off" state can be more than 10^4 Ohm (not shown here) and the resistance of "on" state is very low only about 20 Ohm. The ration of the R_{off}/R_{on} is about 3 orders of magnitude and the threshold voltage by switching "on" and switching "off" are low and well-defined. R_{on} varies only in a small range between 20 Ω to 40 Ω and the threshold voltages to switch "on"- to "off"- state are around -0.5 V. In contrast the stable R_{off} varies in a relatively large range, from $10^3\Omega$ to 10^4 Ω, and consequently the threshold voltage is between 0.5 V and 1.8 V. Fig. 5 illustrates the threshold voltage for switching "off" to "on" depending on the R_{off}. A lower "off" resistance (e.g. switching cycles 2000 to 2005, blue lines) leads to a lower threshold voltage. One possible explanation might be, that a high initial R_{off} is combined with only few conductive locations in the film. So in this case a higher Roff needs a higher threshold voltage to induce a sufficient amount of Cu ions before the material switches in "on" state.

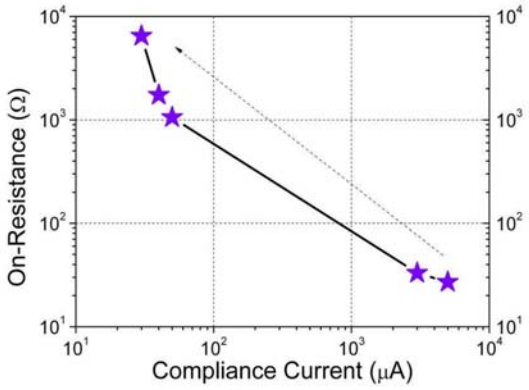

FIG. 6: Compliance current has a great influence on the On resistance (via diameter 140 μm^2).

The compliance current dependence of the "on" resistance is illustrated in Fig 6. Five consecutive measurements are performed with a decreasing compliance current from 5mA to 30μA, which is indicated with the dash arrow. The "on" state resistance difference induced by different compliance currents is more than 2 orders of magnitude comparing the resistance at 5mA to 30μA CC. Such muti-level-capability of the structure is maybe the reason that low and high current switching is found in the same ALD TiO_2 film.

Low power switching of TiO_2 thin films is observed whereby two distinguish resistance states can be switched reversibly. Further investigations will be done to improve their stability and endurance to explore the great potential of integrating TiO_2 into nanoscale memory devices.

[1] F. Argall, Solid-State Electron. **11**, 535 (1968).

[2] T. W. Hickmott, J. Vac. Sci. Technol. **6**, 828 (1969)

[3] J.-W. Park, J.W. Park, D.Y. Kim, and J.K. Lee, J. Vac. Sci. Technol. **A23**, 1309 (2005).

A part of the IFF activity is devoted to the development of novel scattering techniques and the construction and continuous improvement of instruments at large facilities.

Large-Scale Facilities for Research with Photons, Neutrons and Ions

This research programme coordinates the activities taking place at the large scale facilities involved in the HGF research field Structure of Matter. These facilities offer unique research opportunities with photons, neutrons and ions for a multitude of science disciplines, ranging from physics, chemistry, biology and geology to material science, engineering science, and environmental research. A particular feature of this programme is the support of external user groups, which utilize the major part of the available access time. These user groups come mainly from universities, but also from non-university research institutions and industry.

With its excellence in neutron research – manifested in the Jülich Centre for Neutron Science (JCNS) – the IFF supplies a key contribution to this research programme. The strong reputation of the IFF in the German and international neutron landscape is closely related to:

- a powerful in-house research in the area of condensed matter focusing particularly on soft matter and magnetism,
- a large user operation in these research areas being extensively supported by IFF experts and facilities,
- a science-driven programme for the development of new methods and instruments, and
- exploitation of the novel neutron research opportunities provided by pulsed MW spallation sources.

The IFF neutron research is carried out to a large extent at the new state-of-the-art research reactor FRM II in Munich and at the ILL in Grenoble (France), with new opportunities being created at the SNS spallation source in Oak Ridge (USA). These activities are a cornerstone of the HGF programme "Condensed Matter Physics" and provide important contributions also to other HGF programmes, such as "Information Technology with Nano-electronic Systems".

POWTEX: A High Intensity Time-of-Flight Diffractometer at FRM II for Structure Analysis of Polycrystalline Materials

H. Conrad, J. Voigt and Th. Brückel

Institute for Scattering Methods

In order to provide the large chemistry and materials science communities with a powerful tool for rapid data acquisition, a time-of-flight diffractometer to be installed at the new Munich reactor has been designed. The time-of-flight technique is expected to outperform a monochromator instrument by an order of magnitude in intensity on particularily small samples of less than a cubic centimeter. The construction of this innovative type of diffractometer utilizes modern neutron components such as focusing super mirror neutron guides, a 4-unit high speed disk chopper system and linear position sensitive detectors covering a solid angle of about 3 steradian. The diffractometer design enables an easy enlargement of the focal spot size and is therefore equally well suited for the texture analysis of large geological and archeological samples.

Fundamental objectives of solid state chemistry and materials science are the development of new materials, their analytical characterizations and studies of their structures and properties. For that purpose preparative methods have to be directly related to structure determination, since this is a prerequisite for designing materials of specific properties.

Demands of solid state chemists for a neutron diffractometer are a suitable d-spacing resolution ($\delta d/d \cong 0.5\%$), a d-spacing range of about 0.5 Å to 15 Å and high intensity on small samples ($<$ 0.5 cm^3). Even more important is a short-term access to the instrument without a lengthy proposal system and local services for both experiment and data analysis. The material and not the experiment is always the focus of the interest.

A central aspect of geological research is focused on plate tectonics, i.e. relative movements in the lithosphere. Those movements are connected to faults and shear zones where rocks have been deformed temperature dependently. Mineral grains are affected by these deformation processes in forming preferred crystallographic orientations, the so-called texture. Rock texture analysis enables the geologist to reconstruct movements at shear zones and to obtain information on the deformation conditions, e.g. pressure and temperature.

Among others neutron diffraction is the strongest experimental method due to the high penetration capability of neutrons and the large neutron beam cross sections which allow the investigation of volume textures of high grain statistics. An instrument is needed capable of collecting many pole figures of many samples in a reasonable time. A large position sensitive detector installed at a time-of-flight diffractometer compensates for pole figure scanning reducing measuring time by one order of magnitude.

The proposed time-of-flight diffractometer is designed for high intensity even with samples of as little as 0.5cm^3 at a reasonably good resolution of d-spacings, i.e.

$$\delta d/d \leq 5 \times 10^{-3} \qquad (1)$$

Equation (1) can be appropriately expressed in terms of parameters needed for establishing a technical solution of a time-of-flight instrument, viz.

$$\delta d/d = \left[(\delta t/t)^2 + (\delta L/L)^2 + (\delta\Theta \cot\Theta)^2\right]^{1/2} \qquad (2)$$

where t is the neutron flight time across a flight path L and Θ is half the scattering angle. In order to fulfil the requirement of equation (1) each of the terms in equation (2) contributing to the relative uncertainty $\delta d/d$ must not exceed 2.8$\times$10^{-3}. Applying modern technologies like super mirror guides, high speed disk choppers with magnetic bearings and linear position sensitive ^{3}He detectors an instrument can be designed so as to reach these goals. A schematic representation of the instrument is shown in Fig. 1.

Neutrons from the 5$\times$10cm^2 beam channel SR5 of the FRM II are focused onto the slits of a pulse defining double-disk chopper by a 25m long "ballistic" beam compressor made of m=3 super mirror guides, i.e. guides with three times the critical glancing angle of nickel coated guides. The beam of 0.9$\times$10cm^2 at the chopper is then defocused horizontally and focused vertically so as to form an exit cross section of 2.8$\times$2.8cm^2 after a flight path of 11.85m. The focus with a size of 1cm^2 is 0.75m downstream of the exit of that beam tranport guide. In order to prevent direct sight onto the D_2O reflector of the reactor, which minimizes fast neutron background, the guide to the pulse chopper will be mounted at an angle of 10^{-2}radian to the beam center line. The other two choppers of Fig.1 are needed to define both the position of the wavelength band, which will be accessible and to prevent cross talk of consecutive pulses.

The most important features of the instrument are high intensity by exploiting a large fraction of the Debye-Scherrer rings, variable d-spacing and resolution ranges, no limitations in determining peak posi-

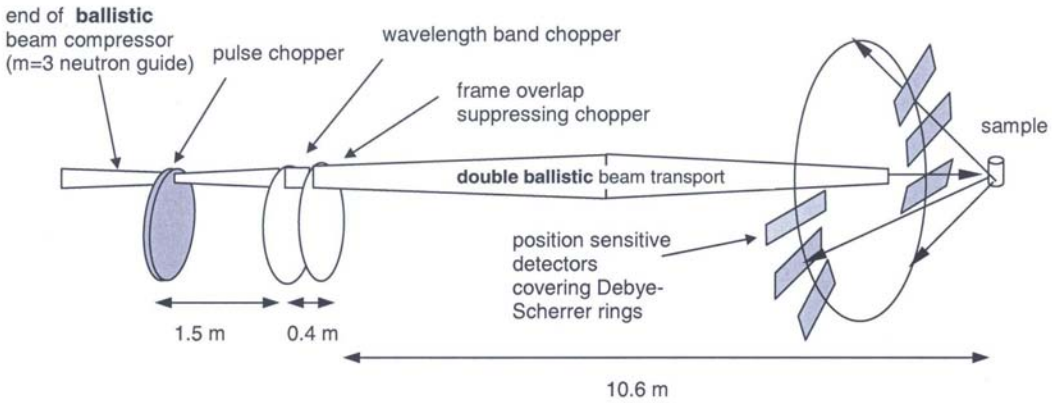

FIG. 1: Schematic layout of the time-of-flight diffractometer POWTEX

tions (using position sensitive detectors without collimators) and unrestricted utilization as both a powder and a texture diffractometer.

Analytical performance estimates have shown that the neutron current at the sample position will be approximately equal for both a monochromator and a time-of-flight diffractometer. However, the absence of the resolution asymmetry of the time-of-flight method will result in an intensity gain for detected neutrons of about an order of magnitude with an initial detector arrangement covering a solid angle of 3 steradian. The optimization of the numerous components of the instrument can be better followed up quantitatively with modern Monte Carlo techniques such as the VITESS code developed at the HMI. Examples of these numerical calculations are given in figures 2 through 4.

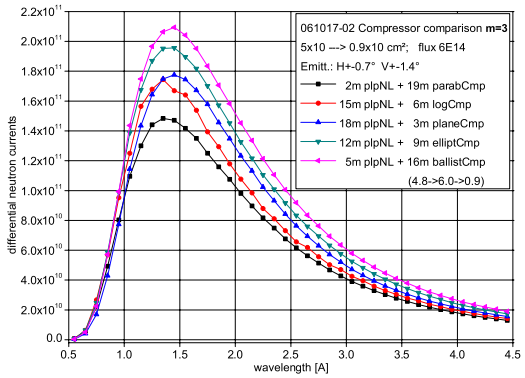

FIG. 2: Intensity as a function of wavelength at the pulse chopper slit for five different compressor geometries

Intensities at the end of different beam compressors are shown in Figure2. Five geometrical shapes have been modeled and independently optimized. Only the optimum performance for each geometry is displayed in Fig. 2.

The results of the Monte-Carlo calculations obtaining the desired focal spot size of 1cm^2 at the sample position is shown in Figure 3. Another important performance feature is the angular divergence $\delta\Theta$ at the sample position (cf. equation 2). The result of the numerical calculations for the 2-dimensional divergence distribution is presented in Figure 4.

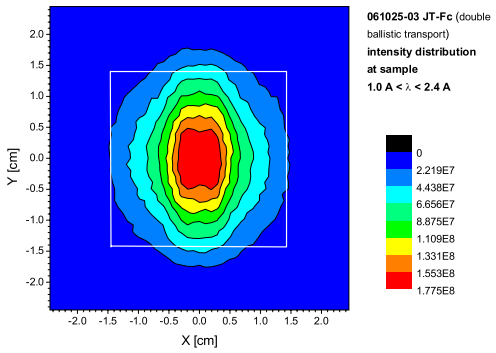

FIG. 3: 2-D intensity distribution at the sample (white square depicts guide exit cross section, 0.75m upstream). Neutron current density in the flat top is 3.5$\times 10^7$ cm^{-2}s^{-1}

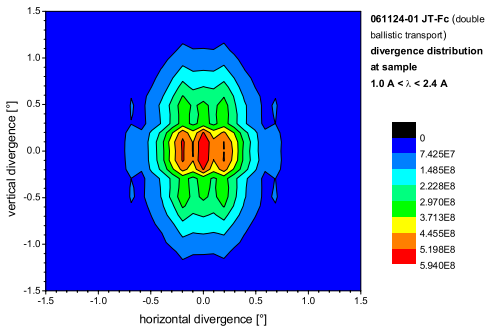

FIG. 4: 2-D beam divergence distribution at the sample

To summarize, our Monte Carlo simulations show that the proposed time-of-flight diffractometer outperforms a conventional monochromator instrument by about an order of magnitude. Based on a proposal by Professor Dronskowski of the RWTH Aachen, representing the large German community of solid state chemists, the “BMBF Verbundforschung” has assented funding for the project to be realized at the FRM II.

The New Reflectometer of the JCNS at the FRM II: MARIA

S. Mattauch[1], U. Rücker[1], A. Ioffe[1], Th. Brückel[1], R. Schmitz[2], V. Fracassi[2]

[1] Institute for Scattering Methods and JCNS
[2] Zentralabteilung Technologie

At the outstation of the Jülich Center for Neutron Science JCNS at FRM-II, a new reflectometer MARIA will be build. This instrument will be optimized for the study of magnetic nanostructures, serving the rapidly growing field of Spintronics or Magnetoelectronics, i.e. information storage, transport and processing using the spin of the electrons. The instrument will have unique features, such as polarization analysis for large angular range, extreme focusing to small sample sizes, high flux, largely variable wavelength band selection, GISANS option, provision for kinematic studies down to the μs range, in-situ sample preparation etc.. Its neutronic performance was optimized by Monte Carlo simulations and specially developed codes for various neutron optical devices.

The new neutron reflectometer MARIA (**MA**gnetism **R**eflectometer with high **I**ncident **A**ngle) of the JCNS (**J**ülich **C**enter of **N**eutron **S**cience) is designed for investigations of thin magnetic layered structures down to the monolayer scale (optimised for layer thicknesses between 3-300Å) with optional lateral structures of nm to μm size. Consequently the instrument is optimised for small sample sizes of 1cm^2 and has polarisation analysis as standard. Beside the reflectometer mode with vertically focused beam and good resolution in the horizontal scattering plane, MARIA will be able to measure in the GISANS mode with additional resolution in the vertical direction. Latter mode allows to measure lateral structures down to the nm scale. In this way MARIA is a strongly improved and extended successor of the HADAS reflectometer at the research reactor DIDO in Jülich which has worked with great success in the last years.

Scattering plane	horizontal
Monochromator	Velocity selector
Wavelength	4.5-10Å
Wavelength spread	1%, 3%, 10%
Expected pol. flux	7x10^7 n/(s*cm^2) (3mrad coll.)
Detector size	400 x 400 mm^2
Detector resolution	1-2mm
Sample detector dist.	2m
Max. detector angle	120°
Q_z-range	0.002 - 3.2Å^{-1}
Q_x-range	6·10^{-5} - 0.001Å^{-1}
α_f	-10 - 90°
Polarisation	double reflection polariser
Polarisation analysis	Radial solid state polariser / ^{3}He
Collim. (scat. plane)	4m long, Slits: 0 - 40 mm
Focussing	vertically focussing elliptic guide
GISANS option	4m long collimation
Q_y-range	0.002 -0.2 Å^{-1}

TABLE 1: Characteristic data of MARIA.

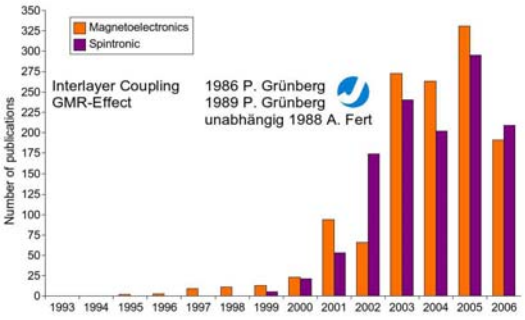

FIG. 1: Literature research at INSPEC with the keywords 'magnetoelectronics' and 'spintronic' from the year 1993 on.

The rising importance of thin magnetic layers with lateral structures in the nanometer scale can be seen in Fig. 1. The rapid increase of articles started with the discovery of the *Interlayer Coupling* in 1986 and the *GMR-Effect* in 1989 by P. Grünberg (IFF) and A. Fert (Paris). These effects allow to store, transport and process information related to the spin of the electron. In combination with lateral structures approaching the nanometer scale in thin film materials, new effects are expected. For the investigation of effects like the behaviour of magnetic domains inside nanostructures buried under nonmagnetic layers, magnetic effects in the vicinity of interfaces of different materials or dipolar interactions of nanostructures, polarised neutrons are a powerful and unique tool. All these phenomena can be studied with a polarised neutron reflectometer designed to have a high signal to noise ratio (8-9 orders of magnitude) with standard polarisation analysis on an area detector.

For layer thicknesses of 3-100Å it is possible to relax the wavelength resolution drastically to $\Delta\lambda/\lambda \sim 10\%$ which increases the intensity at the sample position by a factor of 10 compared to a conventional crystal monochromator reflectometer. Beside the specular reflectivity (incident angle equal to outgoing angle)

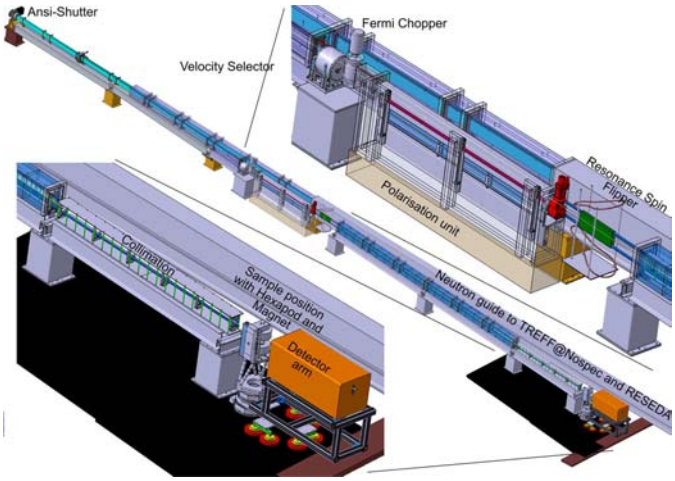

FIG. 2: A view of the new Magnetism Reflectometer MARIA at the FRM-II.

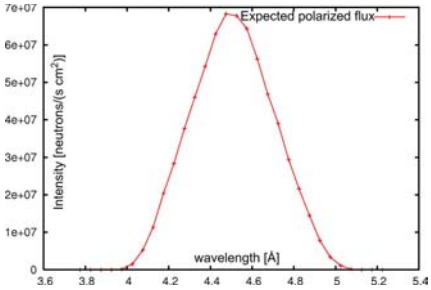

FIG. 3: Intensity distribution at the sample position (1x1cm^2) of a polarized neutron beam with a horizontal collimation of 3mrad simulated by VITESS.

measuring the vertical structure and the layers' magnetisations, a lot of information about the lateral magnetic and chemical structure in the 100nm-μm scale can be seen in the offspecular scattering. Only with polarisation analysis the contributions of the different magnetic and structural phenomena can be distinguished.

In Fig. 2 a schematic drawing of the instrument is shown. On the upper left hand corner the instrument starts with the main shutter and a cross section of 170 x 29mm^2 of the neutron guide. Up to the selector the guide is horizontally curved with a radius of 400m to cut off neutrons with too small wavelengths. At the same time the height of the guide is slightly reduced to fit the window of the velocity selector. To optimise the intensity of the neutron beam at the sample position and the measurement strategy we have decided to use a velocity selector to monochromatise the neutrons. Behind the selector a Fermi-chopper allows to reduce the wavelength spread between 1% and 10% if desired. In the polarisation unit a double reflection polarising or a non-polarising guide for maximum intensity can be selected by the user. With the resonance spin flipper it is possible to change the polarisation of the incoming neutron beam. Already in the polarisation unit the vertical elliptical focussing starts and ends at the last slit of the collimation, 50cm in front of the sample position. The collimation allows one to set the angular resolution of the incident neutron beam. For reflectometer mode the vertically focussing ellipse is continued along the collimation. In GISANS mode, absorbers prevent the vertical focussing and two sets of slits result in two dimensional collimation of the beam. The combination of the two modes without compromising the intensity of any of them is a unique feature and has never before been realised. The combination of these optical devices have been optimised by simulations with the VITESS suite as well as with specialised programs for the detailed understanding of selector, Fermi-chopper and elliptical focussing properties. As an example, Fig. 3 shows the expected intensity distribution at the sample position.

Sample and heavy sample environment can be adjusted flexibly in every direction using a Hexapod. The detector arm carries the detector shielding, housing spin flipper, polarisation analyser and the 2D-detector. The detector arm will be moved with air cushions on a polished granite floor.

The expected polarised flux at 3mrad collimation will be two to three orders of magnitude higher than the flux at HADAS. This will be sufficient to investigate single layers of a few nm material with lateral structures or the interactions of molecular magnets deposited on a substrate. In-situ measurements of layers grown inside a MBE-chamber will be feasible.

Polarising Neutron Beams With Hyper-polarized ^{3}He-Gas Application on Neutron Scattering Instruments

K. Nünighoff, P. Hiller, R. Mueller, A. Ioffe

Institute for Scattering Methods and JCNS

Due to the ever-increasing interest in polarised neutron scattering, development work on neutron spin filter cells using polarised ^{3}He gas is receiving much attention. In this report we describe progress made in cell production at FZJ. Further we report on the construction and test of a magnetostatic cavity for the small angle scattering machine KWS-1, which will be located at the Munich research reactor FRM-II and operated by the Juelich Center of Neutron Science.

^{3}He shows a spin dependent cross section of the ^{3}He(n,p)T reaction[1], which opens the opportunity to use nuclear spin polarised ^{3}He gas as a neutron spin filter. In case of an antiparallel spin orientation of the neutron and the ^{3}He nucleus, the cross section σ is approximately 6,000 barns. But in case of a parallel spin orientation only

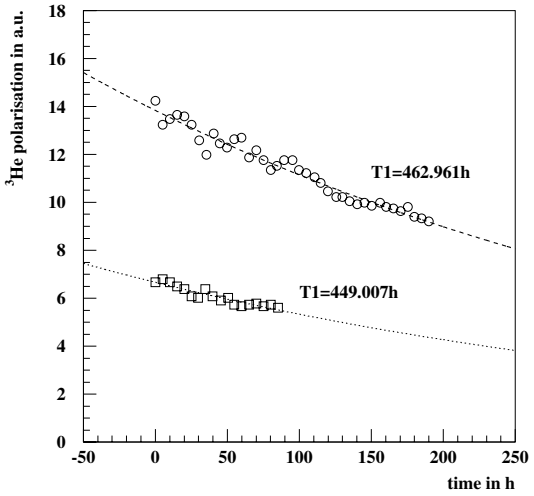

FIG. 1: Measurement of the life time T_1 with nuclear magnetic resonance. After the life time T_1 was measured (open circles) the cell was rotated by 180° and T1 was measured again (open boxes).

elasic scattering is allowed and thus the cross section is reduced by three orders of magnitude and lies in the range of a few barns. This means that nuclear spin polarised ^{3}He is transparent for one spin component and shows a high opacity for the other one. In contrast to other techniques to produce polarised neutron beams, like supermirrors or Haeussler crystals, nuclear spin polarised ^{3}He gas covers a broader wavelength band. The geometry of the cells can be adapted to the instrumental needs and thus can cover a wide angle of scattered neutrons. Two methods exists to polarise ^{3}He: metastable exchange optical pumping (MEOP) [2] and spin exchange optical pumping (SEOP) [3]. Although both techniques are under development in our institute, in this article we focus on the SEOP method and will report on recent developments.
One issue is the production of neutron spin filter cells with a long lifetime T_1. Here T_1 is through the exponential decay, proportional to e^{t/T_1}.

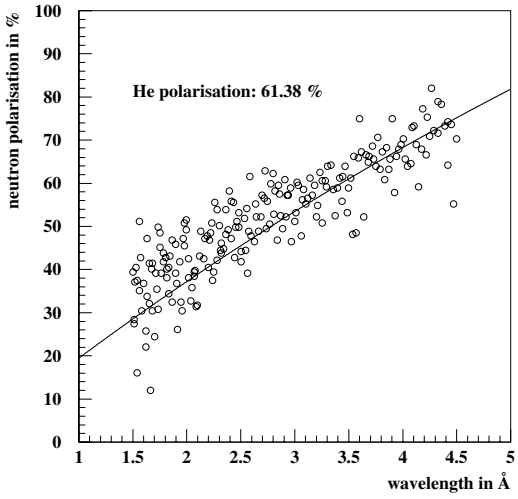

FIG. 2: Measurement of the neutron beam polarisation on the ALF instrument at ISIS (UK).

A first glass cell was made in the glass workshop of the central department of technology. This cell was filled with rubidium and ^{3}He gas at the Rutherford-Appleton-Laboratory. The lifetime was measured by nuclear magnetic resonance. Fig. 1 shows the exponential decay of the ^{3}He polarisation and the results from an exponential fit through the data points. A T_1 of 463 h was measured. After a first measurement of T_1 the cell was rotated by 180° and T_1 was measured again. As can be seen in Fig. 1 no siginificant difference of T_1 was observed, indicating that the amount of paramagnetic impurities inside the cell influencing the lifetime is very low.

On the ALF instrument at ISIS the polarisation of the incident neutron beam was measured. Fig. 2 shows the polarisation of the neutron beam depending on the neutrons wavelengths. From this experiment the polarisation of the ^{3}He gas was determined to be larger than 61 %.
In order to show the influence of paramagnetic impurities, we present further data for a cell manufactured and filled in Juelich. (see Fig. 3).

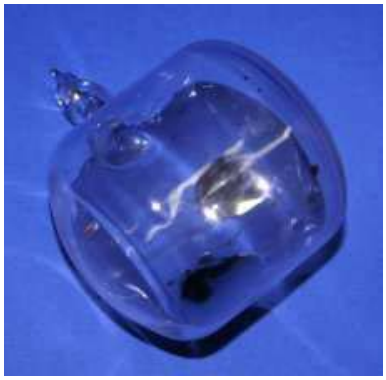

FIG. 3: Neutron spin filter cell produced and filled with rubidium and ^{3}He.

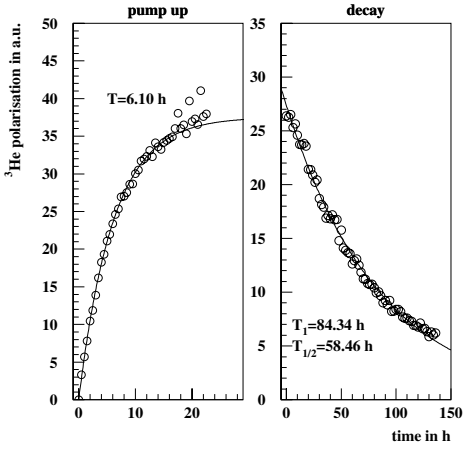

FIG. 4: Polarising the cell (left panel) by optical pumping in the Juelich SEOP aparatus and determining the lifte time T_1.

After the rubidium was condensed into the cell and the cell was filled with a few mbar nitrogen and approximately 1 bar ^{3}He the cell was sealed off. Due to an oxygen intrusion into the cell when filling it with ^{3}He the surface of the rubidium was oxidised. The formation of paramagnetic rubidium oxide inside the neutron spin filter cell will reduce the polarisation lifetime. The left graph in Fig. 4 shows the polarisation in the cell on the Juelich SEOP aparatus. The polarisation of the ^{3}He atoms was again observed by nuclear magnetic resonance. A 40 W laser with λ=795 nm polarises the rubidium atoms and due to collisional mixing the polarised rubidum atoms transfer their spin on the ^{3}He atoms. After 20 h the polarisation achieves saturation. When saturation had been reached the laser was switched off and the decay of the polarised ^{3}He gas was observed. As expected the cell shows a lower lifetime than the cell filled at ISIS, due to rubidium oxide. Only a T_1 of approximately 83 h was achieved.
It is forseen to equip the small angle neutron scattering instrument KWS-1 at the Munich research reactor FRM-II with an analyser based on polarised ^{3}He. To keep the polarisation the analyser cell has to be placed in a magnetic field with a field gradient smaller than 10^{-4} 1/cm. Based on finite element calculations with ANSYS [4] of the magnetic field a magnetostatic cavitiy was constructed and the spatial distribution of the magnetic field was measured and compared with the predictions of the finite element calculations.

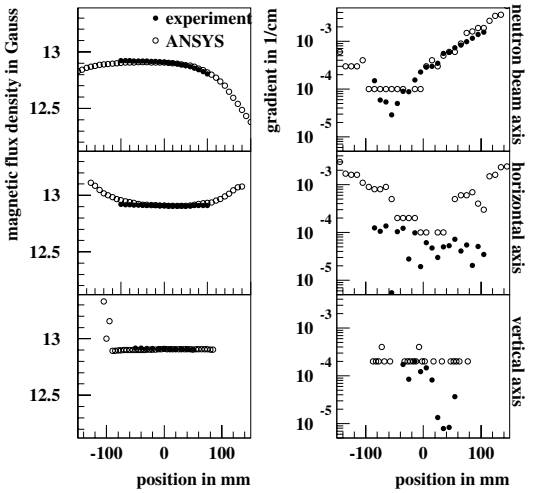

FIG. 5: Comparison of measurements and results from finite element calculations performed with ANSYS.

In Fig. 5 a comparision of the ANSYS calculations and measured data are shown. The experimental data for the magnetic flux density as well as the resulting field gradient are in excellent agreement with the calculated values and the requiered values of the field gradient could be achieved.
To summarize, we have obtained very high ^{3}He polarisation of above 61 % in a cell with a size suitable for neutron scattering experiments. A record value for the lifetime of 450 h was achieved. Finally, we have designed a magnetostatic cavity for a polarisation analyser suitable for the SANS instrument KWS-1 in Munich.
This research project has been supported by the European Commission under the 6^{th} Framework Programme through the Key Action: Strengthening the European Research Area, Research Infrastructures. Contract no: RII3-CT-2003-505925.

[1] L. Passell and R.I. Schermer, Mesurement of the Spin Dependence of he He^3(n,p)T Reaction and of the Nuclear Susceptibility of Adsorbed He^3, Phys.Rev. 150(1966)146

[2] F.D. Colegrove, L.D. Schearer and G.K. Walters, Polarization of He^3 Gas by Optical Pumping,Phys.Rev. 132(1963)2561

[3] M.A. Bouchiat, T.R. Carver, and C.M. Varnum, Nuclear Polarization in He3 Gas Induced by Optical Pumping and Dipolar Exchange, Phys.Rev.Lett. 5(1960)373

[4] ANSYS, Swanson Analysis Systems Inc., USA

TREFF@NOSPEC: A Facility Dedicated to Test Neutron Optical Devices

U. Rücker[1], S. Mattauch[1], K. Bussmann[1], P. Hiller[1], P. P. Stronciwilk[1], F. Gossen[1], A. Ioffe[1], Th. Brückel[1], H. Feilbach[2], K. Hirtz[2], A. Sparbrodt[3], M. Paulzen[3], K.-H. Mertens[3], A. Ofner[4], G. Borchert[4]

[1] Institute for Scattering Methods and JCNS
[2] IFF Joint Service Facilities
[3] Operation Management (Betriebsdirektion)
[4] ZWE FRM II, TU München

In a collaboration with the Neutron Optics Group of the FRM-II, the former very successful neutron reflectometer HADAS (ELLA@FRJ-2; FZ-Jülich) has been adapted and transported to the new research reactor in Munich. The basic idea is to have a powerful reflectometer for testing of neutron optical devices, characterization of samples, monochromator crystals, spin turners, etc. which is available at short notice without the constraints of scheduled user experiments.

The Temporary REFlectometer Facility (TREFF) (Fig.2) is a dedicated reflectometer and diffractometer for the test of neutron optical devices. It is a joint project of the Jülich Center for Neutron Science (JCNS) and the Neutron Optics Group of FRM-II. The instrument is equipped with polarized neutrons, polarization analysis and a 2D position sensitive detector, which is completely covered by the polarization analyzer (see Fig. 1). A zero-field chamber with 3D vector polarization analysis of the transmitted beam will be added soon. TREFF will serve as a flexible high-intensity instrument for investigation of neutron optical devices such as supermirrors (polarizing and non-polarizing), monochromator crystals, spin turners etc. Furthermore, it will host the research activities of FZ Jülich on magnetic thin films until the startup of MARIA (MAgnetism Reflectometer with variable Incident Angle), which is currently being designed and constructed. TREFF is not a regular scheduled user instrument of FRM-II.

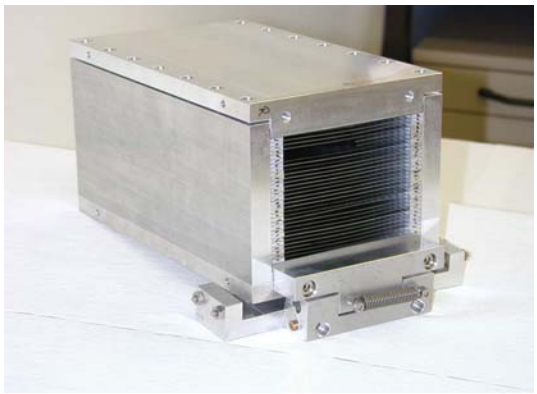

FIG. 1: The polarization analyzer of TREFF.

TREFF is located at the beamport NOSPEC (Neutron Optics' SPECtrometer) of the Neutron Optics Group using the lower part of the neutron guide NL5-S, which it shares with RESEDA (REsonance Spin Echo for Diverse Applications). TREFF uses main components of the HADAS reflectometer [http://www.fz-juelich.de/iff/wns_hadas] that used to be installed at the reactor FRJ-2 in Jülich. The neutrons are extracted from NL5-S with a double monochromator at a Bragg angle of 2θ=90°.

In a first step, TREFF will operate at λ=4.75Å, delivered by P.G.(002) monochromator crystals. A vertically focussing monochromator and a collimation with two pairs of slits in a distance of 170 cm deliver a beam to the sample position, which is 4 cm high, has a vertical divergence of 1.9° and can be collimated horizontally between 0.1 and 16 mrad. To reduce the background, a vacuum tube is inserted between the collimation slits. A transmission polarizer can be placed automatically between the second monochromator and the first slit and offers polarized neutrons with a maximum divergence of 4 mrad. A resonance spin flipper is used to control the polarization of the incident neutron beam. In a second step, we will install Nb(002) monochromator crystals to be used alternatively to P.G.(002) (Pyrolytic Graphite). This will allow to use λ=2.5 Å for the investigation of single crystal quality, mosaic spread and orientation.

The sample table can take and adjust heavy loads of up to 300 kg for all 6 degrees of freedom (3 translations and 3 rotations). An electromagnet with μ_0H=450 mT over 10 cm gap between the poles or 1.9 T over 2 cm gap is available to expose the samples to a magnetic field.

The detector arm carries a lead and B_4C shielding tunnel to protect the detector from gamma and neutron background, that is not coming from the sample. It contains an evacuated beam tube with spin flipper, a beamstop for the part of the primary beam, which is not reflected by the sample, a polarization analyzer (see Fig. 1) and a 2D detector. The inclination of the polarization analyzer can be adjusted automatically either to be polarizing or transparent (for maximum transmission without polarization analysis). It is designed to offer good polarization efficiency without compromising angular resolution and sensitivity over the whole range of scattering angles, which the de-

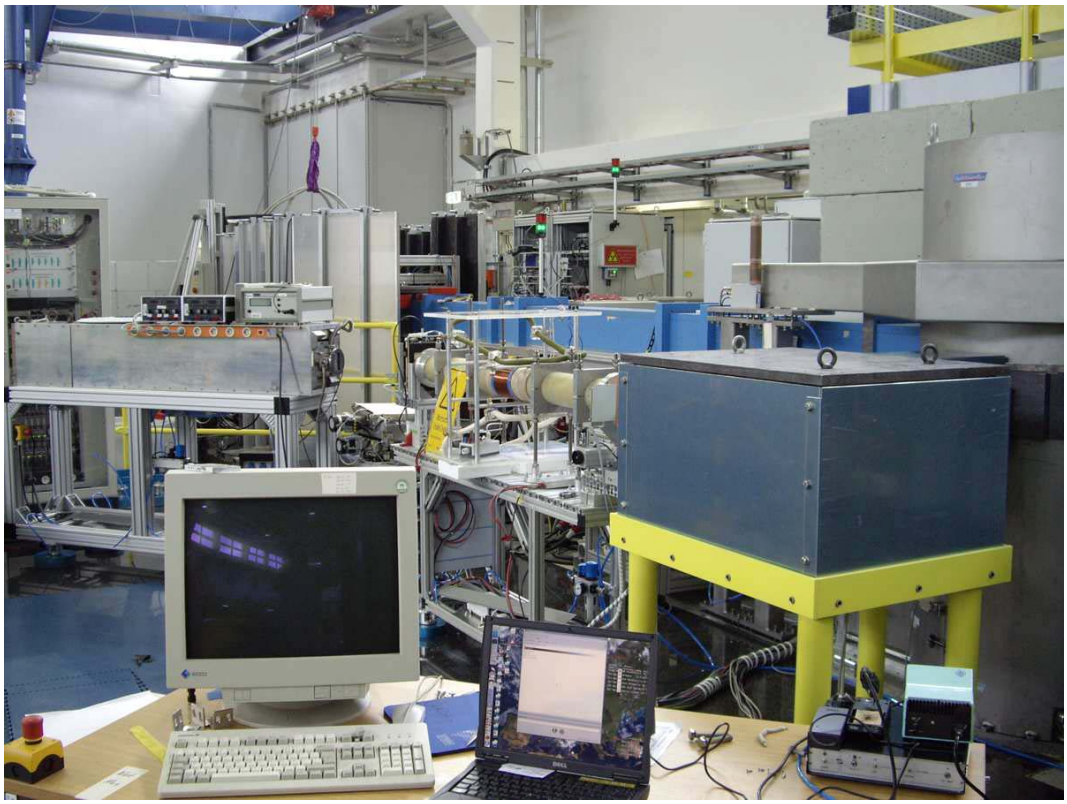

FIG. 2: TREFF@NOSPEC: From the cylindrical shielding of the first monochromator (right) the neutrons are brought to the shielding box of the second monochromator. Then follows the collimation (with the resonance spin flipper coil around the vacuum tube), the sample table and the detector arm (middle left).

tector covers. The detector has a circular sensitive area with 80 mm diameter and a spatial resolution of 1.5 mm. It is mounted at a distance of 1.6 m from the sample, so that it covers a range of scattering angles of 2.2°. Scattering angles of more than 60° can be reached by moving the whole arm on air cushions.
The first parts arrived in Garching in March 2006 after having been assembled and tested in Jülich. During the past months the instrument has been assembled in the Neutron Guide Hall of FRM-II. Today, we are ready to start the commissioning of the instrument as soon as the modification of the neutron guide NL5-S is accomplished and neutrons are available.

We would like to thank the technical staff of the Institute for Scattering Methods, the Jülich Center of Neutron Science and the Central Institute for Electronics (ZEL) for the considerable support given.

DNS – A Versatile Multi-Detector Time-of-Flight Spectrometer With Polarization Analysis

Y. Su[1], W. Schweika[1], E. Küssel[1], K. Bussmann[1], M. Skrobucha[2], Th. Brückel[1]

[1]Institute for Scattering Methods and JCNS
[2]ZAT, FZJ

Neutrons interact not only with nucleus and nuclear spins, but also with the magnetic field produced by unpaired spins in the outmost electronic shells of an atom. Thus one challenge for neutron scattering experiments is to disentangle the scattering contributions from these different sources. DNS, a versatile time-of-flight spectrometer with polarization analysis, to be operated at the most powerful neutron source in Germany, FRM-II, is able to provide unambiguous separation of coherent, spin-incoherent and magnetic scattering simultaneously over a large range of scattering vector Q and energy transfer E. DNS will be therefore highly suitable for investigations of exotic magnetic and structural correlations in a wide range of novel complex materials.

Introduction

The diffuse neutron scattering (DNS) instrument is among several selected instruments being transferred from the Jülich research reactor to FRM-II. Meanwhile, a substantial upgrade and modernization on most of its major components is being carried out. This will transform DNS into a worldwide competitive instrument in its kind. DNS is a cold neutron multi-detector time-of-flight (TOF) spectrometer with both longitudinal (i.e. XYZ-method) and vector polarization analysis [1, 2, 3]. This allows the unambiguous separation of nuclear-coherent, nuclear-spin-incoherent and magnetic scattering contributions simultaneously over a large range of scattering vector **Q** and energy transfer E. With its compact size (only 80 cm distance from sample to detector), DNS is optimized as a high intensity instrument with medium **Q** and energy resolutions. DNS is therefore ideal for the studies of elastic and inelastic diffuse scattering that may arise from short-range magnetic and structural correlations and disordering phenomena in a wide range of emergent materials, such as frustrated magnets, highly correlated electrons, molecular magnets and complex nano-structured compounds. Furthermore, interesting applications to soft matter physics by separating coherent and spin-incoherent scattering can also be found at DNS. DNS uses a vertically and horizontally adjustable double-focusing pyrolytic graphite monochromator, installed in the cold neutron guide NL6a. A schematic layout of DNS at FRM-II is shown in Fig.1. Monochromatic neutron beams with a wavelength ranging from 2.4 to 6 Å are available at DNS. The neutron beam is polarized using a m = 3 Schärpf bender-type focusing supermirror polarizer. The neutron spins are manipulated using a Mezei-type π-flipper, followed by a set of orthogonal XYZ-coils situated around the sample position for providing guide fields. The polarization analysis (PA) is performed by using m = 3 supermirror analyzers in focusing arrangement in front of each ^{3}He detector. 128 new position-sensitive ^{3}He detector tubes will be installed in additional detector banks for non-polarized experiments. This will increase the covered solid angle up to 1.9 sr.

Instrument description

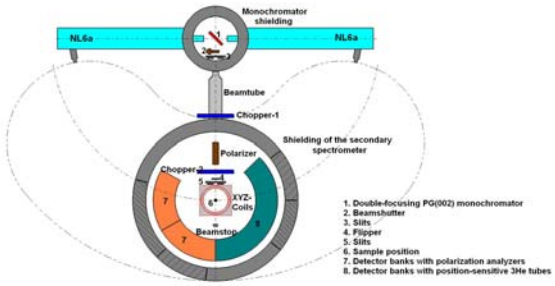

FIG. 1: The schematic layout of DNS at FRM-II

Two new high-frequency (rotation frequency up to 300 Hz corresponding to a repetition rate of 900 Hz for 3 slits) chopper systems will be used at DNS, as shown in Fig.1. Chopper-1 is used for selecting a single harmonic from the reflected orders of neutrons from the monochromator and also for reducing the background. Chopper-2 is the TOF chopper. Various sample environments e.g. cryostat, furnace, dilution cryostat and cryomagnet can be mounted on a heavy loading Huber goniometer on the sample rotation table. The two perpendicular arcs of the goniometer can be used for the orientation of single-crystal samples. The instrument data is summarized in Table. 1.

Monochromator	horizontal- and vertically adjustable double-focusing	PG(002) $d = 3.355$ Å
	crystal dimensions	2.5 x 2.5 cm^2 5 x 7 crystals
	wavelengths	2.4 Å$\leq \lambda \leq$ 6 Å
Double-chopper system	chopper frequency	$<$ 300 Hz
	repetition rate	$<$ 900 Hz
	chopper discs	Titanium, 3 slits $\phi = 420$ mm
Expected flux at sample (n/cm^2s)	non-polarized	$\sim 10^8$, λ=3 Å
	polarized	$\sim 10^7$, λ=3 Å
Detector banks for non-polarized neutrons	position-sensitive ^{3}He detector tubes	128 units, height 101 cm $\phi = 1.27$ cm
	total solid angle covered	1.9 sr
	covered scattering angles	$0° < 2\theta < 135°$
Detector banks for polarized neutrons	polariztion analyzers	24 units, $m = 3$ supermirrors
	^{3}He detector tubes	24 units, height 15cm $\Phi = 2.54$ cm
	convered scattering angles	$0° < 2\theta < 120°$
Q_{max}	$\lambda_i = 2.4$ Å , $E_i = 14.2$ meV	4.84 $Å^{-1}$
	$\lambda_i = 6$ Å , $E_i = 2.28$ meV	1.93 $Å^{-1}$
Expected energy resolution	$\lambda_i = 2.4$ Å , $E_i = 14.2$ meV	1 meV
	$\lambda_i = 6$ Å , $E_i = 2.28$ meV	0.1 meV
Suitable samples	single crystal, powder, soft matter (e.g. polymer, liquid etc.)	
Sample environments	closed-cycle cryostat, Orange-type L-He cryostat, furnace, dilution cryostat and cryomagnet(up to 4T)	

TABLE 1: Instrument data of DNS at FRM-II

In addition to high intensity, the unique strength of DNS lies on its extreme versatility. DNS can be operated in a number of modes for a wide range of samples. There are three PA modes at DNS: uniaxial-PA for separation of coherent and spin-incoherent scattering in non-magnetic samples; longitudinal-PA (XYZ-method) for separation of magnetic scattering in paramagnetic and anti-ferromagnetic samples; (spherical or) vector-PA for the determination of complex magnetic structures. All of these PA set-ups can be operated either in diffraction or in a TOF measurement. With installations of 128 position-sensitive ^{3}He tubes and double choppers, the performance of DNS as a TOF spectrometer will be drastically improved, thus allowing S(**Q**,E) to be measured simultaneously over a large range of **Q** and E on single-crystal samples. As a high intensity cold neutron single-crystal TOF spectrometer, DNS can be very attractive for investigations of spin-wave and phonon excitations.

Current status and outlook

In 2006, we have seen the kicking-off of the relocation of DNS to FRM-II. Both Tanzboden and monochromator shielding have been successfully installed. The year of 2007 will be a major milestone for DNS. The installation of the double-focusing monochromator and the relocation of the secondary spectrometer are expected in the spring of 2007. The delivery of the first neutrons and the starting of the commissioning phase are targeted before the next summer break. The installations of new double choppers and position-sensitive ^{3}He detectors are expected to follow suit.

[1] W. Schweika and P. Böni, Physica B **297**, 155 (2001).

[2] W. Schweika, Physica B **335**, 157 (2003).

[3] W. Schweika, S. Easton and K. U. Neumann, Neutron News **16**, 14 (2005).

TOPAS, the New Thermal Time-of-Flight Spectrometer With Polarisation Analysis

J. Voigt[1], M. Prager[1], Th. Kulessa[2], Th. Brückel[1]

[1]Institut für Streumethoden, Institut für Neutronenstreuung
[2]Zentralabteilung für Technologie

Dynamics give often the clue to understand and/or predict the physical properties of a novel material. TOPAS will be a new spectrometer to determine the excitation spectrum for a wide range of energies on the atomic length scale. It features a 4d data acquisition and a high intensity thanks to focusing neutrons optics, which yields a fast overview of the dynamics particularly for small samples. It will provide polarisation analysis of thermal neutrons as standard tool. This new method will have a strong impact particularly for magnetic systems and sample containing hydrogen, e.g. biological systems.

Inelastic neutron scattering has proven to be one of the most powerful techniques for the study of dynamics in novel materials. Our understanding of phonons, magnetic excitations, hydrogen bonding in materials, and soft-modes at phase transitions has come primarily from the results of inelastic neutron scattering studies. In recent years, this technique has been used to examine an ever-widening range of subjects and phenomena such as the dynamics of polymers, the nature of disordered and amorphous materials, phase transitions in geological materials and subtle electron-lattice interactions. By the use of thermal neutrons, a large range in energy and momentum transfer can be probed. Using the time-of-flight technique, the measurement of the momentum transfer is decoupled from the measurement of the energy transfer. Time-of-flight spectroscopy from single crystals has the potential to explore simultaneously the $(\vec{Q}, \omega)$ space and to map a variety of excitations by covering a large solid angle with detectors. Accordingly, TOPAS can be used for a wide range of applications, particularly for novel materials. Possible application include highly correlated electron systems (e.g. high T_c superconductors), molecular systems, nanoparticle, catalytic processes ....

Up to now, thermal multidetector instruments do not offer the possibility of neutron polarisation analysis. Incorporating this into the spectrometer, offers the opportunity to study the full vector properties of magnetic excitations. On the other hand, hydrogen is a important element for a lot of applications. By polarisation analysis, the strong incoherent scattering from the hydrogen nucleus can be separated, unravelling hidden features.

The scientific case requires an instrument with high intensity, a reasonable energy and momentum resolution and the incorporation of facilities to polarise the incoming neutron beam and to analyze the polarisation of the scattered neutrons.

In a time-of-flight spectrometer the time is measured, in which the neutrons travel from a chopper via the sample to the detector. If the velocity of the neutron at the chopper is known, the velocity after the interaction with the sample can be determined from the time, at which the neutron arrives at the detector. The resolution of such an instrument is given by the length of the neutron pulse, geometric differences in the flight path (i.e. the sample size) and the accuracy of the neutron detection. This timing uncertainties have to be compared to the total time of flight. By increasing the flight path from the sample to the detector the resolution can be improved. However, one has to make sure, that neutrons from the next pulse, that gained energy during the interaction, do not arrive prior those of the previous pulse that lost energy. The time, the slowest neutron, which are wanted to be detected, need to arrive at the detector, determines the time frame. The longer the time frame, the smaller is the repetition rate of the instrument. Of course, the time frame increases if the distance sample to detector increases. The reactor produces neutrons continuously. To make an effective use of the neutrons, a high repetition rate is desireable. In conclusion, on has to trade the requirements of resolution and intensity in designing of the instrument.
For TOPAS, we have chosen a sample to detector distance of 2.5 m. This results in a high intensity of about $5\text{x}10^5 \frac{\text{neutrons}}{cm^2 s}$ at an elastic energy resolution $\frac{dE}{E}$ between 3 and 6 %. The usable repetition rate depends slightly on the incoming wavelength. E.g. we can work at a repetition rate as high as 700 Hz at a wavelength $\lambda = 1.1$ Å.
Furthermore, the comparably short sample to detector distance allows an economical coverage of a large solid angle. The instrument will be sited in a new eastern neutron guide hall of the FRM2 at a distance of about 40 m from the reactor core, see Fig. 1. This gives us the possibility to realize a new concept for the focusing and monochromatisation of a thermal neutron beam. An elliptic shape of the neutron guide focuses the 97x48 mm^2 entrance window onto a 36x16 mm^2 beam spot deduced as the full width at half maximum from Fig. 2. Focusing works well

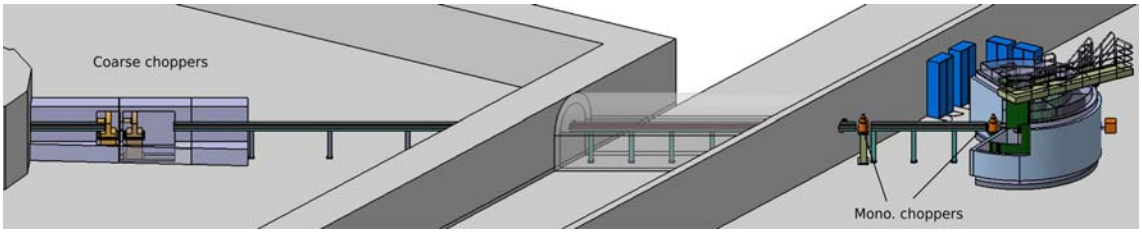

FIG. 1: Overview of TOPAS. The coarse chopper system is shown on the left. Its second chopper can be moved to match the time-of-flight for the desired neutrons to the fixed phase between both discs. The two Fermichoppers in front of the secondary spectrometer monochromatise the neutron beam. The secondary spectrometer around the sample (2.5 m sample to detector distance) is evacuated to reduce the background due to air scattering.

for short wavelength only, if the neutron guide is long enough, as can be seen from Fig. 3. In that case, the guide widens over a longer distance and the neutrons hit the guide wall under a shallower angle.

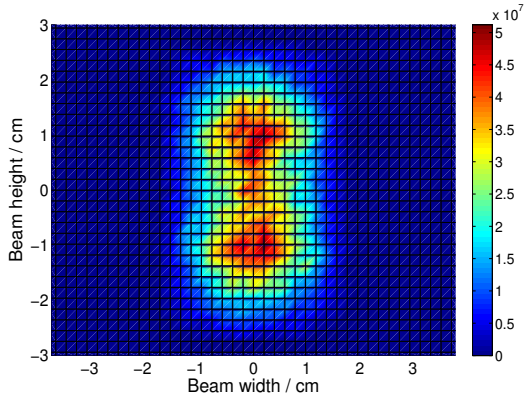

FIG. 2: Beam spot at the focal point, 1.05 Å$< \lambda <$ 1.15 Å. The inhomogeneous intensity distribution can be overcame by displacing the sample position slightly out of focus.

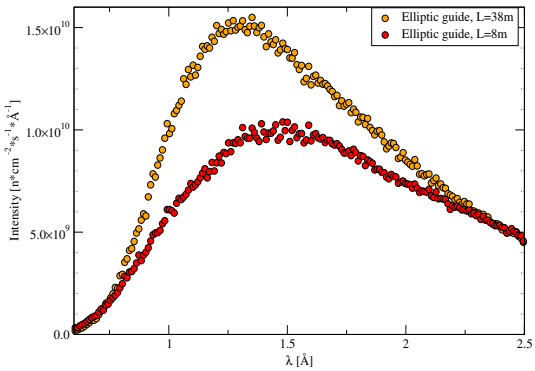

FIG. 3: Spectral flux distribution at the sample position for different lengths of the elliptic neutron guide.

The monochromatisation is done also purely by time-of-flight. Two Fermichoppers will be placed at a distance of 5 m. Neutrons can pass these choppers only during about 15 μs. The incoming wavelength resolution is therefore better than 2 % for thermal neutrons. Close to the reactor neutron source, we have a second set of choppers. They serve several duties: Since the focusing neutron optics require a straight view onto the neutron source, the direct sight has to be prevented by other means than a curved neutron guide. Two massive disc choppers will be placed close to the reactor core, see Fig 1. The phase between them is fixed, such that at a time only one of them is in open position. Hence fast neutron cannot pass them. To allow a maximum transparency for the desired neutron wavelength, the distance between the discs can be adopted to the neutron velocity. These choppers are placed far away from the spectrometer to absorb unwanted neutrons, which would only create background.

The polarisation of the incoming neutron beam will be done by a polarised ^{3}He filter. The absorption cross section is huge, if the neutron spin is antiparallel to the ^{3}He nuclear spin. For a parallel spin configuration ^{3}He is transparent. The ^{3}He cell will be placed between the last Fermi chopper and the sample. For wide angle polarisation analysis, a banana shape ^{3}He cell will be used. A present prototypes at the ILL[1] covers an angular range of 120°. It has proven, that wide angle XYZ polarisation analysis is possible using ^{3}He filter cells. The actual cell has an inner diameter of only 6 cm to accommodate the sample and sample environment. For TOPAS, it has either to be incorporated directly into the sample environment or the cell has to be enlarged. The strong requirements on the magnetic field inhomogeneity represent a major technological challenge.
In conclusion, TOPAS will be a multipurpose spectrometer. Due to its high flux, it will be perfectly suited for measurements on small samples. It will exploit the full potential of time-of-flight spectroscopy, as it simultaneously collects 4d data, yielding the full excitation spectrum in a wide energy and momentum transfer range. With full polarisation analysis, it will offer further degrees of freedom to study the dynamics in novel materials.

[1] www.ill.fr/YellowBook/IN4/pastis.html

Comissioning of the Backscattering Spectrometer SPHERES

J. Wuttke[1], P. Rottländer[1], W. Bünten[1], P. Stronciwilk[1], A. Ioffe[1], M. Prager[2], D. Richter[2], H. Kämmerling[3], M. Drochner[4], F.-J. Kayser[4], H. Kleines[4], F. Suxdorf[4]

[1] JCNS
[2] Institut für Festkörperforschung, FZ Jülich, 52425 Jülich
[3] Zentralabteilung Technologie, FZ Jülich, 52425 Jülich
[4] Zentralinstitut für Elektronik, FZ Jülich, 52425 Jülich

A signal-to-noise ratio of 165:1 is achieved. The energy resolution with unpolished Si[111] crystals is $\delta \mathrm{E}_{\mathrm{res}} = 0.69 \mu \mathrm{eV}$. As a test experiment, the tunneling spectrum of m-xylene was measured. A preliminary comparison with the performance of the HFBS instrument at the NIST, USA, is made.

The commissioning of the backscattering spectrometer SPHERES (SPectrometer with High Energy RESolution) was continued in 2006. The Status 2005 was:

- A neutron flux of $1.9 \cdot 10^9$n/cm^{-2}sec^{-1} was determined at the exit of the neutron guide. This is more than estimated originally.
- The data contained a huge neutron background.
- A large γ background allowed to use the beam only in the presence of radioprotection personnel.
- Shielding restricted the available solid angle.

Technical changes and developments in 2006:

- A standard FRM-II beamshutter, Fig. 1, replaced the old one. This was necessary to minimize spatial constraints for another Jülich instrument, MARIA. The new shutter improves also the safety instrumentation, as it closes automatically on interruption of electricity or pressurised air supply.
- A dedicated lead shielding was build around the neutron velocity selector.
- Lead shieldings were installed around the main γ sources in the spectrometer (chopper, beamstop, monochromator).
- A vacuum flight path between PST chopper and Doppler monochromator was built and installed, Fig. 2. This is a prerequisite for a later argon flooding of the instrument, as it reduces argon activation by an order of magnitude. By eliminating air scattering, the neutron flux at the sample is enhanced by around 20%.
- Most inner surfaces were covered by boron absorber, either as B_4C/PE composite, or in form of a paint.

As result of these measures, the γ background at 50 cm from the spectrometer walls is now weaker than the 3 μSv/h limit. Hereupon we obtained a preliminary permit for self determined test experiment.

Resolution scans with systematic variation of parameters (especially sample thickness) revealed two main sources of noise:

- a sample-independent component due to fast neutrons originating from the LiMg absorber in the chopper rotor.
- a retarded background proportional to the scattering power of the sample from neutrons that somehow bypass the chopper while it is closed.

FIG. 1: The new shutter housing during installation.

With a diaphragm restricting the view from the sample onto the monochromator a signal-to-noise ratio of 165:1 is obtained. In this configuration, the sample should scatter about 20% of the incoming neutrons; in this case, both sources of background are of

equal importance. The loss in flux caused by the diaphragm remains to be quantified; tests of alternative collimators are under preparation.

FIG. 2: Newly installed vacuum flight chamber between the PST chopper (right side) and the Doppler monochromator (left side).

In perspective, considerable improvement seems possible and necessary:

- The fast neutrons background can be avoided if the absorber on the PST will be exchanged against boron. This will be a major action but will improve the signal-to-noise ratio by a factor $\gtrsim$2 for samples with less than 20% scattering probability.
- A further factor 2 can be gained if the chopper which for technical reasons actually runs at only $\frac{1}{3}$ of its final speed reaches its full operation frequency.
- An argon atmosphere will allow about 20% more analyzed neutrons to reach the detectors.
- Coating the backside of the chopper with absorber could make the diaphragm redundant; feasability is under study.

With these factors in mind and cautious extrapolation, we can expect for the final state of the instrument a signal-to-noise ratio above 500.

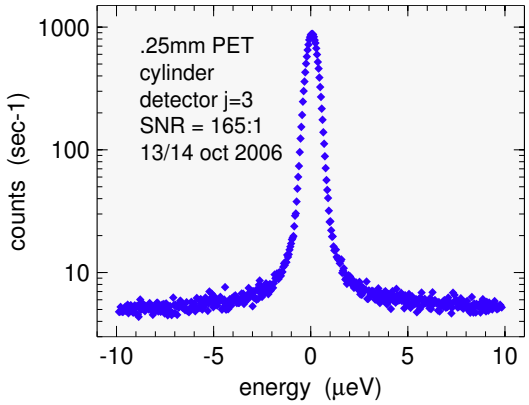

FIG. 3: Resolution curve, measured on a 0.25mm thick polyethyleneterephtalat sample.

Progress is also achieved on the side of the data acquisition software. In addition to the Doppler velocity histograms we are ultimately interested in, we now also collect chopper phase histograms. The acquisition program was developed into a daemon that can be controlled and parametrized through a simple TCP interface. Similarly, sample temperature can be set and read by a simple daemon. Parameters like chopper frequency etc. are now regularly written to a log file. Another process logs human interventions and error states. The entire software is designed such that a graphical user interface can easily be added on top of it.

The actual status of the instrument is presented by two spectra. The elastic scan in Fig. 3 documents the signal-to-noise ratio of 165:1 at an energy resolution of $\delta E_{res} = 0.69 \mu eV$ FWHM. The measuring time was ∼12h.

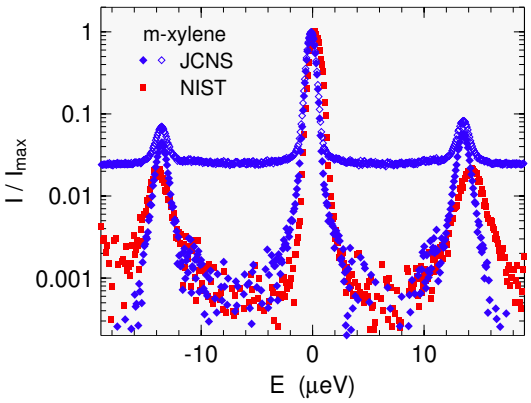

FIG. 4: Tunneling spectrum of m-xylene measured on SPHERES (blue) and HFBS (red) [1]. Normalization to same peak intensities. Sample temperature T=5 K. Momentum transfer: Q∼1.7Å^{-1}. Open symbols: raw data; closed symbols: after subtraction of a flat background.

Fig. 4 shows a tunneling spectrum of m-xylene. This sample was previously measured on the equivalent HFBS instrument at the NIST, USA. signal-to-noise ratio was rather similar and below 100:1. The energy resolution, FWHM, is better on SPHERES while the low intensity wings of the resolution function is less pronounced on HFBS. For SPHERES the energy resolution looks rather independent on energy transfer. This is due to our Doppler monochromator drive based on air bearings, which allows an almost friction free movement compared to the more vibration sensitive cam drive of HFBS.

The improvements of the instrument are going on.

[1] O. Kirstein, M. Prager, R.M. Dimeo, A. Desmedt, J.Chem.Phys. **122**,14502(2005)

Status of the NSE Spectrometer to Be Build at the Spallation Neutron Source in Oak Ridge, USA

M. Ohl[1], R. Achten[2], M. Butzek[2], T. Kozielewski[1], B. Laatsch[2], M. Monkenbusch[1], U. Papbst[2], H. Soltner[2], Ch. Tiemann[2], D. Richter[1]

[1] Institut für Festkörperforschung, FZJ
[2] Central Department of Technology, FZJ

The Research Centre of Jülich is going to build and operate a new high resolution neutron spin echo spectrometer at the Spallation Neutron Source (SNS) in Oak Ridge/TN USA. This contribution presents the current status of the layout and engineering design of the spectrometer and its key components as well as of our R&D work the development of new high current carrying correction elements for the highest field integral of spin echo spectrometer worlwide.

To give an overview of recent work which has been carried out in 2006 we will present the status of each component of the spectrometer as follows:

- The bulk shield insert has been sent to the SNS and is already installed
- Vertical shield plate has been installed during the past reporting period
- Shutter gate has still to be installed. This component is now purchased by SNS. Delivery is expected spring 2007.

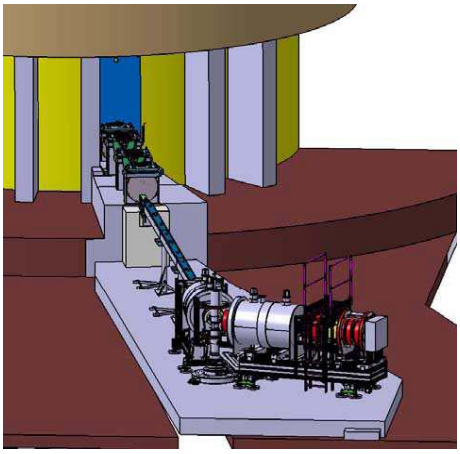

FIG. 1: View on the secondary spectrometer with the downstream choppers, guide system and the revolver drum.

- The chopper systems is currently in our central department of technology (ZAT) under construction. Beside the support structures which are already manufactured one chopper has already been completed. However hardware tests as well as adaption of the electronic components have to be performed within the next few weeks for this chopper. The discussion to handle the master pulse resulted in the use of special electronic cards developed by SNS which will soon be bought by FZJ for test operation.
- The first two neutron guide pieces - section A and section B - will be installed in the first week of January 2007 which is at the same time a time window without the production of neutrons at the SNS. Of course the guide pieces have been produced up to this date and were accepted.

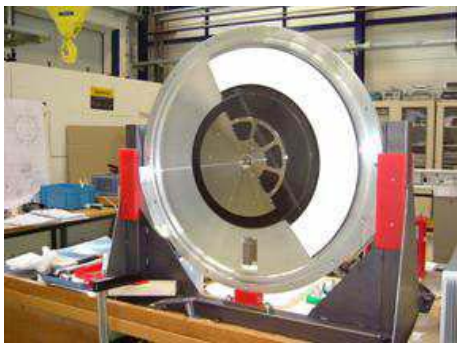

FIG. 2: First chopper completed of the four chopper system in our central department of technology.

- The guide field tests for the polarizers permanent magnet system had been done and specification has been sent to Swiss Neutronics. The first of the requested three polarizers will be available in two weeks as expected. Our central department of technology already startet to manufacture the revolver. Completion date is still in accordance to the project plan spring 2007.
- Our central department of technology already startet to manufacture the revolver. Completion date is still in accordance to the project plan spring 2007.
- We had several meetings with the vendor Babcock Noell Nuclear producing the superconducting main precession coils. Finally the superconducting strand has been choosen and

several considerations to improve the thermal stability have been implemented in the design and layout especially of the winding core. Also manufacturing drawings of the SC coils and its support structure had been proven and were accepted. Subsequently all foreseen milestones have been achieved. Completion date is still end of 2007. Also the field integral has been increased to 1.8Tm instead of 1.5Tm which finally will enhance the worlwide highest resolution of the instrument by 20%.

– The power supply system has been ordered at Bruker Biospin and the contract has been signed already mid of 2006. In this period further electronic implementations have been prepared from our central department of electronics.

– It has been decided to use a granit floor instead of the foresseen NIST Polyethylene floor which has the advantage of non-sensibility to liquid nitrogen. The floor will be installed starting January 2008 after the instrument enclosure has been completed.

– The granit floor has an impact on the final height of the floor to the beam. Thus the height of the already produced sample stage has to be shortened. The impact onto the already produced carrier 1 and 2 is negligible but minor changes will bbe implemented.

– One of our scientist of the electronic department visited the SNS and discussed several interfaces with the SNS. No major challenges were encountered which will not influence the time schedule.

– The order for the 2D detector is placed. Subsequently DENEX in Geesthacht, Germany will produce the detector with the front - end electronics. The 2D detector shall be available mid of 2007.

FIG. 3: The sample stage which has been completed with a lifting mechanism to automatically switch between different samples.

– Swiss Neutronics will produce the analyzer. Delivery is expected mid of 2007. The analyzer housing is now completed in our ZAT department and first tests have been succesfully performed to fit the thin glass plates into the support structure. Also first coatings have been performed by Swiss Neutronics and worked fine.

– The collimator is still under construction. The completion date to spring 2007 did not change.

– The contract to build the instrument enclosure has been given already in the last reporting period to the company AMUNEAL. In the past period we had a kick - off meeting and a 35 % design review meeting with all participating parties AMUNEAL, SNS, FZJ and CH2M (responsible for all concrete work). The schedules was worked out and showed completion date mid of 2008.

– The manufacturing procedure of the correction coils with tilted diagonal cuttings continued during the past year. In detail one correction coil had been produced but showed a short - cut between the backplate and the winding itself. Thus the manufacturing method still has to be more settled to gain a better and higher output of functionable CC's. A new project for the european framework program 7 has been announced with the development of new low small angle scattering Fresnel coils which shall replace existing coils near our sample stage. Cooperation with the Institut Laue Langevin CC development is foreseen. Also a meeting with the NSE team at the Hahn Meitner Institute, Berlin, Germany took place and showed superposition of general interests in the development of low small angle scattering CC's. Common effort is envisaged.

– All five hexapods acceptance test and the amagnetic position mechanism has been completed and are available now.

– 51 solenoids were designed for the secondary spectrometer. Manufacturing started a week ago and will be completed in 2 months.

To summarize, all major components for the spectrometer shall be available until 12/31/2007. Due to the instrument enclosure installation the installation phase of the secondary spectrometer shall start beginning of 2008. Commisioning is planned for 2009.

First Neutrons for J-NSE at the FRM II

O. Holderer[1], M. Monkenbusch[1], R. Schätzler[1], G. Vehres[1], D. Richter[1], W. Westerhausen[2], Ch. Tiemann[2], U. Giesen[2], G. Hansen[2], H. Kleines[3], M. Drochner[3], F. Suxdorf[3], M. Wagener[3], P. Kaemmerling[3], M. Bednarek[4], G. Borchert[5], and C. Breunig[5]

[1] Institut für Neutronenstreuung and Jülich Center for Neutron Science
[2] Zentralabteilung Technologie
[3] Zentralabteilung für Elektronik
[4] Betriebsdirektion Gebäudeleittechnik
[5] ZWE FRM II, TU München

Neutron spin-echo spectrometers have the highest energy resolution of all types of neutron spectrometers [1, 2] and allow for the analysis of slow motions on large and on intermediate scale. They directly measure the Fourier transform of the spectrum, i.e. the intermediate scattering function. The relevant resolution parameter is the maximum achievable Fourier time. The Neutron spin-echo spectrometer that was in operation at the FRJ-2 since 1996 has been moved to the new reactor FRMII in Munich because the DIDO reactor (FRJ-2) has finally stopped operation. It belongs to the JCNS (Jülich Center for Neutron Science) instrument suite. In the course of this moving an update of the electronics has been made and measures to improve resolution have been implemented. The new position at the end of a guide pointing to a high flux cold source yields a considerable flux gain and a wider useable wavelength range compared to the position at the FRJ-2. Together this will extend the useful resolution –expressed in terms of Fourier times– to several $100\,\mathrm{ns}$ corresponding to a few neV quasielastic line width. Currently all main functional parts are installed and first flux measurements and a first echo signal with a pencil beam could be accomplished.

FIG. 1: One of the two main precession coils of the J-NSE spectrometer entering the neutron guide hall

FIG. 2: The NSE spectrometer during installation in the neutron guide hall.

In March 2006 the FRJ2-NSE spectrometer [3] was transferred from the ELLA neutron guide hall in Jülich to the guide hall at the FRMII in Munich (see Fig. 1). To adapt to the beam height at the FRM-II which is about 24 cm below that at Jülich, the carrier structure of the spectrometer arms has been reconstructed. The correction elements are now mounted on motor controlled positioning devices enabling more precise adjustment. The neutron guide system had been designed and installed according to our layout by the neutron guide group of the FRMII. It splits from the NL2 at the entrance of the guide hall casemat where an 8m polarising (FeSi multilayer) section with R=160m curvature follows. A velocity selector and 10m tapered straight guide lead the neutrons to the instrument.

Extra lead shielding around the neutron entrance into the instrument has been installed, first measurments indicate that –after positioning mobile lead walls on the boundary to the neighbouring instrument (Mephisto) area– the radiation levels outside the Tanzboden stay within the required $3\mu\mathrm{Sv/h}$ limit. The electrical installations, cabling of all coils, sensors and motors, took place in 2006. Electrical power and water cooling that comply to the 200KW maximum power consumption of the main coils has been passed to the instrument position. The electronics of the spectrometer has been modernized. In particular new power supplies (except that for the main coils) have been installed, all current sources as well as the SPS modules for hardware control are equipped

with profibus interfaces. The hardware (powersupplies, motors, sensors) is now controlled with Taco servers according to the "Jülich Münchner Standard". The performance of the spectrometer is largely improved at the FRM-II due to several reasons. The spectrometer is now located at the end of the neutron guide NL2a-o, which enables us to select the wavelength in the range of about 4.5 to 16 Å. Short wavelengths (up to about 8 Å) will be polarized in the bent FeSi polarizing neutron guide inside the casemate. For larger wavelengths, a polarizer will be employed that is installed at the end of the neutron guide. The cross section of the guide at exit is $60 \times 60\,\mathrm{mm}^2$.

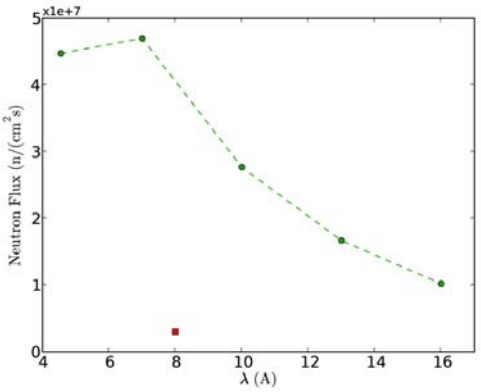

FIG. 3: Neutron flux at the end of the neutron guid NL2a-o. For comparison, the flux at the FRJ-2 is shown (red square).

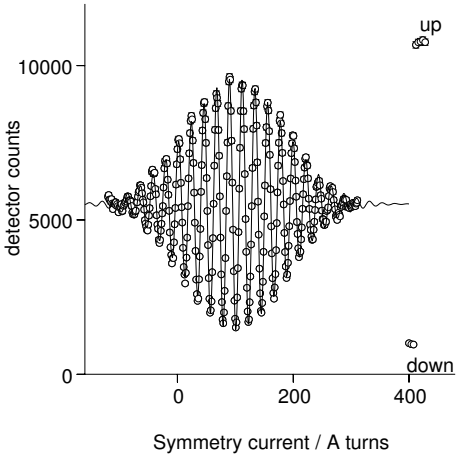

FIG. 4: First echo obtained at $\lambda = 5\,\text{Å}$ of the J-NSE at FRMII. The illumination still with a pencil arund the axis, the main coil current was 8.5A. The count data groups at the right side correspond to the limits of the polarisation anlysis.

New correction coils have been designed and manufactured, the new backplate avoids loss of geometrical precision and yields better heat removal, use of pure Al instead of AlMg3 results in smaller electrical resistance and better heat conduction. This allows the use of higher currents correspondig up to and the maximum field integral of 0.5 Tm of the main precession coils. Tests in Jülich during the last NSE cycle there showed the path to a further necessary modification in the correction coil shape that will improve the correction efficiency. The thus designed coil generation with oblique cuts is under production at the FZJ and will replace the current generation after the first operation cycle.

The neutron flux at the exit of the neutron guide NL2a-o has been measured with gold foil activation analysis (in collaboration with K. Zeitelhack, TUM). The results are presented in Figure 3. At $\lambda = 7$ Å, the flux is about 15 times higher than it was at the neutron guide exit at the FRJ-2, in addition the beam cross section at FRMII is 2.7 larger than that in Jülich. The flux has been compared to McStas simulations (although made with a simplified cold source). The simulated flux agrees reasonably well with the measured values. At higher wavelengths, the neutron flux is smaller than predicted, an observation made also with more sophisticated models of the cold source.

The larger neutron guide exit, the higher flux and the better correction elements push the performance of the instrument to Fourier times $\lambda = 1$ ps to ~ 350 ns, with a q-range of q=$0.02 \cdots 1.5\,\text{Å}^{-1}$

A first test using small diaphragms at the beam entrance and the detector position and straight spectrometer configuration were made to abtain a first echo signal for different wavelength between 5 and 8 Å. Figure 4 shows the resuly for 5 Å neutrons, proving that the main components are operational and work properly.

After the basic function is obtained and confirmed some further work remains until the first samples can be measured, like testing and calibrating the mechanics for the long wavelength polariser, installing the circuitry for maintaining He-athmosphere along the neutron flight path and adjustment of the correction elements. These will be completed in the first month of 2007.

[1] F. Mezei, ed., *Neutron Spin Echo*. no. 128 in Lecture Notes in Physics Vol. 128 (Springer,Berlin, Heidelberg, New York, 1980).

[2] D. Richter, M. Monkenbusch, A. Arbe, and J. Colmenero, *Neutron Spin Echo in Polymer Systems*, no. 174 in Advances in Polymer Science, (2005).

[3] M. Monkenbusch, R. Schätzler, and D. Richter, Nuclear Instruments & Methods In Physics Research Section A-accelerators Spectrometers Detectors And Associated Equipment **399**, 301 (1997).

Publications are the most important medium for presenting research results to the academic and general public.

Publications and Events

Publications

Akola, J.; Jones, R. O.
Density functional calculations of ATP systems I: Crystalline ATP hydrates and related molecules
Journal of Physical Chemistry B, 110 (2006), 8110 – 8120

Akola, J.; Jones, R. O.
Density functional calculations of ATP systems II: ATP hydrolysis at the active site of actin
Journal of Physical Chemistry B, 110 (2006), 8121 – 8129

Akola, J.; Rytkonen, K.; Manninen, M.
Electronic properties of single-walled carbon nanotubes inside cyclic supermolecules
Journal of Physical Chemistry B, 110 (2006), 5186 – 5190

Anders, Chr.; Meßlinger, S.; Urbassek, H. M.
Deformation of slow liquid and solid clusters upon deposition: A molecular-dynamics study of Al cluster impact on an Al surface
Surface Science, 600 (2006), 2587 – 2593

Andreyev, O.; Koroteev, Yu. M.; Sánchez Albaneda, M.; Cinchetti, M.; Bihlmayer, G.; Chulkov, E. V.; Lange, J.; Steeb, F.; Bauer, M.; Echenique, P. M.; Blügel, S.; Aeschlimann, M.
Spin-resolved two-photon photoemission study of the surface resonance state on Co/Cu(001)
Physical Review B, 74 (2006), 195416

Antons, A.; Berger, R.; Schroeder, K.; Voigtländer, B.
Structure of steps on As-passivated Si(111): Ab initio calculations and scanning tunneling microscopy
Physical Review B, 73 (2006), 125327

Arora, S. K.; Sofin, R.G.S.; Shvets, I. V.; Luysberg, M.
Anomalous strain relaxation behaviour of Fe_3O_4/MgO (100) heterostructures grown using molecular beam epitaxy
Journal of Applied Physics, 100 (2006), 073908

Banchio, A. J.; Gapinski, J.; Patkowski, A.; Häußler, W.; Fluerasu, A.; Sacanna, S.; Holmqvist, P.; Meier, G.; Lettinga, M. P.; Nägele, G.
Many-Body Hydrodynamic Interactions in Charge-Stabilized Suspensions
Physical Review Letters, 96 (2006), 138303

Baud, S.; Bihlmayer, G.; Blügel, S.; Ramseyer, Ch.
First-principles investigation of Co wires at Pt(111) step-edges
Surface Science, 600 (2006), 18, 4301 – 4304

Baud, S.; Ramseyer, Ch.; Bihlmayer, G.; Blügel, S.
Relaxation effects on the magnetism of decorated step edges: Co/Pt(664)
Physical Review B, 73 (2006), 104427

Baumgaertner, A.
Biological Nanomachines
Computational Condensed Matter Physics : Lecture Manuscripts of the 37th Spring School of the Institute of Solid State Research ; this spring school was organized by the Institute of Solid State Research in the Forschungszentrum Jülich on March 6 -17, 2006 / ed.: S. Blügel, G. Gompper, E. Koch, H. Müller-Krumbhaar, R. Spatschek, R. G. Winkler. – Jülich, 2006. – (Schriften des Forschungszentrums Jülich. Reihe Materie und Material / Matter and Material ; 32). – 3-89336-430-7. – S. B10.1 – B10.25

Baumgaertner, A.
Biomolecular Machines
Handbook of Theoretical and Computational Nanotechnology / ed.: M. Rieth, W. Schommers. – American Scientific Publishers. – 6 (2006). – S. 73

Bedanta, S.; Kentzinger, E.; Petracic, O.; Kleemann, W.; Rücker, U.; Brückel, T.; Paul, A.; Cardoso, S.; Freitas, P. P.
Modulated magnetization depth profile in dipolarly coupled magnetic multilayers
Physical Review B, 74 (2006), 054426-1 – 054426-3

Bergqvist, L.; Eriksson, O.
Theory of weakly coupled two-dimensional magnets
Journal of Physics: Condensed Matter, 18 (2006), 4853

Bhat, S.; Tuinier, R.; Schurtenberger, P.
Spinodal decomposition in a food colloid-biopolymer mixture: evidence for a linear regime
Journal of Physics: Condensed Matter, 18 (2006), L339 – L346

Bhattacharya, S.; Hermann, R. P.; Keppens, V.; Tritt, T. M.; Snyder, G. J.
Effect of disorder on the thermal transport and elastic properties in thermoelectric Zn_4Sb_3
Physical Review B, 74 (2006), 134108-1 – 134108-5

Bihlmayer, G.
Magnetism in Density Functional Theory
Computational Condensed Matter Physics : Lecture Manuscripts of the 37th Spring School of the Institute of Solid State Research ; this spring school was organized by the Institute of Solid State Research in the Forschungszentrum Jülich on March 6 -17, 2006 / ed.: S. Blügel, G. Gompper, E. Koch, H. Müller-Krumbhaar, R. Spatschek, R. G. Winkler. – Jülich, 2006. – (Schriften des Forschungszentrums Jülich. Reihe Materie und Material / Matter and Material ; 32). – 3-89336-430-7. – S. A2.1 – A2.18

Bihlmayer, G.
Non-Collinear Magnetism: Exchange Parameter and T_c
Computational Nanoscience: Do It Yourself!: NIC Winter School 2006 / ed.: J. Grotendorst, S. Blügel, D. Marx. – (NIC Series ; 31). – 3-00-017350-1. – S. 447 – 467

Bihlmayer, G.; Ferriani, P.; Baud, St.; Lezaic, M.; Heinze, S.; Blügel, S.
Ultra-Thin Magnetic Films and Magnetic Nanostructures on Surfaces
NIC Symposium 2006 : 1 – 2 March 2006, Forschungszentrum Jülich ; proceedings / ed.: G. Münster, D. Wolf, M. Kremer. – Jülich, Forschungszentrum, 2006. – (NIC series ; 32). – 3-00-017351-X. – S. 151 – 158

Bihlmayer, G.; Koroteev, S. B.; Echenique, P. M.; Chulkov, E. V.; Blügel, S.
The Rashba-effect at metallic surfaces
Surface Science, 600 (2006), 18, 3888 – 3891

Blügel, S.
Density Functional Theory in Practice
Computational Condensed Matter Physics : Lecture Manuscripts of the 37th Spring School of the Institute of Solid State Research ; this spring school was organized by the Institute of Solid State Research in the Forschungszentrum Jülich on March 6 -17, 2006 / ed.: S. Blügel, G. Gompper, E. Koch, H. Müller-Krumbhaar, R. Spatschek, R. G. Winkler. – Jülich, 2006. – (Schriften des Forschungszentrums Jülich. Reihe Materie und Material / Matter and Material ; 32). – 3-89336-430-7. – S. A8.1 – A8.36

Blügel, S. (Hrsg.); Gompper, G. (Hrsg.); Koch, E. (Hrsg.); Müller-Krumbhaar, H. (Hrsg.); Spatschek, R. (Hrsg.); Winkler, R. G. (Hrsg.)
Computational Condensed Matter Physics:
Lecture manuscripts of the 37th Spring School of the Institute of Solid State Research; this Spring School was organized by the Institute of Solid State Research in the Forschungszentrum Jülich on March 6 – 17, 2006 – Jülich, Forschungszentrum, Zentralbibliothek, 2006 – Schriften des Forschungszentrums Jülich – Reihe Materie und Material / Matter and Materials ; 323-89336-430-7

Blügel, S.; Bihlmayer, G.
The Full-Potential Linearized Augmented Plane Wave Method
Computational Nanoscience: Do It Yourself! : NIC Winter School 2006 / ed.: J. Grotendorst, S. Blügel, D. Marx. – (NIC Series ; 31). – 3-00-017350-1. – S. 85 – 129

Boese, M.; Heeg, T.; Schubert, J.; Luysberg, M.
HRTEM investigation of the epitaxial growth of scandate/titane multilayers
Journal of Materials Science, 41 (2006), 4434 – 4439

Botti, A.; Pyckhout-Hintzen, W.; Richter, D.; Urban, V.; Straube, E.
A microscopic look at the reinforcement of silica-filled rubbers
Journal of Chemical Physics, 124 (2006), 174908

Bowen, M.; Barthelemy, A.; Bellini, V.; Dederichs, P. H.
Observation of Fowler-Nordheim hole tunneling across an electron tunnel junction due to total symmetry filtering
Physical Review B, 73 (2006), 14, 140408

Breidbach, M.; Bürgler, D. E.; Grünberg, P.
Current-in-plane giant magnetoresistance: The effect of interface roughness and spin-depolarization due to the proximity of a buffer layer
Journal of Magnetism and Magnetic Materials, 307 (2006), 2, L1 – L6

Brener, E. A.; Iordanskiy, S.V.; Saptsov, R. B.
Condensation and vortex formation in a Bose gas upon cooling
Physical Review E, 73 (2006), 016127

Brener, E. A.; Marchenko, V. I.
Elastic Domains in Antiferromagnets on Substrates
Physical Review Letters, 97 (2006), 067204

Brzank, A.; Schütz, G.
Amplication of Molecular Traffic Control in catalytic grains with novel channel topology design
Journal of Chemical Physics, 124 (2006), 214701

Bräuer, J.; Brzank, A.; Kärger, J.
Two-Component Desorption from Anisotropic Pore Networks
Journal of Chemical Physics, 124 (2006), 034713

Buca, D.; Feste, S.; Holländer, B.; Trinkaus, H.; Mantl, S.; Loo, R.; Caymax, M.
Fabrication and Characterisation of patterned SiGe/Si lines with asymmetric biaxial stress
Conference Digest of the Third International Silicon Germanium Technology and Devices Meeting, 15 May – 17 May 2006, Princeton, USA. – 2006. – (IEEE Conference Paper). – S. 252

Buchenau, U.; Ohl, M.; Wischnewski, A.
A new interpretation of dielectric data in molecular glass formers
Journal of Chemical Physics, 124 (2006), 094505

Buchmeier, M.; Bürgler, D. E.; Grünberg, P. A.; Schneider, C. M.; Meijers, R.; Calarco, R.; Raeder, C.; Farle, M.
Anisotropic FMR-linewidth of triple-domain Fe layers on hexagonal GaN(0001)
Physica Status Solidi A, 203 (2006), 7, 1567 – 1572

Budyak, I.L.; Pipich, V.; Mironova, O.S.; Schlesinger, R.; Zaccai, G.; Klein-Seetharaman, J.
Shape and oligomerization state of the cytoplasmic domain of the phototaxis transducer II from Natronobacterium pharaonis
Proceedings of the National Academy of Sciences of the United States of America, 103 (2006), 42, 15428 – 15433

Caciuc, V.; Hölscher, H.; Blügel, S.; Fuchs, H.
Atomic-scale sharpening of silicon tips in non-contact atomic force microscopy
Physical Review Letters, 96 (2006), 016101

Caymax, M.; Delhougne, R.; Ries, M.; Luysberg, M.; Loo, R.
Non-selective thin SiGe strain-relaxed buffer layers: Growth and carbon-induced relaxation
Thin Solid Films, 508 (2006), 260

Chatterji, T.; Koza, M. M.; Demmel, F.; Schmidt, W.; Hoffmann, J.-U.; Aman, U.; Schneider, R.; Dhalenne, G.; Suryanarayanan, R.; Revcolevschi, A.
Coexistence of ferromagnetic and antiferromagnetic spin correlations in $La_{1.2}Sr_{1.8}Mn_2O_7$
Physical Review B, 73 (2006), 104449-1 – 104449-6

Chen, J.; Jung, P.; Nazmy, M.; Hoffelner, W.
In situ creep under helium implantation of titanium-aluminium alloy
Journal of Nuclear Materials, 352 (2006), 36 – 41

Chen, J.; He, Z. Y.; Jung, P.
Microstructure of helium-implanted alpha-Al_2O_3 *after annealing*
Acta Materialia, 54 (2006) , 1607 – 1614

Cherstvy, A. G.; Winkler, R. G.
Strong *and weak adsorptions of polyelectrolyte chains onto oppositely charged spheres*
Journal of Chemical Physics, 125 (2006), 064904

Chioncel, L.; Mavropoulos, Ph.; Lezaic, M.; Blügel, S.; Arrigoni, E.; Katsnelson, M. I.; Lichtenstein, A. I.
Half-Metallic Ferromagnetism Induced by Dynamic Electron Correlations in VAs
Physical Review Letters, 96 (2006), 197203

Conrad, H.
Prospects of a European Spallation Source at Forschungszentrum Jülich
Proceedings of ICANS-XVII, 17th Meeting of the International Collaboration on Advanced Neutron Sources, April 2005, Sante Fe, New Mexico. – Los Alamos National Laboratory, 2006. – (LA-UR-06-3904). – S. 25

Costa, D.; Hansson, P.; Schneider, S.; Miguel, M. G.; Lindman, B.
Interaction between covalent DNA gels and a cationic surfactant
Biomacromolecules, 7 (2006), 1090 – 1095

Costi, T. A.
The numerical renormalization group for quantum impurity models
Computational Condensed Matter Physics : Lecture Manuscripts of the 37th Spring School of the Institute of Solid State Research ; this spring school was organized by the Institute of Solid State Research in the Forschungszentrum Jülich on March 6 -17, 2006 / ed.: S. Blügel, G. Gompper, E. Koch, H. Müller-Krumbhaar, R. Spatschek, R. G. Winkler. – Jülich, 2006. – (Schriften des Forschungszentrums Jülich . Reihe Materie und Material / Matter and Material ; 32). – 3-89336-430-7. – S. A14.1 – 14.24

Da Silva, J. L. F.; Barreteau, C.; Schroeder, K.; Blügel, S.
All-electron first-principles investigations of the energetics of vicinal Cu surfaces
Physical Review B, 73 (2006), 125402

Da Silva, J. L. F.; Schroeder, K.; Blügel, S.
Linear scaling of the interlayer relaxations of the vicinal Cu(p,p,p-2) surfaces with the number of atom-rows in the terraces
Surface Science, 600 (2006), 3008 – 3014

Damm, T.; Buchmeier, M.; Schindler, A.; Bürgler, D. E.; Grünberg, P.; Schneider, C. M.
Magnetic properties of Fe films and Fe/Si/fe trilayers grown on GaAs(001) and MgO(001) by ion-beam sputter epitaxy
Journal of Applied Physics, 99 (2006), 093905

Dasgupta, A.; Premkumar, P.A.; Lawrence, F.; Houben, L.; Kuppusami, P.; Luysberg, M.; Nagaraja, K.S.; Raghunathan, V.S.
Microstructure of thick chromium-nitride coating synthesized using plasma assisted MOCVD technique
Surface and Coatings Technology, 201 (2006), 1401

Dasgupta, A.; Huang, Y.; Houben, L.; Klein, S.; Finger, F.; Carius, R.; Luysberg, M.
Effect of filament and substrate temperatures on the structural and electrical properties of SiC thin films grown by the HWCVD technique
4th International Conference on Hot-Wire CVD (Cat-CVD) Process, October 3.-8.2006, Takayama, Japan : Extended Abstracts. – 2006. – S. 286 – 288

Dasgupta, A.; Klein, S.; Houben, L.; Carius, R.; Finger, F.; Luysberg, M.
Microstructure of highly crystalline silicon carbide thin films grown by HWCVD technique
4th International Conference on Hot-Wire CVD (Cat-CVD) Process, October 3.-8.2006, Takayama, Japan: Extended Abstracts. – 2006. – S. 137 – 139

Dassow, H.; Lehndorff, R.; Bürgler, D. E.; Buchmeier, M.; Grünberg, P. A.; Schneider, C. M.; van der Hart, A.
Normal and inverse current-induced magnetization switching in a single nanopillar
Applied Physics Letters, 89 (2006), 222511

Dederichs, P. H.; Lounis, S.; Zeller, R.
The Korringa-Kohn-Rostoker (KKR) Green Function Method II. Impurities and Clusters in the Bulk and on Surfaces
Computational Nanoscience: Do It Yourself! : NIC Winter School 2006 / ed.: J. Grotendorst, S. Blügel, D. Marx. – (NIC Series ; 31). – 3-00-017350-1. – S. 279 – 298

Dederichs, P. H.; Szotek, Z.; Ordejon, P.
Scientific highlights from the Psi(k) network: Towards atomistic materials design
Physica Status Solidi B, 243 (2006), 11, 2445

Denesyuk, N. A.; Gompper, G.
Mixing A and B homopolymers with AC diblock copolymers: Phase behaviour of asymmetric polymer blends
Macromolecules, 39 (2006), 5497 – 5511

Divin, Y. Y.; Tkachev, D. A.; Pavlovskii, V. V.; Volkov, O. Y.; Liatti, M. V.; Gubankov, V. N.; Urban, K.
Classical and Josephson detection of terahertz radiation using $YBa_2Cu_3O_{7-x}$(100)-tilt bicrystal junctions
Journal of Physics : Conference Series, 43 (2006), 1322 – 1325

Ebert, H.; Bornemann, S.; Minar, J.; Dederichs, P. H.; Zeller, R.; Cabria, I.
Magnetic Properties of Co- and FePt-Clusters
Computational Materials Science, 35 (2006), 279 – 282

Ehrhart, P.; Thomas, R.
Electrical properties of (Ba, Sr) TiO_3 thin films revisited: the case of chemical vapor deposited films on Pt electrodes
Journal of Applied Physics, 99 (2006), 114108

Eisenriegler, E.
Anisotropic colloidal particles interacting with polymers in a good solvent
Journal of Chemical Physics, 124 (2006), 14, 144912

Eisenriegler, E.
Long flexible polymers interacting with ellipsoids, cylinders, and needles
Journal of Chemical Physics, 125 (2006), 204903

Embs, J.; Müller, H. W.; Krill, C. E.; Meyer, F.; Natter, H.; Müller, B.; Wiegand, S.; Lücke, M.; Knorr, G. M.; Hempelmann, R.
Characterization of the Grain Size in Ferromagnetic Colloids: Comparing Torsional-Pendulum Measurements with Standard Complementary Methods
Zeitschrift für physikalische Chemie, 220 (2006), 153 – 171

Faley, M. M.; Jia, C. L.; Houben, L.; Meertens, D.; Poppe, U.; Urban, K.
Meandering of the grain boundary and d-wave effects in high-Tc bicrystal Josephson junctions
Superconductor Science and Technology, 19 (2006), 195 – 199

Faley, M.; Mi, S. B.; Petraru, A.; Jia, C. L.; Poppe, U.; Urban, K.
Multilayer Buffering of MgO Substrates Intended for the Preparation of Strain-Free Epitaxial Quatum Devises
Proceedings of ND 2006 : Conference "Nanoelectronic Days 2006", 9.10. – 11.10.2006 in Aachen. – 2006. – S. 71

Faley, M.; Mi, S. B.; Petraru, A.; Jia, C. L.; Poppe, U.; Urban, K.
Multilayer buffer for high-temperature superconductor devises on MgO
Applied Physics Letters, 89 (2006), 082507

Faley, M.; Poppe, U.; Urban, K.; Paulson, D. N.; Fagaly, R.L.
A new generation of the HTS multilayer DC-SQUID magnetometers and gradiometers
Journal of Physics : Conference Series, 43 (2006), 1199 – 1202

Feuerbacher, M.; Caillard, D.
Dynamics of phason diffusion in icosahedral Al-Pd-Mn quasicrystals
Acta Materialia, 54 (2006), 3233 – 3240

Friedrich, Ch.; Schindlmayr, A.
Many-Body Perturbation Theory: The GW Approximation
Computational Condensed Matter Physics : Lecture Manuscripts of the 37th Spring School of the Institute of Solid State Research ; this spring school was organized by the Institute of Solid State Research in the Forschungszentrum Jülich on March 6 -17, 2006 / ed.: S. Blügel, G. Gompper, E. Koch, H. Müller-Krumbhaar, R. Spatschek, R. G. Winkler. – Jülich, 2006. – (Schriften des Forschungszentrums Jülich. Reihe Materie und Material / Matter and Material ; 32). – 3-89336-430-7. – S. A5.1 – A5.21

Friedrich, Ch.; Schindlmayr, A.
Many-Body Perturbation Theory: The GW Approximation
Computational Nanoscience: Do It Yourself! : NIC Winter School 2006 / ed.: J. Grotendorst, S. Blügel, D. Marx. – (NIC Series ; 31). – 3-00-017350-1. – S. 335 – 355

Friedrich, Ch.; Schindlmayr, A.; Blügel, S.; Kotani, E. A.
Elimination of the linearization error in GW calculations based on the linearized augmented-plane-wave method
Physical Review B, 74 (2006), 045104

Frielinghaus, H.; Maccarrone, S.; Byelov, D.; Allgaier, J.; Richter, D.; Auth, T; Gompper, G.
SANS studies of confined diblock copolymers in microemulsions
Physica B: Condensed Matter, 385-386 (2006), 738 – 741

Fukushima, T.; Sato, K.; Katayama-Yoshida, H.; Dederichs, P. H.
Ab initio study of spinodal decomposition in (Zn,Cr) Te
Physica Status Solidi A, 203 (2006), 11, 2751 – 2755

Fukushima, T.; Sato, K.; Katayama-Yoshida, H.; Dederichs, P. H.
Spinodal decomposition under layer by layer growth condition and high Curie temperature quasi-one-dimensional nano-structure in dilute magnetic semiconductors
Japanese Journal of Applied Physics Part 2: Letters, 45 (2006), 12/16, L416 – L418

Fukushima, T.; Sato, K.; Yoshida, H. K.; Dederichs, P. H.
Theoretical investigations of magnetic properties in (Zn, Cr)Te by first principles calculations
Physica B: Condensed Matter, 376 (2006), 786 – 789

Gabel, F.; Wang, D.; Madern, D.; Sadler, K.; Dayie, M.; Zamanian Daryoush, M.; Schwahn, D.; Zaccai, G.; Lee, X.; Williams, B.R.G.
Dynamic Flexibility of Double-stranded RNA Activated PKR in Solution
Journal of Molecular Biology, 359 (2006), 610 – 623

Galanakis, I.; Özdogan, K.; Sasioglu, E.; Aktas, B.
Defects in CrAs and related compounds as a route to half-metallic ferrimagnetism
Physical Review B, 74 (2006), 140408(R)

Galanakis, I.; Mavropoulos, Ph.; Dederichs, P. H.
Electronic structure and Slater-Pauling behaviour in half-metallic Heusler alloys calculated from first principles
Journal of Physics D – Applied Physics, 39 (2006), 765 – 775

Gareev, R. R.; Bugoslavsky, Yu. V.; Schreiber, R.; Paul, A.; Sperl, M.; Döppe, M.
Carrier-induced ferromagnetism in Ge(Mn,Fe) magnetic semiconductor thin-film structures
Applied Physics Letters, 88 (2006), 222508-1 – 222508-3

Gareev, R. R.; Weides, M.; Schreiber, R.; Poppe, U.
*Resonant Tunneling Magnetoresistive in Antiferromagnetically coupled Fe-based Structures with Multi-layered Si/Ge Spacer*s
Applied Physics Letters, 88 (2006), 172105

Genix, A.-C.; Arbe, A.; Alvarez, F.; Colmenero, J.; Farago, B.; Wischnewski, A.; Richter, D.
Self- and Collective Dynamics of Syndiotactic Poly(methylmethacrylate). A Combined Study by Quasi-elastic Neutron Scattering and Atomistic Molecular Dynamics Simulations
Macromolecules, 39 (2006), 6260 – 6272

Genix, A.-C.; Arbe, A.; Alvarez, F.; Colmenero, J.; Schweika, W.; Richter, D.
Local structure of syndiotactic poly(methyl methacrylate). A combined study by neutron diffraction with polarisation analysis and atomistic molecular dynamics simulations
Macromolecules, 39 (2006), 3947 – 3958

Goerigk, G.; Williamson, D. L.
Temperature induced differences in the nanostructure of hot-wire deposited silicon-germanium alloys analyzed by anomalous small-angle x-ray scattering
Journal of Applied Physics, 99 (2006), 084309-1 – 084309-8

Gompper, G.; Noguchi, H.
Coarse-Grained and Continuum Models of Membranes
Computational Condensed Matter Physics: Lecture Manuscripts of the 37th Spring School of the Institute of Solid State Research ; this spring school was organized by the Institute of Solid State Research in the Forschungszentrum Jülich on March 6 -17, 2006 / ed.: S. Blügel, G. Gompper, E. Koch, H. Müller-Krumbhaar, R. Spatschek, R. G. Winkler. – Jülich, 2006. – (Schriften des Forschungszentrums Jülich. Reihe Materie und Material / Matter and Material ; 32). – 3-89336-430-7. – S. B9.1 – B9.26

Grotendorst, J. (Hrsg.); Blügel, S. (Hrsg.); Marx, D. (Hrsg.)
Computational Nanoscience: Do It Yourself! ;
NIC Winter School, 14 – 22 February 2006, Forschungszentrum Jülich, Germany – Lecture Notes
Jülich, FZJ, John von Neumann Institute for Computing, 2006
NIC series ; 313-00-017350-1

Grushko, B.; Kowalska-Strzeciwilk, E.; Przepiorzynski, B.; Surowiec, M.
An investigation of the Al-Cu-Cr phase diagram: Phase equilibria at 800-1000°C
Journal of Alloys and Compounds, 417 (2006), 121 – 126

Guenther, L.; Peukert, W.; Goerigk, G.; Dingenouts, N.
Microstructure formation in dip-coated particulate films
Journal of Colloid and Interface Science, 294 (2006), 309 – 320

Guo, X.; Waser, R.
Electrical properties of the grain boundaries of oxygen ion conductors: acceptor-doped zirconia and ceria
Progress in Materials Science, 51 (2006), 151

Guzenko, V. A.; Knobbe, J.; Hardtdegen, H.; Schäpers, Th.; Bringer, A.
Rashba effect in InGaAs/InP parallel quantum wires
Applied Physics Letters, 88 (2006), 032102

Harris, R. J.; Rakos, A.; Schütz, G. M.
Breakdown of Gallavotti-Cohen symmetry for stochastic dynamics
Europhysics Letters, 75 (2006), 227 – 233

Hauck, J.; Mika, K.
Interactions from Self-Coordination Numbers – A Physical Relation Without Formula
International Journal of Modern Physics B, 20 (2006), 2065 – 2084

He, J. Q.; Vasco, E.; Dittmann, R.; Wang, R. H.
Growth dynamics and strain relaxation mechanisms in $BaTiO_3$ pulsed laser deposited on $SrRuO_3/SrTiO_3$
Physical Review B, 73 (2006), 125413

He, J.; Dittmann, R.; Karthäuser, S.; Vasco, E.
Geometric shadowing from rippled $SrRuO_3/SrTiO_3$ surface templates induces self-organization of epitaxial $SrZrO_3$ nanowires
Physical Review B, 74 (2006), 205410

Hedström, M.; Schindlmayr, A.; Schwarz, G.; Scheffler, M.
Quasiparticle Corrections to the Electronic Properties of Anion Vacancies at GaAs(110) and InP(110)
Physical Review Letters, 97 (2006), 226401

Heggen, M.; Feuerbacher, M.
Metadislocation arrangements in the complex metallic alloy ksi-Al-Pd-Mn
Philosophical Magazine, 86 (2006), 6/8, 985 – 990

Henry, J.; Vincent, L.; Averty, X.; Marini, B.; Jung, P.
Bending tests on T91 samples implanted with 0.25 at.% helium: Experiments and mechanical analysis
Journal of Nuclear Materials, 356 (2006), 78 – 87

Hermann, R. P.; Grandjean, F.; Keppens, V.; Schweika, W.; Nolas, G. S.; Mandrus, D. G.; Sales, B. C.; Christen, H. M.; Bonville, P.; Long, G. J.
The dynamics of the caged guests in filled germanium clathrates
Materials and Technologies for Direct Thermal-to-Electric Energy Conversion / ed.: J. Yang, T.P. Hogan, R. Funahashi, G.S. Nolas. – Warrendale, PA, MRS, 2006. – (Materials Research Society Symposium proceedings ; 886). – 1-55899-840-3. – S. 389 – 394

Hermes, H. E.; Frielinghaus, H.; Pyckhout-Hintzen, W.; Richter, D.
Quantitative analysis of small angle neutron scattering data from montmorillonite dispersions
Polymer, 47 (2006), 2147 – 2155

Hertel, R.
Theory of the inverse Faraday effect in metals
Journal of Magnetism and Magnetic Materials, 303 (2006), L1 – L4

Hirahara, T.; Nagao, T.; Matsuda, I.; Bihlmayer, G.; Chulkov, E. V.; Koroteev, S. B.; Echenique, P. M.; Saito, M.; Hasagawa, S.
Role of Spin-Orbit Coupling and Hybridization Effects in the Electronic Structure of Ultrathin Bi Films
Physical Review Letters, 97 (2006), 146803

Hoehler, H.; Atodiresei, N.; Schroeder, K.; Zeller, R.; Dederichs, P. H.
Impurity-Vacancy Complexes in Si and Ge
Hyperfine Interactions, 158 (2006), 37 – 40

Holmqvist, P.; Dhont, J. K. G.; Lang, P.
Anisotropy of Brownian motion caused only by hydrodynamic interaction with a wall
Physical Review E, 74 (2006), 021402

Houben, L.
Aberration-corrected HRTEM of defects in strained La_2CuO_4 thin films grown on $SrTiO_3$
Journal of Materials Science, 41 (2006), 4413 – 4419

Hueging, N.; Luysberg, M.; Trinkaus, H.; Tillmann, K.; Urban, K.
Quantitative pressure and strain field analysis of helium precipitates in silicon
Journal of Materials Science, 41 (2006), 4454 – 4465

Hueging, N.; Luysberg, M.; Urban, K.; Buca, D.; Holländer, B.; Mantl, S.; Mörschbächer, M. J.; Fichtner, P. F. P.; Loo, R.; Caymax, M.
Relaxation of SiGe/Si heterostructures by helium implantation and subsequent annealing: Helium acting as dislocation sources
Microscopy of Semiconducting Materials : proceedings of the 14th Conference, April 11-14, 2005, Oxford, UK / ed.: A. G. Cullis ... – Berlin, Springer, 2006. – 3-540-31914-X. – S. 183 – 190

Hur, K.; Winkler, R. G.; Yoon, Do. Y.
Comparison of Ring and Linear Polyethylene from Molecular Dynamics Simulations
Macromolecules, 39 (2006), 3975 – 3977

Jeong, D. S.; Schroeder, H.; Waser, R.
Impedance spectroscopy of TiO_2 thin film showing resistive switching
Applied Physics Letters, 89 (2006), 082909

Jia, C. L.; Houben, L.; Urban, K.
Atom vacancies at a screw dislocation core in $SrTiO_3$
Philosophical Magazine Letters, 86 (2006), 683

Jia, C. L.; Schubert, J.; Heeg, T.; Mi, S. B.; Chen, H. Y.; Joschko, B.; Burianek, M.; Mühlberg, M.; Urban, K.
Tailoring the orientations of complex niobate films on perovskite substrates
Acta Materialia, 54 (2006), 2383 – 2391

Jiang, X.; Jia, C. L.; Hong, R.J.
Microstructure dependence of ZnO:Al films on the deposition conditions and the surface morphology of silicon substrate
Journal of Crystal Growth, 289 (2006), 464

Jones, R. O.
Introduction to Density Functional Theory and Exchange-Correlation Energy Functionals
Computational Nanoscience: Do It Yourself!: NIC Winter School 2006 / ed.: J. Grotendorst, S. Blügel, D. Marx. – (NIC Series ; 31). – 3-00-017350-1. – S. 45 – 70

Jung, P.; Chen, J.; Klein, H.
Recovery of tensile properties in helium implanted EUROFER97 by post-implantation annealing
Journal of Nuclear Materials, 356 (2006), 88 – 94

Kang, K.; Lettinga, M. P.; Dogic, Z.; Dhont, J. K. G.
Vorticity banding in rodlike virus suspensions
Physical Review E, 74 (2006), 026307

Kang, K.; Wilk, A.; Buitenhuis, J.; Patkowski, A.; Dhont, J. K. G.
Diffusion of spheres in isotropic and nematic suspensions of rods
Journal of Chemical Physics, 124 (2006), 044907

Karthäuser, S.; Lüssem, B.; Weides, M.; Alba, M.; Besmehn, A.; Oligschlaeger, R.; Waser, R.
Resistive switching of rose bengal devices: a molecular effect?
Journal of Applied Physics, 100 (2006), 094504

Khan, A.R.; Stangl, J.; Bauer, G.; Buca, D.; Holländer, B.; Trinkaus, H.; Mantl, S.; Loo, R.; Caymax, M.
Study of Relaxation of Strain in Patterned Structures using X-Ray Diffraction Technique
Conference Digest of the Third International Silicon Germanium Technology and Devices Meeting, 15 May – 17 May 2006, Princeton, USA. – 2006. – (IEEE Conference Paper). – S. 116

Kirsch, M.; Mermet, A.; Grimm, H.; Forsyth, V.T.; Rupprecht, A.
Phonon dispersion of oriented DNA by inelastic x-ray scattering
Physical Review E, 73 (2006), 061909

Kirstein, O.; Prager, M.; Grimm, H.; Buchsteiner, A.; Wischnewski, A.
Quasi-elastic neutron spectroscopy and rotational potentials of methyl halides
Physica B: Condensed Matter, 385-386 (2006), 1, 47 – 49

Kita, R.; Polyakov, P.; Wiegand, S.
Soret coefficient of PNiPAM in alcohols and in water
Thermodiffusion : Basics & Applications / ed.: M. M. Bou-Ali, J. K. Platten. – Mondragon University, Arrasate-Mondragon, 2006. – S. 409 – 418

Klein, S.; Carius, R.; Finger, F.; Houben, L.
Low substrate temperature deposition of crystalline SiC using HWCVD
Thin Solid Films, 501 (2006), 169 – 172

Kleshchanok, D.; Strunk, H.; Tuinier, R.; Lang, P.
Interactions and two-phase coexistence in nonionic micellar solutions as determined by static light scattering
Physical Chemistry Chemical Physics, 8 (2006), 869 – 876

Kleshchanok, D.; Tuinier, R.; Lang, P. R.
Depletion Interaction Mediated by a Polydisperse Polymer Studied with Total Internal Reflection Microscopy
Langmuir, 22 (2006), 9121 – 9128

Kleshchanok, D.; Wong, J. E.; von Klitzing, R.; Lang, P.
Potential Profiles between Polyelectrolyte Multilayers and Spherical Colloids Measured with TIRM
Progress in Colloid and Polymer Science, 133 (2006), 52 – 57

Kluge, M.; Schober, H. R.
Diffusion in a binary amorphous metal: Pair-correlation in $Cu_{33}Zr_{67}$
Journal of Non-Crystalline Solids, 352 (2006), 5093 – 5097

Knittel, I.; Wei, J.; Zhou, Y.; Arora, S. K.; Shvets, I. V.; Luysberg, M.
Observation of antiferromagnetic coupling in epitaxial ferrite films
Physical Review B, 74 (2006), 132406

Koch, E.
Electron Correlations
Computational Condensed Matter Physics : Lecture Manuscripts of the 37th Spring School of the Institute of Solid State Research ; this spring school was organized by the Institute of Solid State Research in the Forschungszentrum Jülich on March 6 -17, 2006 / ed.: S. Blügel, G. Gompper, E. Koch, H. Müller-Krumbhaar, R. Spatschek, R. G. Winkler. – Jülich, 2006. – (Schriften des Forschungszentrums Jülich. Reihe Materie und Material / Matter and Material ; 32). – 3-89336-430-7. – S. A9.1 – A9.18

Kohlbrecher, J.; Buitenhuis, J.; Meier, G.; Lettinga, M. P.
Colloidal dispersions of octadecyl grafted silica spheres in toluene: A global analysis of small angle neutron scattering contrast variation and concentration dependence measurements
Journal of Chemical Physics, 125 (2006), 044715

Kriegs, H.; Gapinski, J.; Meier, G.; Paluch, M.; Pawlus, S.; Patkowski, A.
Pressure effects on the alpha and alpha' relaxations in polymethylphenylsiloxane
Journal of Chemical Physics, 124 (2006), 104901

Krivchikov, A. I.; Gorodilov, B. Ya.; Korolyuk, O. A.; Manzhelii, V. G.; Romantsova, O. O.; Conrad, H.; Press, W.; Tse, J. S.; Klug, D. D.
Thermal conductivity of Xe clathrate hydrate at low temperatures
Physical Review B, 73 (2006), 064203-1 – 064203- 6

Kronholz, S.; Karthäuser, S.; Meszaros, G.; Wandlowski, Th.; van der Hart, A.; Waser, R.
Protected Nanoelectrodes of two different Metals with 30 nm Gap-width and Access-window
Microelectronic Engineering, 83 (2006), 1702 – 1705

Kronholz, S.; Karthäuser, S.; van der Hart, A.; Wandlowski, Th.; Waser, R.
Metallic Nanogaps with Access Windows for Liquid-based Systems
Microelectronics Journal, 37 (2006), 7, 591 – 594

Kronholz, S.; Rathgeber, S.; Karthäuser, S.; Kohlstedt, H.; Clemens, S.; Schneller, T.
Self-assembly of diblock-copolymer micelles for template based preparation of $PbTiO_3$ nanograins
Advanced Functional Materials, 16 (2006), 2346 – 2354

Köbler, U.; Hoser, A.
Effective spin description of crystal field effects in $NdAl_2$
Journal of Magnetism and Magnetic Materials, 299 (2006), 145 – 154

Köbler, U.; Hoser, A.; Hoffmann, J.-U.
Crystal field effects in the 3d transition metal compounds
Physica B: Condensed Matter, 382 (2006), 98 – 104

Köbler, U.; Hoser, A.; Hoffmann, J.-U.; Thomas, C.
One-dimensional bulk ferromagnet: $NdAl_2$ and hcp cobalt
Solid State Communications, 137 (2006), 301 – 305

Köbler, U.; Schreiber, R.
Exploring the 2D to 3D dimensionality crossover in thin iron films
Journal of Magnetism and Magnetic Materials, 300 (2006), 519 – 524

Lentzen, M.
Progress in Aberration-Corrected High-Resolution Transmission Electron Microscopy Using Hardware Aberration Correction
Microscopy and Microanalysis, 12 (2006), 3, 191 – 205

Lettinga, M. P.; Kang, K.; Holmqvist, P.; Imhof, A.; Derks, D.; Dhont, J. K. G.
Nematic-isotropic spinodal decomposition kinetics of rodlike viruses
Physical Review E, 73 (2006), 011412

Lezaic, M.; Mavropoulos, Ph.; Bihlmayer, G.; Blügel, S.
Scanning tunnelling microscopy of surfaces of half-metals: an ab-initio study on NiMnSb(001)
Journal of Physics D – Applied Physics, 39 (2006), 797 – 802

Lezaic, M.; Mavropoulos, Ph.; Enkovaara, J.; Bihlmayer, G.; Blügel, S.
Thermal Collapse of Spin Polarization in Half-Metallic Ferromagnets
Physical Review Letters, 97 (2006), 026404

Li, L.Y.; Wang, J.B.; Wang, R. H.; Liu, H.J.; Jia, C. L.; Ma, L.L.; Yu, Y.
Atomistic study on twinning of Cu_2O quantum dots
Applied Physics Letters, 89 (2006), 113109

Liatti, M. V.; Divin, Y. Y.; Poppe, U.; Gubankov, V. N.; Urban, K.
Effect of low-temperature ozone annealing on current-voltage characteristics and 1/f noise of $YBa_2Cu_3O_{7-x}$ (100)-tilt bicrystal junctions
Journal of Physics : Conference Series, 43 (2006), 1211 – 1214

Liatti, M. V.; Poppe, U.; Divin, Y. Y.
Low-frequency voltage noise and electrical transport in (100)-tilt $YBa_2Cu_3O_{7-x}$ grain-boundary junctions
Applied Physics Letters, 88 (2006), 152504

Liebsch, A.
Dynamical Mean Field Theory
Computational Condensed Matter Physics : Lecture Manuscripts of the 37th Spring School of the Institute of Solid State Research ; this spring school was organized by the Institute of Solid State Research in the Forschungszentrum Jülich on March 6 -17, 2006 / ed.: S. Blügel, G. Gompper, E. Koch, H. Müller-Krumbhaar, R. Spatschek, R. G. Winkler. – Jülich, 2006. – (Schriften des Forschungszentrums Jülich. Reihe Materie und Material / Matter and Material ; 32). – 3-89336-430-7. – S. A13.1 – A13.12

Liebsch, A.; Costi, T. A.
Non-Fermi-liquid phases in the two-band Hubbard model: Finite-temperature exact diagonalization study of Hund's rule coupling
European Physical Journal B, 51 (2006), 523

Loewenhaupt, M.; Schedler, R.; Witte, U.; Rotter, M.; Schmidt, W.
Unconventional magnetic excitation in the Kondo lattice $CeCu_2$
Physica B: Condensed Matter, 378-380 (2006), 775 – 777

Long, G. J.; Hermann, R. P.; Grandjean, F.; Chacon, C.; Isnard, O.
A Mössbauer spectral study of the $YCo_{4-x}Fe_xB$ compounds
Journal of Physics: Condensed Matter, 18 (2006), 10765 – 10773

Lounis, S.; Mavropoulos, Ph.; Dederichs, P. H.; Blügel, S.
Surface-state scattering by adatoms on noble metals: Ab initio calculations using the Korringa-Kohn-Rostoker Green function method
Physical Review B, 73 (2006), 195421

Lund, R.; Willner, L.; Richter, D.; Dormidontova, E.
Equilibrium Chain Exchange Kinetics of Diblock Copolymer Micelles: Tuning and Logarithmic Relaxation
Macromolecules, 39 (2006), 13, 4566 – 4575

Lund, R.; Willner, L.; Stellbrink, J.; Lindner, P.; Richter, D.
Logarithmic chain-exchange kinetics of diblock copolymer micelles
Physical Review Letters, 96 (2006), 068302

Lustfeld, H.
Algorithms for Optimization
Computational Condensed Matter Physics: Lecture Manuscripts of the 37th Spring School of the Institute of Solid State Research ; this spring school was organized by the Institute of Solid State Research in he Forschungszentrum Jülich on March 6 -17, 2006 / ed.: S. Blügel, G. Gompper, E. Koch, H. Müller-Krumbhaar, R. Spatschek, R. G. Winkler. – Jülich, 2006. – (Schriften des Forschungszentrums Jülich. Reihe Materie und Material / Matter and Material ; 32). – 3-89336-430-7. – S. D4.1 – D4.20

Luysberg, M.; Feuerbacher, M.; Mayer, J.
Professor Dr. Knut Urban 65 Years
International Journal of Materials Research = Zeitschrift für Metallkunde, 97 (2006), 7, 859 – 860

Lüssem, B.; Müller-Meskamp, L.; Karthäuser, S.; Homberger, M.; Simon, U.; Waser, R.
A STM study of mixed Alkanethiol/Biphenylthiol Self Assembled Monolayers on Au(111)
Langmuir, 22 (2006), 3021

Mallet, F.; Ericsson, J.; Mailly, D.; Ünlübayir, S.; Reuter, D.; Melnikov, A.; Wieck, A.D.; Micklitz, T.; Rosch, A.; Costi, T. A.; Saminadayar, L.; Bäuerle, C.
Scaling of the Low-Temperature Dephasing Rate in Kondo Systems
Physical Review Letters, 97 (2006), 226804

Mavropoulos, Ph.; Lounis, S.; Zeller, R.; Blügel, S.
Fe clusters on Ni and Cu: size and shape dependence of the spin moment
Applied Physics A, 82 (2006), 103 – 107

Mavropoulos, Ph.; Papanikolaou, N.
The Korringa-Kohn-Rostoker (KKR) Green Function Method I. Electronic Structure of Periodic Systems
Computational Nanoscience: Do It Yourself! : NIC Winter School 2006 / ed.: J. Grotendorst, S. Blügel, D. Marx. – (NIC Series ; 31). – 3-00-017350-1. – S. 131 – 158

Melnichenko, Y. B.; Wignall, G. D.; Cole, D. R.; Frielinghaus, H.
Adsorption of supercritical CO_2 in aerogels as studied by small-angle neutron scattering and neutron transmission techniques
Journal of Chemical Physics, 124 (2006), 204711

Mi, S. B.; Jia, C. L.; Faley, M.; Poppe, U.; Urban, K.
Microstructure of $YBa_2Cu_3O_{7-d}/SrTiO_3/BaZrO_3$ Multilayer Films on MgO Substrates
Proceedings of ND 2006 : Conference "Nanoelectronic Days 2006", 9.10. – 11.10.2006 in Aachen. – 2006. – S. 96

Mi, S. B.; Jia, C. L.; Urban, K.; Heeg, T.; Schubert, J.
Growth of $Ca_xBa_{1-x}Nb_2O_6$ thin films on MgO(100) by pulsed laser deposition
Journal of Crystal Growth, 291 (2006), 243 – 248

Micklitz, T.; Altland, A.; Costi, T. A.; Rosch, A.
Universal Dephasing Rate due to Diluted Kondo Impurities
Physical Review Letters, 96 (2006), 226601

Mika, K.
The Ising model without temperature – A possible explanation for the critical energy of the Onsager solution
Physica A, 369 (2006), 577 – 588

Milanov, A.; Bhakta, R.; Baunemann, A.; Becker, H.-W.; Thomas, R.; Ehrhart, P.; Winter, M.; Devi, A.
Guanidinate-stabilized monomeric hafnium amide complexes as promising precursors for MOCVD of HfO_2
Inorganic Chemistry, 45 (2006), 11008 -11018

Milanov, A.; Bhakta, R.; Thomas, R.; Ehrhart, P.; Winter, M.; Waser, R.; Devi, A.
Mixed amide-malonate compound of hafnium as a novel monomeric precursor for MOCVD of HfO_2 thin films
Journal of Materials Chemistry, 16 (2006), 5, 437

Mokrousov, Y.; Atodiresei, N.; Bihlmayer, G.; Blügel, S.
Magnetic Anisotropy Energies of Metal-Benzene Sandwiches
International Journal of Quantum Chemistry, 106 (2006), 3208 – 3213

Mokrousov, Y.; Bihlmayer, G.; Heinze, S.; Blügel, S.
Giant Magnetocrystalline Anisotropies of 4d Transition-Metal Monowires
Physical Review Letters, 96 (2006), 147201

Moras, P.; Ferrari, L.; Spezzani, C.; Gardonio, S.; Lezaic, M.; Mavropoulos, Ph.; Blügel, S.; Carbone, C.
Probing Quasiparticle States Bound by Disparate Periodic Potentials
Physical Review Letters, 97 (2006), 206802

Muresan, A.S.; Dubbeldam, J. L. A.; Kautz, H.; Monkenbusch, M.; Sijbesma, R. P.; van der Schoot, P.; de Jeu, W.H.
Dynamic heterogeneity in hydrogen-bonded polymers
Physical Review E, 74 (2006), 031804

Müller, K.; Kreiling, S.; Dehnicke, K.; Allgaier, J.; Richter, D.; Fetters, L.; Jung, Y.; Yoon, D. Y.; Greiner, A.
Synthesis and rheological properties of poly(5-n-hexyl norbonene)
Macromolecular Chemistry and Physics, 207 (2006), 193 – 200

Müller-Meskamp, L.; Lüssem, B.; Karthäuser, S.; Prikhodovski, S.; Homberger, M.; Simon, U.; Waser, R.
Molecular Structure of Ferrocenethiol Islands embedded into Alkanethiol Self-Assembled Monolayers by UHV-STM
Physica Status Solidi A, 203 (2006), 1448 – 1452

Nagarajan, V.; Junquera, J.; He, J. Q.; Jia, C. L.; Waser, R.; Lee, K.; Kim, Y. K.; Baik, S.; Zhao, T.; Ramesh, R.; Ghosez, Ph.; Rabe, K. M.
Scaling of structure and electrical properties in ultra-thin epitaxial ferroelectric heterostructures
Journal of Applied Physics, 100 (2006), 051609

Neupane, K. P.; Cohn, J. L.; Terashita, H.; Neumeier, J. J.
Doping dependence of polaron hopping energies in $La_{1-x}Ca_xMnO_3$ ($0 \leq x \leq 0{,}15$)
Physical Review B, 74 (2006), 144428-1 – 144428-5

Ning, H.; Buitenhuis, J.; Dhont, J. K. G.; Wiegand, S.
Thermal diffusion behavior of hard-sphere suspensions
Journal of Chemical Physics, 125 (2006), 204911

Ning, H.; Buitenhuis, J.; Wiegand, S.
Thermal diffusion behaviour of interacting colloids
Thermodiffusion : Basics & Applications / ed.: M. M. Bou-Ali, J. K. Platten. – Mondragon University, Arrasate-Mondragon, 2006. – S. 389 – 398

Ning, H.; Kita, R.; Kriegs, H.; Luettmer-Strathmann, J.; Wiegand, S.
Thermal Diffusion Behavior of Nonionic Surfactants in Water
Journal of Physical Chemistry B, 110 (2006), 10746

Ning, H.; Kita, R.; Wiegand, S.
Soret Effect in a Nonionic Surfactant System
Progress in Colloid and Polymer Science, 133 (2006), 111 – 115

Ning, H.; Wiegand, S.
Experimental investigation of the Soret effect in acetone/water and dimethylsulfoxide/water mixtures
Journal of Chemical Physics, 125 (2006), 221102

Noguchi, H.; Gompper, G.
Dynamics of Vesicle Self-Assembly and Dissolution
Journal of Chemical Physics, 125 (2006), 164908

Noguchi, H.; Gompper, G.
Meshless membrane model based on the moving least-squares method
Physical Review E, 73 (2006), 021903-1 – 021903-12

Oh, I. H.; Merz, M.; Mattauch, G. F.; Heger, G.
Structural phase transition and hydrogen ordering of TlH_2PO_4 at low temperature
Acta Crystallographica B : Structural Science, 62 (2006), 5, 719 – 728

Ohly, C.; Hoffmann-Eifert, S.; Guo, X.; Schubert, J.; Waser, R.
Electrical conductivity of epitaxial $SrTiO_3$ thin films as a function of oxygen partial pressure and temperature
Journal of the American Ceramic Society, 89 (2006), 2845

Oligschlaeger, R.; Waser, R.; Meyer, R.; Karthäuser, S.; Dittmann, R.
Resistive switching and data reliability of epitaxial $(Ba,SR)TiO_3$ thin films
Applied Physics Letters, 88 (2006), 042901

Ottaviano, L.; Passacantando, M.; Picozzi, S.; Continenza, A.; Gunnella, R.; Verna, A.; Bihlmayer, G.; Impellizzeri, G.; Priolo, F.
Phase separation and dilution in implanted Mn_xGe_{1-x}alloys
Applied Physics Letters, 88 (2006), 061907

Papadopoulos, G.; Grudinin, S.; Kalpaxis, D.; Choli-Papadopoulou, T.
Changes in the level of poly(Phe) synthesis in Escherichia coli ribosomes containing mutants of L4 ribosomal protein from Thermus thermophilus can be explained by structural changes in the peptidyl-transferase center: a molecular dynamics simulation anal.
European Biophysics Journal : with Biophysics Letters, 35 (2006), 8, 675 – 683

Patil, U.; Thomas, R.; Milanov, A.; Bhakta, R.; Ehrhart, P.; Waser, R.; Becker, R.; Becker, H.-W.; Winter, M.; Merz, K.; Fischer, R. A.; Devi, A.
MOCVD of ZrO_2 and HfO_2 Thin Films from Modified Monomeric Precursors
Chemical Vapor Deposition, 12 (2006), 172

Patkowski, A.; Gapinski, J.; Meier, G.; Kriegs, H.; Le Grand, A.; Dreyfus, C.
Unexpected effect of internal degrees of freedom on transverse phonons in supercooled liquids
Europhysics Letters, 73 (2006), 607 – 613

Patkowski, A.; Gapinski, J.; Pakula, T.; Meier, G.
Physical nature of complex structural relaxation in polysiloxane – PMPTS: alpha and alpha' relaxations
Polymer, 47 (2006), 20, 7231 – 7240

Paul, A.; Kentzinger, E.; Rücker, U.; Brückel, T.
Magnetization reversal with variation of the ratio of the anisotropy energies in exchange bias systems
Physical Review B, 74 (2006), 054424-1 -054424-6

Paul, A.; Kentzinger, E.; Rücker, U.; Brückel, T.
Symmetry and asymmetry during magnetization reversal in exchange biased multilayers and bilayers
Physical Review B, 73 (2006) , 092410-1 – 092410-4

Paul, A.; Kentzinger, E.; Rücker, U.; Brückel, T.
The angular dependence of the magnetization reversal in exchange biased multilayers
Journal of Physics: Condensed Matter, 18 (2006), L149 – L153

Paul, A.; Kentzinger, E.; Rücker, U.; Bürgler, D.; Brückel, T.
Field-dependent magnetic domain structure in antiferromagnetically coupled multilayers by polarized neutron scattering
Physical Review B, 73 (2006), 094441-1 – 094441-8

Paul, A.; Wingbermühle, J.
Surface morphology for ion-beam sputtered Al layer with varying sputtering conditions
Applied Surface Science, 252 (2006), 8151 – 8155

Pavarini, E.
Building model Hamiltonians for strongly correlated materials
Computational Condensed Matter Physics: Lecture Manuscripts of the 37th Spring School of the Institute of Solid State Research ; this spring school was organized by the Institute of Solid State Research in the Forschungszentrum Jülich on March 6 -17, 2006 / ed.: S. Blügel, G. Gompper, E. Koch, H. Müller-Krumbhaar, R. Spatschek, R. G. Winkler. – Jülich, 2006. – (Schriften des Forschungszentrums Jülich . Reihe Materie und Material / Matter and Material ; 32). – 3-89336-430-7. – S. A12.1 – A12.22

Pavarini, E.; Mazin, I. I.
First-principles study of spin-orbit effects and NMR in Sr_2RuO_4
Physical Review B, 74 (2006), 035115

Persson, B. N. J.
Contact mechanics for randomly rough surfaces
Surface Science Reports, 61 (2006), 4, 201 – 227

Persson, B. N. J.
Rubber friction: role of the flash temperature
Journal of Physics: Condensed Matter, 18 (2006), 32, 7789 – 7823

Persson, B. N. J.; Volokitin, A. I.
Rubber friction on smooth surfaces
European Physical Journal E, 21 (2006), 69 – 80

Persson, B. N. J.; Zhao, K.; Zhang, Z.
Chemical contribution to surface-enhanced Raman scattering
Physical Review Letters, 97 (2006), 199702

Persson, B. N. J.; Zhao, K.; Zhang, Z.Y.
Chemical contribution to surface-enhanced Raman scattering
Physical Review Letters, 96 (2006), 20, 207401

Peter, F.; Kubacki, J.; Szot, K.; Reichenberg, B.; Waser, R.
Influence of adsorbates on the piezoresponse of $KnBO_3$
Physica Status Solidi A, 203 (2006), 616 – 621

Peter, F.; Rüdiger, A.; Waser, R.
Mechanical Crosstalk between Vertical and Lateral Piezoresponse Force Microscopy
Review of Scientific Instruments, 77 (2006), 036103

Peter, L.; Rolik, Z.; Kiss, L. F.; Toth, J.; Weihnacht, V.; Schneider, C. M.; Bakonyi, I.
Temperature dependence of giant magnetoresistance and magnetic properties in electrodeposited Co-Cu/Cu multilayers: The role of superparamagnetic regions
Physical Review B, 73 (2006), 174410

Petraru, A.; Nagarajan, V.; Kohlstedt, H.; Ramesh, R.; Schlom, D. G.; Waser, R.
Simultaneous measurement of the piezoelectric and dielectric response of nanoscale ferroelectric capacitors by an atomic force microscopy based approach
Applied Physics A, 84 (2006), 67

Petrov, E.P.; Ohrt, T.; Winkler, R. G.; Schwille, P.
Diffusion and segmental dynamics of double-stranded DNA
Physical Review Letters, 97 (2006), 258101-1 – 258101-4

Picozzi, S.; Lezaic, M.; Blügel, S.
Electronic structure and exchange constants in magnetic semiconductor digital alloys: chemical and band-gap effects
Physica Status Solidi A, 203 (2006), 2738 – 2745

Picozzi, S.; Yamauchi, K.; Bihlmayer, G.; Blügel, S.
First-principles stabilization of an unconventional collinear magnetic ordering in distorted manganites
Physical Review B, 74 (2006), 094402

Pithan, C.; Schneller, T.; Shiratori, Y.; Majumder, S. B.; Haegel, F.-H.; Dornseiffer, J.; Waser, R.
Microemulsion Mediated Synthesis of Nanocrystalline $BaTiO_3$: Possibilities, Potential and Perspectives
International Journal of Materials Research = Zeitschrift für Metallkunde, 97 (2006), 499

Pithan, C.; Shiratori, Y.; Magrez, A.; Mi, S.-B.; Dornseiffer, J.; Waser, R.
Consolidation microstructure and crystallography of dense $NaNbO_3$ ceramics with ultrafine grainz size
Journal of the Ceramic Society of Japan, 114 (2006), 995 – 1000

Pithan, C.; Shiratori, Y.; Waser, R.; Dornseiffer, J.; Haegel, F.-H.
Preparation, processing and characterization of nano-crystalline $BaTiO_3$ powders and ceramics derived from microemulsion mediated synthesis
Journal of the American Ceramic Society, 89 (2006), 2908

Plakhty, V. P.; Wosnitza, J.; Kulda, J.; Brückel, T.; Schweika, W.; Visser, D.; Gavrilov, S. V.; Moskvin, E. V.; Kremer, R. K.; Banks, M. G.
Polarized neutron scattering studies of chiral criticality, and new universality classes of phase transitions
Physica B: Condensed Matter, 385-386 (2006), 288 – 294

Polyakov, P.; Luettmer-Strathmann, J.; Wiegand, S.
Study of the thermal diffusion behavior of alkane/benzene mixtures by thermal diffusion forced rayleigh scattering experiments and lattice model calculations
Journal of Physical Chemistry B, 110 (2006), 51, 26215

Polyakov, P.; Wiegand, S.
Experimental study of the thermal diffusion behaviour of mixtures consisting of simple and chain like molecules using thermal diffusion forced Rayleigh Scattering
Thermodiffusion : Basics & Applications / ed.: M. M. Bou-Ali, J. K. Platten. – Arrasate-Mondragon, Mondragon University, 2006. – S. 399 – 407

Postnikov, A. V.; Bihlmayer, G.; Blügel, S.
Exchange parameters in Fe-based molecular magnets
Computational Materials Science, 36 (2006), 91 – 95

Prager, M.; Grimm, H.; Kirstein, O.
A space and energy focusing hybrid cold time-of-flight spectrometer based on a moving monochromator crystal
Physica B: Condensed Matter, 385-386 (2006), 1098 – 1100

Prager, M.; Pietraszko, L.; Sobczyk, L.; Pawlukojc, E.; Grech, E.; Seydel, T.; Wischnewski, A.; Zamponi, M.
X-ray diffraction and inelastic neutron scattering study of 1:1 tetramethylpyrazine (TMP) chloranilic acid (CLA) complex: temperature, isotope and pressure effects
Journal of Chemical Physics, 125 (2006), 194525

Pérez Aparicio, R.; Arbe, A.; Colmenero, J.; Frick, K. H.; Willner, L.; Richter, D.; Fetters, L. J.
Quasielastic neutron scattering study on the effect of blending on the dynamics of head-to-head poly(propylene) and poly(ethylene propylene)
Macromolecules, 39 (2006), 1060 – 1072

Radulescu, A.; Schwahn, D.; Stellbrink, J.; Kentzinger, E.; Heiderich, M.; Richter, D.; Fetters, L.
Wax crystallization from solution in hierarchical morphology templated by random poly(ethylene-co-butene) self-assemblies
Macromolecules, 39 (2006), 6142 – 6151

Rakos, A.; Paessens, M.
Ergodicity breaking in one-dimensional reaction-diffusion systems
Journal of Physics A – Mathematical and General, 39 (2006), 3231 – 3251

Rameev, B.; Yildiz, F.; Kazan, S.; Aktas, B.; Gupta, A.; Tagirov, L.; Rata, D.; Bürgler, D. E.; Grünberg, P.; Schneider, C. M.; Kammerer, S.; Reiss, G.; Hütten, A.
FMR investigations of half-metallic ferromagnets
Physica Status Solidi A, 203 (2006), 7, 1503 – 1512

Rata, A. D.; Braak, H.; Bürgler, D. E.; Cramm, S.; Schneider, C. M.
Structural and magneto-transport characterization of $Co_2Cr_xFe_{1-x}Al$ Heusler alloy films
European Physical Journal B, 52 (2006), 445 – 451

Rata, A.D.; Braak, H.; Bürgler, D. E.; Cramm, S.; Schneider, C. M.
Structural and magneto-transport characterization of $Co_2Cr_xFe_{1-x}Al$ Heusler alloy films
European Physical Journal B, 52 (2006), 445 – 451

Rathgeber, S.; Monkenbusch, M.; Hedrick, J. L.; Trollsas, M.; Gast, A. P.
Starlike dendrimers in solutions: Structural properties and internal dynamics
Journal of Chemical Physics, 125 (2006), 204908

Ripoll, M.
Mesoscale Hydrodynamic Simulations
Computational Condensed Matter Physics : Lecture Manuscripts of the 37th Spring School of the Institute of Solid State Research ; this spring school was organized by the Institute of Solid State Research in the Forschungszentrum Jülich on March 6 -17, 2006 / ed.: S. Blügel, G. Gompper, E. Koch, H. Müller-Krumbhaar, R. Spatschek, R. G. Winkler. – Jülich, 2006. – (Schriften des Forschungszentrums Jülich . Reihe Materie und Material / Matter and Material ; 32). – 3-89336-430-7. – S. B5.1 – B5.31

Ripoll, M.; Winkler, R. G.; Gompper, G.
Star polymers in shear flow
Physical Review Letters, 96 (2006), 188302

Roke, S.; Berg, O.; Buitenhuis, J.; van Blaaderen, A.; Bonn, M.
Surface molecular view of colloidal gelation
Proceedings of the National Academy of Sciences of the United States of America, 103 (2006), 36, 13310 – 13314

Rosenbaum, R. L.; Grushko, B.; Przepiorzynski, B.
Electronic Transport Behaviors of Insulating Icosahedral Al-Pd-Re Bulk Samples
Journal of Low Temperature Physics, 142 (2006), 1/2, 101 – 113

Rusz, J.; Bergqvist, L.; Kudrnovsky, J.; Turek, I.
Exchange interactions and Curie temperatures in $Ni_{2-x}MnSb$ alloys: first-principles study
Physical Review B, 73 (2006), 214412

Rzhevsky, A. A.; Krichevtsov, B. B.; Bürgler, D.; Schneider, C. M.
Investigation of the interfacial magnetization in exchange coupled Fe/Cr/Fe structures by second harmonic generation
New Magnetic Materials of Microelectronics (NMMM-20), 12.-16.06.06, Moscow, Russia : Proceedings of the XX-th Anniversary School-Seminar. – 2006. – S. 232 – 234

Rzhevsky, A. A.; Krichevtsov, B. B.; Bürgler, D.; Schneider, C. M.
Magnetization dynamics in Cr/Fe/Ag/Fe/GaAs(100) thin films measured by pump-probe technique
New Magnetic Materials of Microelectronics (NMMM-20), 12.-16.06.06, Moscow, Russia : proceedings of the XX-th Anniversary School-Seminar. – 2006. – S. 877 – 879

Rzhevsky, A. A.; Krichevtsov, B. B.; Rata, A.D.; Chang, C.F.; Sutarto, R.; Tjeng, L. H.; Schneider, C. M.
Magnetization-induced second-harmonic generation in epitxial magnetite thin films $Fe_3O_4/MgO(100)$
Journal of Applied Physics, 99 (2006), 08J702

Saalfrank, R. W.; Scheurer, A.; Bernt, I.; Heinemann, F.W.; Postnikov, A. V.; Schünemann, V.; Trautwein, A. X.; Alam, M. S.; Rupp, H.; Müller, P.
The $Fe^{III}[Fe^{III}(L^1)_2]_3$ star-type single-molecule magnet
Dalton Transactions, 23 (2006), 2865 – 2874

Sangiovanni, G.; Gunnarsson, O.; Koch, E.; Castellani, C.; Capone, M.
Electron-Phonon Interaction and Antiferromagnetic Correlations
Physical Review Letters, 97 (2006), 046404

Sangiovanni, G.; Toschi, A.; Koch, E.; Held, K.; Capone, M.; Castellani, C.; Gunnarsson, O.; Mo, S.-K.; Allen, J. W.; Kim, H.-D.; Sekiyama, A.; Yamasaki, A.; Suga, S.; Metcalf, P.
Static versus dynamical mean-field theory of Mott antiferromagnets
Physical Review B, 73 (2006), 205121

Sapmaz, S.; Meyer, C.; Beliczynski, P.; Jarillo-Herrero, P.; Kouwenhoven, L. P.
Excited state spectroscopy in carbon nanotube double quantum dots
Nano Letters, 6 (2006), 7, 1350 – 1355

Sasioglu, E.; Sandratskii, L.M.; Bruno, P.
Magnetic phase diagram of the semi-Heusler alloys from first principles
Applied Physics Letters, 89 (2006), 222508

Sato, K.; Dederichs, P. H.; Katayama-Yoshida, H.
Curie temperatures of dilute magnetic semiconductors from LDA+U electronic structure calculations
Physica B: Condensed Matter, 376 (2006), 639 – 642

Schindlmayr, A.
Time-Dependent Density-Functional Theory
Computational Condensed Matter Physics : Lecture Manuscripts of the 37th Spring School of the Institute of Solid State Research ; this spring school was organized by the Institute of Solid State Research in the Forschungszentrum Jülich on March 6 -17, 2006 / ed.: S. Blügel, G. Gompper, E. Koch, H. Müller-Krumbhaar, R. Spatschek, R. G. Winkler. – Jülich, 2006. – (Schriften des Forschungszentrums Jülich. Reihe Materie und Material / Matter and Material ; 32). – 3-89336-430-7. – S. A4.1 – A4.19

Schneider, C. M.
Complex thin film systems for magnetoelectronics
Metal-Based Thin Film Systems / ed.: K. Wetzig, C. M. Schneider. – 2nd ed. – Weinheim, Wiley-VCH, 2006. – 3-527-40650-6. – S. 71

Schneider, C. M.
Soft x-ray photoemission electron microscopy
Neutron and X-ray Spectroscopy / ed.: F. Hippert, E. Geissler, J.-L. Hodeau, E. Lelievre-Berna, J.-R. Regnard. – Kluwer Acad. Publ., 2006. – 1-402-03336-2. – S. 456

Schneider, C. M.; Thomas, J.
Thermal stability of magnetic multilayers
Metal-Based Thin Film Systems / ed.: K. Wetzig, C. M. Schneider. – 2nd ed. – Weinheim, Wiley-VCH, 2006. – 3-527-40650-6. – S. 283

Schober, T.
Phase diagrams in the proton conductor systems $Sr_6Ta_2O_{22}$ x n H_2O and $Sr_{5.92}Ta_{2.08}O_{11.12}$ x n H_2O
Solid State Ionics, 177 (2006), 471

Schroeder, H.
A leakage current model for a "flash-like", non-volatile resistive switch memory cell
Electroresponsive Polymers and their Applications / ed.: V. Bharti, Y. Bar-Cohen, Z.-Y. Cheng, Q. Zhang, J. Madden. – Warrendale, PA, 2006. – (Materials Research Society Symposium proceedings ; 889). – 1-55899-843-8. – S. W08-04

Schroeder, H.
On the Mechanism of Resistive Switching in MIM Capacitors – An Approach with in-Situ TEM Experiments
In-situ Electron Microscopy of Materials / ed.: P. J. Ferreira, I. M. Robertson, G. Dehm, H. Saka. – Warrendale, PA, 2006. – (Materials Research Society Symposium proceedings ; 907). – MM06-02

Schweins, R.; Goerigk, G.; Huber, K.
Shrinking of anionic polyacrylate coils induced by Ca^{2+}, Sr^{2+} and Ba^{2+}: A combined light scattering and ASAXS study
European Physical Journal E, 21 (2006) , 99 – 110

Schönhense, G.; Elmers, H.-J.; Nepijko, S. A.; Schneider, C. M.
Time-resolved photoemission electron microscopy
Advances in Imaging and Electron Physics / ed.: P. Hawkes. – San Diego, Academic Press. – 142 (2006). – 0-12-014784-X. – S. 160

Schütz, G. M.
Phase separation in one-dimensional stochastic particle systems?
Bulletin of the Brazilian Mathematical Society, 37 (2006), 523 – 535

Spatschek, R.
Elasticity, Friction and Fracture
Computational Condensed Matter Physics : Lecture Manuscripts of the 37th Spring School of the Institute of Solid State Research ; this spring school was organized by the Institute of Solid State Research in the Forschungszentrum Jülich on March 6 -17, 2006 / ed.: S. Blügel, G. Gompper, E. Koch, H. Müller-Krumbhaar, R. Spatschek, R. G. Winkler. – Jülich, 2006. – (Schriften des Forschungszentrums Jülich. Reihe Materie und Material / Matter and Material ; 32). – 3-89336-430-7. – S. C4.1 – C4.28

Spatschek, R.; Hartmann, M.; Brener, E. A.; Müller-Krumbhaar, H.; Kassner, K.
Phase Field Modeling of Fast Crack Propagation
Physical Review Letters, 96 (2006), 015502

Sperotto, M.M.; May, S.; Baumgaertner, A.
Modelling of Proteins in Membranes
Chemistry and Physics of Lipids, 141 (2006), 2 – 29

Sun, J.; Mikkelsen, A.; Fuglsang Jensen, M.; Koroteev, Y.M.; Bihlmayer, G.; Chulkov, E. V.; Adams, D. L.; Hofmann, Ph.; Pohl, K.
Structural determination of the Bi(110) semimetal surface by LEED analysis and ab initio calculations
Physical Review B, 74 (2006), 245406

Svanberg, C.; Pyckhout-Hintzen, W.; Börjesson, L.
Network structure of poly(methyl methacrylate)-based gels and gel electrolytes
Electrochimica Acta, 51 (2006), 4153 – 4156

Szot, K.; Speier, W.; Bihlmayer, G.; Waser, R.
Switching the electrical resistance of individual dislocations in single-crystalline $SrTiO_3$
Nature Materials, 5 (2006), 4, 312

Szot, K.; Tiedke, S.; Reichenberg, B.; Peter, F.; Waser, R.
Electrical characterization of perovskite nanostructures by SPM
Scanning Probe Microscopy : Electrical and Electromechanical Phenomena at the Nanoscale / ed.: S. V. Kalinin, A. Gruverman. – New York, Springer, 2006. – 978-0-387-28667-9. – Chapter III 9

Tabatabaei, F.; Schütz, G. M.
Shocks in the asymmetric exclusion process with internal degree of freedom
Physical Review E, 74 (2006), 051108-1 – 051108-8

Takahasi, K.; Suzuki, M.; Kojima, T.; Watanabe, T.; Sakashita, Y.; Kato, K.; Sakata, O.; Sumitani, K.; Funakubo, H.
Thickness dependence of dielectric properties in bismuth layer-structured dielectrics
Applied Physics Letters, 89 (2006), 082901

Tartaglino, U.; Samoilov, V. N.; Persson, B. N. J.
Role of surface roughness in superlubricity
Journal of Physics: Condensed Matter, 18 (2006), 17, 4143 – 4160

Tartaglino, U.; Sivebaek, I. M.; Persson, B. N. J.; Tosatti, E.
Impact of molecular structure on the lubricant squeeze-out between curved surfaces with long range elasticity
Journal of Chemical Physics, 125 (2006), 014704

Theis-Bröhl, K.; Wolff, M.; Westphalen, A.; Zabel, H.; McCord, J.; Höink, V.; Schmalhorst, J.; Reiss, G.; Weis, T.; Engel, D.; Ehresmann, A.; Rücker, U.; Toperverg, B.
Exchange-bias instability in a bi-layer with an ion beam imprinted stripe pattern of ferromagnetic/antiferromagnetic interfaces
Physical Review B, 73 (2006), 174408-1 – 174408-14

Thomas, R.; Ehrhart, P.; Luysberg, M.; Boese, M.; Waser, R.; Roeckerath, M.; Rije, E.; Schubert, J.; van Elshocht, S.; Caymax, M.
Dysprosium scandate thin films as an alternate amorphous gate oxide prepared by metal-organic chemical vapor deposition
Applied Physics Letters, 89 (2006), 232902

Thomas, R.; Milanov, A.; Bhakta, R.; Patil, U.; Winter, M.; Ehrhart, P.; Waser, R.; Devi, A.
Liquid injection MOCVD of ZrO_2 thin films using a novel zirconium Bis(diethylamido)-bis(di-tert-butylmalonato) as a novel precursor
Chemical Vapor Deposition, 12 (2006), 295 – 300

Tillmann, K.; Houben, L.; Thust, A.
Atomic-resolution imaging of lattice imperfections in semiconductors by combined aberration-corrected HRTEM and exit-plane wavefunction retrieval
Philosophical Magazine, 86 (2006), 29/31, 4589 – 4606

Tillmann, K.; Houben, L.; Thust, A.; Urban, K.
Spherical-aberration correction in tandem with the restoration of the exit-plane wavefunction: synergetic tools for the imaging of lattice imperfections in crystalline solids at atomic resolution
Journal of Materials Science, 41 (2006), 4420 – 4433

Tillmann, K.; Thust, A.; Houben, L.; Luysberg, M.; Lentzen, M.; Urban, K.
Spherical aberration correction and exit-plane wave function reconstruction: Synergetic tools for the atomic-scale imaging of structural imperfections in semiconductor materials
Proceedings of the 14th Conference on Microscopy of Semiconducting Materials, Oxford, UK, 11.04. – 14.04.2005 / ed.: A. G. Cullis, J. L. Hutchison. – Berlin, Springer, 2006. – 3-540-31914-X, 978-3-540-31914-6. – S. 183 – 190

Tripadus, V.; Radulescu, A.; Pieper, J.; Buchstainer, A.; Podlesnyak, A.; Janssen, S.; Serban, A.
Molecular dynamics in triglycine sulphate by cold neutron spectroscopy
Chemical Physics, 322 (2006), 323 – 330

Tsymbal, E.Y.; Kohlstedt, H.
Tunneling across a ferroelectric
Science, 313 (2006), 181 – 183

Tuinier, R.; Dhont, J. K. G.; Fan, T.-H.
How depletion affects sphere motion through solutions containing macromolecules
Europhysics Letters, 75 (2006), 6, 929 – 935

Tuinier, R; Fleer, G. J.
Critical Endpoint and Analytical Phase Diagram of Attractive Hard-Core Yukawa Spheres
Journal of Physical Chemistry B, 110 (2006), 20540 – 20545

Urban, K.; Mayer, J.; Luysberg, M.; Tillmann, K.
Frontiers of Electron Microcopy in Materials Science 2005
Journal of Materials Science, 41 (2006), 14, 4377 – 4381

Urban, K.; Mayer, J.; Luysberg, M.; Tillmann, K.
Introduction: A Special Issue on Frontiers of Electron Microscopy in Materials Science
Microscopy and Microanalysis, 12 (2006), 6, 441

van der Gucht, J.; Lemmers, M.; Knoben, W.; Besseling, N. A. M.; Lettinga, M. P.
Multiple shear-banding transitions in a supramolecular polymer solution
Physical Review Letters, 97 (2006), 10, 108301

Varga, Z.; Bóta, A.; Goerigk, G.
Localization of Dibromophenol in DPPC/Water Liposomes Studied by Anomalous Small-Angle X-ray Scattering
Journal of Physical Chemistry B, 110 (2006), 11029 – 11032

Vetter, S.; Abetz, V.; Goerigk, G.; Buder, I.; Pereira Nunes, S.
Polyetherketones for fuel cell application
Desalination, 199 (2006), 1/3, 289 – 290

Vliegenthart, G. A.
Monte Carlo Simulations
Computational Condensed Matter Physics : Lecture Manuscripts of the 37th Spring School of the Institute of Solid State Research ; this spring school was organized by the Institute of Solid State Research in the Forschungszentrum Jülich on March 6 -17, 2006 / ed.: S. Blügel, G. Gompper, E. Koch, H. Müller-Krumbhaar, R. Spatschek, R. G. Winkler. – Jülich, 2006. – (Schriften des Forschungszentrums Jülich . Reihe Materie und Material / Matter and Material ; 32). – 3-89336-430-7. – S. B2.1 – B2.32

Vliegenthart, G. A.; Gompper, G.
Forced crumpling of self-avoiding elastic sheets
Nature Materials, 5 (2006), 216 – 221

Vliegenthart, G. A.; Gompper, G.
Mechanical Deformation of Spherical Viruses with Icosahedral Symmetry
Biophysical Journal, 91 (2006), 834 – 841

Vliegenthart, G. A.; Gompper, G.
Mechanical Properties of Icosahedral Virus Capsids
Proceedings of the Third International Conference on "Multiscale Materials Modeling" – Stuttgart., Fraunhofer IRB Verlag, 2006. – S. 615 – 621

Voigt, J.; Kentzinger, E.; Rücker, U.; Schweika, W.; Wermeille, D.; Schmidt, W.; Brückel, T.
Structural and magnetic properties of [Er/Tb] multilayers
European Physical Journal B, 49 (2006), 441 – 451

Volokitin, A. I.; Persson, B. N. J.; Ueba, H.
Enhancement of noncontact friction between closely spaced bodies by two-dimensional systems
Physical Review B, 73 (2006), 165423

Von Bergmann, K.; Heinze, S.; Bode, M.; Vedmedenko, E. Y.; Bihlmayer, G.; Blügel, S.; Wiesendanger, R.
Observation of a Complex Nanoscale Magnetic Structure in a Hexagonal Fe Monolayer
Physical Review Letters, 96 (2006), 167203

Walter, G.; Goerigk, G.; Rüssel, C.
The structure of phosphate glass evidenced by small angle X-ray scattering
Journal of Non-Crystalline Solids, 352 (2006), 4051 – 4061

Walterfang, M.; Keune, W.; Trounov, K.; Peters, R.; Rücker, U.; Westerholt, K.
Magnetic and structural properties of epitaxial c-FeSi-films grown on MgO (100)
Physical Review B, 73 (2006), 214423-1 – 214423-10

Watanabe, T.; Funakubo, H.
Controlled crystal growth of layered-perovskite thin films as an approach to study their basic properties
Journal of Applied Physics, 100 (2006), 5, 051602

Watanabe, T.; Hoffmann-Eifert, S.; Hwang, C. S.; Waser, R.
Liquid-injection atomic layer deposition of TiO_x and Pb-Ti-O films
Journal of the Electrochemical Society, 153 (2006), F199 – F204

Wegner, D.; Bauer, A.; Koroteev, Yu. M.; Bihlmayer, G.; Chulkov, E. V.; Echenique, P. M.; Kaindl, G.
Surface electronic structures of La(0001) and Lu(0001)
Physical Review B, 73 (2006), 115403

Weides, M.; Kemmler, M.; Goldobin, E.; Koelle, D.; Kleiner, R.; Kohlstedt, H.; Buzdin, A.
High quality ferromagnetic 0 and pi Josephson tunnel junctions
Applied Physics Letters, 89 (2006), 12, 122511

Weides, M.; Kemmler, M.; Kohlstedt, H.; Waser, R.; Koelle, D.; Kleiner, R.; Goldobin, E.
O-pi Josephson tunnel junctions with ferromagnetic barrier
Physical Review Letters, 97 (2006), 247001

Weides, M.; Tillmann, K.; Kohlstedt, H.
Fabrication of High Quality Ferromagnetic Josephson Junctions
Physica C, 437-438 (2006), 349

Welnic, W.; Pamungkas, A.; Detemple, R.; Steimer, Ch.; Blügel, S.; Wuttig, M.
Unravelling the interplay of local structure and physical properties in phase-change materials
Nature Materials, 5 (2006), 56

Wetzig, K.; Schneider, C. M.
Metal-based thin film systems for electronics
2., überarb. und erw. Aufl. – Weinheim, Wiley-VCH, 2006 – 3-527-40650-6

Wiegand, S.; Ning, H.; Kita, R.
To the warm or to the cold? Thermal diffusion in aqueous systems
Thermodiffusion : Basics & Applications / ed.: M. M. Bou-Ali, J. K. Platten. – Mondragon University, Arrasate-Mondragon, 2006. – S .23 – 32

Winkler, R. G.
Molecular Dynamics Simulations
Computational Condensed Matter Physics : Lecture Manuscripts of the 37th Spring School of the Institute of Solid State Research ; this spring school was organized by the Institute of Solid State Research in the Forschungszentrum Jülich on March 6 -17, 2006 / ed.: S. Blügel, G. Gompper, E. Koch, H. Müller-Krumbhaar, R. Spatschek, R. G. Winkler. – Jülich, 2006. – (Schriften des Forschungszentrums Jülich. Reihe Materie und Material / Matter and Material ; 32). – 3-89336-430-7. – S. B3.1 – B3.34

Winkler, R. G.
Semiflexible Polymers in Shear Flow
Physical Review Letters, 97 (2006), 12, 128301

Winkler, R. G.; Cherstvy, A. G.
Critical Adsorption of Polyelectrolytes onto Charged Spherical Colloids
Physical Review Letters, 96 (2006), 066103-1 – 066103-4

Winkler, R. G.; Keller, S.; Rädler, J. O.
Intramolecular dynamics of linear macromolecules by fluorescence correlation spectroscopy
Physical Review E, 73 (2006), 041919-1 – 041919-14

Wortmann, D.
Ab Initio Description of Electronic Transport
Computational Nanoscience: Do It Yourself! : NIC Winter School 2006 / ed.: J. Grotendorst, S. Blügel, D. Marx. – (NIC Series ; 31). – 3-00-017350-1. – S. 469 – 490

Yang, C.; Tartaglino, U.; Persson, B. N. J.
A multiscale molecular dynamics approach to contact mechanics
European Physical Journal E, 19 (2006), 1, 47 – 58

Yang, C.; Tartaglino, U.; Persson, B. N. J.
Influence of surface roughness on superhydrophobicity
Physical Review Letters, 97 (2006), 116103

Zamponi, M.; Wischnewski, A.; Monkenbusch, M.; Willner, L.; Richter, D.; Likhtman, A. E.; Kali, G.; Farago, B.
Molecular Observation of Constraint Release in Polymer Melts
Physical Review Letters, 96 (2006), 238302

Zastrow, U.; Houben, L.; Meertens, D.; Grohe, A.; Brammer, T.; Schneiderlöchner, E.
Characterization of laser-fired contacts in PERC solar cells: SIMS and TEM analysis applying advanced preparation techniques
Applied Surface Science, 252 (2006), 19, 7082 – 7085

Zecha, Ch.; Ebert, H.; Akai, H.; Dederichs, P. H.; Zeller, R.
Hyperfine Fields of Light Interstitial Impurities in Ni
Hyperfine Interactions, 158 (2006), 59 – 62

Zeller, R.
Spin-Polarized DFT Calculations and Magnetism
Computational Nanoscience: Do It Yourself! : NIC Winter School 2006 / ed.: J. Grotendorst, S. Blügel, D. Marx. – (NIC series ; 31). – 3-00-017350-1. – S. 419 – 445

Zorn, R.; Monkenbusch, M.; Richter, D.; Alegría, A.; Colmenero, J.; Farago, B.
Plasticizer effect on the dynamics of polyvinylchloride studied by dielectric spectroscopy and quasielastic neutron scattering
Journal of Chemical Physics, 125 (2006), 154904

Özdogan, K.; Sasioglu, E.; Aktas, B.; Galanakis, I.
Doping and disorder in the Co_2MnAl and Co_2MnGa half-metallic Heusler alloys
Physical Review B, 74 (2006), 172412

Conferences and Schools

February 14 – 22	NIC Winter School Computational Nanoscience: Do it Yourself! Forschungszentrum Jülich, Germany
February 16 – 17	JCNS Symposium and EU User Meeting Forschungszentrum Jülich, Germany
March 6 – 17	IFF-Ferienschule Computational Condensed Matter Physics Forschungszentrum Jülich, Germany
March 13 – 24	10th Neutron Scattering Labcourse Forschungszentrum Jülich, Germany
April 5 – 7	Mesoscale Simulation Techniques for Soft Matter Systems Forschungszentrum Jülich, Germany
September 25 – 29	CNI-Ferienpraktikum Nanoelektronik Forschungszentrum Jülich, Germany
October 2 – 4	Computational Magnetism and Spintronics 2006 Forschungszentrum Jülich, Germany
October 11 – 13	Nanoelectronics Days 2006 RWTH Aachen, Germany
November 14 – 17	Jülich Soft Matter Days 2006 Gustav-Stresemann-Institut Bonn, Germany

Kolloquia

January 20	Prof. Dr. Jürg Osterwalder Physik-Institut, Universität Zürich, Switzerland *Electronic Structure of Nanostructured Surfaces and Interfaces*
January 27	Prof. Dr. Alan Tennant Hahn-Meitner-Institut Berlin, Germany *Neutrons, Magnetic fields, and Quantum States*
March 24	Prof. Dr. S. Dietrich Max-Planck-Institut für Metallforschung, Stuttgart, und Institut für Theoretische und Angewandte Physik,Universität Stuttgart, Germany *Thermodynamic Casimir Forces*
May 5	Prof. Dr Warren E. Pickett University of California, Davis, USA *Strong Coupling Superconductivity: Paradigm Shifts, Alternative Universes*
May 12	Prof. Dr Stephan W. Koch Physik Department, Universität Marburg, Marburg, Germany *Optics in semiconductor nanostructures*
June 30	Prof. Dr Walter Schirmacher Physik Department E13, Techn. Universität München, Garching, Germany *Vibrational and Thermal Anomalies in Disordered Solids*
July 14	Prof. Manfred Fiebig Universität Bonn, Bonn, Germany *Ultrafast magnetization dynamics of antiferromagnetic compounds*
August 9	Prof. William van Megen Applied Physics Department, Royal Melbourne Institute of Technology, Australia *Colours Opal and Packing – What we can learn about solidification dynamics from a colloidal suspension*
November 10	Prof. Dr. Peter N. Pusey University of Edinburgh, United Kingdom *Colloidal Glasses*
December 12	Prof. Manuel Bibes Institut d'Electronique Fondamentale, Univ. Paris-Sud, France *Ultrathin multiferroic films for spintronics*
December 15	Prof. Chuck Fadley Department of Physics, University of California Davis, Materials Sciences Division, Lawrence Berkeley National Laboratory, USA *Some new directions in materials and nanostructure studies with photoemission: standing waves and hard x-rays*
December 22	Prof. Dr. Paul Kögerler RWTH Aachen und Forschungszentrum Jülich, Germany Molecular Magnetism, Quo Vadis?

Ph.D. Theses

Braak, H.
Mit Mangan und Eisen ko-dotiertes Germanium: Ein ferromagnetischer Halbleiter?
Jülich, Forschungszentrum, Zentralbibliothek, 2006
Berichte des Forschungszentrums Jülich ; 4223
JUEL-4223
Köln, Univ., Diss., 2006

Brzank, A.
Molecular traffic control and single-file diffusion with two species of particles
Jülich, Forschungszentrum Jülich, Institut für Festkörperforschung, 2006
Leipzig, Univ., Diss., 2006

Lüssem, B.
Molecular electronic building blocks based on self-assembled monolayers
Jülich, Forschungszentrum, Zentralbibliothek, 2006
Schriften des Forschungszentrums Jülich . Reihe Informationstechnik / Information Technology ; 12
3-89336-454-4
Aachen, Techn. Hochsch., Diss., 2006

Peter, F.
Piezoresponse force microscopy and surface effects of perovskite ferroelectric nanostructures
Jülich, Forschungszentrum, Zentralbibliothek, 2006
Schriften des Forschungszentrums Jülich . Reihe Informationstechnik / Information Technology ; 11
3-89336-444-7
Aachen, Techn. Hochsch., Diss., 2006

Pohlmann, L.
Experimente zum Einfluss elektrischer Spannung auf die magnetische Kopplung in Fe/Si/FeDreischicht-systemen
Jülich, Forschungszentrum Jülich, Zentralbibliothek, 2006
Berichte des Forschungszentrums Jülich ; 4204
JUEL-4204
Köln, Univ., Diss., 2005

Sarau, G.
Spin-dependent transport in cobalt nanocontacts
Jülich, Forschungszentrum Jülich, Institut für Festkörperforschung, 2006
Duisburg, Univ., Diss., 2006

Steeb, A.
Untersuchung der Morphologie und magnetischen Eigenschaften von ionenstrahl-gesputterten Eisen-Einzelschichten, Fe/Cr/Fe- und Fe/MgO/Fe-Schichtsystemen
Jülich, Forschungszentrum Jülich, Institut für Festkörperforschung, 2006
Duisburg, Univ., Diss., 2006

Diploma Theses

Dolfen, A.
Massively parallel exact diagonalization of strongly correlated systems
Jülich, Forschungszentrum Jülich, Institut für Festkörperforschung, 2006
Aachen, Techn. Hochsch., Dipl., 2006

Fleck, M.
Influence of stress on the evolution of coherent interfaces including dynamic elasticity
Jülich, Forschungszentrum Jülich, Institut für Festkörperforschung, 2006
Aachen, RWTH, Dipl., 2006

Göhring, L.
Diffusion Constant in the Rubinstein-Duke model for reptation
Jülich, Forschungszentrum Jülich, Institut für Festkörperforschung, 2006
Bonn, Univ., Dipl., 2006

Hüter, C.
Diffusion limited propagation of a melting zone along a grain boundary
Jülich, Forschungszentrum Jülich, Institut für Festkörperforschung, 2006
Aachen, RWTH, Dipl., 2006

211 students and young scientists from all over the world attended the 37th IFF Spring Scool in March 2006.

Appendix

Institute of Solid State Research (IFF)

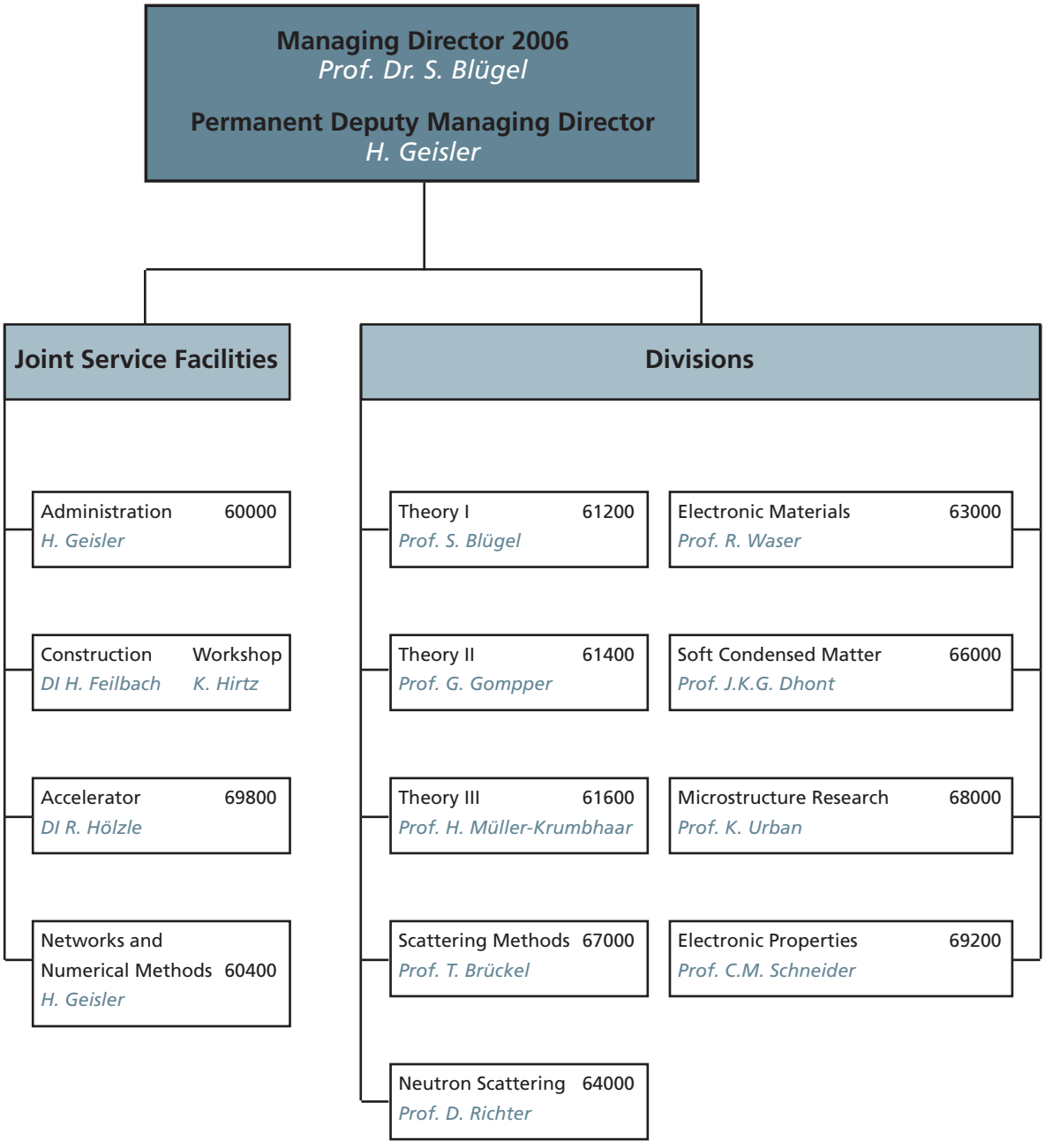

(2 January, 2006)

Personnel

Staff members (centrally financial)	
• Scientific Staff	113
Including those funded externally	*15*
• Technical Staff	51
Including those funded externally	*2*
Post-doc (HGF)	17
Including those funded externally	*2*
Staff members of service-groups	38
Administrations incl. Secretaries	*19*
Graduate students	47
Including those funded externally	*8*
Diploma students	21
Trainees	24
Guests Scientists staying for two weeks or longer	70
Invited lectures	139

Scientific Advisory Board

Joint Scientific Council
The joint Scientific Council of the IFF and IBN advises the Institute and the committees of Research Centre Jülich and functions as a supervisory board. The members of the council are leading scientists from research and industry. They are appointed for five years.

Prof. Dr. Georg Bednorz
IBM Research GmbH, Rüschlikon (CH)

Prof. Dr. Wim J. Briels
University Twente, AE Enschede (NL)

Dr. Kurt Clausen
Paul Scherrer Institut, Villingen (CH)

Dr. Manfred Horstmann
AMD Saxony LLC & Co. KG, Dresden (D)

Prof. Dr. Klaus Kern
Max-Planck-Institut, Stuttgart (D)

Prof. Dr. Jürgen Kirschner
Max-Planck-Institut, Halle (D)

Prof. Dr. Beate Klösgen
University of Southern Denmark, Odense (DK)

Prof. Dr. Hilbert von Löhneysen
Forschungszentrum Karlsruhe (D)

Prof. Dr. Werner Press (Chairman)
Christian Alberts-Universität Kiel (D)

Prof. Dr. Friederike Schmid
Universität Bielefeld (D)

Prof. Dr. Herbert Schöller
RWTH Aachen (D)

Prof. Dr. Clivia M. Sotomayor-Torres
University College Cork (IRE)

Prof. Dr. Hans-Rainer Trebin
Universität Stuttgart (D)

Prof. Dr. Gero Vogl
Universität Wien (A)

List of IFF Scientists

Adam, Roman	Electronic Properties
Albrecht, Wolfgang	Electronic Materials
Allakhiarov, Elchad	Theory II
Allgaier, Jürgen	Neutron Scattering
Arend, Nikolas	Scattering Methods
Atodiresei, Nicolae	Theory I
Auth, Thorsten	Theory II
Barthel, Juri	Microstructure Research
Bauer, Günter	Scattering Methods
Baumgarten, Lutz	Electronic Properties
Baumgärtner, Artur	Theory II
Bechthold, Paul-Siegfried	Electronic Properties
Bhattacharyya, Somnath	Soft Condensed Matter
Biehl, Ralf	Neutron Scattering
Bihlmayer, Gustav	Theory I
Bodnarchuk, Victor	Scattering Methods
Boese, Markus	Microstructure Research
Braak, Heiko	Electronic Properties
Brener, Efim	Theory III
Bringer, Andreas	Theory I
Buchmeier, Matthias	Electronic Properties
Buitenhuis, Johan	Soft Condensed Matter
Bürgler, Daniel-Emil	Electronic Properties
Busch, Peter	JCNS
Carsughi, Flavio	Neutron Scattering
Claver-Cabrero, Ana	Neutron Scattering
Conrad, Harald	Scattering Methods
Costi, Theodoulos	Theory III
Cramm, Stefan	Electronic Properties
Dahbi, Louissa	Neutron Scattering
Dassow, Henning	Electronic Properties

Denesyuk, Natasha	Theory II
Dittmann, Regina	Electronic Materials
Divin, Yuri	Microstructure Research
Ebert, Philipp-Georg	Microstructure Research
Ehrhart, Peter	Electronic Materials
Eisenriegler, Erich	Theory II
Faley, Mikhail	Microstructure Research
Feuerbacher, Michael	Microstructure Research
Frielinghaus, Henrich	JCNS
Goerigk, Günter	Scattering Methods
Götze, Ingo Oliver	Theory II
Grimm, Hans	Neutron Scattering
Grudinin, Sergey	Theory II
Grushko, Benjamin	Microstructure Research
Guo, Xin	Electronic Materials
Harris, John	Theory I
Harris, Rosemary Jane	Theory II
Hauck, Jürgen	Soft Condensed Matter
Heinrich, Martine	Neutron Scattering
Hermann, Raphael	Scattering Methods
Hertel, Riccardo	Electronic Properties
Hillebrecht, Franz Ulrich († 8.8.2006)	Electronic Properties
Hoffmann-Eifert, Susanne	Electronic Materials
Holderer, Olaf	JCNS
Holmqvist, Peter	Soft Condensed Matter
Hölzle, Rainer	Accelerators
Houben, Lothar	Microstructure Research
Ioffe, Alexander	JCNS
Jakes, Peter	Electronic Properties
Jia, Chunlin	Microstructure Research
Jones, Robert	Theory I
Jung, Peter	Scattering Methods

Kakay, Attila	Electronic Properties
Kang, Kyongok Ok	Soft Condensed Matter
Karthäuser, Silvia	Electronic Materials
Kentzinger, Emmanuel	Scattering Methods
Köbler, Ulrich	Scattering Methods
Koch, Erik Eduard	Theory I
Kohlstedt, Herbert Hermann	Electronic Materials
Kriegs, Hartmut Oskar Kurt	Soft Condensed Matter
Kronholz, Stephan Detlef	Electronic Materials
Kügeler, Carsten	Electronic Materials
Lang, Peter Robert	Soft Condensed Matter
Lentzen, Markus	Microstructure Research
Lettinga, Minne Paul	Soft Condensed Matter
Lezaic, Marjana	Theory I
Liebsch, Ansgar	Theory I
Lonetti, Barbara	Neutron Scattering
Lounis, Samir	Theory I
Lund, Reidar	Neutron Scattering
Lustfeld, Hans	Theory I
Luysberg, Martina	Microstructure Research
Mattauch, Stefan Hans Josef	JCNS
Matthes, Frank	Electronic Properties
McPhie, Mathieu Gordon	Soft Condensed Matter
Meier, Gerhard	Soft Condensed Matter
Meuffels, Paul	Electronic Materials
Meyer, Carola	Electronic Properties
Meyer, René	Electronic Materials
Mi, Shaobo	Microstructure Research
Monkenbusch, Michael	Neutron Scattering
Müller-Meskamp, Lars	Electronic Materials
Nägele, Gerhard	Soft Condensed Matter
Niu-Ebert, Aizhen	Neutron Scattering

Noguchi, Hiroshi	Theory II
Nünighoff, Kay Uwe	Scattering Methods
Ohl, Michael	Neutron Scattering
Paul, Amitesh	Scattering Methods
Pavarini, Eva	Theory I
Persson, Bo	Theory I
Perßon, Jörg	Scattering Methods
Peter, Frank	Electronic Materials
Petraru, Adrian Ion	Electronic Materials
Pipich, Vitaliy	JCNS
Pithan, Christian	Electronic Materials
Plucinski, Lukasz	Electronic Properties
Pollmeier, Klaus	Scattering Methods
Poppe, Ulrich	Microstructure Research
Prager, Michael	Neutron Scattering
Pyckhout-Hintzen, Wim	Neutron Scattering
Radulescu, Aurel	JCNS
Rata, Aurora Diana	Electronic Properties
Rottländer, Johannes Peter	Neutron Scattering
Rücker, Ulrich	Scattering Methods
Rüdiger, Andreas	Electronic Materials
Sager, Wiebke	Soft Condensed Matter
Schindlmayr, Arno	Theory I
Schmalzl, Karin Elisabeth	JCNS
Schmidt, Wolfgang	JCNS
Schneider, Stefanie	Theory II
Schober, Herbert	Theory III
Schroeder, Herbert	Electronic Materials
Schroeder, Kurt	Theory III
Schütz, Gunter-Markus	Theory II
Schwahn, Dietmar	Neutron Scattering
Schweika, Werner	Scattering Methods

Spatschek, Robert Philipp Maximilian	Theory III
Stellbrink, Jörg	Neutron Scattering
Su, Yixi	JCNS
Szot, Krzysztof	Electronic Materials
Tao, Yu-Guo	Theory II
Terashita, Hirotoshi	Scattering Methods
Thust, Andreas	Microstructure Research
Tillmann, Karsten	Microstructure Research
Tuinier, Remco	Soft Condensed Matter
Vizdrik, Gennady M.	Electronic Materials
Vliegenthart, Gerard Adriaan	Theory II
Voigt, Jörg Jakob	JCNS
Watanabe, Takayuki	Electronic Materials
Weides, Martin Peter	Electronic Materials
Wiegand, Simone	Soft Condensed Matter
Willner, Lutz	Neutron Scattering
Winkler, Roland	Theory II
Wischnewski, Andreas	Neutron Scattering
Wortmann, Daniel	Theory I
Wuttke, Joachim	JCNS
Yan, Ming	Electronic Properties
Yurechko, Mariya	Microstructure Research
Zamponi, Michaela	JCNS
Zeller, Rudolf	Theory III
Zorn, Reiner	Neutron Scattering

List of Graduate Students

Al-Zubi, Ali	Theory I
Belhadji, Brahim	Theory III
Brodeck, Martin	Neutron Scattering
Chen, Han Yuan	Microstructure Research
Dolfen, Andreas	Theory I
Feygenson, Mikhail	Scattering Methods
Frank, Sandra	Theory II
Freimuth, Frank	Theory I
Gliga, Sebastian	Electronic Properties
Gögelein, Christoph	Soft Condensed Matter
Gorelik, Eugene	Scattering Methods
Kaiser, Alexander	Electronic Properties
Kleshchanok, Dzina	Soft Condensed Matter
Korolkov, Denis	Scattering Methods
Krug, Ingo Peter	Electronic Properties
Lehndorff, Ronald	Electronic Properties
Li, Haifeng	Scattering Methods
Lipinska-Chwalek, Marta Agata	Microstructure Research
Lüssem, Björn	Electronic Materials
Maccarrone, Simona	Neutron Scattering
Mayorova, Maria	Neutron Scattering
Meier, Matthias	Electronic Materials
Menke, Tobias	Electronic Materials
Meßlinger, Reginhard Sebastian	Theory III
Mlynarczyk, Marcin	Electronic Materials
Müller, Martina	Electronic Properties
Müller-Gugenberger, Clemens	Theory III
Münstermann, Ruth Christine	Electronic Materials
Nandy, Bidisha	Theory III
Nauenheim, Christian	Electronic Materials
Niedzwiedz, Katarzyna	Neutron Scattering
Niesert, Manfred	Theory I

Pavlyuchkov, Dmytro	Microstructure Research
Puchalla, Jochen	Electronic Materials
Rahmanizadeh, Kourosh	Theory III
Röhrig, Serge	Electronic Materials
Roitsch, Stefan	Microstructure Research
Sarau, George	Electronic Properties
Schindler, Christina	Electronic Materials
Schützendorf, Patrick Rene	Electronic Materials
Shen, Wan	Electronic Materials
Soni, Rohit	Electronic Materials
Spudat, Christian	Electronic Properties
Steeb, Alexandra	Electronic Properties
Tabatabaei Panah, Fatemeh Sadat	Theory II
Tranca, Ionut Claudiu	Theory III
Woodford, Simon	Theory I
Wysocki, Adam	Theory II
Yang, Chunyan	Theory I
Yang, Lin	Electronic Materials
Yang, Yingzi	Theory II
Zhang, Zhenkun	Soft Condensed Matter

List of IFF Technical and Administrative Staff

Böhr, Heinz-Peter	Administration
Bongartz, Dieter	Administration
Griesen, Johann Engelbert	Administration
Kinzel, Gernot	Administration
Mirea, Elena	Administration
Schmitz, Silke	Administration
Sittardt, Hanne	Administration
Wassenhoven, Gertrud	Administration
Wenzik, Angela	Administration
Bläsen, Franz	Networks and Numerical Methods
Funk-Kath, Ursula	Networks and Numerical Methods
Heinen, Josef	Networks and Numerical Methods
Henkel, Dorothea	Networks and Numerical Methods
Olefs, Bodo-August	Networks and Numerical Methods
Schätzler, Liane	Networks and Numerical Methods
Thomas, Rita	Networks and Numerical Methods
Westphal, Elmar	Networks and Numerical Methods
Wingerath, Kurt	Networks and Numerical Methods
Bremen, Arnd	Design/Workshop
Eickenberg, Peter	Design/Workshop
Emmerich, Hans-Matthias	Design/Workshop
Esser, Heinz-Peter	Design/Workshop
Feilbach, Herbert	Design/Workshop
Gehlhaar, Reimund Werner	Design/Workshop
Hecker, Michael Rüdiger	Design/Workshop
Heinrich, Vladimir	Design/Workshop
Hirtz, Kurt	Design/Workshop
Jansen, Thomas	Design/Workshop
Johnen, Karl-Heinz	Design/Workshop
Leuchtenberg, Anton	Design/Workshop
Lingenbach, Peter Josef	Design/Workshop

Matulewski, Anton	Design/Workshop
Pohl, Maria	Design/Workshop
Radermacher, Bert Hubert	Design/Workshop
Rehfisch, Jessica	Design/Workshop
Sachsenhausen, Hans-Rudolf	Design/Workshop
Schnitzler, Helmut-Hubert	Design/Workshop
Schnitzler, Jens-Willi	Design/Workshop
Schramm, Franz-Josef	Design/Workshop
Stefelmanns, Hans-Peter	Design/Workshop
Winkler, Ute	Theory I
Paffen, Helga	Theory II
Snyders, Friederike-Luise	Theory III
Bierfeld, Hermann-Josef	Electronic Materials
Friedrich, Jochen	Electronic Materials
Garcia y Gonzales, Maria	Electronic Materials
Gebauer, Manfred	Electronic Materials
Gerst, Marcel	Electronic Materials
Haselier, Johann	Electronic Materials
Hermanns, Bernd	Electronic Materials
John, Holger	Electronic Materials
Makovicka, Cerstin	Electronic Materials
Borges, Martina	Neutron Scattering
Bünten, Ulrich	Neutron Scattering
Bünten, Wilhelm Detlef	Neutron Scattering
Frech, Stephan	Neutron Scattering
Heiderich, Manfred	Neutron Scattering
Hintzen, Maria Elisabeth	Neutron Scattering
Kluck, Günther	Neutron Scattering
Kozielewski, Tadeusz	Neutron Scattering
Nguyen, Vu-Thanh	Neutron Scattering
Oubenkhir, Saida	Neutron Scattering

Sausen-Malka, Ulrike	Neutron Scattering
Schätzler, Reinhardt	Neutron Scattering
Starc, Thomas	Neutron Scattering
Stollenwerk, Robert	Neutron Scattering
Vehres, Guido	Neutron Scattering
Ziebarth, Tanja	Neutron Scattering
Erven, Andreas	JCNS
Gossen, Frank	JCNS
Hölzle, Micha Marc Gerhard	JCNS
Janaschke, Sven	JCNS
Kohnke, Thomas	JCNS
Mintmans, Stephanie	JCNS
Stronciwilk, Peter	JCNS
de Waal, Sylvia-Maria	Soft Condensed Matter
Göcking, Marie-Luise	Soft Condensed Matter
Hoffmann, Hans-Jürgen	Soft Condensed Matter
Sellinghoff, Karin	Soft Condensed Matter
Triefenbach, Dieter	Soft Condensed Matter
Bergs, Wolfgang	Scattering Methods
Bussmann, Klaus Max	Scattering Methods
Dohmen, Ludwig	Scattering Methods
Hiller, Peter	Scattering Methods
Horriar-Esser, Christel	Scattering Methods
Jungbluth, Heinrich	Scattering Methods
Klein, Horst	Scattering Methods
Köppchen, Barbara-Dorothea	Scattering Methods
Kox, Sebastian	Scattering Methods
Küssel, Eckhard	Scattering Methods
Schmitz, Berthold-Klaus	Scattering Methods
Graf, Karl-Heinz	Microstructure Research
Holten, Kathrin	Microstructure Research

Meertens, Doris	Microstructure Research
Pieper, Werner	Microstructure Research
Rische-Radloff, Ingrid	Microstructure Research
Schmidt, Marita	Microstructure Research
Speen, Hans-Rolf	Microstructure Research
Sybertz, Wilma	Microstructure Research
Thomas, Carsten	Microstructure Research
Wassenhoven, Gabriele-Marie	Microstructure Research
Würtz, Eva Maria	Microstructure Research
Bickmann, Konrad	Electronic Properties
Gollnick, Jutta	Electronic Properties
Köhne, Franz-Josef	Electronic Properties
Küpper, Bernhard	Electronic Properties
Lauer, Jürgen	Electronic Properties
Pfeifer, Heinz	Electronic Properties
Schreiber, Reinert	Electronic Properties

List of IFF Scientists on Leave

Dr. Thorsten Auth	Weizmann Institut, Israel
Martin Brodeck	Donostia International Physical Center, Spain
Dr. Günter Goerigk	HASYLAB bei DESY, Hamburg, Germany
Dr. Herbert Hermann Kohlstedt	University of California, Berkeley, USA
Dr. Rainer Lässer	FZ Karlsruhe, Projekt Kernfusion EU, Germany
Dr. René Meyer	Stanford University, Kalifornien, USA
Marcin Mlynarczyk	Jagellonische Universität Krakau, Poland
Christina Schindler	Arizona State University, USA
Dr. Arno Schindlmayr	Universität Paderborn, Germany
Dr. Karin Elisabeth Schmalzl	ILL Grenoble, France
Dr. Wolfgang Schmidt	ILL Grenoble, France
Dr. Piotr Swiatek	DLR (PT-DLR) Bonn, Germany

List of Guest Scientists

Prof. Dr. Anthony S. Arrott	Simon-Fraser-Universität, Canada
Dr. David Avila	Universidad Complutense, Madrid, Spain
Dmitro Barankov	National Science Center of Ukraine, Ukraine
Maxim Belushkin	Joint Inst. f. Nuclear Research, Russia
Dr. Lars Tore Bergqvist	Universität Uppsala, Sweden
Dr. Valery Borysenko	National Science Center of Ukraine, Ukraine
Prof. Dr. Oleg Braun	Institute of Physics UNAS, Ukraine
Prof. Theodore Burkhardt	Temple University, Philadelphia, USA
Prof. Dr. Zhixu Cheng	China Institute of Atomic Energy, China
Dr. Bogdan Cichocki	Universität Warschau, Poland
Dr. Hitoshi Endo	Department of Polymer Chemistry, Kyoto, Japan
Prof. Dr. Charles Fadley	ALS Berkeley, USA
Dr. Lewis J. Fetters	University Cornell, USA
Dr. Leslie John Ray Foster	University of New South Wales, Australia
Markus Gilbert	Fachhochschule Münster, Germany
Prof. Vadim Gurevich	IOFFE-Institut, St. Petersburg, Russia
Jean-Feng Gwan	National Center for High Performance, Taiwan
Andreas Hönig	Stiftung Caesar, Bonn, Germany

Prof. Sergei Iordanski	Landau Institut für Theor. Physik, Russia
Ying Jiang	Chinese Academy of Sciences, China
Swetlana Jungblut	Johannes-Gutenberg-Universität, Mainz, Germany
Prof. Dr. Dragi Karevski	Universität Nancy, France
Dr. Dmitry Kholin	Institute for Physical Problems, Moskau, Russia
Sönke Klinkhammer	Heinrich- Heine-Universität Düsseldorf, Germany
Dr. Paul Kögerler	Ames Laboratory Iowa State University, USA
Wojciech Kowalski	Schlesische Universität Katowice, Poland
Dr. Boris Krichevtsov	Ioffe Physical Technical Institute of the Russian Academy of Sciences, St. Petersburg, Russia
Dr. Antonio Lamura	Physics Department, Complesso Monte Sant' Angelo, Napoli, Italy
Tianfu Li	China Institute of Atomic Energy, China
Prof. Yaowen Liu	Tongji University, Shanghai, China
Prof. Dr. Jutta Luettmer-Strathmann	University Akron, Ohio, USA
Prof. Dr. Vladimir Marchenko	Akademie der Wissenschaften, Russia
Dr. James Liam Yates McWhirter	University of Utah, USA
Anton Menshutin	Landau Institut für theoretische Physik, Russia
Lei Na	Fundan University, Shanghai, China

Dr. Masako Ogura	Osaka University, Japan
Prof. Dr. Christina Oligschleger	Fachhochschule Rheinbach, Germany
Dr. Nikolaos Papanikolaou	Universität Athen, Greece
Prof. Dr. Dmitri Parshin	Technische Staatsuniv. St. Petersburg, Russia
Prof. Adam Patkowski	A. Mickiewicz University, Poznan, Poland
Dr. Yuri Petrusenko	National Science Center of Ukraine, Ukraine
Dr. Silvia Picozzi	Universita di L'Aquila, Italy
Michai Pilch	Schlesische Universität Katowice, Poland
Bartosz Przepiorzynski	Universität of Silesia, Katowice, Poland
Ruslan Puscasu	University of Iasi, Romania, Romania
Dr. Mohammad Qureshi	Indian Institute for Technology, India
Dr. Monika Ratajczyk	A. Mickiewicz University, Poznan, Poland
Camila Francalossi Rediguieri	Universität Sao Paulo, Brazil
Dr. Alexey Rzhevsky	Ioffe Physical Technical Institute of the Russian Academy of Sciences, St. Petersburg, Russia
Prof. Dr. Vladimir Samoilov	Moscow State University, Russia
Roman Saptsov	Landau Institut für Theor. Physik, Russia
Ersoy Sasioglu	Fritz-Haber-Institut d. MPG, Germany
Dr. Kazunori Sato	Osaka University, Japan

Dr. Ugur Serincan	Middle East Technical University, Ankara, Turkey
Swanee Shin	University of California, USA
Yaroslav Shirshov	Moscow State University, Russia
Dr. Tatsuya Shishidou	Hiroshima Science University, Japan
Ion Sivebak	Technical University of Denmark, Denmark
Elena Skripka	Moscow State University, Russia
Prof. Ekkehard Straube	Universität Merseburg, Germany
Dr. Marian Surowiec	Schlesische Universität Katowice, Poland
Dr. Ugo Tartaglino	Inst. Nazionale di Fisica della Materia, Italy
Takao Tsumuraya	Hiroshima Science University, Japan
Dr. Sabolcz Vass	KFKI Budapest, Hungary
Dr. Bart Verberck	Universität Antwerpen, Belgium
Prof. Alexander Volokitin	State Technical University Samara, Russia
Dr. Volodymyr Voronko	National Science Center of Ukraine, Ukraine
Dr. Hongli Wang	China Institute of Atomic Energy, China
Junhai Xia	Universität Siegen, Germany
Dr. Kunihiko Yamauchi	Universität Osaka, Japan
Dr. Susumu Yanagisawa	Universität Osaka, Japan

List of IFF Scientists Teaching at Universities

Lecturer:	University:
PD Dr. Baumgärtner	Duisburg
Prof. Bechthold	Köln
Prof. Blügel	Aachen
Dr. Bringer	Düsseldorf
Prof. Brückel	Aachen
PD Dr. Bürgler	Köln
Prof. Dhont	Düsseldorf
Dr. Ebert	Aachen
Dr. Ehrhart	Aachen
Prof. Gompper	Köln
PD Dr. Hertel	Halle-Wittenberg
Dr. Koch	Stuttgart
Dr. Kohlstedt	Köln
Dr. Lang	Düsseldorf
Dr. Lustfeld	Duisburg
Prof. Müller-Krumbhaar	Aachen
Prof. Nägele	Düsseldorf
Prof. Richter	Münster
Prof. Schneider	Duisburg-Essen
Prof. H. Schroeder	Aachen
Prof. K. Schroeder	Aachen
Prof. Schütz	Bonn
Dr. Schweika	Aachen
Prof. Szot	Katowice
Prof. Urban	Aachen
Prof. Waser	Aachen
Dr. Wiegand	Köln
Prof. Winkler	Ulm
Dr. Zorn	Münster

Honours

Prof. Peter Heinz Dederichs was awarded the Ernst Mach Honorary Medal by the Czech Academy of Sciences.

Prof. Jan Dhont has been appointed as a guest professor at the Department of Chemical Engineering at the Catholic University Leuven, Netherlands.

Prof. Peter A. Grünberg has been awarded the "European Inventor of the Year" prize of the European Patent Office and the European Commission in the "University and Research Institutions" category for his discovery of giant magnetoresistance (GMR).

Dr. Riccardo Hertel obtained his habilitation from the Physics Department at the Martin Luther University Halle-Wittenberg with a habilitation thesis on "Static and dynamic magnetisation in nanostructures".

Denis Korolkov won the “Student Poster Prize” at the International Workshop of Nanomagnets by Self-organization (8.-11.10.2006) in Eisenerz/Austria for his poster entitled “Nanotemplate fabrication using self-organized diblock-copolymers”.

Dr. Bo Persson has been awarded the prize of the Japanese Society for the Promotion of Science.

Prof. Knut Urban has been honoured by the Von Hippel Award of the American Materials Research Society.

Prof. Knut Urban received one of the two Karl Heinz Beckurts Awards 2006.

Prof. Knut Urban has been elected a senator of the Wissenschaftsgemeinschaft Gottfried Wilhelm Leibnitz e.V. (WGL).

Prof. Dr. Rainer Waser was granted full membership of the Academy of Sciences of North Rhine-Westphalia on 7 June 2006.

Imprint

Published by:
Research Centre Jülich GmbH
Institute of Solid State Research (IFF)
52425 Jülich, Germany

Phone: +49 2461 61-4465
Fax: +49 2461 61-2410

E-mail: wwwiff@fz-juelich.de
Internet: www.fz-juelich.de/iff/e_iff

Conception and Editorial:
Angela Wenzik
Claus M. Schneider

Design and Graphics:
Clarissa Reisen
Dieter Laufenberg
Graphic Department
Research Centre Jülich

Layout work on 2-page reports:
Ursula Funk-Kath
Dorothea Henkel
Liane Schätzler
Kurt Wingerath

Pictures:
Research Centre Jülich, if nothing else mentioned

Print:
Medienhaus Plump GmbH
Rheinbreitbach